NUMERICAL MODELLING OF THE ALUMINIUM EXTRUSION PROCESS

ZHI PENG

A thesis submitted in partial fulfilment of the requirements of Bournemouth University for the degree of Doctor of Philosophy

April 2005

Bournemouth University

Numerical Modelling of the Aluminium Extrusion Process

Zhi Peng

Abstract

The extrusion of aluminium alloys involves the shaping of the product from an homogenised billet into a complex shape. In addition the properties of the extrudate are closely related to the processing parameters (temperature, stain rate, and material morphology). Since all the parameters vary throughout the ram stroke and throughout the billet the prediction of the condition of the extrudate is complex. In this study the analysis is accomplished by the use of finite element analysis coupled with sub-modelling of the structural features. The study is extended to include the heat-treatment process necessary for precipitation hardened alloys subsequent to the process. The author has published these results in a number of learned journals and these are given in Appendix.

After a concise introduction and cririca1 literature review chapter3 analyses the basic operation of the finite element package(FEM) discussing the procedures involved, the equilibrium equations and the more practical aspect of the mesh morphology and size. Finite Element analysis and material structural models have been integrated using parallel processing technology and program sub-routines. In this section the external inputs are also defined paying particular attention to the friction conditions and the constitutive equations. The thesis then proceeds to describe and analyse the integrated modelling of the process necessary to introduce the user introduction of the equations necessary to produce a comprehensive analysis of the material structural problems. This includes the cellular automata techniques. Various complex extrusion geometries are analysed and the effects of scaling considered.

Development of the extrudate surface and criteria for ptedicting this important feature are comprehebsively covered in chapter 5 whilst chapter 6 considers some special technologies such as the use of pockets to obtain homogenous structures. Isothermal extrusion is also included in this section.

List of Contents

List of Figures

List of Tables

Acknowledgements

The author would like to express his sincere thanks to Professor Terry Sheppard for his supervision, guidance and encouragement during the production of this thesis and for his assistance in overcoming many of the problems encountered during the research.

Thanks are due to Dr. Xavier Velay who offered practical help and support throughout various stages of the thesis.

A special mention must also be made to Dr. Xinjian Duan for his invaluable guidance to my research at the beginning stage.

The help received from Dr. Isaac Flitta, Dr. Kamran Tebeshfar, Professor Peter Hogarth, and other members within design group were much appreciated.

Finally I am very grateful to my aunts and uncles for their encouragement for my study.

1 Introduction

1.1 Aluminium alloy and extrusion process

Aluminium and its alloys, which can be of widely differing properties. are readily fabricated into simple and complex shapes. Consequently a large extrusion industry has emerged around these products.

Wrought aluminium alloys are divided into seven classes according to their principal alloy elements (Sheppard 1999a, p.69). Each alloy is described by a four digit number plus a further letter and number indicating the temper or condition of the alloy. Furthermore, alloy classes can be divided into two categories according to whether they are strengthened only by work hardening or also by heat treatment (precipitation hardening). The former applies to 1XXX, 3XXX, 4XXX and 5XXX alloys, while the latter applies to 2XXX, 6XXX and 7XXX alloys. Most of the work in this thesis is concerned with 2XXX and 6XXX alloys. The specification of these two alloy series are shown in Table 1.1.

Table 1.1 2XXX and 6XXX alloy properties

Designation	Major alloying element	Characteristic	Typical alloys and their main application
2XXX	Cu, Si	Hard alloy, heat treatable, low extrudability	2017, 2014, 2024 for aircraft industry
6XXX	Mg, Si	Soft to medium alloy, good extrudability	6061, 6063, 6351 6082 for structural and architectural application

Historically, mechanical working has been used as the primary means of changing the size and shape of materials while transforming the cast structure of an ingot into what is generally referred to as a wrought product. Extrusion is one of the major processes by which this has been achieved. The process is typically conducted at relatively high temperatures because the lower flow stress of the material under these conditions permits larger section reductions to be achieved; lowering the power requirements and processing times.

Extrusion is a plastic deformation process in which a billet of cast and homogenised metal (billet) is forced to flow by compression through the die opening of a smaller cross-section of area than that of the original billet. Figure 1.1 illustrates the essential principle of the extrusion process, and, at the same time, the distinction between two methods of working, known as direct and indirect extrusion. These depend on the arrangement of the tools. The extrusion process must usually produce an engineered product satisfying strict geometric, cosmetic and property specifications. This complex process involves interaction between the process variables and material high-temperature characteristics.

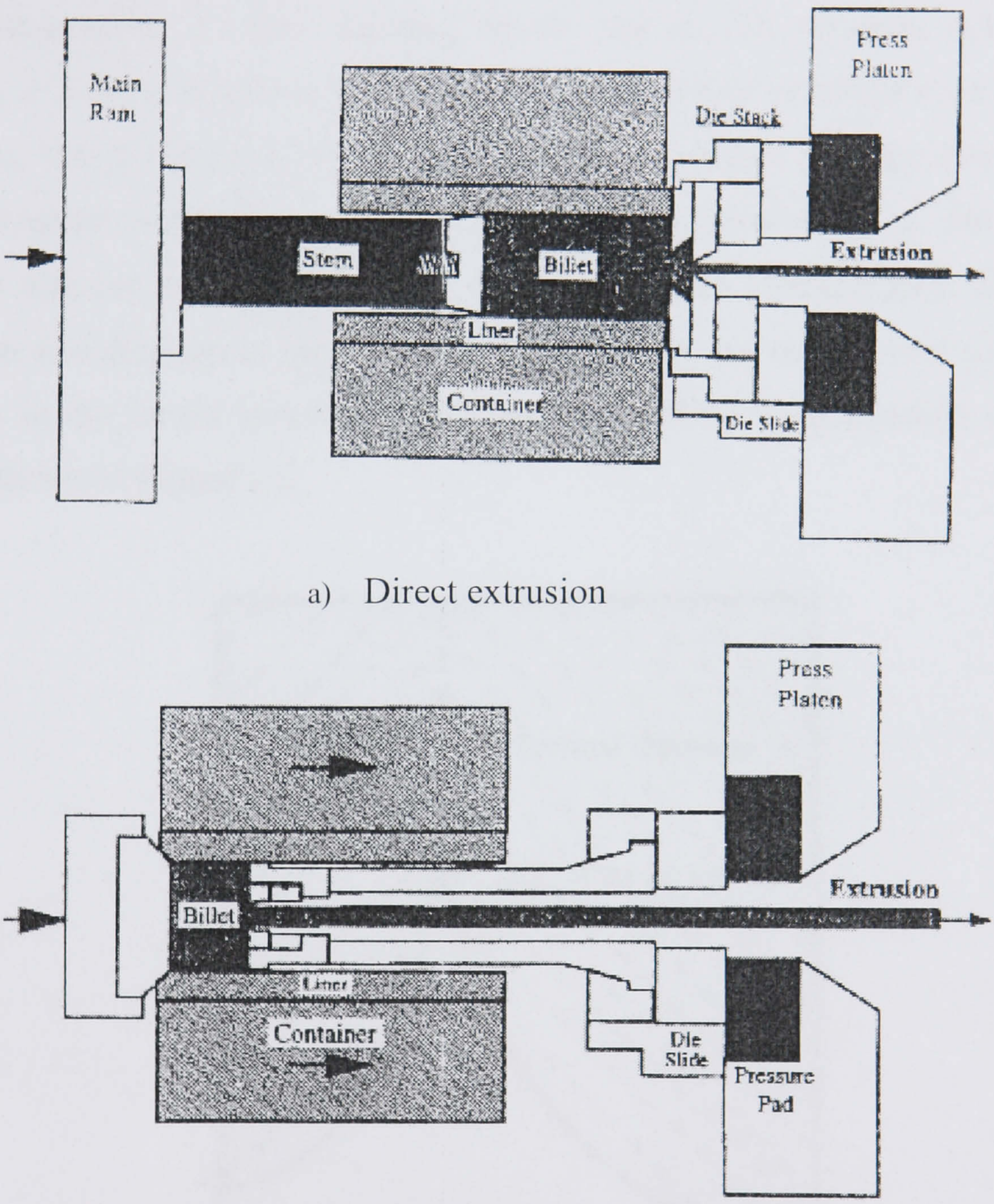

a) Direct extrusion

b) Indirect extrusion

Figure 1.1 Extrusion tools (Saha 2000, p11)

The specific steps of an extrusion process (excluding billet preparation and product heat treatment) are:

1. Loading of the die holder and die。

2. Loading of the billet;

3. Extrusion;

4. Separation of the die holder with the die and the discard from the extrusion.

Process variables available for control are the extrusion ratio R, the ram speed V and the extrusion temperature T. One limiting factor lies in the inherent stiffness (The relationship of load to deformation for a particular material) of alloys even at elevated temperatures. The stiffness may make the required load higher than the extrusion press capacity. Another major factor limiting the process parameters is the maximum temperature that can be tolerated during the process. The representation of these two factors upon one diagram is termed limit diagrams and the most useful form of such diagrams is in the format developed by Sheppard (1999a). One example of the limit diagram is shown in Figure 1.2.

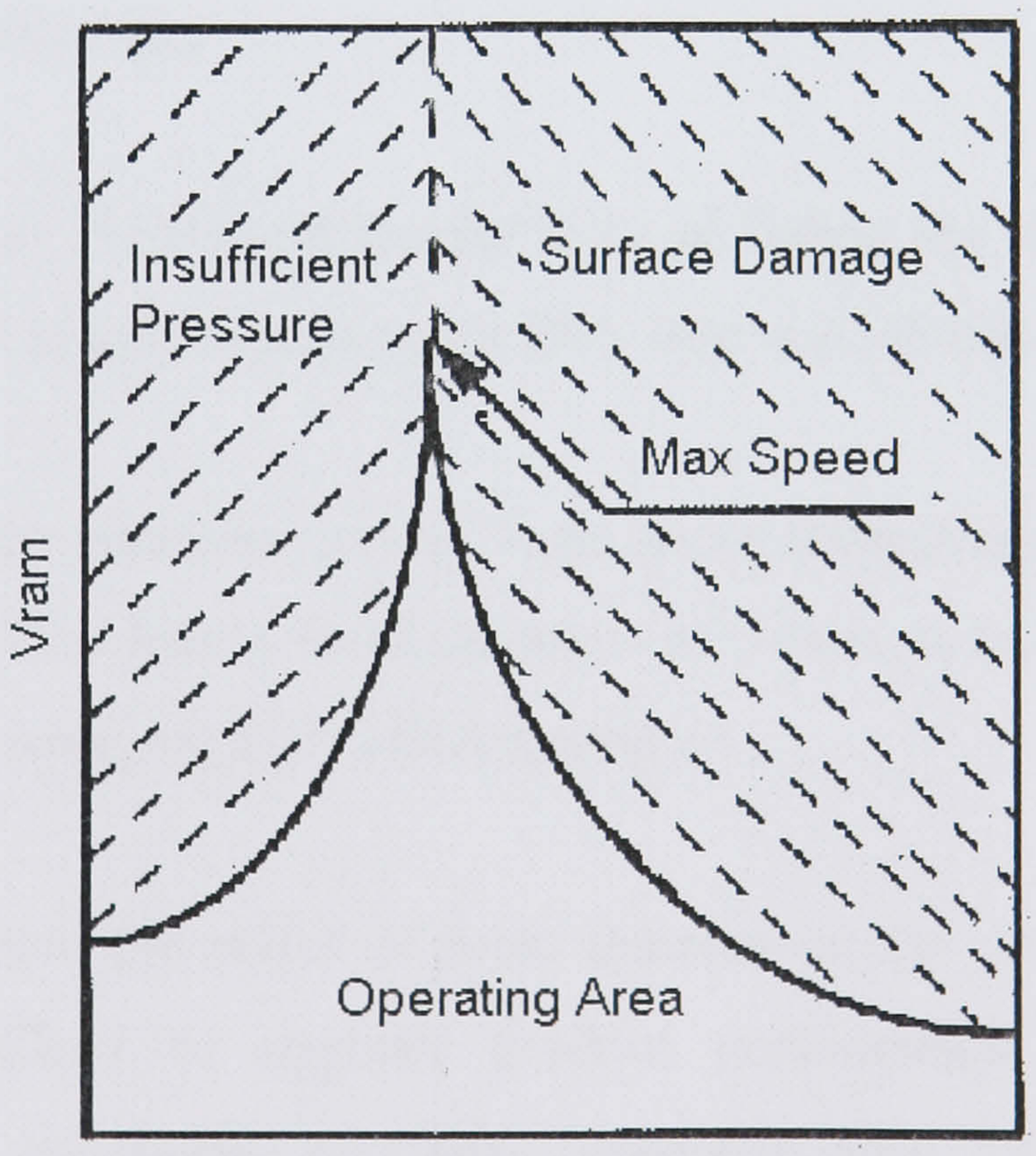

Figure 1.2 Limit Diagram (Sheppard 1999a)

The fundamental way to control the final product properties is to study the complex relationship between forming parameters, metallurgical response and final properties.

Since 1970s, Sheppard and his co-workers have carried out extensive experimental work in this field and accumulated a considerable amount of primary data (Sheppard 1999).

It is now generally recognized (Sellars et al. 1986, Shercliff and Lovatt 2001) that the microstructure of the material also requires careful control and hence the integrated process must be considered. For extrusion, the integrated process (the thermo-mechanical process) will consist of the unit processes involved: homogenization (the alloy is heated up to its eutectic temperature and kept at this temperature during some time), heating to working temperature, extrusion, stretching, solution treatment and ageing. Microstructural features of importance for property control of aluminium alloys include:

(a) the coherency and distribution of strengthening precipitates;

(b) the degree of recrystallization;

(c) the grain and /or subgrain size and shape;

(d) crystallographic texture and

(e) size and distribution of intermetallic particles including the dispersoids (present by design) and constituent phases (which result from iron and silicon impurities).

(f) There are also trace elements arising from grain refinement during casting using Titanium Boride rod. This leaves small amounts of Titanium oxide and Boride. There have been no reported works on their affect during all

The ability to understand the effect of these features on the properties of aluminium alloys has led to efforts to upgrade product performance by modifications in conventional primary processing methods. Beginning with the as-cast ingot which exhibits a heterogeneous morphology, processing includes a homogenization treatment, to reduce segregation, remove the low melting point phases and thus improve workability. This thermal treatment also serves to precipitate dispersoid-forming elements such as chromium, manganese and zirconium, so that they may perform their role of grain control during processing.

The extrusion process breaks down the billet and effects the required shape change. Since aluminium and its alloys have a high stacking fault energy (Jonas et al. 1969), sufficient dynamic recovery normally occurs during hot deformation, i.e. at temperatures above 0.5 T_h (homologous temperature, which is defined as the extrusion temperature divided by the lowest melting temperature of the phase) (Jonas et al. 1969), to give rise to a stable polygonized substructure. The subgrains remain equiaxed during hot working although the grains elongate in the direction of flow and do not recrystallise. Some of the alloying additions are in solution during hot working but the dispersoid-forming transition elements (such as $CuAl_2$) precipitate and may become strung out in the working direction (Sheppard 1999a).

Extrusion is the dominant process in producing complex shape products. The section shape is quite clearly the most important factor in the extrudability considerations. Typical examples of complex shapes are shown in Figure 1.3. The harder alloys of the 2XXX, 5XXX ($>3\%Mg$), and 7XXX series are more difficult to extrude and consequently are used for more demanding applications such as aerospace. Generally these alloys are of less complex shape than is shown in Figure 1.3

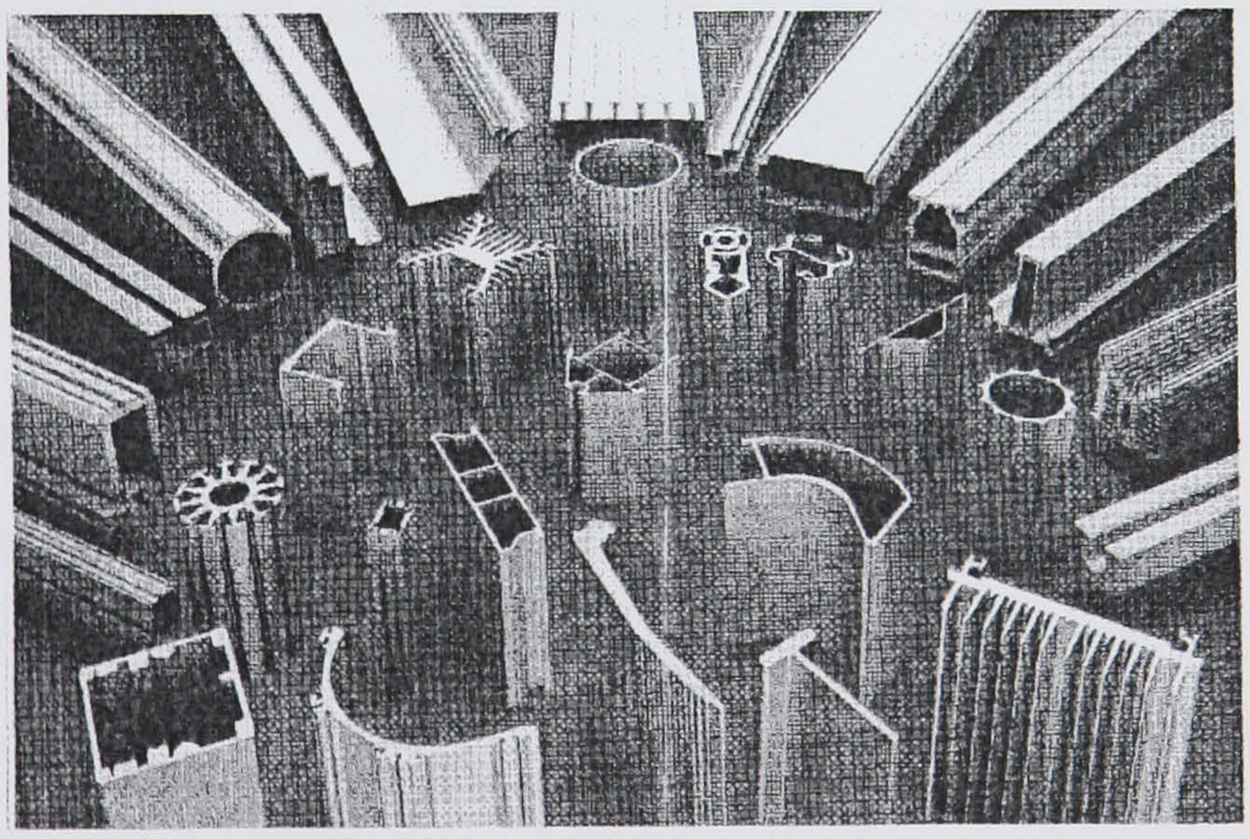

Figure 1.3 Examples of extruded shapes. (Courtesy of Hoogovens Aluminium)

1.2 The role of process modelling in manufacturing processes design

The selection and optimising of a suitable manufacturing process often involves considering the complex coupling between characteristics of the design, the material and

the process. Requirements and attributes of a process selection and optimisation can be greatly improved by process modelling. The use of modelling opens up great opportunities for making maximum use of sparse process data, for optimum co-selection of material and process, and for providing the designer with feedback on the likely influence of processing on the viability and cost of a design as well as indicating promising processing parameters (Shercliff and Lovatt 2001).

It is widely recognised that the most appropriate approach to selection during engineering design depends on the design context. Pahl and Beitz (1977) split the context of design into conceptual (preliminary), embodiment (intermediate) and detail (final) stages. Although different design objectives are undertaken in different design stages, the task-based selection is particularly important whenever (Shercliff and Lovatt 2001):

(1) The quality or functionality of the component is strongly influenced by the interaction of the process with specific design features;

(2) The economics of the process depend on detailed aspects of the design.

A single methodology for approaching task-based selection, which can incorporate this breadth of complexity, has been described in the literature (Grong and Shercliff 2002, Shercliff and Lovatt 2001).

The employment of numerical methods in materials science is promoted by the ever-increasing capability of computer systems in terms of speed and information storage, and by the growing demands for quantitative predictions in industry and research. The scientific branch that has matured within this interdisciplinary field, is often refereed to as "computational material science" (Evans 1993). This science branch brings together approaches from materials science, physics, computer science, mathematics, chemistry, and mechanical engineering. The applications of microstructure simulation into extrusion modelling are discussed in depth in the present work.

The application of various models in simulation of the extrusion process will be illustrated in the present work.

1.3 Modelling of extrusion process

Exact mathematical analysis of the extrusion process requires a complete solution to the equilibrium equations, the instantaneous yield criterion, the plasticity equations, and the compressibility condition. Theoretically, it is possible to do this, but the mathematical complexities become enormous and have not been fully resolved. In addition, there is often insufficient knowledge regarding the stress-strain relationship of the extruding metal at various strain rates, and the friction effects at the die/metal interface. Thus, the solution becomes approximate. Many analytical and semi-analytical methods such as ideal work, slab (or equilibrium), slip line, upper bound, visco-plasticity, integral profile, and energy methods are well established and have been discussed in numerous text books and scientific studies (Ruppin and Strehmel 1977, Sheppard and Raybould 1973b, Castle and Sheppard 1976, Sheppard and Wood 1980, Bianchi and Sheppard 1987).

In extrusion, both the frictional work and the work of deformation generate heat. Heat generation and transfer take place simultaneously from the commencement of the ram stroke during extrusion. Some of the generated heat remains in the extruded metal, some is transmitted to the container and the die, and some increases the temperature of the section of the billet that is not yet extruded. With knowledge of these factors it should be possible to calculate the mean exit temperature and several mathematical models (Finite difference method, Integral profile models, etc.) have been developed for this calculation. However, all these models involve certain assumptions to simplify the analysis. These models are detailed in individual references (Humphreys 1979, Zaidi and Sheppard 1984, Paterson and Sheppard 1982, Q. Li et al. 2003).

With the development of process modelling technology, more advanced numerical thermal-mechanical combined simulation has been provided by the Finite Element Method (FEM). The implementation of the model in the form of computer codes, with thermo-mechanical balance and kinematics compatibility built in, has introduced a modelling tool driven only by the external boundary conditions and the material behaviour. Thus, additional assumptions such as the pre-setting of discontinuity lines – as in upper bound techniques – are not necessary. Because of their flexibility in reproducing almost any required geometry, finite-element techniques must be regarded as potentially the most practical tool presently available. The details of the comparison

between the FEM with upper-bound and slip-line field techniques can be found in Sheppard's work (1999).

In recent years, the thermal-mechanical and microstructure integrated simulation has also been developed. By empirical and physically based means, a modest degree of prediction of microstructure can be achieved, for example, linking recrystallisation after deformation to the average process conditions (Shercliff 1997, Shercliff and Lovatt 1999, Raabe 1998).

1.4 Objective of this research

All of the work that has been developed will be applied into the modelling of the manufacturing process, specifically, hot extrusion of aluminium alloys (Peng and Sheppard 2003, 2004a-g).

FEM simulation is employed in the 2D and 3D thermal-mechanical simulation of the extrusion process, which has achieved successful results (Q Li et al. 2003, Peng and Sheppard 2003). Metallurgical models are applied to the modelling of the substructure evolution and have been proved to be effective (Peng and Sheppard 2003, 2004a,b,f,g). Special extrusion technologies, such as pocket die extrusion (Peng and Sheppard 2005a) and isothermal extrusion (Peng and Sheppard 2004e) were modelled and 3D visualised simulation results have been published. Product quality controls were established numerically and quantitative analysis results had been provided (Peng and Sheppard 2004c).

With the appropriate metallurgical model, fracture models applicable to surface cracking and three dimensional modelling technologies, FEM simulation is proved to be a powerful tool for the aluminium industry, especially when combined other numerical models which can be compactly integrated into the FEM software (Peng and Sheppard 2004d, 2005b,c).

2 literature review

2.1 Mechanics of hot extrusion

Although extrusion is a modern process (rolling and forging being much older) it precedes the development of aluminium which was only commercially available following the invention in 1886 (Sheppard 1999a, Castle 1974), concurrently by Hall and Heroult, of the electrolytic process to extract the metal from bauxite. The conventional extrusion process is complex. Among the industrial methods by which aluminium billets can be transformed to exceedingly complex shapes, extrusion has no rival and has firmly established itself as a major industrial process (Farag and Sellars 1975, Sheppard and Chare 1972, Wood and Sheppard 1975).

2.1.1 Direct and indirect extrusion

It is noted in section 1.1 that almost since the inception of the extrusion process there have been two modes of operation. The difference between the two modes are provided in great detail in previous studies (Morse 1970, Spiers et al. 1969, Mueller 2002, Sheppard and Paterson 1982, Long 1986).

The major difference is that in the indirect mode there is no friction between the billet and container whereas in the direct mode the outer shell of the billet moves relative to the container as extrusion proceeds (Chadwick 1970, Cockroft 1969, Tuschy 1971, Berezhnoy 1997). Thus in direct extrusion the surface of the billet is sheared at, or slides along, the container wall (Hodges 1970, Hirobumi and Hiromasa 1974). In every case, part of the extrusion load, depending on the length of the billet, is expended in overcoming the friction between the billet and the container, or in shearing the inner material from the slower-moving peripheral layer adjacent to the container wall. As one would expect, this results in considerable variation in flow behaviour, which is considered in detail in Chapter 3.

Generally, direct extrusion is more widely used and some of the complex extrusions employed in the subsequent chapters are introduced below, including:

(1) Multihole-die extrusion:

When extruding shaped sections which would normally require pressures in excess of the press capacity, and where it is more productive to extrude shorter lengths or when extruding forge stock, it is common to use multi-hole dies (Castle 1974, Gunasekera 1984, Romana and Jozef 1985). The literature describing or analysing this process is sparse although the industrial application is quite common. The majority of experimental extrusion reported has been concerned with plane or axi-symmetric extrusion of sheet or rod. There are few studies reported concerning the pressure requirements or the temperature variations and material flow when considering complex shapes or multi-hole dies (Johnson and Kudo 1962, Ulysse and Johnson 1998, Rahman et al. 2002) although these are important considerations to the press designer and to the operator. Reports concerning the use of a commercial FEM code FORGE3® to study the influence of the number and the distribution of die holes on extrusion parameters can be found in Chapter 4. The flow pattern, pressure requirements, and temperature histories developed are established and the difference in the properties of the extrudate using multiple holes (compared with single hole) are also reported in Chapter 4.

(2) Shape extrusion:

Extrusion is the preferred method to produce complex shaped components (Doar 1969, Ferguson 1996, Lof and Blokhuis 2002, Sheikh et al. 2004, Rong 1998). As an example to demonstrate the effectiveness of numerical simulation in modelling extrusion process, T shape extrusions (representative of the aircraft wing axe) at various initial conditions are studied in the following chapters. The dimensions of the section are shown in Figure 2.1. The distribution of equivalent strain, strain rate, temperature and the evolution of the substructure including static recrystallisation have been studied and results are presented in Chapter 4.

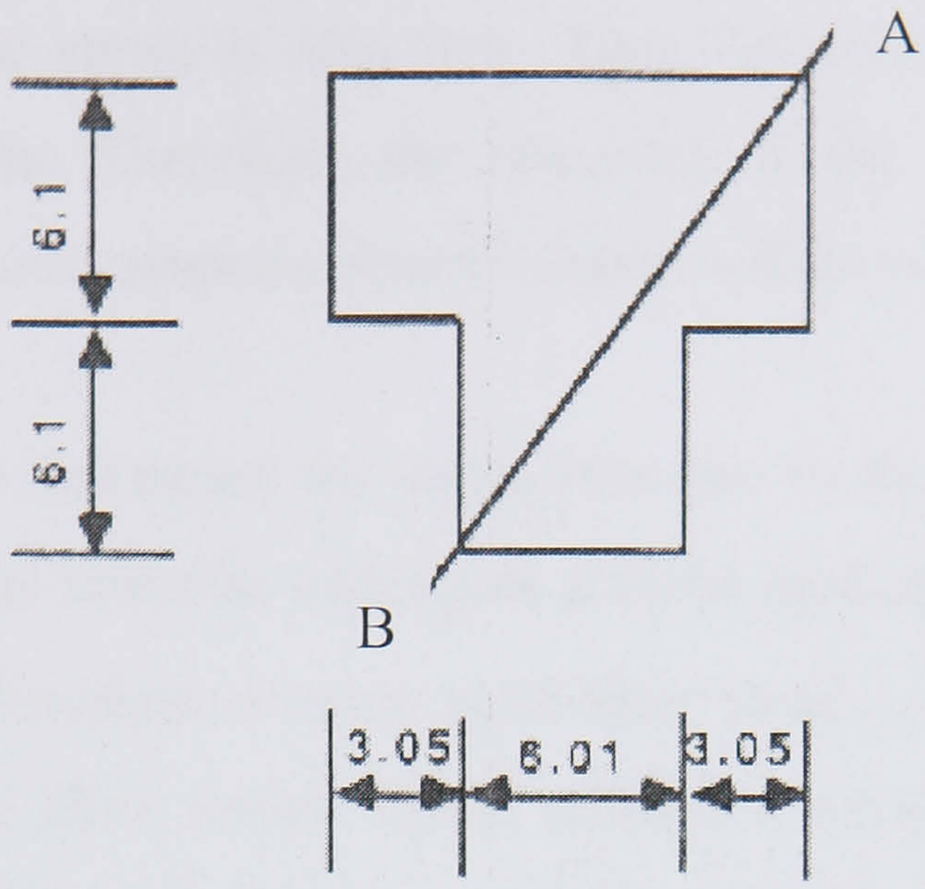

Figure 2.1 Dimensions of T shape section

2.1.2 Physical parameters and principles used in modelling of extrusion

2.1.2.1 Extrusion ratio

In conventional extrusion the extrusion ratio R is defined as:

$$R = \frac{Ac}{nA_E} \tag{2.1}$$

where Ac is the area of the container cross section, A_E is the total cross sectional area of the extrudate and n the number of holes in the die (for multi hole extrusion). The effective extrusion ratio range in industry practice for soft alloys is from 10:1 to 100:1.

2.1.2.2 Plastic strain and strain rate

The actual strain, $\bar{\varepsilon}$, obtained by integration is a logarithmic function. Therefore, the effective strain in direct extrusion is usually approximated as the fractional cross-sectional area and is defined in an elementary notation as:

$$\bar{\varepsilon} = \ln \frac{Ac}{A_E} = \ln R \tag{2.2}$$

where Ac is the cross sectional area of the container bore and A_E is the cross section area of the extrudate (Sara 2000). It is worth noting that when the extrusion ratio is low, the amount of plastic strain is also low. Thus the amount of work done during the extrusion will be less. Therefore, the structure of the extrudate will be under less deformation and physical property specifications will be compromised.

It is very difficult to determine the strain rate due to the complex flow pattern in the deformation zone. The material undergoes a rapid acceleration as it passes through the deformation zone. Therefore, a mean equivalent strain rate, $\dot{\bar{\varepsilon}}$, has to be estimated for determination of the flow stress. After extensive optimisation of the upper bound solution, Castle (1976a) and Tutcher (1979) suggested the following equation for the mean equivalent strain rate:

$$\dot{\bar{\varepsilon}} = \frac{6D_C^2 V_R (a + b \ln R)(c + d \tan \omega)}{D_C^3 - D_E^3} \qquad (2.3)$$

where a, b, c and d are constants, D_C is the container diameter, D_E is the extrudate diameter, V_R is the ram speed and ω is the deformation cone semi-angle with $\omega = i + j \ln R$, where i and j are constants. Of course more accurate calculation of $\dot{\bar{\varepsilon}}$ may be obtained when using FEM (Lof 2001, Peng 2004a).

2.1.2.3 Friction

Friction in aluminium extrusion is a complex and still not fully understood phenomenon (Wagener 1994, Renne 1989, Muller 2002, Nakamura and Ishibashi 1995). The environment of hot extrusion (i.e. high pressure, high temperature and material flow) prevents efficient investigation of the frictional interfaces. The temperature distribution depends heavily on the frictional heat flux generated at the interfaces between the tooling and the material. Temperature increases also occur due to shearing at the dead metal zone interface (Abtahi 1996, Sara 1998, Tokizawa et al. 1976, Sivaram 1988).
Generally the direct hot extrusion of aluminium alloys is performed without any lubricant. However a small amount of graphite based grease is sometimes used on the

face of the container which could become washed in below the extrudate surface during extrusion. This can lead to surface lamination and blistering.

In direct extrusion (with a flat die) friction occurs at four interfaces (Bowden and Tabor 1964, Schey 1983, Benedyk 2001, Gamache 1999, Lin 2003, Guha and Lengyel 1974): (a) container-billet, (b) die bearing-material, (c) dead metal zone-material, and (d) dummy block-billet, as shown in Figure 2.2.

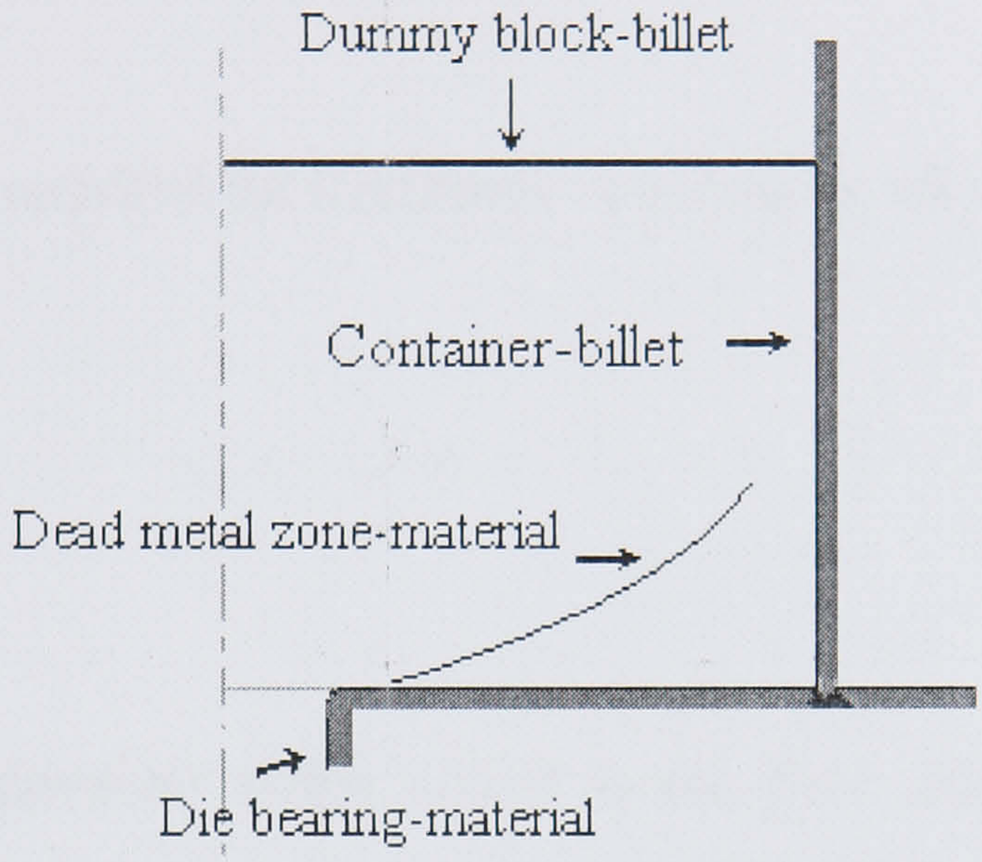

Figure 2.2 Friction interfaces at direct extrusion

The numerical description of friction is introduced in detail in Chapter 3 and it is not repeated here.

2.1.2.4 Extrusion pressure

The study of pressure during aluminium extrusion has been extensively reported (Oki 1990, Arif 2001, Chadwick 1970, Sonmez 2002, Ohuchi and Takahashi 1988). The pressure required for the process is the principal consideration in the selection of an extrusion press. The pressure can vary depending on: the alloy and its condition, the extrusion ratio, diameter and length of the billet, temperature of the billet and tooling, ram speed and the shape of the extrudate (Sheppard 1993, 1999a).

An early estimation of the extrusion pressure, p, was suggested by Siebel and Fangmeir (1931 cited Sheppard 1999a, L Li et al. 2004, Moshksar and Ebrahimi 1999, Bessey 2004) in the form of:

$$p = \bar{\sigma} \ln R \tag{2.4}$$

where $\bar{\sigma}$ is the equivalent stress. Unfortunately, this equation underestimates the real extrusion pressure by about 60%. It does not take account of the friction and the peak pressure. It is now generally accepted that the extrusion pressure (or the pressure exerted on the ram), p, can be divided into four parts as follows (Castle and Sheppard 1976b).

$$p = p_D + p_F + p_{RW} + p_B \tag{2.5}$$

where p_D is the pressure required for the plastic deformation of the billet, which is given in the functional form as:

$$p_D = f(\bar{\sigma}, \bar{\varepsilon}) \tag{2.6}$$

where $\bar{\varepsilon}$ is the mean equivalent strain and $\bar{\sigma}$ is the flow stress. p_F is the pressure required to overcome the friction mainly at the container wall, p_{RW} is the pressure required to compensate redundant or internal deformation work. p_B is the pressure required to overcome the higher number of dislocation density present in the billet before steady state extrusion is reached.

From experimental observations and numerical analysis (slip line or upper bound) the following formulae can be derived (Sheppard and Raybould 1973):

$$p = \bar{\sigma}(a + b \ln R + cL) \tag{2.7}$$

where a is the contribution to the redundant work, b is linked to the semi-dead metal zone angle, L is the length of the billet and c is dependent on the friction coefficients.

Further work (Castle and Sheppard 1980a,b, Sheppard and Wood 1980, Sheppard 1993, Vierod and Sheppard 1985, 1987, Langseth 1994) demonstrated the importance of the shape of the extruded product on the extrusion pressure. Therefore a peripheral ratio parameter, λ, defined as the ratio of the periphery of the section to the periphery of a rod

of equivalent cross-section, was introduced into the pressure equation. One example helping to understand the definition of the peripheral ratio is shown below:

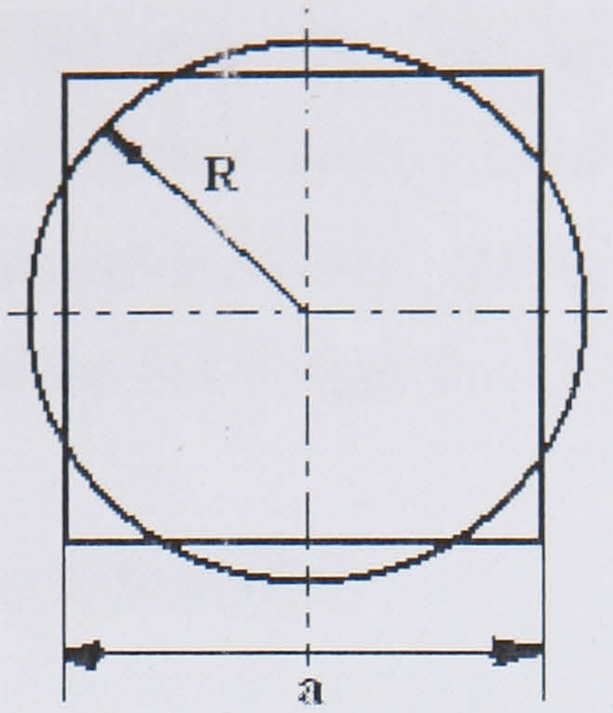

In case a round and a square enclose an equal area, $\lambda = 2a / \pi R$

Figure 2.3 Example of peripheral ratio parameter

Here the square and the round have the same extrusion ratio. Thus the shape factor is given by the peripheral values for the square 4a divided by the peripheral distance of the round $2\pi R$.

It has already been well recognised that Finite Element Method (FEM) can give more precise prediction of extrusion pressure than the methods introduced above. FEM is also more flexible than other methods, especially when complex boundary conditions are under consideration (for example, in the analysis of multi-hole or complex shape extrusion). The detail of the discussion can be found in Chapter 3 and 4.

2.1.2.5 Heat transfer and balance during extrusion process

Heat transfer is one of the most important phenomena to consider in extrusion as it defines the temperature parameter. This is one of the process variables that can be controlled. In general it has been shown that variations in temperature are mainly due to the extrusion ratio and ram speed (Wu et al. 1995, Guice and Witte 1987, Kamal and Kalyon 1983) The flow stress and therefore the pressure can be reduced if the temperature is increased. However, there is a risk of localised incipient melting with high ram velocity (Chen 2000, Gopalakrishna 1991).

Heat transfer occurs throughout the extrusion process from the initial stage of homogenisation to the following extrusion stage, during which heat transfers to the die (from the billet) and air (from the extrudate), until the stage of stretching and finally at the stage of solution treatment and ageing (Sheppard and Wood 1980, Lange 1971,

Castle and Sheppard 1976, Macey and Salim 1988, Chenot 1992). However, the heat generation and heat transfer occuring during the extrusion are critical because they define the exit temperature of the extrudate. The temperature of the extrudate just leaving the die is important for product quality (dimensional stability and extrusion defects) and die life (wear and performance). Castle (1992) and Sheppard (1999b) divided the heat balance between the following processes:

(1) Heat generation due to plastic deformation,

(2) Heat generation due to friction at the container-billet, dead metal zone-material and die land-material interfaces,

(3) Heat exchange between the billet and the tooling (container, pressure pad, die land).

The detail of theory of numerical modelling of thermal behaviour during extrusion process can be found in Chapter 3.

2.2 Optimising extrusion conditions and the role of modelling

The extrusion process must produce a product satisfying strict geometric, cosmetic and property specifications. The extrudability of aluminium alloys, which means the compatibility of an alloy to withstand high speed extrusion, varies with the material variables, which include alloy elements, homogeneity and billet conditions. One measure of extrudability is the flow stress of the alloy since this parameter, for any given section, determines the pressure locus on the extrusion limit diagram (McShane 1978, Patterson 1981, Sheppard and Wright 1979, Sheppard 1999a).

The representation of press capacity and maximum temperature which can be tolerated during process in one diagram is termed a limit diagram and one example is schematically shown in Figure 1.2 and it is not repeated here. The most useful form of such diagrams is in the format developed by Sheppard and Raybould (1973a). The format utilises constant strain rate curves and also shows that limit diagrams could provide specific metallurgical data on the structure of the final extrudate, thus providing the press operator with the capacity for metallurgical process control.

The application of numerical techniques to the continuum mechanics problem. developed over the last three decades, has improved the capability for an integrated treatment of both tool-load demands and internal micromechanics (Bianchi and Sheppard 1987, Childs 1974, Baskes 1999, Harrison 1994). Their implementation as computer codes, with thermo-mechanical balance and kinematics compatibility built in, has introduced a modelling tool driven only by the external boundary conditions and the material behaviour. The Finite Element method now provides sufficient information for many 'mechanical' problems, such as load prediction, speed optimisation, temperature and residual stress, etc. to be solved. Whilst most of the early finite element methods used in computational science postulated isotropic, homogeneous, linear, and continuous materials properties (Zienkiewicz et al. 1990), a number of advanced methods consider material heterogeneity, crystal anisotropy, nonlinear material response, and nonlinear geometrical aspects (Gittus and Zarka 1986, Mchugh et al. 1993, Dawson et al. 1994, Fleck et al. 1994, Schmauder and Weichert 1996, Sarma 1996).

However, FEM is mainly applied in thermal-mechanical continuum analyses. To simulate the evolution process of the material structure (for example, recovery and recrystallisation) and predict the final structure, FEM has to be combined with other structural models. Microstructure modelling is now often seen as the most profitable way to add value when applied to industrial based FEM simulation (Shercliff and Lovatt 2001). Various microstructure models have been developed, although many of them are still in an early stage. Different methods, such as physically based model using internal state variables, statistical mechanism models, Monte Carlo and Cellular Automata, etc. have been applied in simulations of different scales (Micro, Meso and Macroscale) (Smolander 1985, Hunter et al. 1990, Srolovitz et al. 1986) A new branch of science: "computational material science" is under development (Raabe 1998a).

The greater part of process modelling is developed for detailed design, or to enhance scientific understanding of processing. The challenge is to extract an appropriate level of detail and approximation to provide useful discrimination as dictated by the needs of the designer. Process modelling could also play a more significant role in improving understanding of the response of the material in the numerous standard laboratory tests used by industry. This modelling could provide a more robust basis for making design decisions on the basis of these tests.

An important aspect of modelling in selection. which has to be considered here. is the degree of uncertainty in the predictions, the work on simulation using different models must take this into account (Shercliff and Lovatt 2001).

2.3 Numerical modelling and simulation

The term "modelling" has two meanings, one falls into the domain of model formulation or model design. By selecting the independent variable (typically time t and space x) and dependent variables (functions of the independent variables), underlying kinematics and structure evolution equations could be established, in the form of algebraic, differential, and/or integral expressions. The second meaning of modelling is the numerical solution of the governing equations associated with models. This procedure can be referred to as "numerical modelling" or "simulation" (Ashby 1992, Biner 1992, Miller 1987, Kirtley 2001, Jekl et al 1991). Both terms paraphrase the solution of a set of mathematical expressions, i.e., of a number of path-dependent and path-independent functions, which quantify the underlying model formulation using appropriate boundary- and initial-value conditions.

One common approach is to use the notion "numerical modelling" for the entire procedure of model formulation and program code generation, while the term "simulation" is often used in the sense of numerical experimentation. The details of the definition and discussion of the terms can be found in Raabe's work (1998a).

The application fields, for example, mechanical engineering or materials science, commonly classify different modelling methods (Murphy and Perera 2002). The modelling applied in different research fields in the present work are introduced in the sections below. However, the trend is to integrate different research fields and thus "integrated modelling" is introduced at the end of this chapter.

2.3.1 Thermal-mechanical modelling by Finite Element Method

The simulation calculation of an extrusion sequence in an industrial environment consists principally of a thermo-mechanical analysis of the plastic deformation (Dyja and Korczak 1999, Kowalsky and Ahrens 1997, Meguid 2001). Modelling of thermo-mechanical processing of metals is one of a number of industrial modelling activities

which has been reviewed in response to the technology foresight exercise (Shercliff 1997). This illustrated the breadth of industrial processes and alloys for which there are common underlying challenges in process modelling (Shercliff and Lovatt 1999).

The term thermodynamics refers to the study of heat related to matter in motion. Modelling of thermomechanical processing of metals is one of a number of materials modelling activities. The Finite Element Method (FEM) is a general numerical means of obtaining approximate solutions in space to boundary and initial-value problems. It is based on generating the governing differential equations and the discrete algebraic counterparts of the problem under investigation using a variation formulation. The development of the state variable being approximated by appropriate interpolation functions. The application of numerical techniques to the continuum mechanics problem, developed over the last three decades (Iwata et al 1972, Livesley 1983, Reinikainen 1994, Herberg and Skauvik 1993, Udagawa 1992, L Li et al 2004) has improved the capability for an integrated treatment of both tool-load demands and internal micromechanics.

Currently, computer modelling and simulation of the material forming process has been developed to the point where it may b4e used to solve industrial problems. Computer modelling is often treated as a universal tool in all problems of metal forming processes. Taking a general view of the present state of the art in terms of numerical modelling, it appears that the finite element method is most suited to the three-dimensional analysis of material forming processes. In fact, the finite element method can take into account practical non-linearity in the geometry and material properties, besides producing accurate predictions of stress, strain, strain rate and temperature throughout the deforming billet (Mathur and Dawson 1989, Becker 1991, Liu et al. 2000, Chanda 2000).

For many deformation processes, there is a view that continuum mechanics FEM is well established, both for simulating the manufacturing process itself and the less obvious task of modelling the 'standard test' used, for example, to determine constitutive behaviour (Huang 1998). The greatest limiting factors at the continuum level in all metal-forming analyses are poor characterisation of interfacial friction conditions (and to a lesser degree heat transfer), and the need for improved models of material constitutive behaviour for complex deformation histories and for heterogeneous materials (Shercliff 1997, Marthinsen 2003).

2.3.2 Microstructure modelling

Observations of the structure developed by hot working have been made on a wide range of materials deformed either by forging, rolling, or extrusion, or by high-strain-rate tension, compression, or torsion tests (Sheppard and Tutcher 1979a,b, Tibbetts and Wen 1998, Sellars 2003, Nes 1994). In general, the results obtained using different modes of deformation are in good agreement and they indicate that there are two broad groups of metals and solid-solution alloys which may behave differently under hot working conditions. Aluminium and aluminium alloys, commercial-purity α-iron and ferrite alloys are observed to develop subgrains during deformation when specimens are cooled rapidly after either small or large amounts of deformation. The structural changes during hot working of this group of metals are similar to those during creep, and where activation energies have been observed to remain nearly constant over the whole range of strain rates and temperature (Jonas et al. 1969).

In contrast, copper and copper alloys, nickel alloys and austenitic steel show a substructure within the distorted original grains after low deformations, but after higher deformations, when steady-state conditions have been attained, they develop an equiaxed recrystallised grain structure. Activation-energy measurements for creep and hot working on materials in this group show distinct differences (Jonas et al. 1969). This form of deformation is known as dynamic recrystallisation.

The work in the present study concentrates on deformation of aluminium alloys in which dynamic recovery and static recrystallisation are the main restoration process. Since the beginning of the 1990's, much progress has been made in computer modelling of microstructure evolution during the hot deformation process. Excellent reviews of modelling of static recrystallisation (SRX) have been given by Gottstein et al. (2000) and by Shercliff and Lovatt (1999). There are several approaches to modelling microstructure evolution in hot deformation and subsequent annealing, the most commonly used methods include: (a) Empirical methods, (b) Network models (Humphreys 1992), (c) Statistical modelling (Crotaz et al. 2002) (d) 'Physically based' (PB) state variable methods (Nes 1998, Sellars and Zhu 1999, Gottstein 1998, Furu 1999, Zhu et al. 2003) which have been proposed to describe the hot rolling of aluminium alloys. One of the important tasks of the present project is to verify and apply these

models to the extrusion process as well as (e) the cellular automaton (CA) and the Potts model (MC) (Liu 1996, Davis 1997).

The various scales of microstructure modelling can also be roughly grouped into the nanoscopic, microscopic, mesoscopic, and macroscopic regimes (Raabe 1998a). In this context the term nanoscopic refers to the atomic level, microscopic to lattice defects ensembles below the grain scale, mesoscopic to lattice defect ensembles at the grain scale, and macroscopic to the sample geometry. This subdivision is to a certain extent deterministic, various alternative subdivisions are conceivable. In the present work, most studies are concentrated on the macro and mesoscopic scale simulation with physically based metallurgical models and other numerical models, for example, the Cellular Automata model. Some work concerned with the microscopic simulation is also discussed.

2.3.2.1 Empirical models

The greater part of process modelling is developed for detailed design, or to enhance scientific understanding of processing. The challenge is to extract an appropriate level of detail and approximation to provide useful discrimination as dictated by the needs of the designer. The inherent complexity of some process physics also calls for a degree of pragmatism, so that purely empirical models are used if required in order that as wide a range of options as possible is considered.

The established empirical approach (Sellars 1990, Mclaren & Sellars 1992) to predict flow stress and subsequent recrystallisation is based on the Zener-Hollomon parameter:

$$Z = \dot{\bar{\varepsilon}} \exp(\frac{\Delta H}{RT}) \qquad (2\text{-}8)$$

where $\dot{\bar{\varepsilon}}$ is the mean equivalent strain rate, ΔH is the activation energy and T is the temperature. Flow stress in the above study is commonly described by an equation of the form

$$\sigma = \frac{1}{\alpha'} \operatorname{arcsin} h(\frac{Z}{Z^*})^{1/n} \qquad (2\text{-}9)$$

where α', Z^* and n are material constants. Recrystallised grain size, d_{rex}, and the time to 50% recrystallisation, t_{50} (a common measure of recrystallisation kinetics), are described by power laws:

$$d_{rex} = k d_0^{\alpha} \varepsilon^{-b} Z^{c} \qquad (2\text{-}10)$$

$$t_{50} = \beta d_0^{p} \varepsilon^{-q} Z^{-r} \exp(Q_{def} / RT) \qquad (2\text{-}11)$$

where α, β, k are constants, d_0 is the initial grain size (Nes 1994, 1998), and ε is the Von Mises equivalent strain. The other parameters are empirical constants.

The volume fraction recrystallised factor can also be related to the temperature and the other forming parameters, which can be expressed as:

$$Xv = f(K, T, \lambda, Z, \varepsilon, \dot{\varepsilon}) \qquad (2\text{-}12)$$

where T is the temperature, λ is the peripheral ratio, R is the extrusion ratio, K is a constant (Sheppard 1993, 1999a).

Other empirical models have been developed to describe:

(1) The relations between the subgrain size and recrystallised grain size to processing parameters:

On the finer scale, the extrudates contain a well recovered subgrain structure whose sizes are modified by the presence of the inclusion and precipitates. The subgrain size is commonly given as reported in a considerable volume of literature (Sheppard and Tutcher 1979, Sheppard and Raybould 1973a, Paterson 1981, Sellars 1986) as:

$$\delta^{-1} = A\mathrm{Ln}(Z) + B \qquad (2\text{-}13)$$

and the constants A and B have been given for various aluminium alloys (Sheppard 1982. Zaidi 1983, Sheppard 1999, Nes 1994, Sellars 1996).

Empirical equations were also given to relate the recrystallised grain size to the deformation conditions (Nes 1994). Empirical models have also been combined with FEM to predict the final structure in rolling in many previous studies (Chen 1992. Duan 2002). Some of them have been introduced in the introductory chapter and they are not repeated here.

(2) Volume fraction recrystallised factor.

The volume fraction of a material Xv which recrystallises in a time t during isothermal annealing produces a curve of sigmoidal shape as reported by Sheppard and Raghunathan (1989), and is consistent with the recovery, nucleation, and growth equation proposed by Johnson and Mehl and Avrami which takes the form:

$$Xv = 1 - \exp(-\beta t^{n}) \qquad (2\text{-}14)$$

where β and n are constant for any fixed time and temperature conditions. Rearranging this equation yields:

$$\ln\ln(\frac{1}{1 - Xv}) = \ln\beta + n \ln t \qquad (2\text{-}15)$$

By introducing the concept of temperature compensated time, shape factor λ (defined as the ratio of the periphery Ω_s of the section to the periphery Ω_r of a rod of equivalent cross-section) and the strain rate, Sheppard (1993) has reported the expression for the extrusion process as:

$$\ln\ln(\frac{1}{1 - Xv}) = K_0 + K_1 T + K_2 \ln(\lambda^2) R - K_3 \ln[\lambda^2 (\frac{Z}{A})] + K_4 \lambda^2 \qquad (2\text{-}16)$$

Subjecting the experimental measurements to multiple regression analysis to obtain the relevant equation yields, for example, for direct extrusion of AA2024: K_0=1.95, K_1=-0.012, K_2=1.16, K_3=0.04, K_4=0.04 (correlation coefficient 0.9907), for indirect extrusion, K_0=-2.05, K_1=-0.005, K_2=1, K_3=0.003, K_4=0.02 (correlation coefficient 0.9615).

(3) Working hardening phenomenon.

Various empirical equations have been given in predicting the proof stress by Nes (1998), or used to relate the work hardening to the variation of subgrain size or the recrystallised grain size (Nes 1994, Sellars 1986, Nes 1998, Urcola 1987, Vernon-Parry 1996) and now they have been developed into a physically based model, which is fully physically based (Nes and Marthinsen 2002).

However, it is important to point out here that it is not the aim of present work to develop any empirical methods to predict the structural evolution. The only use of these equations is to give a reference data to correlate the simulation results when the detailed experimental results are not available.

As can be seen from the discussion above, by empirical means, a modest degree of prediction of microstructure can be achieved, for example, linking recrystallisation after deformation to the average process conditions. However, the empirical expressions depend on the accuracy of experiments and are regarded mainly as a case study method.

2.3.2.2 Network models

The network model is an efficient way to represent microstructural evolution in discretised form (Humphreys 1992). These models are efficient because they abstract a key Feature of the grain structure, i.e., the vertices or triple junctions between grain boundaries, and are therefore, efficient because only the motion of the joint points needs to be calculated, provided that local equilibrium can be assumed at triple junctions.

2.3.2.3 Physically based internal state variable model

A certain amount of the modelling work has been achieved in the field of hot rolling (Duan 2002a, Chen 1992, Mclaren 1992, Zhu 2003, Marthinsen 2003), and recently in the field of hot extrusion by Duan and Sheppard (2004a,b). Some models introduce many tuning parameters, especially for the physically based models. These parameters depend mainly on the material. To estimate their real values, specific and numerous experiments would be required. Recently, the inverse method combined with FEM has been adopted to tune the values of these parameters. The FEM is run iteratively until the appropriate value is found to match the experimental measurement. Duan and Sheppard (2004a,b) have used the inverse method to give the parameters for alloy 5083 and 2014. The method has also been used in simulations of the extrusion process by Peng (2004a,c).

Modelling of microstructure evolution explicitly in differential form has been the basis for most classical theories of work hardening and annealing. The internal state variables are now physically meaningful quantities that can, at least in principle, be measured by electron microscopy (dislocation densities etc.). Developments of this approach can now benefit from the recent advances in microscopy, such as semiautomatic electron back scatter diffraction (EBSD), which enables substructures to be quantified with far greater speed and precision (Hurley and Humphreys 2003a,b). Differential physically based state variable models have the potential to follow complex process histories and provide a means of conveying microstructure explicitly from one processing stage to the next.

The approach summarised here comes largely from the research groups in Trondheim, Sheffield and Cambridge (Nes 1994, Sellars 1986, Shercliff and Lovatt 1999). There are three separate modelling tasks: (a) describing the evolution of deformation substructure, in particular the subgrain size, dislocation density and subgrain boundary misorientation; (b) coupling substructure to flow stress; and (c) predicting recrystallisation behaviour.
The Trondheim group (Nes et al. 1994, Nes 1995, Nes & Furu 1995) have used evolution laws for subgrain size and dislocation density to study steady-state flow stress in constant strain-rate hot deformation, when work hardening and dynamic softening processes are balanced. Complex developments of this approach have been proposed to provide a 'universal model' for work hardening (at constant strain rate) across all

deformation temperatures both for pure FCC metals and Al-Mg alloys, based on a statistical view of dislocation storage (Nes 1998. Marthinsen & Nes 1997).

The Sheffield (IMMPETUS) group have approached hot working of aluminium alloys from a background of FE analysis of the transient nature of the deformation history in flat rolling, in terms of temperature, strain rate and strain path. Models for predicting the evolution of internal state variables such as internal dislocation density, subgrain size and misorientation between subgrains, as well as subsequent recrystallisation behaviour are developed for both constant and transient deformation conditions (Furu et al. 1999, Zhu et al. 2000). The detail of the model can be found in Appendix A.

However, criticism of the physically based models is that they have mainly been concentrated on a specific alloy (Al-1%Mg) and developed from experiments utilising plain strain compression (PSC), in which plastic strains greater than 2 are difficult to achieve. The interaction of recrystallisation and precipitation (Jones and Humphreys 2003) has not been considered in detail in the models.

At the present time, it is still difficult to obtain a precise measurement of some of the parameters used in the physically based models, such as the dislocation density. It has been reported by Sellars (1994), Shahani (1994) and reviewed by Nes (1994) that during steady state the dislocation within the cells ($1/\sqrt{\rho_i}$) is inversely proportional to the cell size δ:

$$\sqrt{\rho_i} = C_\delta / \delta \qquad (2\text{-}17)$$

where C_δ is a constant of typical value of the order 5. The stored energy can be written (Nes 1994):

$$P_D = \Gamma \rho_i + \kappa \gamma_{SB} \frac{1}{\delta} \qquad (2\text{-}18)$$

where Γ is the dislocation line tension, γ_{SB} is the sub-boundary energy:

$$\gamma_{SB} \approx \alpha_4 Gb\theta(\ln e\theta_c / \theta) \qquad (2\text{-}19)$$

with:

$$\alpha_4 = 1/4\pi(1-\nu) \qquad (2\text{-}20)$$

ν is the Poisson coefficient. $\theta(\approx 3^{\circ})$ is the sub-boundary misorientation and κ is a geometrical constant ($\kappa \approx 3$ for a uniform, regular substructure). Although the expression of the stored energy has been refined further (Furu and Sellars 1999), it is still at its early stage since the dislocation densities are difficult to measure in detail. There are still many phenomena to be understood to describe the complete physical nature of recrystallisation (Doherty et al. 1997) and this retards the development of physically based models.

2.3.2.3.1 Subgrain size

The as-deformed state microstructures in aluminium alloys have been characterised by a subgrain structure of low misorientation consistent with the operation of dynamic recovery and repolygonisation during extrusion (Marthinsen 2002, Ryen et al 2002, Nes 2004).

Examples of the substructures in the 5% Cu alloys at low extrusion temperature and high temperature are shown in Figure 2.4. As can be seen from Figure 2.4(a), the subgrains are elongated in the extrusion direction and have a relatively high internal dislocation density indicating that recovery is not complete at low temperatures. The substructure from high temperature extrudates in Figure 2.4 (b) shows that an increase in extrusion temperature results in a steady state substructure of larger subgrains with lower internal dislocation densities and narrower subboundary walls. The increase in thermal activation permits easier cross slip and climb of dislocations. The subgrains are generally more equiaxed in nature which can be associated with the need to reduce the grain boundary area and thus reduce the free energy of the structure, which is further enhanced by the increased mobility of the subboundary dislocations. The subgrain size can be related to the temperature compensated strain rate Z and hence the process condition by:

$$d^{-m} = a + b\mathrm{Ln}Z \qquad (2\text{-}21)$$

where a, b and m are constants (Jonas et al. 1969, Nes 1994,1998). A value of m=1 is normally used since it has been found to give the best overall correlation.

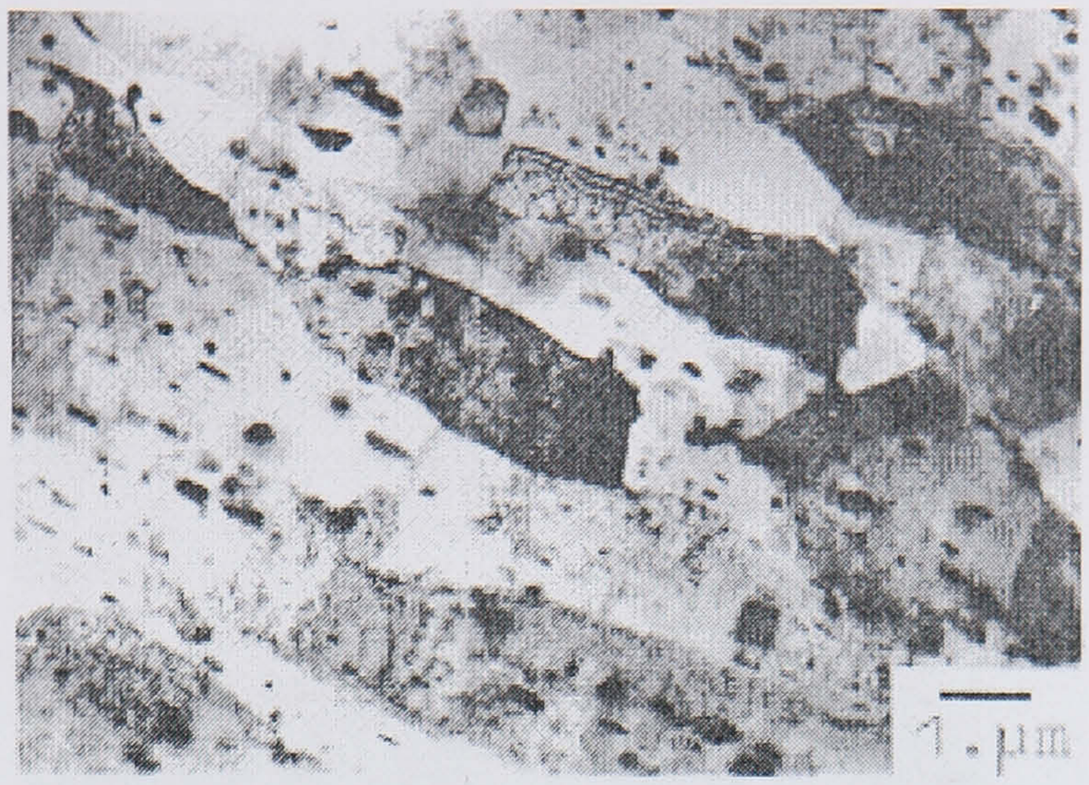

a) Ti=350°C LnZc=26.56

b) Ti=450°C LnZc=23.58

Figure 2.4 substructures observed in the longitudinal plane of the press quenched direct extrudates of the 5% Cu alloys (Vierod 1983)

2.3.2.3.2 Recrystallised grain size

Static recrystallisation can occur subsequently to extrusion after the material travels out of the die. Apart from the heavily worked outer region, the structure can be fully recrystallised, fibrous, or a combination of both. The structures may be classified into three main typical types as shown in Figure 2.5. Frequently the structure is a combination of one or more of these types.

In the case of solutionised rod extrusion, Subramaniyan gives an empirical relationship, in which the volume percentage recrystallisation is related to $\mathrm{Ln}Z_i$ (Subramaniyan 1989).

$$\text{volume}\% = a + b \ln Z_i \qquad (2\text{-}22)$$

where volume% is the volume percentage recrystallisation, a and b are constants, Z_i is the Zener-Holomon parameter calculated using the initial temperature:

$$Z_i = \dot{\varepsilon} \exp(\frac{\Delta H}{RT_i}) \qquad (2\text{-}23)$$

where T_i is the initial temperature, ΔH is the activation energy for deformation, R is the universal gas constant.

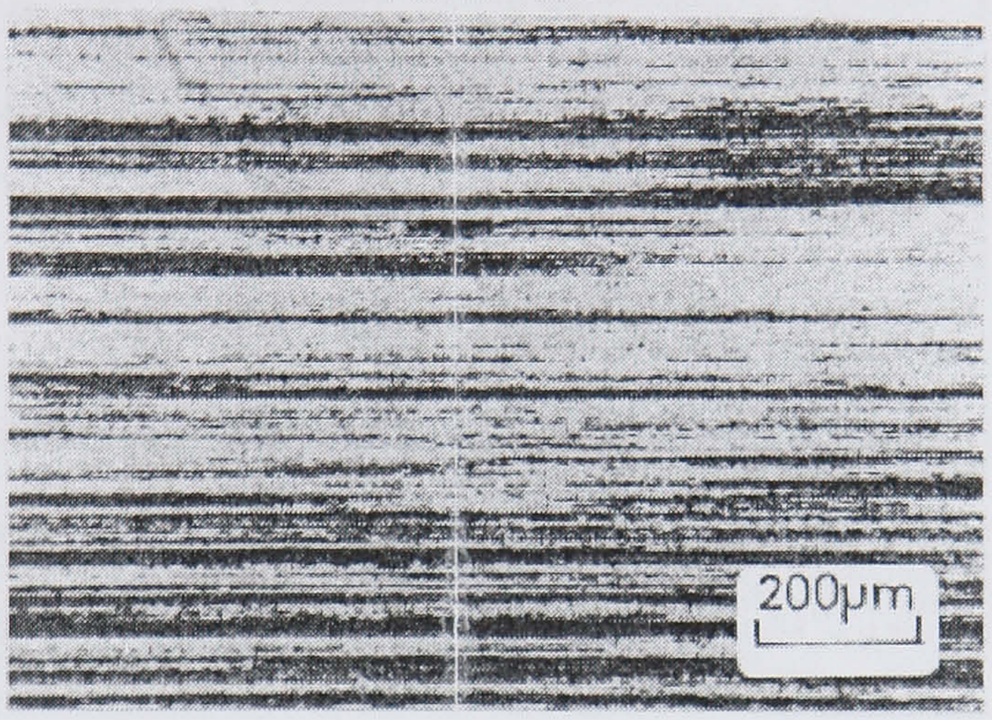

(a) 30:1, 338°C, 5 mm/sec

(b) 60:1, 353°C, 5 mm/sec

(c) 60:1, 468°C, 5 mm/sec

Figure 2.5 Optical micrographs of typical structures of the extrudate showing the fibrous, mixed and recrystallised morphologies possible (Castle 1974)

The relationship of equation 2-23 can only be regarded as an approximation, since the quench delay varies with the strain rate and, in addition, is virtually doubled during indirect extrusion due to the difference in the tooling arrangement. The constants a and b vary significantly for different alloys and depend heavily on the forming conditions. Therefore, precautions should be taken when using this type of empirical equation.

Heat treatments are usually applied after extrusion of heat treatable aluminium alloys to improve the mechanical qualities. Static recrystallisation usually occurs during this heat treatment, and the as extruded structures are replaced by a newly-formed grain structure (Sheppard, 1993, Nes et al. 2002, Sellars et al. 2003). Fully recrystallised structures are produced in all extrudates produced below an initial temperature of about 350°C for 2014 alloy.

Typical examples of longitudinal and transverse sections are shown in Figure 2.6, taken from a 350°C extrudate, showing full recrystallisation with an average grain size of 0.3 mm in the transverse direction (Subramanian 1989).

The extrusion conditions, such as the initial temperature, the ram speed and the condition of the heat treatment have great influence on the final product structures, and this is studied in detail in Chapter 4. One example of the influence of the initial extrusion temperature on the fraction recrystallised factor is shown in Figure 2.7.

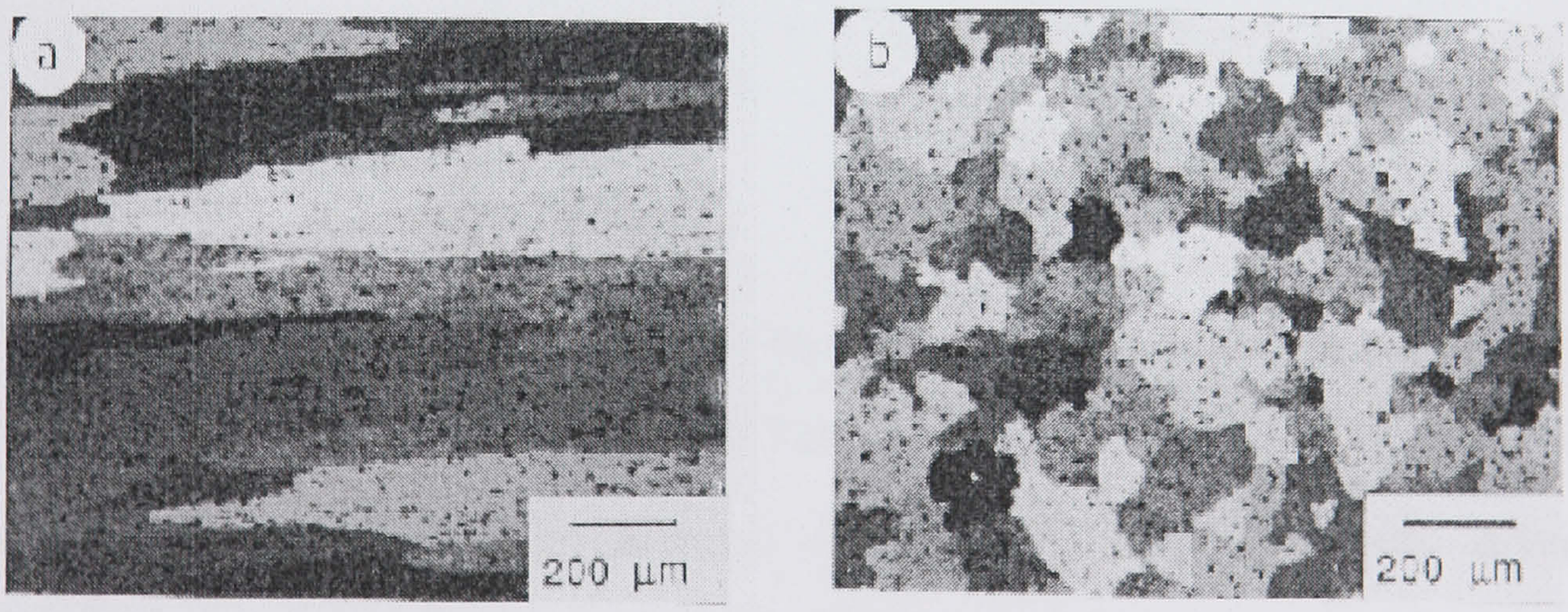

(a) Longitudinal (b) Transverse

Figure 2.6 350 °C extrudate, 0.5 hour soak, 500°C (Subramaniyan 1989)

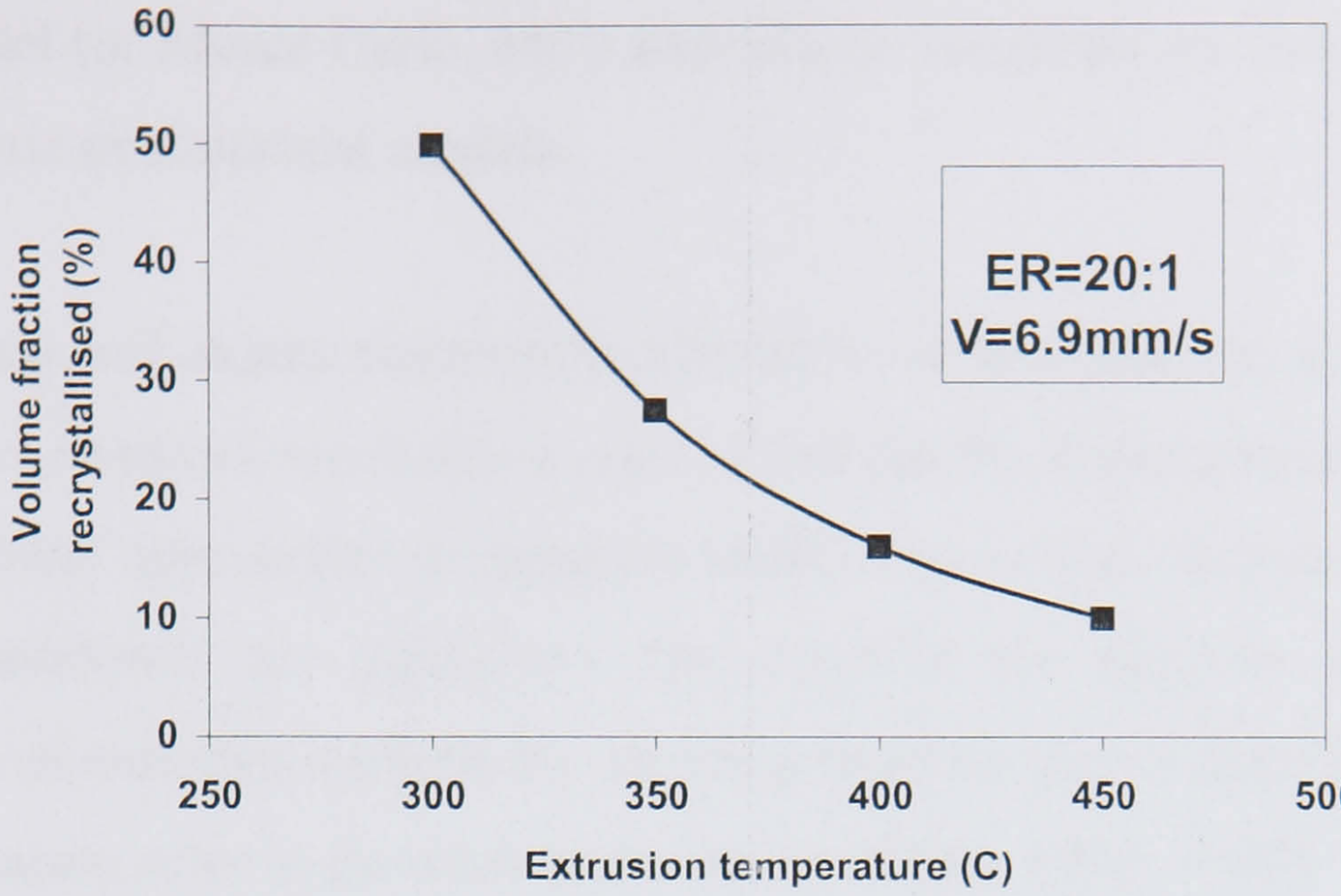

Figure 2.7 Volume percent recrystallised vs initial billet temperature for solutionised extrudates (Subramaniyan 1989)

2.3.2.3.3 Kinetics of Recrystallisation

The relationship between the volume fraction recrystallised (Xv) and the holding time (t) is generally represented by the Johnson-Mehl (1939)-Avrami (1939)-Kolmogorov (1937) equation (JMAK), which predicts the relationship between the volume fraction recrystallised (Xv) and the holding time (t) and is generally represented as:

$$Xv = 1 - \exp\{-0.693(\frac{t}{t_{50}})^{k}\} \qquad (2\text{-}24)$$

where t is annealing time, k is the Avrami exponent with a commonly reported value of 2, t_{50} is the time to 50% recrystallisation. For the calculation of t_{50}, the physical model is commonly regarded as the method of revealing the mechanics driving the transformation. Previous studies (Furu et al. 1999), have shown that the physical models describe the experimental results well for uniform processing conditions. The model was also successfully applied to tests in which the strain rate was increased (when microstructure transients were not observed). Recently, Sheppard and Duan (2003) have confirmed that the physical model will give better computed results than the empirical model in the simulation of aluminium extrusion. Only the physical model proposed by Furu et al. (1996) and Zhu and Sellars (2000) has been used in this study.

2.3.2.4 Cellular Automata (CA) and Potts model (MC)

Potts model (or Monte Carlo, MC) and cellular automata are two well known analogous probabilistic or statistical models.

The various techniques commonly referred to as Monte Carlo methods comprise direct approaches to mimic stochastic events which can be decomposed into isolated processes and statistical approaches to integrate multi-dimensional definite integrals numerically. Cellular automata are algorithms that describe the discrete spatial and/or temporal evolution of complex systems by applying local or global deterministic or probabilistic transformation rules to the sites in the lattice (Raabe 1998, 2002).

Computer simulation of grain growth and recrystallisaton was strongly stimulated in the early 1980s by the realisation that MC models could be applied to problems of grain structure evolution. By extension of the Ising model for domain modelling of magnetic domains to the Potts model, it was then possible to represent grains (domains) by regions of similarly oriented (lattice) points (Anderson et al. 1984, Baxter and Behringer 1991).

The simulation of recrystallisation by the CA method is reported by Hesselbarth and Gobel (1991), Pezzee and Dunand (1994). Davies (1995, 1997, 1999) also gave detailed discussions of the effect of neighbourhood and the possibility of the application of CA into aluminium rolling.

However, neither the MC model nor the CA model in their standard form is entirely satisfactory for studying boundary migration under the combined influence of two different driving forces (Zandler 1994, Sreekumar 1998). In grain growth, the driving force derives from the curvature of a boundary, for which the MC model is satisfactory. In primary recrystallisation, the driving force is the removal of stored dislocations by the migration of the recrystallisation front, for which the CA model is satisfactory. In both cases, we expect to find a linear relationship between driving force and migration rate (velocity). The actual behaviour of the MC model does not give this for stored energy as a driving force (except for low driving forces), and the CA model does not allow for boundary curvature as a driving force. Although both of the models have been developed extensively in the last decade and various hybrid models have been provided (Rollett and Raabe 2001), difficulty still exists in integrating the two methods without arbitrary

control by the user. In the following studies, only the CA model is adopted since most of the time only primary recrystallisation applies to the present research.

2.3.2.4.1 Definition of CA

Cellular automata are algorithms that describe the discrete spatial and/or temporal evolution of complex systems by applying local or global deterministic or probabilistic transformation rules to the sites of a lattice (Raabe 1998, 2002).

It is well known that a cellular automaton (CA) is an arrangement of cells characterised by three Features:

(1) The number and the kind of states a cell can possess

(2) The geometry and the definition of the neighbourhood of a cell

(3) The rules of transition for a CA that determine the state of each cell in the next time step, depending on the actual state of the cell, and the state of the cells in its neighbourhood.

Different definitions of neighbourhood that have been used in the previous studies are shown in Figure 2.8. A new type of neighbourhood is adopted in this study due to the elongated nature of the recrystallisation grain shape in the extrudate, as shown in Figure 2.8e.

It has been pointed out by Janssens (2003) that the main reason why the scientific community is searching for new computational approaches to simulate and predict recrystallization and grain growth processes is the heterogeneous nature of these processes.

The as deformed structures are spatially nonhomogeneous, however, the continuum theory at the present time has some difficulty in precisely simulating the heterogeneity at the process size (macro-) scale, although great improvements have been achieved in crystal modelling at the micro- or meso-scale in the last decade.

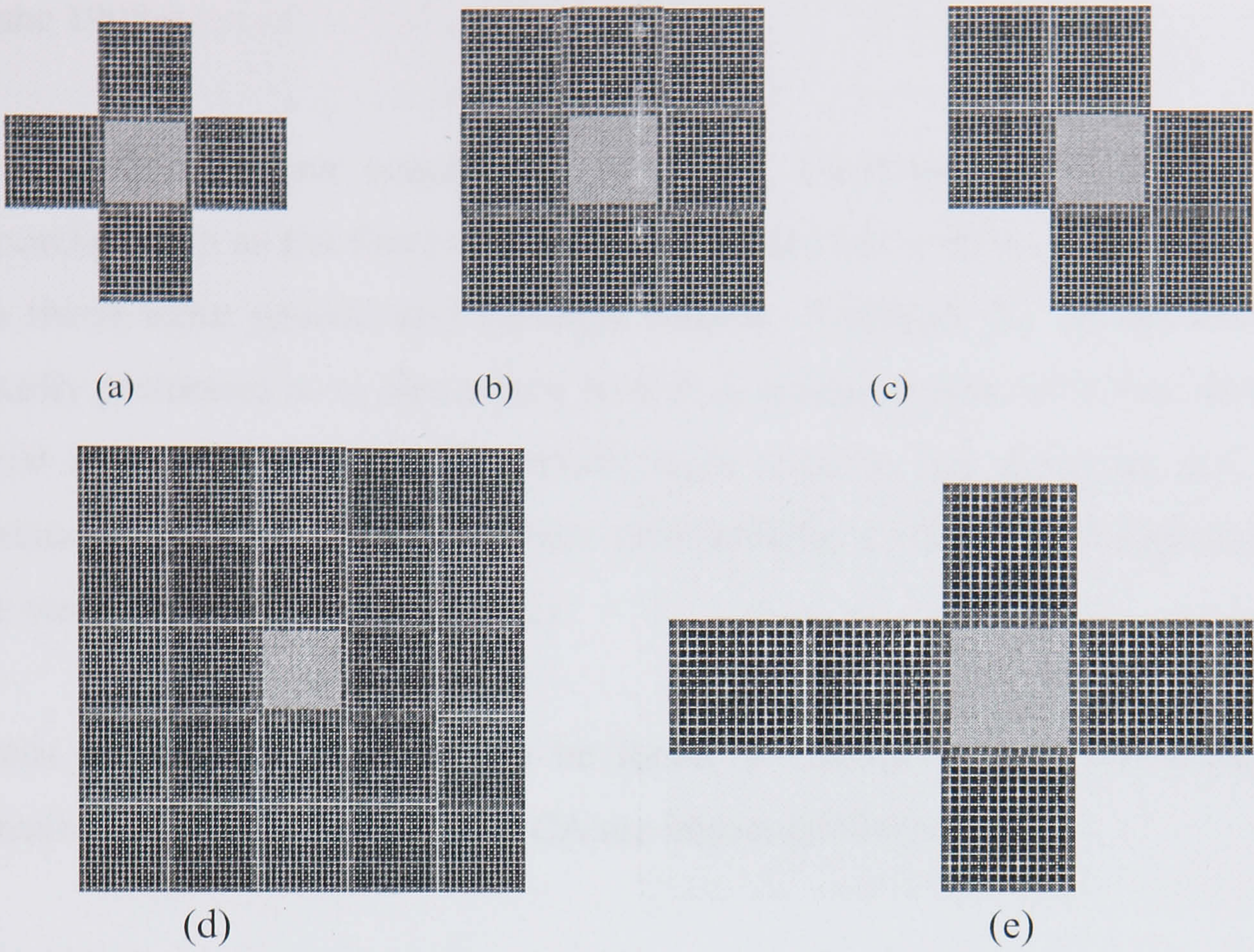

Figure 2.8 Definition of neighbourhoods: (a) Von Newmann, (b) Moore, (c) 7-cells-neighbourhood, (d) 25-cells-neighbourhood (e) side-prefer-neighbour

The crystal plasticity finite element model, which accounts for plastic deformation by crystallographic slip and for the rotation of the crystal lattice during deformation, could predict the deformation behaviour of one or several coalescing grains or subgrains, but was not fully capable of simulation of the deformation process at the macro-scale. The FEM simulation at the macro-scale did not take account of the material heterogeneity, however, it is still a powerful tool in predicting the necessary variables, such as strain, strain rate and stress, which are necessary for microstructure simulation. The recently developed physically based models relate the final recrystallised structure to the as deformed state, but it ignores the evolution process of the recrystallisation. Every method has its own merits and shortcomings. However, if the macro-scale FEM can be integrated with the physically based metallurgical model and CA, it could have a promising future in the simulation of structural evolution at different scales (macro-, micro and meso-scale).

By mapping the state variables on a two- or three-dimensional spatial grid, cellular automaton simulations are capable of accounting for microstructural inhomogeneities such as second phases, microbands, shear bands, transition bands, heterophase interfaces, grain boundaries, or twins. These local defect structures can be described in terms of

corresponding values of the state variables (such as temperature) or their gradients (Raabe 1998a).

The cellular automata concept is not simply identical to conventional simulation approaches such as the finite difference, finite element or Potts methods, but is defined in a much more general and versatile manner. Although CA simulations have been typically performed at an elementary level (e.g. atoms, clusters of atoms, dislocations), it should be emphasised that particularly those variants that discretise and map into a continuum space are not intrinsically calibrated by a characteristic physical length or time scale (Bolt 2005, Alonso 2005)

Details of discussion on CA can be found in Chapter 5, only the definition of the deterministic and the probabilistic CA are introduced below.

2.3.2.4.2 Deterministic CA

The local interaction of neighbouring sites in a cellular automaton is specified through a set of deterministic or stochastic transformation rules (Gallas et al. 1992, Grassberger 1983, Kagaris and Tragoudas 1977, Lopez et al. 1999). The value of an arbitrary state variable ξ assigned to a particular site at a time $(t_0 + \Delta t)$ is determined by its present state (t_0) (or its last few states $t_0, t_0 - \Delta t$, et al.) and the state of its neighbours. Considering the last two steps for the evolution of a one-dimensional cellular automaton, this can be expressed formally by writing

$$\xi_j^{t_0+\Delta t} = f(\xi_{j-1}^{t_0-\Delta t}, \xi_j^{t_0-\Delta t}, \xi_{j+1}^{t_0-\Delta t}, \xi_{j-1}^{t_0}, \xi_j^{t_0}, \xi_{j+1}^{t_0}) \qquad (2\text{-}25)$$

where $\xi_j^{t_0}$ indicates the value of the variable at a time t_0 at the node j. The positions $j+1$ and $j-1$ indicate the nodes in the immediate neighbourhood of position j. The function f specifies the set of transformation rules, such as provided by standard finite difference algorithms. The value of a variable at a node is derived from the state of the neighbours through the employment of transformation rules. These rules are identical at each node. However, nonhomogeneous materials are more easily simulated by assigning corresponding properties to the state of the nodes and exploiting the huge variety of

possible switching rules rather than by changing the transformation laws locally. The simulation of microstructure evolution with consideration of stochastic processes can be achieved by rendering deterministic into probabilistic transformation rules (Raabe, 1998b).

2.3.2.4.3 Probabilistic CA

In order to avoid confusion when discussing nondeterministic cellular automata, one must clearly indicate the stochastic element that appears in the algorithm (Pemantle 2005, Adell and Sanguesa 2005, Makowice 1993, Meghdadi 2002). There are essentially two possible ways of transforming a deterministic cellular automaton into a nondeterministic one. The first approach consists in selecting the investigated lattice sites randomly, rather than systematically in sequential order, but using a deterministic transformation law. The second approach consists in using a probabilistic instead of a deterministic transformation law. Probabilistic cellular automata are in their elementary setup very similar to conventional cellular automata, except for the fact that the transition rules are stochastic rather than deterministic. The local switching probability can be quantified by the ratio of the local and the maximum mobility m^{local}/m^{max}, which is a function of the grain boundary character and by the ratio of the local and the maximum driving pressure p^{local}/p^{max}.

$$\hat{w}^{local} = \left(\frac{m^{local} p^{local}}{m^{max} p^{max}}\right) = \left(\frac{\dot{x}^{local}}{\dot{x}^{max}}\right) = \left(\frac{t^{max}}{t^{local}}\right) \tag{2-26}$$

t is the local time required by a grain boundary with velocity $\dot{x}$ to cross the automation cell. The detail of the transition rule can be found in Raabe's work (1998).

2.4 Product quality control

With the different models introduced before, there is a great potential to apply numerical simulation to the extrusion process to improve the product quality.

During extrusion, imperfections in the quality of the extrudate may arise, ranging from a rough or uneven surface to a complete severance of the extrudate. The quality of the

extrudate can be measured by the degree of internal precision (substructure. grain size. metallurgical structure, precipitates, non-homogeneous metal flow, variation of structure across the extrudate, etc.), external defects (surface finish), geometrical tolerances and mechanical physical properties. The mechanical properties are mostly dependent on the internal structural variations (Wang et al. 2001.Bunting 1983, Venkatesan 2003. Taver 2004, Potente 1996). The surface finish of the product is as important as the mechanical properties, and the control of defects is often the deciding factor in determining the extrusion conditions. Defects that may occur vary from visible blemishes such as cracks (Clode and Sheppard 1990), blisters, and die lines, to invisible ones that show up after anodising. In high-strength aluminium alloys where die lines and surface scoring have only secondary importance to the mechanical property requirements (because the surface often has to be machined to remove recrystallized layers) the defect is tolerated provided the die lines are not so coarse that stress concentrations arise (Sheppard 1993).

The peripheral coarse grain (PCG) is also identified as one of the common defects in all alloys. the factors affecting recrystallisation in the outer band grain structure are: the degree of deformation (extrusion ratio); exit temperature; alloy composition, with particular reference to its transitional element (Mn, Cr, Zr) content; metallurgical structure of the alloy, with particular reference to the changes taking place in it during extrusion; and flow stress, the solvus, solidus and recrystallisation temperatures of the alloy under the given extrusion conditions.

Various methods have been forwarded to minimise the defects. One important means is isothermal extrusion. The isothermal extrusion process has the potential to maximise productivity and product quality (Bryant 1999).

2.4.1 Surface cracking

Surface cracking is generally recognised as one of the main defects occurring during the process of aluminium extrusion, especially in the case of the so-called hard aluminium alloys (Kaida 1997, Gupta and Hughes 1979, Onawola and Adeyemi 2003) For the 4% Cu alloys, surface cracking (or speed cracking) is a major problem, especially at high temperatures and strain rates. Previous experiments suggest that this type of defect is caused by the rise in temperature as the process proceeds. Some other experiments

indicate the surface quality is good even though the temperature may be high during extrusion.

Since the product must be scrapped due to poor surface quality and inferior mechanical properties, it is of primary importance to study the occurrence of surface cracking in the extrusion of hard alloys.

In order to evaluate surface cracking the extrudates have been placed into one of three categories (Sheppard and Raybould 1973a, Dixon 2004).

A – No evidence of cracking.

B – Cracking commences at some distance along the extrudate.

C – Cracking occurs along the entire length of the extrudate increasing in severity as extrusion proceeds.

Typical examples of these three categories are shown in Figure 2.9, the examples are taken from the same position along the extrudate length corresponding to a position at 0.5L, i.e. halfway along the extrudate length. Detail study on surface cracking can be found in Chapter 6.

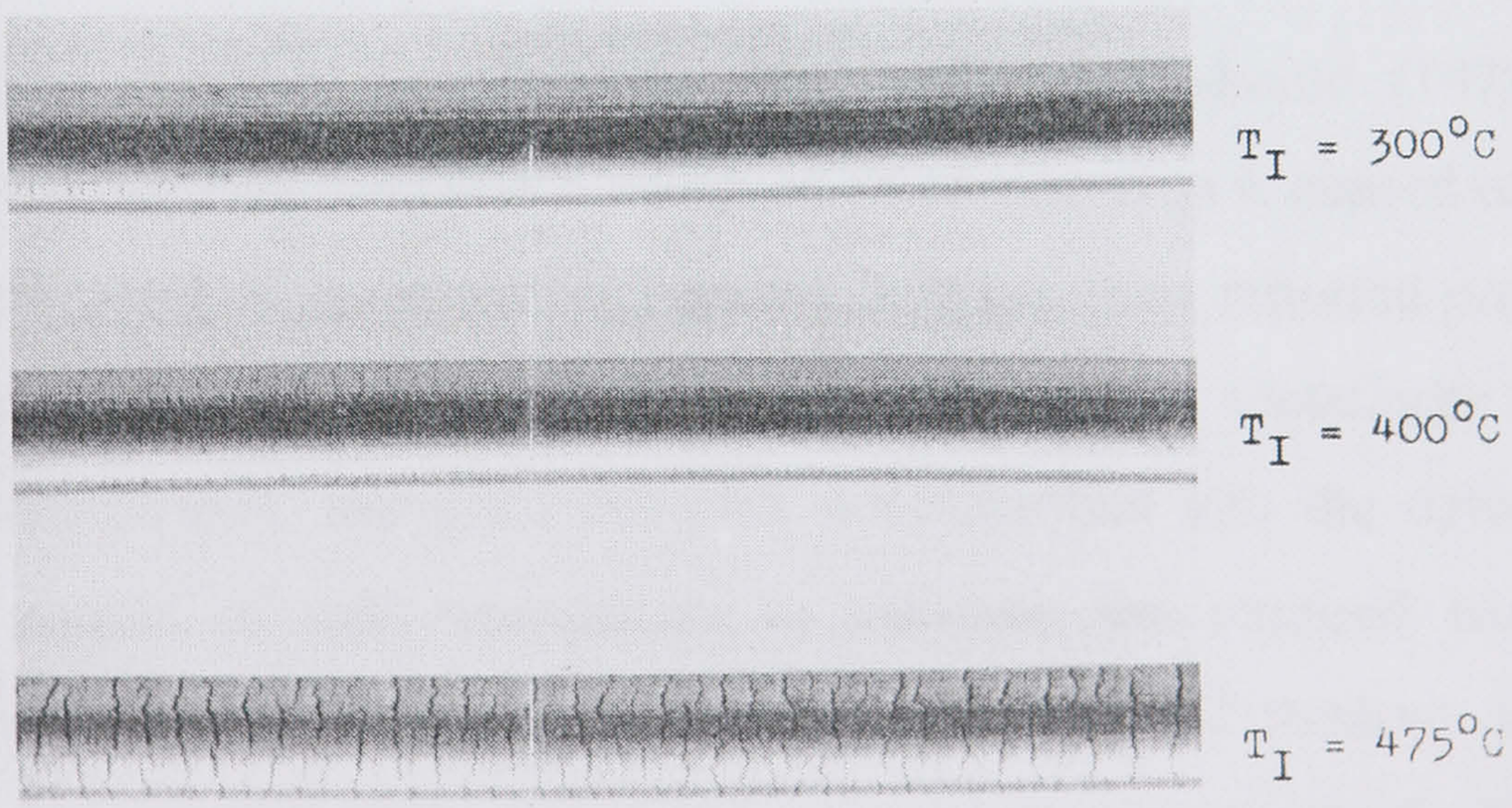

Figure 2.9 Three categories of surface cracking (Sheppard 1993)

2.4.2 Microstructure control

Dynamic recovery and static recrystallisation are the most common plasticity restoration processes that occur during aluminium alloy extrusion. The size of subgrains, resulting from recovery, and the recrystallised grains are closely related to the conditions of extrusion process and the subsequent heat treatment. Ideally, the reaction of the substructure to solution soaking should be subgrain coalescence without recrystallisation, but if static recrystallisation is to occur then the extrusion conditions must be controlled to ensure a uniform small recrystallised grain size (Sheppard 1999). In fact, the process conditions, the structure and properties of the extrusion product interact with each other and therefore it is important to control the microstructure to obtain the best quality by optimising the extrusion parameters.

2.4.3 Effect of isothermal extrusion

Isothermal extrusion is defined as an extrusion procedure which results in the extrudate leaving the die at a constant temperature. Although there are difficulties in temperature control, significant gains in productivity and product quality can be realised by adopting processes and process controls to achieve "close to" isothermal conditions.

2.4.3.1 Benefit of isothermal extrusion

Referring to the limit diagram developed by Sheppard and Raybould (1973c), the maximum productivity ignoring structure is achieved when extrusion is carried out at the apex of the operation window, as shown in Figure 1.2. It has been reported previously that the process variables, such as the ram speed, ram load, billet metallurgy and the different tooling temperatures, introduce complex nonlinearities into the deformation equations so that control of exit temperature to maintain the required isothermal condition is difficult to achieve. However, the sophistication of modern radiation pyrometry and the cyclic nature of the commercial extrusion process, which allows for iterative changes, have increased the possibility of developing algorithms for satisfactory feedback control for isothermal operation (Bryant, 1999). There is the added fact that accurate simulation could negate temperature measurement.

2.4.3.2 Establishment of isothermal extrusion

Numerous methods have been or are being adopted to achieve isothermal extrusion operation, these may be divided into two types:

(1) Setting up a longitudinal thermal gradient in the billet (tapered billet) before feeding it to the press.

This is done by applying differential heating along the billet length in the preheat furnace (taper heating) or by applying a differential quench to the billet during its travel from preheat furnace exit to the press (taper quenching). In direct extrusion, the hot end of the billet would be placed at the front of the container against the die. The cold end would then be heated by frictional deformation resistance during the extrusion stroke.

(2) Controlling extrudate exit temperature by varying ram speed.

In this case, which is an example of the principle of feedback control, the ram speed and exit temperature are continuously measured and transmitted to a microprocessor. The ram speed is then adjusted in the appropriate sense to maintain constant exit temperature.

There are also numerous examples of in-plant attempts to achieve isothermal or near isothermal extrusion based on ram load or some expert knowledge and shop-floor experience to set up the appropriate control procedures.

For the first method mentioned above, the "longitudinal thermal gradient" can be linear, i.e. the temperature decreasing linearly from the front to the back end of the billet, or the gradient can be non-linear, in which the temperature decreases more rapidly in the front part of the billet than in the rear. Some results of process optimisation by linear temperature gradient have been presented by SMS Schloemann (Biswas 1996), and recently some studies concerning non-linear gradients were also reported (L Li et al. 2003). Detail study on isothermal extrusion can be found in Chapter 7.

2.5 Application of Integrated FEM simulation into extrusion process

The "modelling" and "simulation" are classified by different approaches. Often they are simply grouped according to their underlying characteristic scale. A coarse spatial subdivision would suggest four classes of models, namely, macroscopic (refers to the sample geometry), mesoscopic (lattice defect ensembles at the grain scale), microscopic (lattice defects below grain scale), and nanoscopic models (atomic level). However, the most commonly used classification is by the field the modelling is applied to, for example, thermo-mechanical modelling and structural modelling.

Figure 2.9 illustrates the interactions in thermo-mechanical process modelling at the 'macro' level. Given the volume of detailed FE output about the distribution of deformation and temperature history, there is great potential to exploit this output for microstructure modelling (Evans 1993).

In most cases, microstructure modelling will be a 'post-processing' activity, but, in more complex situations, microstructure prediction may be in parallel, determining the constitutive response of the material in the next time-step. Figure 2.10 summarises the necessary inputs required for process modelling at this 'micro' level. It is clear that there is potential great 'added value' that may be obtained by incorporating microstructure modelling, in particular offering:

(1) Wider scope for predicting properties, damage and subsequent material process-ability.

(2) Linking upstream and downstream material behaviour through multi-stage process histories.

It is the modelling interactions illustrated in Figures 2.10 and 2.11 that currently provide the most fertile opportunities for collaborative research between academia and industry.

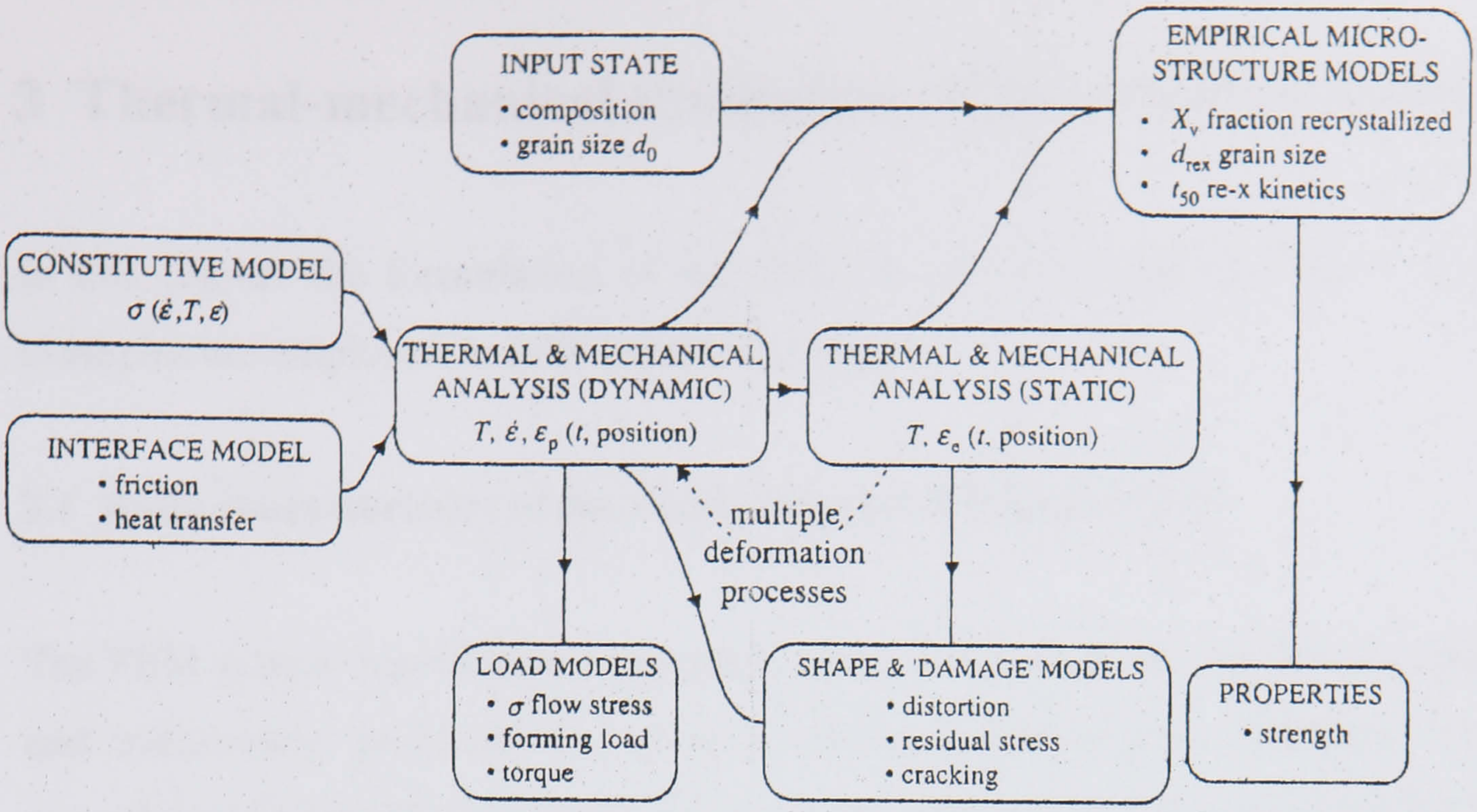

Figure 2.10 Thermo-mechanical process modelling: sub-models and connectivity at the 'macro' level (Shercliff and Lovatt 1999)

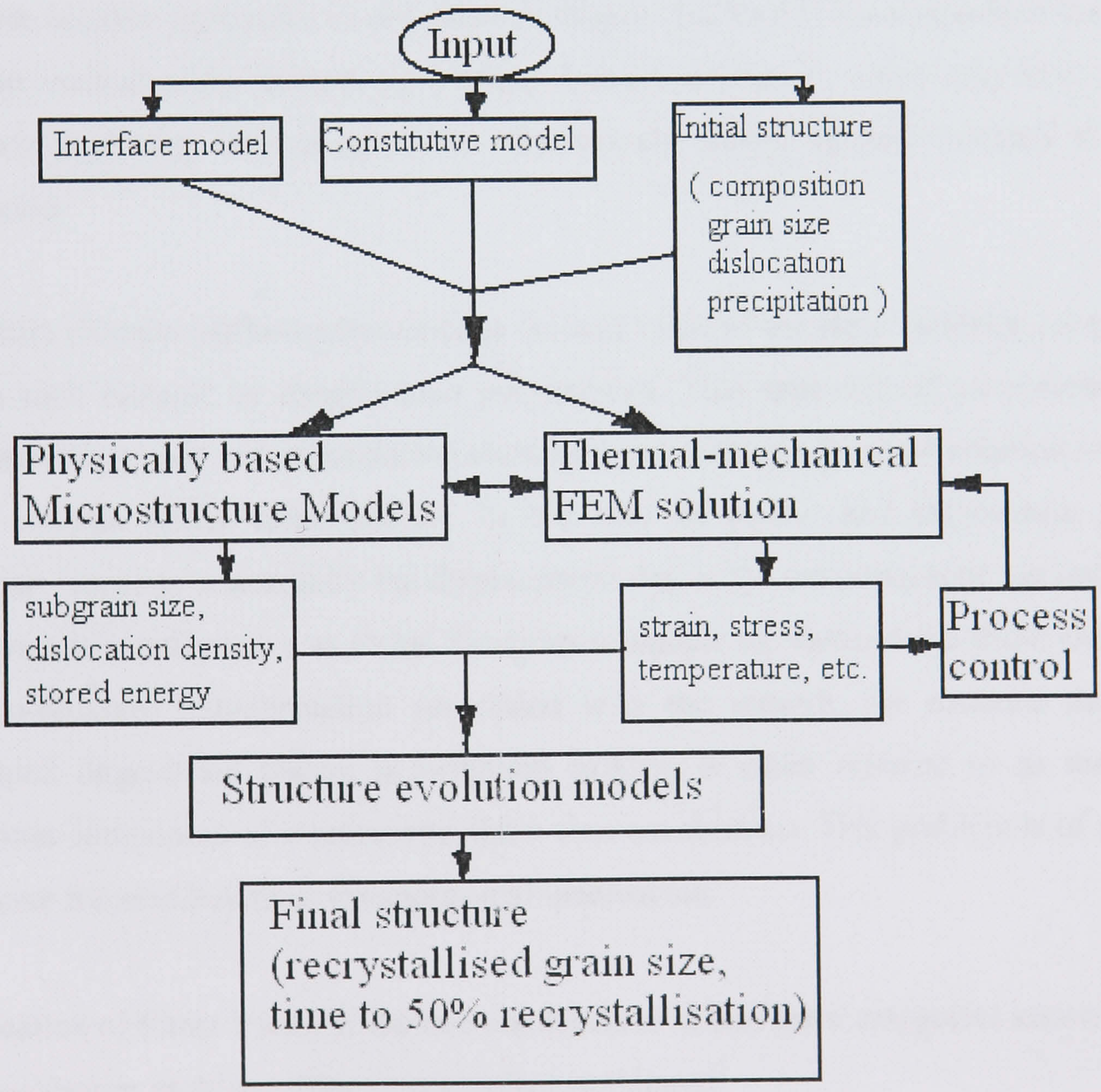

Figure 2.11 Thermo-mechanical process modelling: sub-models and connectivity at the 'micro' level

3 Thermal-mechanical simulation of the extrusion process

In this chapter the formulation of the FEM code is investigated and 2-D simulation examples are employed to fully validate its use.

3.1 Basic characteristics of the Finite Element Method (FEM)

The FEM is now regarded as a powerful method for obtaining solutions to boundary- and initial-value problems by using polynomial interpolation functions. The FEM procedures are employed extensively in the analysis of solids and structures and of heat transfer and fluids, and indeed, finite element methods are useful in virtually every field of engineering analysis (Bathe 1982). In contrast to analytical techniques, finite elements are also applicable to complicated shapes. The basic characteristic of the finite element method is the discretisation of the domain of interest, which may have nearly arbitrary geometry, into an assembly of relatively simply shaped elements that are connected.

The finite element method approximates the real value of the state variables considered within each element by interpolation polynomials. This approach of interpolating the variable within each cell amounts to assuming a piecewise polynomial solution over the entire domain under consideration. In the case of elastic and large-strain plastic materials response it is usually the displacement that is the unknown state variable. The polynomials usually serve as shape functions to update the form of the finite elements. The co-ordinate transformation associated with the remesh, for instance during a simulated large-strain plastic deformation process is often referred to as the most important component of a successful finite element solution. This problem is of special relevance for simulations at the meso- and macroscale.

Application of Finite Element Method can be divided into three categories known as:

(1) equilibrium problems (time independent problems)

(2) eigenvalue problems

(3) propagation problems (time dependent problems)

3.1.1 Finite Element Procedure

The most widely used finite element formulation in solid mechanics is the displacement approach. The displacement field within the element is defined in terms of assumed functions (interpolation functions) and unknown parameters at the nodes which are either displacements or displacement related quantities such as slopes and curvatures. For each finite element, a displacement function in terms of the element coordinates (x, y, z) and the nodal displacement parameters is chosen to represent the displacement field, and thereby the strain and stress, within the element. A stiffness matrix relating the nodal forces to the nodal displacements can be derived through the application of the principle of virtual work or the principle of minimum total potential energy. The stiffness matrices of all the elements in the domain can be assembled to form the overall stiffness matrix for the system. After modifying the global stiffness matrix in accordance with the boundary conditions and establishing the force vector, the system of equations can be solved to yield firstly the nodal displacements, and then subsequently the stresses at any point in each individual element.

The steps of a finite element analysis can be summarised as follows (Cheung 1996, p5):

1. Discretisation of the problem domain into finite elements.
2. Selection of nodal displacement parameters and element interpolation functions.
3. Evaluation of individual element properties.
4. Assembly of system stiffness matrix.
5. Introduction of boundary conditions.
6. Formation of global force vector.
7. Solution of system matrix equations for nodal displacements.
8. Additional calculation for stresses and other parameters.

3.1.2 The equilibrium equation in FE simulations

Depending on the character of the material response to external and internal loads, the material dynamics are conveniently described in terms of the "strong form" of the differential equation of motion, the "weak form" of the virtual work principle, or the stable equilibrium quantified by the "minimum mechanical energy".

A simple straightforward approach to deriving the equations for displacement-based finite element codes starts from the general principle of virtual work. This is the work done by arbitrary small virtual displacements due to the forces and moments acting on a solid body in accord with continuity and displacement boundary constraints. For the most general cases this principle can be written as:

$$\delta\bar{W} = \iiint_V \sigma_{ij}\delta\bar{\varepsilon}_{ij}dV = \iiint_V P_j\delta\bar{u}_j dV + \iint_S T_j\delta\bar{u}_j dS + F_j\delta\bar{u}_j \qquad (3.1)$$

where $\delta\bar{W}$ is the virtual work which results from the strain due to the virtual displacements $\delta\bar{\varepsilon}$ that act on the stresses σ. This work equals the sum of the virtual work which results from the virtual displacements $\delta\bar{u}$ due to the body force **P**, to the traction **T**, and to point forces **F**. **S** is the surface that enclosed the volume **V**.

Equation 3.1 is generally valid for an arbitrary body. However, the finite element method decomposes the solid under investigation into a large number n of simply shaped volume elements which are connected at nodes. Thus, equation 3.1 applies for each individual element under implicit consideration of equilibrium and compatibility. The course of the displacement is approximated in each finite element by interpolation polynomials that enter all n equations of the form of equation 3.1. This amounts to calculating the volume and surface integrals over each finite segment individually and subsequently summing up all elements. Assuming that the point forces are only applied at the nodal points, equation 3.1 may then be rewritten

$$\sum_n \iiint_V \sigma_{ij}\delta\hat{\varepsilon}_{ij}dV = \sum_n \iiint_V P_j\delta\hat{u}_j dV + \sum_n \iint_S T_j\delta\hat{u}_j dS + \sum_n F_j\delta\hat{u}_j \qquad (3.2)$$

3.1.3 Finite Element kinematical description

The Algorithms of continuum mechanics usually make use of two classical descriptions of motion: the Lagrangian description and the Eulerian description (Malvern 1969).

Lagrangian algorithms, in which each individual node of the computational mesh follows the associated material particle during motion, are mainly used in structural mechanics.

The Lagrangian description allows an easy tracking of free surfaces and interfaces between different materials. It also facilitates the treatment of materials with history-dependent constitutive relations. Its weakness is its inability to follow large distortions of the computational domain without recourse to frequent remeshing operations.

Eulerian algorithms are widely used in fluid dynamics. The computational mesh is fixed and the continuum moves with respect to the mesh. In the Eulerian description, large distortions in the continuum motion can be handled with relative ease, but generally at the expense of precise interface definition and the resolution of flow details.

Because of the shortcoming of purely Lagrangian and purely Eulerian descriptions, a technique has been developed that succeeds, to a certain extent, in combining the best features of both the Lagrangian and the Eulerian approaches. Such a technique is known as the arbitrary Lagrangian-Eulerian (ALE) description. In the ALE description, the nodes of the computational mesh may be moved with the continuum in normal Lagrangian fashion, or be held fixed in Eulerian manner, or be moved in some arbitrary specified way to give a continuous remesh capability. Because of this freedom in moving the computational mesh offered by the ALE description, greater distortions of the continuum can be handled than would be allowed by a purely Lagrangian method, with more resolution than that afforded by a purely Eulerian approach.

3.1.4 Finite element discretisation and element type

The first step of a finite element analysis is to divide the continuum or problem domain into valid finite elements. The discretisation of the problem domain involves a decision on the number, size and shape of sub regions used to model the real structure. The element should be small enough to give useful results and large enough to reduce the computational effort. The actual discretisation process can be divided into two parts - the division of the system into elements and the labelling of the elements and nodes (Cheung 1996, p5).

Figure 3.1 shows the basic shapes available (Fagan 1992, p23) in the finite element method. As might be expected, they range from a single point through to volumes or

three-dimensional shapes. Before choosing the element type, the engineer should try to predict what is taking place in the problem to be examined. The finite element method works by approximating the distribution of an unknown variable in a precise manner across the body to be analysed. The size and number of elements in a finite element model are clearly inversely related. As the number of elements increase, the size of each element must decrease, and consequently the accuracy of the model generally increases.

Shape	Type	Geometry
Point	Mass	
Line	Spring, beam, spar, gap	
Area	2D solid, axisymmetric solid, plate	
Curved area	Shell	
Volume	3D solid	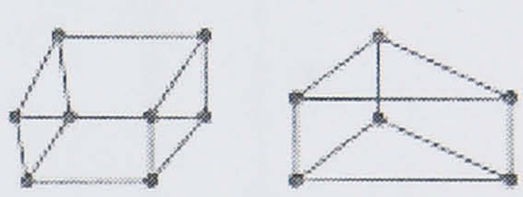

Figure 3.1 Basic element shapes (Fagan 1992, p. 23)

The unknown variables are only reliably produced if the shapes of the elements are not excessively distorted. As element distortion increases, so errors in the element formulations start to become increasingly important. The allowable limits of distortion are difficult to quantify, and depend very much on the variable distribution that the elements are representing. The two methods of assessing element distortion are known as:

(1) Aspect ratio, which is the ratio of the longest side of an element to the shortest side, as illustrated in Figure 3.2.

(2) Internal angles of the element. Rectangular elements should include angles as close to 90° as possible, whereas the corners of triangular elements should be near to 60°.

The range of allowable distortion may vary from problem to problem, but as a guide, if no other information is available, the values suggested in Figure 3.3 may be used.

The finite element discretisation is outlined with the mixed velocity and pressure formulation and the time discretisation is presented with the incremental contact problem.

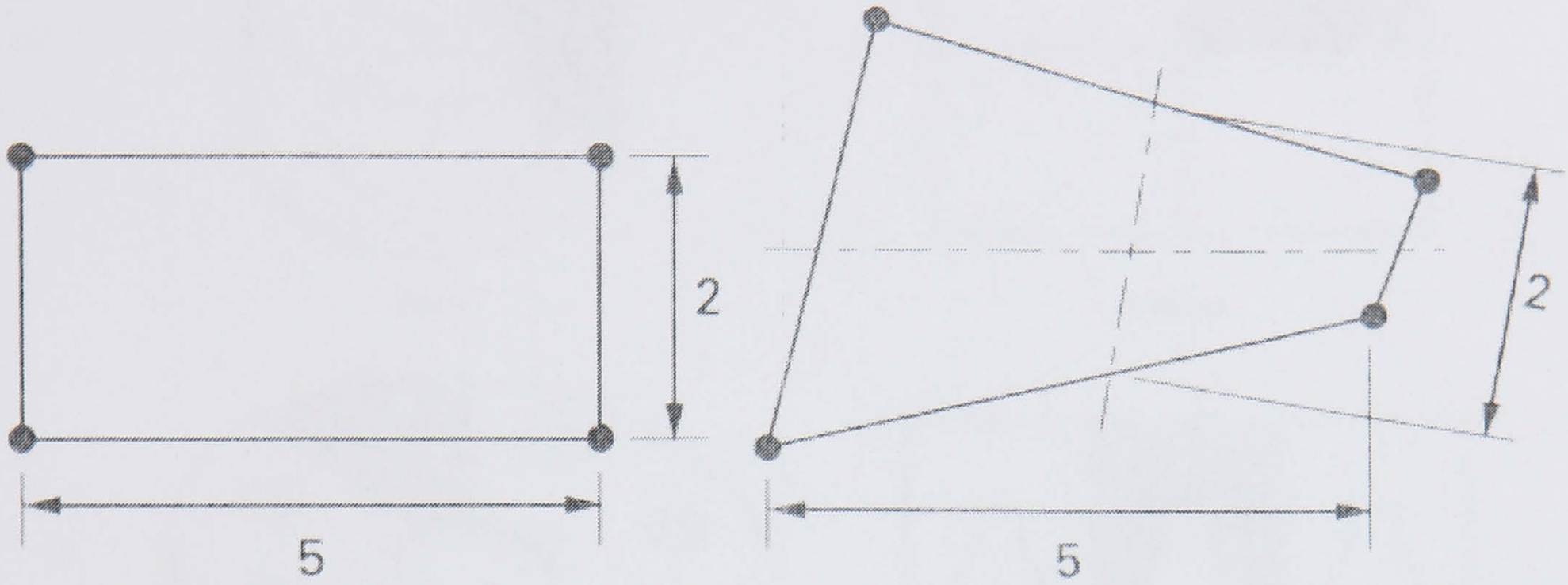

Aspect ratio = 2.5 Aspect ratio = 2.5

Aspect ratio = 2 Aspect ratio = 1

Figure 3.2 Examples of aspect ratio, to measure element distortion

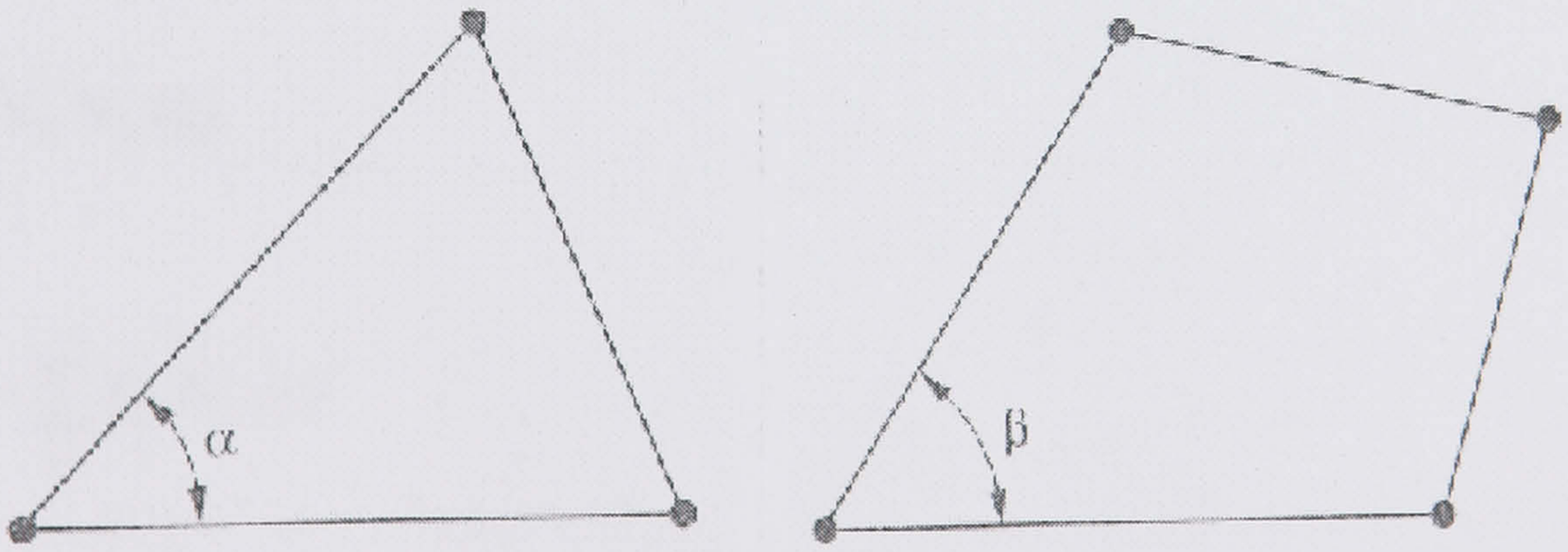

$45° < \alpha < 75°$ $45° < \beta < 135°$

Figure 3.3 Allowable element distortions

Symmetry is the most effective way to improve the efficiency of FEM calculations. If the configuration of the body and the external conditions (i.e. boundary conditions) are

similarly symmetric, then only the repeated part of the structure needs to be modelled. There are four common types of symmetry encountered in engineering problems: axial, planar, cyclic and repetitive, as illustrated in Figure 3.4.

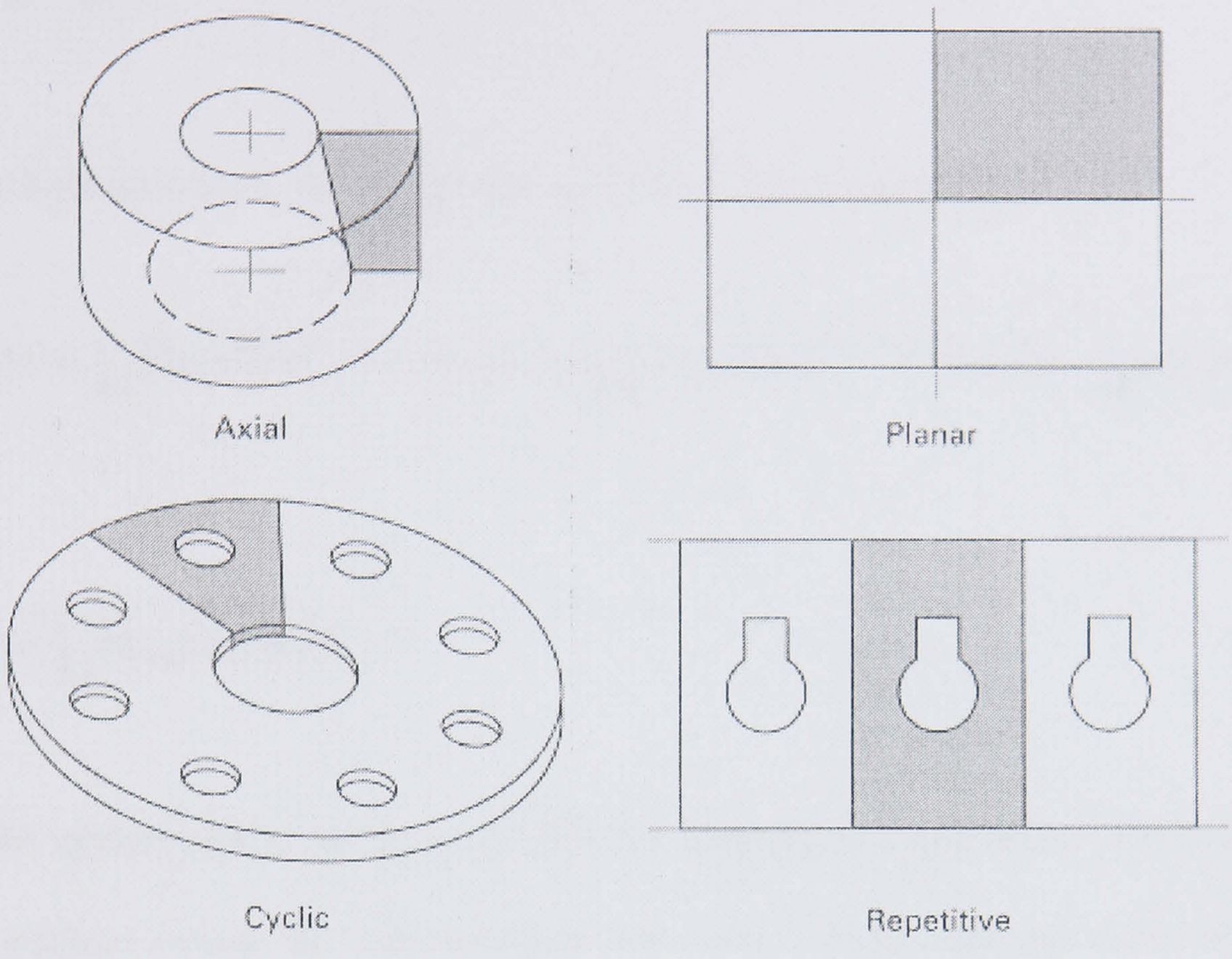

Figure 3.4 Types of symmetry

3.1.5 Increment approach

Using isoparametric elements, the velocity field v, is discretised with the help of the nodal velocity vectors V_n, shape functions N_n and local co-ordinate vector ξ as:

$$v = \sum_n V_n N_n(\xi) \tag{3-3}$$

$$\text{and } x = \sum_n X_n N_n(\xi) \tag{3-4}$$

the strain rate tensor is expressed with the B operator:

$$\dot{\varepsilon} = \sum_n V_n B_b \tag{3-5}$$

Similarly the pressure field is discretised in terms of nodal pressure P_m . with compatible shape functions M_m :

$$p = \sum_m P_m M_m(\xi) \tag{3-6}$$

for the mixed approach, we obtain the set of non-linear equations

$$R_n^V(V,P) = \int_\Omega 2K(\sqrt{3}\dot{\bar{\varepsilon}})^{m-1}\dot{\varepsilon} : B_n dV + \int_{\partial\Omega_C} \alpha_f K|\Delta v|^{p-1}\Delta v N_n dS - \int_\Omega p\,tr(B_n)dV = 0 \tag{3-7}$$

$$R_m^P(V) = \int_\Omega M_m \,div(v)dV = 0 \tag{3-8}$$

The nodal update can be performed with the simplest scheme (Euler explicit). If X_n^t is the co-ordinate vector of node number n at time t, with velocity vector V_n^t, at time $t + \Delta t$ the new co-ordinate vector will be:

$$X_n^{t+\Delta t} = X_n^t + \Delta t V_n^t \tag{3-9}$$

A semi implicit second order scheme was shown to improve the accuracy (Surdon 1987):

$$X_n^{t+\Delta t} = X_n^t + \frac{1}{2}\Delta t(V_n^t + V_n^{t+\Delta t}) \tag{3-10}$$

3.1.6 Constitutive equation

Three constitutive equations, the Norton Hoff law, the hyperbolic sine function and the Hansel-Spittle's model, have usually been adopted in those FEM simulations using a commercial code (Transvalor 2001).

The exponential form of the Norton Hoff law is written as (Transvalor 2001):

$$\bar{\sigma} = K \cdot \exp(\beta T) \cdot \dot{\bar{\varepsilon}}^m (\bar{\varepsilon} + \bar{\varepsilon}_0)^n \tag{3-11}$$

where K, β are material constants, m is the strain rate sensitively index, which ranges between 0.1 and 0.2 for ordinary metals, and between 0.5 and 0.7 for superplastic metals. n is the strain-hardening index, $\bar{\varepsilon}$ is the equivalent strain, $\dot{\bar{\varepsilon}}$ is the equivalent stain rate, $\bar{\varepsilon}_0$ is a small constant (Transvalor 2001). Critically the formulation does not include any term related to the physical state.

To describe the deformation of aluminium alloys the most commonly used equation is that proposed by Zener and then by Sellars (1973) and subsequently modified by Sheppard and Wright (1979) to yield the steady state flow stress $\bar{\sigma}$ as:

$$\bar{\sigma} = \frac{1}{a} \mathrm{Ln}\left\{\left(\frac{Z}{A}\right)^{1/n} + \sqrt{\left(\frac{Z}{A}\right)^{2/n} + 1}\right\} \tag{3-12}$$

where the Zener-Hollomon parameter Z is given by:

$$Z = \dot{\varepsilon} \exp\left\{\frac{\Delta H}{GT}\right\} = A[\sinh(a\sigma)]^n \tag{3-13}$$

$\dot{\varepsilon}$ is the strain rate, G is the universal gas constant (8.314 J $\mathrm{mol}^{-1}\mathrm{K}^{-1}$), ΔH is the activation energy, T is the absolute temperature, and A, a, n are constants. Here ΔH is closely related to the activation energy for self diffusion.

The flow stress is given as a function of the process parameters and the constants are established experimentally. The relationship is widely used both in extrusion and rolling (Sheppard and Richards 1987, Raghunathan 1989, Sheppard and Jackson 1997) and has been used by the aluminium industry for on-line control in extrusion and tandem mill rolling. The criticism of the equation is that it says nothing concerning the structural events occurring and does not consider the evolution of structure, which determines the current flow stress for subsequent operations. However, it has been shown that the Z parameter is important both in the development and definition of the flow structure.

The Hansel-Spittle's model is expressed as:

$$\overline{\sigma} = Ae^{m_1 T}\overline{\varepsilon}^{m_2}\dot{\overline{\varepsilon}}^{m_3}e^{m_4/\overline{\varepsilon}} \tag{3-14}$$

A, m_1, m_2, m_3, m_4 are constant (Spittel et al. 1990, Transvalor 2001). It is a purely empirical equation that is regressed from experimental results.

Among the three constitutive equations, the hyperbolic-sine function is the only one revealing the physical nature of the flow stress and can be derived without the need for statistical analysis, while the other two are pure empirical methods with the tuneable constants to comprise experimental measurements (Sheppard 1999a).

3.1.7 Friction Model

The locally varying and time-dependent friction values in the contact zone between workpiece and tools represent one of the required boundary conditions. The value of the friction influences the calculated contact shear stresses and, hence, the accuracy of the numerical process model. The friction values used in numerical modelling are either estimated on the basis of knowledge and experience or determined using tribological model tests. To what extent the friction values obtained in a model test apply to the process to be modelled essentially depends on how accurate the model test reflects its tribological conditions and dominating wear mechanism. The tribological conditions in forming at elevated temperatures are very complex and can only be determined with the help of a numerical model. The local and time-dependent distributions of contact temperature, contact normal stress, sliding length and sliding velocity are especially important.

Three kinds of friction laws are commonly employed in the metal forming process: Tresca, Viscoplastic and Coulomb. The Tresca friction law developed by using the Tresca yield criterion is written in the following form:

$$\tau = -m\tau_{max} \tag{3-15}$$

where τ_{max} is a property of the material m is commonly referred to as a friction factor. ΔV is the velocity difference at the interface. The Tresca law treats the interface friction as pressure independent and relates the friction stress directly to the yield strength of the deformed material. When $m = 1$, sticking friction occurs. The range of m is $0 \le m \le 1$. This development of friction is the most used in numerical analysis of hot deformation processes.

The viscoplastic friction law arises from the consideration of a thin interface layer of a viscoplastic lubricant between the workpiece and tool. The Viscoplastic friction law is written in the following form:

$$\tau = -aK\Delta V^{p-1}\Delta \mathbf{V} \tag{3-16}$$

where a is a Viscoplastic friction coefficient and $0 \le a \le 1$, which is a function of the normal stress. p is the sensitivity parameter to the sliding velocity. K is the consistency of the material, which is defined by:

$$K = K_0(\bar{\varepsilon}_0 + \bar{\varepsilon})^n \exp(\beta / T) \tag{3-17}$$

K_0 is a constant. $\bar{\varepsilon}_0$ is the term of strain hardening regulation. n is the strain-hardening sensitivity, β is the temperature term.

The modified Coulomb friction law can be written as:

$$\tau = \mu\sigma_n \qquad \text{if } \mu\sigma_n < \frac{\bar{\sigma}}{\sqrt{3}} \tag{3-18}$$

and

$$\tau = m\frac{\bar{\sigma}}{\sqrt{3}} \qquad \text{if } \mu\sigma_n \ge m\frac{\bar{\sigma}}{\sqrt{3}} \tag{3-19}$$

where $\bar{\sigma}$ is the von Mises stress. With this relationship, the friction shear stress is equal to the normal stress σ_n multiplied by the friction coefficient μ or to a fraction of the

maximum shear stress sustainable by the material. Figure 3.5 illustrates this friction law against the value of the normal stress.

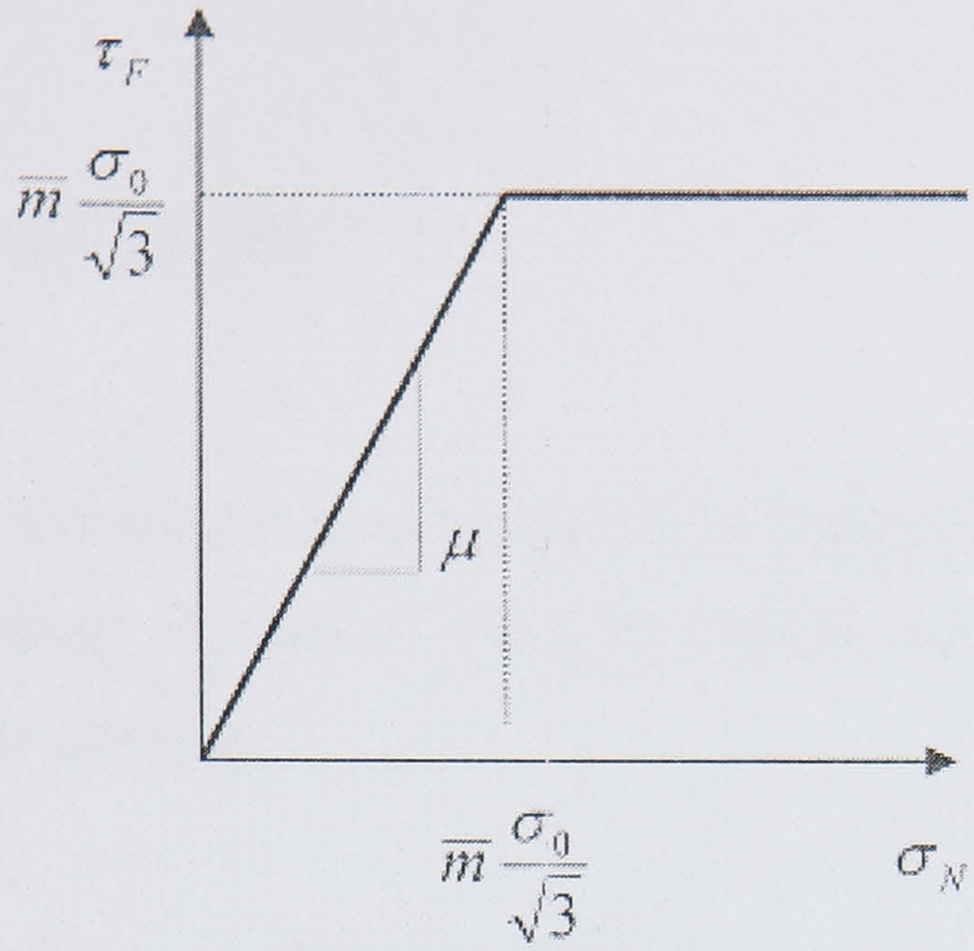

Figure 3.5 Coulomb friction law

3.1.8 Thermal-mechanical simulation by FEM

In a FEM simulation, the temperature field is discretised with the same elements as for the velocity field.

$$T = \sum_n T_n N_n(\xi) \tag{3-20}$$

The temperature evolution inside any physical system is the result of the competition between the phenomena of internal heat conduction and internal heat dissipation, under the constraints defined on the area boundary in terms of interchange (radiation, conduction, convection …) or in terms of imposed temperature.

The classical semi-discretised form is easily obtained from the equation:

$$C \cdot \frac{dT}{dt} + H \cdot T + F = 0 \tag{3-21}$$

where **T** is the nodal temperatures vector, **C** is the capacity matrix and **H** is the conductivity matrix. **C** and **H** are computed by:

$$C_{ij} = \int_{\Omega} \rho c N_i N_j dV \tag{3-22}$$

and

$$H_{ij} = \int_{\Omega} k \, \mathrm{grad}(N_i).\mathrm{grad}(N_j) dV \tag{3-23}$$

while the **F** vector contains the viscoplastic heat dissipation and boundary conditions. For the finite element solution of the heat transfer problem we use the principle of virtual temperature given as:

$$\int_V \bar{t}'^T k t' dV = \int_V \bar{t} q^B dV + \int_{S_q} \bar{t}^s q^s dS + \sum_i \bar{t}^i Q^i \tag{3-24}$$

where:

$$t'^T = [\frac{\partial t}{\partial x} \quad \frac{\partial t}{\partial y} \quad \frac{\partial t}{\partial z}] \tag{3-25}$$

and

$$k = \begin{bmatrix} k_x & 0 & 0 \\ 0 & k_y & 0 \\ 0 & 0 & k_z \end{bmatrix} \tag{3-26}$$

the Q^i are concentrated heat flow inputs, q^B is the rate of heat generated per unit volume, q^s is the prescribed heat flux input on the surface of the body, k_x, k_y, k_z are the thermal conductivities corresponding to the principle axes x, y and z.. Each Q^i is equivalent to a surface heat flow input over a very small area. The bar over the temperature t indicates that a virtual temperature distribution is being considered.

3.1.9 FEM software (FORGE2® and FORGE3®)

The French developed FEM software FORGE2® and FORGE3® are used in the present work. FORGE2® is dedicated to the simulation of hot. warm and cold forging of axi-symmetric (revolution) parts and parts with high length-to-width ratios (Plain Strain). FORGE3® is constructed for the simulation of three dimensional problems.

The geometry of a FORGE3® die is described only through its surface, represented by a triangular mesh. A complete tooling file is composed of different dies (for example, the ram, container and the bottom die in extrusion). Each die is described through one specific surface mesh. These meshes have to be prepared with CAD system (I-deas). FORGE2® and FORGE3® provide interfaces for standard output formats.

Several technology difficulties have been met in the present work when using FORGE2&3 in the simulation of extrusion, including:

(1) There is a small gap between the die land and the material, which will never occur in practice. Details of the problem and the solution method can be found in Appendix B. Some of the communications between the virtual manufacturing group of Bournemouth University and Transvalor software company can also be found in Appendix C.

(2) Time needed for a complete three dimensional simulation of extrusion process is too long to be acceptable.

The first problem has already been solved. In two dimensional simulations, by adopting small time increments in the input file of FORGE2, the orifice can be eliminated. In three dimensional simulations, an upgraded version of Forge3 has been developed by Transvalor and satisfactory simulation results have already been obtained.

The second problem was also partially solved by using auto-trim technology, which is introduced below. However, the time scale for a complete three dimensional simulation is still long and further attempts have to be made, such as the employment of cluster computers, to solve the problem.

3.1.10 Auto-trim applied in FEM Simulation

A new technology called "auto-trim" is adopted in the present work and the calculation time can then be significantly reduced. The method involved is to "kill" the elements when they are extruded out of the die orifice after a certain distance. It can be seen from Figure 3.6 that after the technology is adopted, the elements shown in the box at (a) are eliminated and then the remesh time used in simulation (b) is much less than required in simulation (a). The complete extrusion process can be performed in a relatively short time with this technology.

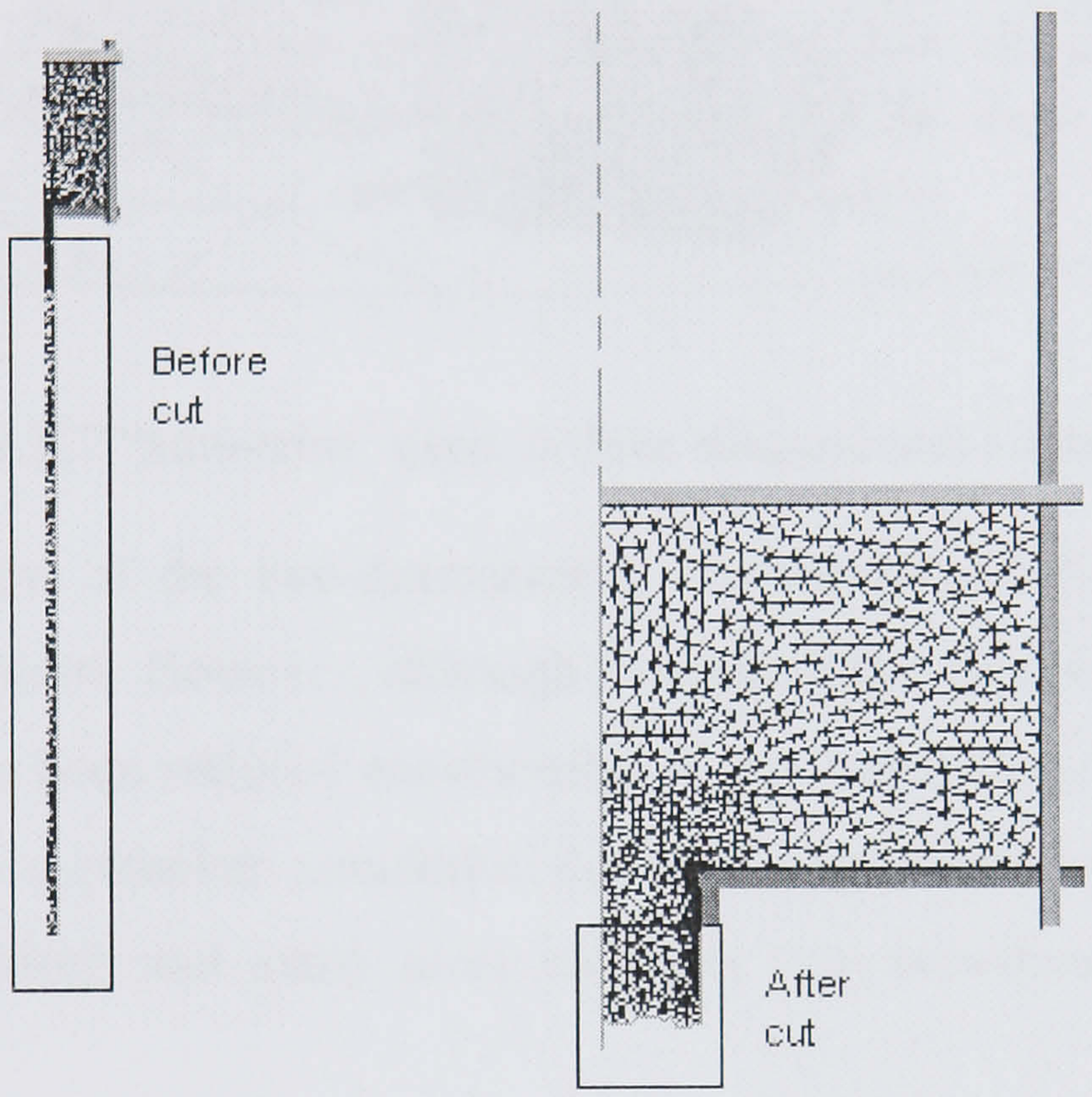

Figure 3.6 "auto-trim" used to shorten computing time

The new technology can be applied to either two-dimensional simulation or three-dimensional simulation. An example of the application of the auto-trim in three-dimensional T shape extrusion is shown in Figure 3.7.

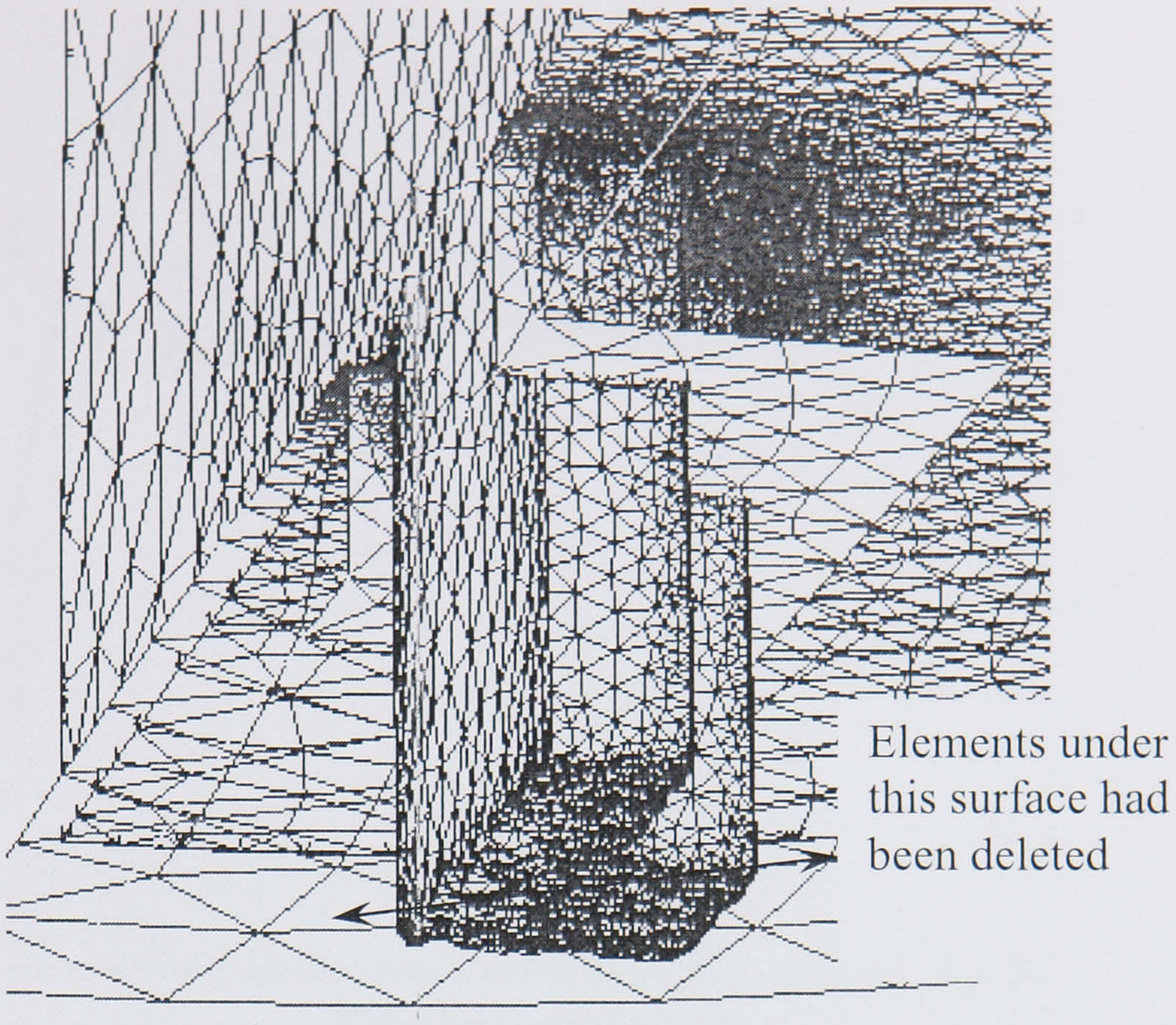

Figure 3.7 "auto-trim" used in three dimensional simulation

With auto-trim, most of the two-dimensional simulations can be completed in 36 computer working hours. However, although the calculation time in three-dimensional simulations has also been reduced enormously, it was found that much time was still required to perform a complete simulation due to the asymmetric nature of the three-dimensional simulations and many more elements than two-dimensional simulation were employed.

3.2 Validation of simulation results: Extrusion load

Figure 3.8 depicts an idealised load-displacement curve for direct extrusion and shows how this curve may be divided into three distinct stages. During stage I the billet is upset to fill the container and there is limited ram travel for an increase in the load to a maximum.

Stage II is referred to as steady state flow and shows a decrease in load with ram travel since the frictional force generated by the movement of the billet relative to the container is reduced as the billet length decreases. Stage III involves a rapid rise in load as the pressure pad impinges on the deformation zone. For this reason a discard is left in the container and is ejected before the next extrusion.

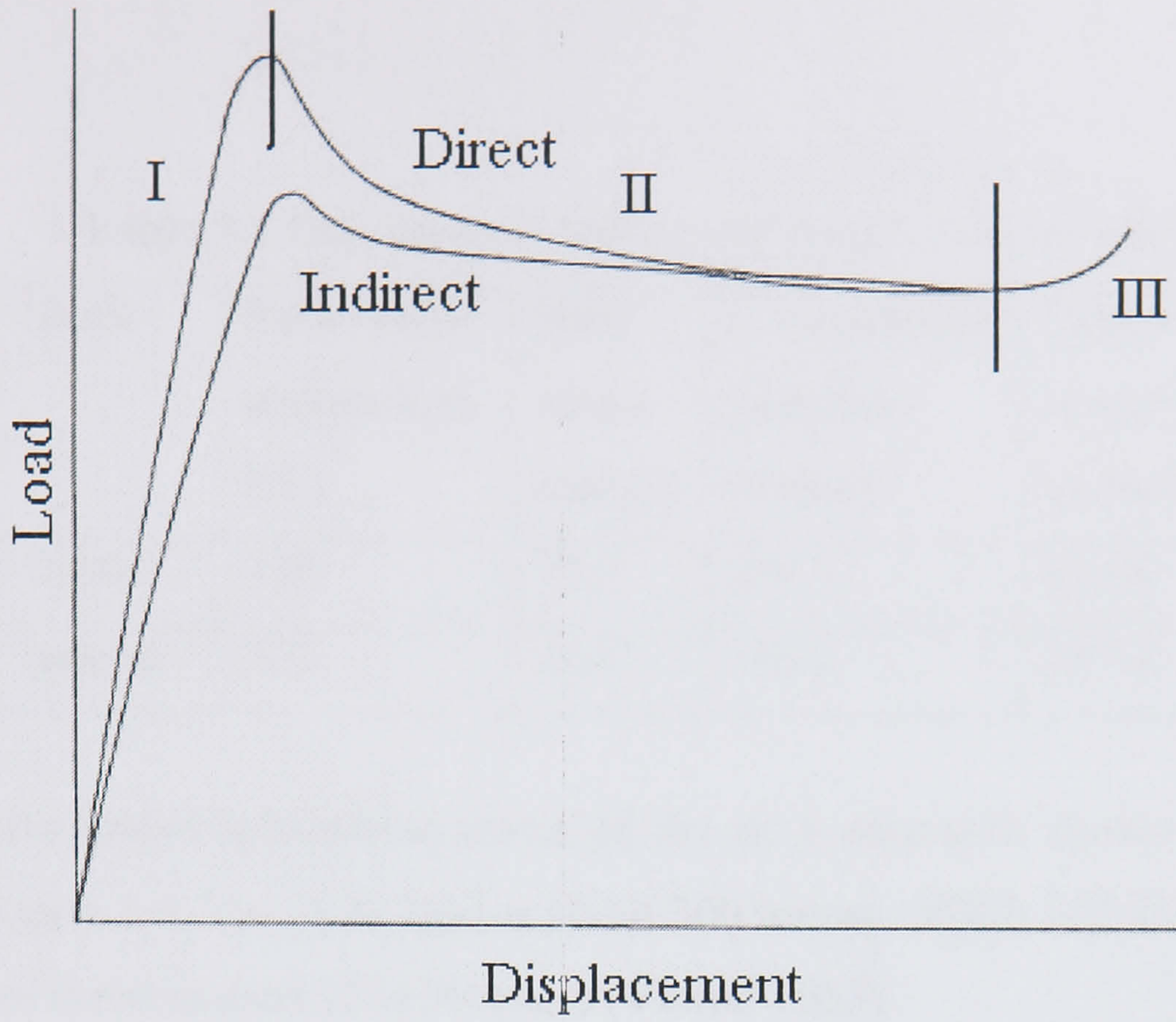

Figure 3.8 Typical load-displacement curves

The controlling feature, which will determine whether extrusion is possible or not, is the maximum pressure which occurs at the boundary between stages I and II. This pressure is referred to as the peak or breakthrough pressure and must lie within the capacity of the press. The magnitude of this pressure is dependent on the extrusion ratio, the initial billet temperature, the ram speed, and the billet length/diameter ratio. The existence of the peak, although it is not always detected, has been recognised for many years.

In aluminium extrusion the shape of the shear region between the deforming billet and the dead metal region has been described as approximately elliptical.

Simulations were performed for one direct extrusion and one indirect extrusion. The extrusion conditions are shown in Table 3.1. In both of the extrusions, the extrusion ratio is 20, the container temperature is 50°C lower than the billet temperature,

Table 3.1 Experimental setting and results (Vierod 1983)

Run	Mode	Initial billet temperature (°C)	Ram speed (mm/s)	Experimental peak load (tonnes)	Experimental load at end of extrusion (tonnes)
1	Direct	400	12.4	284.7	214.8
2	Indirect	400	10.6	196.2	197.4

The complete load-displacement curve of the no.1 extrusion shown in Table 3.1 is shown in Figure 3.9. The peak load is about 300 tonnes, which is 5.4% higher than the experimental measurement (284.7tonnes) (Vierod 1983).

The predicted load-displacement curve of the no.2 extrusion shown in Table 3.1 is shown in Figure 3.10. The predicted peak load is 210 tonnes (7.0% higher than the experimental result) and the predicted load at end of extrusion is 215 tonnes (8.2% higher).

As can be seen from the simulation results, the predicted loads are in reasonable agreement with the experimental results. The difference between the peak load and the minimum load in the indirect extrusion is smaller than that in the direct extrusion. In stage II of the direct extrusion, the extrusion load decreases nearly linearly, which is caused by the decrease of contact area between the container and the billet. However, the same phenomenon has not been found in the indirect extrusion, which indicates a different material flow pattern exists between the direct and indirect extrusion and the influence of the friction on extrusion load is more significant in direct extrusion than in indirect extrusion.

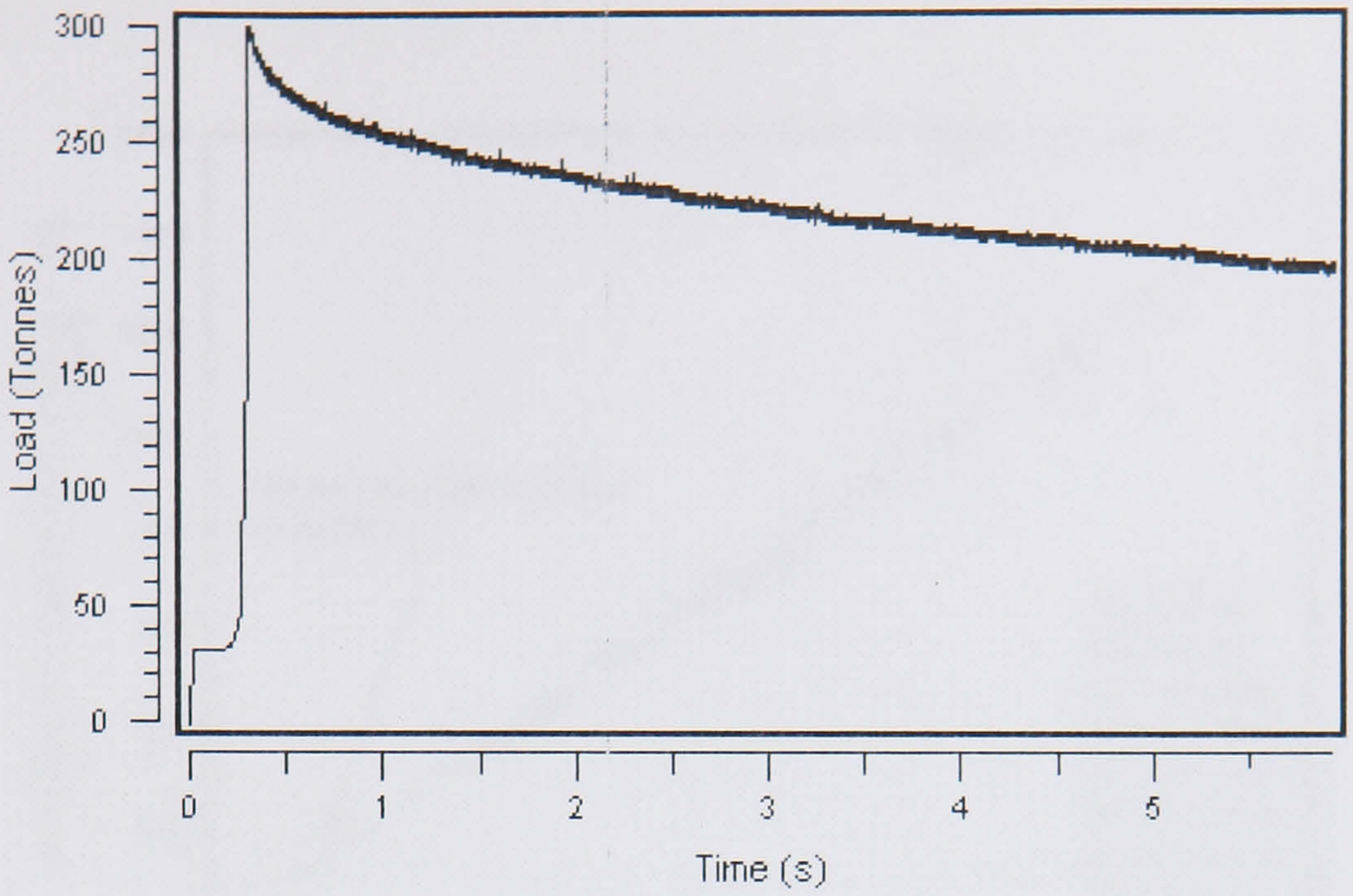

Figure 3.9 Load-displacement curve for run 1

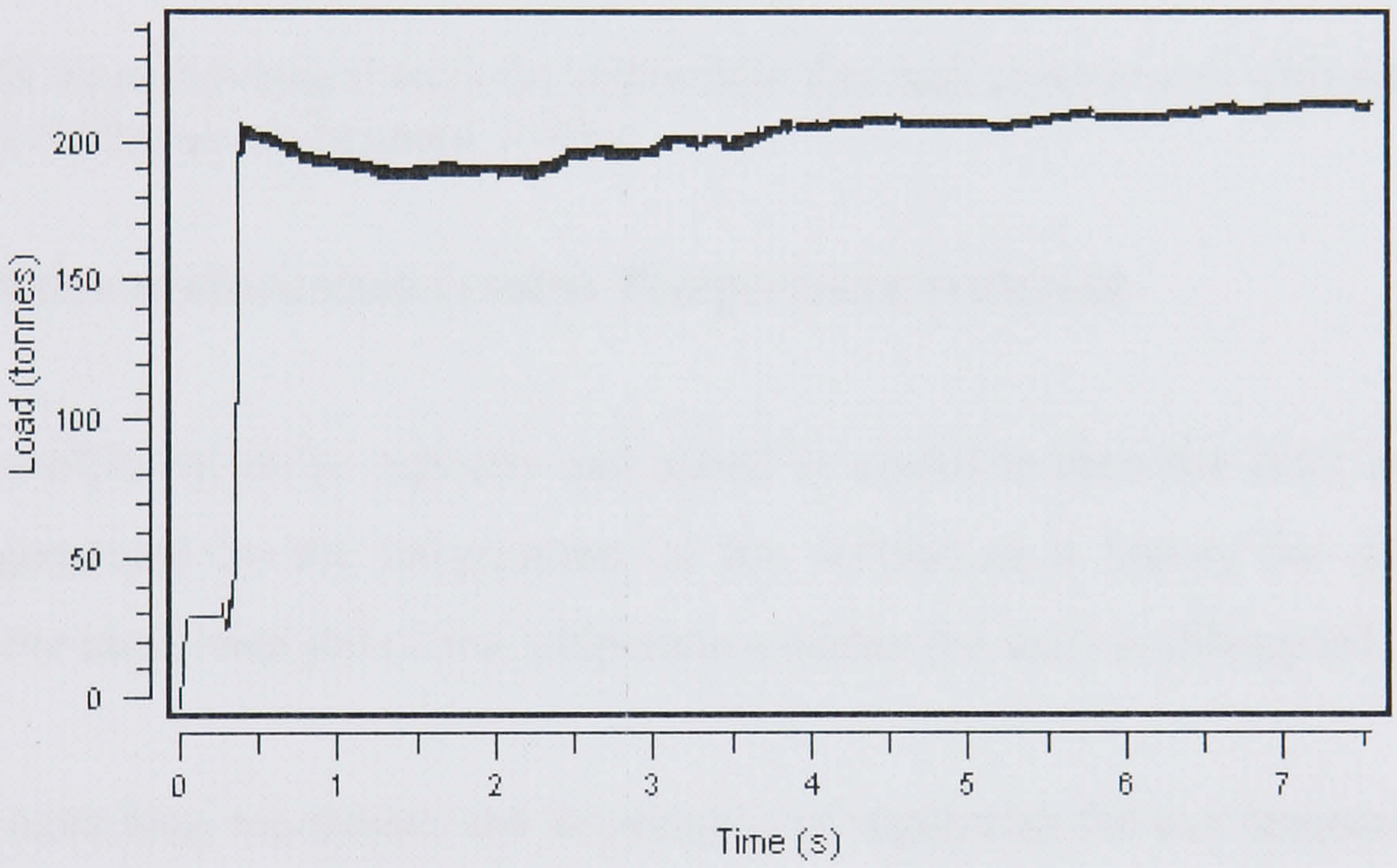

Figure 3.10 Load-displacement curve for run 2

Complex shapes and multi-hole die extrusions are more complex than rod extrusion. One example is shown in Figure 3.11. However, once the basic problem, such as FEM simulation of rod extrusion has been solved and proved to be effective, there is a great potential for FEM to develop a comprehensive and deep understanding of complex shapes extrusions, which are discussed in detail in Chapter 4.

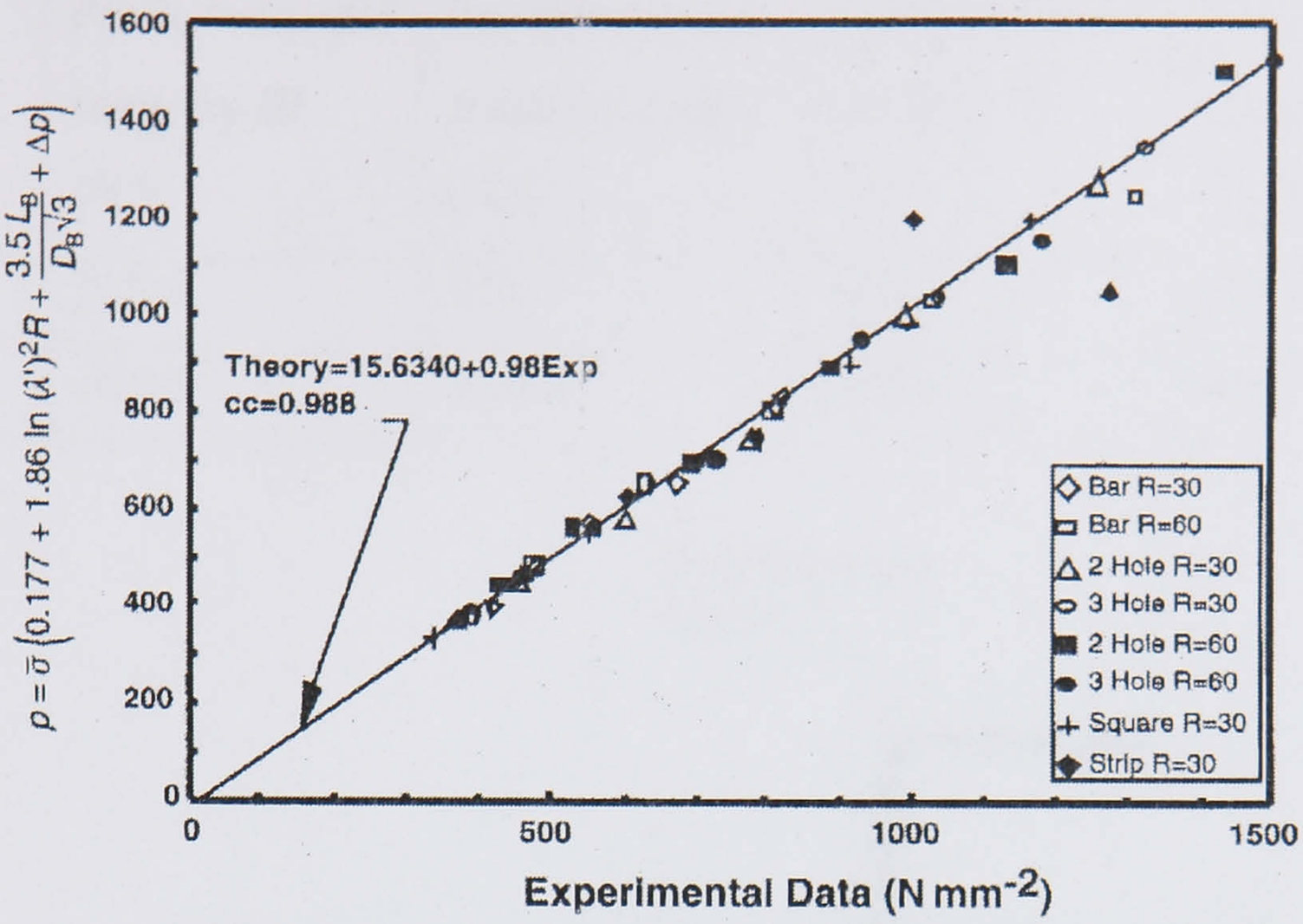

Figure 3.11 Experimental results for multi-hole dies and comparison with single-hole and shaped extrusions (Sheppard 1999a)

3.3 Validation of simulation results: Temperature evolution

Assuming sufficient press capacity and speed is available then the limit of extrusion speed is governed by the temperature of the section as it leaves the die or, more correctly, the maximum permitted temperature within the section (Sheppard, 1999a).

Extruders have long recognised the importance of regulating the exit temperature either to maintain a good surface quality or to achieve properties specified by the customer.

The predicted peak temperature (the temperature at the time when peak load occurs) and the final temperature by integral profile method are shown in Table 3.2. The typical extrusion area near the die land is shown in Figure 3.12 and temperature rises at the centre point and the side point (as shown in Figure 3.12) are extracted as shown in Figures 3.13 and 3.14. However, the temperature difference between the surface and the centre has not been considered by the integral profile method (IP). Therefore only an approximate comparison can be made between the results given by the finite different method and by FEM simulation.

Table 3.2 Temperature predicted by IP and FEM (IP results from Vierod 1983)

Run (same as in Table 3.1)	Predicted peak temp by IP (°C)	Predicted peak temp by FEM (°C)	Predicted final temp by IP (°C)	Predicted peak temp by FEM (°C)
1	315.0	312.1	452.8	453.2
2	406.0	403.2	460.9	456.5

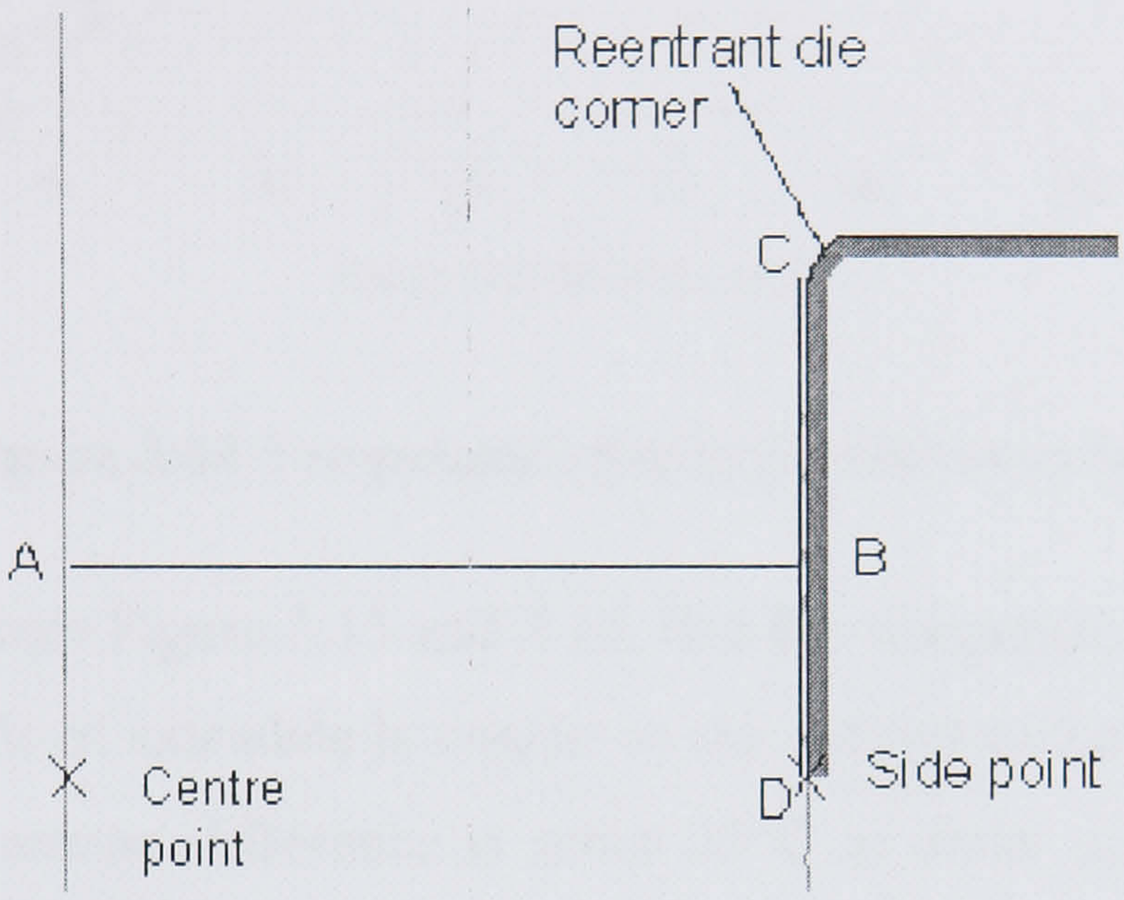

Figure 3.12 Deformation area near the die (a complete die has been shown in Figure 3.6)

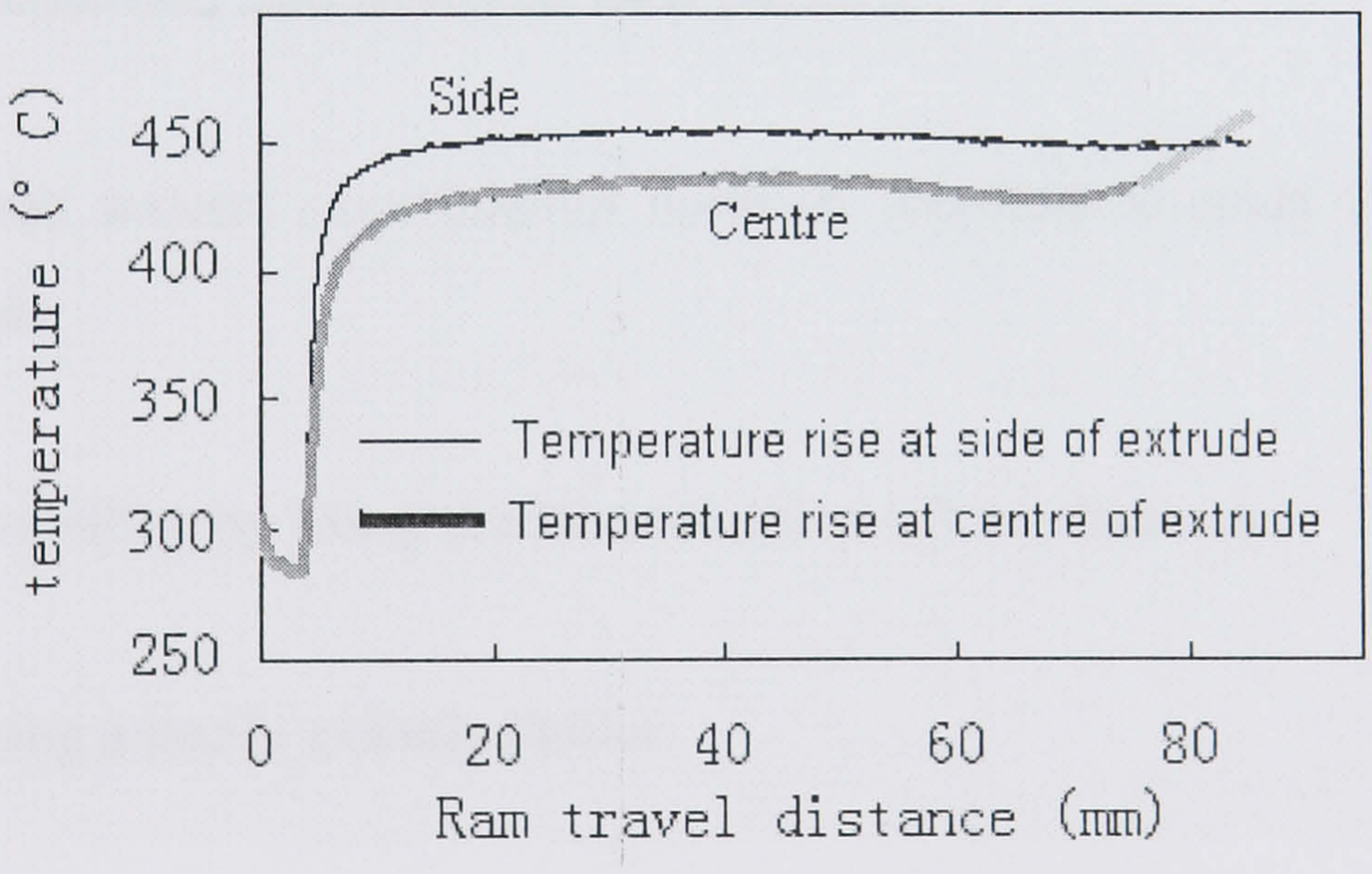

Figure 3.13 Temperature rise in direct extrusion

As can be seen in Figure 3.13, the temperature at the side of the extrudate is higher than that at the centre of the extrudate except at the end of extrusion (stage III as shown in Figure 3.8), the temperature at the surface rises sharply and overwhelms the temperature at the centre. This has been reported previously (Valberg 1992) and was

regarded as caused by the different material flow pattern occurring at the end of extrusion.

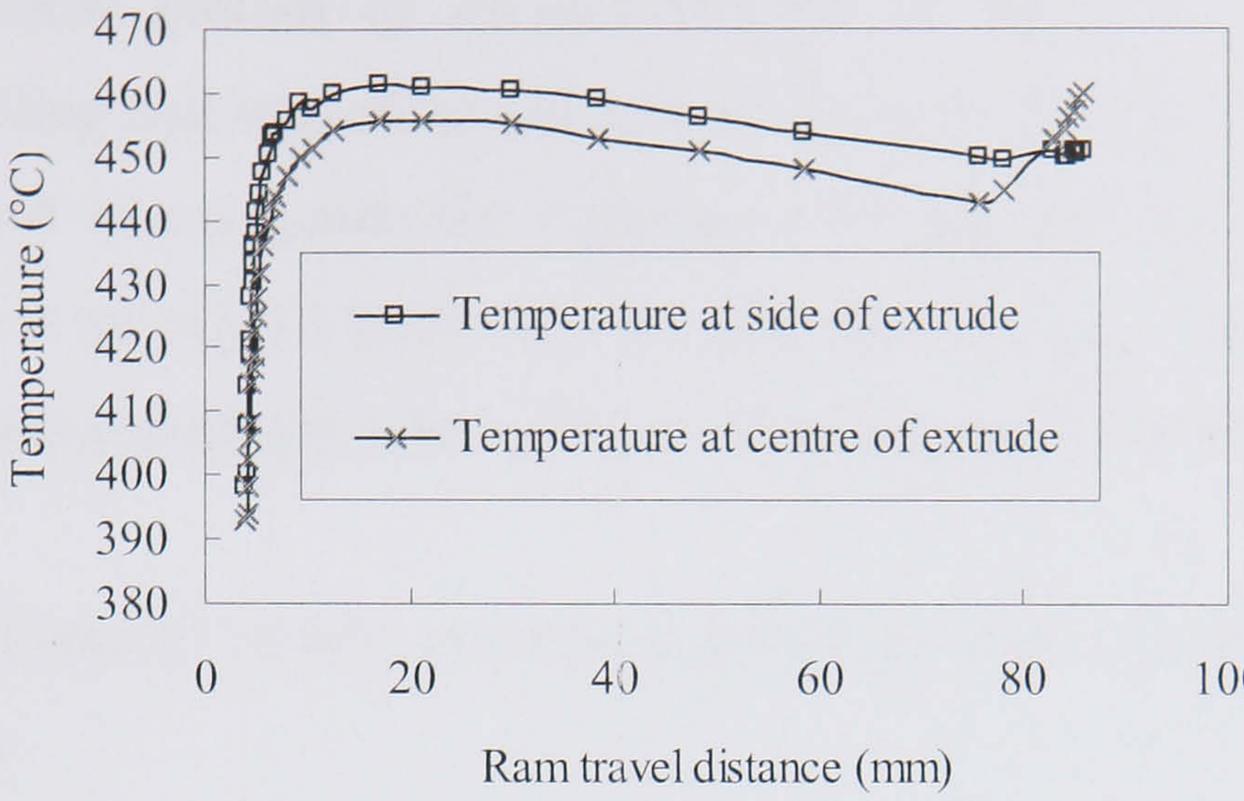

Figure 3.14 Temperature rise in indirect extrusion

It can also be seen from Figure 3.13 and 3.14, that the temperature difference between the centre and the side of extrudate is smaller in the indirect extrusion then in the direct extrusion. The temperature difference is about 25°C in direct extrusion and no more than 10°C in indirect extrusion.

3.4 Surface formation and material flow pattern

There have been several experimental methods reported to study the material flow during extrusion:

[1] Physical modelling by using model materials such as plasticine.

[2] Macro-etching a partly extruded billet.

[3] Inscribing a grid on one half of a billet prior to extrusion. One method developed in the 1960's by Thomson (1965) and his co-workers is the visioplastic technique.

A split-billet, with a grid inscribed in one half, is extruded in incremental steps and by removing the billet at the end of each step, the instantaneous velocity of a material particle can be found. By applying basic plasticity theory the stress and strain variation in the material can be studied.

[4] Numerical simulation

The material flow pattern of axi-symmetrical extrusion has been established by physical modelling and numerical simulation. Arentoft et al. (1998, 2000) have studied the material flow in axi-symmetric extrusion with physical and two dimensional FEM simulation. Li et al. (Q. Li 2003) has studied the influence of pocket die designs on metal flow in aluminium extrusion with two dimensional FEM simulation.

Based on experimental results, Pearson and Parkins (1961) classified the flow patterns into three types

.

A – Found in lubricated and indirect extrusion, where the billet undergoes no deformation until it reaches the deformation zone.

B – Similar to type A except that no lubricant is used, and shear occurs between the billet and the container surface.

C – A more complex form found in many industrial extrusions, where a fairly thick rim of dead material extends down the sides of the stagnant zone, under the shoulder of the die, to the back of the billet. The material at the back is gathered into the centre and eventually forms the back end defect. This type of flow is avoided during aluminium extrusion by ensuring a lack of lubricant at the container/die interface.

The methodology and the procedures used in the present study of surface formation can be found in the literature (Velay et al. 2003) and are not repeated here. The billet was extruded down to a discard of 30mm (without the auto-trim technology) in the simulation.

One vertical line (AB, with a length of 2000 mm, as shown in Figure 3.15) that is 0.05 mm under the extrudate surface, is adopted to study the flow behaviour of the billet skin. The surface location points are shown in Figure 3.15 in detail. The location in the billet from which the outer surface layers of the profile originates can be determined with a high degree of precision. As can be seen from Figure 3.15, a 0.05mm thick outer surface layer of the rod in axi-symmetric direct extrusion would form from a relatively

small crescent wedge-shaped region located near to the dead metal zone during the extrusion. In aluminium extrusion the shape of the shear region between the deforming billet and the dead metal region has been described as approximately elliptical. This has been reported previously in the study of outer surface layer formation in extrusion of AlMgSi alloy (Valberg 1986) as shown in Figure 3.16. In Valberg's study, the experiments were performed by implanting a complete grid pattern inside the billet, which is the same as shown in Figure 3.17 and 3.18.

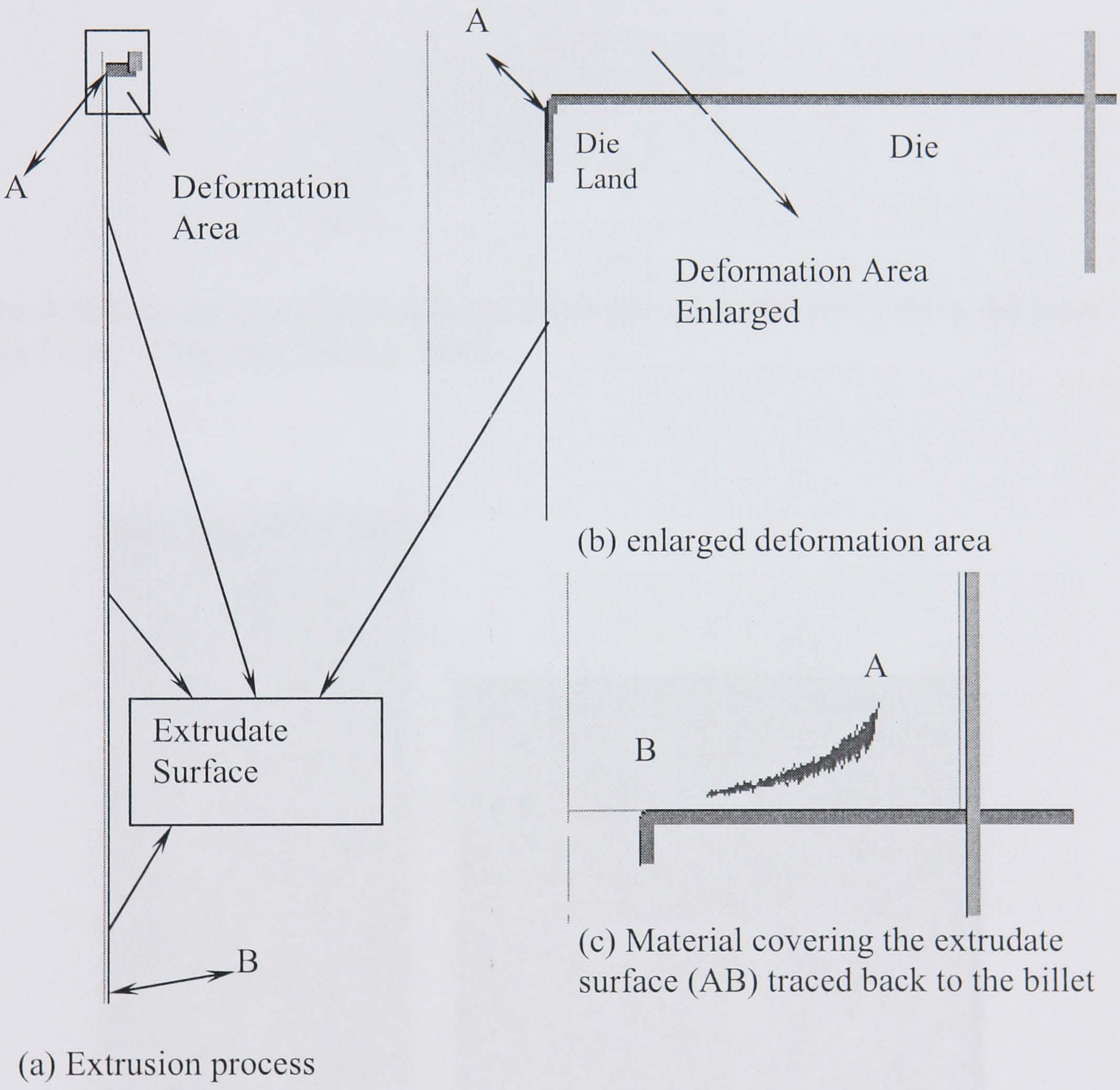

(a) Extrusion process

Figure 3.15 Surface formation in the conventional extrusion

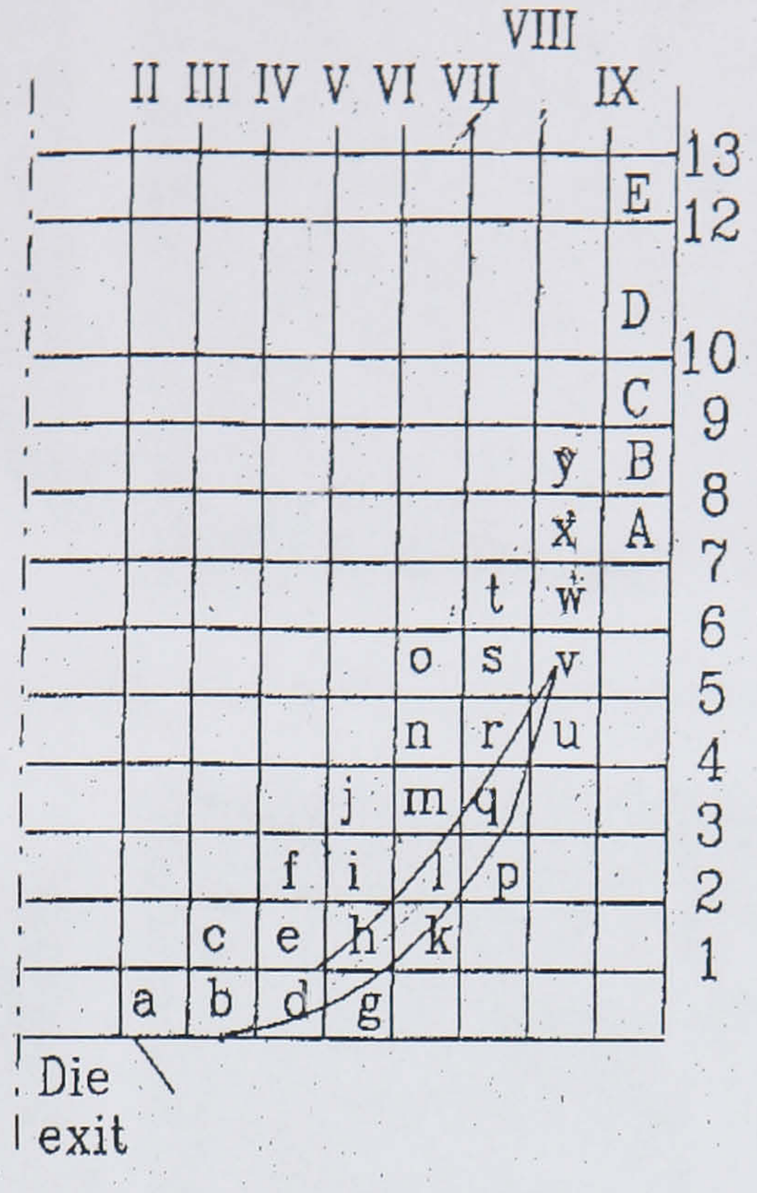

Figure 3.16 Grid elements of the billet in direct extrusion (R=40) forming the outer surface layers of the rod (Valberg 1986).

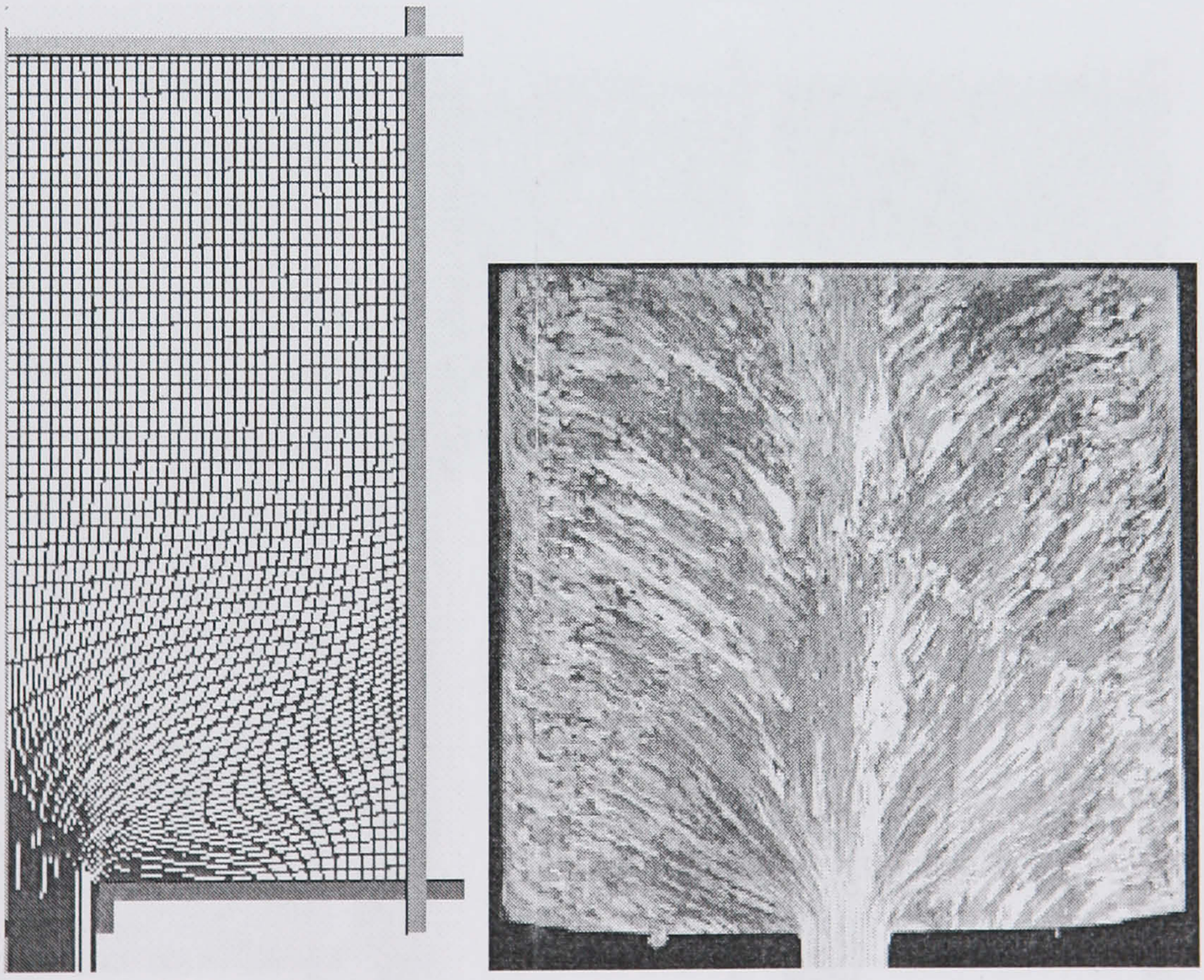

Figure 3.17(a) at the beginning of extrusion (experiments after Castle 1974)

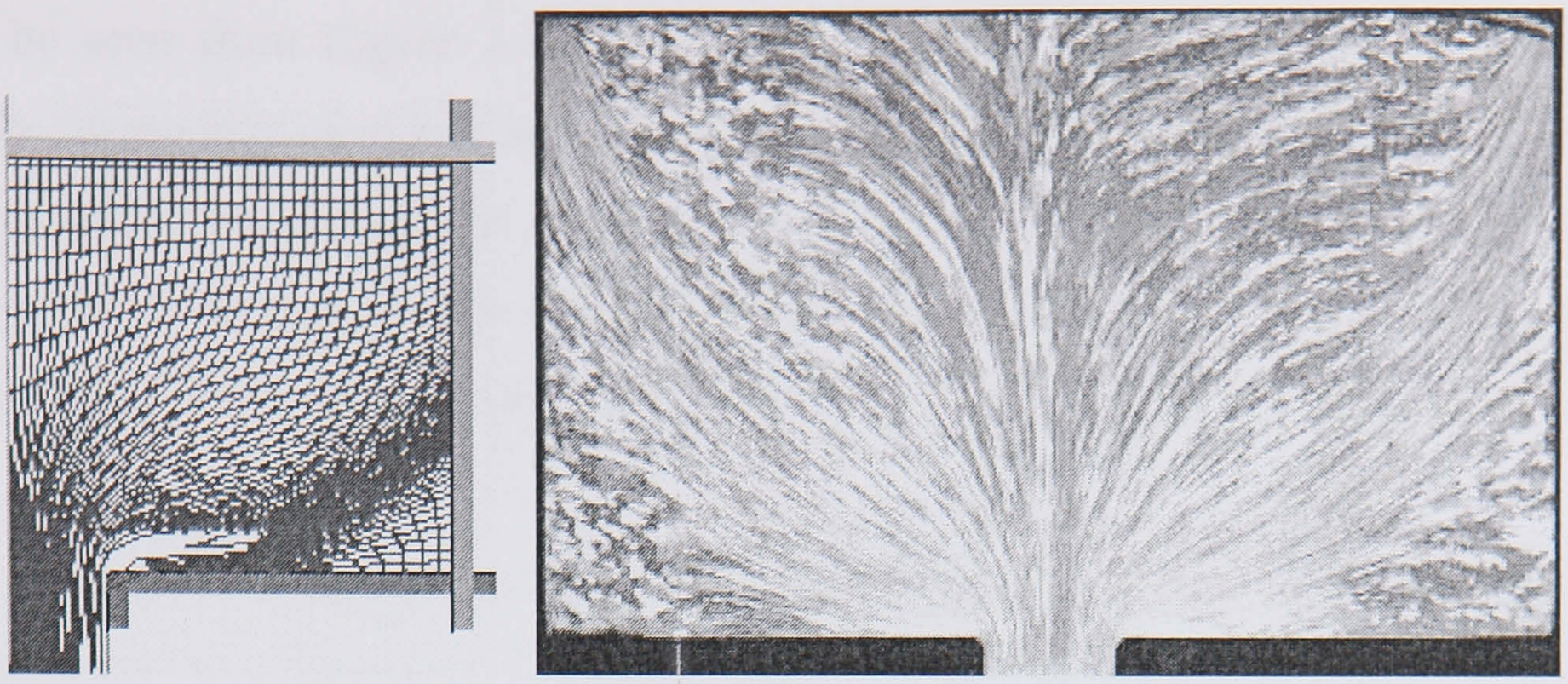

Figure 3.17(b) at the middle of extrusion

Figure 3.17(c) at the end of extrusion

Figure 3.17 Material flow in the direct extrusion (experiments after Castle 1974)

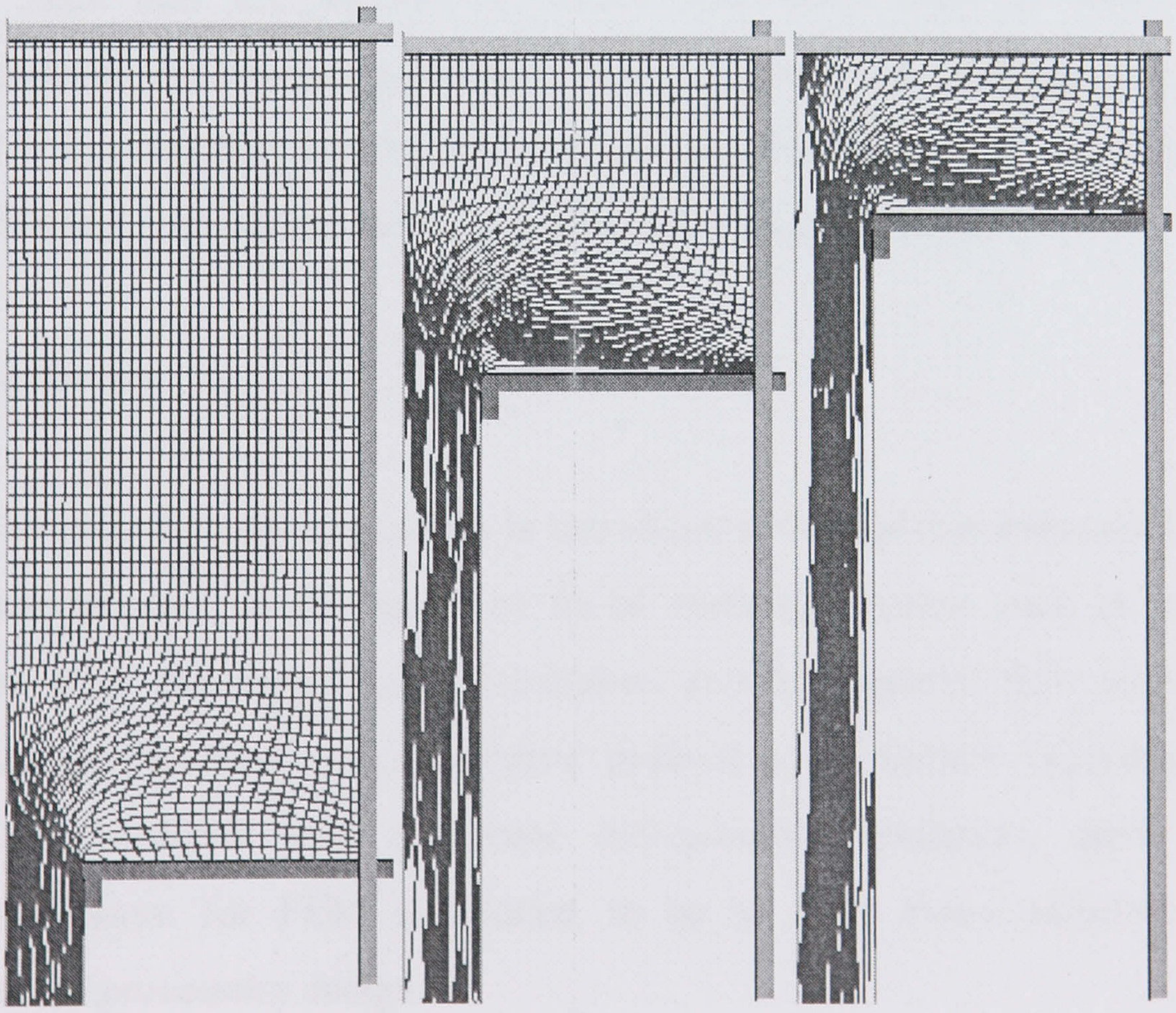

Figure 3.18 Material flow in indirect extrusion

As can be seen from Figure 3.18, the material flows from the wedge-shaped region gradually during extrusion and forms a surface layer that completely covers the rod. The mechanical properties, the extrusion pressure and the surface finish will all be related to the flow pattern, the more complex the flow the more inhomogeneous the working. Many studies have been carried out on axi-symmetrical extrusion.

Due to the axi-symmetric nature of the rod extrusion, two dimensional simulations were performed to study the material flow. The simulation results of direct and indirect extrusion are shown in Figure 3.17 and Figure 3.18 individually. As can be seen from these Figures, the simulation results are in reasonable correspondance with the previous experimental results. Some experiments, performed by inscribing a grid on one half of a billet prior to extrusion, are shown in Figure 3.19 and Figure 3.20. The different material flow occurring during direct and indirect extrusion can also observed from the simulation results of shear stress, which are shown in Figure 3.21 and Figure 3.22. The location of the maximum shear stress in direct extrusion is found to be at the die entrance area and shear stress between the billet and the die can be discerned, while in the indirect extrusion, there is no shear deformation between the billet and the die. It can be seen that the simulation results correspond well to these experimental measurements. Although quantitative analyses were not performed due to lack of detailed experimental results, the simulation results can at least provide some qualitative and basic information about the deformation process.

3.5 Conclusion

As can be seen from the discussion in this chapter, thermal-mechanical FEM simulation is a powerful tool in the study of metal forming process such as extrusion. The extrusion load, the temperature distribution and the material flow pattern can all be simulated at the level of quantitative prediction. If further experiments could be performed combined with the three dimensional simulation, there is a definite promising future for FEM simulation to be an even more effective tool for the manufacture processing design.

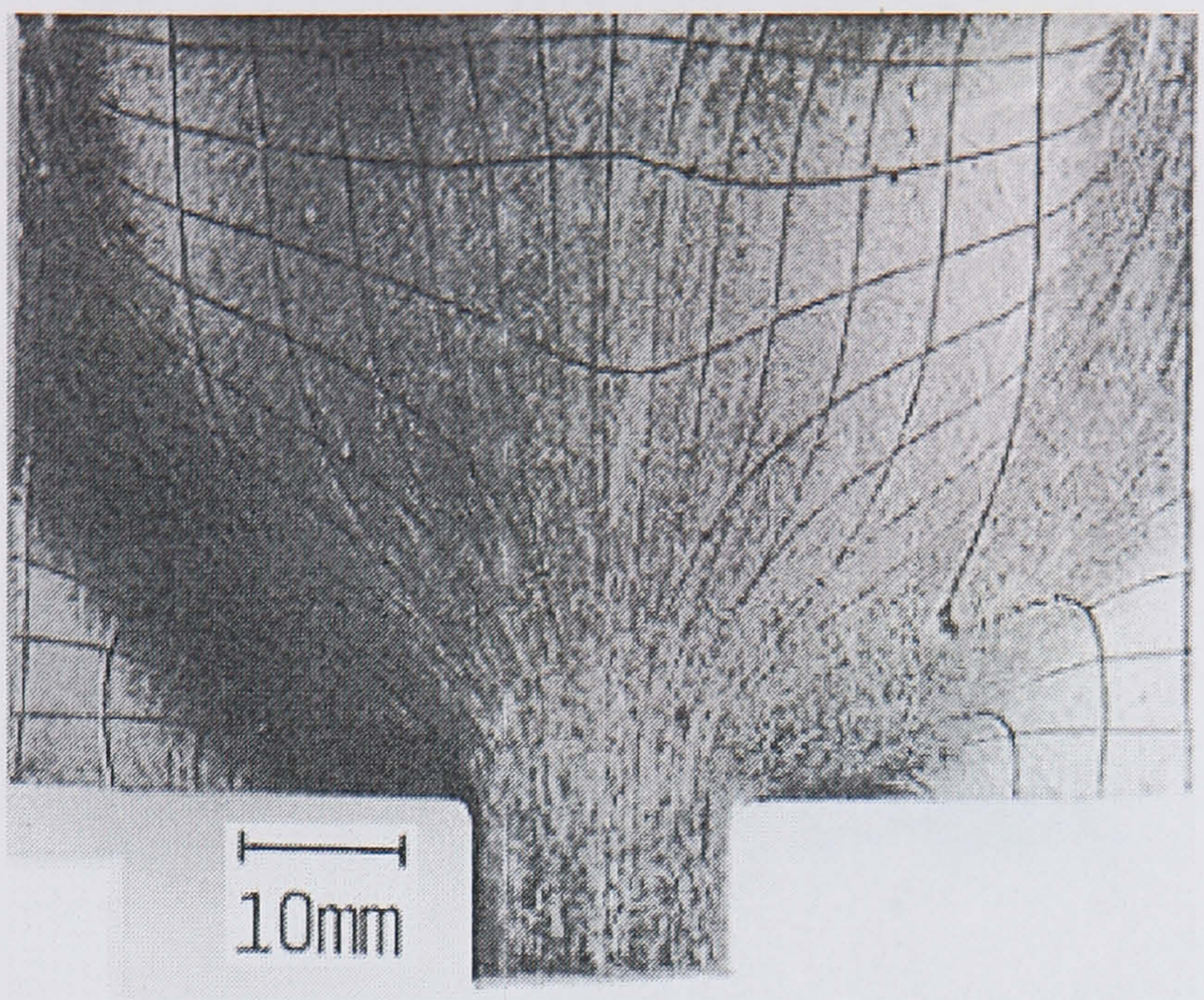

Figure 3.19 Experimental results of direct extrusion (Castle 1974)

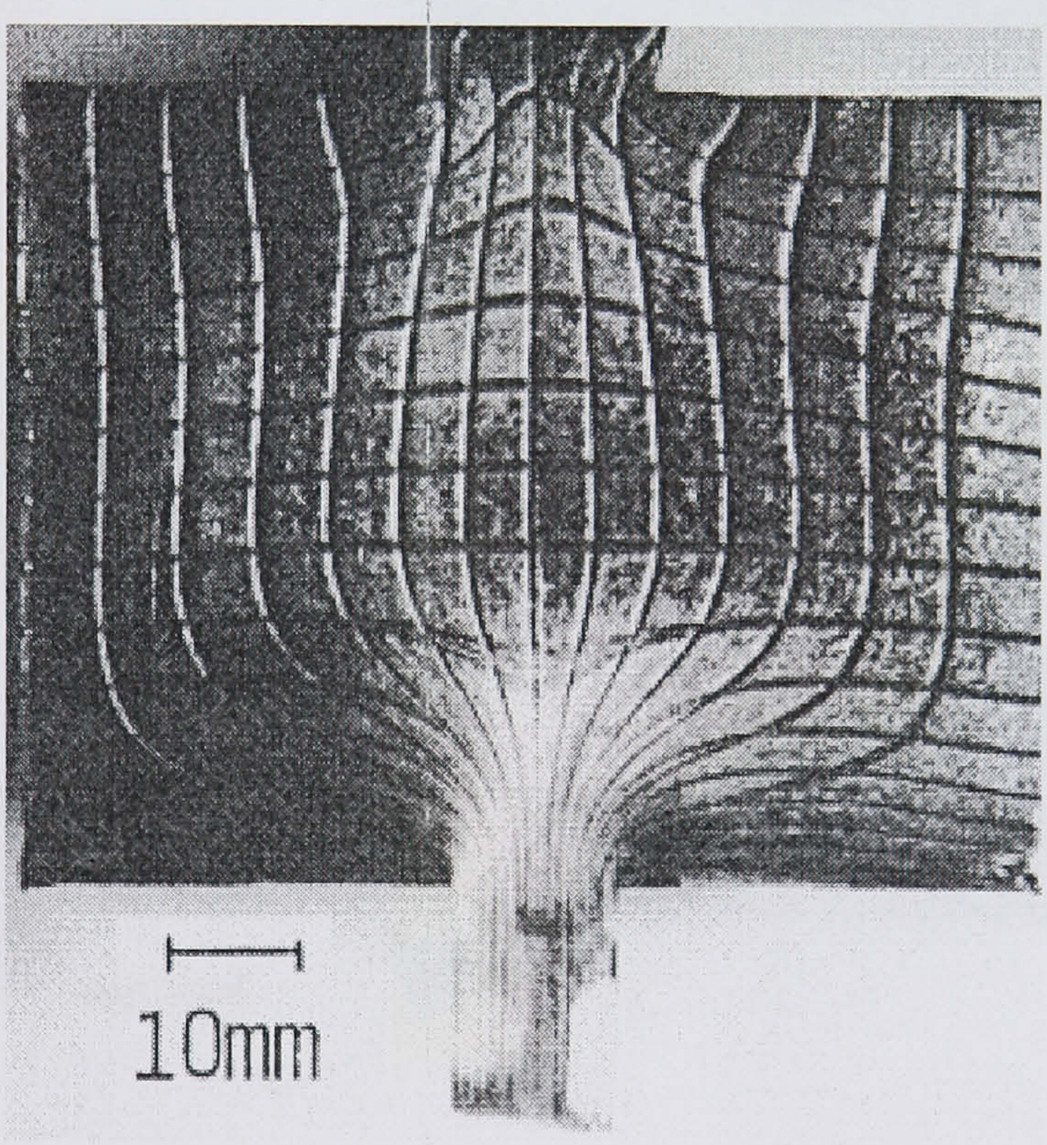

Figure 3.20 Experimental results of indirect extrusion (Castle 1974)

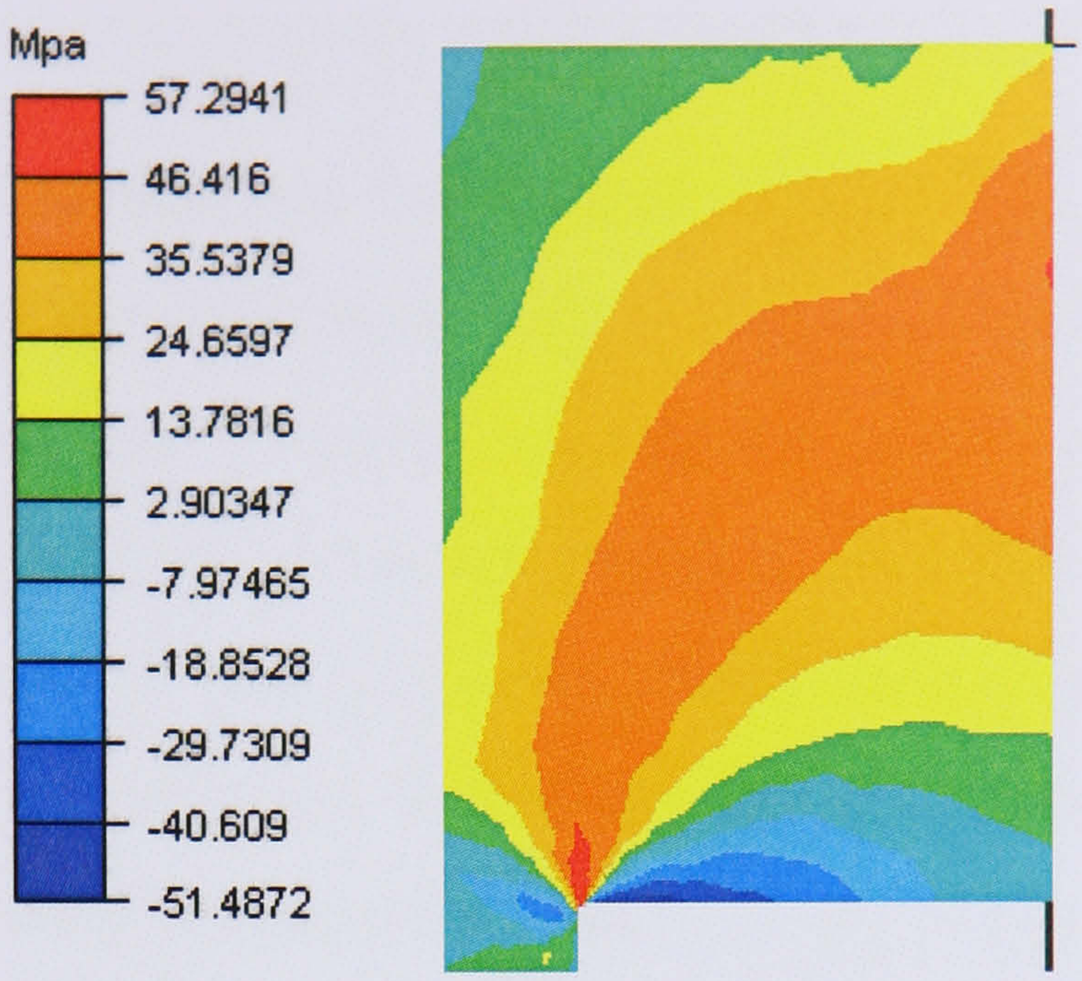

Figure 3.21 Shear stress distributions in direct extrusion

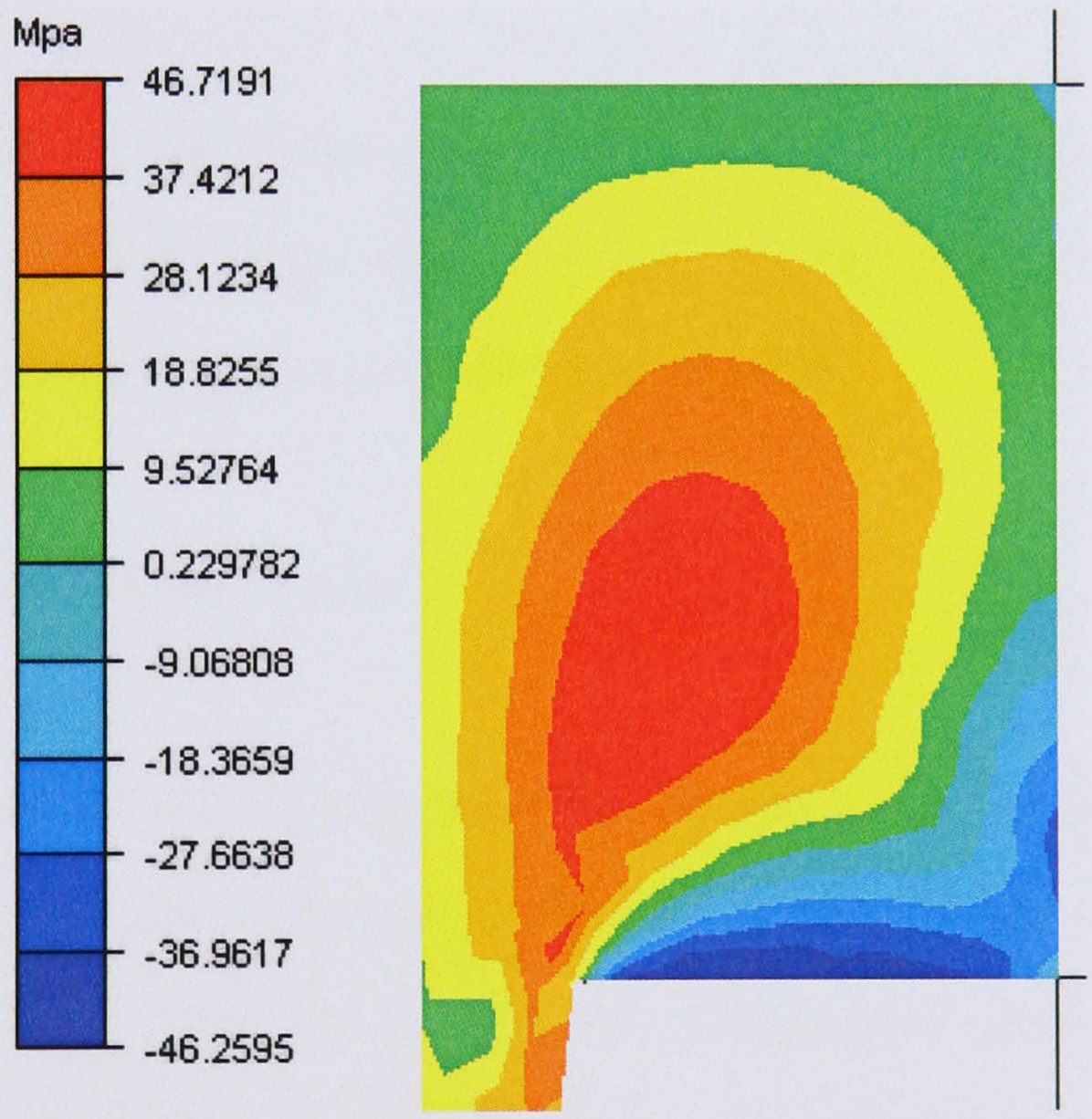

Figure 3.22 Shear stress distributions in indirect extrusion

4 Integrated modelling of the extrusion process

Various methods used to model the microstructure evolution process and predict the final structure state were introduced in Chapter 2 and 3. Combined with FEM and structural models, the integrated models are capable of producing a comprehensive modelling of aluminium extrusion from the metal forming process to the following heat treatment. In this chapter, the models that have been successfully employed in structural simulation in the field of extrusion and the following heat treatment are discussed in detail.

4.1 Rod extrusion

Examples of the thermal-mechanical simulation results of rod extrusions have been provided in Chapter 3 and they are not repeated here. The structural simulation results are presented in the following sections.

4.1.1 Structural modelling results

Although the microstructure models provided by Furu and Sellars (1999) are physically based (presented in Appendix A), which means there should be no restriction to applying them to a different aluminium alloy or different deformation, it is still of primary importance to give a justification before any application of the model. Here a rod extrusion process was selected and the effectiveness of the model combined with FEM in predicting the final structure was tested. The experimental setting is shown in Table 4.1. The container temperature is 50°C lower than the billet temperature.

Table 4.1 Experimental setting (Vierod 1983)

Billet temp ($^{\circ}C$)	Extrusion ratio	Ram speed (mm/s)	Extrusion mode
410	40	3	Direct

The Tresca friction law is adopted in the FEM simulation. To obtain the friction coefficient, the inverse method was adopted. Three simulation results, which are shown in Table 4.2, are compared with the experimental measurements. The friction coefficient, which gave the best agreement with the experimental result, was finally applied to the following simulations:

Table 4.2 Simulation runs to judge the friction coefficient

Run No.	Friction coefficient	Peak load (tonnes)	Quasi-static state Load (tonnes)
1	0.8	305.5	258.9
2	0.9	321.7	270.5
3	1.0	349.8	285.8

The experimental peak load was 339 tonnes and the steady state pressure was 659 MPa, which is equal to 291 tonnes. As can be seen from the group of simulations above, full sticking condition, which was used in No.3 run, gave the best result when compared with the experimental data. The predicted peak load was 349.8 tonnes, which is 3.2% higher, and the predicted quasi-static state load was 285.8 tonnes, which is 1.8% lower than the experimental result. It should be noted here that due to the lack of exact information concerning the discard length, it is acceptable that there is a small difference between the simulated and the experimental loads. Thus full sticking condition was used here and throughout the later simulations in the next section.

4.1.1.1 Subgrain size

The predicted subgrain sizes at the transverse direction are shown in Figure 4.1.

It can be seen from Figure 4.1 that the difference between the calculated subgrain size at the centre (2.27 μm) and the experimental measurement (2.22 μm) is no more than 0.3%. At the edge of the extrudate, the predicted subgrain size is 2.52 μm , which is just 0.3% higher than the experimental result (2.45 μm). It is clear from Figure 4.1 that the predicted subgrain size increases as the temperature rises along the tranverse direction of the extrudate. This phenomenon is the same as that observed previously (Sheppard 1993).

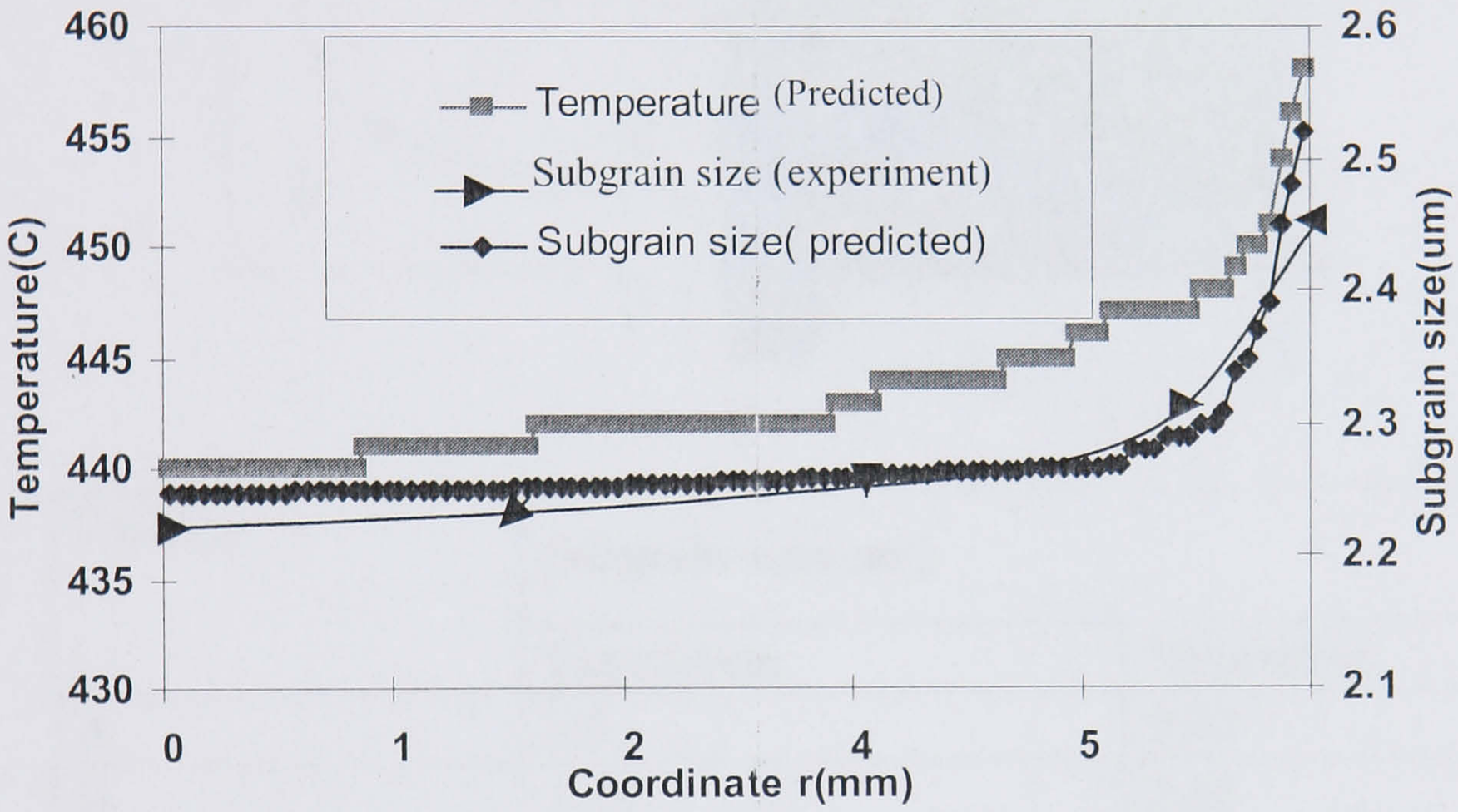

Figure 4.1 Subgrain size and temperature

It should be noted that all of the above discussion is focused on deformation area 1 (extrudate), as shown in Figure 4.2. For the area 2 (billet, or the inside of container), the predictions show a little higher value than the experimental results. Although at test points A, C and D the predictions correlate to experimental measurement quite well, the prediction at point B is higher because of proximity to the dead metal zone. The predicted subgrain size at this point is 2.68 μm , while the experimental measurement is 2.28 μm . The difference between them is about 17.5%. However, it should be noted that there is a relative error of 9% in any subgrain size measurement. Therefore the prediction can be taken as reasonable. Furthermore, because the current work is concentrated on the area of

the extrudate surface, the problem of inaccurate prediction of the subgrain size of the billet within the container area will not affect this study.

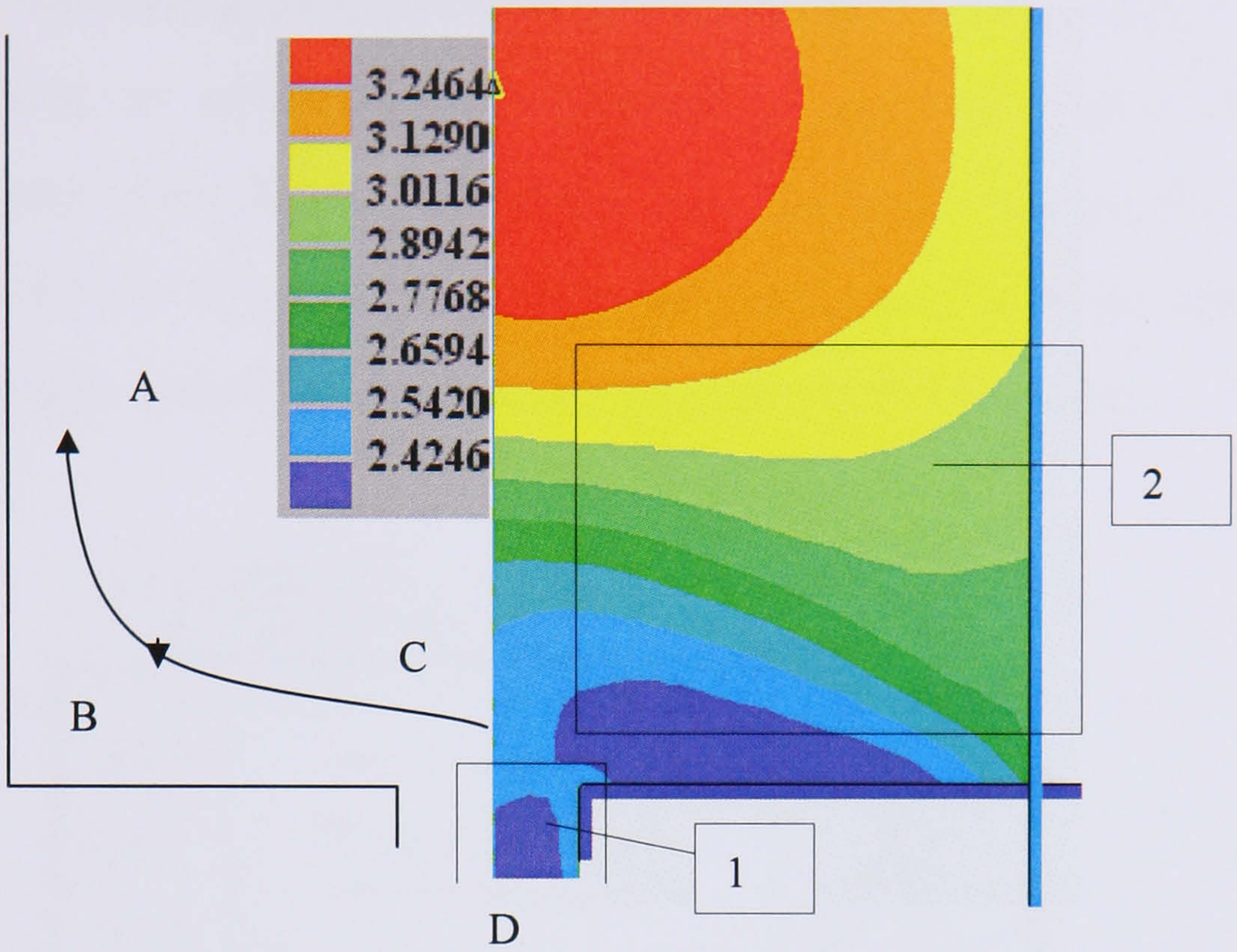

Position	Subgrain size(μm)	
	Experiment	Simulation
A	3.0	2.92
B	2.28	2.68
C	2.37	2.50
D	2.40	2.42

Figure 4.2 Subgrain size distributions

4.1.1.2 Recrystallised grain size

From Figure 4.3, the recrystallised grain size shows a sharp decrease at the surface of the extrudate, and it is easy to see the recrystallised grain size is in inverse proportion to the equivalent strain. This has also been observed before by Vierod and many others (Vierod 1983, Sellars 2000). The predicted value is 0.455mm, which is 3.2% lower than the experimental results.

The given misorientation is shown in Figure 4.4. The value of the misorientation rises up to about 3° and then remains constant. The prediction correlates well

with previous studies (Furu 1999, Sellars 2000).

One problem concerning the shear deformed surface layer at the outside of the extrudate should be addressed here. Aukrust et al. (1997) have given a quantitative study of the sheared sub-surface of aluminium extrudates. As can be seen in Figure 4.3, the predicted value of the equivalent strain increases sharply at the subsurface area indicating that the shear stresses will also increase,

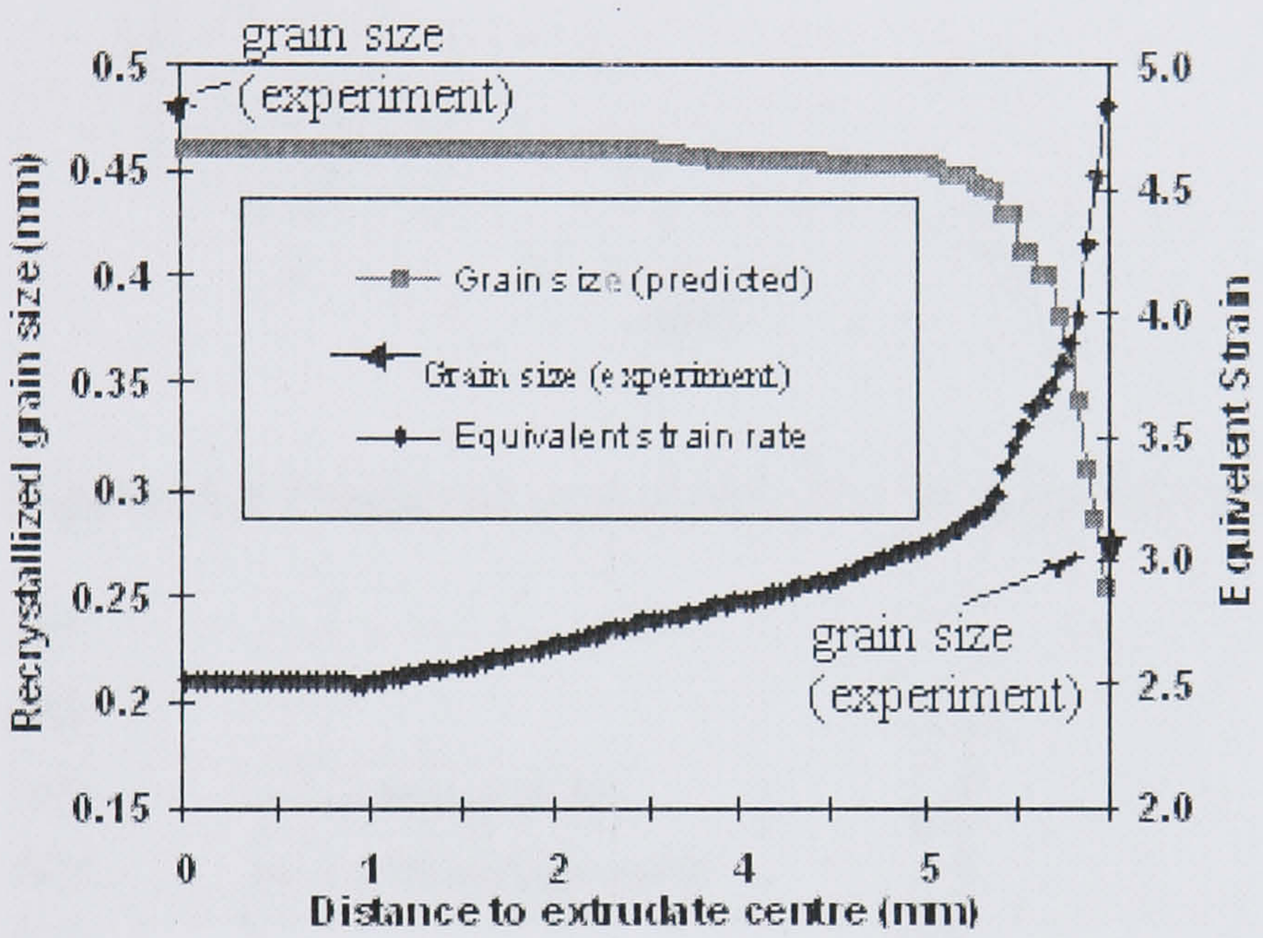

Figure 4.3 Recrystallized grain size and equivalent strain

According to the physically based model, the density of nucleation sites is much higher and the recrystallised grain size is expected to be considerably smaller at the subsurface area under shear deformation than the areas below. The values of grain boundary area per unit area Sv and the nucleation site density Nv (calculated from equation A3 amd A4 in Appendix A) across the extrudate are shown individually in Figure 4.5 and 4.6. As can be seen in these two graphs, the value of Sv and Nv increases sharply in the sub-surface area of the extrudate. This is due to the shear deformation suffered at the surface area of the extrudate, which has been reported by many studies (Castle 1976).

However, in experiments, the extremely small recrystallised grain was not

observed, only a relatively small decrease of the grain size was found in this area. Two causes may lead to this phenomenon: one is that the physically based (PB) model needs to be improved to predict the recrystallisation in extremely sheared structures, and the second is that secondary recrystallisation is likely to occur in this special area.

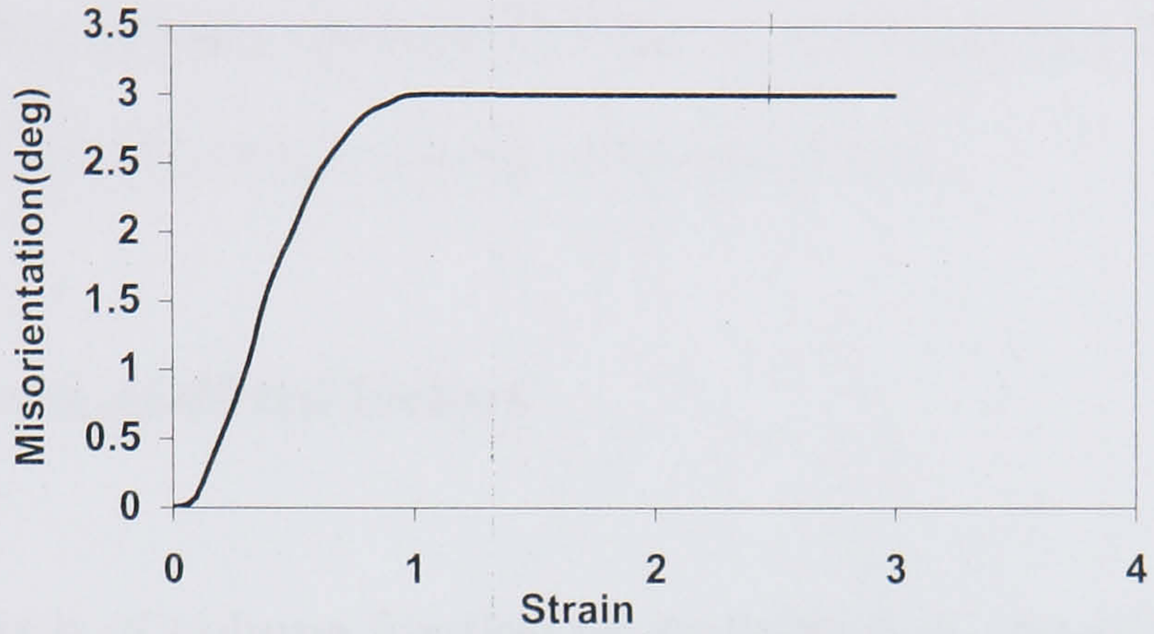

Figure 4.4 Predicted misorientation of the subgrain

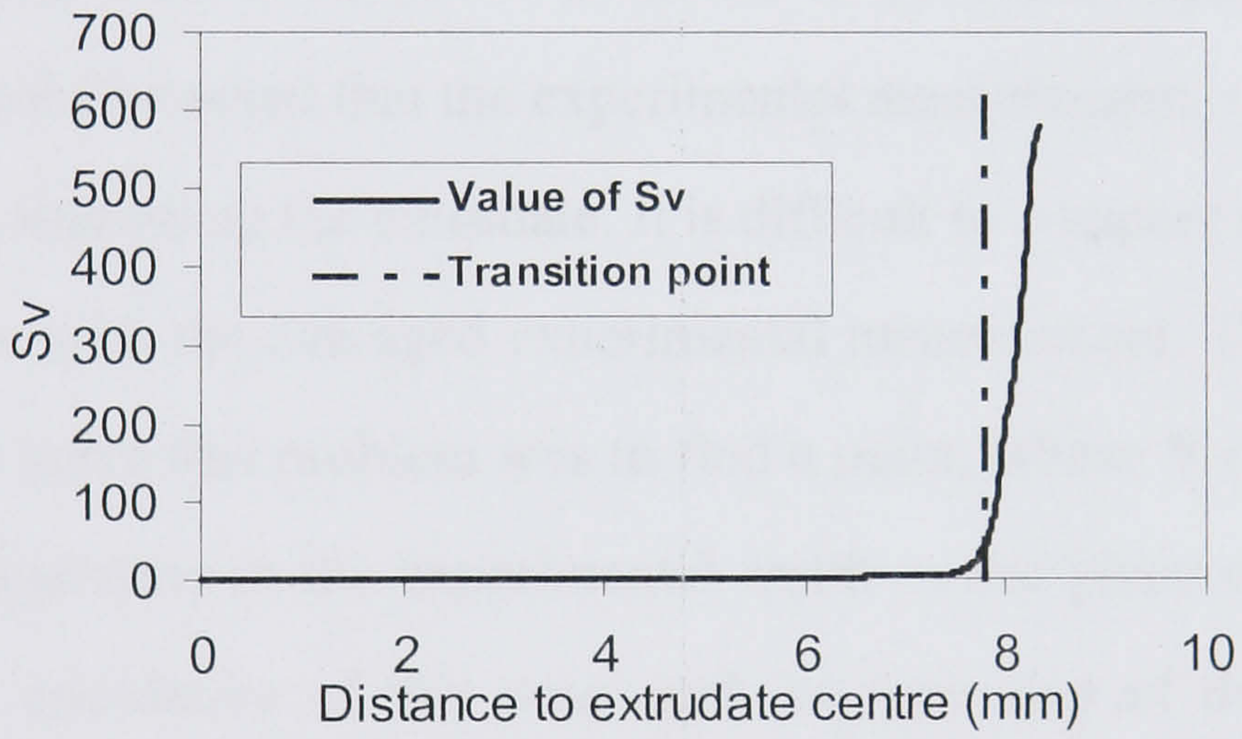

Figure 4.5 Ratio of grain boundary arer per unit area (Sv) across the extrudate

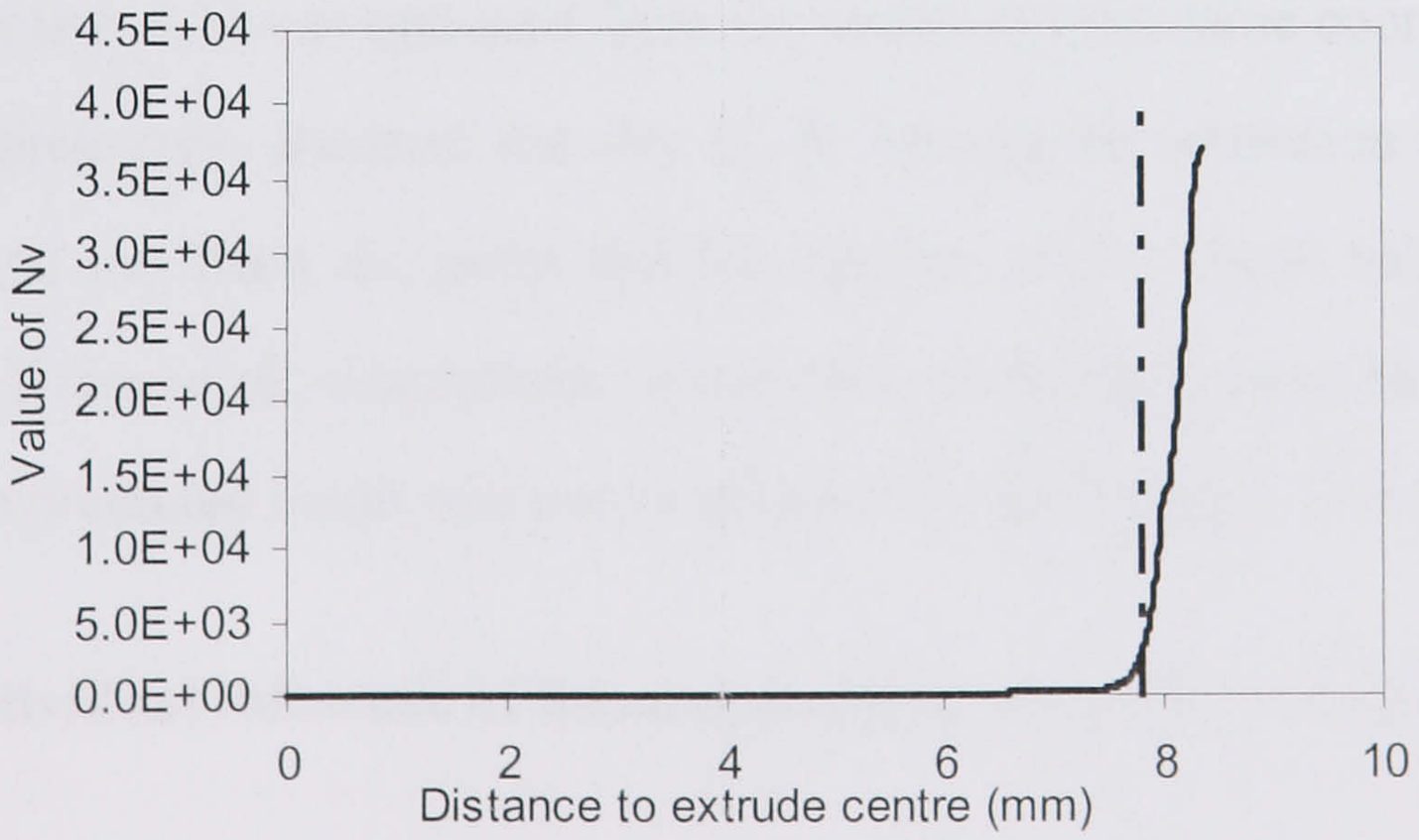

Figure 4.6 Density of nucleation sites (Nv) across the extrudate

However, with the lack of experimental evidence, it is difficult to reach any conclusion. Some arbitrary solution has to be applied to simulate the structure evolution for this special area. According to the experimental results, the nuclei number at this area was regarded as approximately 1.4 times more than the area 500 μm below the surface. Because the outer surface layer with 0.5mm thickness is a very small portion of the extrudate (5.93mm), the approximate solution will not influence the final result of the macro-scale simulation.

4.1.1.3 Fraction recrystallised factors

For the predicted result of volume fraction recrystallisation, the simulation gave a slightly rising value along the extrudate surface, as can been seen from Figure 4.7. This phenomenon has been observed in previous experiments (Sheppard 1993). It should be noted that the experimental measurement, which is 27.37%, is an average value along the extrudate. It is difficult to compare the variation of the predicted Xv with the averaged experimental measurement. The method used in this study to solve this problem was to find a point, whose Y coordinate gave the best correspondence to the experimental result in the given curve. At the same time, the X coordinate of this point and the time step of the simulation were picked out, and the predicted Xv of the other simulations employed in the next section (section 4.3) was obtained from the point with the same coordinate and at the same time step. Because the rise of Xv during the extrusion is small, the value picked out from the point can be regarded as the mean value along the extrudate. Because all simulations in the next section are using the same FEM setting, the predicted result will not be affected by the meshing or tooling.

4.1.2 Individual influence of forming parameters on the structure

As can be seen from the discussions above, the physically based models can be applied to the simulation of extrusion process successfully to predict the final

structure. In the following sections, the simulations with the physically based models used to analysis the individual influence of forming parameters on the final structure will be discussed in detail.

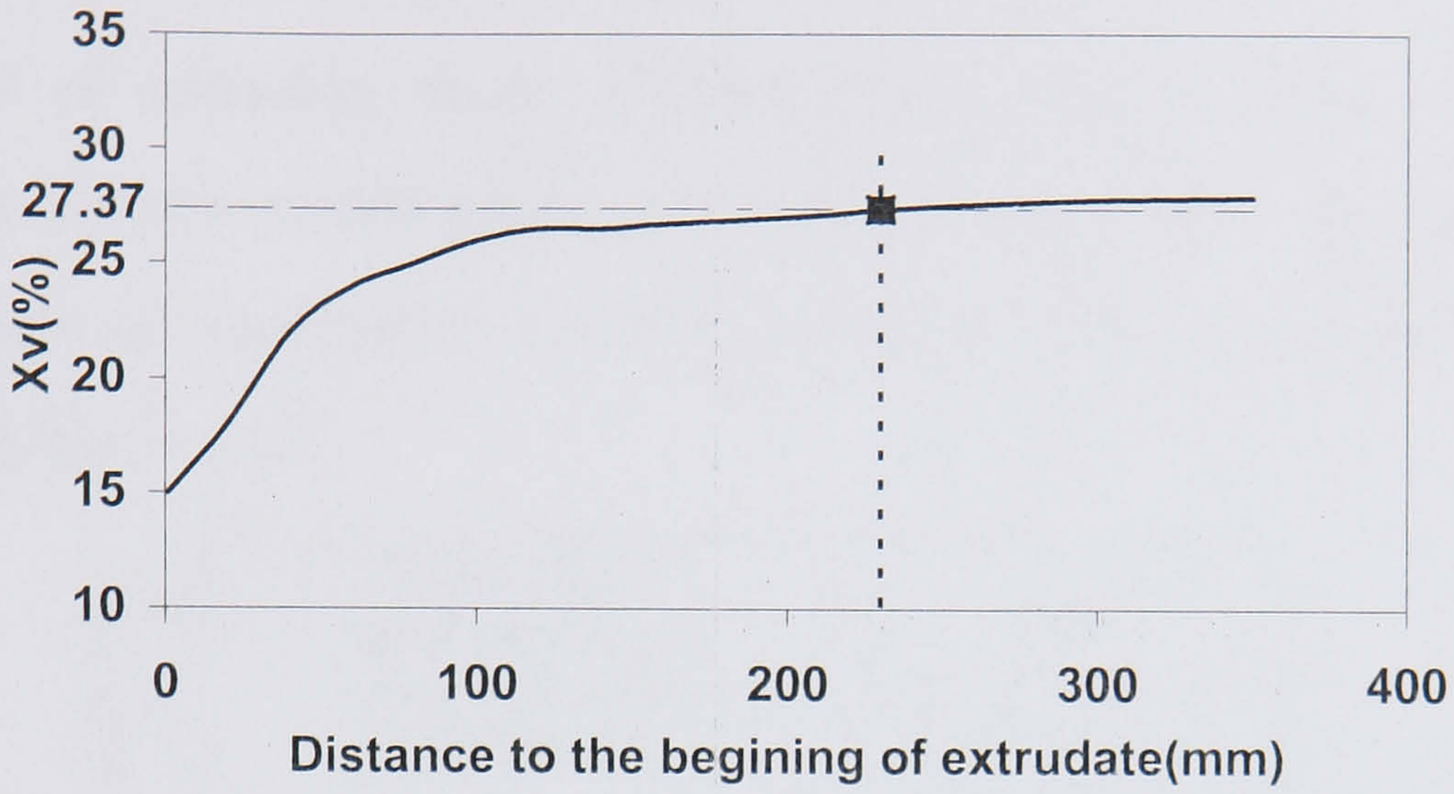

Figure 4.7 Predicted volume fraction recrystallised factor (Xv) along extrudate surface and the selected point

Special heat treatments are required for most of the heat treatable aluminium alloys after extrusion to improve the mechanical properties. For alloy AA2024, fully recrystallised structures are produced in all extrudates below an extrusion temperature of about 350°C, solution treated at 500°C for 30 minutes and water quenched, followed by ageing at 160 °C for 18 hours. Below this temperature the fibrous structure observed in the central region of the extrudate is no longer retained, static recrystallisation having formed new strain free grains. Above this temperature the extrudates exhibited a fibrous core similar to the as-quenched specimens surrounded by a recrystallised grain structure as shown in Figure 4.8 (Vierod 1983). It is well known that when surface recrystallisation occurs, the percentage of recrystallisation increases with decreasing extrusion temperature. As has been shown in Chapter 2, Figure 2.6, the percentage of recrystallisation decreases from about 50% to 10% with increase of the temperature. This is due to the increased stress and hence the driving force for static recrystallisation. The surface recrystallisation is of major importance because in these applications requiring good fracture toughness together with corrosion resistance, an

unrecrystallised structure is preferred, thus the surface and sub-surface recrystallisation determine the volume of material wasted by the necessary machinery operations.

The effect of extrusion mode (direct/indirect) on the volume percentage recrystallised is represented graphically in Figure 4.8. There is a large reduction of percentage recrystallisation for both extrusion ratios investigated when the indirect process is used.

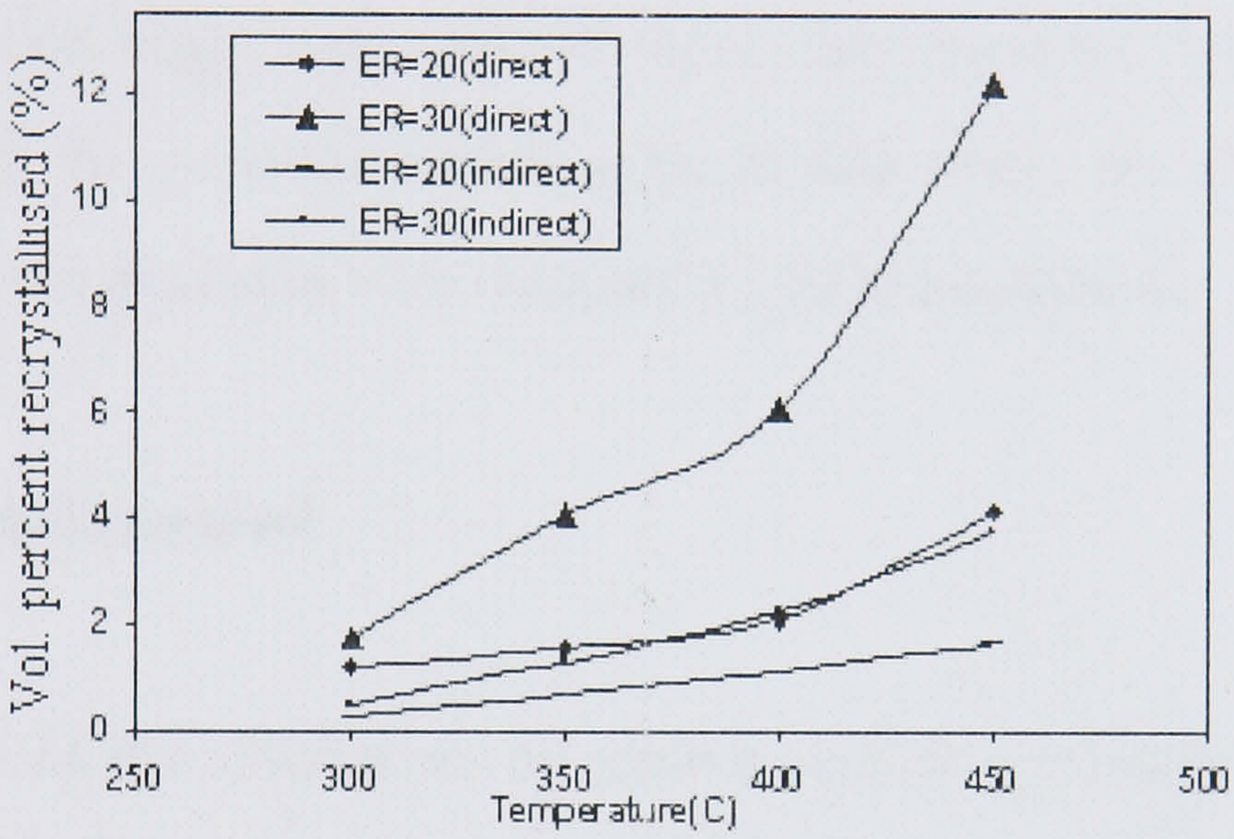

Figure 4.8 Influence of extrusion mode on surface recrystallisation

As can be seen from the above discussion, relationships exist only between the surface recrystallisation and one or two parameters. There are no comprehensive literature reviews concerning the contribution of each parameter to the process of surface recrystallisation. The absence of this type of study may be caused by the non-linear relationships between the forming parameters and the recrystallisation behaviour. The complexity of the extrusion process and the subsequent heat treatment may also prevent such studies from giving a comprehensive and simple relationship. Moreover, the recrystallisation behaviour varies when the composition of the alloy changes, which adds to the complexity of the study. However, the knowledge of the contribution of individual factors is key to deciding the nature of the control to be established in a production process. If this

information is established, even for a specific alloy and a limited range of temperature, it will still be helpful to the design of the extrusion process.

In the following sections, an investigation is made into the relationship of the fraction recrystallised coefficient to the main extrusion parameters in the extrusion of AA2024: extrusion ratio, ram speed, billet temperature and extrusion mode. The individual influence of these four parameters on the percentage recrystallisation is discussed by the use of the Taguchi method. To carry out this analysis, at least eight experimental results are required, but only five were available from the previous experiments. In this study, the other data that are necessary but not available were obtained by FEM simulation.

4.1.2.1 Taguchi method

The sequence of the simulations to predict surface recrystallisation is possible using the Taguchi method. The Taguchi method is designed to improve the quality of products and processes where the performance depends on many factors. Its approach to enhance quality in the design phase involves two steps (Fowlkes 1995):

1. Optimising the design of the product/process (system approach).

2. Making the design insensitive to the influence of uncontrollable factors (robustness).

The Taguchi method is most effective when applied to experiments with multiple factors. Taguchi constructed a special set of general designs for factorial experiments that cover many applications. The special set of designs consists of orthogonal arrays. The use of these arrays helps determine the least number of experiments needed for a given set of factors (Ranjit 1990).

An L8 orthogonal array is shown in Table 4.3. For the L8 array, there are two linear graphs available as shown in Figure 4.9. These two linear graphs indicate that several factors may be assigned to different columns and several different interactions may be evaluated in different columns.

Table 4.3 L8 Orthogonal Array Matrix

Trial no.	Column no.						
	1	2	3	4	5	6	7
1	1	1	1	1	1	1	1
2	1	1	1	2	2	2	2
3	1	2	2	1	1	2	2
4	1	2	2	2	2	1	1
5	2	1	2	1	2	1	2
6	2	1	2	2	1	2	1
7	2	2	1	1	2	2	1
8	2	2	1	2	1	1	2

Table 4.4 Simulation schedules according to Figure 4.9(a)

Runs	A (Billet temp) $^{\circ}C$	B (Extrusion ratio)	$A\times B$	C (Ram speed) mm/s	$A\times C$	$A\times D$	D (Extrusion mode)
1	360	40	1	7	1	1	Direct
2	360	40	1	3	2	2	Indirect
3	360	20	2	7	1	2	Indirect
4	360	20	2	3	2	1	Direct
5	410	40	2	7	2	1	Indirect
6	410	40	2	3	1	2	Direct
7	410	20	1	7	2	2	Direct
8	410	20	1	3	1	1	Indirect

For instance, linear graph (a), Factors A, B, C, and D may be assigned to columns 1,2,4 and 7 respectively. This places the $A\times B$ interaction in column 3, the $A\times C$ interaction in column 5, and the $A\times D$ interaction in column 6. The other linear graph provides an alternative arrangement with other interactions assigned. Both of these two possible interpretations are discussed in this thesis.

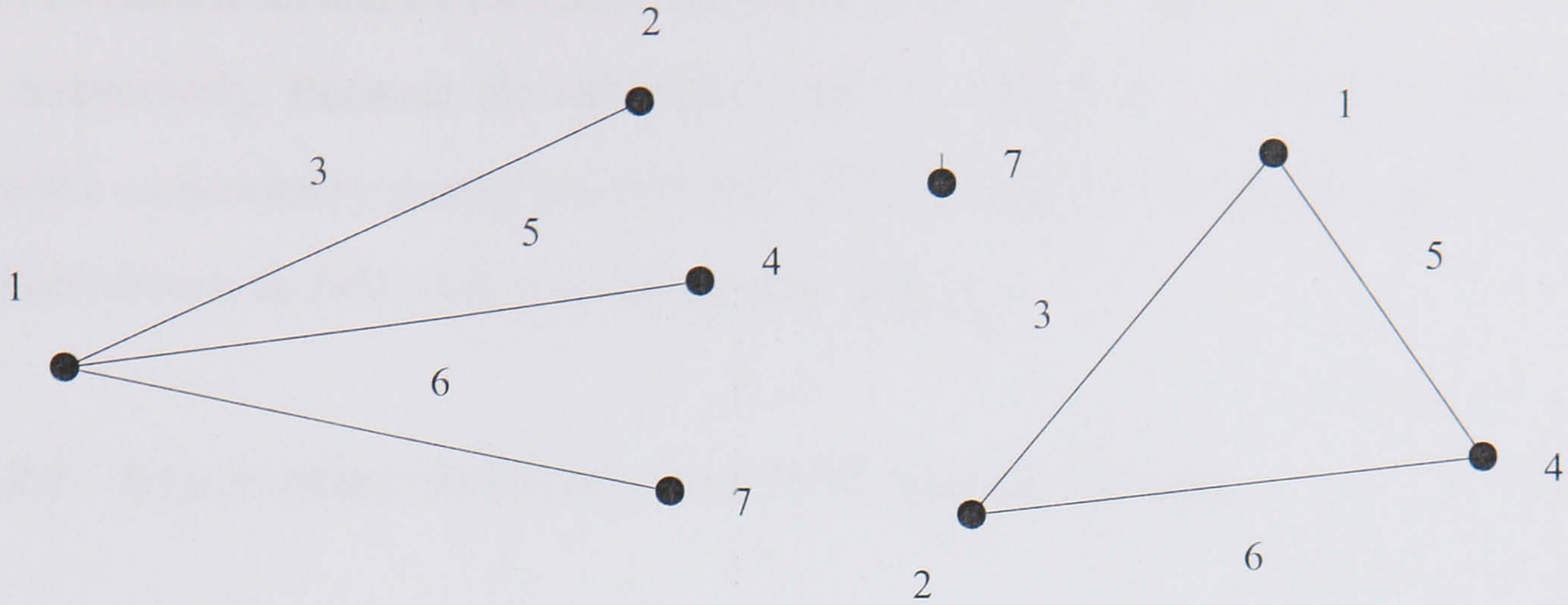

(a) Linear graph a (b) Linear graph b

Figure 4.9 L8 linear graphs arranged by Taguchi Method

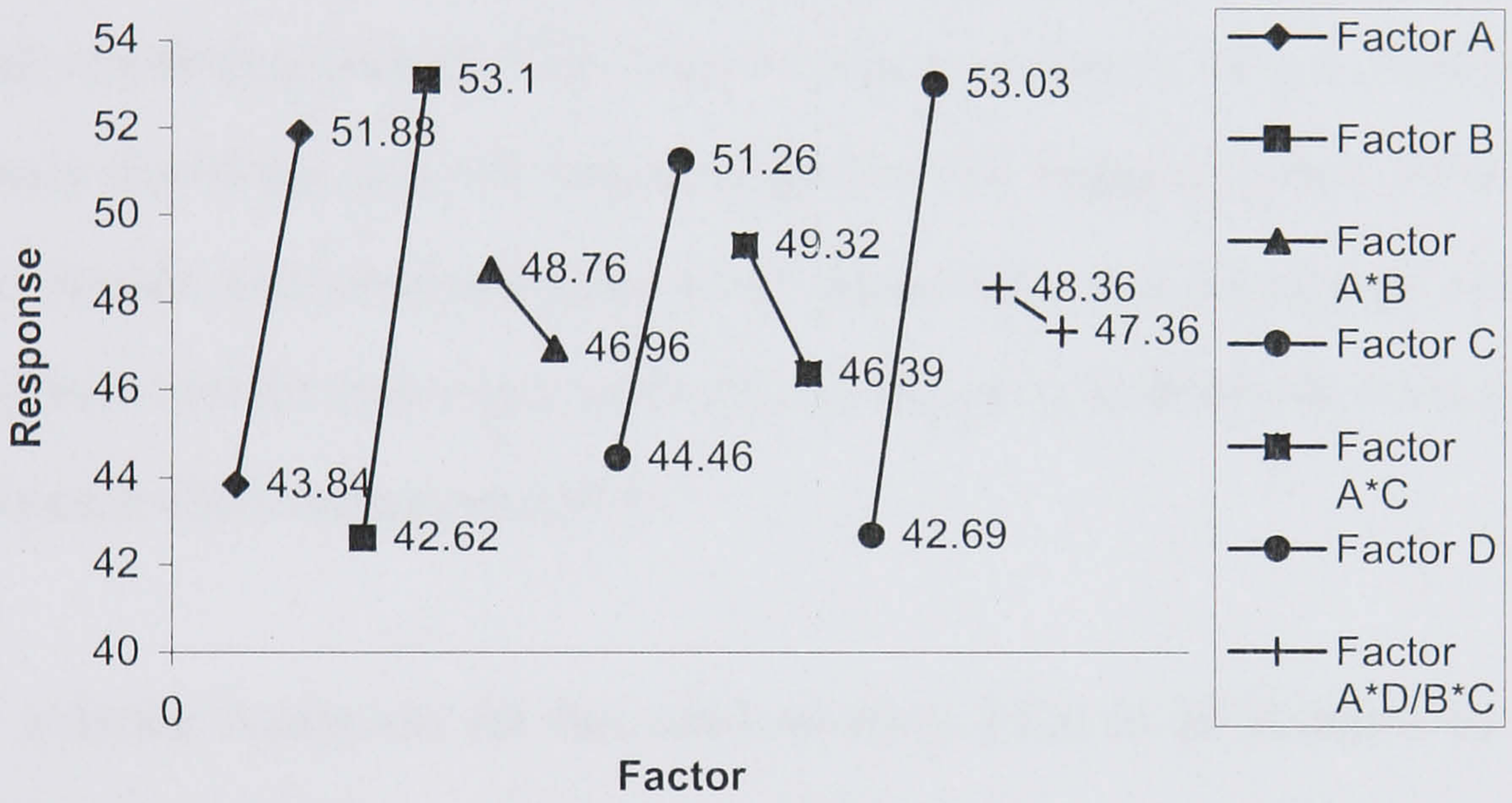

Figure 4.10 Effect of each factor (each number represents a level of a factor)

Table 4.5 Simulation schedules according to Figure 4.9(b)

Runs	A (Billet temp $^{\circ}C$)	B (Extrusion ratio)	$A \times B$	C (Ram speed) mm/s	$A \times C$	$B \times C$	D (not in use)
1	360	40	1	7	1	1	
2	360	40	1	3	2	2	
3	360	20	2	7	1	2	
4	360	20	2	3	2	1	
5	410	40	2	7	2	1	
6	410	40	2	3	1	2	
7	410	20	1	7	2	2	
8	410	20	1	3	1	1	

The simulation schedules for these two linear graphs are shown in Table 4.4 and 4.5 respectively. Because the extrusion mode is a parameter which can not be adjusted conveniently during the process of production and has been used in the analysis shown in Table 4.4, it is not used in Table 4.5.

4.1.2.2 Experimental Procedure and FEM Analysis setting.

Experiments performed by Subramaniyan (Subramaniyan 1989) are used to correlate the prediction results in this study. Extrusion was performed on a 5 MN press operating with tooling set up for direct and indirect extrusions. The billets were 75mm diameter ×95mm long and were heated in an induction heater or in an air circulating furnace. The load was measured by a Mayes load cell situated directly above the ram, the output from the cell being recorded on a Labmaster. Ram speeds and displacements were measured by a rectilinear potentiometer fixed between the moving crossheads and the press bolster that transmitted to the Labmaster (Subramaniyan 1989).

The solution treatment for hot worked alloy 2024 is 20 minutes to 2 hours at 500°C (depending on section size), followed by water quenching to obtain a supersaturated solution.

The FEM program, FORGE2® is used in the present study. It is a process simulation tool based on the Finite Element Method. The hyperbolic sine function was combined into the FEM to describe the material behaviour. For aluminium alloy AA2024, ΔH =146880KJ/mol, α =0.016 m^2 / MN , n=4.27, LnA= 19.6 (Sheppard 1999). The Tresca friction law with full stick friction is adopted in the present work.

4.1.2.3 Results and discussion

The runs, the experimental results and the simulation results are shown in Table 4.6. It is easy to see that the simulation runs according to Table 4.4 as shown in Table 4.6 can be used for Table 4.5 without any adjustment, that is, the same 8 runs can be used for both of the two possible schedules. Because the variation of each parameter is small in this study, it is reasonable to appoint only two levels to each parameter. $A\times B$, $A\times C$, $B\times C$ and $A\times D$ shown in Table 4.4 are the interactions between two parameters.

There are two methods to analyse the results: the signal-to-noise (S/N) ratio analysis and the standard deviation analysis (Ranjit 1990). Whenever an experiment involves repeated observations at each of the trial conditions, the S/N ratio has been found to provide a practical way to measure and control the combined influence of deviation of the population mean from the target and the variation around the mean. In this study, the S/N ratio analysis was adopted.

In cases when a smaller response is better, the formula of S/N ratio is:

$$S/N = -10 * \mathrm{Log}(MSD) \qquad (4\text{-}1)$$

where MSD is the Mean Squared Deviation (MSD) of the set. If the smaller response is the best quality characteristic, then:

$$MSD = (\frac{1}{n}\sum_{i=1}^{n} Y_i^2) \qquad (4\text{-}2)$$

where Y_i is the repeated simulation results in each run.

Table 4.6 Experimental and Simulation results

Runs	Experimental result (%)	Simulation results (%)			S/N
		1	2	3	
1	38.79				8.23
2		27.12	27.54	27.33	11.27
3	23.10				12.73
4		27.21	26.85	27.04	11.40
5		25.12	25.41	25.01	11.98
6	27.37	27.47	27.30	27.52	11.24
7	25.50				11.87
8		13.91	13.85	13.95	17.14

The analysis of variance (ANOVA) for the schedule shown in Table 4.4 and Table 4.5 is shown in Table 4.7 and Table 4.8 respectively. In this study, the S/N ratio analysis will use the experimental result if it is available, and if not, the three repeated simulation results of the same run shown in Table 4.6 will be used. The effect of each factor is plotted in Figure 4.10. The factorial effect is the difference between the two average effects of the factor at the two levels. The greater the difference between levels, the greater the effect.

Table 4.7 ANOVA for Table 4.4

Source	df	S	V	S'	ρ (%)
A (Billet temp)	1	9.25	9.25	8.75	20.57
B (Extrusion ratio)	1	13.59	13.59	13.09	30.77
$A\times B$	1 (pooled*)	0.17 (pooled*)	-		
C (Ram speed)	1	4.86	4.86	4.36	10.25
$A\times C$	1(pooled*)	0.99 (pooled*)	-		
D (Extrusion mode)	1	13.47	13.47	12.97	30.49
$A\times D$	1(pooled*)	0.34 (pooled*)	-		
e	3 (df_e)	1.5	0.5 (V_e)	3.5	7.92
Total	7	42.67		42.67	1

* When the contribution of a factor is small, as $A\times B$, $A\times C$ and $A\times D$ in the

Table, the sum of squares for that factor is combined with the error e. The detail of the pooling procedure is not mentioned here.

Table 4.8 ANOVA for Table 4.5

Source	df	S	V	S'	ρ (%)
A (Billet temp)	1	9.25	9.25	8.75	30.0
B (Extrusion ratio)	1	13.59	13.59	13.09	44.8
$A \times B$	1(pooled)	0.17(pooled)	-		
C (Ram speed)	1	4.86	4.86	4.36	14.9
$A \times C$	1(pooled)	0.99(pooled)	-		
$B \times C$	1(pooled)	0.34(pooled)	-		
e	3	1.5	0.5	3.0	10.3
Total	7	29.2		29.2	1

The parameters used in Table 4.7 and 4.8 are explained below:

df : Degree of freedom.

df = Number of trial conditions for a factor-1

df_e :Degree of freedom of Error Term.

$$df_e = df_T - (df_M + df_R + df_B + df_E + df_c) \quad (4\text{-}3)$$

S: Sum of squares:

$$S = A_1^2 / N_{A1} + A_2^2 / N_{A2} - T^2 / n \quad (4\text{-}4)$$

Where A_1 and A_2 are the sum of run results in each level of a factor, N_{A1} and N_{A2} are the number of trials for each level of a factor (4 in this case), T is the grand total of all results, n is the total number of runs.

V: Variance.

$$V_i = S_i / df_i \quad (4\text{-}5)$$

S' : pure sum of squares.

$$S_i^{'} = S_i - V_e \tag{4-6}$$

From these Tables, it is easy to see that the extrusion ratio is the most important in terms of surface recrystallisation. The influence of the extrusion ratio is 30.77% and the influence of extrusion mode is 30.49% as shown in Table 4.7. When the extrusion mode is excluded, the influence of the temperature (30.0%) and the ram speed (14.9%) is also less than the influence of extrusion ratio (44.8%) on surface recrystallisation. The influence of the interaction effects can be ignored both in Table 4.7 and 4.8. Because all of the parameters studied here each have influences on the temperature rise, which is important for the metallurgical behaviour during aluminium extrusion, it seems surprising that interaction effects are very small. When noting that the different extrusion parameters tend to result in a very small exit temperature range, it not difficult to understand this result. In related research work performed by the present author (Peng and Sheppard 2004a), the individual influence of forming parameters (extrusion mode, billet temperature, container temperature and ram speed but excluding extrusion ratio) on the surface recrystallisation have also been determined using an identical method that is used in this study. The study result shows the extrusion mode and the initial temperature are the most influential factors, which clearly correlate with the conclusion of the present study.

It is worthwhile to reiterate that in this study, the temperature is limited between two levels: $360^{\circ}C$ and $410^{\circ}C$. Below or beyond this temperature range, the billet temperature shows a much more important influence than the other parameters. However, surface integrity factors dictate that such data may not be used in this analysis.

As can be seen from the discussion above, with the use of the metallurgical model, the recrystallisation behaviour at the extrudate surface of aluminium alloy can be predicted by FEM simulation. The mode of extrusion is clearly of paramount importance and if the highest quality material is required, then this mode should be used, despite the mechanical drawbacks. The analysis using the Taguchi method shows that the extrusion ratio has the most significant influence on the volume fraction recrystallisation when compared with the other forming parameters. However this is not a commonly accepted proposition (because extrusion ratio is not in general controllable) and it would appear that careful control of temperature and ram speed would be the method generally attaining the desired structure. Moreover, the extrusion ratio is normally a fixed parameter in the industrial context.

4.2 T shape extrusion

Practical experience indicates that very large increases in the extrusion load can be encountered as the section geometry diverges from simple rounds to complex shapes containing re-entrant corners or thin wall sections, depending on the complexity of the shapes. An example of a thin wall extrusion is shown in Figure 4.11. In the following discussions, the simulations of T shape section extrusion are adopted to illustrate the application of FEM in this field. The dimension of the T section has been shown in Figure 2.1 and it is repeated here for the convenience of the reader.

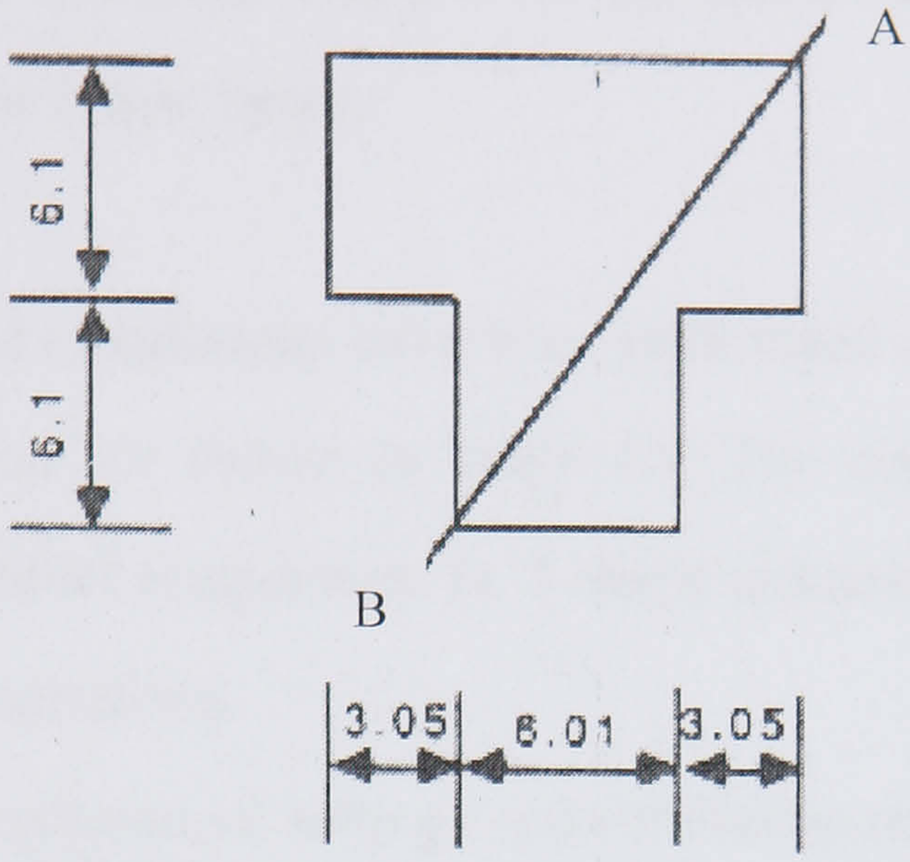

Figure 4.11 Dimension of the T shape extrudate (Subramaniyan 1989)

4.2.1 Thermal-mechanical simulation results

Compared with axi-symmetric extrusion, the flow pattern of shape extrusions is more complex.

For the present work, the peripheral ratio, λ, defined as the ratio of the periphery Ω_s of the section to the periphery Ω_r of a rod of equivalent cross-section, has been used to represent the complexity of the die. For example, Sheppard and Wood (1980) have shown that the total pressure requirement would be predicted by an equation of the form:

$$p = f(\lambda, R, Z, A) \qquad (4\text{-}7)$$

where R is the extrusion ratio, Z is the Zener-Hollomon parameter, A is a constant, λ is the shape factor.

Experiments and simulations have been performed and the individual results for T-shape extrusion are shown in Table 4.9. The container temperature is 50°C lower than the billet temperature in T-shape extrusions and remains at 300°C in multi-hole die extrusions.

Table 4.9 Experimental settings and simulation results of T-shape extrusion

(Experiments after Subramaniyan 1989)

Run	Ratio	Temperature (°C)	Ram speed (mm/s)	Experimental load (tonnes)	Predicted load (tonnes)
1	40	350	3	458	460
2	40	452	7	326	340

The predicted time-load curve of run 2 is shown in Figure 4.12. As can be seen from the simulation results, the predicted loads are in reasonable agreement with the experimental results.

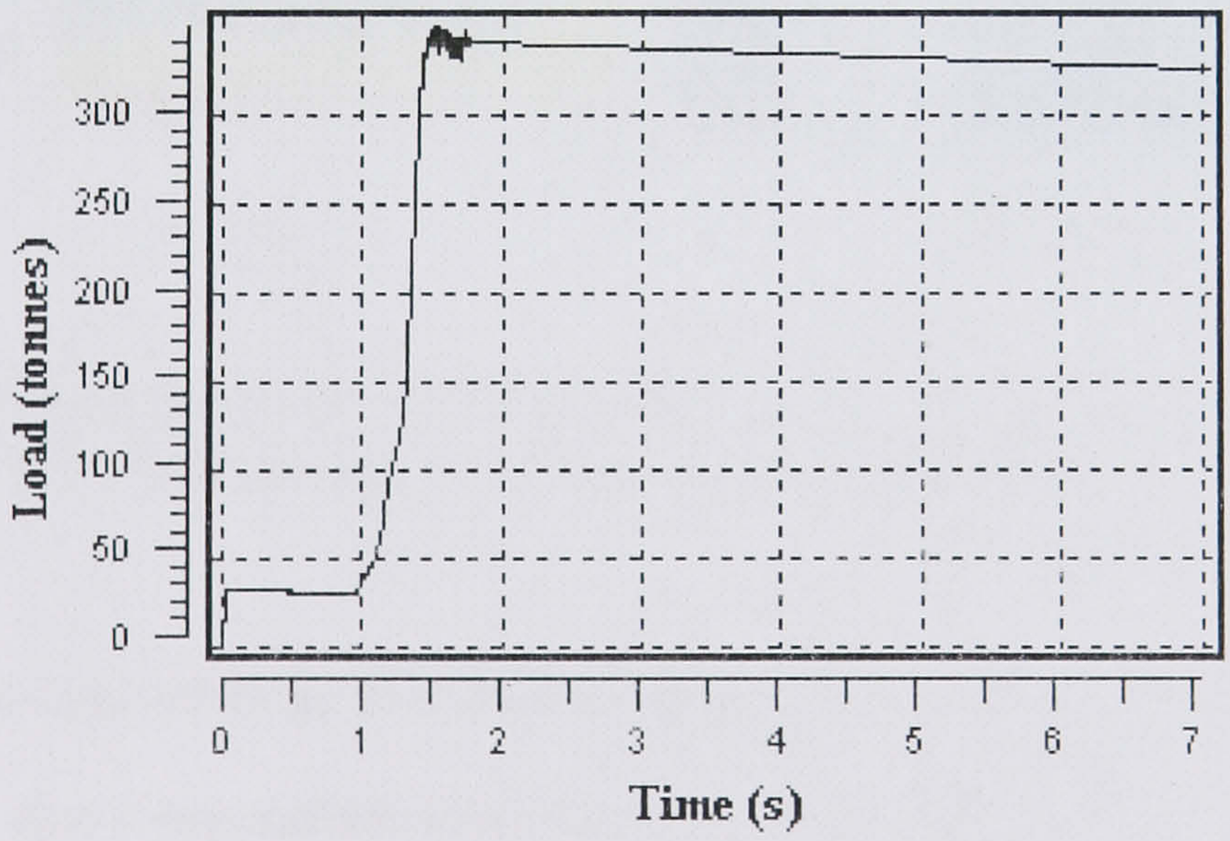

Figure 4.12 Predicted peak loads in T-shape extrusion (run 2)

Due to the asymmetric nature of the complex shape dies, the temperature distribution in the extrudate in the transverse direction is quite inhomogeneous

when it exits the die orifice. Because the temperature is to be strictly controlled to give a product with satisfactory quality, it is therefore important to study the temperature distribution and its influence on the product quality.

The most important information is the temperature distribution in the cross section of the extrudate. In Figure 4.13 and Figure 4.14, the temperature at the sections of extrudate of the run 1 (as shown in Table 4.9) was provided. As can be seen from these two figures, the highest temperature occurs at the position with sharp configuration changes.

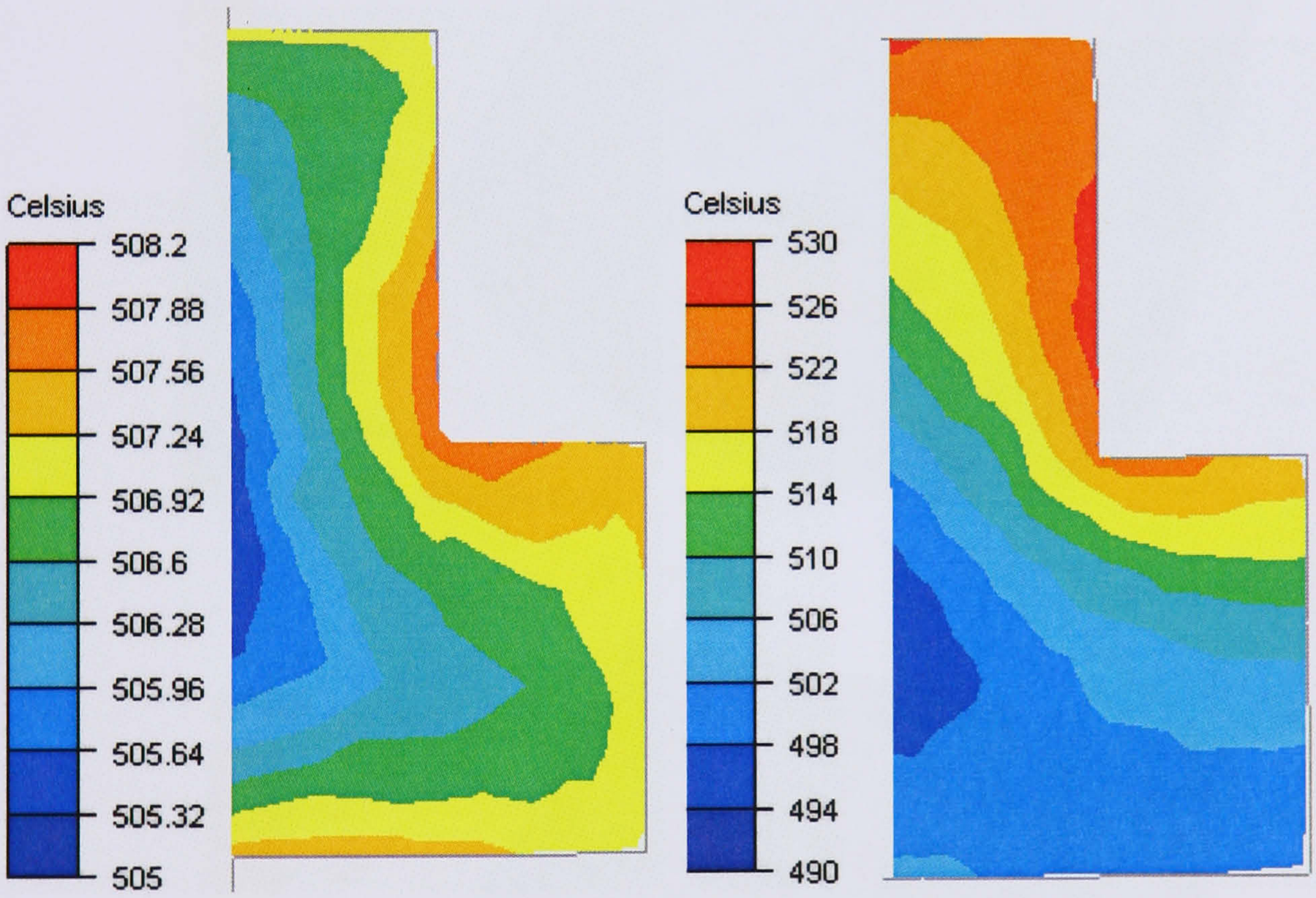

(a) run 1 (b) run 2

Figure 4.13 Temperature distribution at the die exit cross section (run 1: initial temperature 350°C, 3mm/s, run 2: initial temperature 452°C, 7mm/s).

In addition, the temperature distribution inside the billet is also shown in Figure 4.13 and 4.14, the temperature rises sharply at the die entrance corners, which is also where the highest strain rate occurs. The temperature continues to rise until the material exits the die. As can be seen in Figure 4.13, the temperature distribution at the cross section is similar although a larger range of temperature can be observed when the ram speed is higher.

However, the present study is just a demonstration of the application of the FEM simulation into the study of aluminium extrusion. Because of the lack of experimental means to measure the temperature distribution inside the billet precisely, it is difficult to provide any comparison analysis at the present time. The justification of FEM given in Chapter 3 gives confidence that these results can be acceptable.

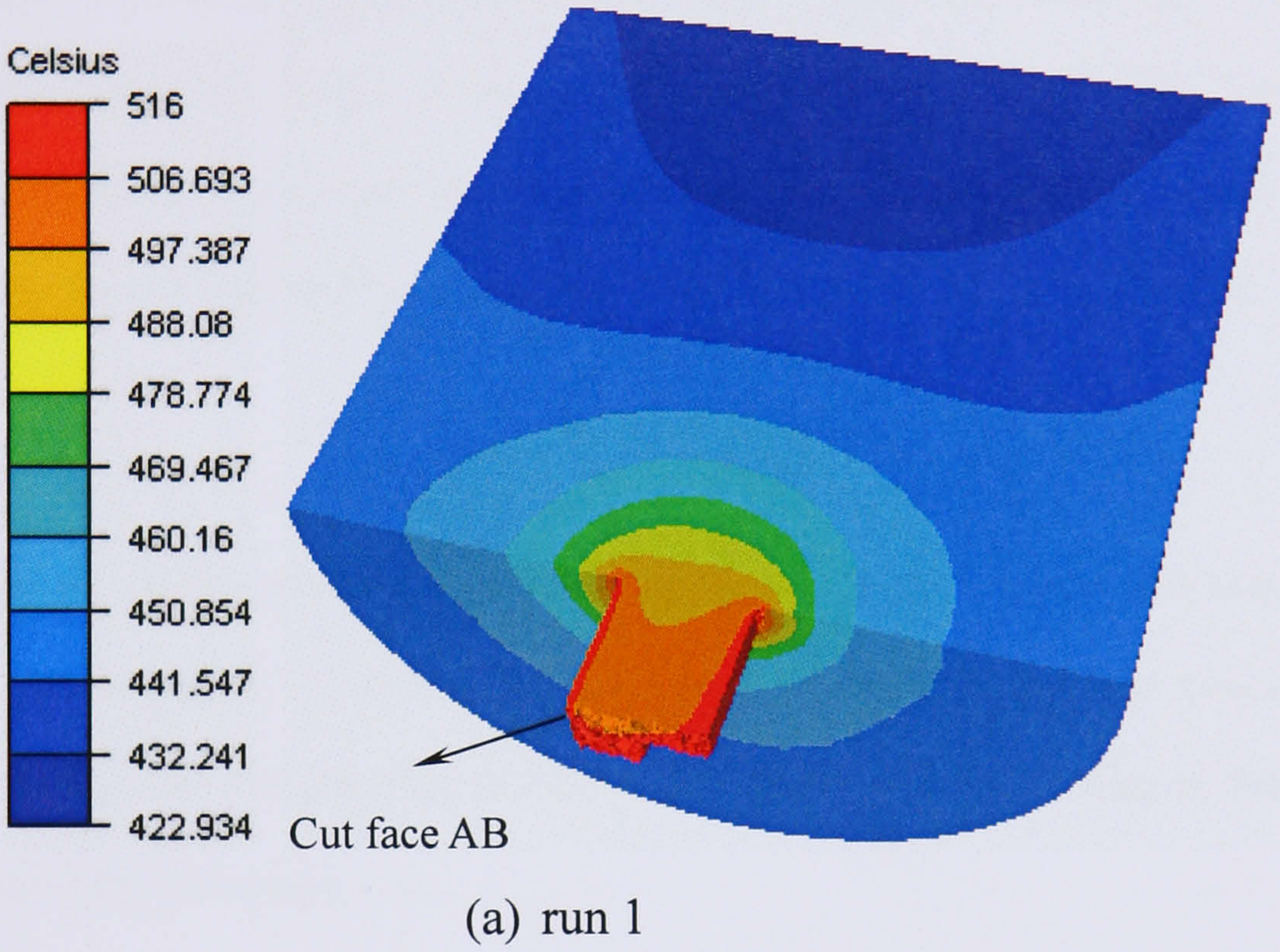

(a) run 1

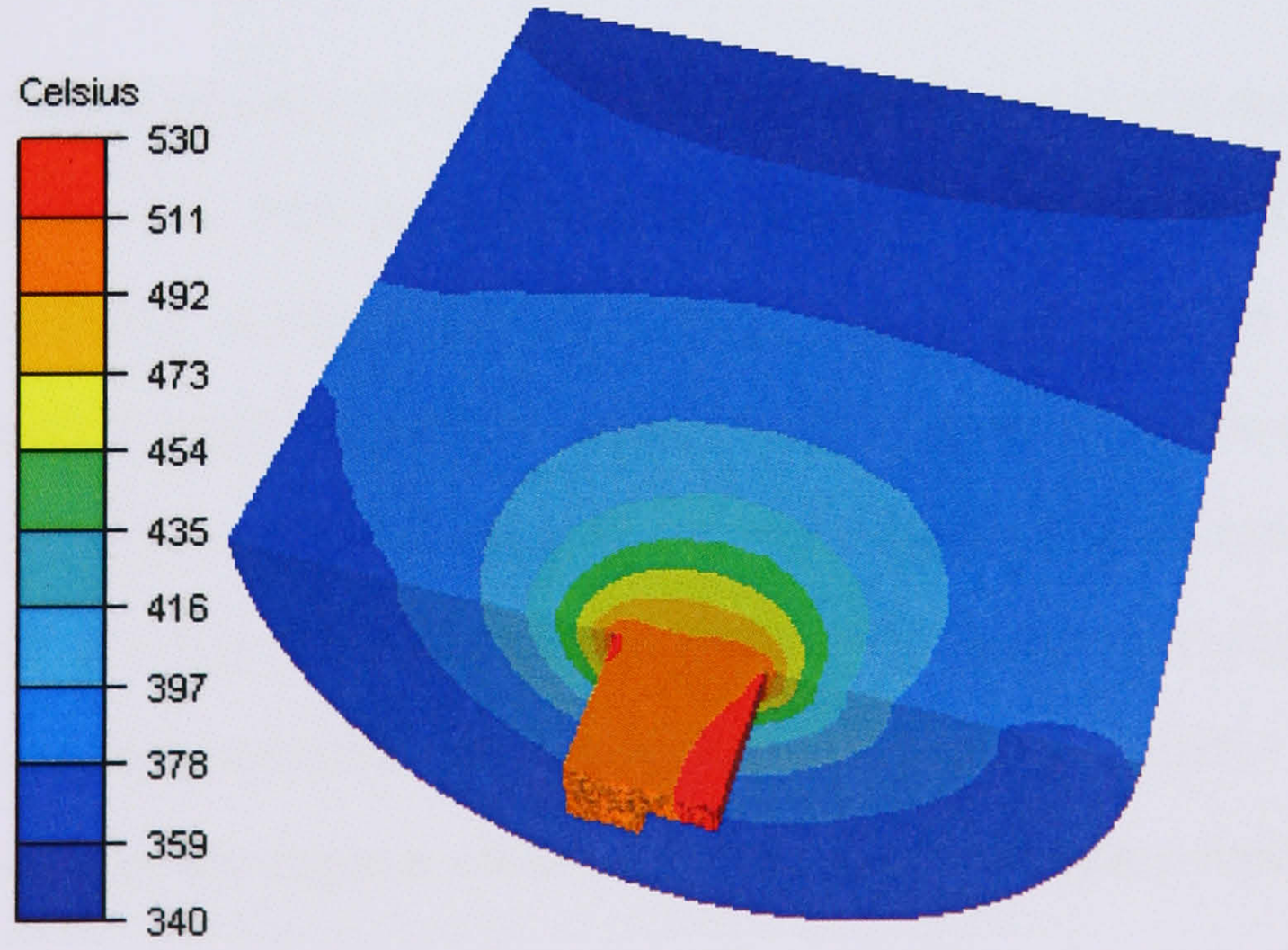

(b) run 2

Figure 4.14 Temperature distribution at the symmetric section (run 1: initial temperature 350°C, 3mm/s, run 2: initial temperature 452°C, 7mm/s).

4.2.2 Structural and substructural simulation results

In the extrusion of AA2024, due to the stored deformation energy within the extrudate, static recrystallisation usually occurs and extends to 100% of the material in some cases. The production of coarse grains during heat treatment is not beneficial because it causes a reduction in mechanical properties. Damage tolerance, fatigue crack propagation or corrosion, which are three very import technical indices required by the aerospace industry, are significantly affected by the recrystallised grain size and the volume fraction recrystallised. It has also been shown that this problem becomes greater as the complexity of section shape increases.

Hence, knowledge of the variation of the recrystalised grain size with time and space assists optimisation of the extrusion process. In the studies below, all discussions are focused on the formation of the grain size, the volume fraction recrystallised and the subgrain size.

Compared with axi-symmetrical extrusion, the material flow is nonhomogeneous in shaped extrusion. The flow pattern corresponding to the extrusion of rod and shape section is shown in Figure 4.15. The shape sections are cut from face AB as shown in Figure 2.1 and Figure 4.14. The cross plane section and the expected metal flow patterns for a T shape are also shown in Figure 4.16. It can be seen from Figure 4.15 and 4.16 that although the general flow pattern remains similar to that in rod extrusion, a certain amount of asymmetry about the billet axis can be seen, especially in the regions close to the die shoulders (dead metal zone). This can be explained on the basis that. if the flow is expected to be radial from the container wall, at least on the plane of projection parallel to the die place, the distance ab and cd as shown in Figure 4.16 over which the metal flows will be different. This can to some extent cause the asymmetry observed in the present instance. The asymmetrical material flow pattern has an important influence on

the metallurgical behaviour during shape extrusion, which will be discussed below.

The equivalent strain and the recrystallised grain size distribution of the two sections are shown in Figure 4.17 and Figure 4.18 respectively. As can be seen in Figure 4.18, unlike the axi-symmetrical extrusion, the recrystallised grain size around the periphery of the shape section is nonhomogeneous. The inverse relationship between the recrystallised grain size and the equivalent strain does exist in shape sections. In the area where the greater deformations occur, the recrystallised grain size is smaller than the other areas.

The predicted fraction recrystallised factors (Xv) at the periphery of the T shape section are shown in Table 4.10. The positions of the points used in these Tables are shown in Figure 4.19. For the shaped section, estimation of the depth of the recrystallised layer was difficult in previous experiments, since the layer was no longer uniform. With FEM simulation, the distribution of the volume fraction recrystallised factors can be predicted and extracted more easily. It has been found that both in previous experiments and FEM simulations that the recrystallised layer was thicker for more complex sections due to the larger temperature rise. As can be seen in Table 4.10, at the positions where the deformation is more complex, that is, where the strain and the temperature are higher, the fraction recrystallised factor is also higher. The experimental measurement of the average fraction recrystallised factor is 75%, the average value of the Xv as shown in Table 4.10 is 68%, which is about 7% lower than the experimental result. It should be pointed out here that the relative error for the method of measurements was approximately 9% and there was a variation in the value of Xv in the thickness around the extrudate. Considering these factors, the predicted results can be regarded as in reasonable agreement with the experimental measurements.

Table 4.10 Fraction recrystallised factors of T shape extrusion

Point	Equivalent strain	Xv	Point	Equivalent strain	Xv
1	2.1	61%	8	3.19	70%
2	3.37	62%	9	3.36	78%
3	3.04	65%	10	3.38	68%
4	2.97	60%	11	3.40	72%
5	4.06	69%	12	3.17	65%
6	4.15	82%	13	3.4	68%
7	4.81	72%			

The temperature distribution across the shape extrudates is shown in Figure 4.20. It can be seen that at the place where a sharper deformation occurs, the temperature and the volume fraction recrystallised are higher.

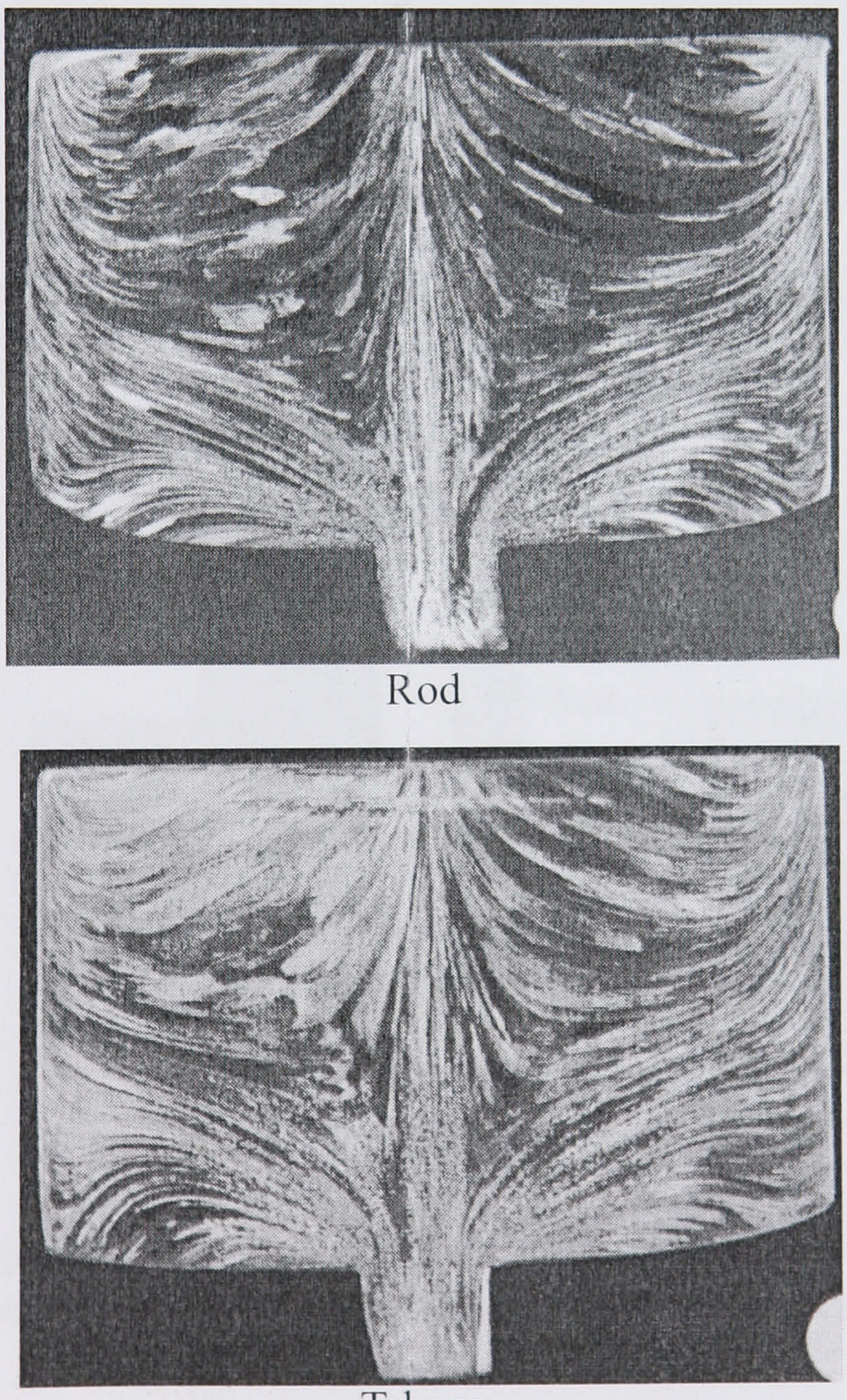

Rod

Tshape

Figure 4.15 Macrosections of partially extrudated billets

It can be seen from the discussions above, due to the different flow pattern in axi-symmetrical extrusion, the recrystallised grain size and the volume fraction recrystallised factor are nonhomogeneous around the periphery of the shaped section.

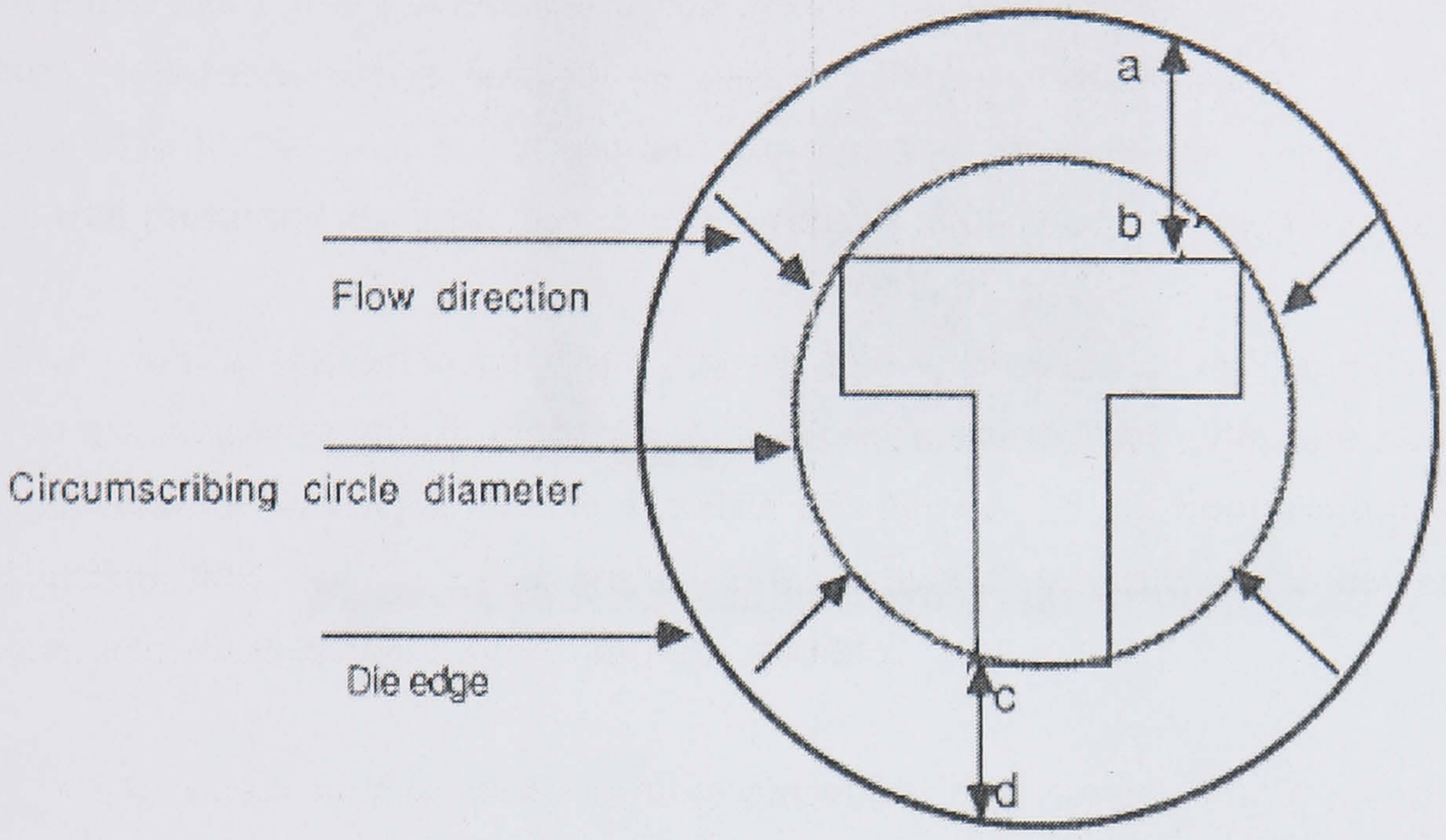

Figure 4.16 Metal flow expected in a T-Shape

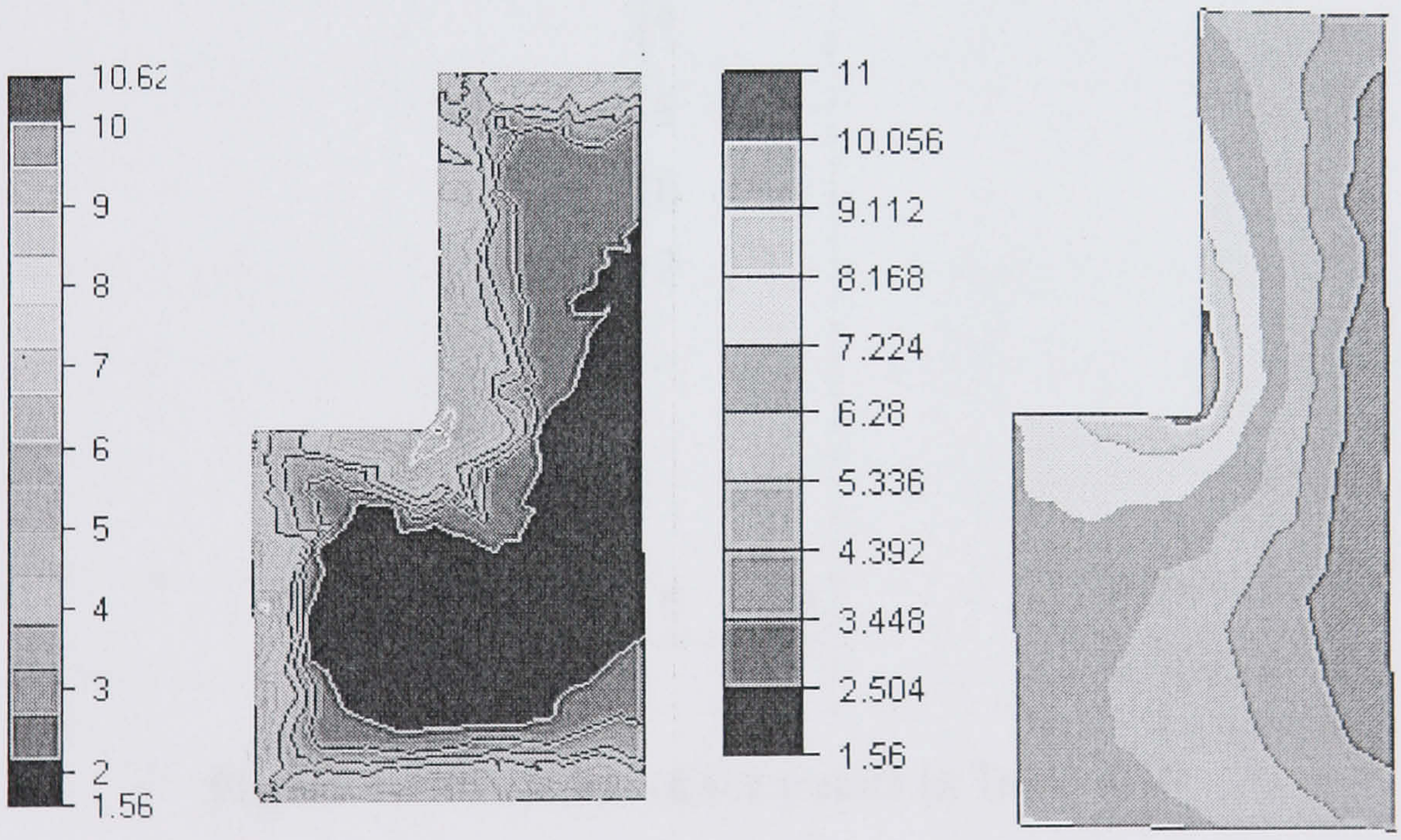

Run (1) Run(2)

Figure 4.17 Equivalent strain distribution (run 1:initial temperature 350°C, 3mm/s, run 2: initial temperature 452°C, 7mm/s)

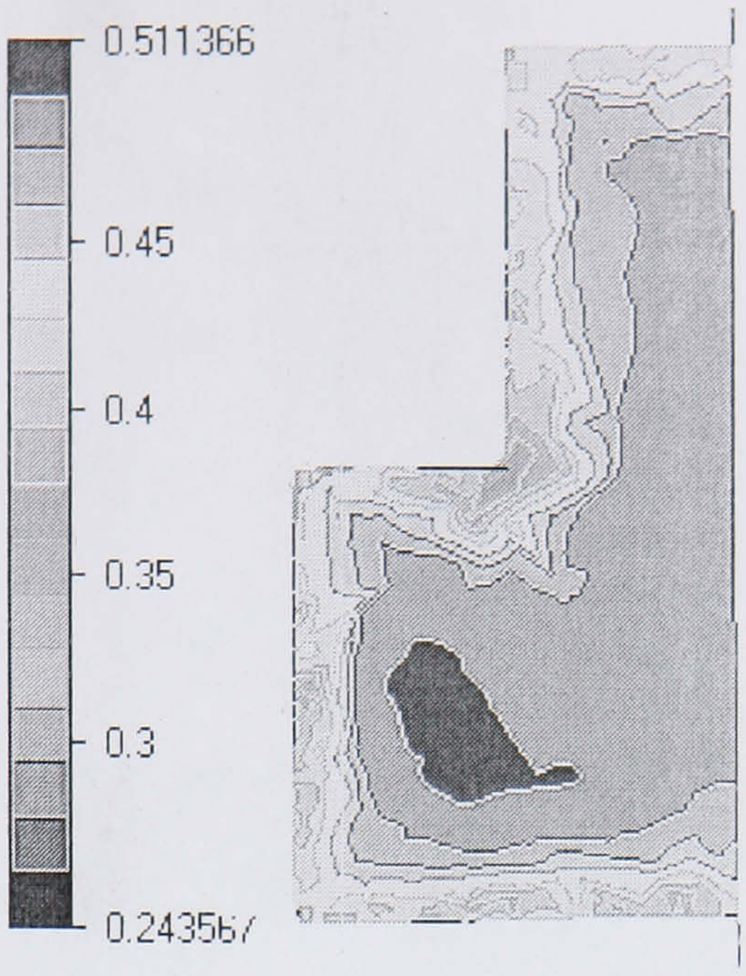

Figure 4.18 Recrystallised grain size (mm) (run 2)

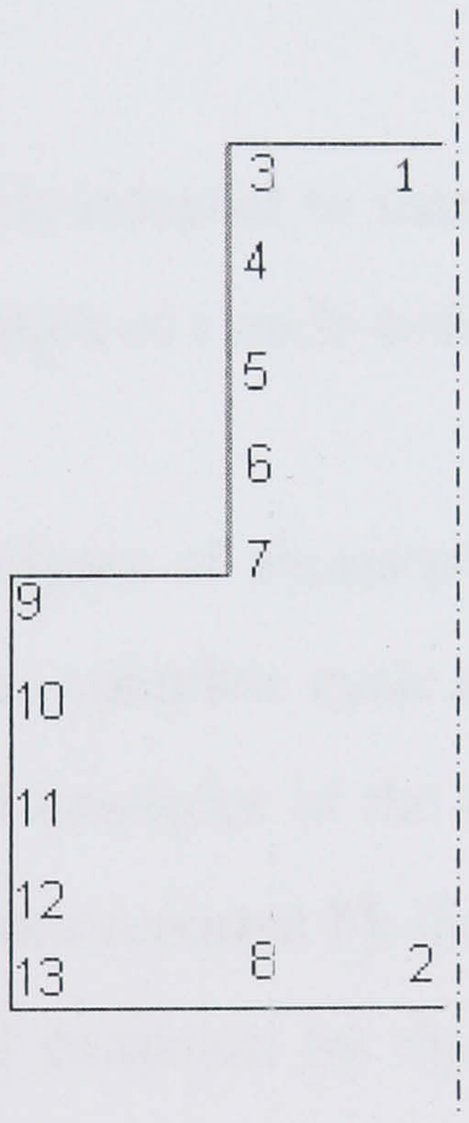

Figure 4.19 Position of the points in Table 4.10

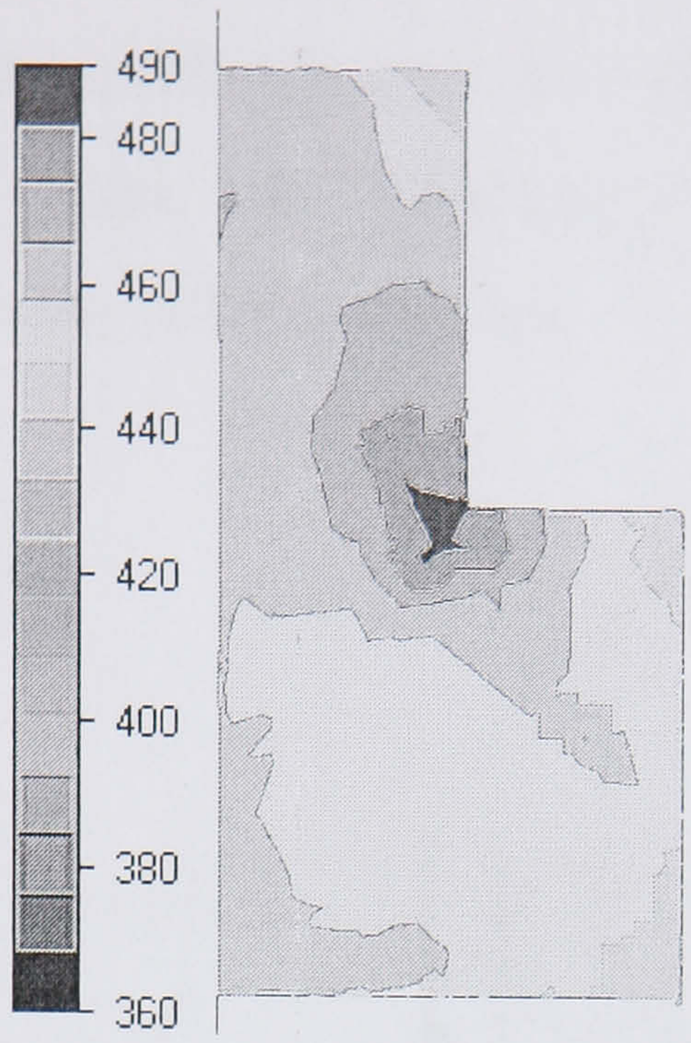

Figure 4.20 Temperature distribution ($^{\circ}C$) (run 2)

4.3 Multi-hole die extrusion

Multi-hole extrusion is widely adopted to increase productivity or where short lengths are required. An example of a multi-hole die is shown in Figure 4.21.

Three-dimensional FEM analyses of symmetric extrusion have been reported. Zhou et al. (2003) studied the complete cycle of an aluminium extrusion with a reduction ratio of 8:1. Some examples of the material flow pattern of complex shape extrusion have also been reported by Gouveia et al. (2001), they studied the round-to-square forward extrusion by three-dimensional FEM simulation. Milenin et al. (2002) studied a very complex shape extrusion with three-dimensional computer simulation, but little information about the material flow is provided in the study.

Compared with axi-symmetric extrusion, the flow pattern of multi-hole extrusion is more complex. The flow that occurs is asymmetrical and depends on the distribution of the holes. This can have important consequences on subsequent heat treatment and any further working. Experiments concerning material flow in

multi-hole extrusion reported, both using plasticine, and metals. Vater and Koltzenburg (1970) have also published some flow patterns for more complex shapes. By extruding two billets, one behind the other, after separation, the complex shape of the zone in the billet can be seen.

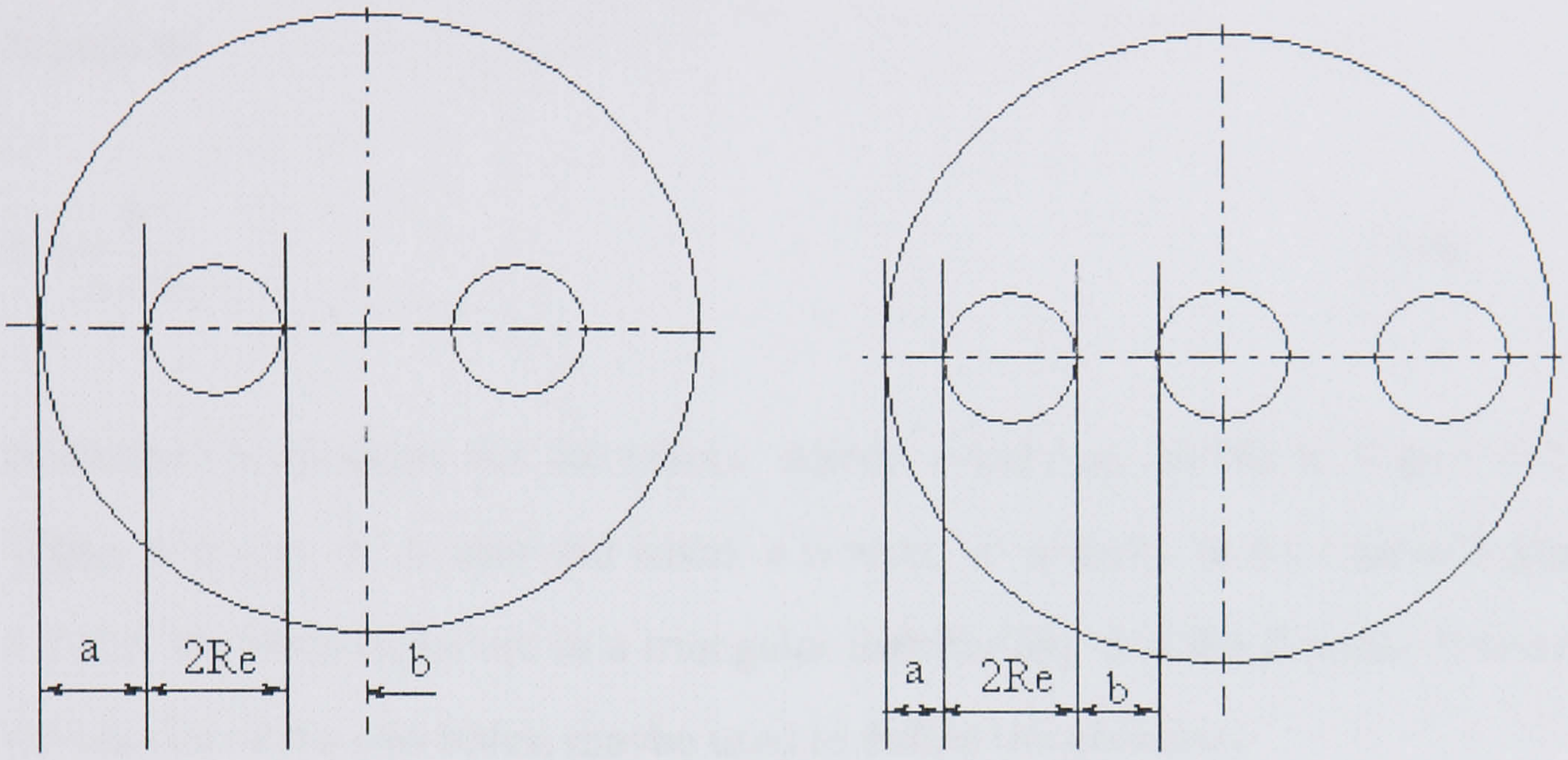

(a) Three hole die

(b) Two hole die

(c) Three hole die (triangle distribution)

Figure 4.21 Definition of eccentricity in multi-hole dies

There is no literature reported to predict the flow pattern of multi-hole extrusion from theory. The exception is those utilising slip-line field or upper bound approaches. Because the upper bound approach assumes the flow stress is a constant value, this method can only give approximate patterns in a limited

number of cases. With the development of three-dimensional FEM, the problem can be solved by numerical simulation. In this study, the material flow during the extrusion process is demonstrated clearly by such simulation.

In the case of two-hole or three-hole die extrusion, the eccentricity, which is defined as

$$\varepsilon = \frac{b}{a+b} \tag{4-8}$$

is adopted to evaluate the die layout, where a and b are shown in Figure 4.21. When b is zero ε is zero and when a is zero, ε is unity. In the case of Figure 4.21(c), the three holes are in a triangular distribution. d is the distance between the centres of the two holes, maybe used to define the geometry.

Castle (1974) reported experiments concerning the extrusion of shapes as well as extrusion through multihole dies. Sheppard (1999) has used the experimental data to show that for multihole extrusion the correction factor required may be expressed in terms of the peripheral ratio calculated using all the holes (i.e. for the extrusion of multiple rounds the ratio is simply $\sqrt{N}$ where N is the number of holes) and the pitch circle diameter such that $\lambda' = \lambda(D_B/(D_B - D_P))$ where D_P is the pitch circle diameter and D_B is the billet diameter. Table 4.9 shows the results of the analysis and the experimental data published by Castle (1974).

4.3.1 Thermal-mechanical simulation results

To analyse the influence of the multi-hole die on the extrusion load, some extra rod extrusions for comparison of multi-hole die extrusions were performed as shown in Table 4.11. The simulated peak load-time curves of the multi-hole die extrusions are shown in Figure 4.22 and some experimental measurements are also shown in Table 4.11.

The experimental measurement of the peak load is 245 tonnes for the No. 3 run as shown in Table 4.11. The predicted value is 229.5 tonnes, which is 6.5% lower. The experimental measurement of the No.6 run is 281 tonnes and the simulation result is 270.5 tonnes, which is 3.7% lower. Due to the lack of precise measurement of the friction at the interface of the billet and the dies, it is foreseeable that there are differences between the predicted and experimental loads. However, the FEM simulation results correlate well with the experimental measurements.

Some empirical work on the multi-hole extrusion of rods reported previously (Johnson and Kudo 1962) indicated that the load increased as the number of holes increased. For the two-hole die, the minimum is at an eccentricity of 0.45, which is almost identical to the symmetrical position of a and b being equal in Figure 4.21. The minimum for the three-hole extrusion pressure is at an eccentricity of 0.6, which again almost corresponds to the symmetrical configuration of a equal to $\frac{b}{2}$ (a and b are shown schematically in Figure 4.21).

The peak loads have also been studied by slip line solutions. The dependence of the peak load on the eccentricity of the die was also calculated. As can be seen from Figure 4.22, for both the two and the three hole configurations a minimum load is predicted at a certain value of the eccentricity, which is practically

independent of the extrusion ratio (R). The increase in the extrusion ram pressure $\Delta\bar{p}/2k$ (The increase in the extrusion ram pressure caused by the eccentricity ε, k is the maximum shear stress in simple shear) caused by the eccentricity ε in multi-hole extrusion is clearly shown (Johnson and Kudo 1962). The R shown in Figure 4.23 is defined as:

The two hole extrusion:

$$R = 1 - [2R_E / (a + b + 2R_E)] \tag{4-9}$$

The three hole extrusion:

$$R = 1 - [3R_E / (a + b + 3R_E)] \tag{4-10}$$

where a, b, R_E are shown in Figure 4.21.

Table 4.11 Experimental settings of multi-hole die extrusion

Run	Type	R (Extrusion ratio)	$2R_E$ (In Fig.3.8) (mm)	ε	Predicted peak load (tonnes)	Experimental peak load (tonnes) (Castle 1974)
1	One hole	120:1	6.86	0	298.0	313
2	One hole	60:1	9.68	0	170.8	190
3	Two hole	60:1	6.86	0.27	229.5	245
4	Two hole	60:1	6.86	0.45	196.2	
5	Two hole	60:1	6.86	0.7	211.3	
6	Three hole	60:1	5.59	0.22	270.5	281
7	Three hole	100:1	4.32	0.17	310.2	
8	Three hole (Triangular Distribution)	60:1	5.59	d = 12.61 (mm)	342.8	
9	Three hole	60:1	5.59	0.6	304.2	

It can be seen that there are some differences between the prediction, the theoretical solutions and the empirical work with regard to the two-hole extrusion. Using slip-line field theory, the eccentricity at which the minimum

load occurs is 0.7 in the two hole extrusion, whilst it is 0.45 according to the experiments as shown in Figure 4.23 (Johnson and Kudo 1962, p65). It should be pointed out that in Johnson's work, plain strain condition was assumed, and the work hardening and the friction condition were not considered. This explains the discrepancy existing between this and FEM. It also clearly indicates the necessity for the FEM approach. Further research examining the peak load and geometry of multi-hole extrusion is now under investigation.

The conclusions from the empirical experiments, the slip line solution and the FEM simulation are:

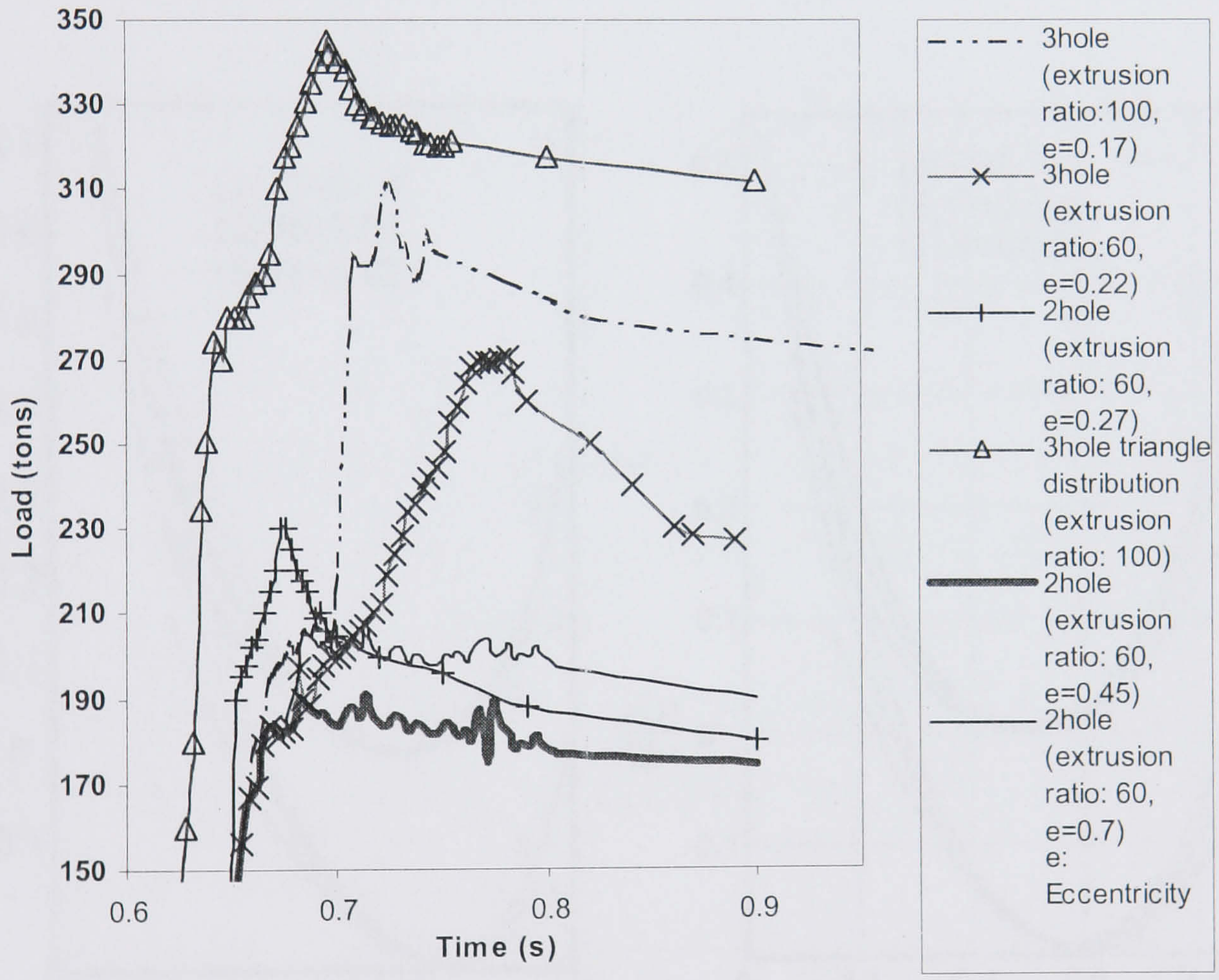

Figure 4.22 Peak load obtained for the runs given in Table 4.11

(1) The peak load increases as the number of holes increases. That is, the peak load of three hole extrusion is the highest and the peak loads of two hole extrusion are higher than the single hole extrusion at the same extrusion ratio.

(2) Three holes in a line in the diameter plane produce lower loads than a triangular distribution. However the reader should note that this work does not address the possibilities of the stress and "sinking".

(3) The least peak load of the three-hole extrusion occurs at an eccentricity of about 0.22 compared with a slip line field value of 0.6 (Figure 4.23). For the two hole extrusions the corresponding values are 0.45 and 0.75.

These values clearly demonstrate that the predictions based on a perfectly plastic material coupled with a plane strain model are quite unacceptable. The obvious advantages of FEM analysis are clear.

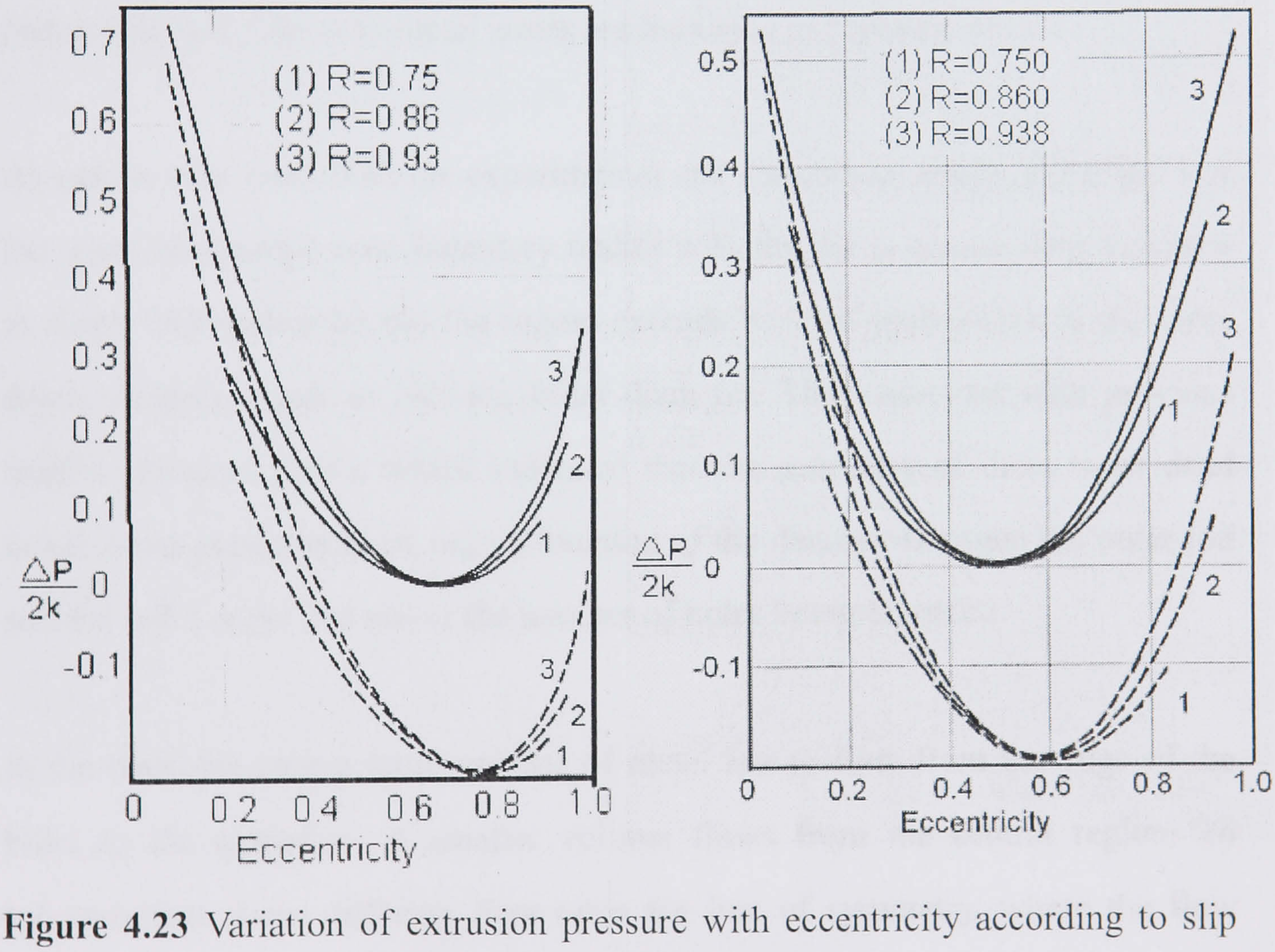

Figure 4.23 Variation of extrusion pressure with eccentricity according to slip line solutions (Johnson and Kudo 1962, p65)

However, to establish a quantitative relationship between the shape factor and the peak load, many more simulations and experiments need to be performed. The analyses in this section are just demonstrations of FEM applications to the

simulation of the extrusion process.

Examples from experimental and simulation results of the material flow pattern are shown in Figure 4.24. The experimental work showing the flow patterns for multi-hole extrusion were all taken in the vertical plane containing all the holes and typical examples are given to the left of Fig 4.24. The simulation outputs are given to the right of the Fig. Dead metal zones are seen in the circumferential extremities and can just be discerned in the area between the holes when the velocity vectors indicate stagnation. There are many basic similarities to the single-hole extrusion, with regions of intense shear bordering the dead metal zones, but there is also a shear region down the central axis in the case of the three-hole extrusion. In between these zones of shear the metal flows in a curved path to the exit. The dead metal zones are indicated in Figure 4.24.

As can be seen from both the experimental and simulation results, the angle that the outer dead metal zone boundary makes with the die is greater than that seen in single hole extrusion but the region extends back to approximately the same depth, roughly equal to half the billet diameter. This coincides with previous studies (Pearson 1961), which indicated that the geometry of these outer dead metal zones appeared to be only a function of the distance between the outer rod and the billet edge, and not of the number of holes being extruded.

In the two-hole case a large volume of metal has to flow from the edge of the billet to the extrudate. A smaller volume flows from the central region. To accommodate these differing flow rates the line of symmetry, where the flow rates are equal, will be displaced towards the centre. The three-hole extrusions are similar but more complex.

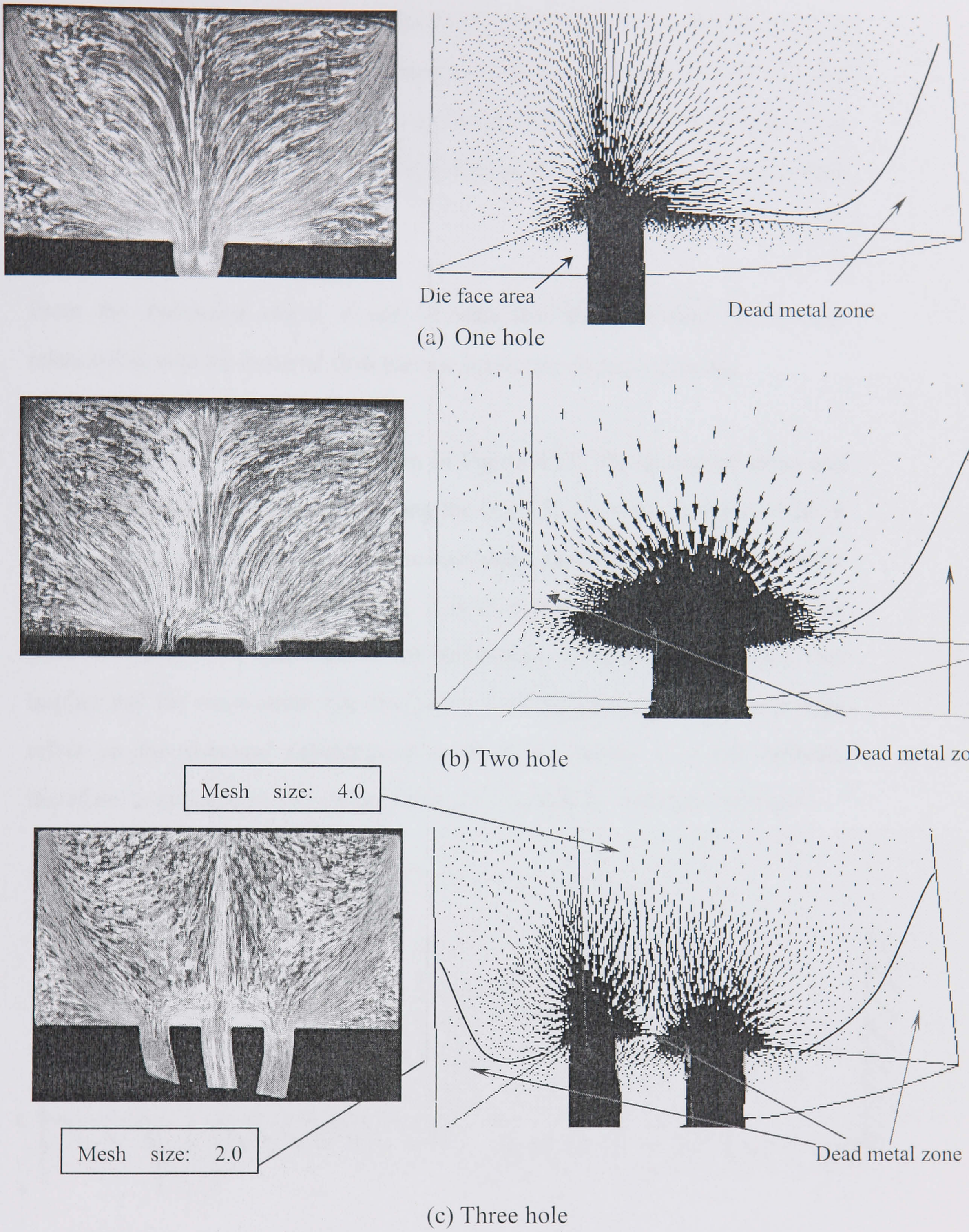

Figure 4.24 Experimental and simulation results indicating the agreement between micrograph and simulation output.

It is worth noting that the mesh size of the FEM setting can influence the interpretation of results. As can be seen from Figure 4.24(c). The back of the

billet is in coarse mesh size and the front of the billet is in fine mesh. The simulated vector distribution in the fine mesh area is fairly good but it is not very clear in the coarse mesh area. The conclusion can be easily drawn that a fine mesh is preferred, but at the same time it means that much more calculation time is needed.

From the discussion above, it can be seen that the peak load has a close relationship with the material flow pattern developed during extrusion.

The position of the line CD is shown in Figure 4.25. Th equivalent stress and equivalent strain-rate distribution along the line CD is shown in Figure 4.26. It can be seen that the flow stress and the equivalent strain-rate are higher when the flow pattern becomes more complex. It is noticeable that there is a strain rate peak associated with each hole (1 for single-hole, 2 for double-hole etc.) This implies that the mean strain rate also varies with the geometry. This has a large effect on the structure development as discussed below. It is not difficult, therefore, to understand why higher loads are expected in multi-hole extrusion.

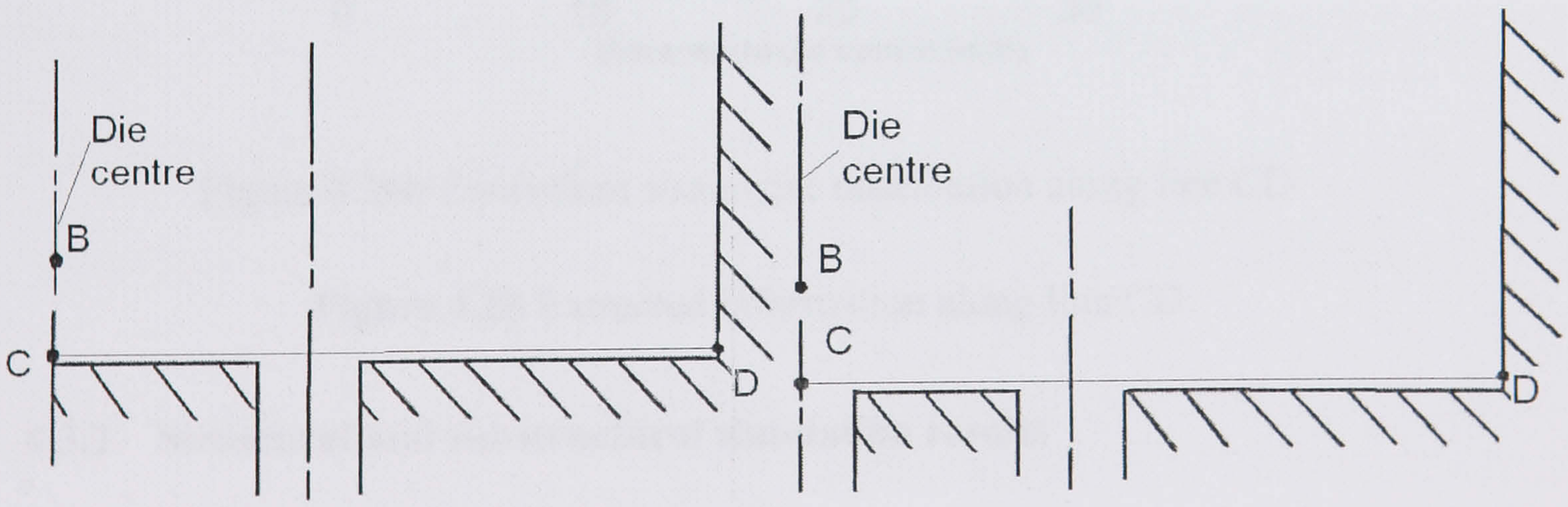

(a) two hole die extrusion (b) three hole die extrusion

Figure 4.25 The position of line CD

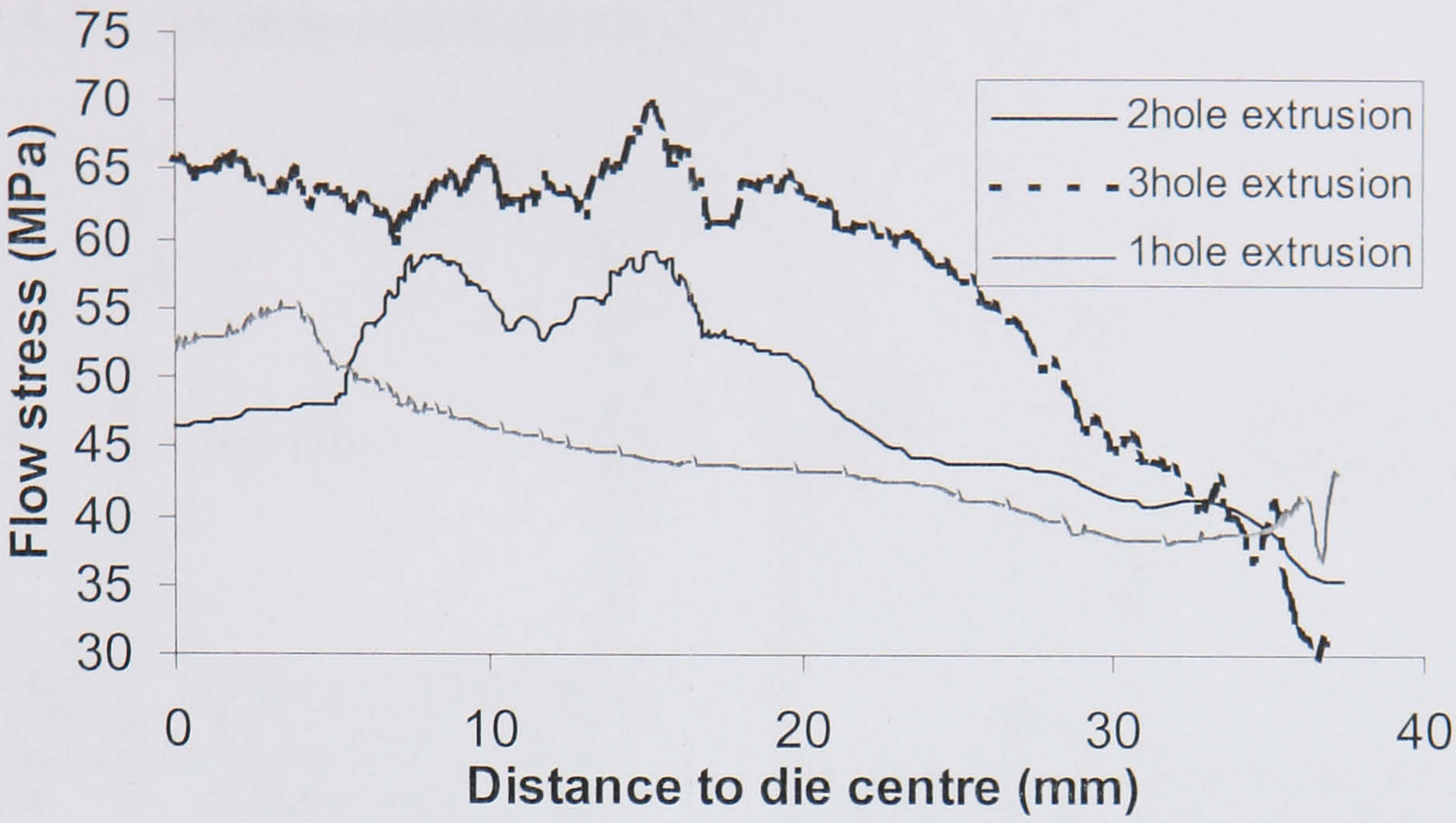

Figure 4.26a Equivalent stress distribution along line CD

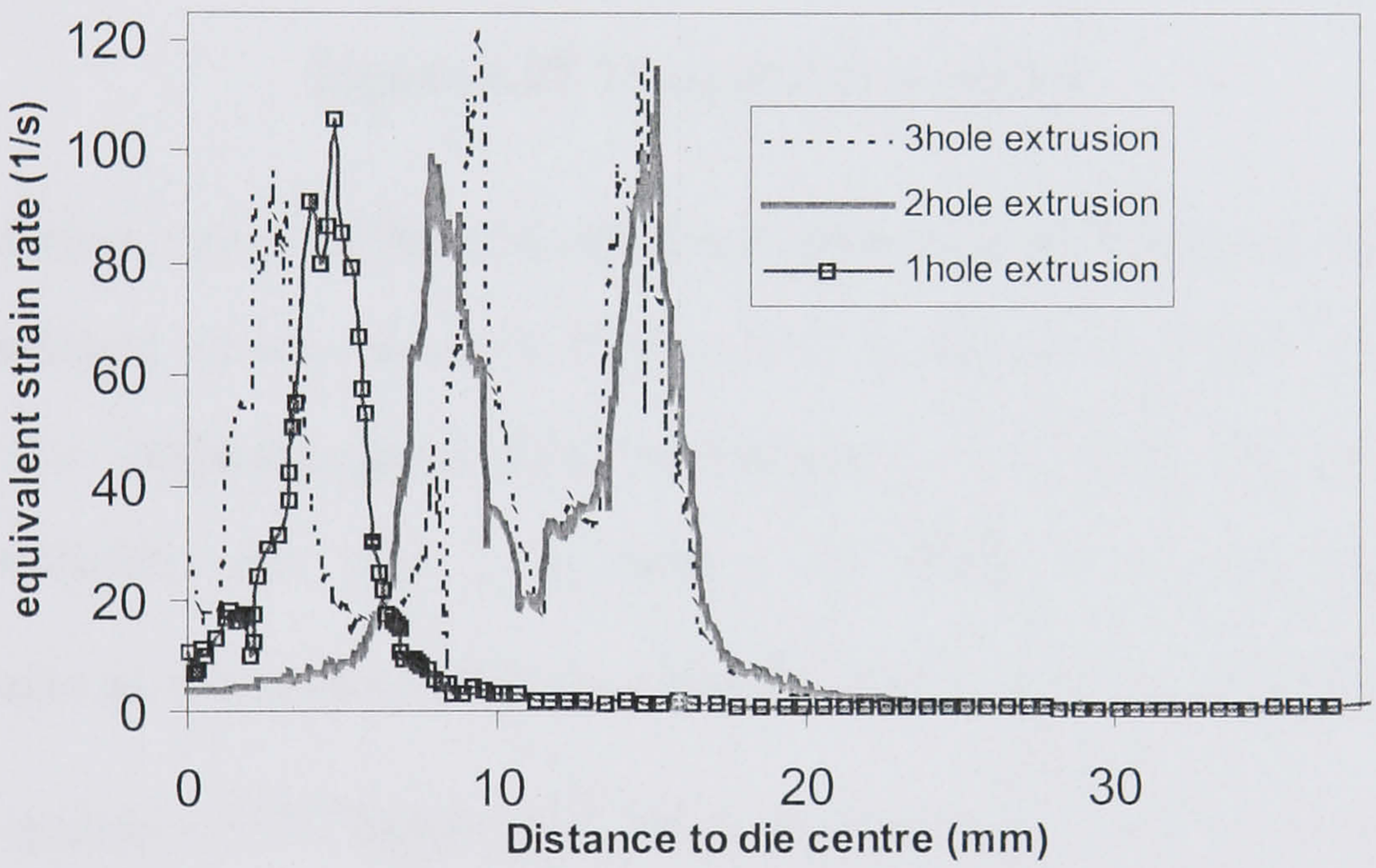

Figure 4.26b Equivalent strain-rate distribution along line CD

Figure 4.26 Extracted information along line CD

4.3.2 Structural and substructural simulation results

The simulation result regarding the restoration behaviour is discussed in this section. Three-dimensional simulations were carried out when studying the multi-hole extrusion. It should be noted that in the no.8 simulation as shown in Table 4.11, d=12.61mm, which is equal to $b+2R_E$ of the no. 6 simulation.

The value of d (shown in Figure 4.21) in the run 8 is equal to the value of b (Figure 4.21), which is used in the run 6.

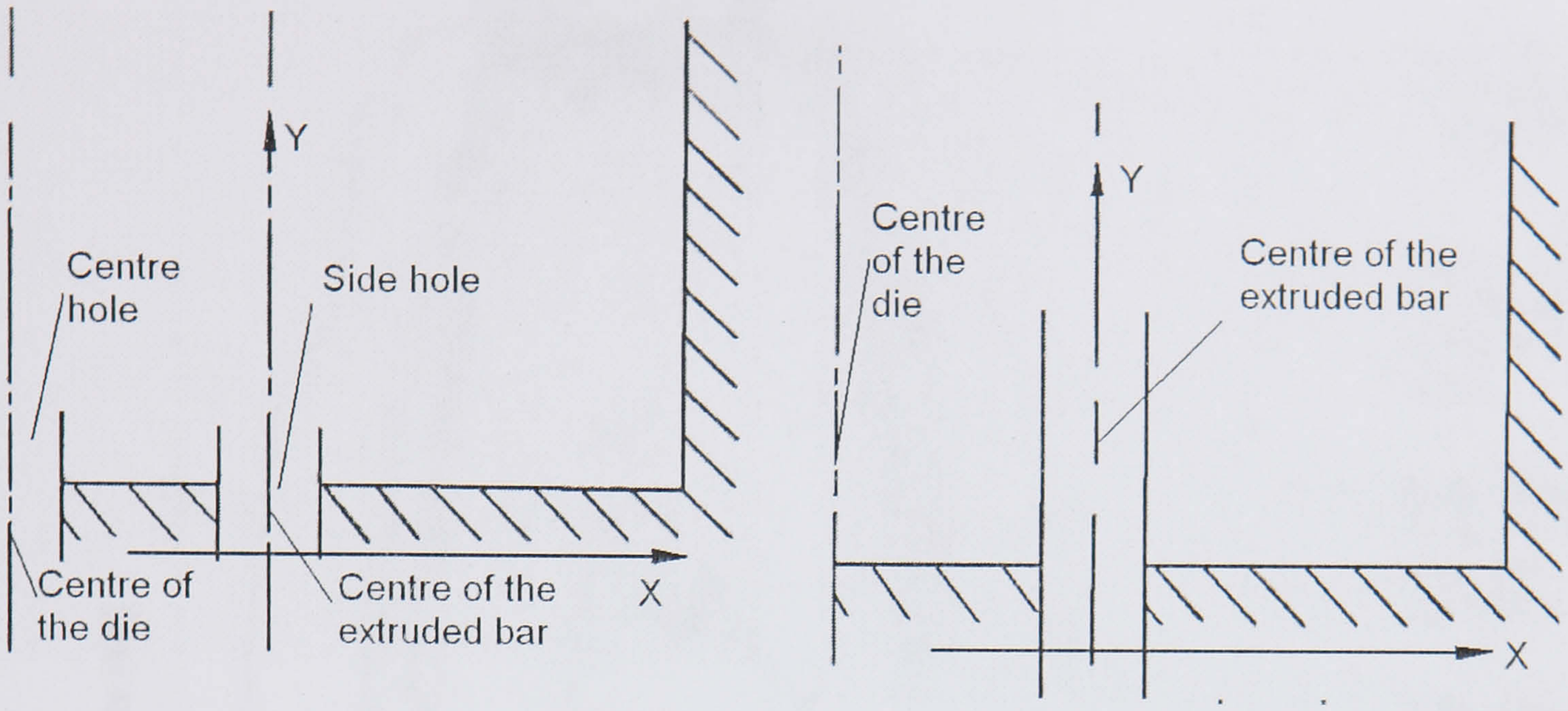

(a) Three hole extrusion

(b) Two hole extrusion

Figure 4.27 The coordinate system

The simulation results of the recrystallised grain size are shown in Figure 4.28. The co-ordinate system used in Figure 4.28 is shown in Figure 4.27(a) and 4.27(b). The predicted grain sizes corresponded well with the experimental results available. For run 2 as shown in Table 4.11, the experimental measurement at the centre of the extrudate is 40 μm and the predicted value is 42.3 μm , which is 5.7% higher. For run 3, the predicted value is 41.2 μm , which is 4.2% lower than the experimental measurement (43 μm). The detail of the effectiveness of the model can be found in literature (Duan and Sheppard 2003).

There are some conclusions that can be drawn from the simulation results.

It can be seen that for extrusions with the same reduction ratio, the minimum grain size occurs in the three-hole extrusion. As the extrusion ratio increases, the size of the grain decreases.

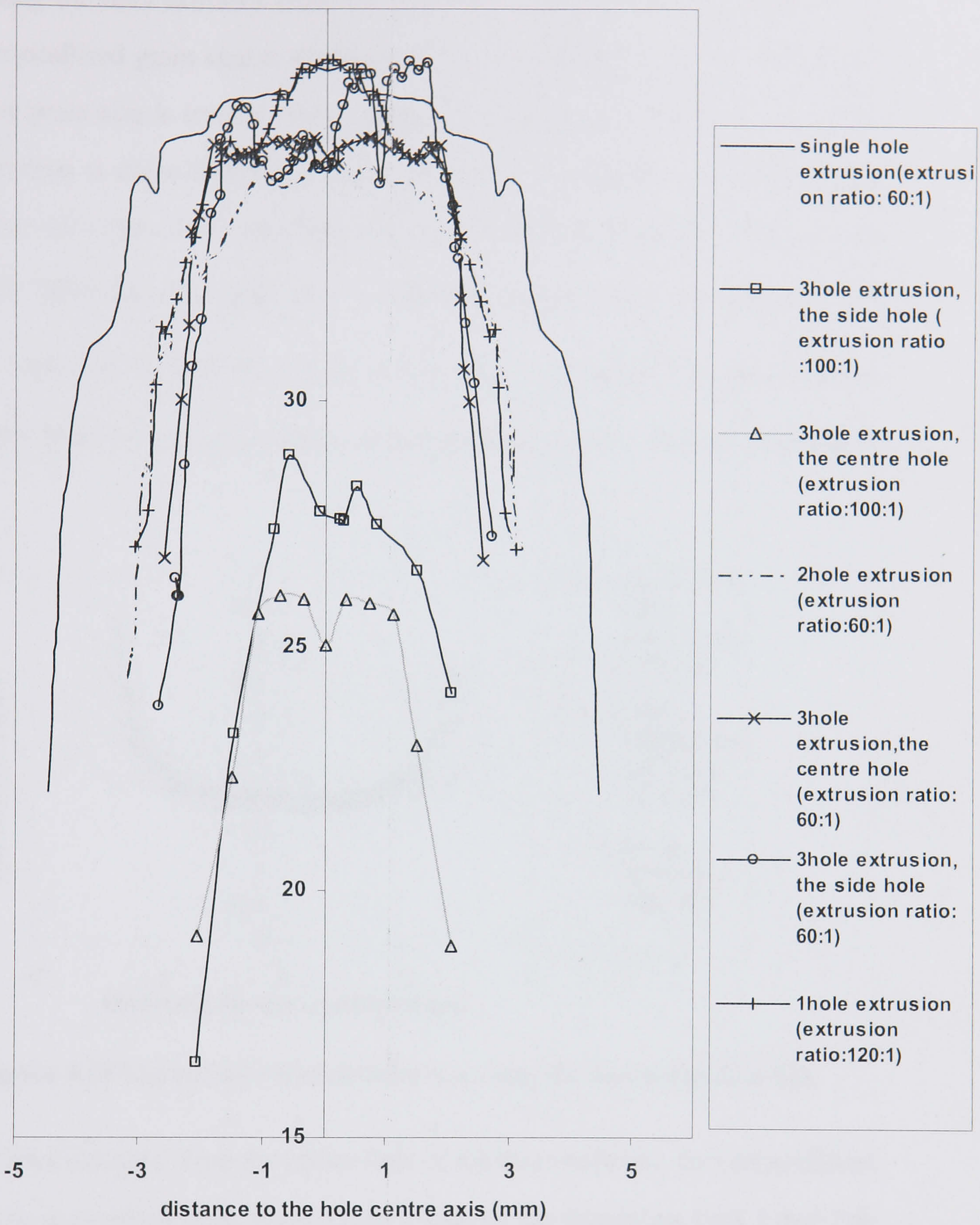

Figure 4.28 Recrystallised grain size along the tranverse direction

The recrystallised grain size on the surface of the extrudate is smaller than at the centre. From Figure 4.28, it can be seen that the recrystallised grain size shows a sharp decrease at the surface of the extrudate, and it is easy to see the recrystallised grain size is in inverse proportion to the equivalent strain. This has also been observed by other workers (Sellars 2000).

Regarding the bars extruded from the two-hole extrusion, one can observe that the recrystallised grain size is slightly different at opposite surfaces of the same bar. The grain size is smaller on the surface that is nearer to the die centre. This phenomenon is more significant in the three-hole extrusion, which has a high extrusion ratio. As can be seen from Figure 4.28, for the simulation results of the run 7 in Table 4.11, the grain size is 16 μm at the side that is nearer to the die centre, while on the opposite surface, the grain size is 24 μm. This phenomenon is closely related to the distribution of the equivalent strain, as plotted in Figure 4.29.

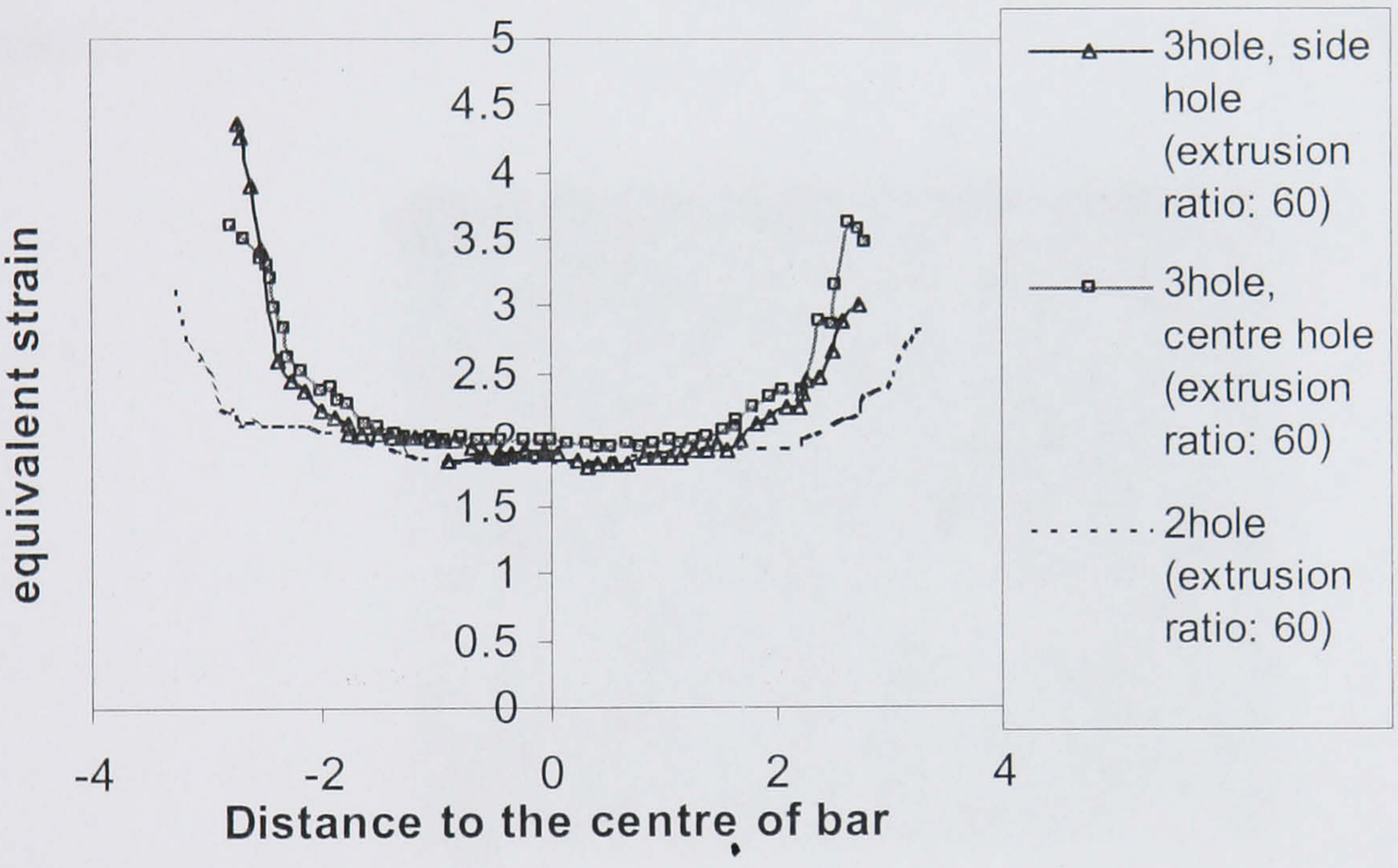

Figure 4.29 Equivalent strain distribution along the transverse direction

For the bars extruded from the centre hole of the three-hole die, the recrystallised grain size is axi-symmetric. It can be seen that for the simulation runs 1 and 3 as shown in Table 4.11, the extruded bars are of the same size (2Re). In these two simulations, the recrystallised grain sizes in the transverse direction are similar, as shown in Figure 4.28. Only on the circumferential surface are there some differences when comparing the recrystallised grain sizes to each other. Whilst these differences may appear trivial, and certainly the degree of precision in the model would suggest this, the reader should note the remark in the previous paragraph and also the deleterious nature of the differing grain size at opposing

circumferential locations as reported above.

In Figure 4.30, part of the cross-section of a multihole extrudate is seen. The main structure is the fibrosity, which is radiating from the surface and demonstrates one of the distinctive features of multi-hole extrusion. For the rods of two-hole extrusion, and the outer rods of the three-hole extrusion, only one of these regions of radiating lines was seen. Two were found in the centre rod of the three-hole extrusion. This non-uniform flow is a direct result of the flow occurring in multi-hole extrusion. It is clear to see that the radial point coincides with the location at which the corresponding recrystallised grain size is at a minimum.

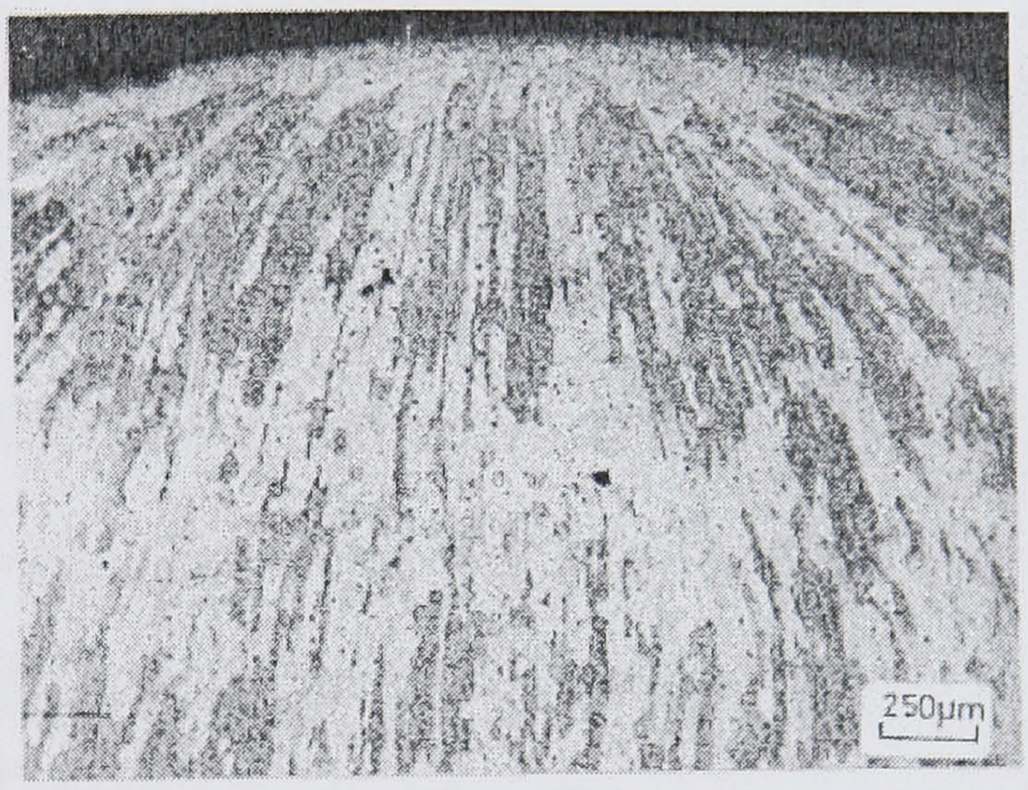

Figure 4.30 Cross section of a multi-hole extrudate shows the fibrous nature of the radial grain distribution. (R=30:1, three hole, $420\,^{\circ}C$, $11.1\,\mathrm{mm/sec^{-1}}$) (Castle 1974, p.233)

Meanwhile, it should be pointed out that in some of the experiments, when recrystallisation had still occurred no such radiating structures were seen and the recrystallised grain sizes on the extrudate surface are not different to each other. This is caused by the extrusion ratio being no greater than 60 in these experiments. As mentioned above in the two-hole and three-hole extrusion, the size of the recrystallised grain varies on the extrudate surface even when the extrusion ratio is low. It should also be noticed that there is a relative error (9%)

in the size measurements in the experiments. When the size differences are small. inaccuracies may clearly occur.

Furthermore, means to minimise or eliminate the deformation and the following recrystallisation unbalanced behaviour are discussed in Chapter 6, in which pocket die extrusion or isothermal extrusion are introduced in detail.

4.4 Scaling effect on numerical simulation of aluminium extrusion process

The finite element method is only approximate. The way in which the problem is modelled, for example the approximations in the geometry or material properties, and the method of description (i.e. the number and type of elements used), both affect the accuracy of the final answer. This section is concerned with modelling procedures and use of finite element software to obtain solutions.

Taking a general view of the present state of the art in terms of numerical modelling, it appears that the finite element method is most suited to the three-dimensional analysis of material forming processes. In fact, the finite element method can take into account practical non-linearity in the geometry and material properties, besides producing accurate predictions of stress, strain, strain rate and temperature throughout the deforming billet. However, in some cases, this stage is extremely time consuming and there are limitations, which could cause fault in the design process. Physical simulation, in which a sealed down process is adopted, would result in the time spent in design to be significantly reduced. It is therefore of great interest to investigate if a small-scale model can be adopted in numerical simulations. The relevant question that is frequently being asked concerns the difference in accuracy between simplified modelling and simulation (Gouveia 2001). When some simplification (for example, a smaller-scale but geometrically similar process) is adopted, will the simulation still be of sufficient accuracy? Can the simplified simulation reproduce most of

the important forming parameters of the real process?

It should also be borne in mind that at the present time, the trend of numerical simulation is not only thermally and mechanically coupled, but also structurally or metallurgically combined. Excellent reviews of modelling of static recrystallisation (SRX) have been given by Gottstein et al. (2000) and by Shercliff and Lovatt (1999). Recently, the inverse method combined with FEM has been adopted to integrate those values of parameters reported in the literature. The FEM is run iteratively until the appropriate value is found to match the experimental measurement. Duan and Sheppard (2002) have used the inverse method to give the parameters for alloy 2014.

In the following studies, the possibility of the application of a small-scale model to numerical simulation of extrusion is discussed. It was found that although the small-scaled model is effective in saving computing time, there are some serious deviations in the simulation results.

The alloy used in the present work is AA2014 and the main simulation tooling is shown in Table 4.12. Two simulations of rod extrusion were performed and the billet size in Run 2 was 2.5 times smaller than that in Run 1, in terms of diameter and length. In these two simulations, the extrusion ratio was 20, the ram speed was 12.4mm/sec, the initial temperature of the billet was 350 $^{\circ}C$ and the container temperature was 50 $^{\circ}C$ lower than the billet.

Table 4.12 Tooling of FEM model (As shown in Fig 1)

Run	Billet length (mm)	Billet diameter (mm)
1	95	75
2	38	30

The hyperbolic sine function was integrated into the FEM to describe the

material behaviour. For aluminium alloy AA2014, ΔH =144408KJ/mol, α = $0.0152\,m^2 / MN$, n = 5.27, LnA = 24.41 (Sheppard and Jackson 1997).

The Tresca friction law is adopted in the numerical model in the present work and the friction coefficient $m = 0.85$ was adopted (Flitta 2003).

In the following sections, the thermal-mechanical and the structural combined simulation results of the two runs are compared. The discussion concerning the computation time and material flow pattern is presented first.

4.4.1 Thermal-mechanical simulation

When modelling a complex problem, approximations might be made in one or more of the following:

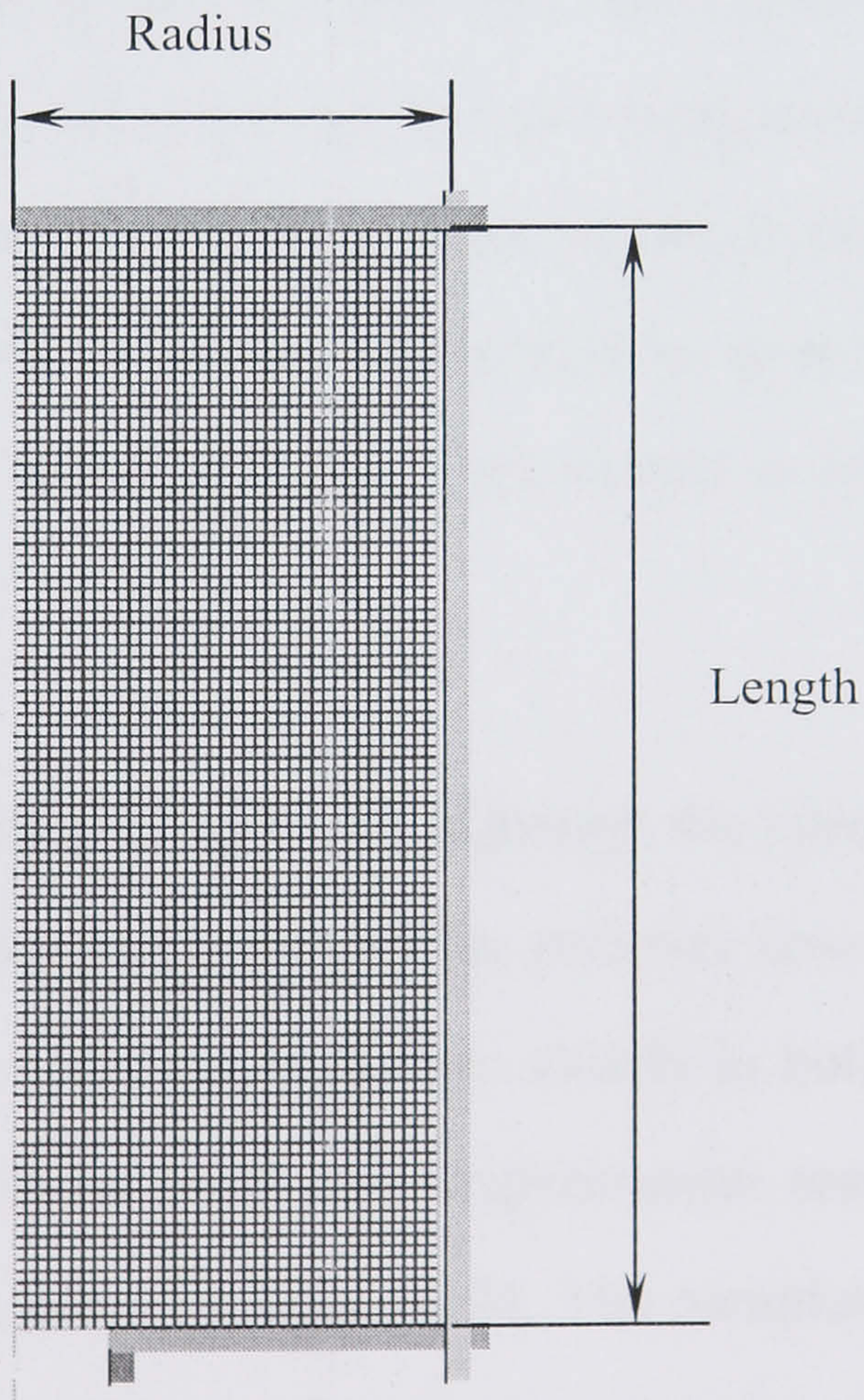

Figure 4.31 Reference grid pattern (undeformed)

(a) geometry,

(b) material properties

(c) loading conditions

(d) constraint conditions.

The acceptability of those approximations depends on the purpose of the investigation, and indeed some comparative analyses do not require absolute accuracy. The final answer produced by the analysis depends on the validity and accuracy of the model, and the user should give some consideration to whether the model is valid and accurate enough. The degree of validation may well be checked by comparison with the previcus experiments or with answers obtained by approximate hand calculations, such as the results from upper bound theory.

4.4.1.1 Material flow pattern

Previous studies have confirmed that FEM simulation is effective in predicting the material flow pattern. Arentoft et al. (2000) have studied the material flow in axi-symmetric extrusion with physical and two dimensional FEM simulation. Some studies in multi-hole die extrusion by three dimensional FEM simulation have also been published by Peng (2004). In the following study, a reference grid pattern was adopted to study the material flow pattern, as shown in Figure 4.31. The simulation results of Run 1 and Run 2 are shown in Figure 4.32 and 4.33 respectively.

As can be seen from Figure 4.32 and 4.33, although the billet sizes are different in these two runs, the simulation results of the material flow pattern are similar. The different deformation areas can be shown clearly in both of these two runs and the predictions correspond well with experimental results (Sheppard and Tutcher 1980), which are shown in Figure 4.34. The complete computation time of the first run is 25 hours whilst in Run 2, the total time is not more than 15 hours. It is evident therefore that computation time can be significantly saved (40%) with a small-scale simulation and the simulation result is still approximate compared with the material flow pattern of the original process. In fact, it is

worth noting that small-scale simulation has been used in the field of physical simulation, in which soft materials were adopted in experiments and the cost of design was then significantly saved (Aretz 2000). However, the majority of the cases reported in the literature show that the use of physical modelling is limited to qualitative analyses of the material flow.

It has been pointed out by Arentoft et al. (2000) that the basic problem lies in the transferral of the model-experiment results to reality. In the case of extrusion, in which temperature rise is significant and strain rate is quite high, more important factors in addition to the material flow need to be considered, for example, the structure evolution. To ensure accurate results and interpretation, the model and the real process must be similar. For metalworking processes the following important similarity conditions must be created (Wanheim 1988, Ferguson 1993): geometrical, plastic, frictional, thermal, elastic and dynamic. The fulfilment of all of these conditions is practically impossible. In most cases, the first four conditions are the most important, although they are also perhaps the hardest to fulfil. Therefore, it is essential to determine and select which material properties and process parameters are the most relevant for the purpose of the experiment. During the process of extrusion, the press load, temperature rise, surface quality and extrudate mechanical properties are the most important factors to be considered. If any simulation is applied in extrusion, it has to be effective in predicting all of the above factors. In the following discussions, the analysis results of these forming parameters in the small-scaled simulation are set out.

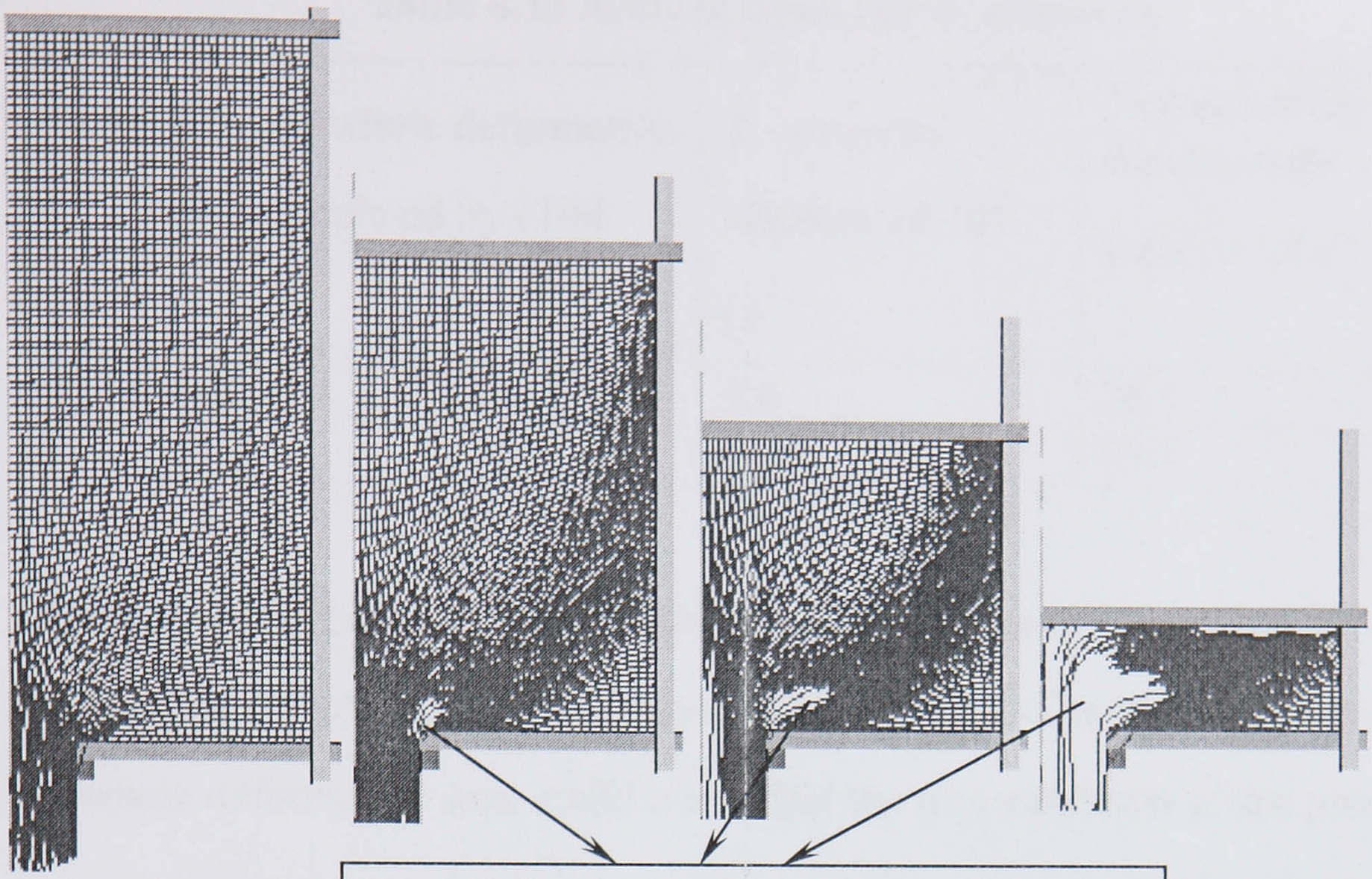

Figure 4.32 Simulation result using the full size billet (Run 1)

4.4.1.2 Equivalent strain rate

The simulated instantaneous strain rate distributions ($Ln(\dot{\varepsilon})$) in these two runs are compared as shown in Figure 4.35 and Figure 4.36.

Table 4.13 shows the average strain rate of the whole deformation area calculated by the FEM program and given by the upper bound method (Sheppard 1999a) according to equation (4-11):

$$\bar{\dot{\varepsilon}} = \frac{6V_B D_B^2 (0.171 + 1.86\mathrm{LnR})\mathrm{Tan}(38.7 + 6.9\mathrm{LnR})}{D_B^3 - D_E^3} \qquad (4\text{-}11)$$

Where V_B is the ram speed, D_B is the billet diameter, D_E is the extrudate diameter and R is the extrusion ratio.

Table 4.13 Average strain rate of extrusion

Run	$\dot{\bar{\varepsilon}}$ of the whole deformation area calculated by FEM (s^{-1})	$\dot{\bar{\varepsilon}}$ given by equation (4-16) (s^{-1})	Average strain rate in the area with $Ln(\dot{\varepsilon})>1$. (s^{-1})
1	6.57	5.6	20.3
2	15.1	14.4	23.7

However, in the process of extrusion, the main deformation occurred at the area near the die orifice as shown in Figure 4.35 and 4.36. The average strain rate of the whole deformation area could not reflect the true condition of the process, so the average strain rate of the area with $Ln(\dot{\varepsilon})>1$ was calculated and the results are also shown in Table 4.13.

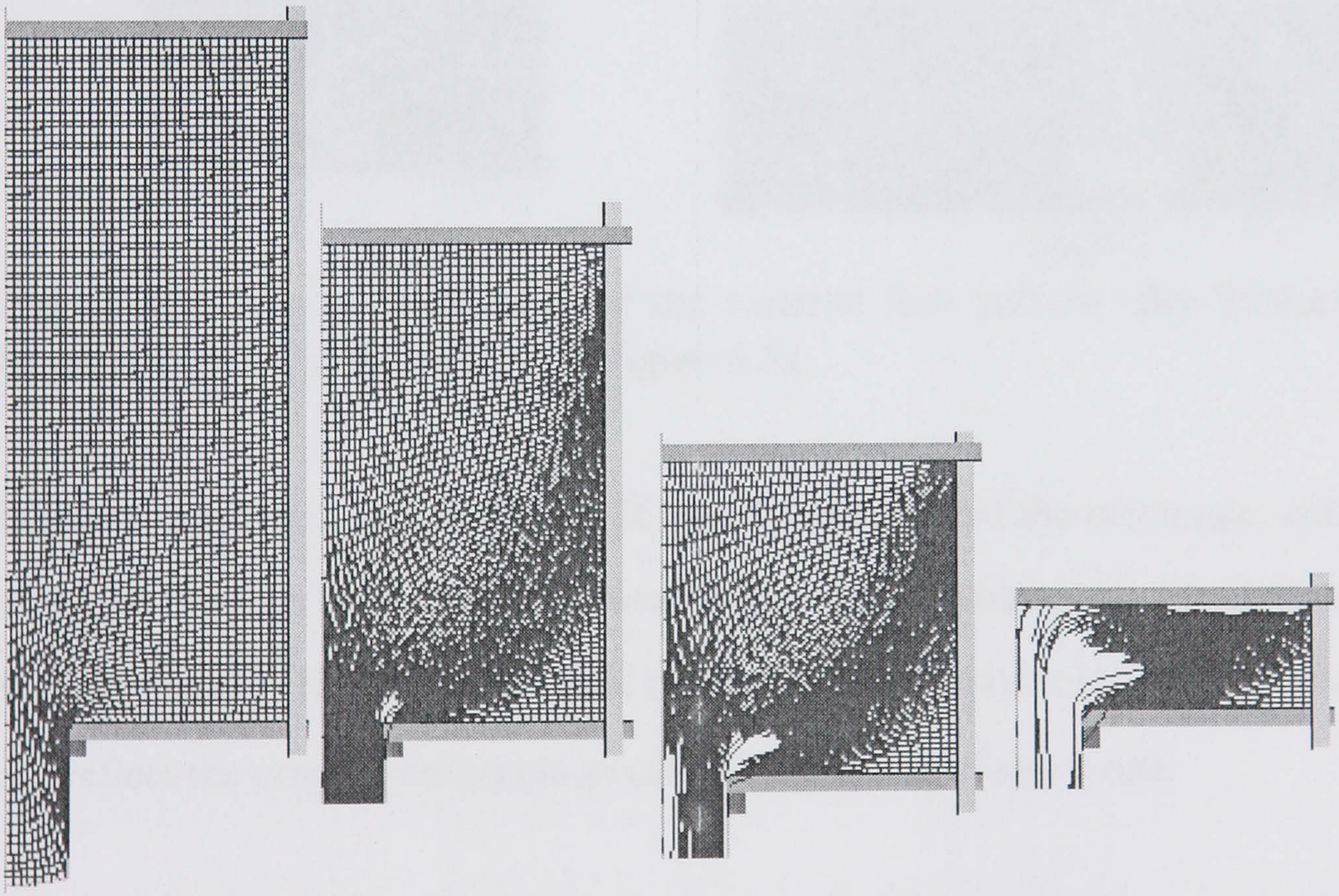

Figure 4.33 Simulation result using the small-scale billet (Run 2)

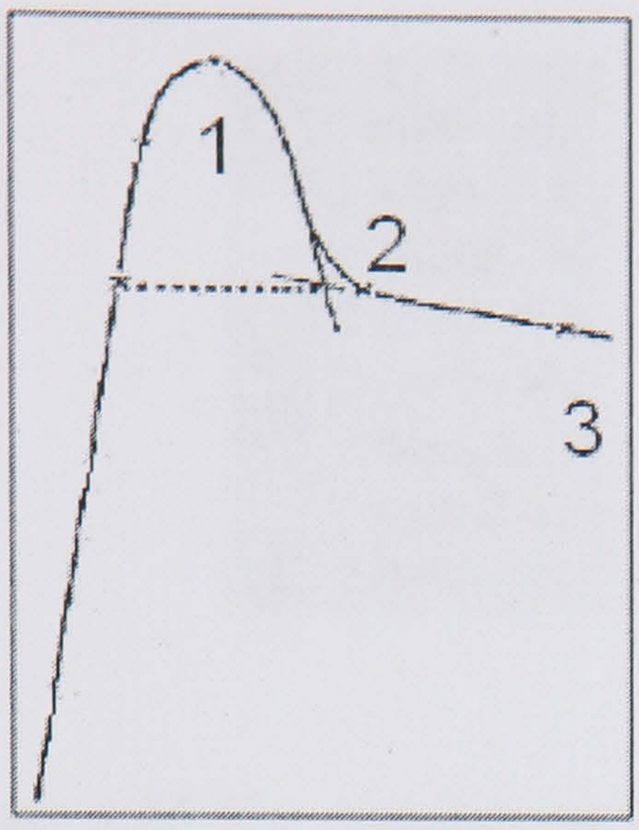

Extrusion stages

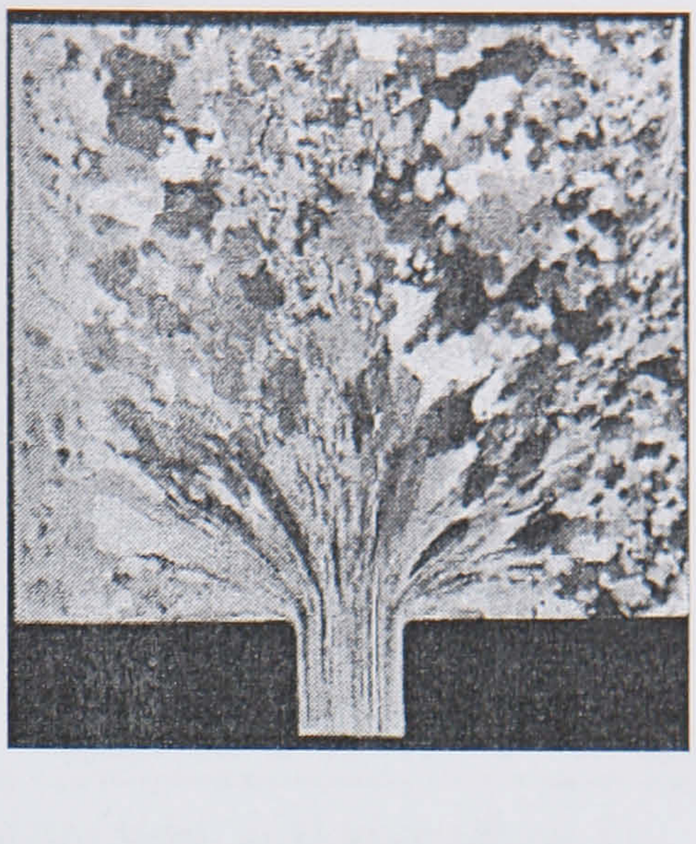

Stage 1

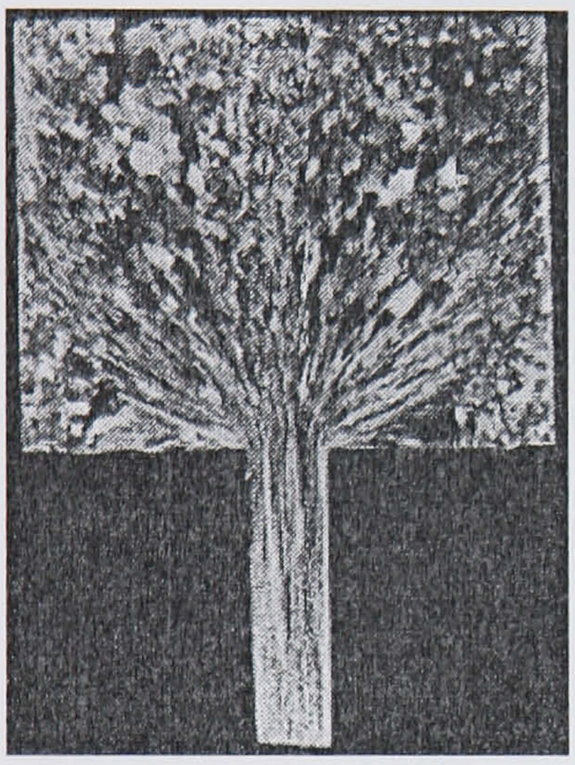

Stage 2

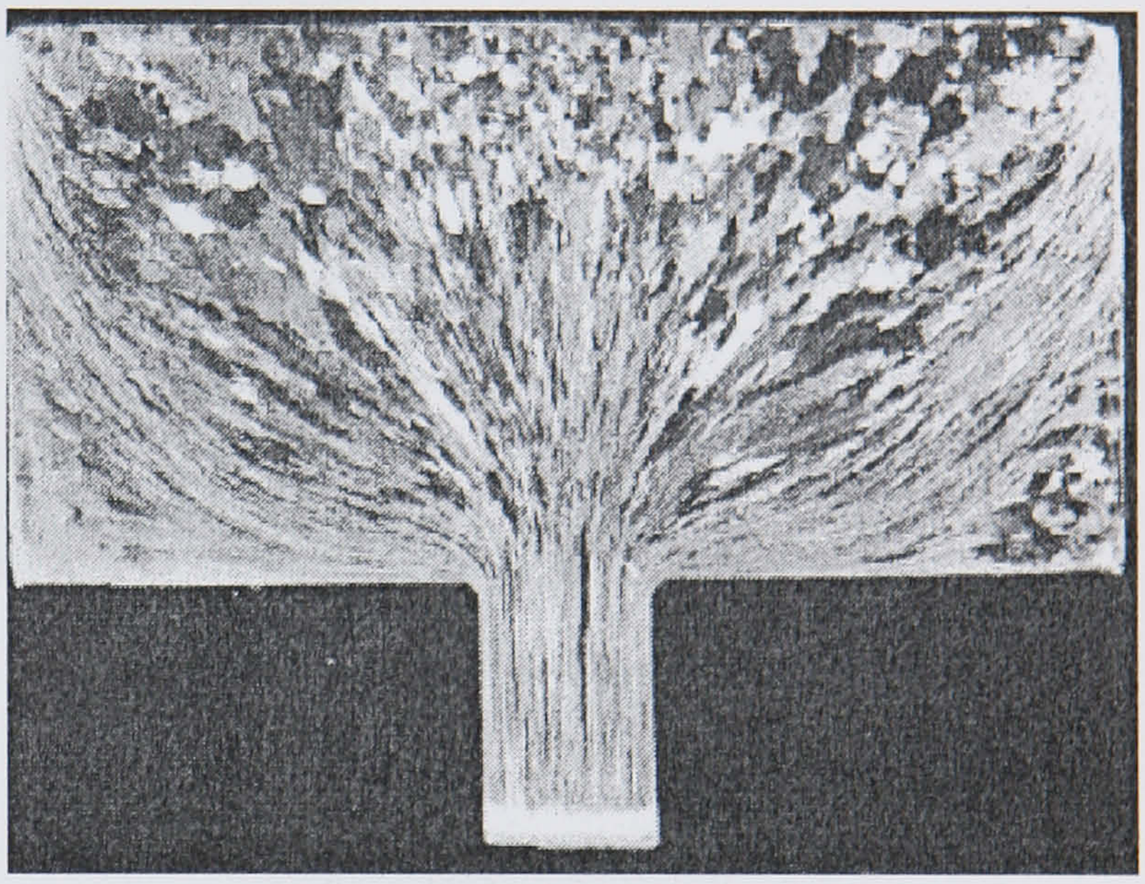

Stage 3

Figure 4.34 Experimental result of the material flow pattern after Tutcher and Sheppard (1979), comparing with Figure 4.32

It can be seen from Figure 4.35, 4.36 and Table 4.13 that the strain rate, either in terms of 'average' or 'instant', is much higher in the small-scale simulation than that predicted in Run 1. So, it could be said that the small-scale simulation could not reflect the original deformation correctly in terms of strain rate.

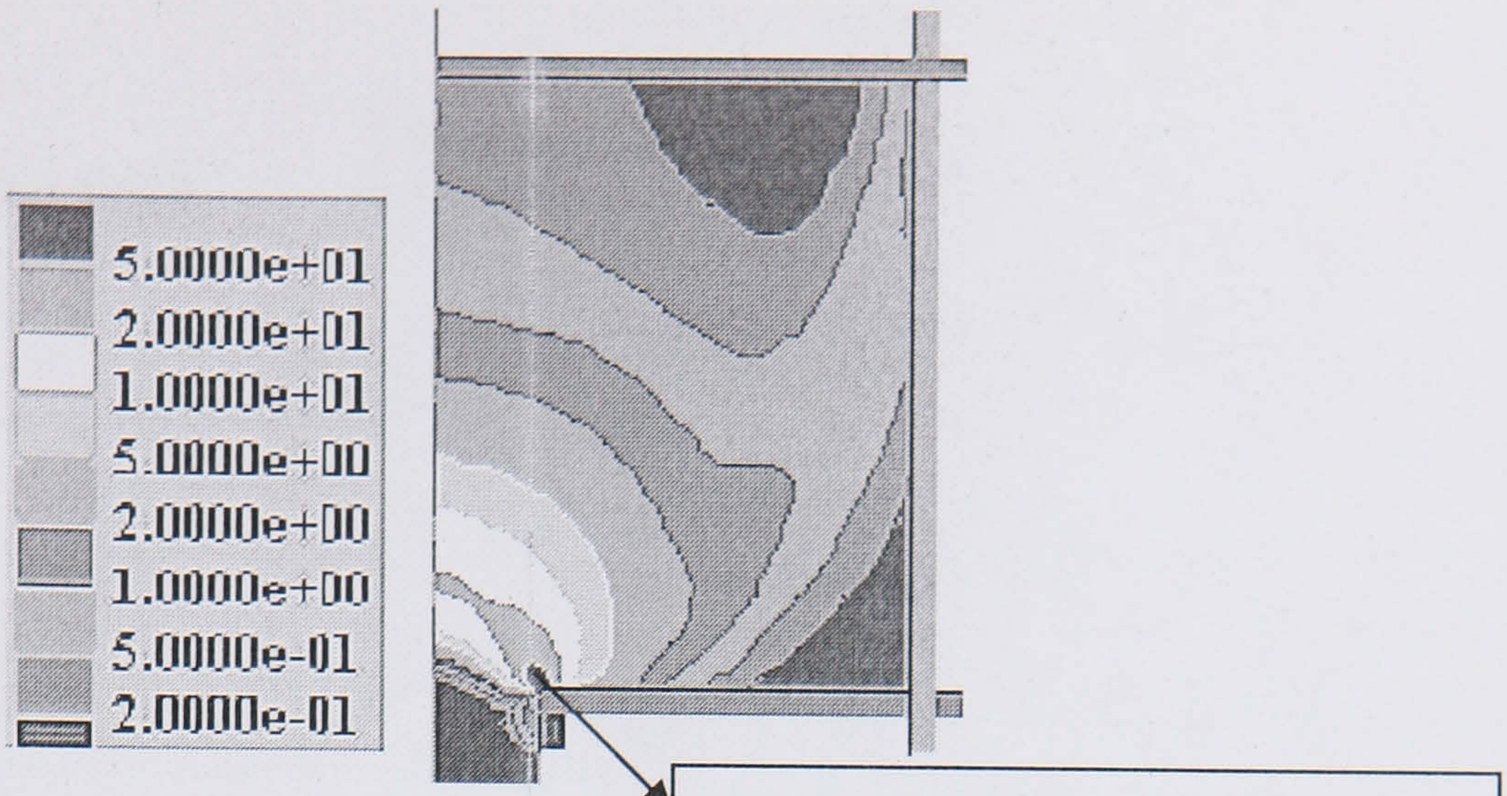

Figure 4.35 The distribution of the $\bar{\dot{\varepsilon}}$ in the billet with full size (Run 1)

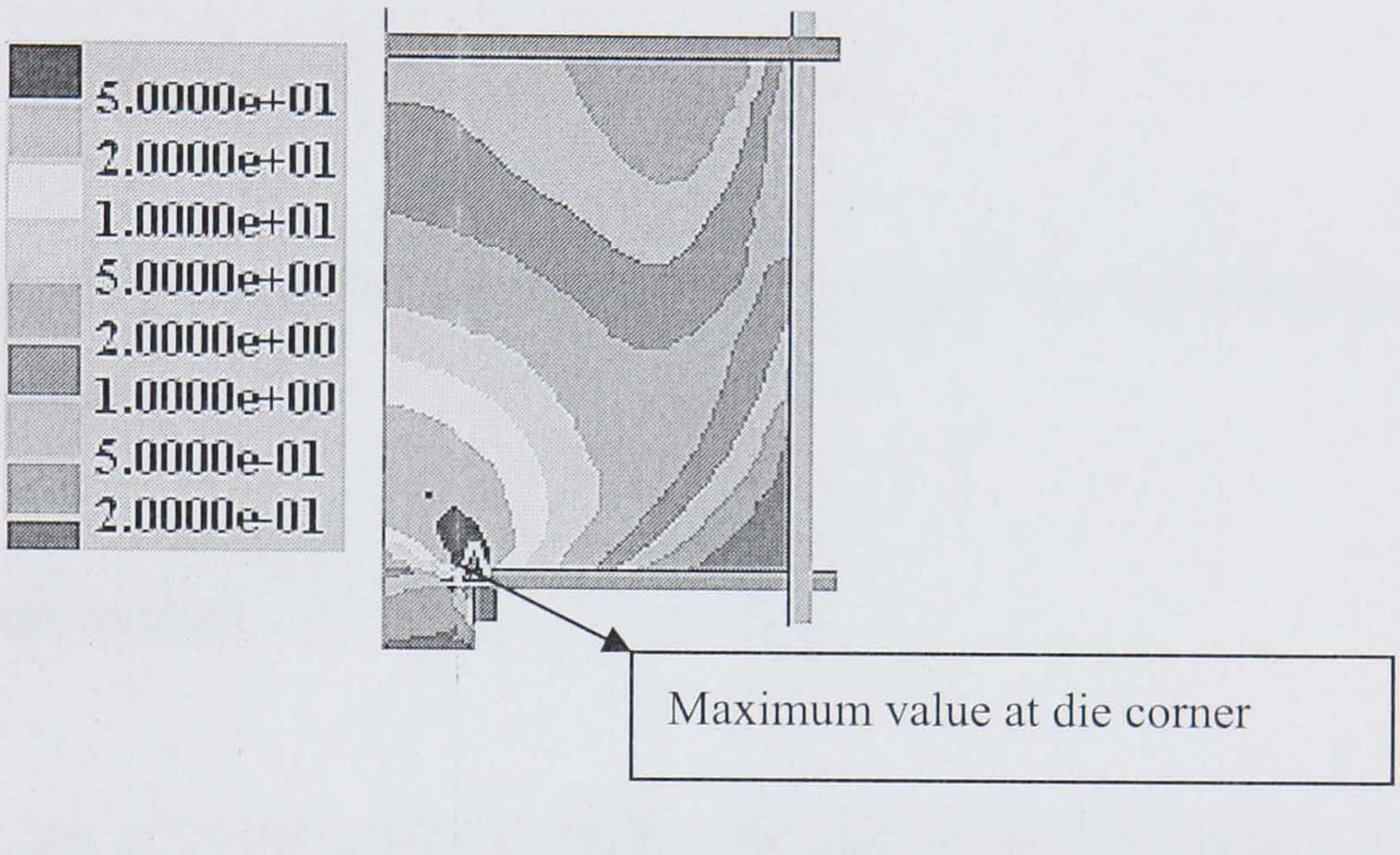

Figure 4.36 The distribution of the $\bar{\dot{\varepsilon}}$ in the small-scale billet (Run 2)

4.4.1.3 Temperature rise during extrusion

The temperature rise during extrusion was also studied. In extrusion, the temperature distribution in the billet is a critical process variable, affecting extrusion pressure, speed, surface finish and mechanical properties. Extrusion exit temperature also determines the surface finish and shape dimensions. The temperature rise is actually more significant than most of the other metal forming variables. The side temperature and the centre temperature are extracted from the side point and the centre point, which are shown in Figure 4.37. The simulation results of the exit temperatures of Run 1 and Run 2 are shown in Figure 4.38 and 4.39 respectively.

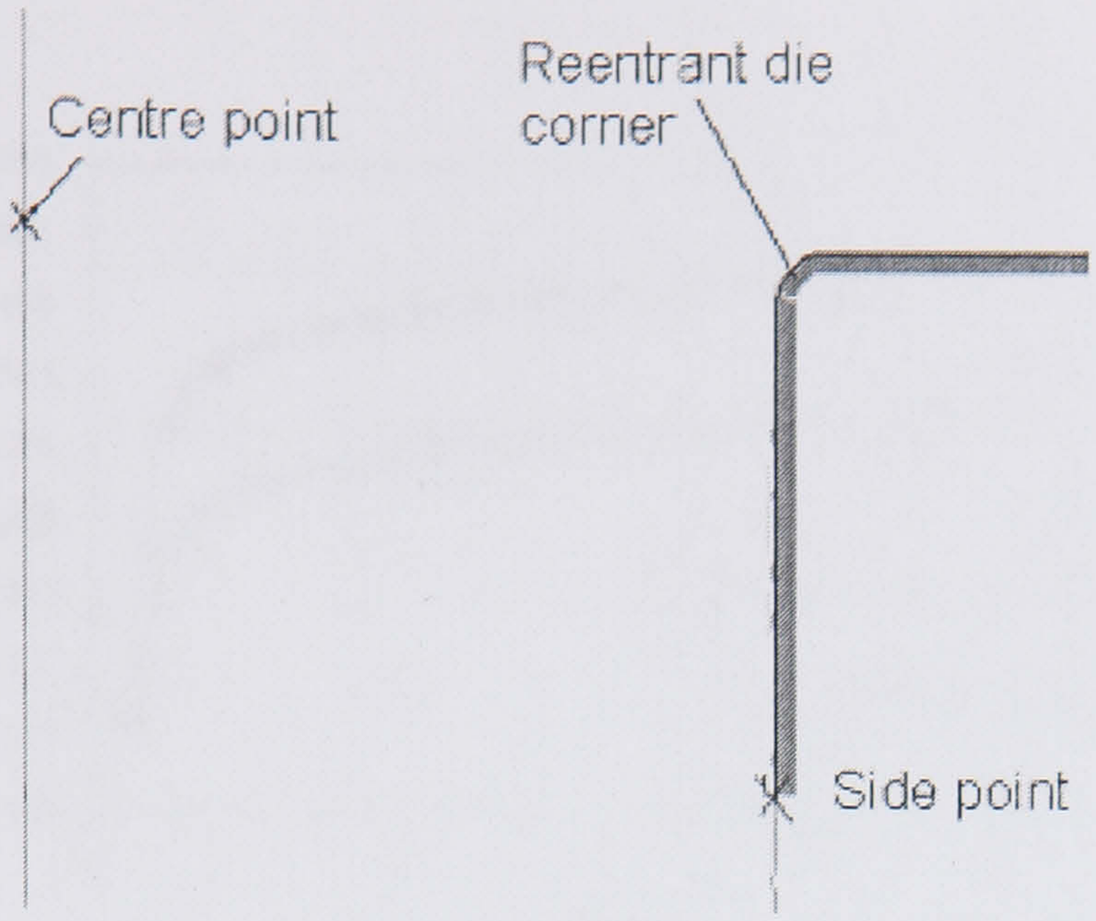

Figure 4.37 The deformation area

The main difference concerning the temperature rise in these two runs can be summarised in two points:

(1) The maximum temperature

In the present study, the extrusions were carried to the end of the billet length. It should be borne in mind that in real situations, extrusion is normally stopped when the billet has extruded to about 90% of its length, which is marked in Figure 4.38 and 4.39 with a vertical line. It can be seen from Figure 4.38 and Figure 4.39 that the maximum temperature on the surface of the extrudate in Run 1 is 475$^{\circ}C$ while it is 466$^{\circ}C$ in Run 2. The maximum temperature in the centre of the extrudate in Run 1 is 432$^{\circ}C$ whilst it is 447$^{\circ}C$ in Run 2.

(2) The temperature gradient along the transverse direction (between the surface and the centre of the extrudate)

In Run 1, the temperature difference between the surface and the centre is maintained at 43$^{\circ}C$ while it is only 19$^{\circ}C$ in Run 2.

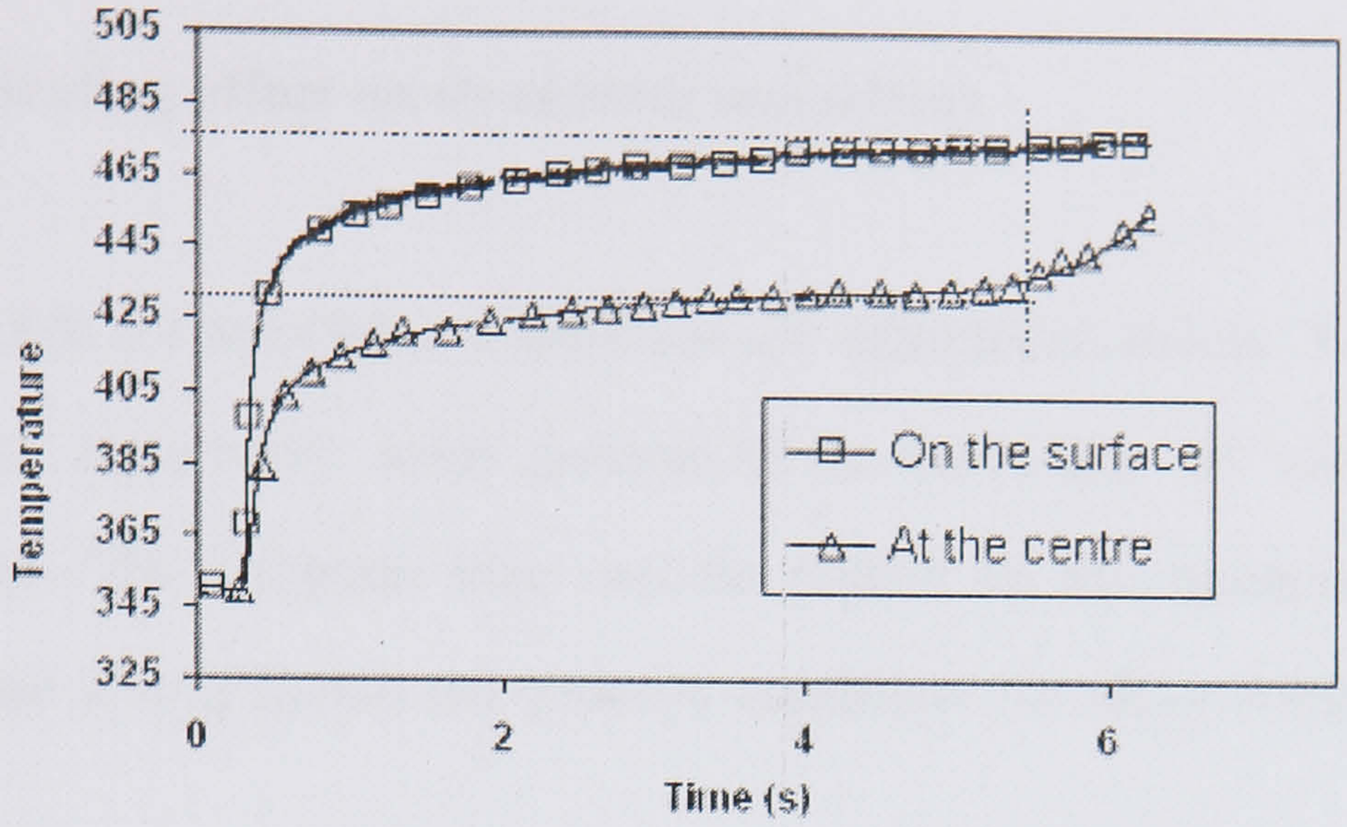

Figure 4.38 Temperature rise in the full size billet (Run 1, Temperature in Celsius)

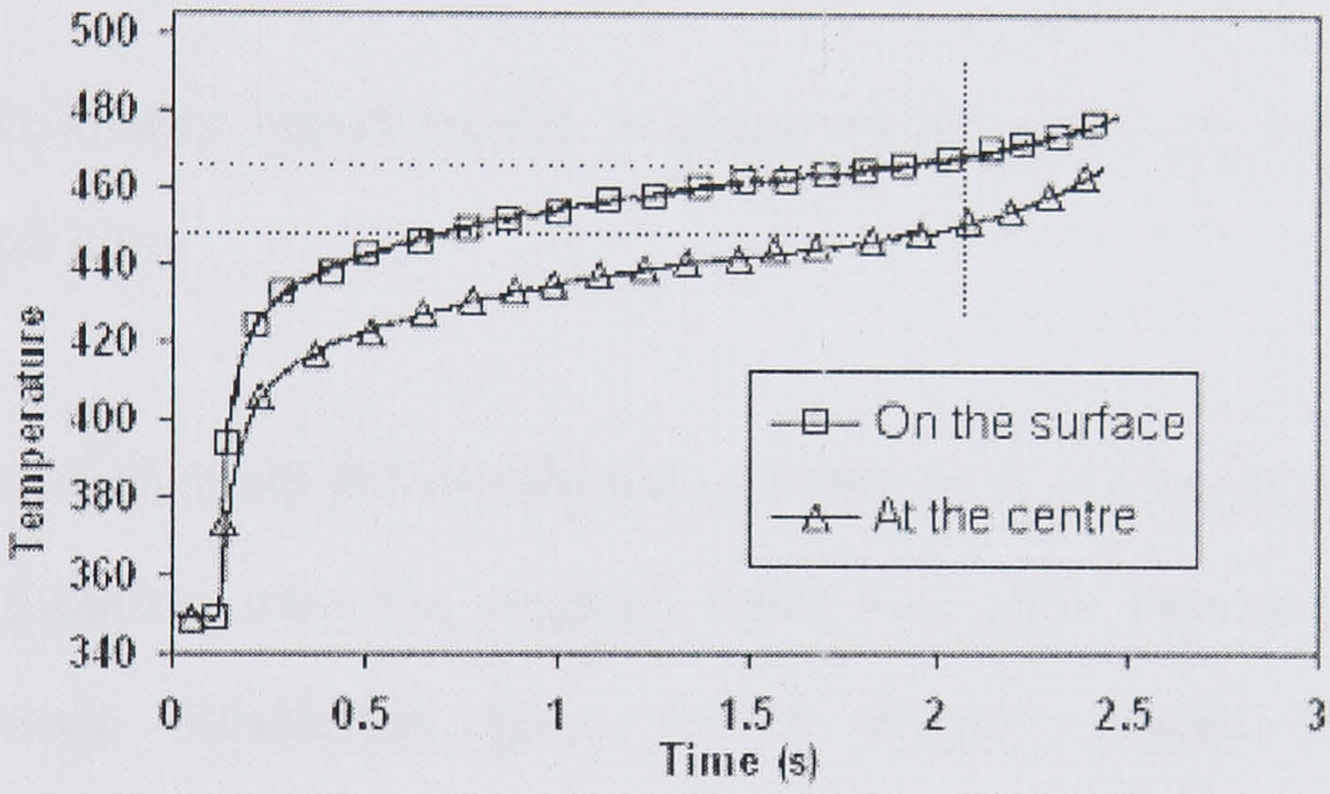

Figure 4.39 Temperature rise in the small-scale billet (Run 2, Temperature in Celsius)

As can be seen from the discussion above, although the geometrical conditions are similar in these two runs, there is no similar or proportional result concerning the exit temperature. The small-scale simulation failed to predict the correct temperature distribution, especially in the die orifice area. It is well known that the exit temperature depends on the initial billet temperature, the magnitude of the work carried out during extrusion, and how this is divided between the work needed to overcome friction on one hand, and the heat losses to the tooling (Sheppard 1999a) on the other. The geometrically similar conditions cannot

guarantee that the simulation result is correct.

4.4.2 Scaling effect on structural simulation

The models for structural simulation are introduced below. The subgrain size is the most commonly used parameter in the study of aluminium extrudate structures. The subgrain size can be related to the temperature compensated strain rate Z and hence the process condition for alloy AA2014 by (Sheppard 1999):

$$d^{-1} = 0.096 \mathrm{Ln}Z - 1.747 \qquad (4\text{-}12)$$

The physically based model is given in Appendix A in detail, and it is not repeated here.

The calculation results are shown in Table 4.14. As can be seen from Table 4.14, the simulation with the original billet size gave reasonable results while the small-scale simulation gave rather deviant results compared with the experimental results. The small-scale simulation proved to give incorrect results in material structural simulation.

Table 4.14 The predicted material structures (experiments from Castle 1974)

Run	Predicted subgrain size (μm)	Predicted grain size (mm)		Experimental subgrain size (μm)	Experimental grain size (mm)	
		Centre	Edge		Centre	Edge
1	1.75	0.294	0.273	$1.43^{+}_{-}0.25$	$0.321^{+}_{-}0.04$	$0.266^{+}_{-}0.04$
2	2.26	0.250	0.232			

4.4.3 Further discussion on scaling effect

A finite element analysis will only produce the correct answer if the model is both valid and accurate. Validity depends on how faithfully the physical problem is represented in the computer, while accuracy depends on how close the model is to convergence. To investigate whether the scaling effect could be modified by a sample scaling factor we now attempt to obtain similar strain rates by such method.

4.4.3.1 Similar strain rate obtained by changing ram speed

As has been shown in the previous two sections, the scaled down simulation can not reproduce the deformation histories and material properties concerned with the original models with manufacturing scale sizes. However, suggestions following that study indicate that a similar strain rate could be expected if the ram speed is also scaled down according to equation 4-11. Run no.3 as shown in Table 4.15 is the run which is designed to investigate whether this is feasible. Run 1 and 2 in Table are identical to the corresponding runs of Table 4.13 but have been rerun and modifications are made in the way of interpolating the simulation results.

The billet sizes in Run 2, 3 and 4 are scaled down to 2.5 times smaller than those of Run 1 in terms of diameter and length. In these simulations, the extrusion ratio is 20, the initial temperature of the billet is 350°*C* and the container temperature is 50°*C* lower than the billet. All other FEM data are the same as in the paper previously published (Peng 2004d).

Table 4.15 Tooling of FEM model

Run	Billet length (mm)	Billet diameter (mm)	Ram speed (mm/s)	Calculation time (hours)
1	95	75	12.4	23
2	38	30	12.4	15
3	38	30	4.93	17
4	38	30	8.0	16

The simulation results concerning the equivalent strain rate distribution of each run detailed in Table 4.15 are shown in Figure 4.40. As can be seen in Figure 4.40, the deformation area with the equivalent strain rate greater than 1 in run 2 is obviously larger than the field found in the other simulations. At the die entrance area, a much larger area with the strain rate greater than 30 was also observed. One problem which must be addressed is that at the location very close to the die entrance radius, the predicted strain rate rises sharply as shown in Figure 4.41 which is an enlarged picture of Figure 4.40a. Inside the location of the triangle, the strain rate is shown to be greater than 50 (at one or two specific nodes even greater than 100). Until the present time, no experimental measurements have been found to justify this simulation result. It would seem that the value at this point is greatly influenced by the small penetration of nodes into the die. Since the number of the nodes with a strain rate greater than 100 is limited, it is justifiable when calculating the mean equivalent strain rate that these nodes may be ignored. This criterion was followed for all of the simulation runs. This may cause some discrepancy when comparing the calculation results with the previous study, however, this should not influence the conclusion of the present study since at every run in Table 4.15, the rogue nodes (with equivalent strain rate greater than 100) are not included in the overall average strain rate.

As can be seen in Table 4.16, the calculated equivalent strain rate of run 1 according to equation 1 is 5.6, which is larger than the calculated average $\dot{\bar{\varepsilon}}$ of the whole deformation area. Since the equation 4.16 is the approximate result of $\dot{\bar{\varepsilon}}$ of

the deformation area but not the whole area, the discrepancy between the two numbers is acceptable. The calculated average strain rate of the area with $\dot{\bar{\varepsilon}}$ greater than 0.1/s is much closer to the prediction results of equation 4.16 than the results from other areas used in Table 3, which indicates the deformation area assumed in equation 4.16 is closer to this specific area.

Table 4.16 Average strain rate of extrusion

Run	$\dot{\bar{\varepsilon}}$ given by equation 4-16 (s^{-1})	$\dot{\bar{\varepsilon}}$ of the whole area (s^{-1})	Area with $\dot{\bar{\varepsilon}}>0.1(s^{-1})$	Area with $\dot{\bar{\varepsilon}}>5(s^{-1})$
1	5.6	3.75	8.4	25.9
2	14.4	4.79	12.5	28.2
3	5.6	2.77	7.5	22.2
4	9.1	3.79	10.4	26.4

As can also be seen in Table 4.16, the average strain rates calculated from all the specific areas of run 3 are smaller than that of run 1. Therefore, it can be concluded that the scaled down ram speed according to equation 4.16 can give approximately the same average strain rate when the area with $\dot{\bar{\varepsilon}} > 0.1$ is chosen. However, it will not be unusual for some differences to emerge when the equation is compared directly to FEM simulation, which should give more precise predictions.

Furthermore, the first three running results gave a promising probability to obtain a similar strain rate to run 1 if a suitable ram speed can be chosen between that of run 2 and 3. There is no strict scientific method to infer the selected ram speed, except for an observation that the average strain rate of run 1 is approximately at the middle of run 2 and run 3. Therefore, run 4 with a ram speed of 8mm/s is

established and the average strain rates of the specific areas are calculated by FEM subroutines. It can be seen that in the areas within a certain range of equivalent strain rates the result of run 4 is very close to run 1.

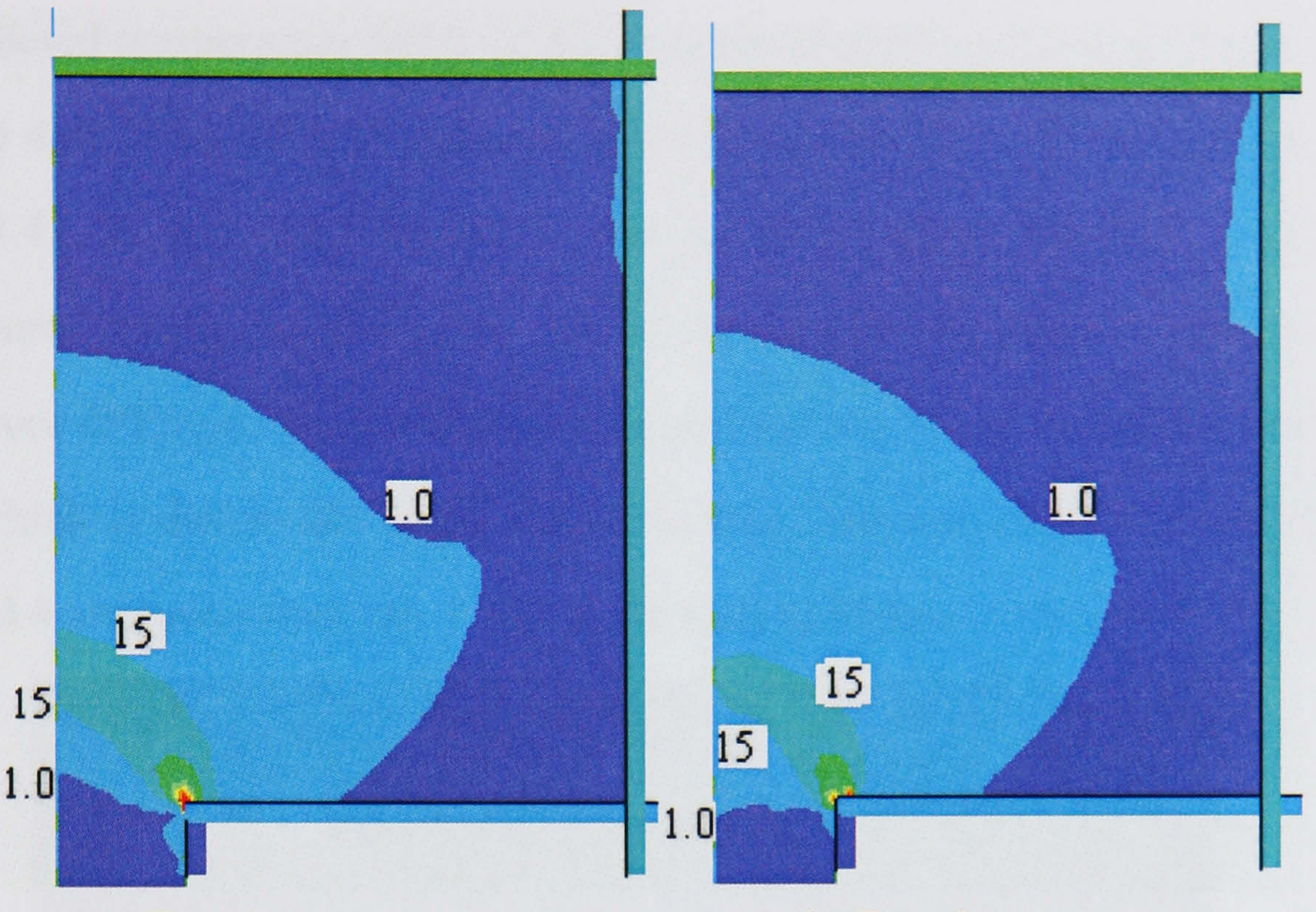

a) Run 1 b) Run 3

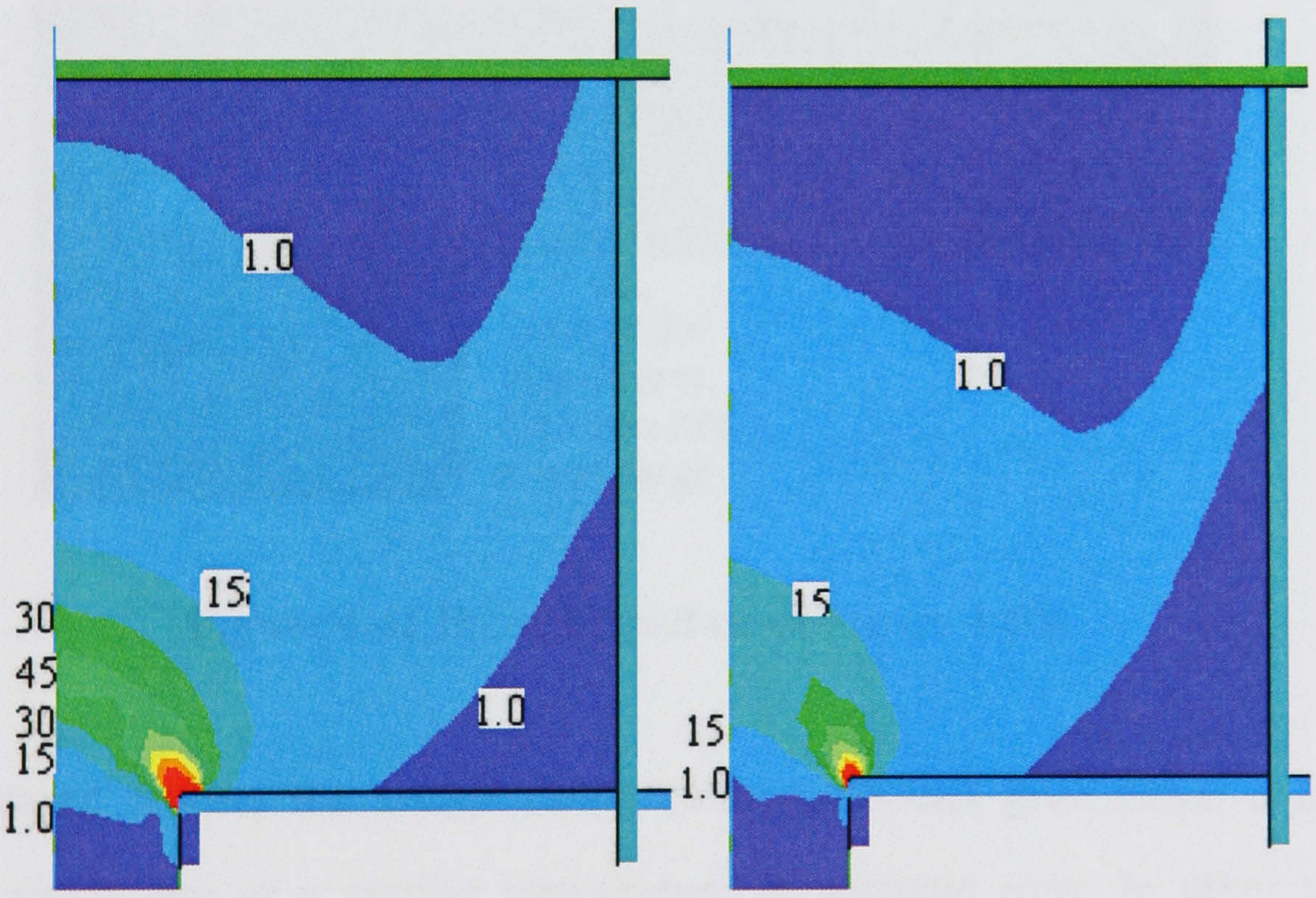

c) Run 2 d) Run 4

Figure 4.40 Equivalent strain rate distribution in billet

It can also be seen from Table 4.15 that although run 3 is expected to give the closest simulation results compared to run 1, the run 4 is in fact most similar to run 1 in the sense of equivalent strain rate.

4.4.3.2 Effect of scaling on Zener-Hollomon Parameter

The predicted temperature fields of the four simulations in Table 4.15 are shown in Figure 4.42. The billet is extruded down to half length in all of the figures in Figure 4.42. It has been shown in the previous section that the maximum temperature during extrusion in run 1 is similar to run 2, although the temperature difference between the centre and surface of the extrudate is larger in run 1, which is due to the larger extrudate size. The maximum temperatures in run 3 and 4 are lower than run 1, as can be seen in Figure 4.42c and 4.42d.

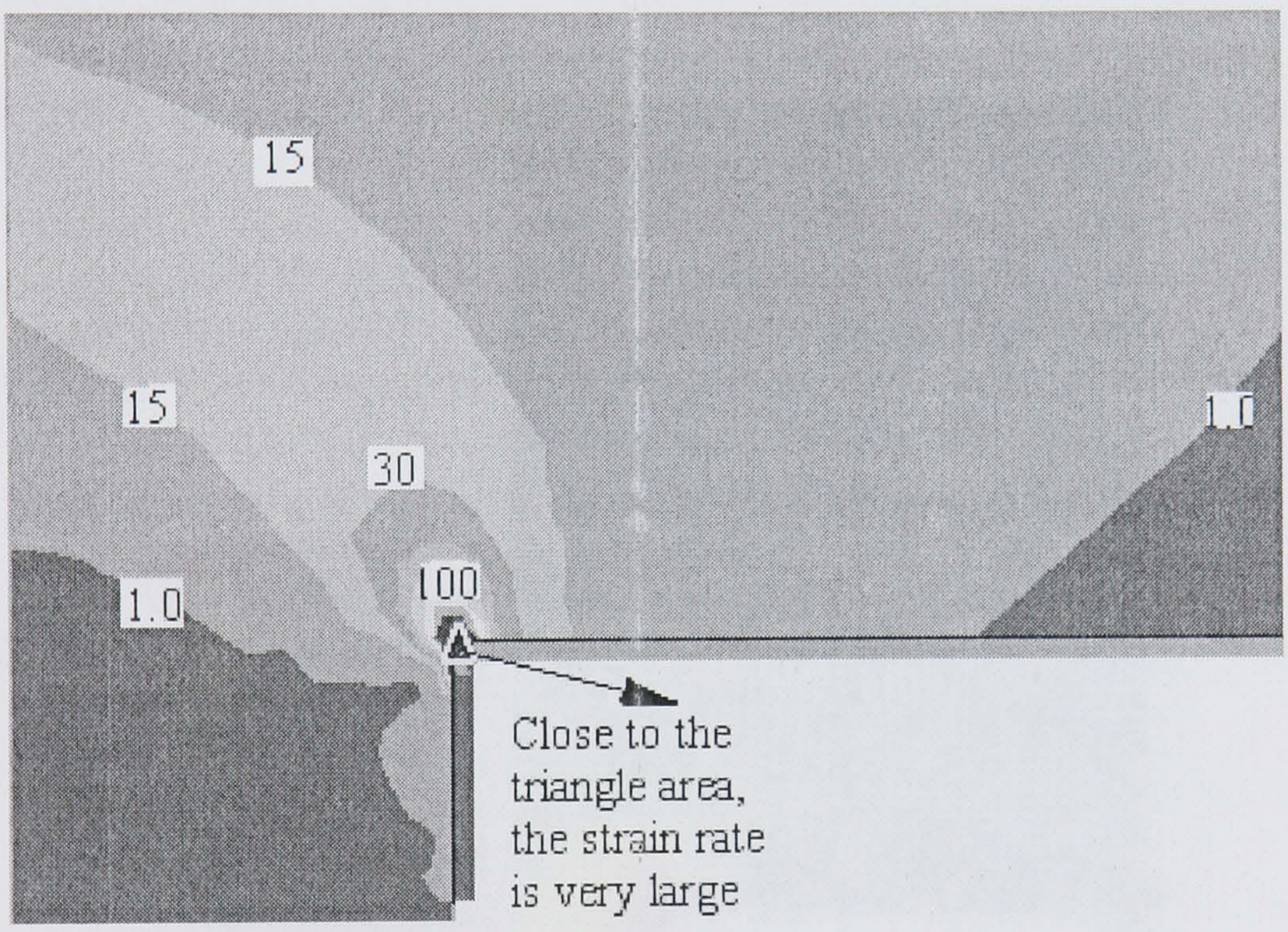

Figure 4.41 Enlarged picture of Figure 4.40a.

As discussed before, the scaled down simulations can give either a similar average strain rate or a similar temperature in separate runs. In other words, when the temperature is similar, the strain rate is higher (as in run 2), while when the strain rate is similar, the temperature is lower (as in run 4). It has not been found that the average strain rate and the temperature can both be reproduced in one run. Since the Zener-Hollomon parameter is in direct proportional to the equivalent strain rate and in inverse re ationship to the temperature, differences are also expected for the calculated Z value between run 1 and the other runs.

The predicted value given by FEM subroutines are shown in Table 4.17. The values are extracted from the same stage of extrusion for run 1 and 3. The predicted values in run 3 are higher than in run 1.

Table 4.17 Predicted value of Zener-Hollomon parameter

Run (according to Table 2)	The whole deformation field	Area with $\dot{\bar{\varepsilon}}>1$	Area with $\dot{\bar{\varepsilon}}>0.1$	Area with $\dot{\bar{\varepsilon}}>0.05$
1	1.87e8	6.54e8	5.22e8	3.15e8
3	2.18e8	1.18e9	8.25e8	4.29e8

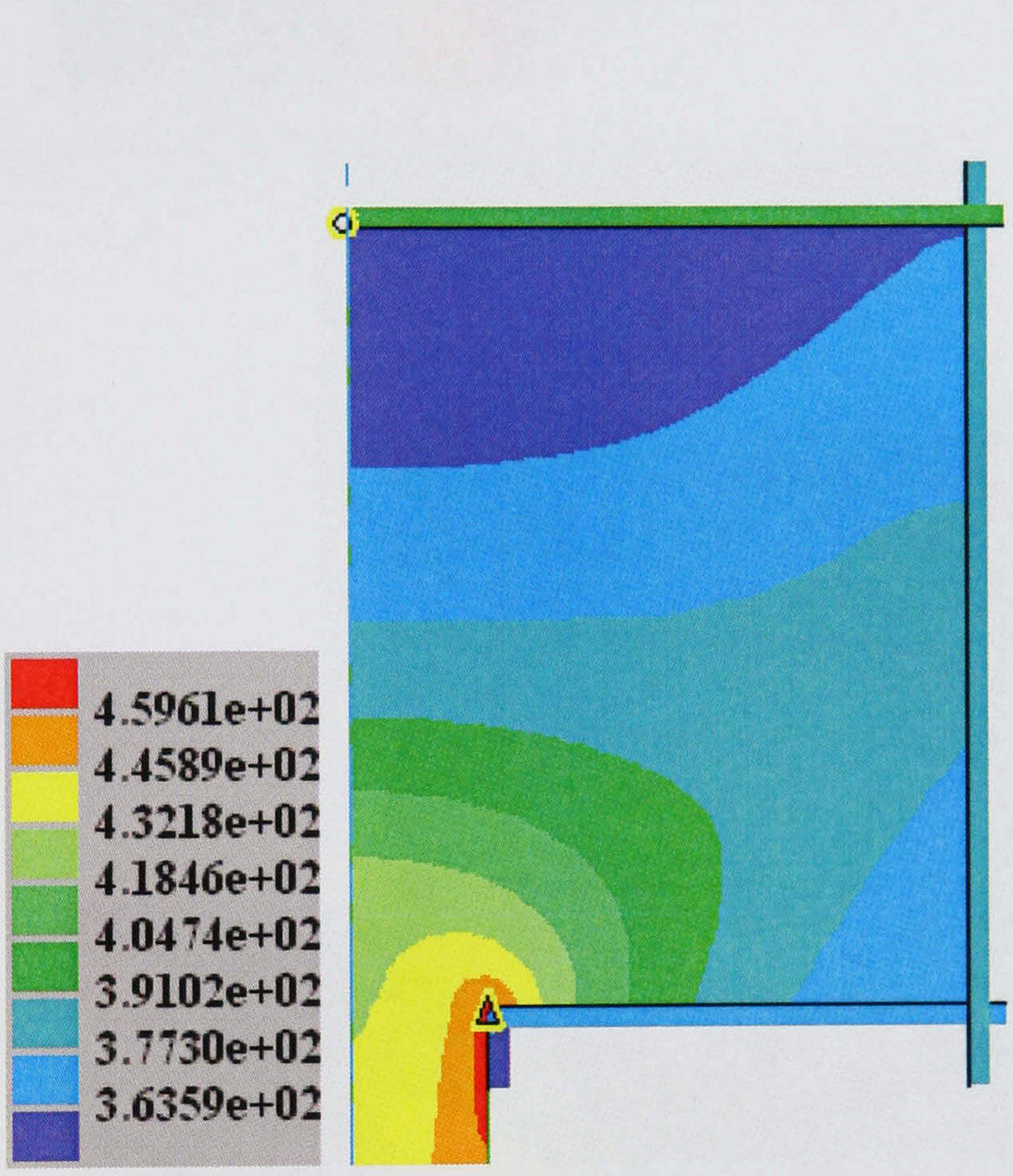

Figure 4.42(a) Temperature distribution in Run 1

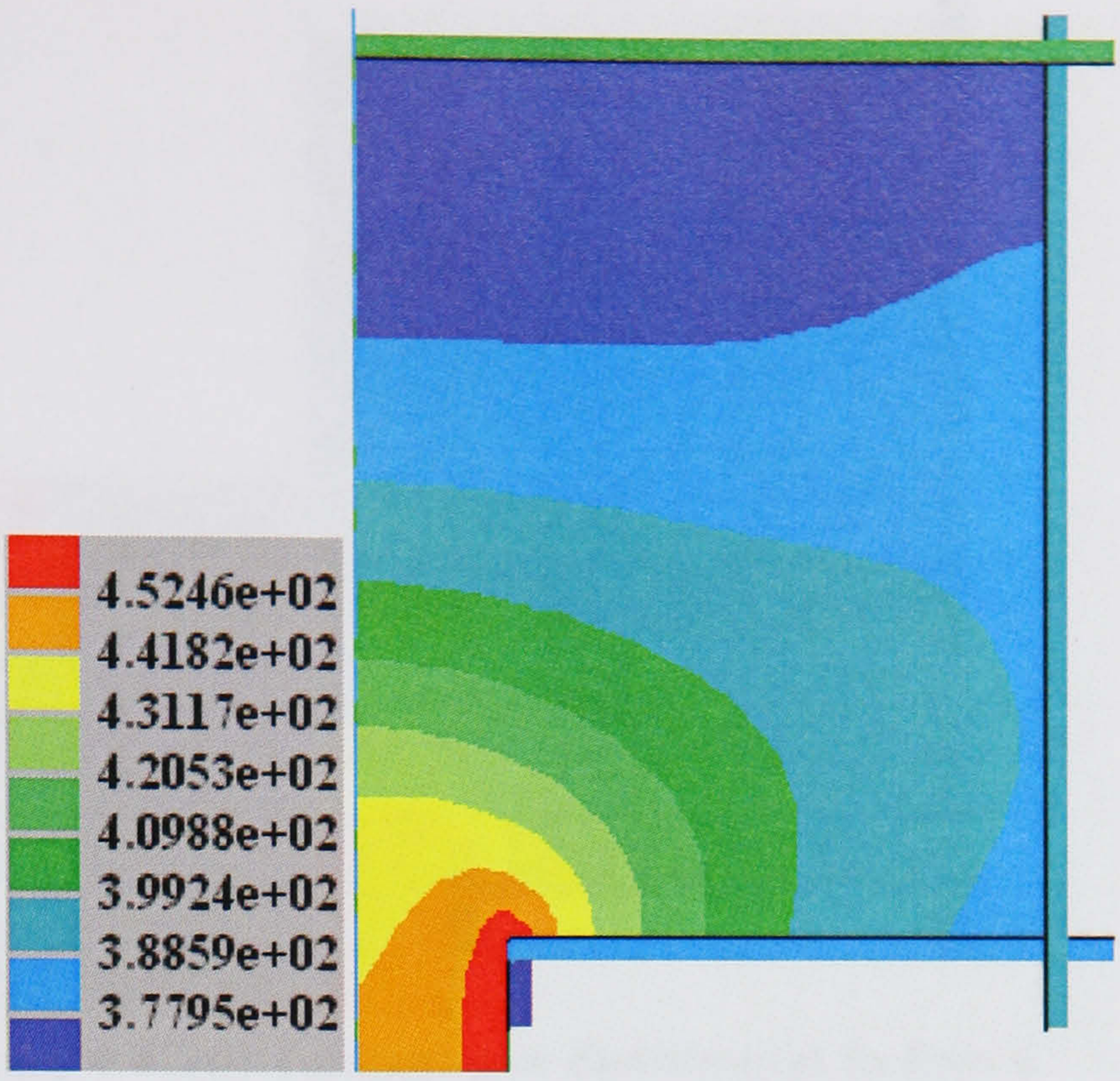

Figure 4.42(b) Temperature distribution in Run 2

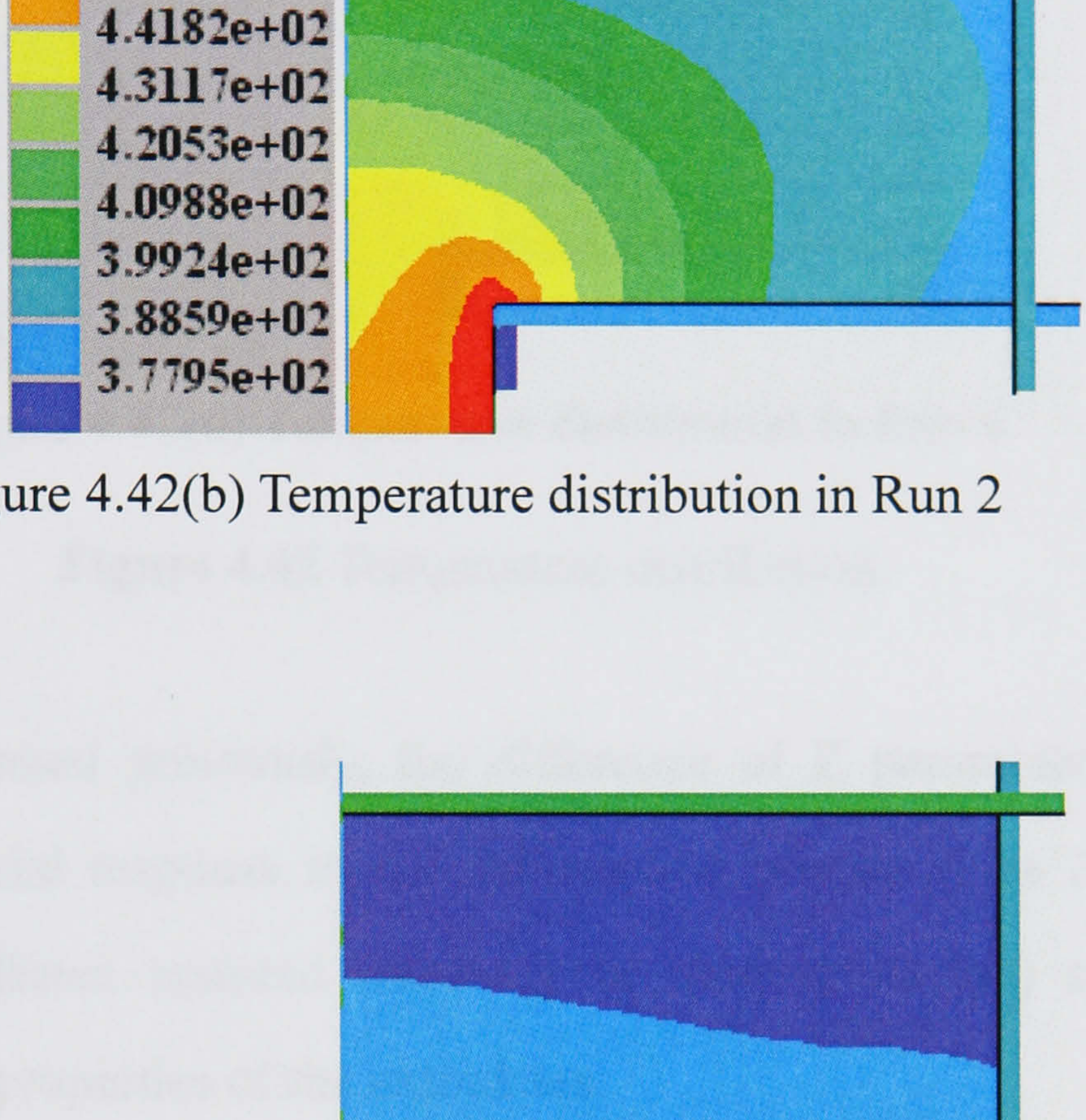

Figure 4.42(c) Temperature distribution in Run 3

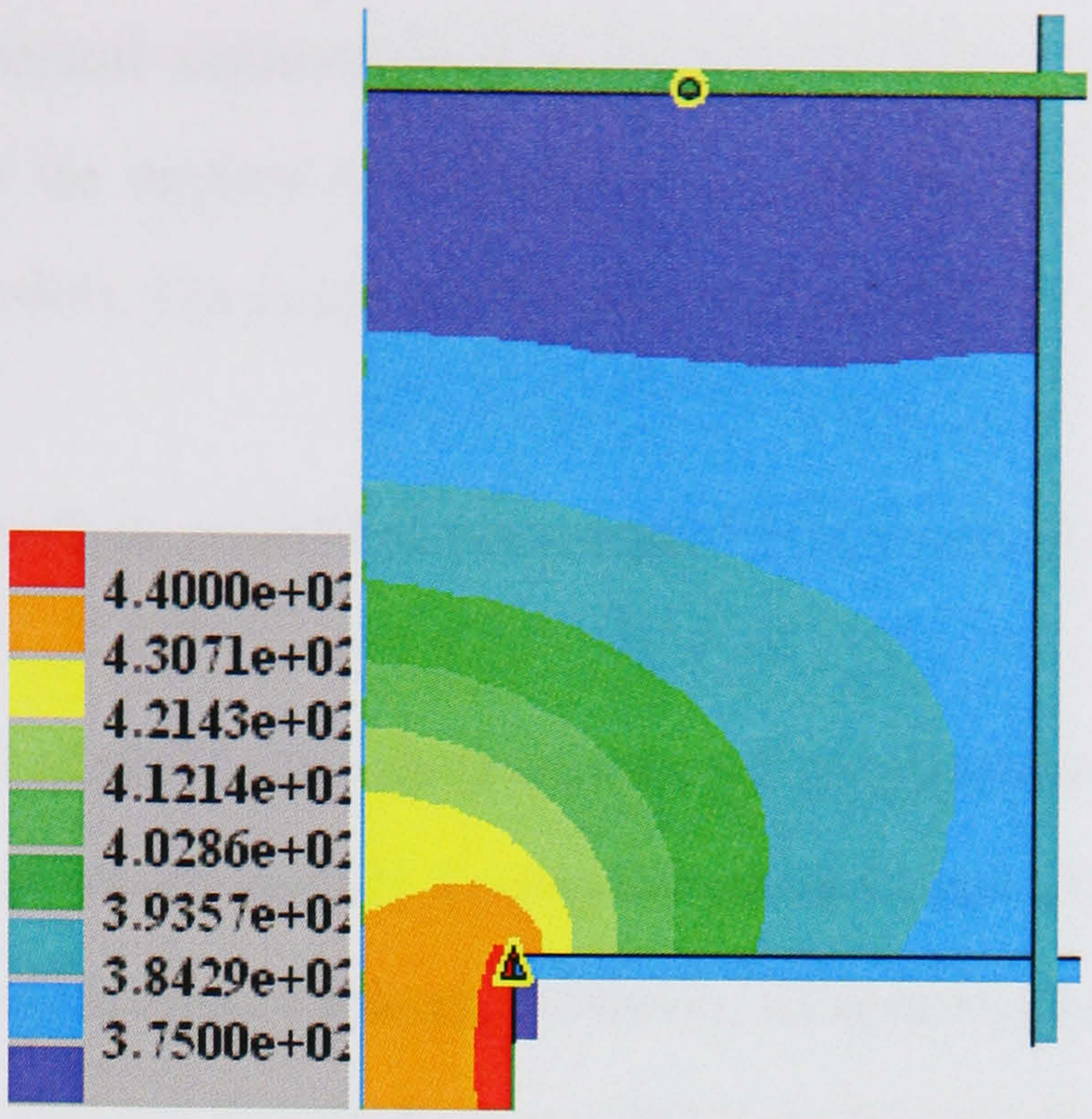

Figure 4.42(d) Temperature distribution in Run 4

Figure 4.42 Temperature distribution

As has been discussed previously, the difference of Z parameter indicates a difference of material response to the deformation process (Nes 2002), which will lead to a different restored (recovery or recrystallisation) structure and therefore, the final properties of the extrudates.

Although it is possible to give an identical Z value by choosing another ram speed, which will be different to all of the runs in Table 4.15, the influence on the material property is not clear as regards the material properties when the deformation temperature, the deformation strain and strain rate are different (Sheppard 1993, Peng 2004a). Another problem will also emerge concerned with how to evaluate the imposed ram speed in a scaled down model to give a similar Z to the original run. The method of trial and error will not be admissible since the time and economic cost will be too high and the advantages of the scaled modelling will be diluted. Detailed discussion will not be addressed here but the main point is that caution must be taken because of uncertainty when employing the scaled down model to study the manufacture process.

Moreover, in numerical simulations concerned with finite element method, a larger mesh could be applied to modelling the manufacturing process when establishing the models. The detail of this discussion can be found below.

4.4.3.3 Effect of mesh in manufacturing scale FEM simulation

The Finite Element Method, after three decades of development, has reached that point of maturity at which nobody doubts its effectiveness and power to solve various kinds of engineering problems. However, its results, as those of any other numerical method, can not be relied upon without an assessment of their accuracy. The accuracy of the finite element solution depends on the discretisation which is characterised by the finite element mesh and the choice of element (Krishnamorthy 1997).

After the importance of developing both a valid and an accurate representation of the problem is examined, element mesh refinement is discussed in detail in this section, and comparisons of the performance of different mesh densities are reported.

The accuracy of a model can be improved in two ways. Either the geometry can be divided into smaller elements, so that the mesh density is increased, or the accuracy of the elements themselves can be improved by using higher-order interpolation functions. These two techniques to improve a model's accuracy are known as h-refinement and p-refinement, respectively (Fagan, 1992). The latter appears the simpler of the two methods for the user of a finite element package, but in practice commercial programs only offer linear and quadratic elements, so that the opportunity for p-refinement is limited. Also, increasing the element order from linear to quadratic, for example, leads to a significant increase in the computer time needed to analyse the structure. To confirm the convergence of a model by progressive h-refinement of the mesh, all previous meshes should be

contained in the finer meshes. This is generally referred to as a reducible net (Fagan, 1992).

Considerable work has been done to investigate the various criteria involved in designing the 'best' mesh. Notable among this are the studies of Melosh and Ebner etc. (Melosh and Utku, 1987). These studies expose the complexity involved in designing the mesh and provide some guidelines covering problems of idealisation and discretisation. It is only recently that researchers have focused their attention on the main problems of the 'reliability' of solutions of the finite element method.

Normally a finite element analyst designs a mesh based on his previous experience, intuition and guesswork. The results are accepted if they reasonably match with what he has guessed. If the initial solution is not acceptable, the analyst has to prepare an entirely new set of input data for a finer mesh. This is a very costly and time consuming procedure, and does not guarantee that the new mesh will sufficiently accurate results. However, in the software of Forge2 and Forge3, automatic mesh generation has been developed and it is a technique that can generate subregions of node points and element connectivity for an object given its overall geometry and limited meshing information.

The refinement strategy depends on the criteria to be adopted to attain the level of accuracy required. The refinement scheme and data structure that supports it are crucial since they strongly influence the practical feasibility, storage overheads and related considerations.

To discuss the effect of mesh size on FEM simulation, two extra simulations, which utilise a model of true manufacturing scale, are established as shown in Table 4.18. The billet length is 400mm, the diameter is 300mm and the ram speed is 12.4 mm/s. The radius of the die entrance is 2.5mm, the die land length

is 25mm. The model has been built up in a more complex mesh, which is detailed in Table 4.18. The positions of the mesh boxes are shown in Figure 4.43. To avoid errors caused by element distortion, the mesh size difference between mesh boxes in contact should be controlled at a limited range, usually smaller than 3, which can be checked in Table 4.18.

Table 4.18 Mesh sizes (unit mm)

Run	Default mesh size	Box 1	Box 2	Box 3	Box 4	Calculation time (hours)
5	11.82	8.1	3.0	--	--	12
6	8.1	4.0	2.0	1.0	0.4	39

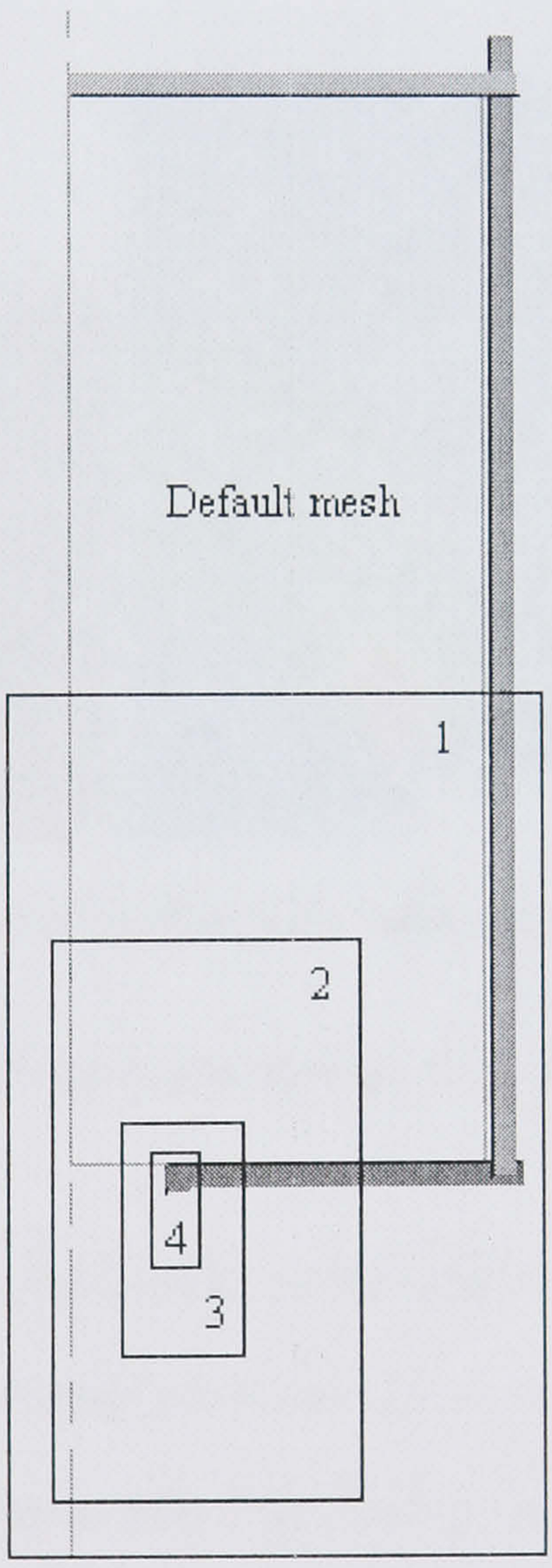

Figure 4.43 Mesh boxes used in FEM simulation

As can be seen in Table 4.18, by using the coarse mesh size, the calculation time is even less than that needed in the previous simulations shown in Table 4.15. When finer meshes are employed, as in run 2 of Table 4.15, the amount of time

increased significantly. However, the time implication is still acceptable and the simulation results compared with run 1 are similar. This can be seen in Figure 4.44 as an example of the predicted results of strain rate.

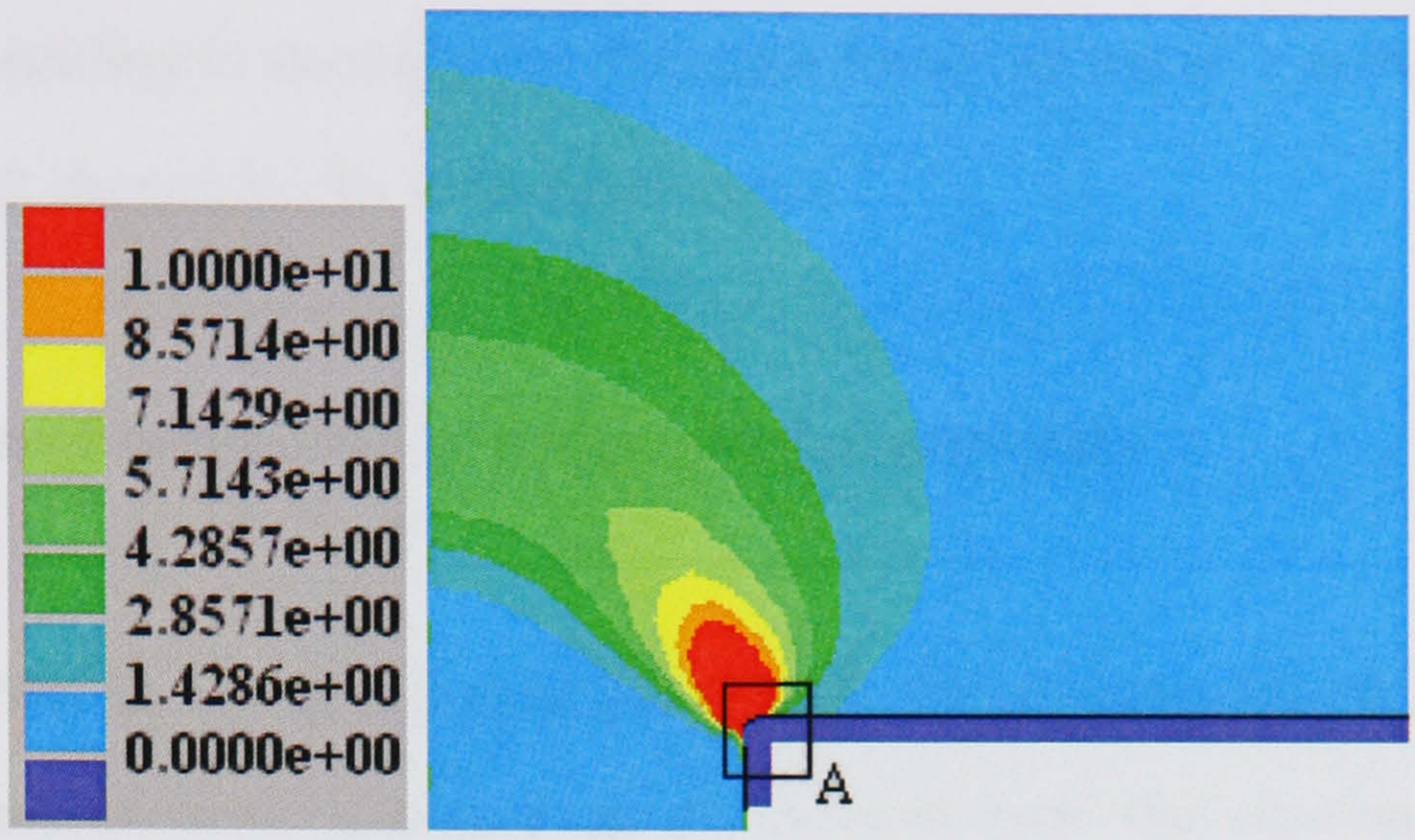

(a) Predicted results with fine mesh

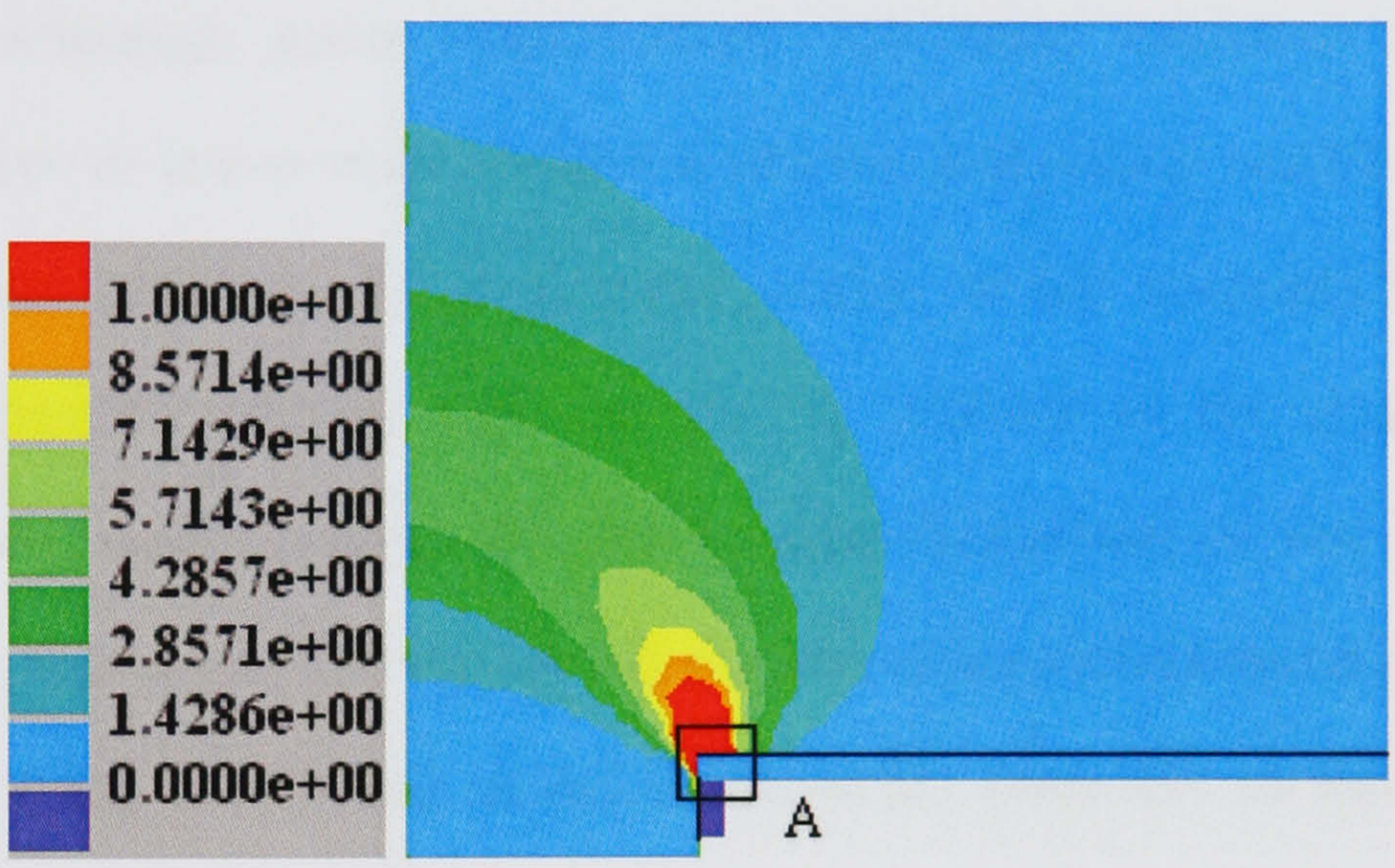

(b) Predicted results with coarse mesh

Figure 4.44 Predicted strain rate with different mesh sizes

The calculated strains in the two runs at the deformation area are almost identical, except at the die entrance corner as marked as area A in Figure 4.44. It is found that the maximum strain rate in run 5 is 70 but the maximum strain rate in run 6 is nearly 100. The discrepancy of the prediction at the die entrance corner is caused by the mesh penetration, which is influenced by the mesh size. As reported it is prudent to ignore the abnormal and probably erroneous Figure. There is no experiment or theoretical analysis which would rectify the predicted results. However, it is generally agreed that the finer the mesh, the more precise

the simulation. Whilst the prediction of the simulation with coarse mesh can still be regarded as acceptable, a balance could be achieved between the time and precision when a suitable mesh size is chosen. Therefore, full modelling of the process without scaling is strongly recommended and the use of a suitable design of optimum mesh should be the simulation route.

4.5 Simulation of recrystallisation by cellular automata

It has been shown in the discussion above that the as-extruded structures are spatially nonhomogeneous, however, at the present time the continuum theory has some difficulty in precisely simulating the heterogeneity at the process size (macro-) scale, although great improvement has been achieved in crystal modelling at micro- or meso-scale (between macro- and micro- scale) in the last decade. The crystal plasticity finite element model, which accounts for plastic deformation by crystallographic slip and for the rotation of the crystal lattice during deformation, could predict the deformation behaviour of one or several coalescing grains, but is not mature for simulation of the deformation process on the macro-scale. FEM simulation at the macro-scale does not include material heterogeneity. However, it is still a powerful tool in predicting the necessary variables, such as strain, strain rate and stress, which are necessary for microstructure simulation. The recently developed PB models can relate the final recrystallised structure directly to the as deformed state, but ignore the evolution process of the recrystallisation. Every method has its own merit and shortcomings. However, if the macro-scale FEM can be integrated with the physically based metallurgical model and CA, it could have a promising future in the simulation of structural evolution at the macro-, micro or meso-scale.

The transition rule at the beginning state of CA depends in an arbitrary way (Liu et al. 1996), purely on the geometry of the matrix. However, it has now reached a rather complex and probabilistic state (Raabe and Becker 2000), which depends

on the mobility of the grain boundary and the stored energy of the structure. It has been pointed out previously (Raabe and Becker 2000) that although spatially discrete microstructure simulations have already profoundly enhanced our understanding of microstructure and texture evolution over the last decade, their potential is sometimes simply limited by an insufficient knowledge about the external boundary conditions that characterise the process and an insufficient knowledge of the internal starting conditions that are, to a large extent, inherited from the preceding process step.

Different definitions of neighbourhood have been used in the previous studies as shown in Chapter 2, Figure 2.7 and they are not repeated here (for the convenience of the reader, the novel Figure 2.7e is shown again below). The preferred ratio is defined as the number of cells at the preferred side to the number of the cells at the other side (the preferred ratio is 2 as shown in Figure 2.7e). It should be pointed out that a preferred ratio of 15 is adopted in construction of the initial structures and a ratio of 2 is employed at the nucleation and growing state of simulation. The exact value of the preferred ratio is difficult to judge from the experiments because of the uncertainty in original grain shape. Consequently a process of iteration has been carried out by the present author and only the ratios giving the most appropriate results have been presented in this study.

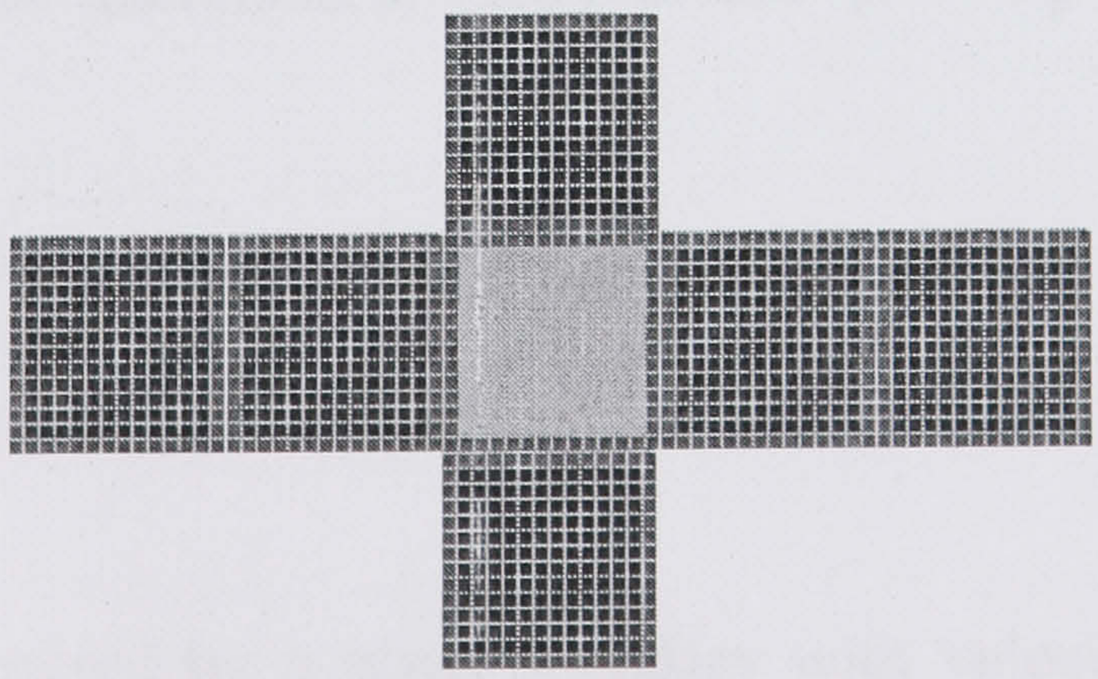

Repeated figure 2.7e Side-prefer-neighbour (preferred ratio 2) (repeat of Figure 2.7 for the convenience of the reader)

Before grains begin to touch each other, the shape of the grain and its growth rate depend on the definition of the neighbourhood. The recrystallised structure is more or less independent of the neighbourhood that was chosen. After the grains have grown together, and the process is terminated, the grain pattern is virtually independent of the neighbourhood chosen. It was also reported by Davies (1995) that on average, to within 95% certainty the neighbourhood used in a cellular automaton does not affect the JMAK (Johnson-Mehl-Avrami-Kolmogorov) time exponent. However, in discrete cases the model may yield time exponents which differ significantly from the theoretical values and this must be accounted for in any simulation attempts. In the present study, research in predicting the recrystallisation time has not been completed, so the impact of different neighbourhoods is mainly on the shape of the recrystallised grain before the grain impact on each other. The side preferred neighbourhood was found most suitable for the present case, which is determined by the nature of the recrystallised grain size found in experiments.

As for the transition rules, the recrystallisation designed with a probabilistic-switching rule was adopted in this study. The local switching probability can be quantified by the ratio of the local and the maximum mobility m^{local} / m^{max}, which is a function of the grain boundary character and by the ratio of the local and the maximum driving pressure p^{local} / p^{max}.

$$\hat{w}^{local} = \left(\frac{m^{local} p^{local}}{m^{max} p^{max}}\right) = \left(\frac{\dot{x}^{local}}{\dot{x}^{max}}\right) = \left(\frac{t^{max}}{t^{local}}\right) \qquad (4\text{-}13)$$

t is the local time required by a grain boundary with velocity $\dot{x}$ to cross the automaton cell.

In Raabe's study (2000), nucleation in the simulation is performed in accord with

two aspects, i.e. potential nucleation sites must fulfil both the kinetic and the thermodynamic instability criterion. At the beginning of the simulation, the thermodynamic criterion, i.e. the local value of the dislocation density, was first checked for all grid points. If the dislocation density was larger than some critical value of its maximum value in the checking area (for example, 30%, 60% or 90%), the cell recrystallised without any orientation change (dislocation density assigned as zero and original crystal orientation reserved). The ordinary growth algorithm was started and the kinetics for conditions for nucleation was checked by calculating the misorientations among all recrystallised cells and their neighbourhood. If any pair of cells found a misorientation above 15°, the cell flip of the unrecrystallised cell was calculated according to equation 4-13. The detail of the transition rule can be found in Raabe's work.

As a result of the lack of means for predicting the crystal orientation at the macro-scale simulation and the shortage of experiment results, a statistical method was adopted in the present study to give the misorientation between the grains. For each cell, a randomly allocated orientation number, q, was assigned to each grain. The orientation number indicates primarily the orientation of a cell and maximum number of q was 936, which represents 936 texture components, these were equally distributed in orientation space. Geiger et al. (2001) has discovered that $q \geq 64$ crystal orientations were necessary to simulate the recrystallisation process, and the number of 936 was taken from Raabe's study (2003).

The misorientation is obtained from the q numbers of the neighbouring grains:

$$\theta' = \pi / 2 * |\Delta q| / q_{max} \qquad (4\text{-}14)$$

where Δq is the difference between orientation numbers of two adjacent grains (Doherty et al. 1995) and $0 \leq |\Delta q| / q_{max} < 1$.

In the present study, an adjustment of the nucleation criterion used in Raabe's study (1998b) was adopted. At the beginning of simulation, the dislocation density was also checked, in the same way as Raabe's study, but the total number of the nucleation site was controlled to no more than a certain number (30, in macro-scale simulation) at the first step decreasing gradually at the following time steps. In other words, only the cells having the 30 highest dislocation densities could be the nucleation sites and in the following steps this number decreased slightly and gradually. The recrystallised grain grows continually until it impacts on the other growing grains.

The second phase particles (mainly θ phase and S phase) were considered in the simulation. A certain number of pixels, which were set as the particles, were distributed into the automata matrix. Their states were unchangeable during simulation and when the grain boundary impacts on these cells, the boundary will stop moving forward until the particle is surrounded and bypassed by the boundary. This corresponds to the experiments in which these small or medium sized particles are interfering with the dislocations during the solution soaking treatment and retard the recrystallisation process (Doherty et al. 1997).

In this chapter, finite element simulation combined with the physically based model is adopted to give the initial parameters for the calculation of the as deformed structures, as introduced below.

4.5.1 Simulation setting and initial state of simulation

The Finite element method (FEM) is adopted to give the initial state variables for the structure models, such as the equivalent strain, the temperature and the equivalent strain rate. The subgrain size, and dislocation densities are calculated from physically based models and are transferred to CA models to construct the data required to define initial state of recrystallisation. Simulation results are compared with experimental measurements. It is demonstrated that CA integrated with the physically based models is effective in predicting the structural changes by selecting a suitable neighbourhood and reasonable transition rules.

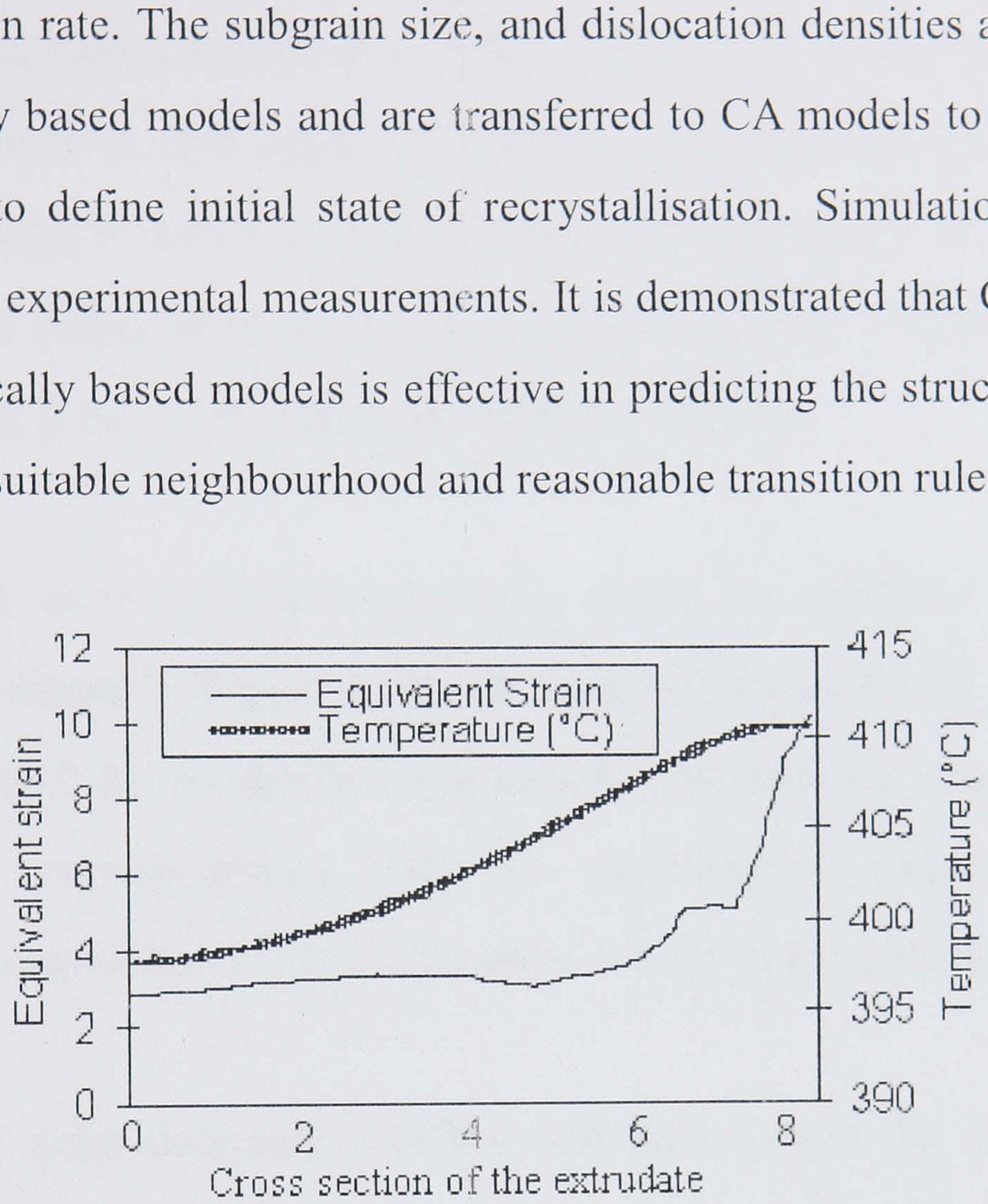

Figure 4.45 Equivalent strain and temperature distribution

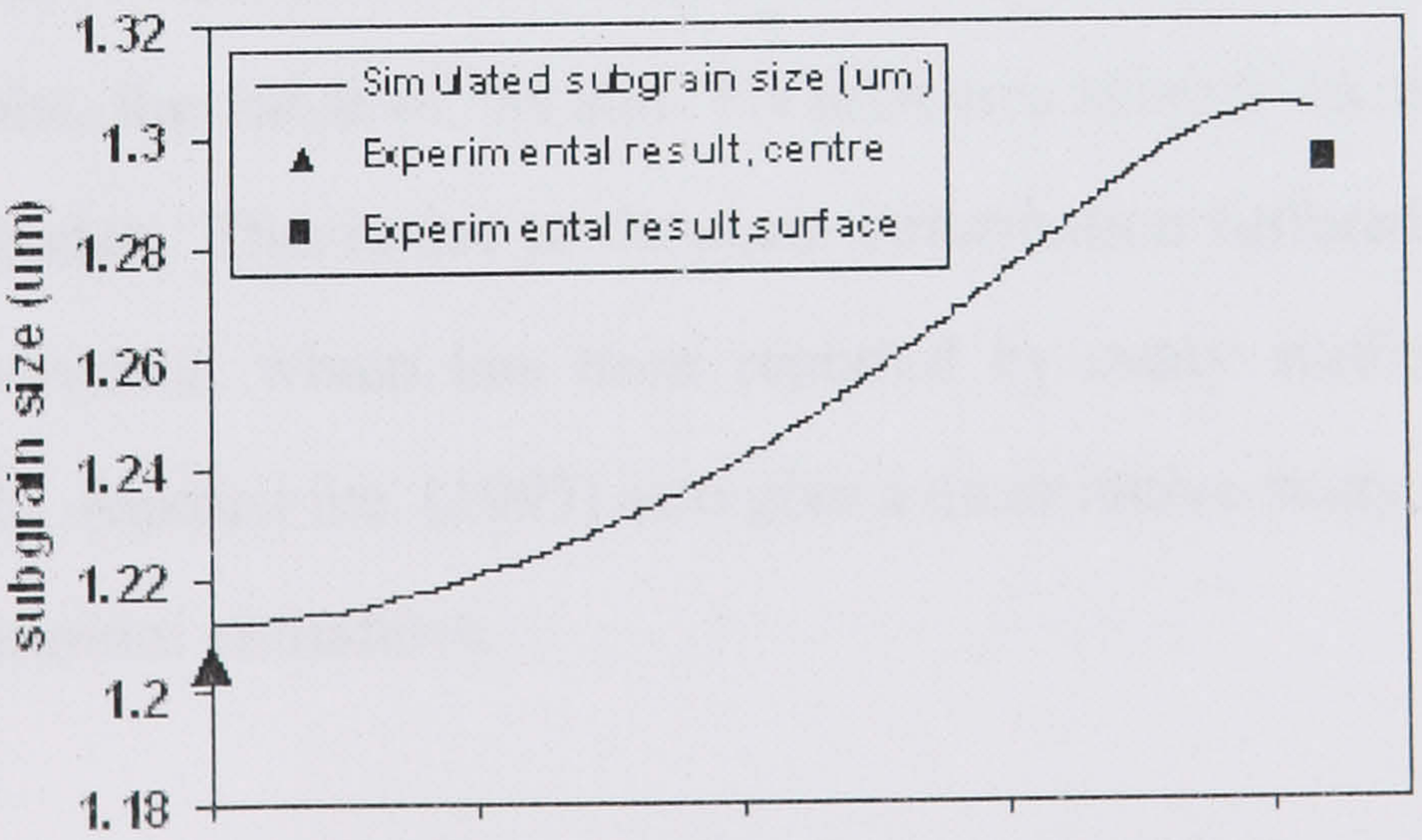

Figure 4.46 Subgrain size

For the solution soaked aluminium alloy used in this study, ΔH =176867KJ/mol, α =0.0118 m^2 / MN , n= 5.86, ln A =31.43 (Sheppard 1999a). Experiments have been performed by Vierod (1983) and Paterson (1981). The extrusion ratio was 20. Initial billet temperature was between 350°C. The length of the billet was 95mm. The container temperature was 50°C lower than the billet temperature, and the ram speed is 12.8 mm/s. The billet is homogenised at 500°C for 30 minutes. The billet is then heated to the extrusion temperature. After extrusion, the extrudate is subjected to a solution treatment at 500°C for 30 minutes and water quenched, followed by ageing at 160°C for 18 hours.

The equivalent strain and the temperature, which are predicted by the FEM simulation (as shown in Figure 4.45), are used in calculating the subgrain size with the equation 2-21. As shown in Figure 4-12, the predicted subgrain sizes are in reasonable correspondence with the experimental measurement. The difference is no more than 1% at either centre or edge of the extrudate.

The values of grain boundary area per unit area Sv and the nucleation site density Nv (calculated from equations A-3 and A-4 in Appendix A) across the extrudate are shown individually in Figures 4.47 and 4.48 (this has been shown in Chapter 4, but is repeated for the convenience of the reader). As can be seen in these two graphs, the value of Sv and Nv increases sharply on the sub-surface area of the extrudate. This is due to the shear deformation suffered at the surface area of the extrudate, which has been reported by many studies (Castle and Sheppard 1976). Aukrust etc. (1997) also give a quantitative study on the sheared surface of aluminium extrudates.

In the analyses performed by Aukrust, a transition from grains which are lamella to the point at which the lamella structure is broken up was found. It was reported to take place around 200μm below the surface. Results in another experiment

carried out by the same author reported where the transition from a bulk region with a rolling type of texture to a surface boundary layer with shear type of texture takes place between 400 μm and 165 μm. The main component of the texture in the surface in both experiments mentioned above is close to (113)[332], which corresponds to the idealised shear texture, the skew cube (001)[110], rotated about 25° about the transversal axis. In the present study, the transition location was regarded as 500 μm below the surface area, where the sharp rise of Sv or Nv occurs. The transition point is shown in Figures 4.47 and 4.48, as the cross point between the dashed point line and the predicted curve.

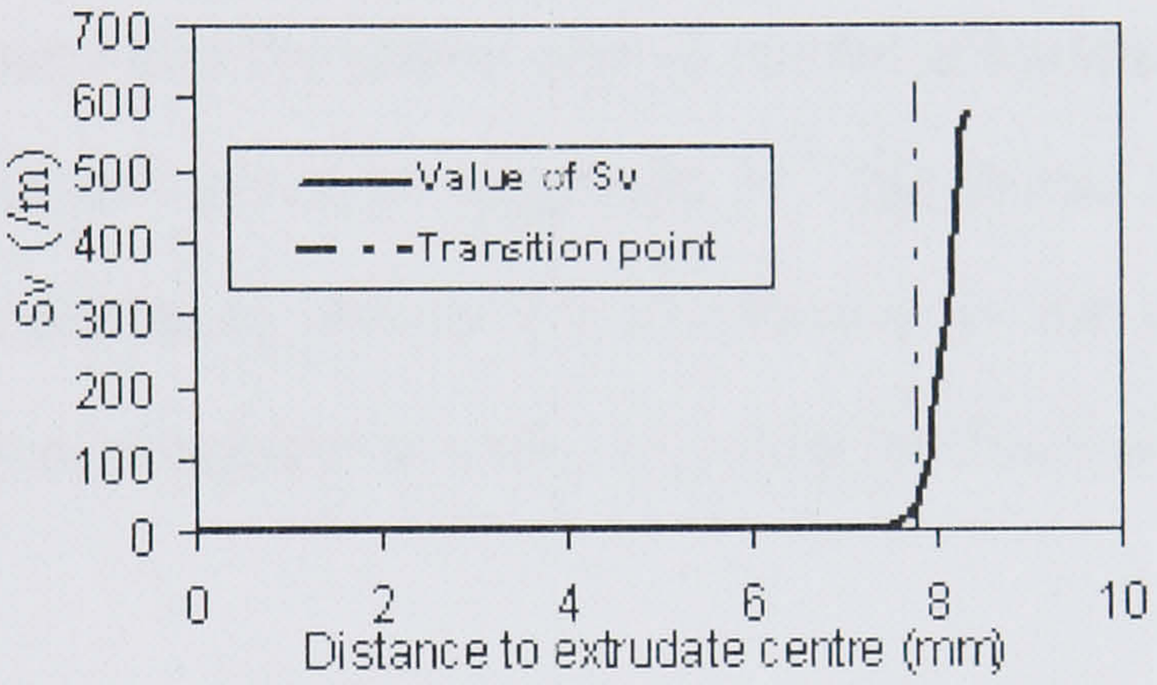

Figure 4.47 Value of Sv across the extrudate

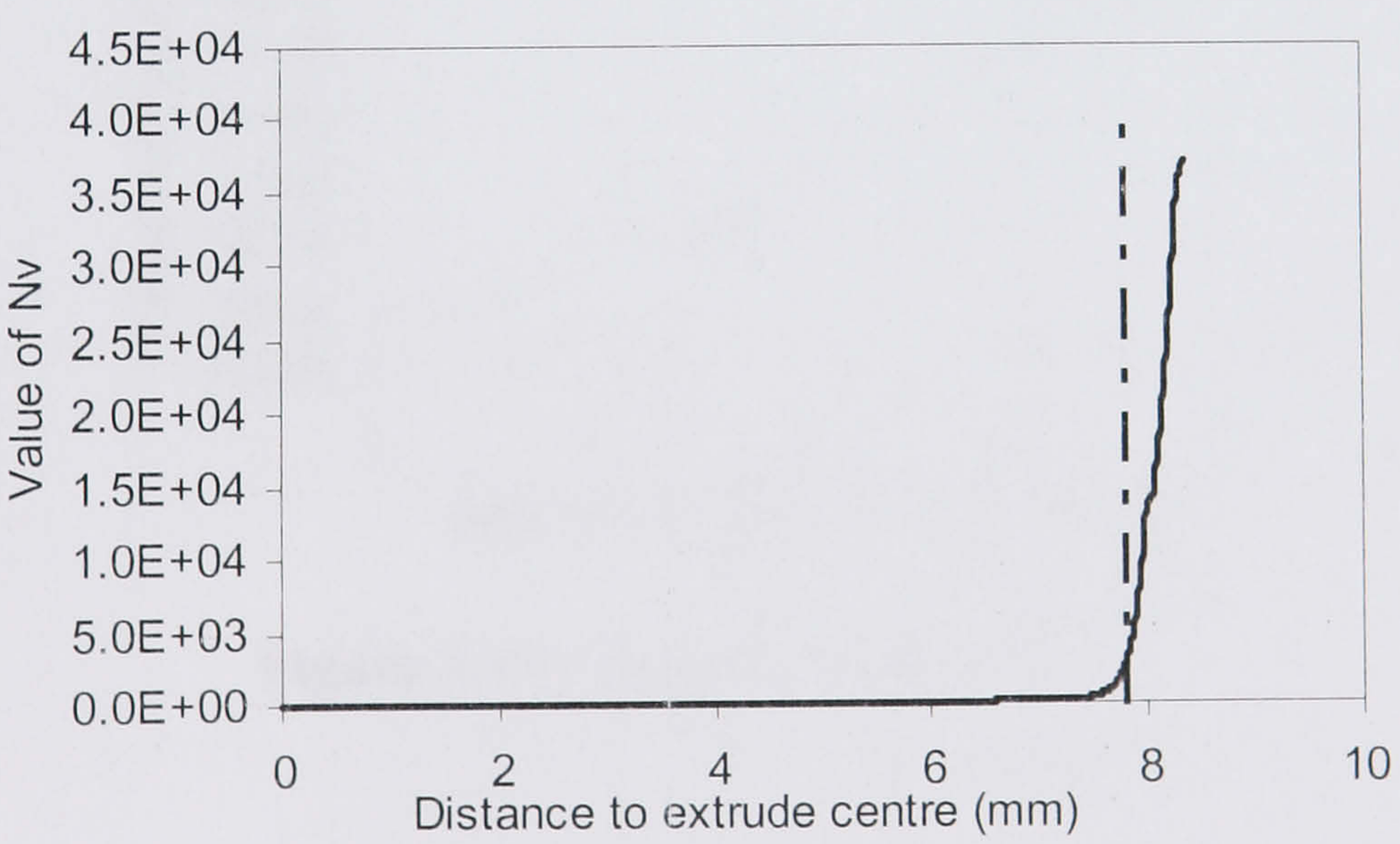

Figure 4.48 Value of Nv across the extrudate

According to the physically based model, the density of nucleation sites is much higher and the recrystallised grain size is expected to be substantially smaller at

the subsurface area under shear deformation than the areas below. However, in experiments, this phenomenon has not been observed, only a relatively small decrease of the grain size was found in this area. Two causes may lead to this phenomenon: one is that the PB model needs to be improved to predict the recrystallisaton in extremely sheared structures, and the second is that secondary recrystallisation is likely to occur in this special area. However, with the lack of experimental evidence, it is difficult to make any conclusion. According to the experimental observation, the nuclei number at this area was approximately regarded as 1.4 times more than the area 500 μm below the surface.

The dislocation density and the stored energy can be calculated by the physically based models, which are given in Appendix A. The stored energy is shown in Figure 4.49. The calculation results are transferred to the initial state for CA calculation by Fortran programs in order to match the Fortran format of the base program.

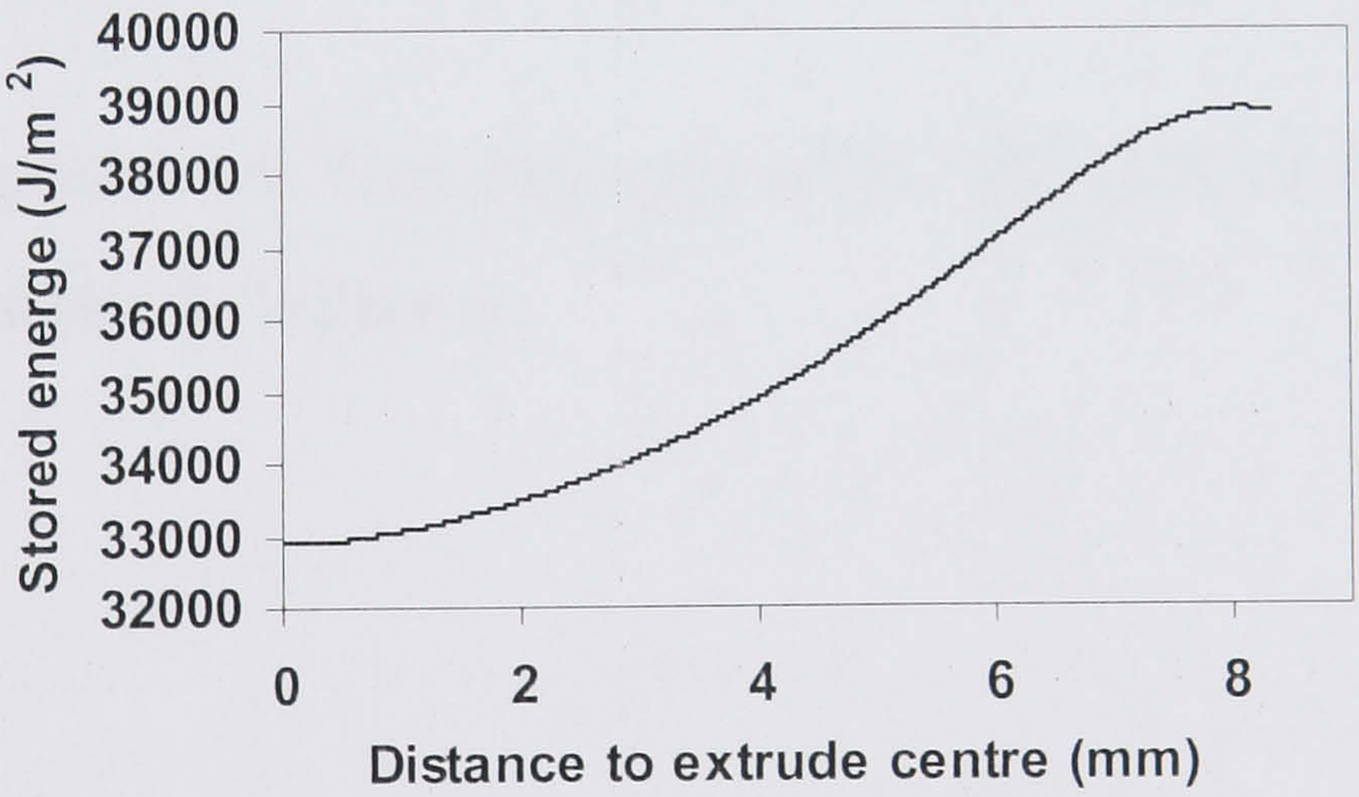

Figure 4.49 Predicted stored energy

4.5.2 Meso-scale simulation

At the meso-scale simulation, 1000×500 square cells were used as shown in Figure 4.50. Each pixel corresponds to a cell: thus the terms pixel and cell may be used interchangeably. Each pixel represents the size of $1\mu m$, and thus the graph represents $1\times0.5mm^2$ of the material at the surface area. The initial fibrous structure was constructed and each fibre of the as extruded structure was appointed with a q number, which represents the crystal orientation. To help display on a screen, each q number has a different colour, which is allocated by the program automatically. The finite element and PB simulation results (for example, the stored energy and the subgrain size across the transverse direction of the extrudate) are transferred to the initial state of the CA model by the FEM program subroutines and a further computer program, compiled in Visual Fortran 6.1.

The empirical equation has been employed to give the width of the as extruded elongated grain, which is written as:

$$D_1 = D_0 / \sqrt{R} \qquad (4\text{-}15)$$

where D_1 is the width of the fibrous grain and D_0 is the initial grain width (approximately 90 μm), R is the extrusion ratio (20). The width of the fibrous structure using this calculation is $20\mu m$. However, due to the heavily sheared deformation suffered during extrusion, the width of the elongated grain at the subsurface area is much less than the calculated result. There is no experimental

measurements in the literature and the value of 8 μm has been adopted from experimental observations and consideration of the variation of equivalent strain across the extrudate section (the equivalent strain has been shown in Figure 4.45).

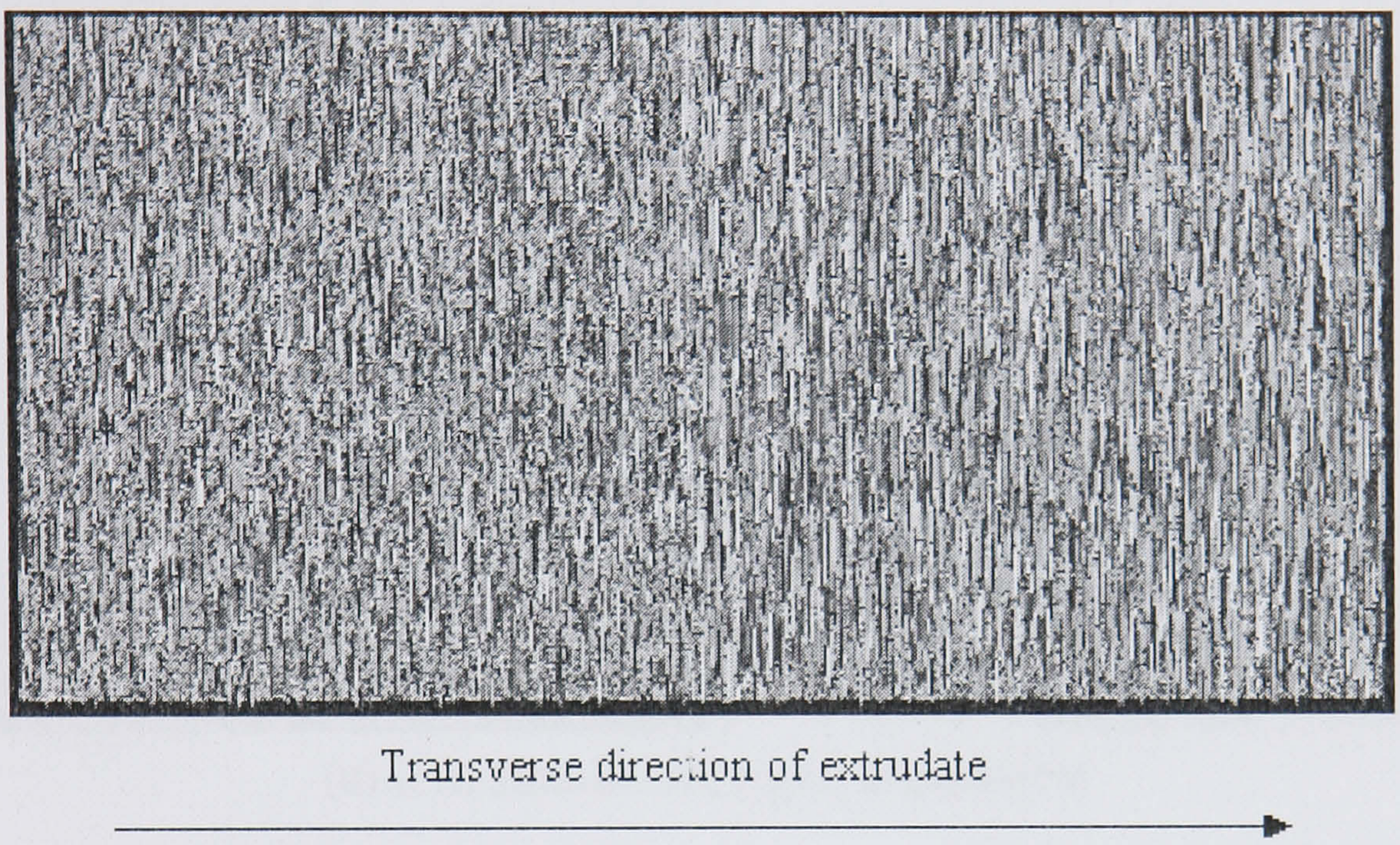

Figure 4.50 The initial state of CA (1000×500 cells)

The simulation results are compared with the experimental measurement as shown in Figure 4.51.

The program measured the size of different recrystallised grains in both the transverse section and the extrusion direction automatically. The calculated average grain size is 188μm in the extrusion direction and 92μ*m* in the transverse direction. The average value is140μm , which is 7.9% lower than the experimental measurement (152 ± 0.013μm). However, the grain size distribution is inhomogeneous and the shape of every grain is quite different, it is difficult to achieve a very precise measurement either in simulation or in experiments.

The reason for the formation of the elongation nature of the recrystallised grain has been discussed previously by many studies in metal forming processes and was regarded as caused by orientation pinning (Doherty etc. 1995, Subramaniyan 1989).

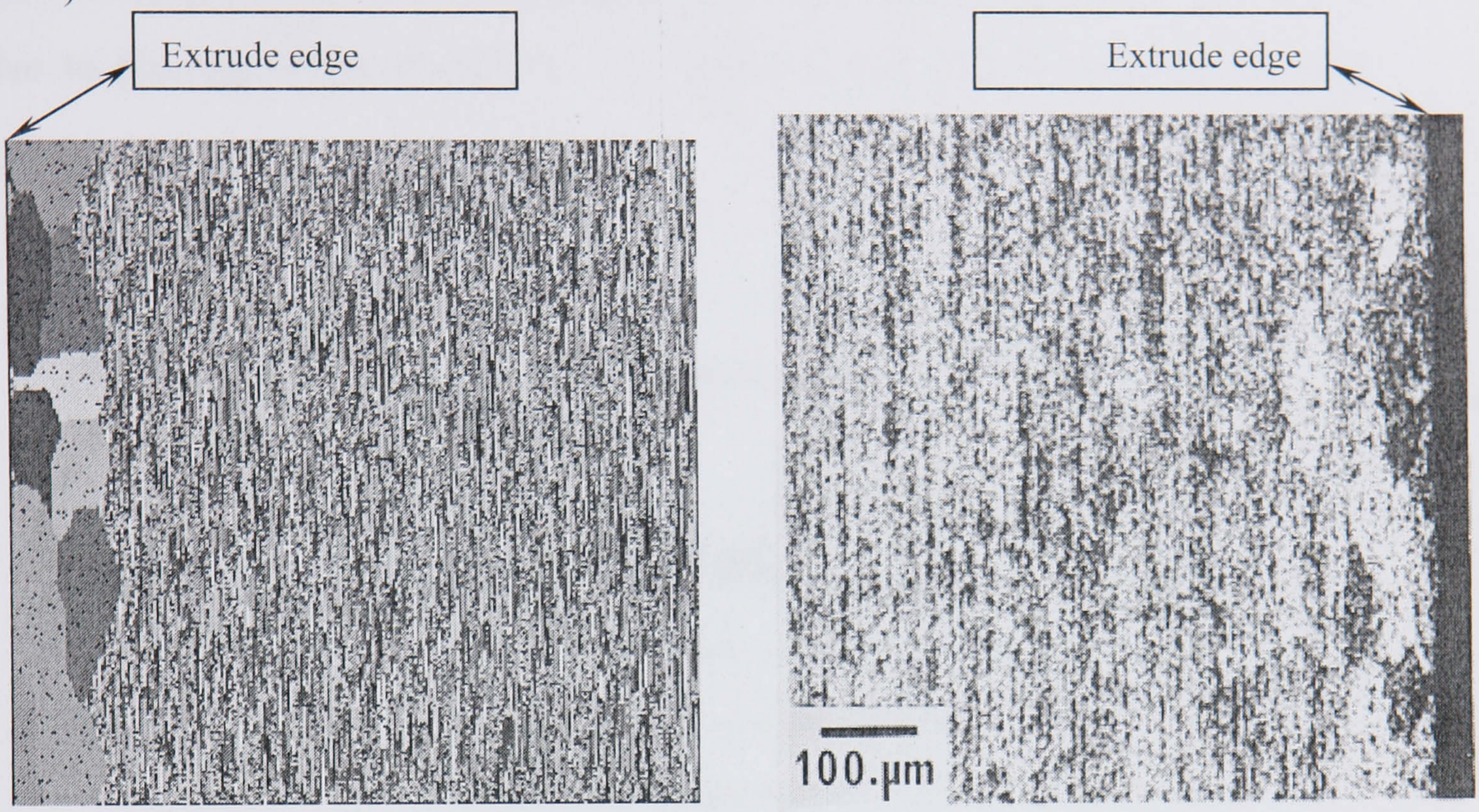

(a) left: simulation, right: experiment

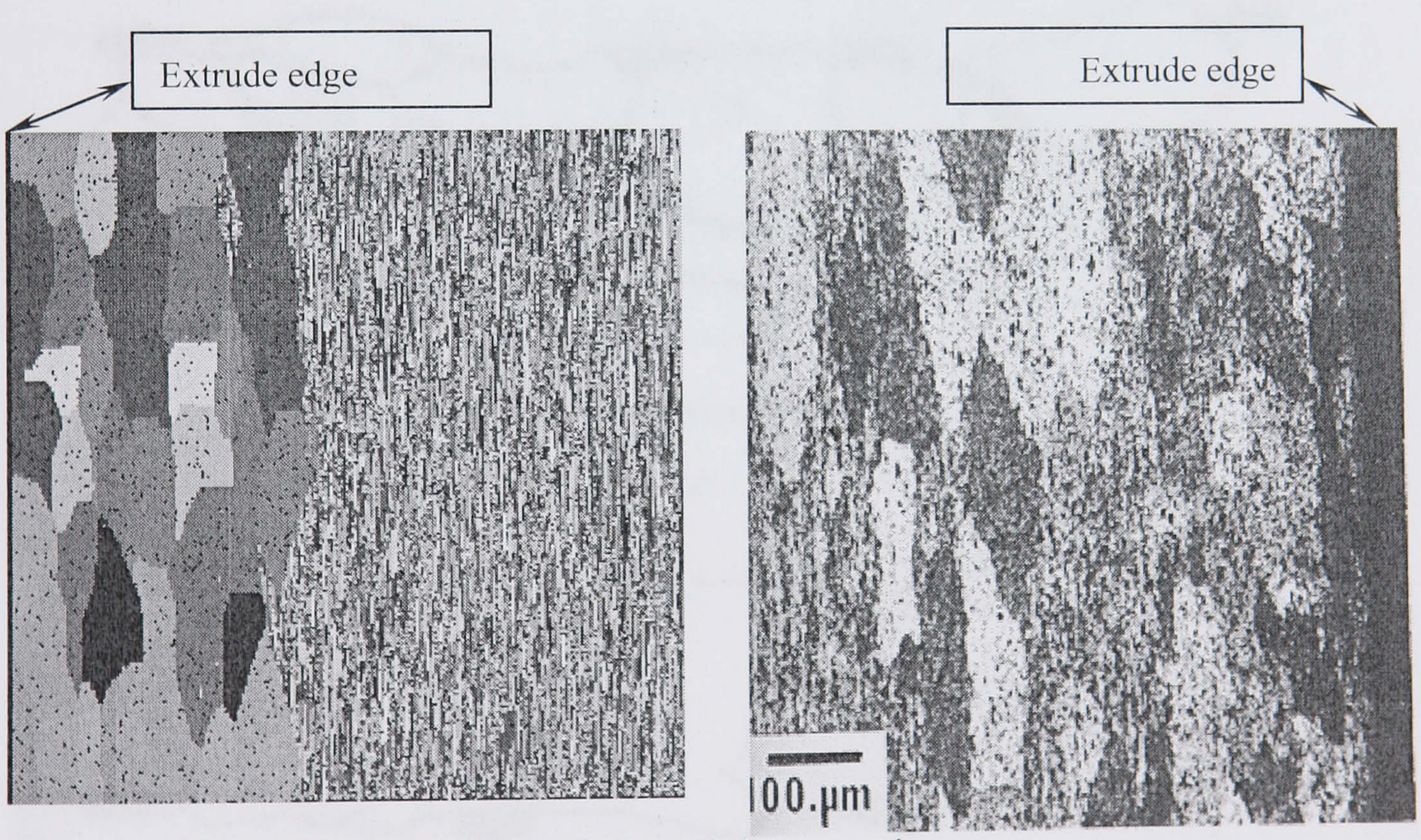

(b) left: simulation, right: experiment

Figure 4.51 Meso-scale simulation: recrystallisation at the surface area (a) at the beginning, (b) recrystallisation occurred to the centre.Experiments after Paterson (1981)

Based on experimental studies of warm plane strain extruded aluminium, the deformed bands of nearly constant orientation are stretched out in the extrusion,

similar but more pronounced than in the hot rolling process. Very strong inhibition of growth in the transverse (normal) direction will occur. A similar analysis proposed by Subramaniyan (1989) but involving precipitates is shown schematically in Figure 4.52. The elongated nature in the extrusion direction is due to pinning of the boundaries by second phrase particles (no larger than 1 μm).

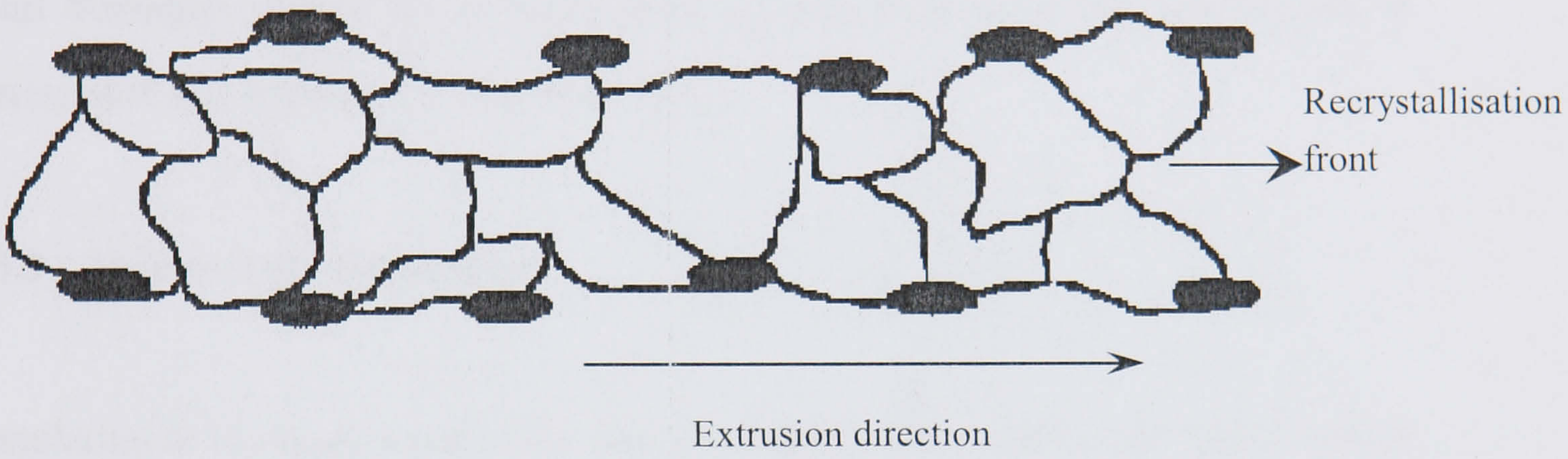

(a) low temperature

(b) high temperature

Figure 4.52 Mechanism of grain growth in high and low temperature extrudates: after Subramaniyan (1989)

As shown in Figure 4.52a at low temperature extrudates, the density of second phase particles is high and coalescence is difficult, whereas for high temperature extrudates, the propensity for subgrain coalescence to be predominant is high, as shown in Figure 4.52(b). The grain is not impeded in either the transverse or longitudinal direction due to the reduced density of particles, resulting in the equiaxed nature of the grains. The black points in the new-formed grains as shown in Figure 4.51 are the particles and as previously explained, when the grain boundary moves up to these cells, growth will stop until the particle is surrounded and bypassed by the boundary.

4.5.3 Macro-scale simulation

Simulation at the macro-scale was also performed. The 1000×500 pixel matrix is used, but represents $8.38\times4.19mm^2$ of the extrudate. The simulation and the experimental results are shown in Figure 4.53. The micrographs of the experimental results are obtained from extrusion under slightly different conditions, however, the results are quite similar to the measurements under the present experiment conditions.

The predicted recrystallised grain sizes by CA, physically based model across the transverse direction are compared with the experimental results, as shown in Figure 4.54. The results at the surface and centre by every method are also shown in Table 4.19. It can be seen from Table 4.19, either by physically based model or by CA, the simulation results correspond reasonably well with the experimental measurement.

Table 4.19 Results of recrystallised grain size

Method	Edge (mm)	Centre (mm)
Experiments	0.152 ± 0.013	0.297 ± 0.110
PB	0.149	0.312
CA	0.16	0.30

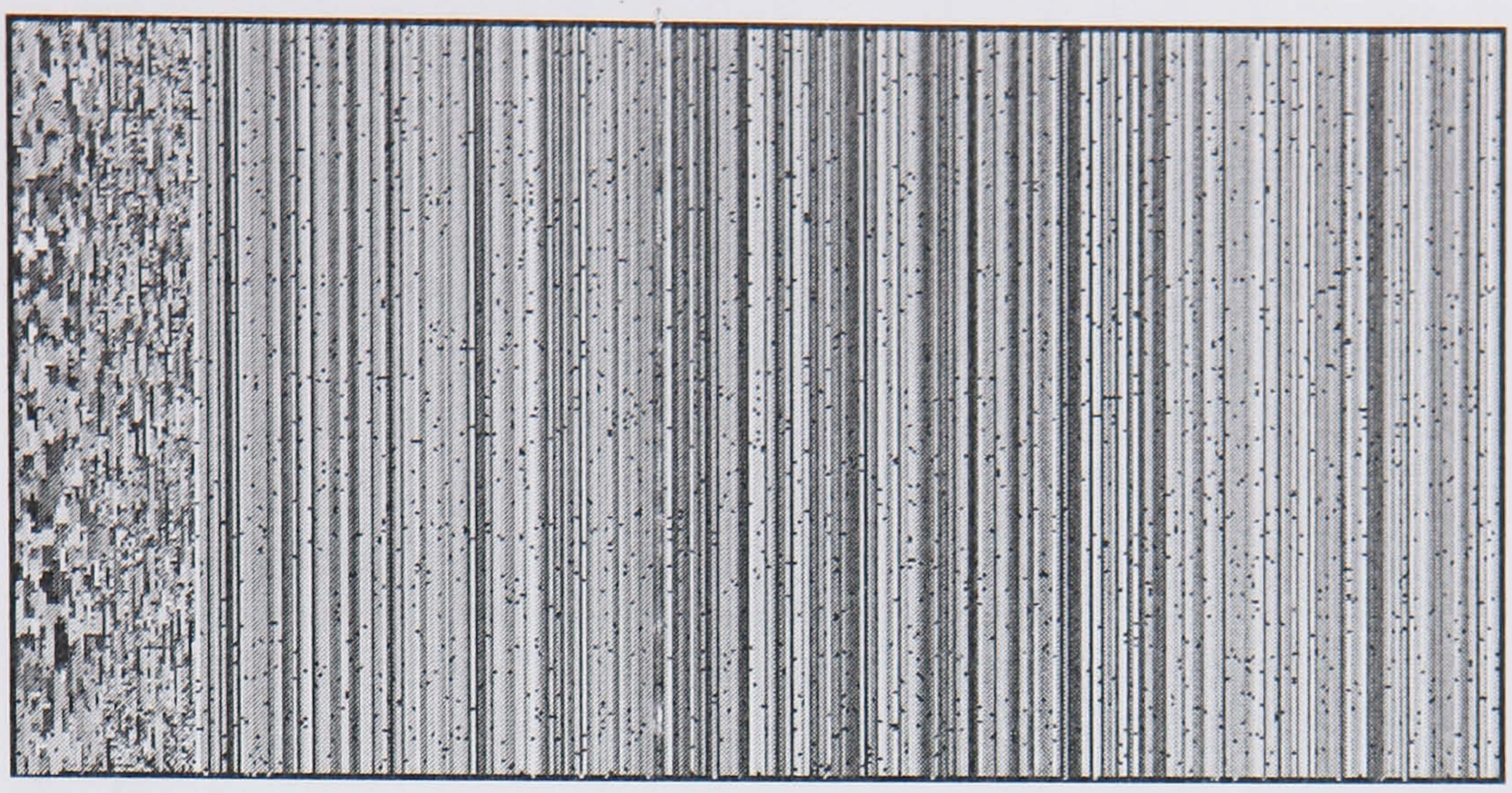

Edge Centre

Simulation

Edge Centre

Experiment

Figure 4.53(a) at the beginning of recrystallisation process

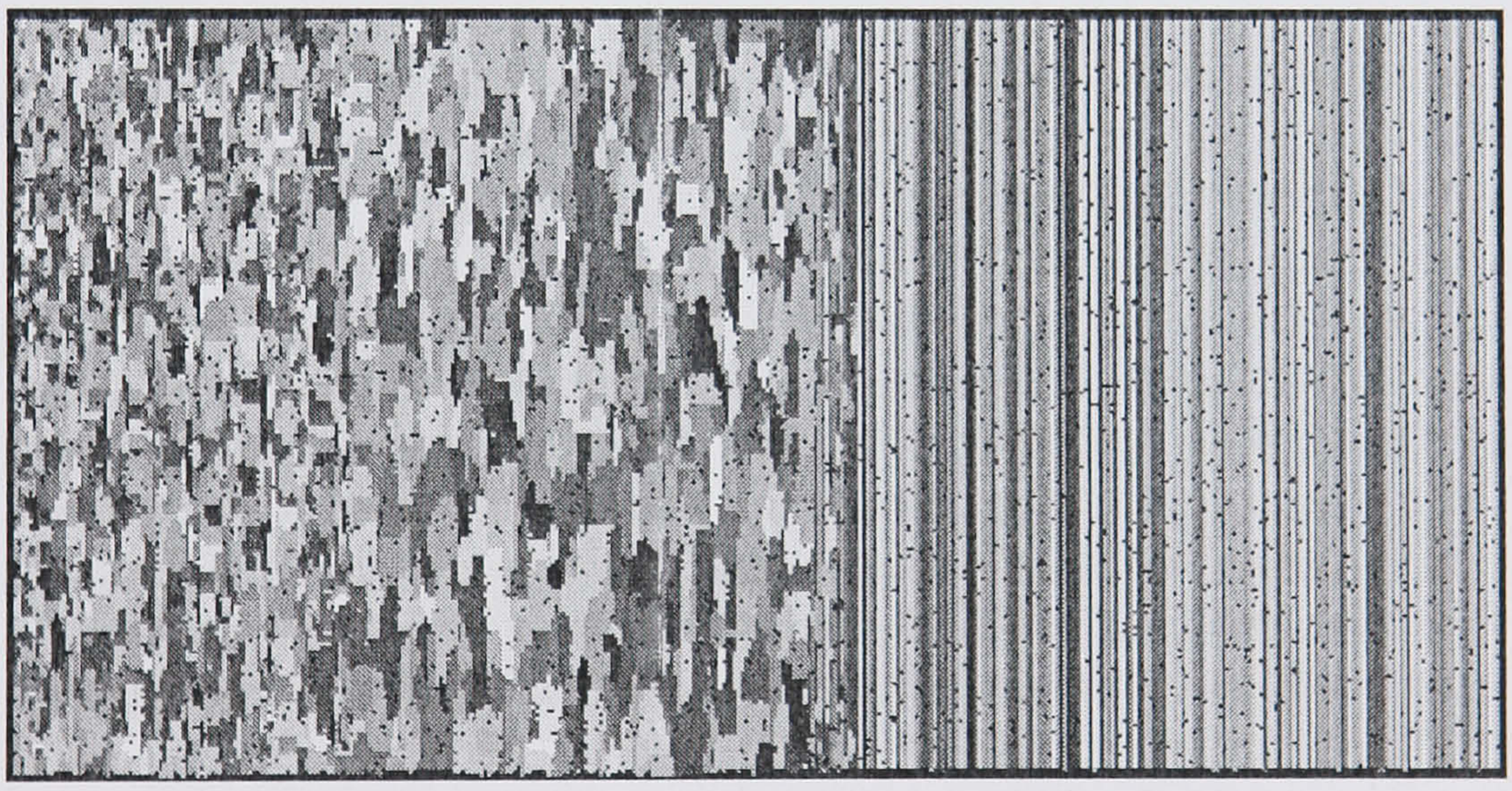

Simulation

Experiments

Figure 4.53(b) the recrystallisation grow into the inner side of extrudate

Figure 4.53 Macro-scale simulation

However, because the lack of full experimental records in the transverse direction of the extrudate, further comparisons within various methods must be completed with a matrix of different extrusions.

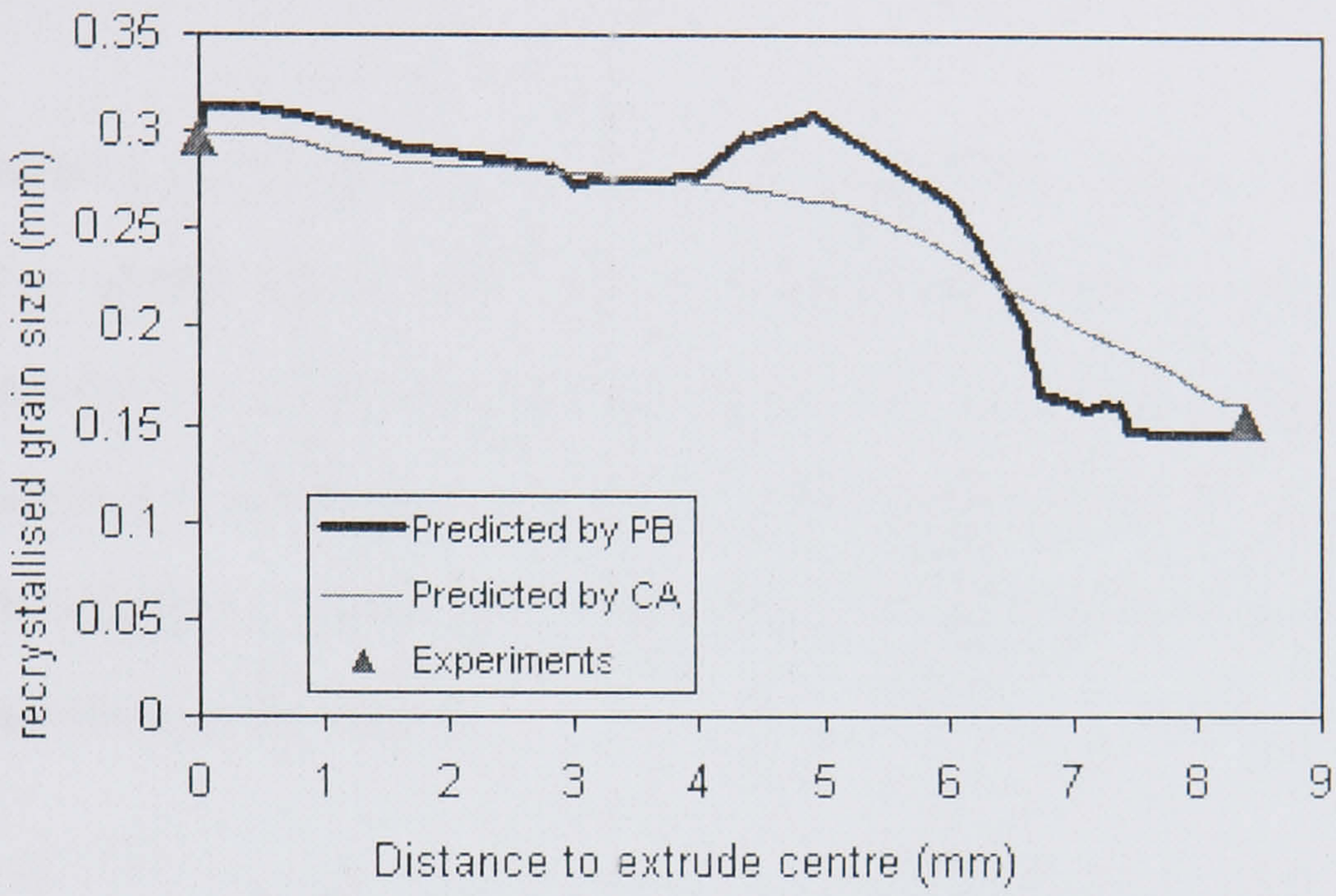

Figure 4.54 Experiment and simulation results of recrystallised grain size

4.6 Conclusion

As can be seen from the discussion above, the empirical models, the internal state variables models (physically based models) are effective in simulation of the recrystallisation process occurring in the extrusion and heat treatment of aluminium extrudates. With the combination of FEM and integrated metallurgical model, the substructure evolution and recrystallisation could be predicted quantitatively.

The influence of the scaled down modelling on the prediction results of numerical simulation is significant. Although the average strain rate, the temperature and the Zener-Hollomon parameter could be similar to the model with the original size in separate runs, it is difficult to reproduce all of the variables in one simulation run. Scaled modelling could reproduce some

information at the macroscopic level, for example, the material flow pattern. However. quantitative analysis using scaled down numerical modelling should be avoided. Full size modelling is recommended for the simulation of manufacturing processes, but requires detailed comparison with parameters colleted from industry.

As can be seen from the discussion above, the empirical models, the internal state variables model (physically based model) and cellular automata are effective in simulation of the recrystallisation process occurring in the extrusion and heat treatment of aluminium extrudates. With the combination of FEM and integrated metallurgical model, the substructure evolution and recrystallisation could be predicted quantitatively.

However further improvement must be made either to the PB model or to the CA model if more precise simulation is to be performed. The assumptions, for example, the neighbourhood, the assumed initial nucleation sites and the statistical cases for initial crystal orientations, have to be adopted to give a satisfactory simulation.

The improvements to eliminate the assumptions depend on the development, concurrently of several scientific research fields and one strong limitation is the fact that it is not entirely clear how the computational kinetics of these models relate to the actual kinetics of recrystallisation.

5 Surface Quality Control

The surface finish of the product is as important as the mechanical properties, and the control of defects is often the deciding factor in determining the extrusion conditions. Defects that may occur vary from visible blemishes such as cracks, blisters, and die lines, to invisible ones that show up after anodising. While in high-strength aluminium alloys where die lines and surface scoring have only secondary importance to the mechanical property requirements (because the surface often has to be machined to remove recrystallized layers) the defect is tolerated provided the die lines are not so coarse that stress concentrations arise (Sheppard 1993). For the 4% Cu alloys surface cracking (or speed cracking) is a major problem, especially at high temperatures and strain rates.

Copper is one of the most important alloying constituents for aluminium because of its appreciable solubility and strengthening effect, the strength increasing with increasing copper content up to a maximum of approximately 6%. Magnesium is used in combination with copper to accelerate and increase the age hardening at room temperature. The equilibrium compounds for this system are $CuAl_2$ (θ-phase) and $CuMgAl_2$ (S-phase) (Sheppard 1999, Mondolfo et al. 1976). These are soluble in the matrix during solution heat treatment.

The effects of particles on recrystallisation are complex. During deformation, particles will affect the deformation microstructure and texture through effects such as an increase in dislocation density, the production of large deformation heterogeneities at larger particles, and the alteration of the homogeneity of slip, e.g. shear bands. During annealing, the primary effect of closely spaced particles is to pin grain boundaries (Zener pinning), but the deformation heterogeneities at large particles may be sites at which recrystallisation originates (particle stimulated nucleation or PSN) (Doherty et al. 1997).

5.1 Integrating cracking criteria into FEM simulation

It is also well known that crack criteria (the criteria developed by Rice and Tracey, Cockroft and Latham, Oyane and empirical method) have been adopted to explain the cracking that occurs in extrusion, blanking and rolling, etc. In this chapter, FEM is used in differing ways to predict the surface cracking during hot extrusion. The crack criteria are integrated into the FEM code FORGE®2.0. The effectiveness of these criteria in predicting the surface cracking in the case of hot extrusion is discussed. The FEM simulation also provides some other quantitative data, such as the temperature rise during the extrusion at different initial temperatures. In addition, the principal stresses at the die land area at different stages of the extrusion are also shown.

A typical simulation procedure carried out by FEM, can consider the effect of:

(1) The geometry of the die and workpiece,

(2) Operating variables such as temperature and the rate of deformation, and the bulk constitutive response of the material and the interaction with solid boundaries.

The stresses and strains can then be calculated as functions of time from which predictions regarding the occurrence of fractures are obtained.

5.1.1 Traditional criteria

There exists a wide variety of criteria for assessing rupture in metal forming processes (Hambli and Reszka 2002, Clift et al. 1990), which are based on experimental work which utilise a deformation process that is related to actual industrial applications. The initiation of ductile fracture in metals depends strongly on the stress and strain histories. Many ductile-fracture criteria have a form which leads to fracture when the value of a damage parameter, which is given as an integral form of stress and strain, reaches a particular value. In this study, several of the criteria were combined into the FEM subroutine to see if there was a critical value to indicate the initiation of the surface cracking in hot extrusion. The details of the selected criteria are:

(1) Oyane:

$$\int_0^{\varepsilon_R} (1 + A\frac{\sigma_H}{\sigma_{eq}})d\varepsilon_{eq} \geq C1 \tag{5.1}$$

where A and C1 are constants, σ_H is the hydrostatic stress, σ_{eq} is the equivalent stress, ε_{eq} is the equivalent strain. The process by which fractures occur in metal forming has been widely modelled as void initiation and growth, followed by coalescence to form a crack. Based on this hypothesis, criteria for ductile fracture have been suggested by McClintock et al. (1996) and Oyane et al (1978).

(2) Cockroft and Latham (C-L1):

$$\int_0^{\varepsilon_R} \sigma^* d\varepsilon_{eq} \geq C2 \tag{5.2}$$

$$\sigma^* = \mathrm{Max}(\sigma_1, \sigma_2, \sigma_3, 0) \tag{5.3}$$

where C2 is a constant, σ^* is the maximum principle stress. Cockcroft and Latham (1968) considered the effects of the maximum principal tensile stress over the plastic strain path to fracture.

(3) Cockroft and Latham normalised (C-L2):

$$\int_0^{\epsilon_R} \frac{\sigma^*}{\sigma_{eq}} d\varepsilon_{eq} \geq C3 \tag{5.4}$$

where C3 is a constant. This criterion has a dependence on hydrostatic stress.

(4) Ayada:

$$\int_0^{\epsilon_R} (\frac{\sigma_H}{\sigma_{eq}}) d\varepsilon_{eq} \geq C4 \tag{5.5}$$

where C4 is a constant.

(5) Generalised work criterion (GW), or Freudenthal criterion:

$$\int_0^{\epsilon_R} \sigma_{eq} d\varepsilon_{eq} \geq C5 \tag{5.6}$$

$$\int_0^t (\sigma_1 \dot{\varepsilon}_1 + \sigma_2 \dot{\varepsilon}_2 + \sigma_3 \dot{\varepsilon}_3) dt \geq C5' \tag{5.7}$$

where C5 and C5′ are constants. σ_1, σ_2 and σ_3 are the principle stresses and $\dot{\varepsilon}_1$, $\dot{\varepsilon}_2$ and $\dot{\varepsilon}_3$ are the corresponding principle strain rates.

Freudenthal (1950) proposed that energy represents the critical parameter measuring fracture. In this criterion, the fracture occurs in a material element when the rate of

plastic energy dissipation reaches a critical value when integrated with respect to time, following the element as it travels through the die. This is the only criterion that accurately predicted the site of fracture initiation for all three metal-forming processes considered: Upsetting, extrusion (Brass) and strip deformation in the work of Clift et al (1990).

(6) Temperature:

$$T \geq C6 \tag{5.8}$$

where C6 is a constant. If the heat generation near the die land area increases the local temperature such that the applied stresses exceed the resistance to deformation then severe cracking at the surface may be expected. This temperature generation is a function of the alloy chemistry, extrusion speed, extrusion ratio, aspect ratio, container temperature and the initial billet temperature (Sheppard 1993). Much of the heat generation to the surface occurs through the dead metal zone and the deformation zone shear band, which terminates on the face of the die immediately prior to the die land area. This results in a steep rise in the temperature as the material approaches the die land (Sheppard 1999a). Heat generation is comparatively less in the indirect mode of extrusion compared to the direct mode.

According to the six criteria mentioned above, when the constants, i.e. C1-C6, reach the critical value, the crack occurs.

By integrating the crack criteria into FEM programs, research has been carried out to study various criteria adapted to the metal forming process.

Hambli and Reszka (2002) have checked the fracture criteria validity using an FEM model of the blanking operation by an inverse technique approach. Their study showed the valid critical values for crack initiation generated by shearing mechanisms could be

predicted by the fracture criteria of: Rice, Freudenthal, Cockroft and Latham, Atkins, Oyane, Ayada and Plastic strain.

Clift et al (1990) described the use of the finite-element technique to predict fracture initiation in a range of simple metal forming operations, which included simple upsetting, axisymmetric extrusion and strip compression and tension. In the case of axisymmetric extrusion, their study showed the numerically predicted sites of fracture agreed with the experiment when the criteria of Oyane, Freudenthal and C-L are adopted. However, the extrusion ratio was very small in their study and the influence of temperature rise, which is a very important factor for crack initiation during extrusion, was again ignored.

In the work of Ko et al. (1996), The C-L criterion was adopted for FEM simulation and it was confirmed a valid predictor of crack initiation during aluminium extrusion. However, the extrusion ratio they used was also very small and the temperature rise was not considered.

It is interesting to see that some studies of paste extrusion, which can be assumed to be a real isothermal process, have been performed previously by Domanti et al (2002). The C-L Criterion and the Generalised Work Criterion are discussed in their study and these criteria are shown to be successful in predicting the increase in fracture with increasing die entry angle. They are also proved to be at least qualitatively correct in considering the effect of extrusion ratio on surface fracture. The work of Domanti et al is an ideal example of an isothermal extrusion, which can be contrasted with the present work, in which the temperature evolution has to be involved.

Some investigations (Ko 1996, Sheppard 1993, Hambli 2002) have shown that it is difficult to choose a fracture criterion that is "universal" enough in the sense that it gives consistent results for operating conditions outside the calibration range. Applications of critical values of fracture criteria are only successful when they are both characterised and applied under similar loading conditions. A material might crack at a relatively small

deformation during forging, yet might be satisfactorily deformed to a very large strain by extrusion. The onset of cracking depends both on the details of the working process to which the material is subjected and on its basic ductility.

5.1.2 Empirical model

In addition to the criteria mentioned above, there also exists an empirical method to predict surface cracking occurring in hot extrusion, proposed by Sheppard and Tutcher (1980) as shown in Figure 5.1. They investigated the incidence of speed cracking in the rod form of AA5456 alloy and showed that the Z parameter may be used to correlate results over widely varying temperature and speed conditions.

For acceptable surface quality:

$$\ln\left(\frac{Z_i}{A}\right) \leq \frac{6.35\times10^{20}}{T_i^{7.06}} \tag{5.9}$$

where Z_i is the Zener-Holloman parameter using the average strain rate and the initial temperature,

$$Z_i = \dot{\bar{\varepsilon}} \exp\left(Q/RT_i\right) \tag{5.10}$$

$\dot{\bar{\varepsilon}}$ is the average strain rate, which can be defined by

$$\dot{\bar{\varepsilon}} = \frac{6D_B^2 v(a + b\mathrm{Ln}R)(c + d\mathrm{Tan}\omega)}{D_B^3 - D_E^3} \tag{5.11}$$

D_B is the billet diameter, D_E is the extrudate diameter, v is the ram speed, R is the extrusion ratio, ω is the deformation zone cone semi-angle (Sheppard 1999), which is defined by

$$\omega = 38.7 - 6.9 \mathrm{LnR} \qquad (5.12)$$

a, b, c and d are constants. ($a = 0.171$, $b = 1.86$, $c = 38.7$, $d = 6.9$), T_i is the initial temperature.

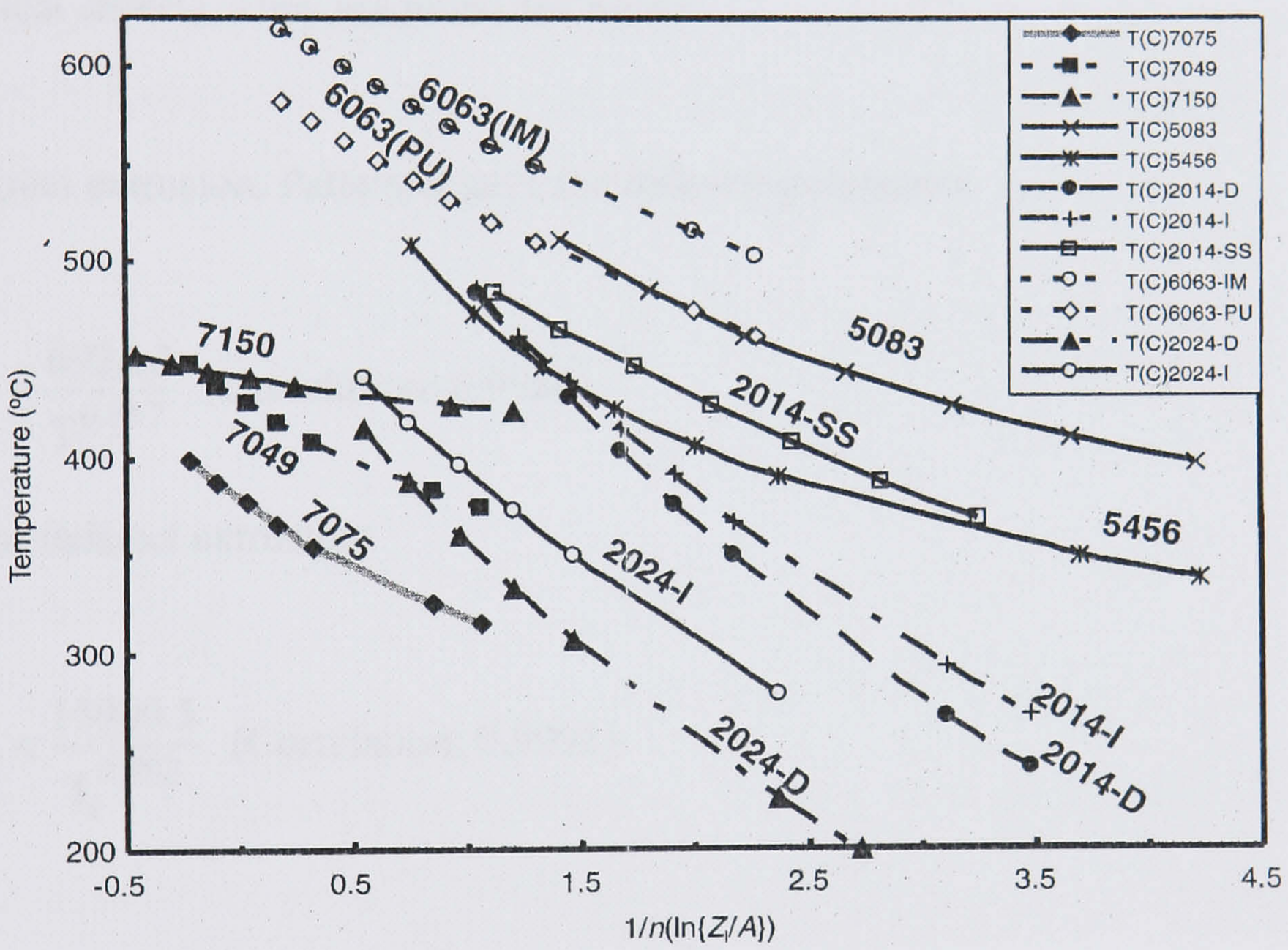

Figure 5.1 Extrusion limit

This type of analysis has also been applied to the observed surfaces of shaped extrusions in 2024 alloy and introducing the λ^2 modification for shaped extrusion acceptable surfaces were achieved when:

$$\frac{1}{n} \ln(\lambda^2 \frac{Z_i}{A}) \leq \frac{2.113 \times 10^9}{T_i^{2.866}} \qquad (5.13)$$

for direct extrusion and

$$\frac{1}{n}\ln(\lambda^2 \frac{Z_i}{A}) \geq \frac{2.113\times10^9}{T_i^{2.866}} \qquad (5.14)$$

for indirect extrusion. λ is the shape factor. These criteria are shown in Figure 5.1 for a number of Al-alloys.

In the case of 2014 extrusion, Patterson (1981) and Vierod (1985) both provided the empirical criteria. They are presented below.

For direct extrusion, Patterson gave the following equation:

$$\ln Z_I < \frac{6924.2}{T_i^{0.857}} \text{ (Correlation: 0.9986)} \qquad (5.15)$$

and for indirect extrusion:

$$LnZ_i < \frac{15909.5}{T_i^{0.982}} \text{ (Correlation: 0.9991)} \qquad (5.16)$$

where T is the initial billet temperature in degrees Kelvin.

Vierod (1983) also reported that differing preheat approaches affected this criterion such that for conventional heating (CH, indicating heating continuous to the extrusion temperature)

$$LnZi < \frac{67954}{T_i^{1.199}} \text{ (correlation 0.998)} \qquad (5.17)$$

and for material that has been presolution soaked (SS, heat solution soak temperature and cool to extrusion temperature).

$$\mathrm{LnZi} < \frac{97955}{T_i^{1.223}} \text{ (correlation 0.999)} \tag{5.18}$$

It can be seen from the above equations that in these empirical equations, only the initial temperature and the average strain rate are considered. Presently, with the FE method, the evolution of the instant Zener-Hollomon parameter, in which the real time strain rate and the real time temperature are used. can be conveniently obtained from the output program. In this paper, the instant Zener-Hollomon parameter is integrated into the FEM program to observe the evolution of its value during extrusion and the initial $\mathrm{LnZ_i}$ and the real time $\mathrm{Ln}(Z_r)$ values are compared. The real time Zener-Hollomon parameter is defined by:

$$Z_r = \dot{\varepsilon} \exp(Q/RT) \tag{5.19}$$

where $\dot{\varepsilon}$ is the real time strain rate and T is the real time temperature. With the combination of the initial Z value anc the instant Z history, the surface cracking is studied again by the use of the empirical equations.

5.2 Justification of cracking criteria by FEM simulation

If a criterion can explain the following four phenomena, then it can be regarded as effective in predicting the surface cracking which occurs in hot extrusion of aluminium alloy AA2014,

1. Phenomenon 1 (P1):

The cracking occurs on the extrudate surface and has not been seen at other locations.

2. Phenomenon 2 (P2):

The extrusion suffers surface cracking seriously during extrusion at high initial temperatures, such as in RUN 3. It is not a serious problem for extrusion at low initial temperatures.

3. Phenomenon 3 (P3)

In some cases, for instance RUN 2 extrusion used in this study, surface cracking occurs in the middle period of the process and becomes more serious as the process continues.

4. Phenomenon 4 (P4)

The severity of cracking is less in the indirect mode than in the direct mode. We should recall that the higher value of the damage parameters, i.e. the C1-C6 mentioned above, indicate the greater the chance of cracking. If the assumed "critical value" does exist, then the surface cracking will occur if the predicted value is higher than the "critical value"

The main simulation tooling and experimental results used in this study is shown in Table 5.1.

The data are extracted from two points (side point and centre point) and two lines (AB and CD) at the die land area, as shown in Figure 5.2.

Table 5.1 Tooling of FEM model

Run code	Extrusion mode	Initial billet temperature (C°)	Container temperature (C°)	Ram speed (mm/s)	Surface Condition*
1	Direct	298	275	7.9	A†
2	Direct	396	350	7.0	B†
3	Direct	470	375	7.3	C†
4	Direct	474	430	3.3	B
5	Indirect	464	375	3.4	A

†A- The surface condition is good throughout the extrusion

†B- The surface cracking occurs from the middle stage of extrusion to the end

†C- The surface cracking occurs at the very beginning of extrusion

* experimental results from (Vierod 1983).

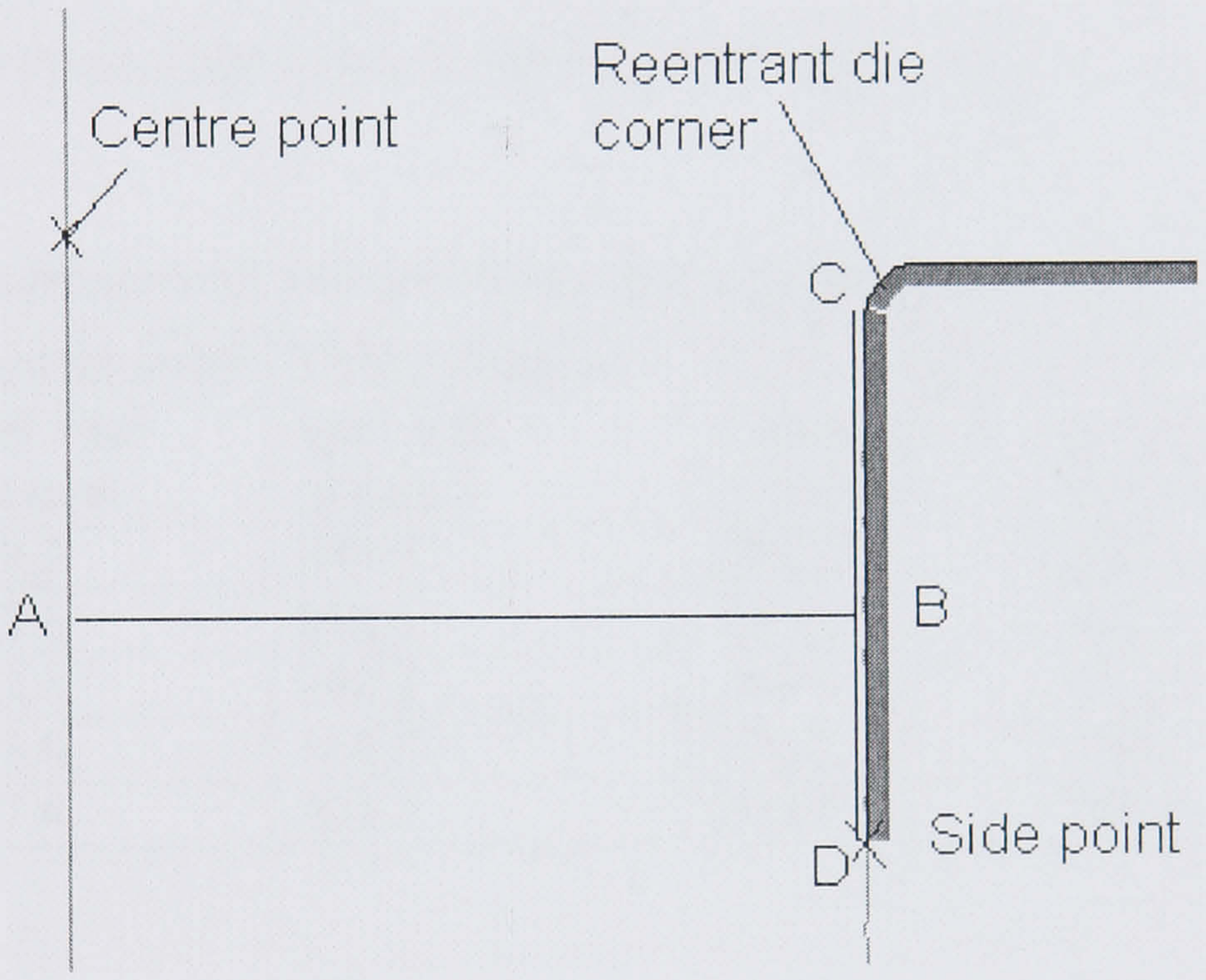

Figure 5.2 The positions of the area analysed

The temperature evolutions at the side point and centre points of the entire direct extrusion runs are shown in Figure 5.3. For the indirect extrusion RUN 5, the positions of the two points were changing throughout the extrusion because they were moving with the die. It is therefore difficult to extract the data continuously as performed for direct extrusions. The temperatures in this case are extracted from line AB at different stages of extrusion, as shown in Figure 5.4.

This difference between the temperature of the extrudate face and that of the centre in this paper is close to $30^\circ C$, while in Venas's work (1986), the difference is stated to

be $60^{\circ}C$. Because the billet size used in this study is quite different to that used in Venas's work, it is not strange that there is some discrepancy. The very sharp temperature gradient near the surface is of great significance since it is the surface temperature, but not average exit temperature that is critical for surface failure such as cracking.

Table 5.2 shows that the predicted loads correlate well with the experimental results. The predicted temperatures, as shown in Table 5.3, are also in good agreement with the experimental measurements. Due to the lack of exact knowledge of the friction, extrusion process control and critically the discard length, the differences are acceptable.

Table 5.2 Experimental and simulation loads (experiments from Vierod 1983)

Extrusion code	Experimental max load (tonnes)	FEM predicted max load (tonnes)	Experimental min load (tonnes)	FEM predicted min load (tonnes)
1	439.2	445.9	285.8	280.1
2	295.6	286.1	208.6	195.7
3	243.8	240.2	204.6	192.2
4	193.0	190.2	179.3	160.2
5	197.4	203.2	209.7	205.8

Table 5.3 Experimental and simulation temperature (experiments from Vierod 1983)

Extrusion code	Peak temp† (C°)	FEM predicted peak temp (C°)	Final temp† (C°)	FEM predicted final temp (C°)
1	309.1	315.2	470.8	465.7
2	403.5	408.9	501.2	498.2
3	476.1	479.2	546.3	539.6
4	478.0	482.1	529.0	520.4
5	471.3	478.3	488.8	493.2

†Peak temp means the temperature of the extrudate when the peak load occurs. Both the Peak temp and the Final temp here are obtained from the integral profile model.

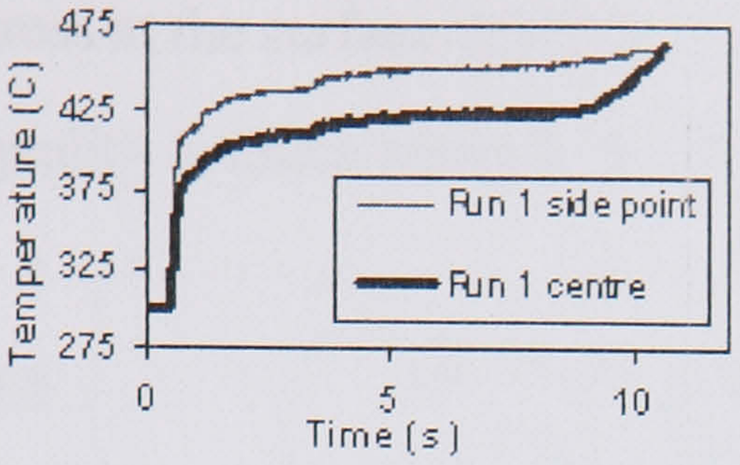

(a) Run 1

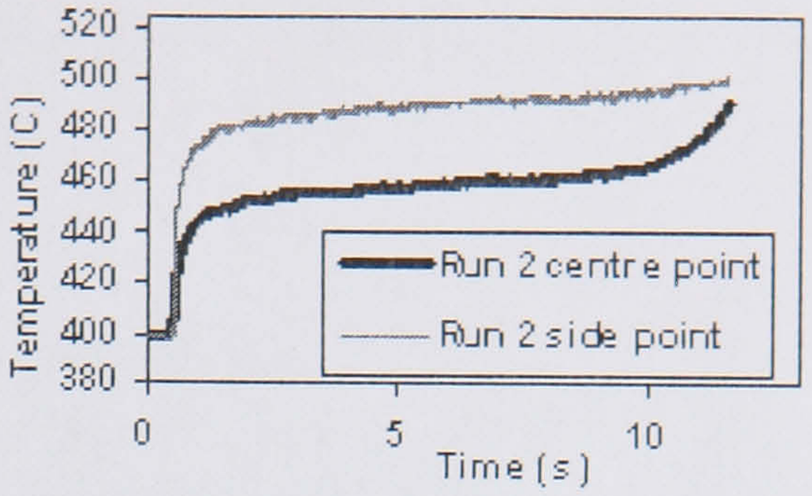

(b) Run 2

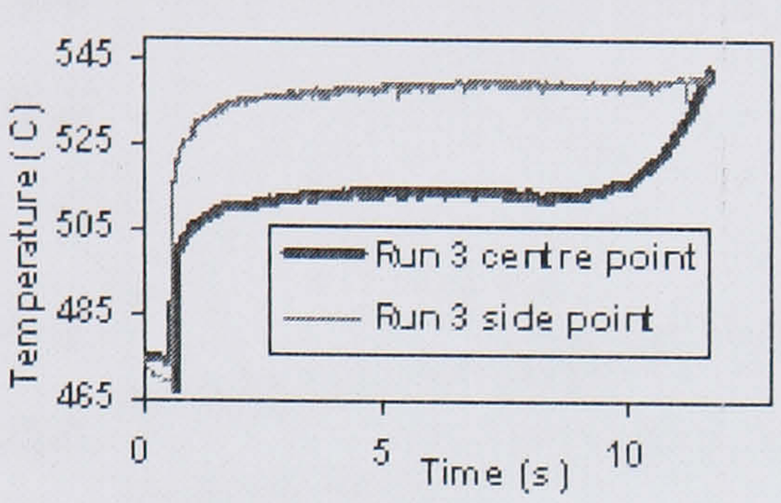

(c) Run 3

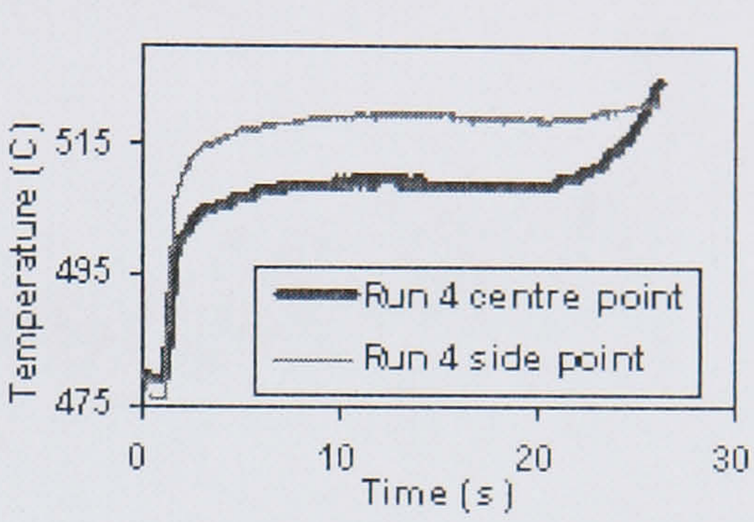

(d) Run 4

Figure 5.3 Temperature evolution

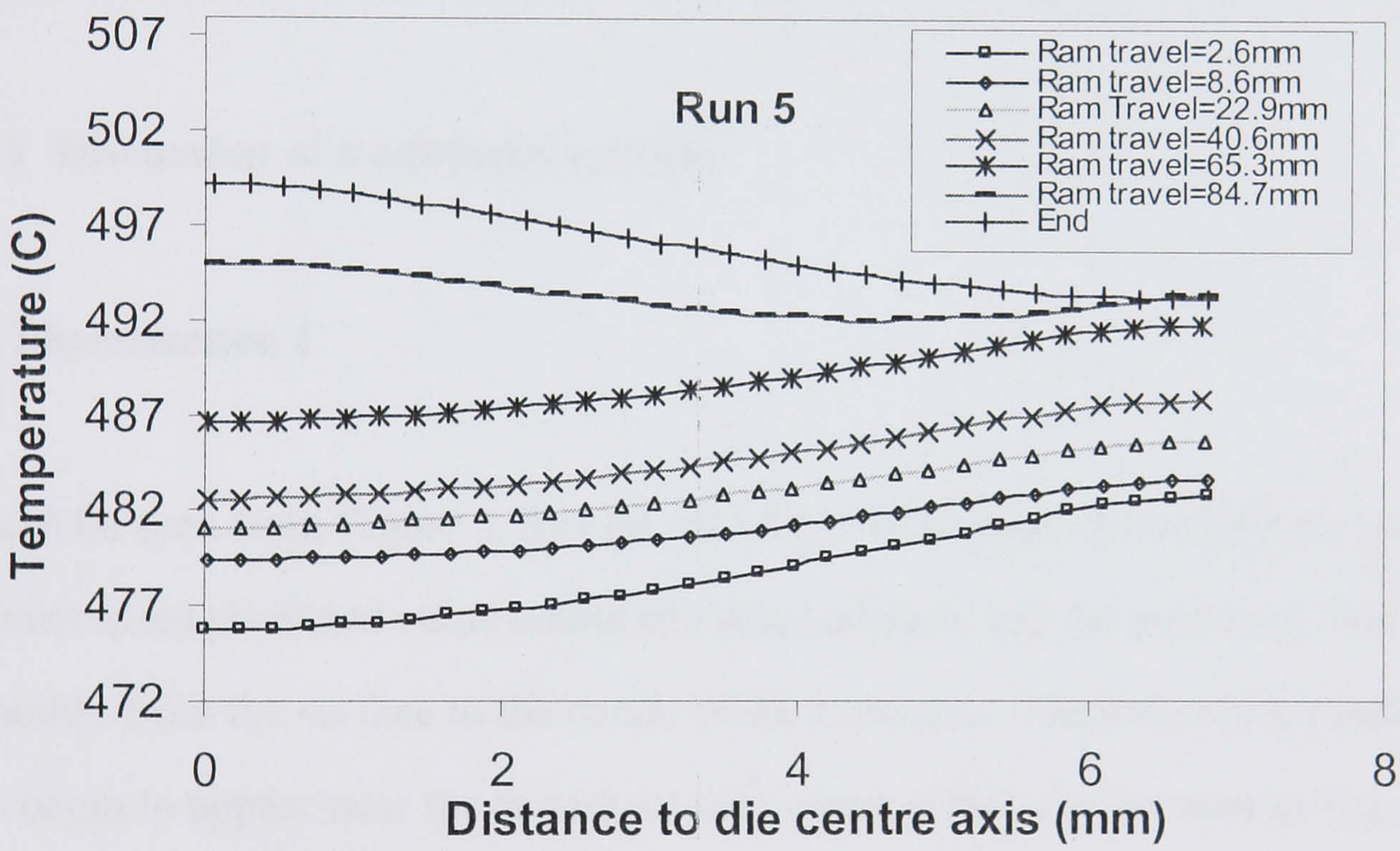

Figure 5.4 Temperature evolution of Line A-B in the extrusion run 5

The principal stress distributions at different extrusion stages along the line AB (as shown in Figure 5.2) are shown in Figure 5.5. Compared with the longitudinal stress in paste extrusion, which is shown in Figure 5.6, the distributions of the longitudinal stress in aluminium extrusion are different. As can be seen from Figure 5.6, the stress is linear along the transverse direction when the extrusion ratio is high in paste extrusion while it is totally different in hot aluminium extrusion. It can also be seen from Figure 5.5 that the

maximum stress at the surface of RUN 1 extrusion is higher then that of RUN 3 although the surface quality is much better in RUN 1.

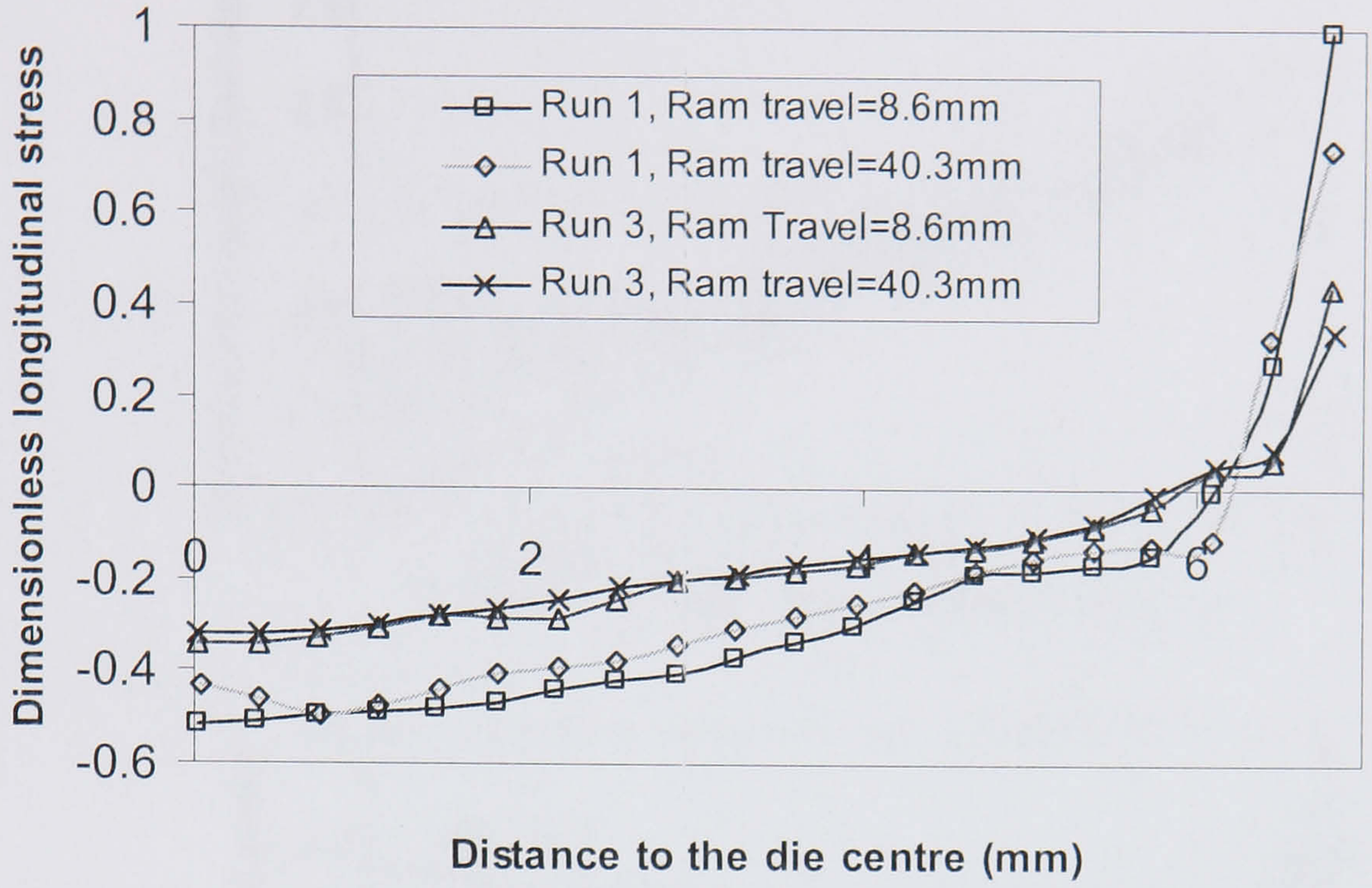

Figure 5.5 Principal stress distribution along line AB at different stages in hot extrusion

5.2.1 Discussion of traditional criteria

(1) Phenomenon 1

As can be seen from Figure 5.7(a)-(f), all of the simulations with different criteria give the maximum predicted value on the extrudate surface, and the predicted value decreases smoothly from the surface to the centre of the extrudate. The maximum predicted values also begin to appear near the re-entrant die corner, which can be seen in Figure 5.7(f). It follows that if there is a critical value for a cracking criterion mentioned above, then this value would be reached first on the surface, according to all of the criteria adopted in this study. Then the cracking would appear on the surface according to all the criteria and this has been proved after the crack function of the software was triggered, which can be seen in Figure 5.7(g).

Hence we may conclude that all of the criteria are effective in predicting the first phenomenon.

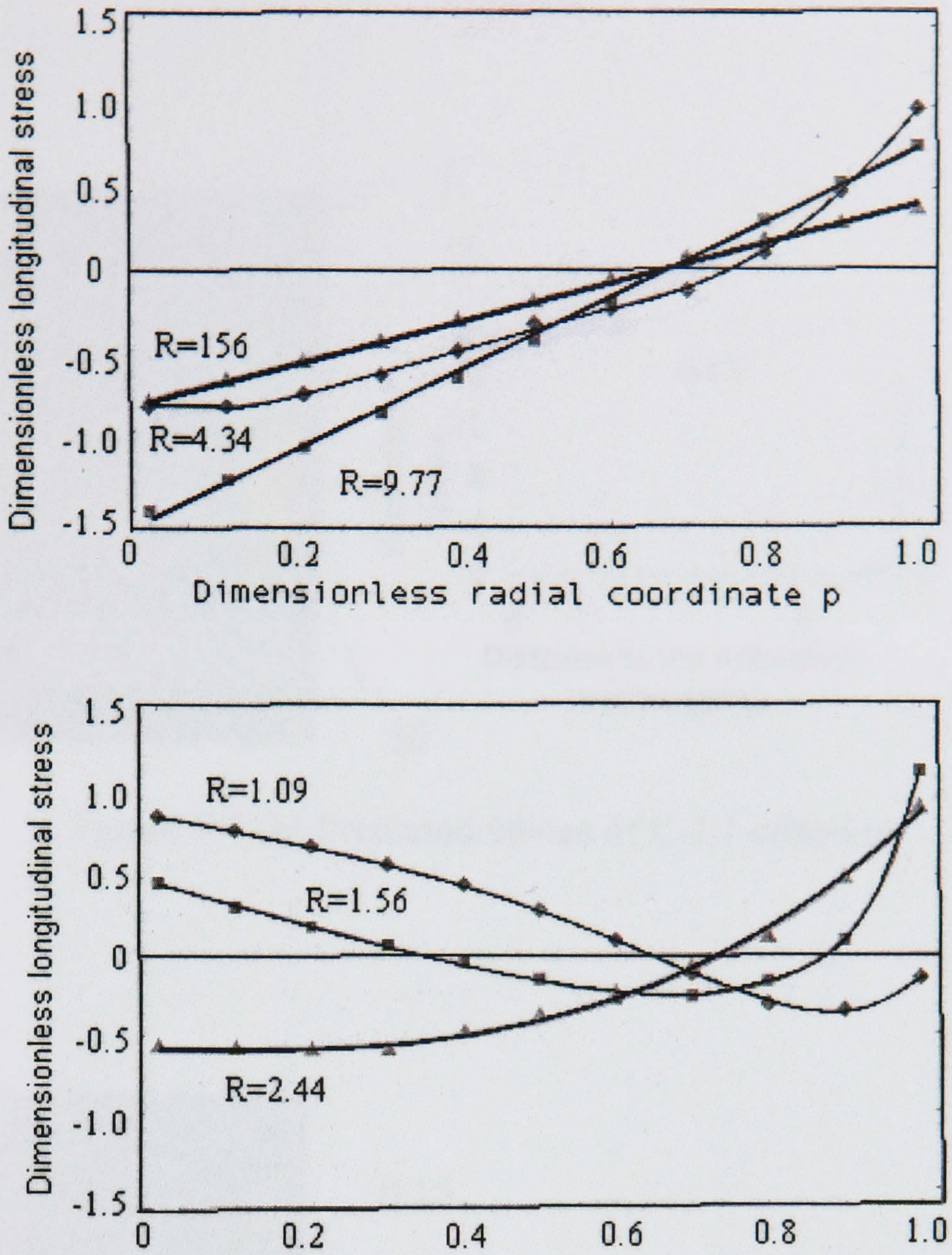

Figure 5.6 Principle stress distribution at transverse direction in paste extrusion (R represents extrusion ratio) (Domanti 2002)

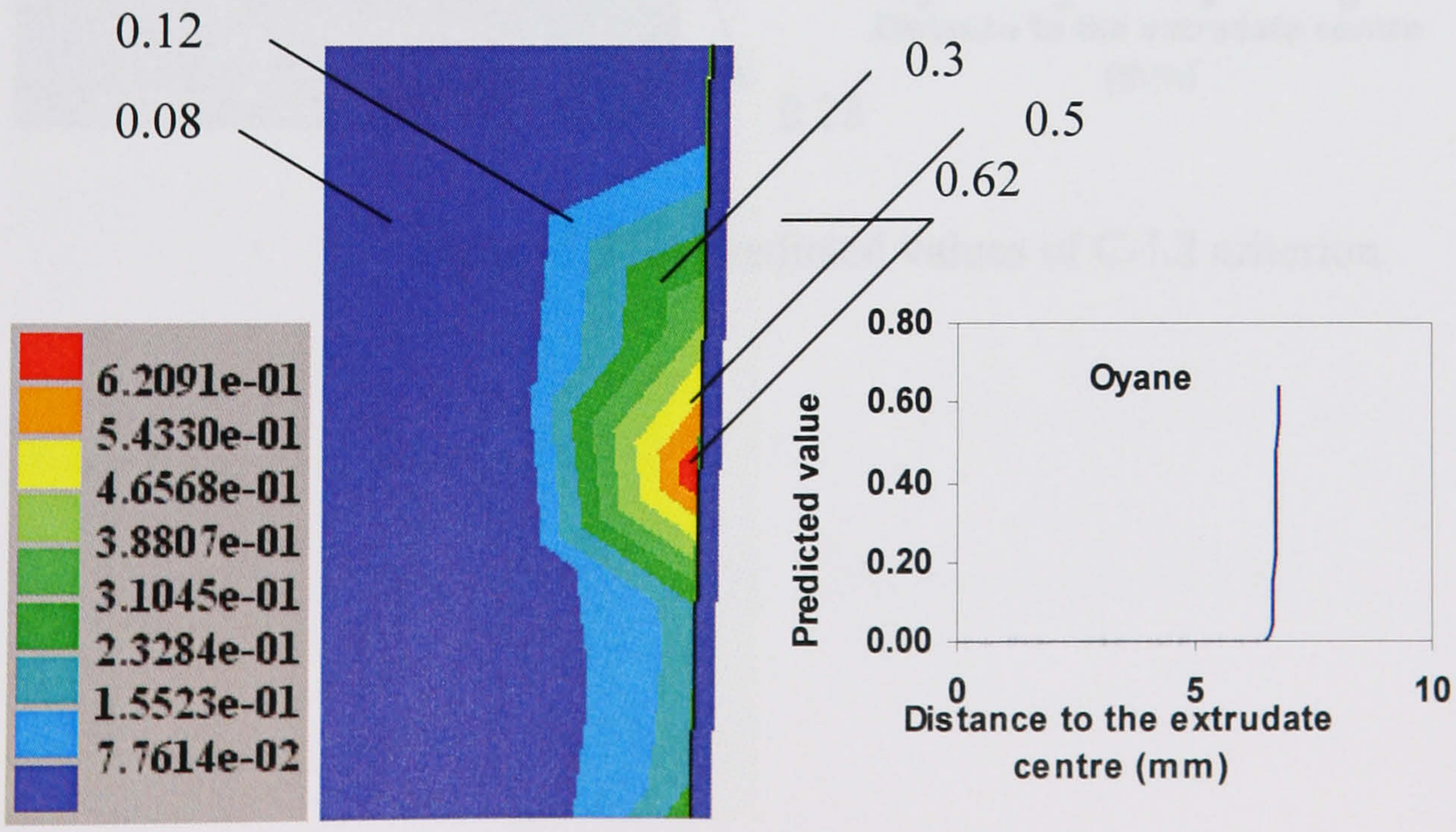

Figure 5.7 (a) Predicted values of Oyane criterion

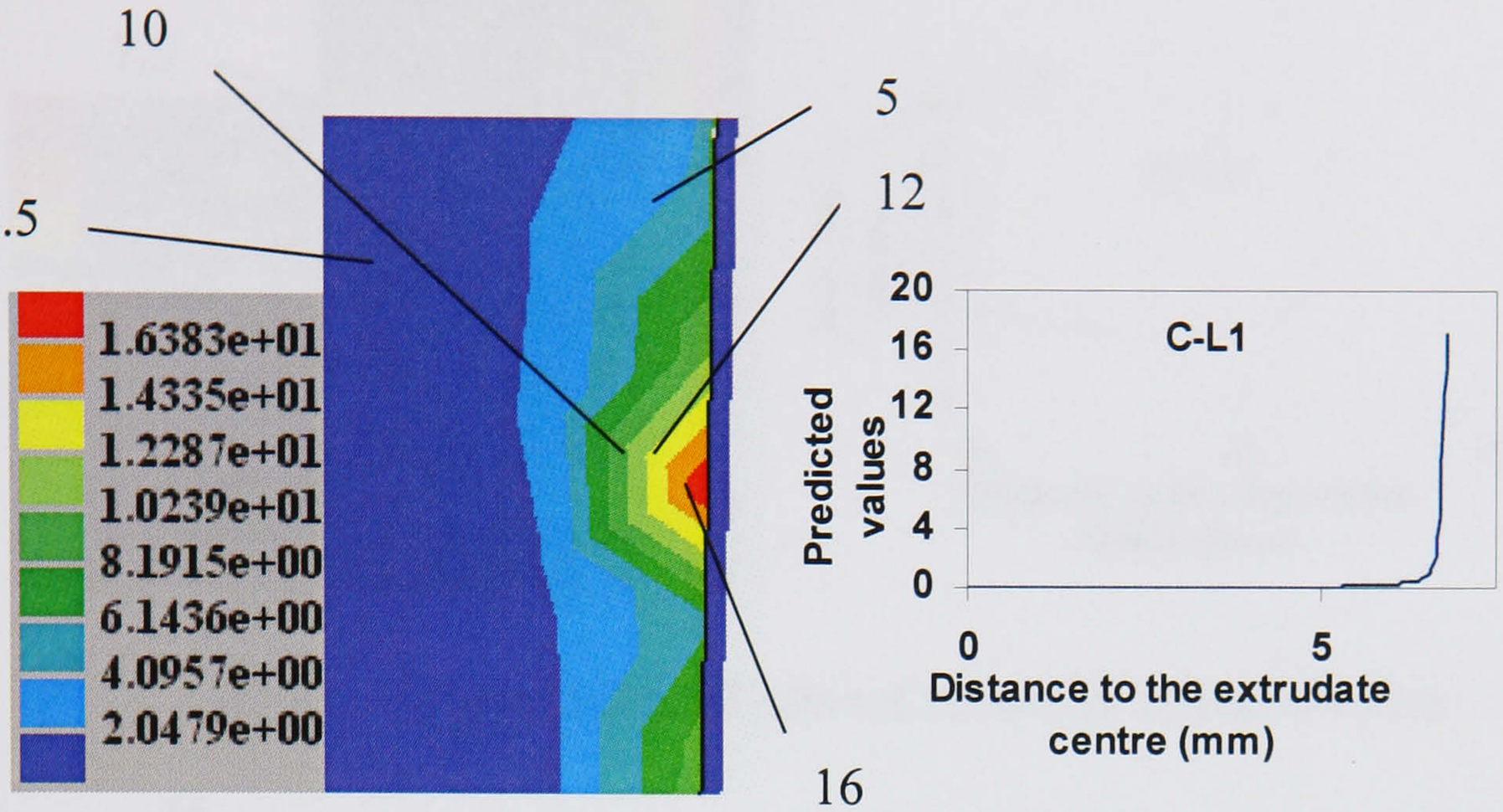

Figure 5.7 (b) Predicted values of C-L1 criterion

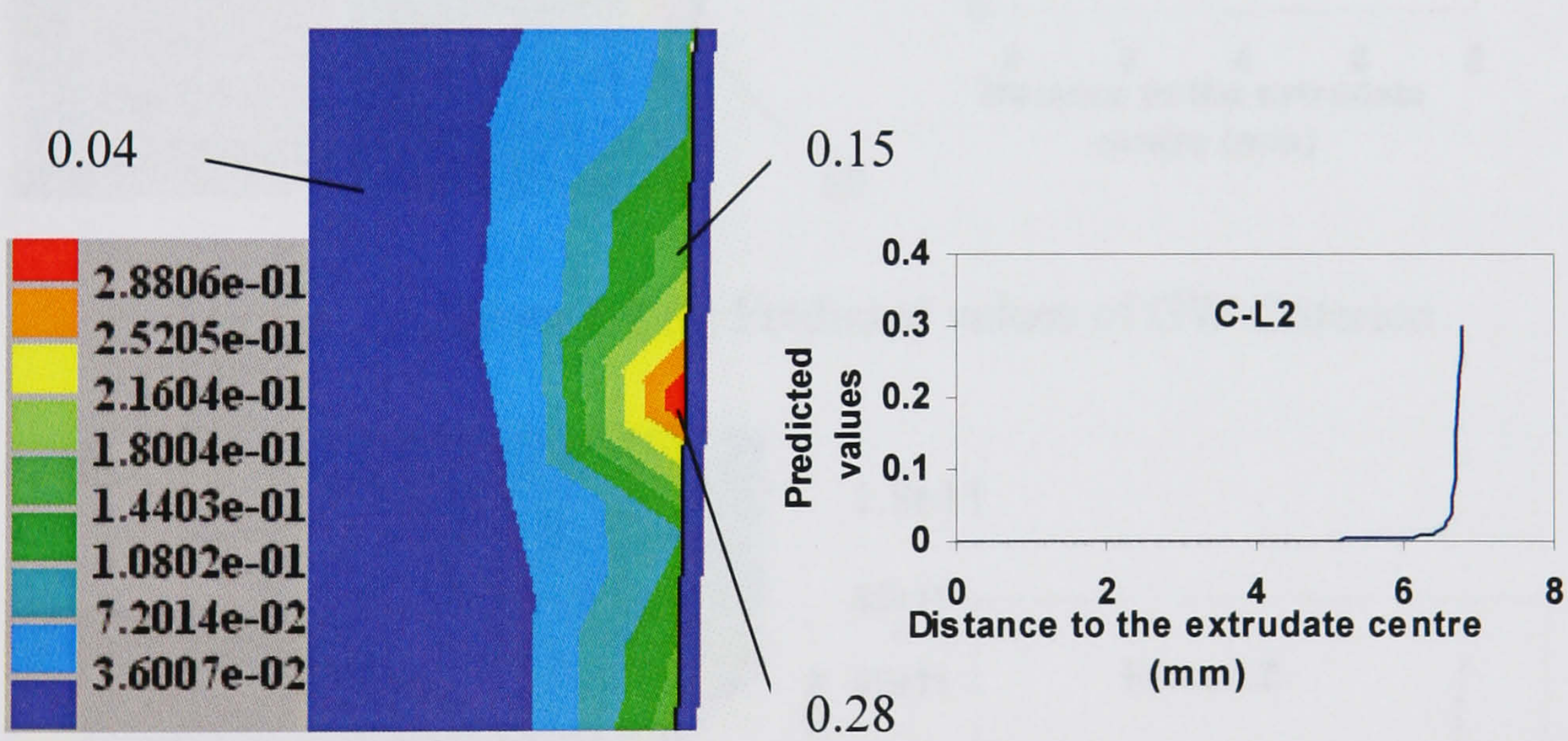

Figure 5.7 (c) Predicted values of C-L2 criterion

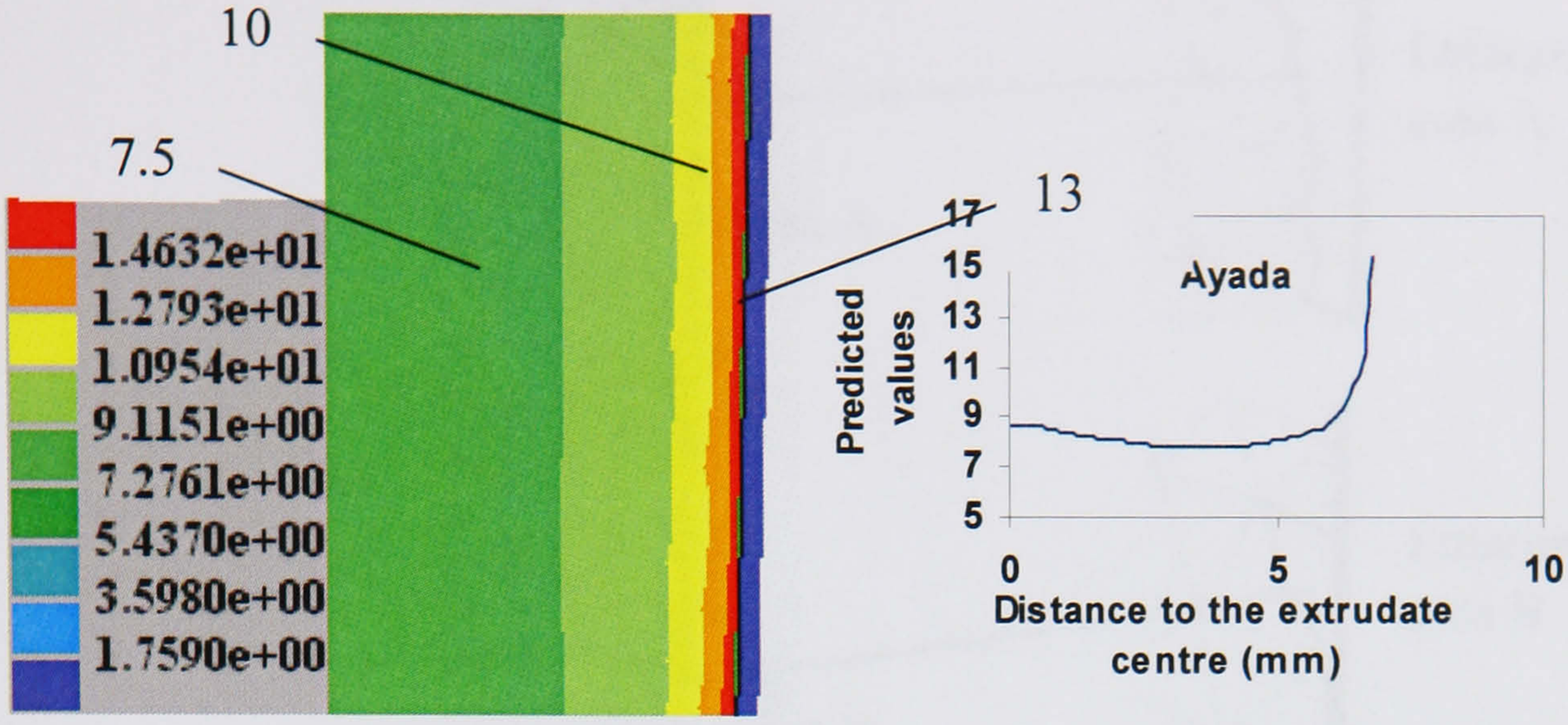

Figure 5.7 (d) Predicted values of Ayada criterion

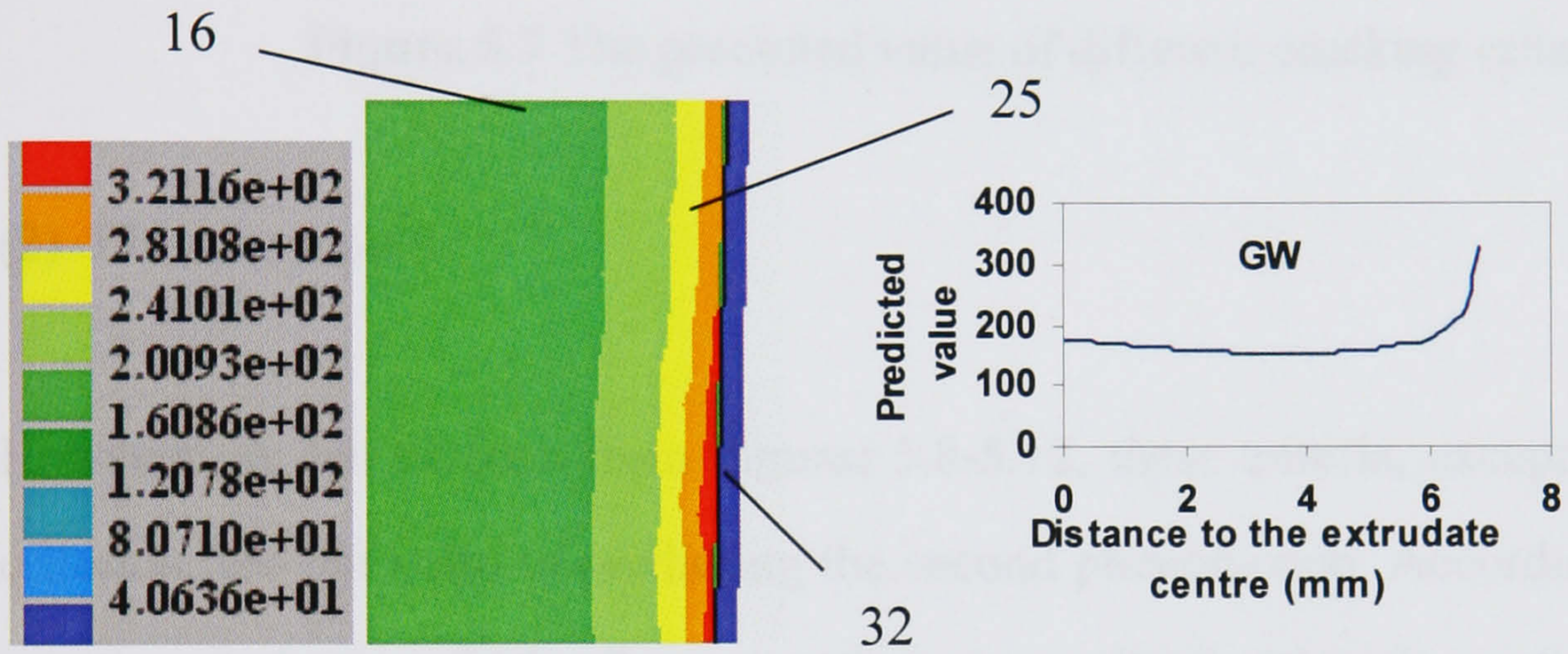

Figure 5.7 (e) Predicted values of GW Criterion

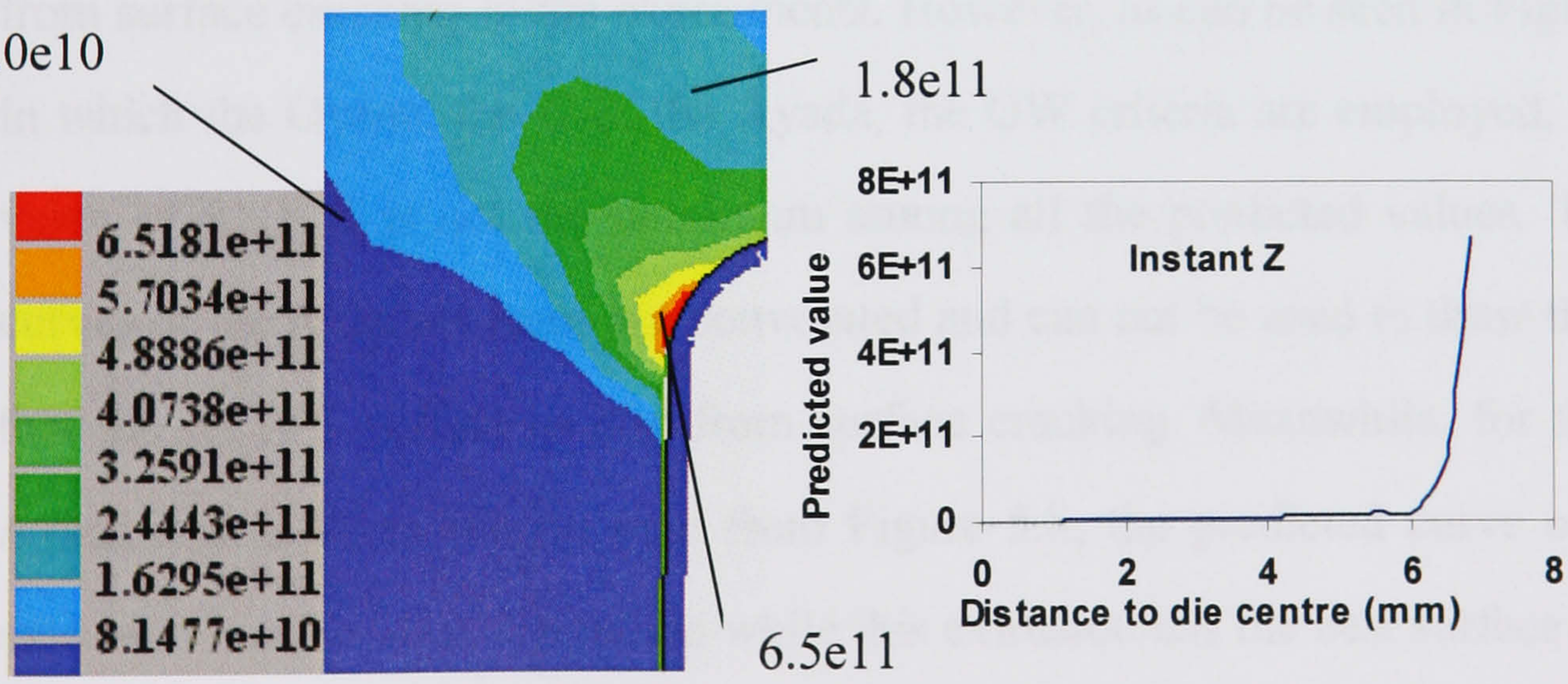

Figure 5.7 (f) Predicted Instant Z value

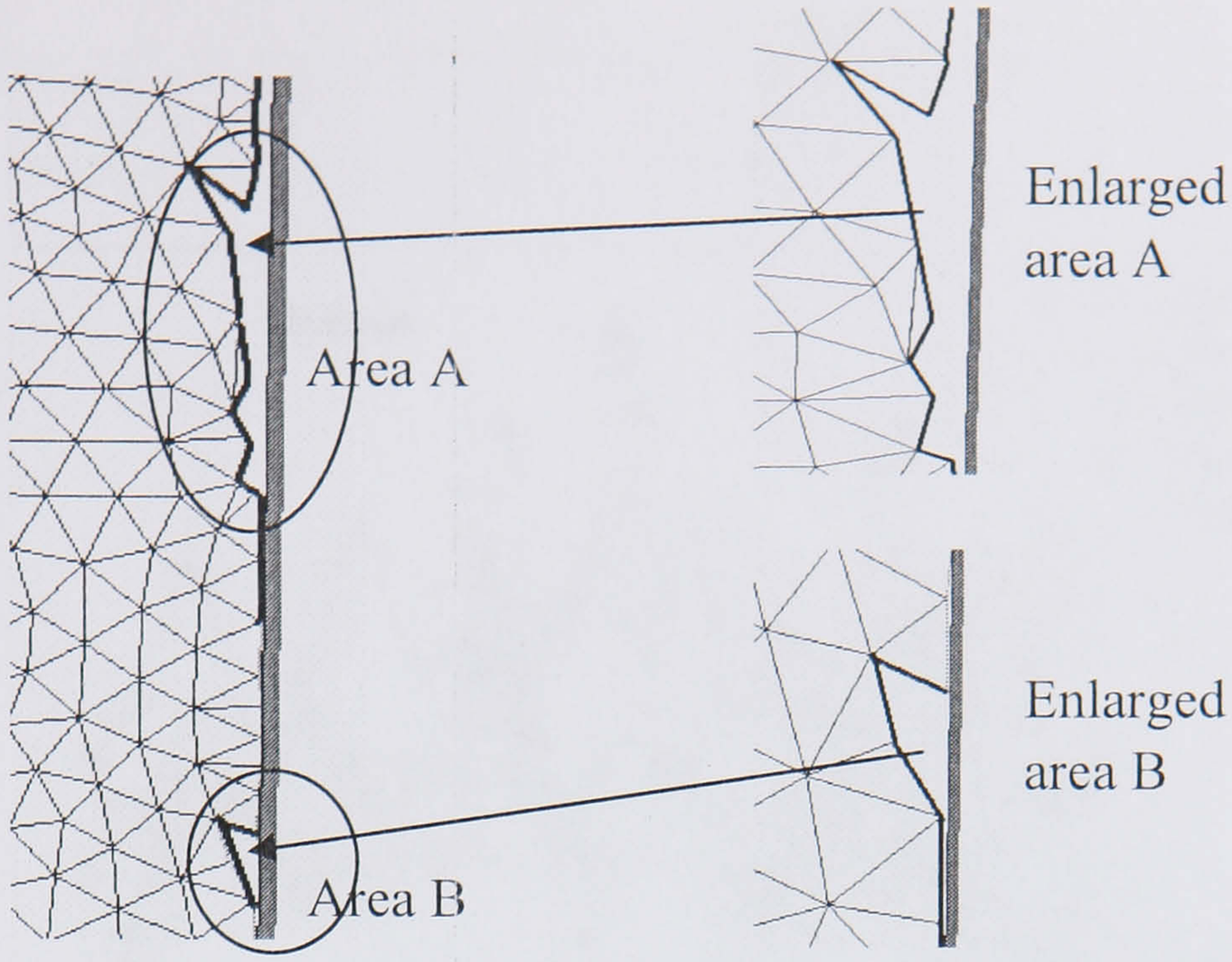

Figure 5.7(g) Surface cracking (After the crack function was triggered)

Figure 5.7 The predicted value of different cracking criteria

(2) Phenomenon 2

However, as can be seen from Figures 5.8-5.12, these criteria, except the temperature criterion, are not valid in predicting the second phenomenon. According to the criteria mentioned above, which all assume there is a critical value for surface cracking, the critical value should be reached first in the extrusion of RUN 3, which suffers mostly from surface cracking in the experiments. However, as can be seen in Figures 5.8-5.12, in which the Oyane, the C-L, the Ayada, the GW criteria are employed, the predicted value of RUN 3 is not the maximum among all the predicted values. The predicted curves of the different Runs are convoluted and can not be used to draw the conclusion that the RUN 3 suffers mostly from surface cracking. Meanwhile, for the criteria of Ayada and GW, as can be seen from Figure 5.8, the predicted curve of the RUN 1 extrusion has the highest position while this extrusion has the best surface quality in the experiments. In Figure 5.12, the curve of RUN 3 is a little lower than the curve of RUN 2, while in experiments surface cracking which happened in RUN 2 is less serious than that in RUN 3. The data shown in Figures 5.8-5.10 was extracted from line CD, as shown in Figure 6.2, after the ram travelled the same distance. The data shown in Figures 5.11-5.12 are extracted from the point D, as shown in Figure 5.2.

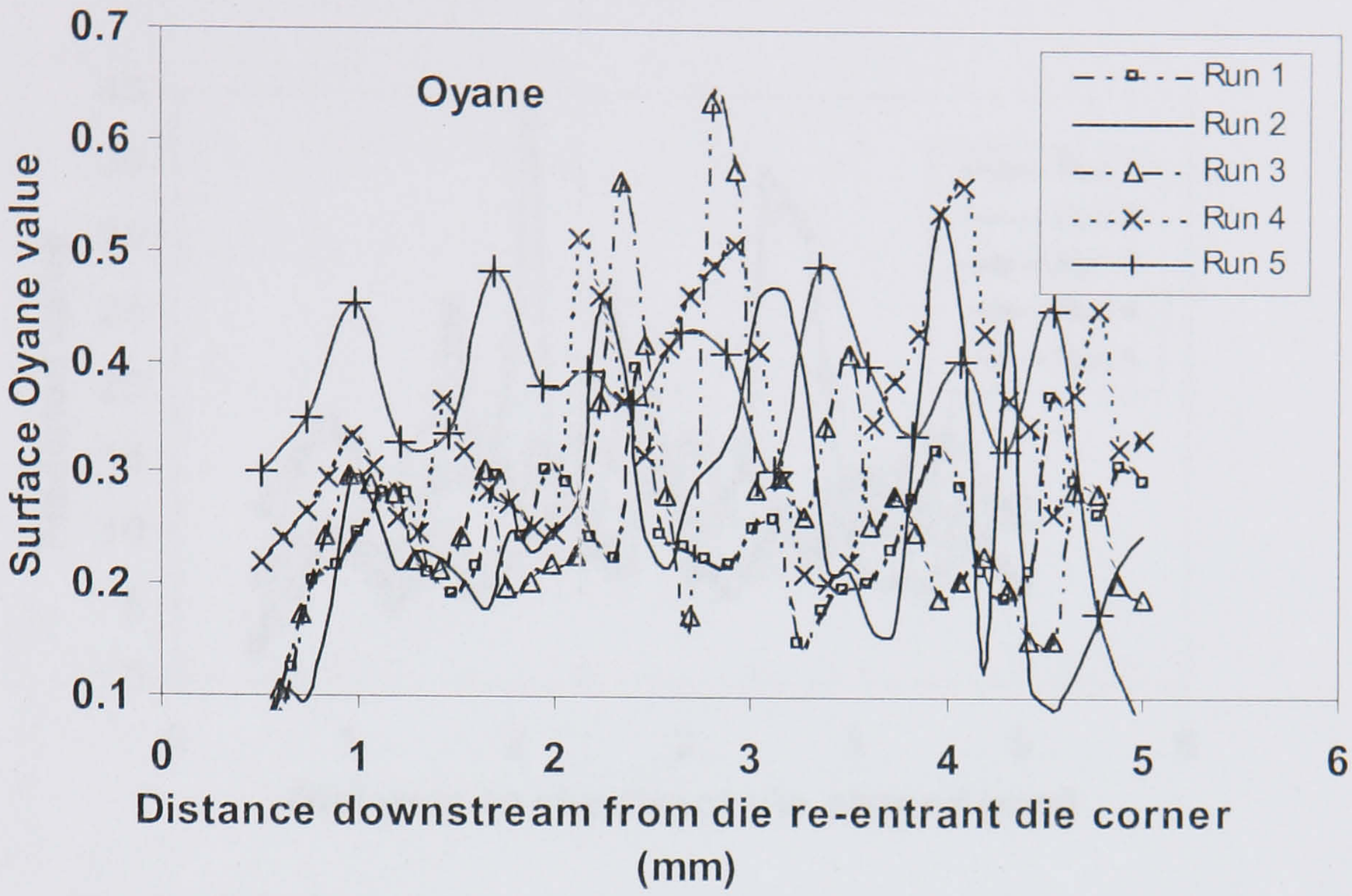

Figure 5.8 Simulation results using Oyane criterion for phenomenon 2

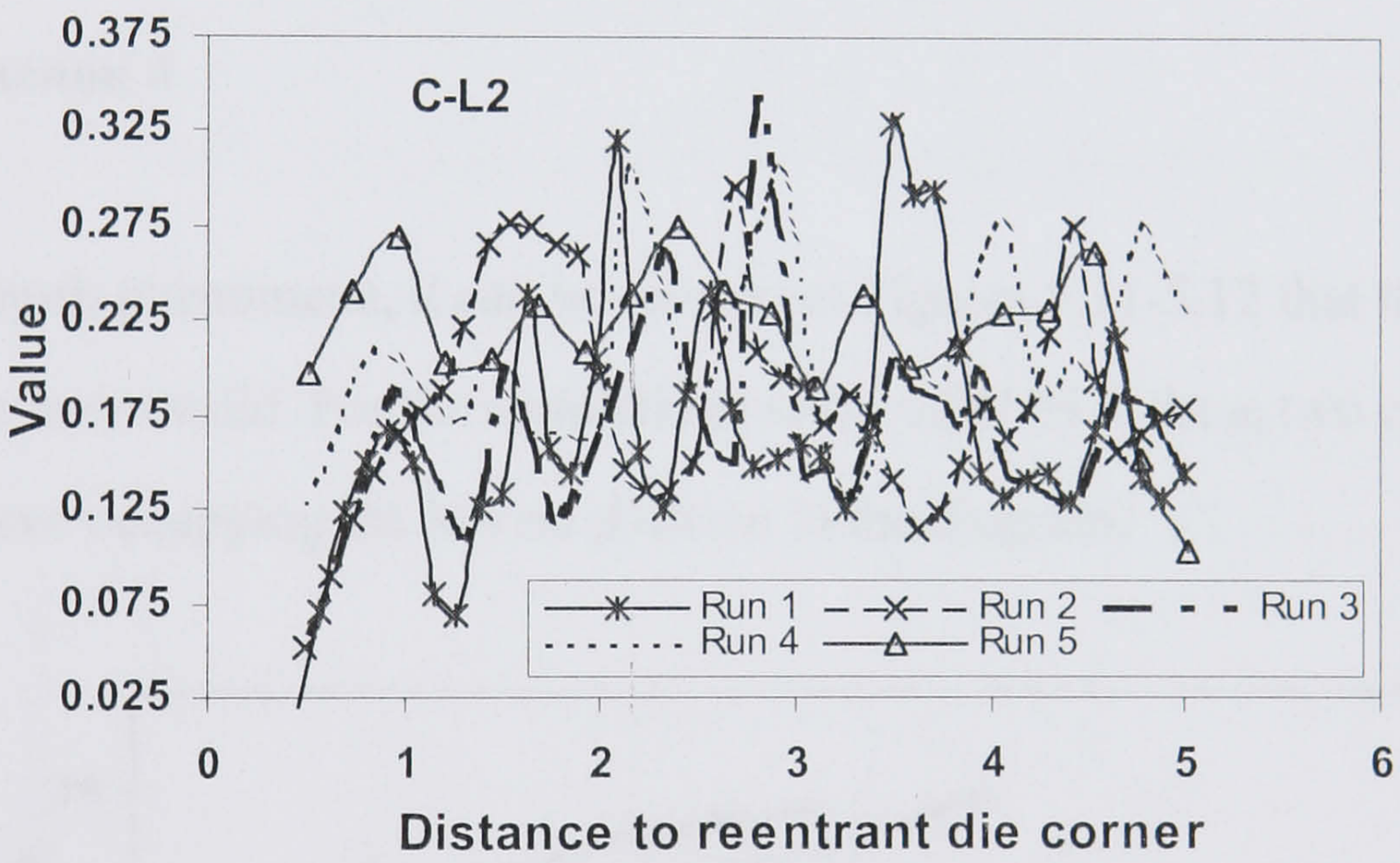

Figure 5.9 Simulation results using C-L2 for phenomenon 2

(3) Phenomenon 3

As for the third phenomenon, it can be seen from Figures 5.13-5.15 that the first three criteria, i.e. the Oyane, the C-L1 and the C-L2 criteria are valid. The predicted peak values at the middle of extrusion are higher than the maximum value at the beginning of extrusion. It can also be seen from Figures 5.16 and 5.17, that the Ayada and the GW criteria are obviously effective. The predicted values of these two criteria are

continuously rising through out the extrusion, and this corresponds with the concept that if surface cracking occurs, it will become more and more severe as the process proceeds.

Figure 5.10 Simulation results using C-L1 for phenomenon 2

(4) Phenomenon 4

As for the fourth phenomena, it can be seen from Figures 5.11-5.12 that the Ayada and the GW criteria are valid. For the simulation results of RUN 5, these two criteria give the predicted curve occupying the lowest position in the diagram.

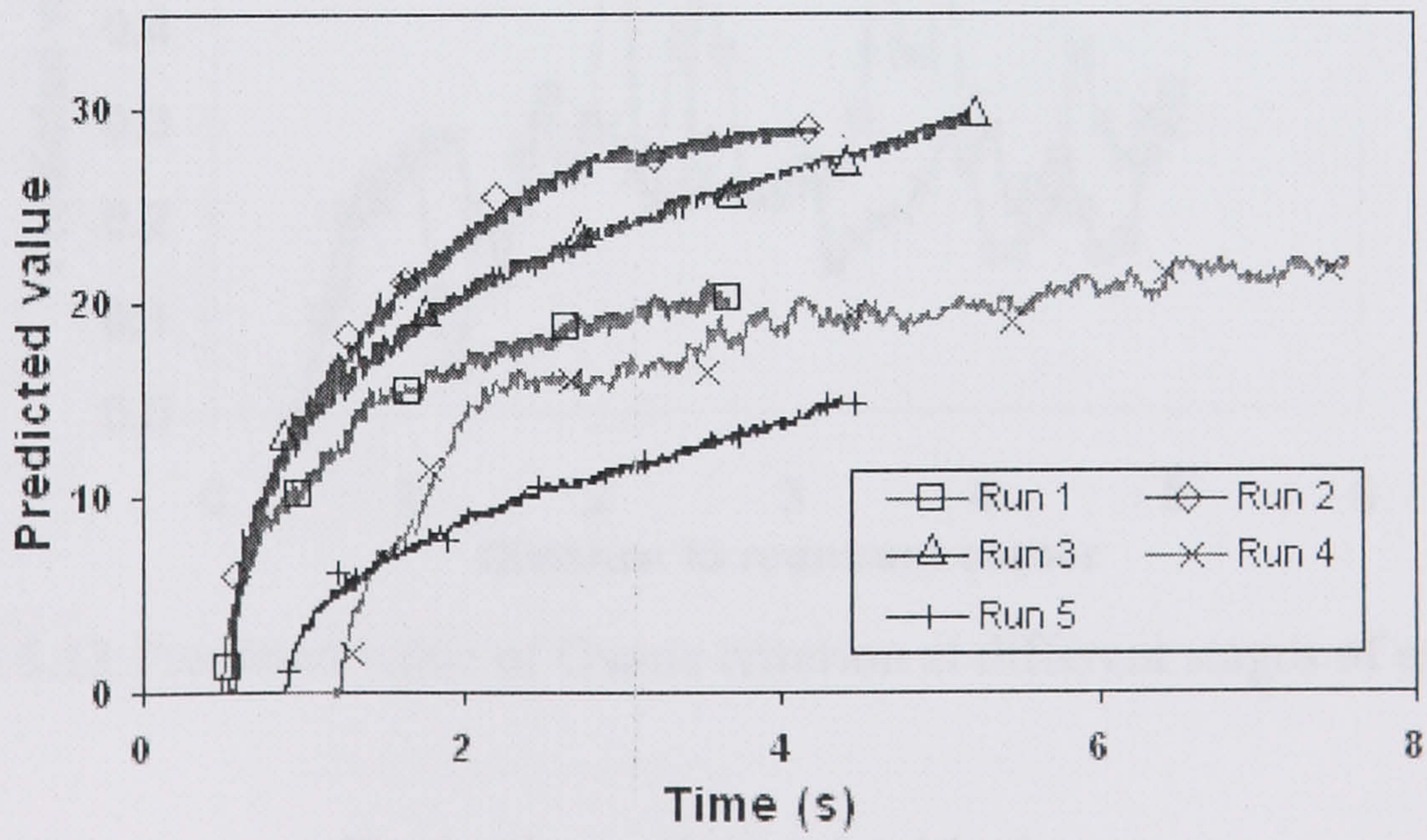

Figure 5.11 Simulation results using Ayada criterion for phenomenon 2

The temperature criterion is also valid in explaining the fourth phenomenon, as can be seen from Figure 5.3. As has been discussed previously, the temperature rise during extrusion results in incipient melting of the second phase particles, which form an intergranular network when quenched, resulting in a brittle product with poor mechanical properties (Vierod 1983).

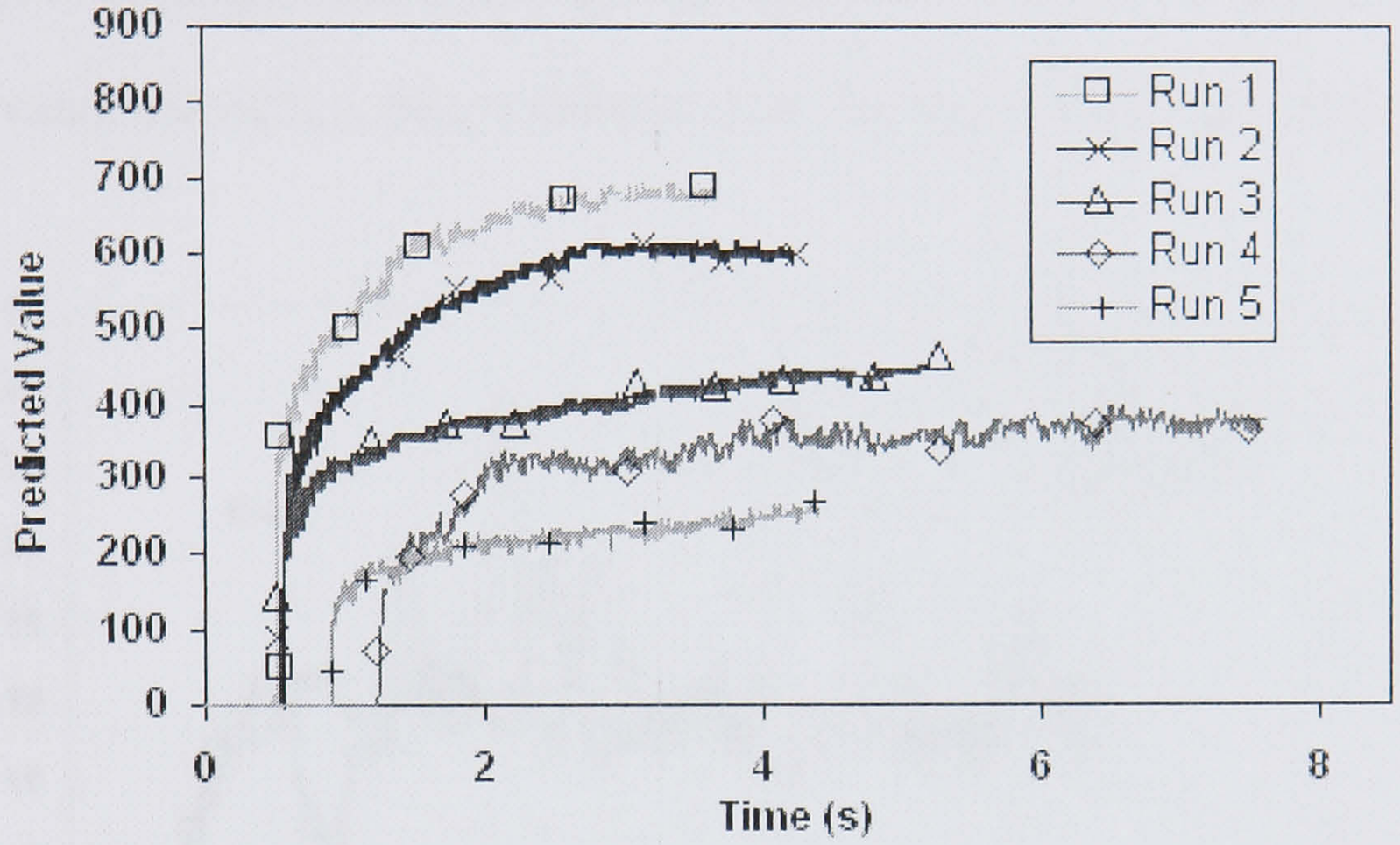

Figure 5.12 Simulation results using GW (Freudenthal) for phenomenon 2

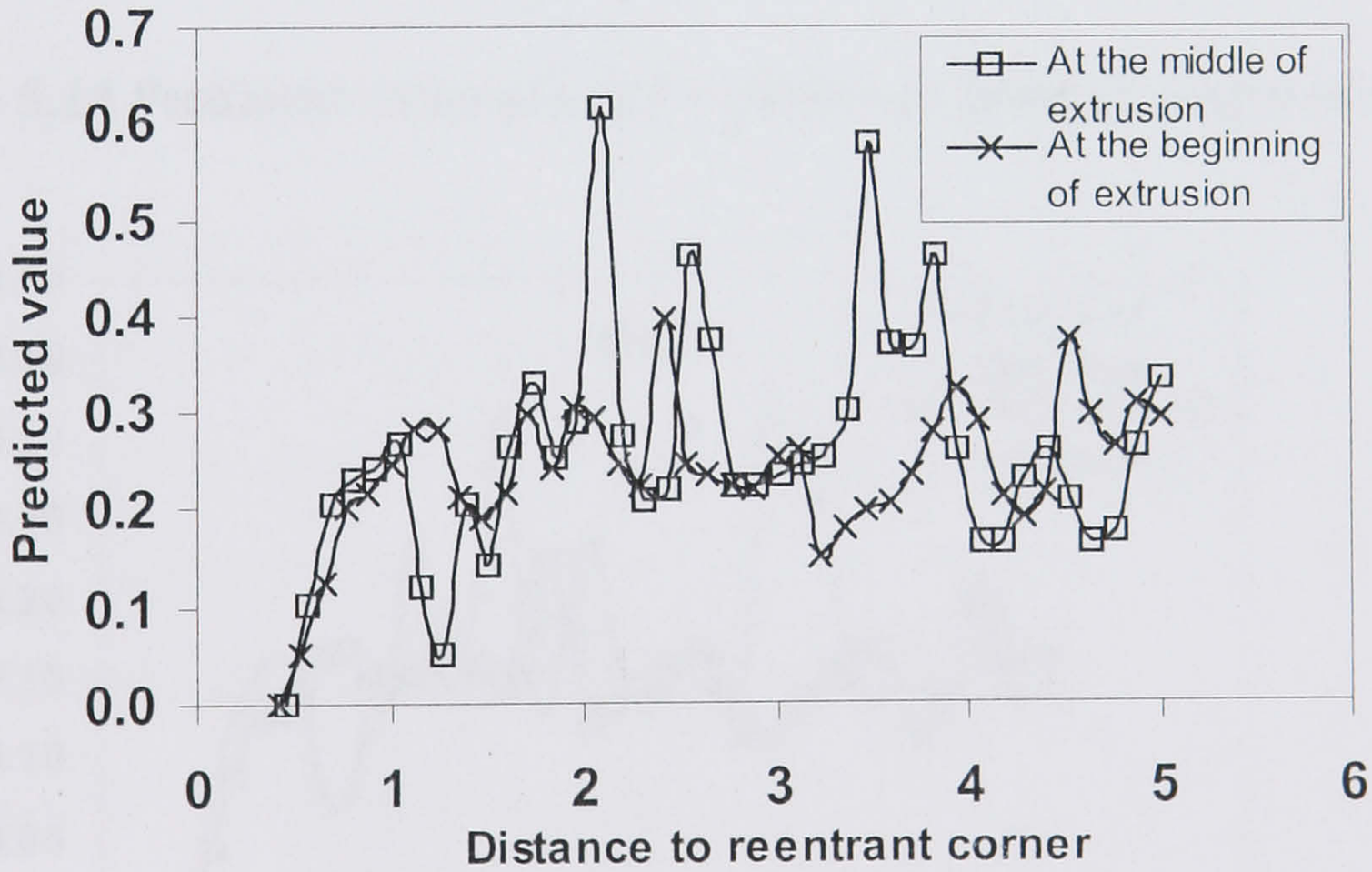

Figure 5.13 Predicted value of Oyane criterion at different stages of extrusion

The other criteria are not effective in predicting the 4th phenomena.

5.2.2 Discussion of the empirical criterion

Because the empirical method is regressed from all of the experiments, it is evident that it is effective in predicting the phenomena 1, 2, 4 and 5 mentioned above. Meanwhile, if only judged from the $\mathrm{Ln}(Z_i)$ value, it is difficult to predict if the surface cracking will occur at the beginning of extrusion or at the middle of extrusion. However, with the FEM predicted value of $\mathrm{Ln}(Z_r)$, this problem can be solved, as discussed below.

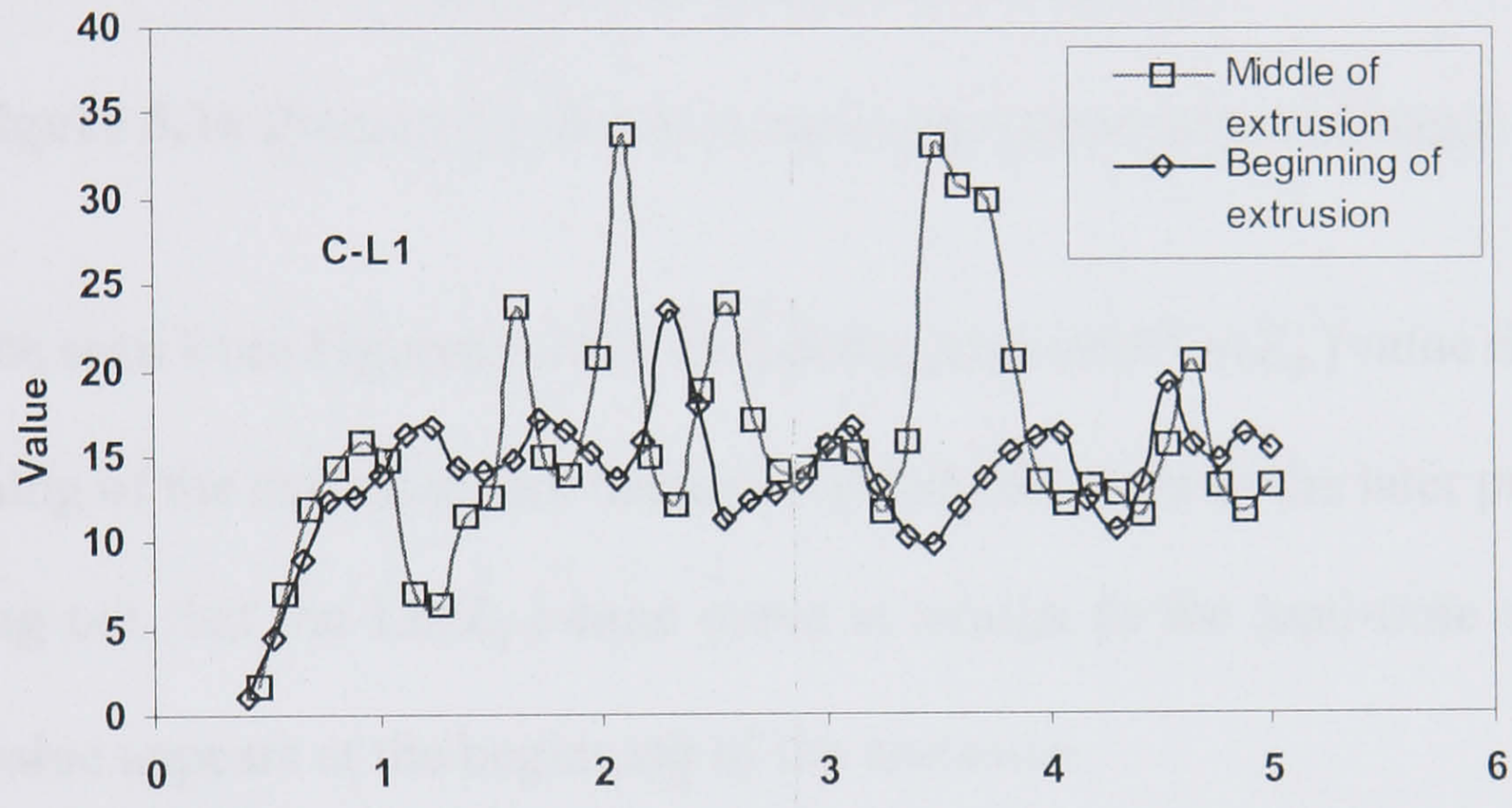

Figure 5.14 Predicted value of C-L1 criterion at different stages of extrusion

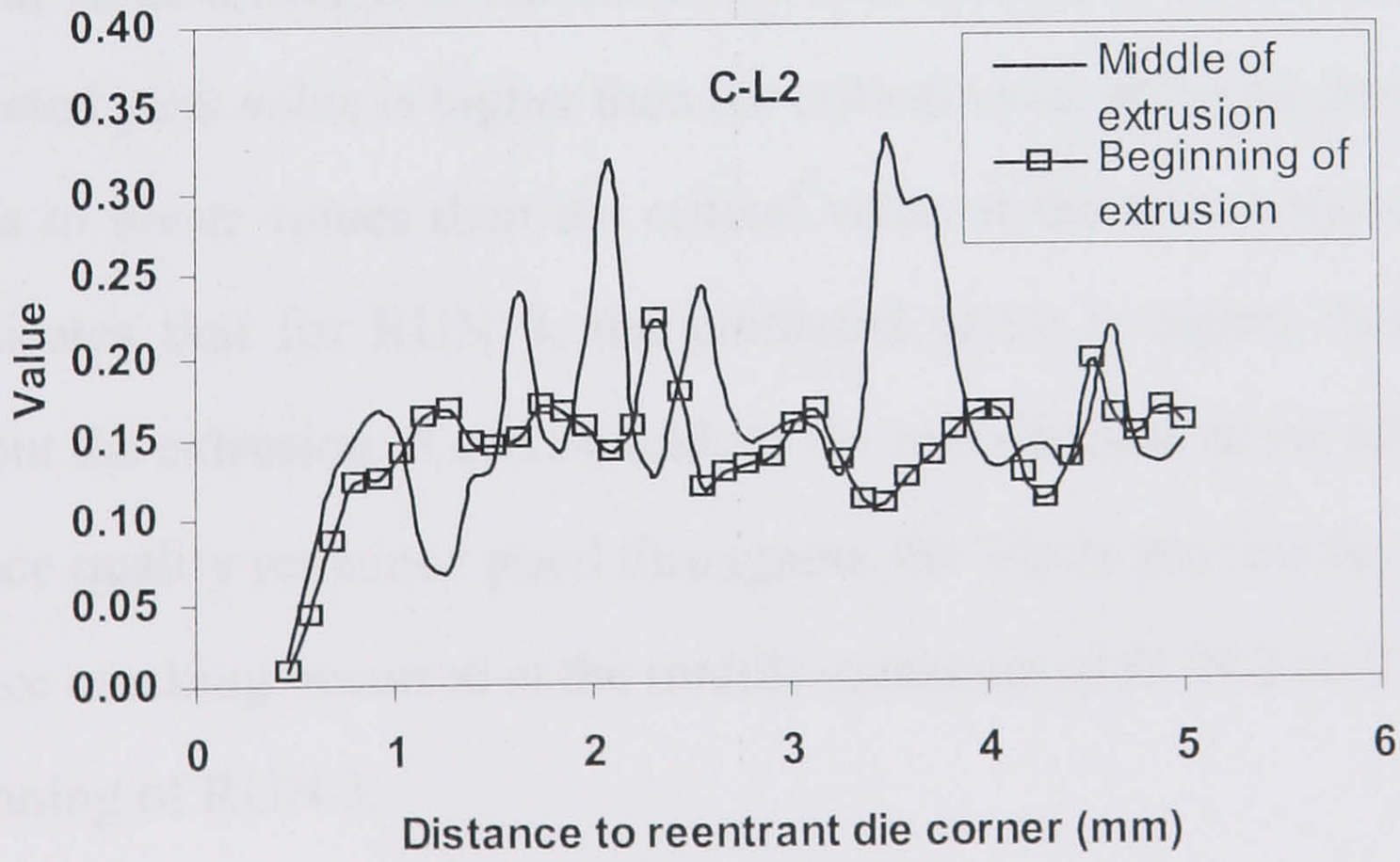

Figure 5.15 Predicted value of C-L2 criterion at different stages of extrusion

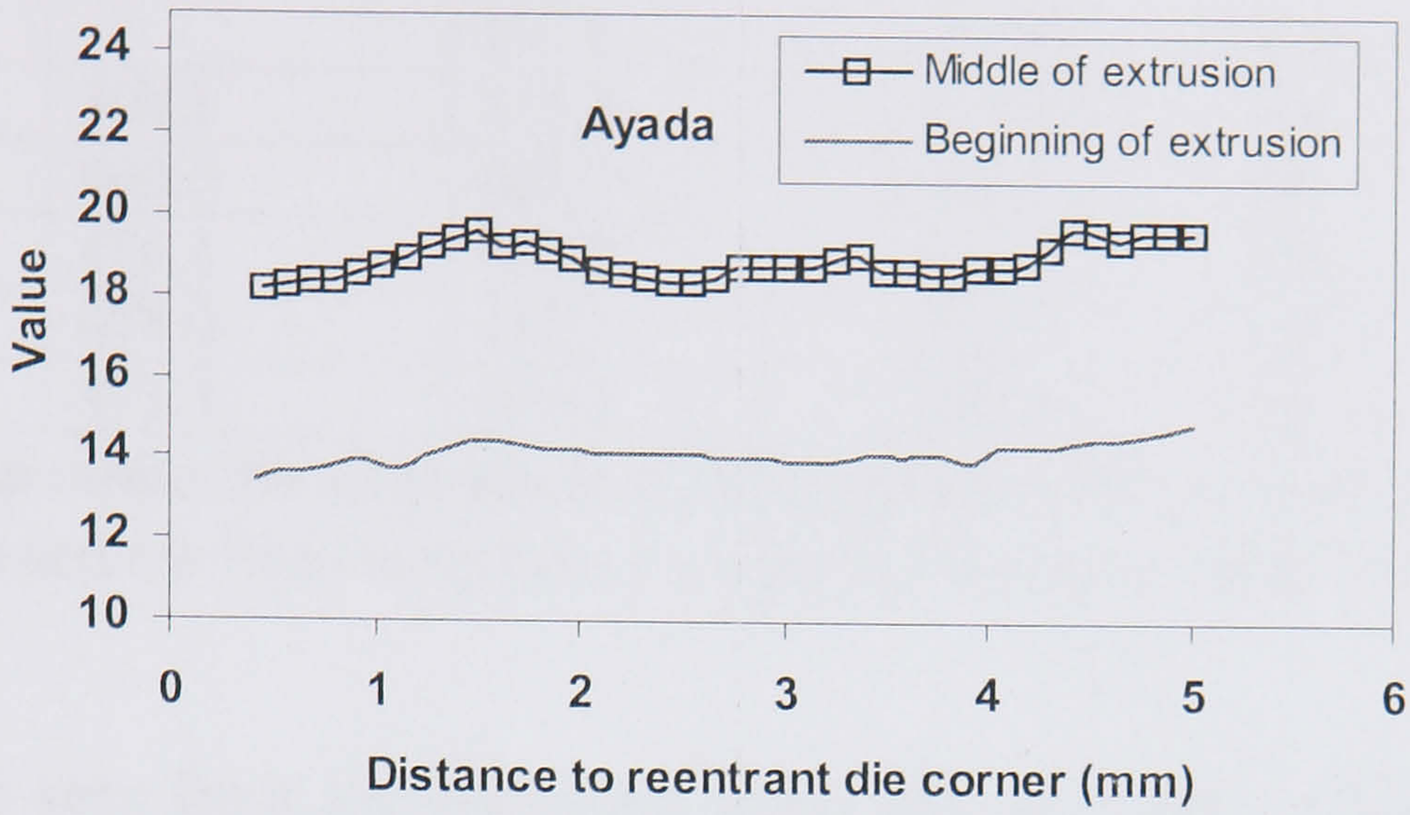

Figure 5.16 Predicted value of Ayada criterion at different stages of extrusion

It can be seen from Figures 5.18-5.21 that the predicted $\mathrm{Ln}(Z_r)$ value rises sharply at the beginning of the extrusion, but decreases slowly throughout the later process. It is worth pointing out that the $\mathrm{Ln}(Z_r)$-time curve is similar to the load-time curve, in which a peak value appears at the beginning of the extrusion.

As shown in Table 5.4, for runs 1 and 4, the predicted instant $\mathrm{Ln}(Z_r)$ value is lower than the critical value throughout the extrusion. For RUN 2, as can be seen from Figure 5.20, the predicted peak value is higher than the critical value at the beginning of extrusion but decreases to lower values than the critical value at the later stage of extrusion. Figure 5.21 indicates that for RUN 3, the predicted value is higher than the critical value throughout the extrusion. It corresponds to the real situation in the experiments, in which the surface quality remained good throughout the whole process for runs 1 and 4, while the surface cracking occurred at the middle extrusion of RUN 2 and it began to appear at the beginning of RUN 3.

Table 5.4 Predicted temperature (experiments from Vierod 1983)

Extrusion code	Peak temp† (C°)	FEM predicted peak temp (C°)	Final temp† (C°)	FEM predicted final temp (C°)
1	309.1	315.2	470.8	465.7
2	403.5	408.9	501.2	498.2
3	476.1	479.2	546.3	539.6
4	478.0	482.1	529.0	520.4
5	471.3	478.3	488.8	493.2

†Peak temp means the temperature of the extrudate when the peak load occurs. Both the Peak temp and the Final temp here are obtained from the integral profile model.

As can be seen from the discussion above that with the combination of $\mathrm{Ln}(Z_i)$ and $\mathrm{Ln}(Z_r)$, the surface cracking can be predicted. If the $\mathrm{Ln}(Z_i)$ is higher than the critical value given by equation 5.19, then surface cracking will happen, and if the $\mathrm{Ln}(Z_r)$ is higher than the critical value throughout the extrusion then the extrudate will suffer from surface cracking throughout the extrusion.

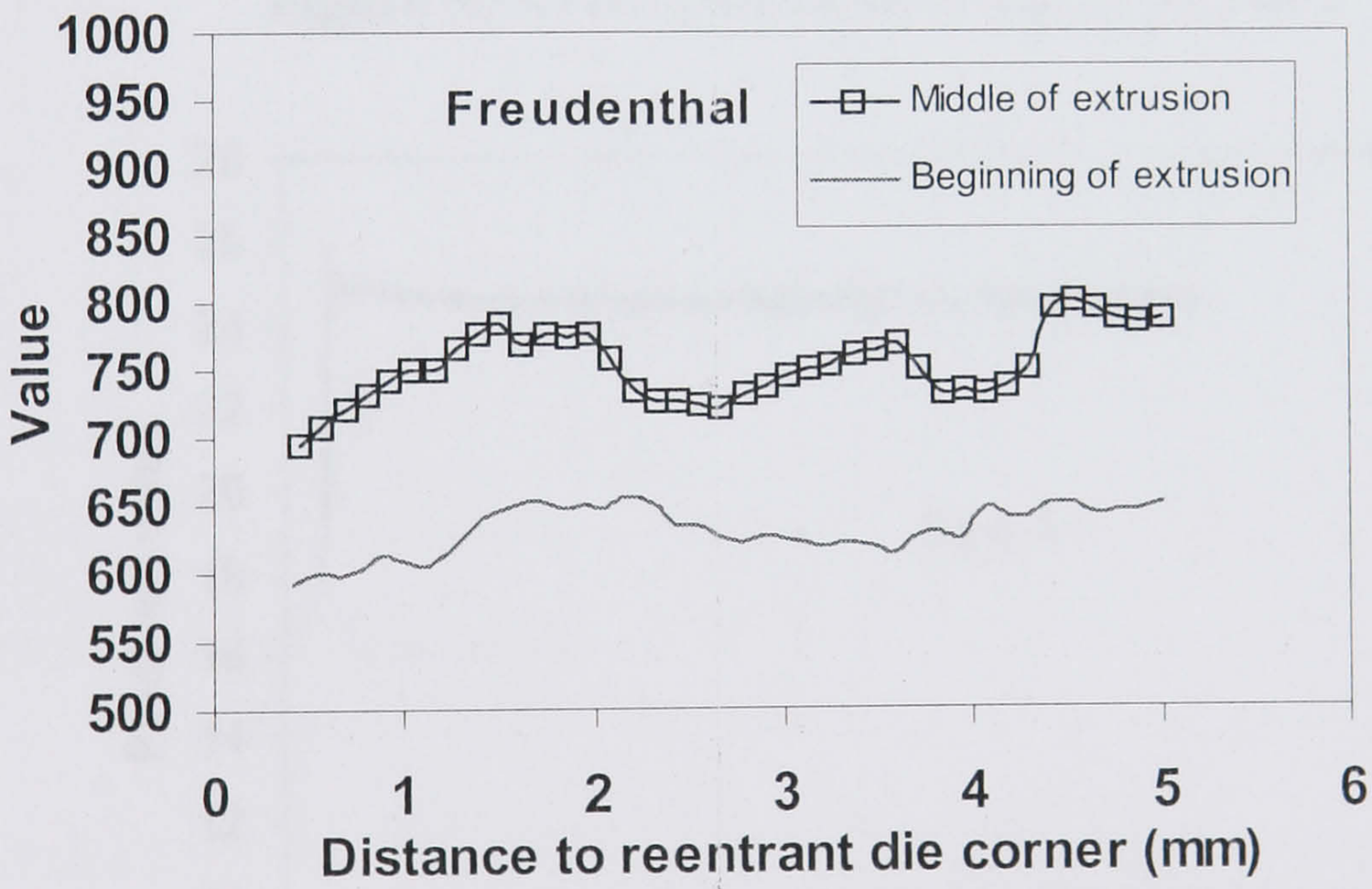

Figure 5.17 Predicted value of GW criterion at different stages of extrusion

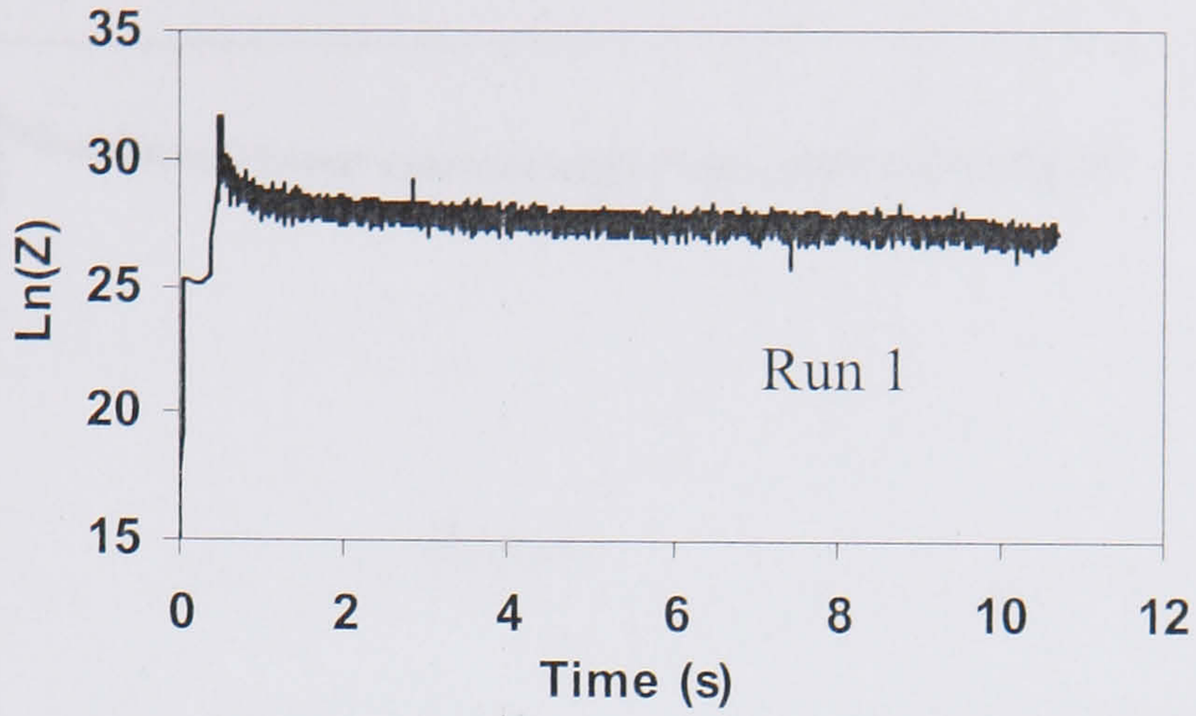

Figure 5.18 Predicted value of $Ln(Z_r)$ in run 1

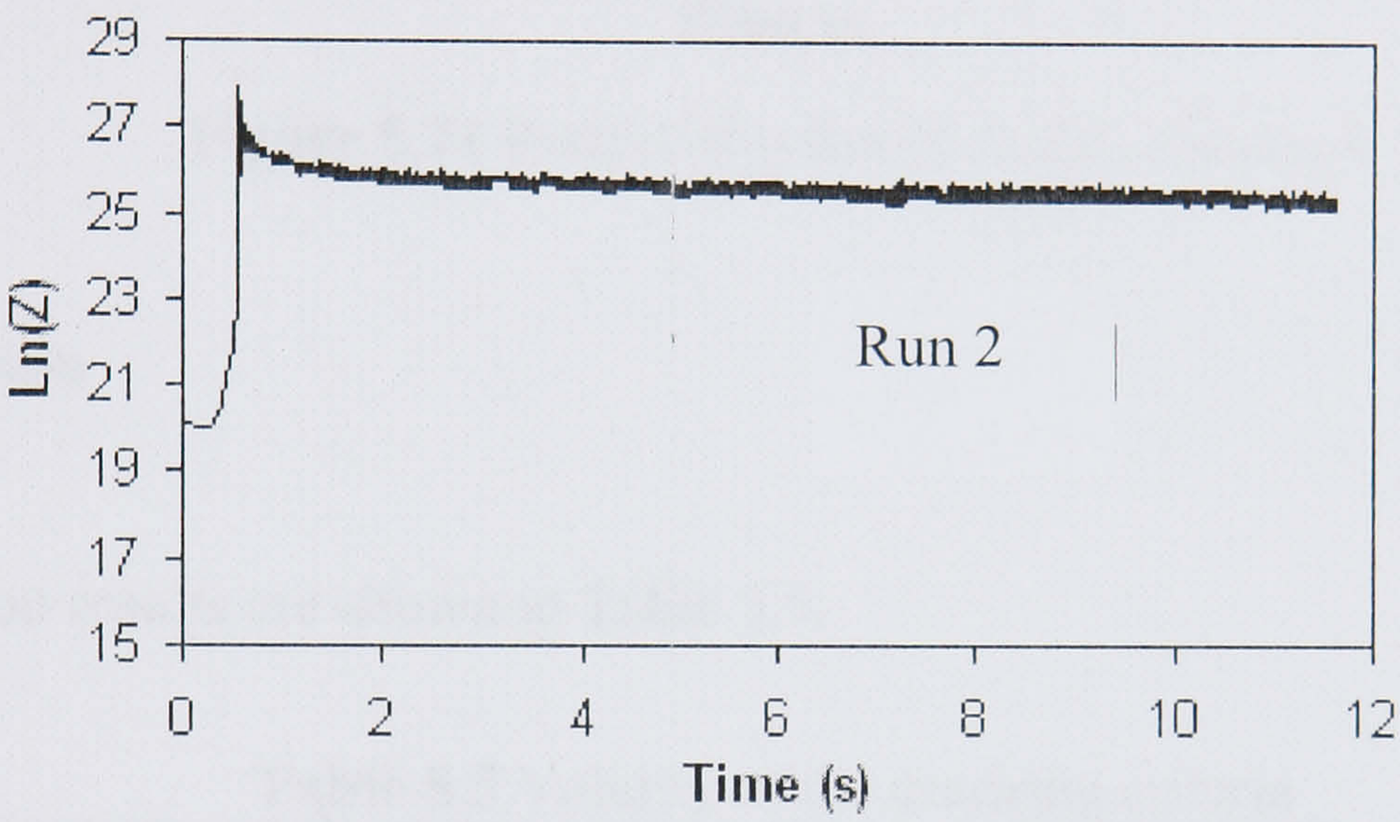

Figure 5.19 Predicted value of $Ln(Z_r)$ in run 2

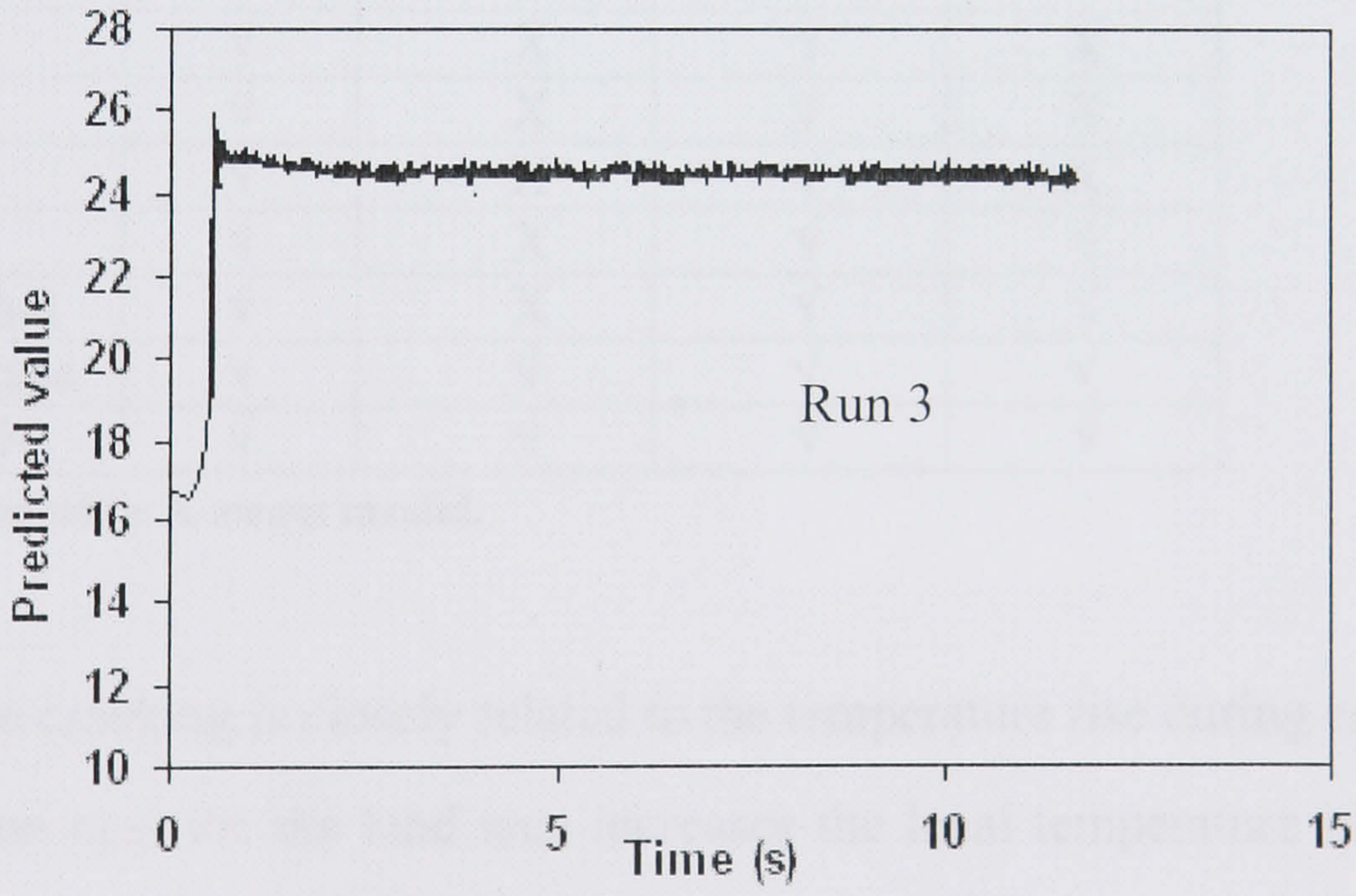

Figure 5.20 Predicted value of $Ln(Z_r)$ in run 3

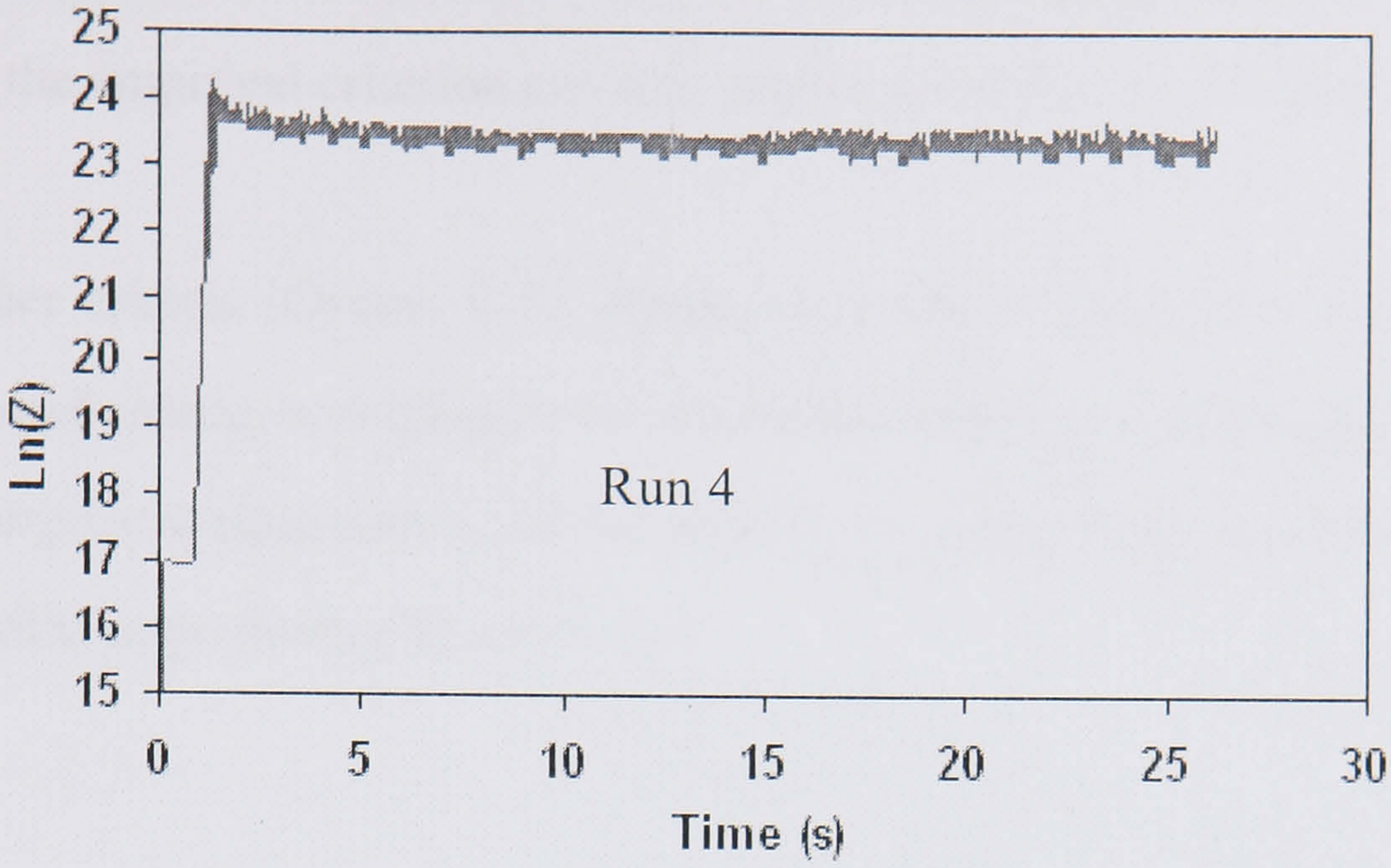

Figure 5.21 Predicted value of $\mathrm{Ln}(Z_r)$ in run 4

5.3 Conclusion

The discussion results are shown in Table 5.5.

Table 5.5 Validity of the cracking criteria

Criterion	Phenomenon			
	1	2	3	4
Oyane	√	X	√	X
C-L1	√	X	√	X
C-L2	√	X	√	X
Ayada	√	X	√	√
Freudenthal	√	X	√	√
Temperature	√	√	√	√
Empirical	√	√	√	√

√ means effective while X means invalid.

1) The surface cracking is closely related to the temperature rise during extrusion. If the heat generation near the die land area increases the local temperature in excess of the solidus point, localised melting can occur, which can cause severe cracking of the surface. This conclusion coincides with many previous studies (Sheppard 1999a, Paterson 1981, Vierod 1983).

2) Given a so-called "critical value" that depends on the initial condition but not assumed universal, the empirical criterion can also predict all of the five phenomena.

3) The other criteria (Oyane, C-L, Ayada, etc.) can't successfully predict all the four cracking mechanisms occurring in hot aluminium extrusion. Although they are capable of predicting some phenomena, all the criteria excepting temperature and the empirical formula failed in predicting phenomenon 2.

6 Simulation of Special Extrusion Technologies

6.1 Pocket die extrusion

It is well known that pocket technology if properly adopted in the extrusion process can, to some extent, balance the material flow. However, the literature describing or analysing this process is sparse although the industrial application of pocket die extrusion is quite common. In this chapter, the influence of the pocket on material flow is modelled by three-dimensional FEM. The exit velocity profiles, the temperature difference, the deformation history of the material across the die orifice are clearly illustrated, and they correspond well with experimental data. It is shown that the material flow can be more homogeneous than normal extrusion if the appropriate pocket die design is applied. The influence of pocket die design on material structure is also studied by the use of physically based models combined with FEM simulation.

Figure 6.1 shows the crescent-like effect obtained by Northcott (1949). As with single hole extrusion, the heavily worked crescent zone may contain a substructure condition or may contain large grains, according to the conditions of the operation and subsequent treatment. The phenomenon was next studied in detail in the early 1970s, when Sheppard and Castle (1974) made a comprehensive study on multi-hole die extrusion.

In the case of multi-hole die extrusion without pocket, the eccentricity of the die is defined by:

$$\varepsilon = \frac{b}{a+b} \tag{6-1}$$

where a and b have been shown in Figure 4.21 and been revised as shown in Figure 6.2. When the pocket is adopted, the offset of the pocket is shown in Figure 6.2 as C. To aid in discussion, two points on the cut plane (which is 0.5mm under the die exit): M and N are

defined. M represents the extrudate side which is farthest from the centre axis of die, and N represents the side which is nearer to the die centre axis.

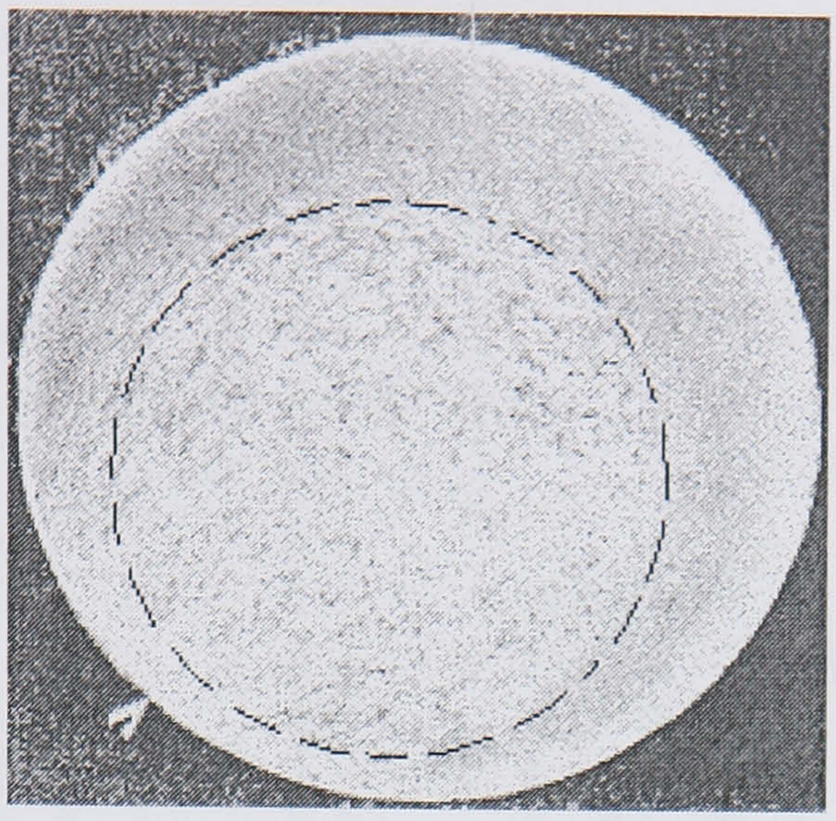

Figure 6.1 Microstructure of bar extrudated through a multihole die reported by Northcott (1949), showing crescent type feature indicating more severe deformation on the right hand side.

The inhomogeneous nature of recrystallisation around the periphery of extrudate from multi-hole die extrusion is shown in Chapter 4. This is undesirable both in terms of further processing and when the extrudate is applied for normal application (i.e. is a finished product). The object of this work is to demonstrate that dies utilising pockets favourably affect the material flow and subsequent recrystallisation and processing.

Four simulations are performed in this study as shown in Table 6.1. In all of the simulation running, the temperature of the billet is 433°C, the temperatures of the tooling (ram, container and die) are 300 °C , and the ram speed is 5mm/sec.

Table 6.1 Simulation runs

Run	Eccentricity	C (offset, mm)
1 (without pocket)	0.27	----
2	0.27	0
3	0.27	0.5 (offset towards die centre)
4	0.27	-0.5 (offset away die centre)

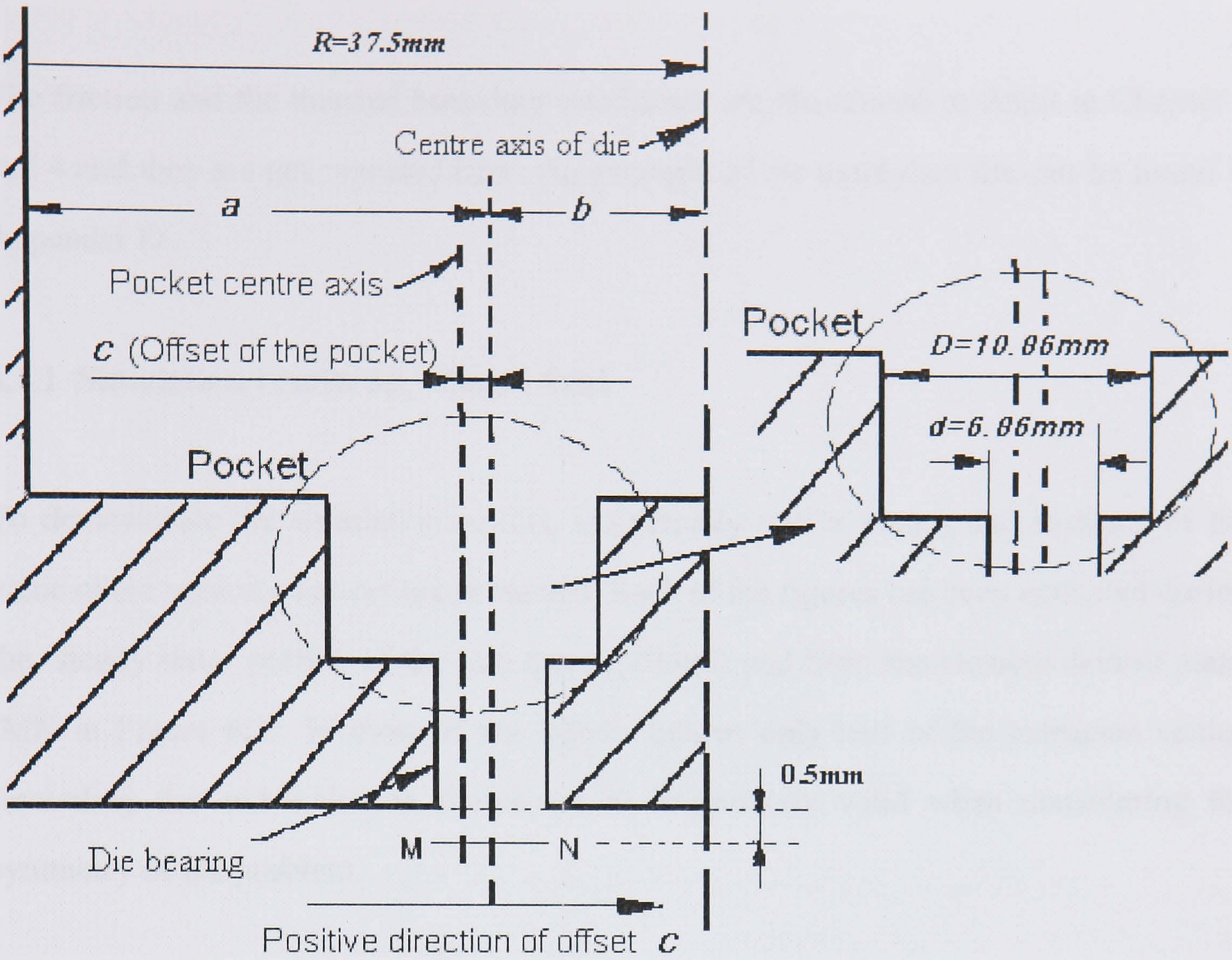

Figure 6.2 Indicating the offset 'C' of the pocket

The FEM program, FORGE3® is used in the present study. The hyperbolic sine function was combined into the FEM to describe the material behaviour. The constitutive equation can be written as:

$$\bar{\sigma} = \frac{1}{\alpha} \mathrm{Ln}[(\frac{Z}{A})^{\frac{1}{n}} + [(\frac{Z}{A})^{\frac{2}{n}} + 1]^{\frac{1}{2}}] \qquad (6\text{-}2)$$

where $\bar{\sigma}$ is the flow stress. α, A, n are temperature independent constants, Z is the Zener-Hollomon parameter:

$$Z = \dot{\varepsilon} \exp(\frac{\Delta H}{RT}) \qquad (6\text{-}3)$$

where $\dot{\bar{\varepsilon}}$ is the mean equivalent strain rate, ΔH is the activation energy and T is the temperature (Sheppard 1993).

The friction and the thermal boundary conditions are introduced in detail in Chapter 3 and 4 and they are not repeated here. An example of the input data file can be found in Appendix D.

6.1.1 Simulation results on velocity field

To demonstrate the simulation results, iso-velocity vector planes and surfaces of the value of the velocity vectors are presented. Each of the figures has been extracted during the 'steady state' portion of the ram travel (20mm) and from the element delimit plane (MN in Figure 6.2). In most of the figures below, only half of the extrusion setting (including die and billet) is shown which is perfectly valid when considering the symmetry of the problem.

The velocity contour lines and the iso-velocity surfaces of the first run are shown in Figures 6.3(a) and 6.3(b) individually.

As can be seen from Figure 6.3(a), in which there is no pocket, the velocity field is inhomogeneous at the die bearing area. The material flows faster at the die bearing area nearer to the die centre axis (N in Figure 6.2) than at the opposite site (M). This is demonstrated more clearly in Figure 6.3(b) by stereo visage results, in which both of the two iso-velocity surfaces, whose velocity are lower than the average exit velocity, expanding further at the side of M than at the opposite site N.

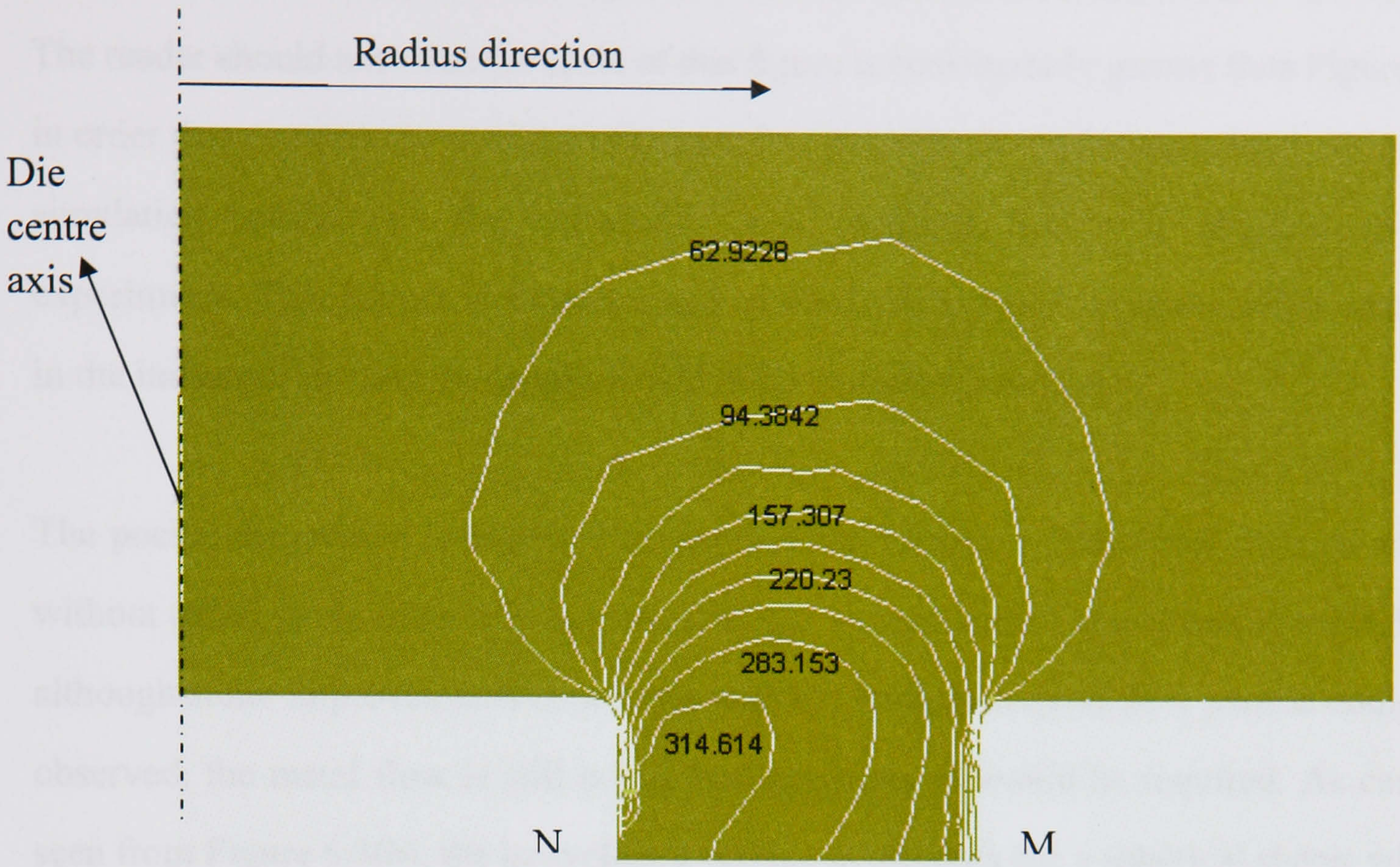

Figure 6.3a Material iso-velocity vector field of run 1 (mm/sec)

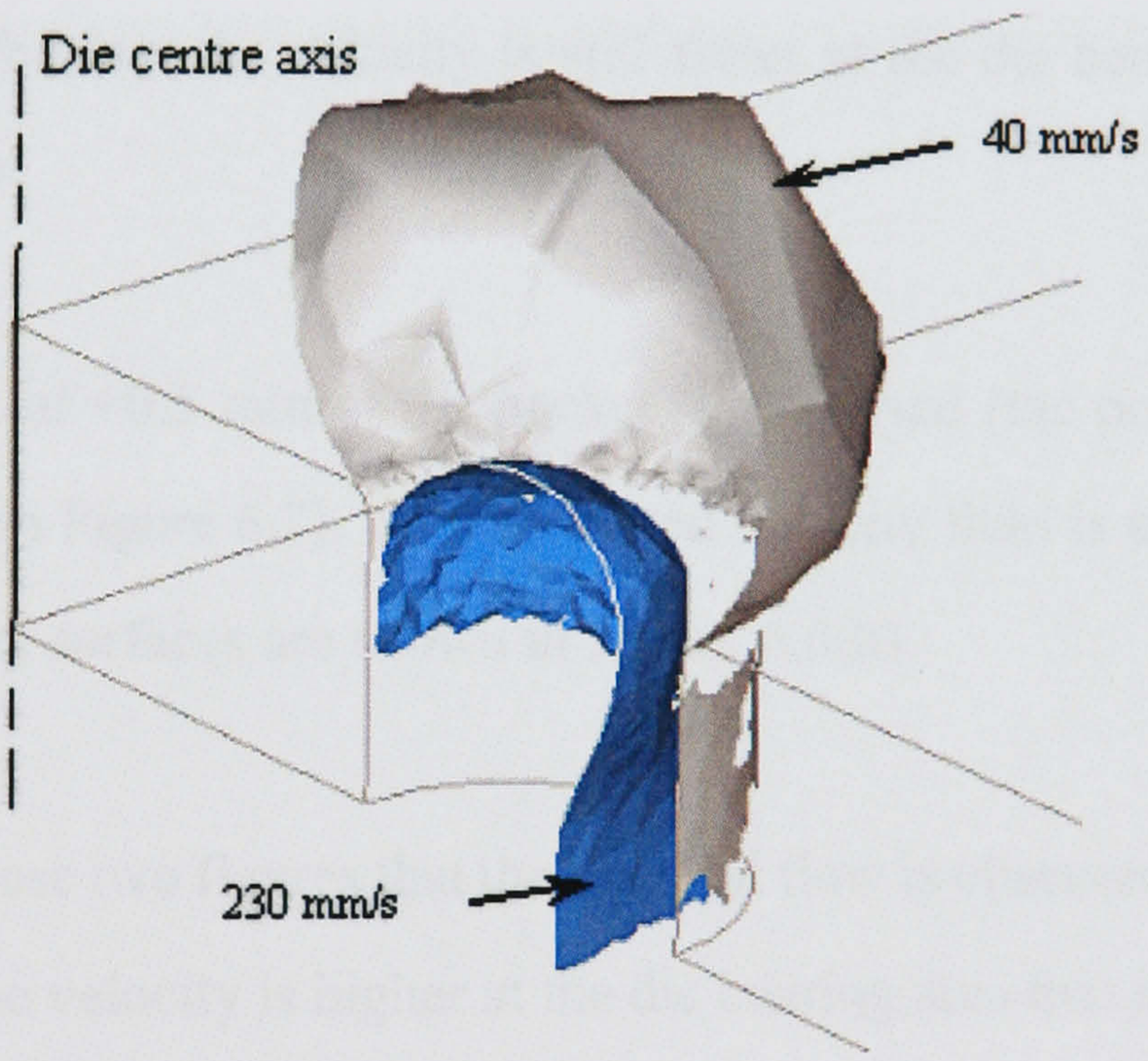

Figure 6.3b Iso-velocity surfaces of run 1 (40mm/sec and 230 mm/sec)

Figure 6.3 FEM simulation output in run 1.

These observations indicate that the material flows faster at the N side than at the opposite M site in the deformation area.

In Figure 6.4, an example of the experimental and simulation results of run 1 are shown. The reader should note that the scale of this figure is considerably greater than Figure 6.3 in order that comparison with the micrograph is possible. It can be seen clearly from the simulation results that the extrudate bends outwards, which is identical to the experiments. This feature is a direct result of the die land length being constant whereas in the industrial context the length would differ around the periphery.

The pocket die, which is expected to improve the balance of the metal flow, is added without offset in simulation 2. However, as can be seen from Figures 6.5(a) and 6.5(b), although some improvements concerned with the homogeneity of flow pattern could be observed, the metal flow is still not as homogeneous as would be required. As can be seen from Figure 6.5(b), the iso-velocity surface of 40mm/s has a spherical shape, which indicates a nearly balanced flow, while the iso-velocity surface of 230mm/s has no such symmetrical distribution, the velocity is still faster at the die bearing nearer to the die centre (the N side).

In run 3, an offset of +0.5 mm of the pocket is employed (the positive direction of the offset was shown in Figure 6.2). The calculated velocity field is shown in Figure 6.6(a) and the iso-velocity surfaces are shown in Figure 6.6(b).

It can be seen in these two figures that the material flow is observed to be almost a mirror image of run 2. The velocity is higher at the die bearing area that is furthest from the die centre axis (M side). The material flows faster at the location where the flow velocity is lowest in runs 1 and 2. The metal flow in this run is still quite inhomogeneous suggests that the offset of the pocket is incorrectly positioned.

It is should be noted that the offset (0.5mm) is small compared with the dimension of the die. The fact that a small offset can lead to such a significant change in the metal flow velocity field indicates the complex nature of the material flow and the challenge for the die designer to remedy defects.

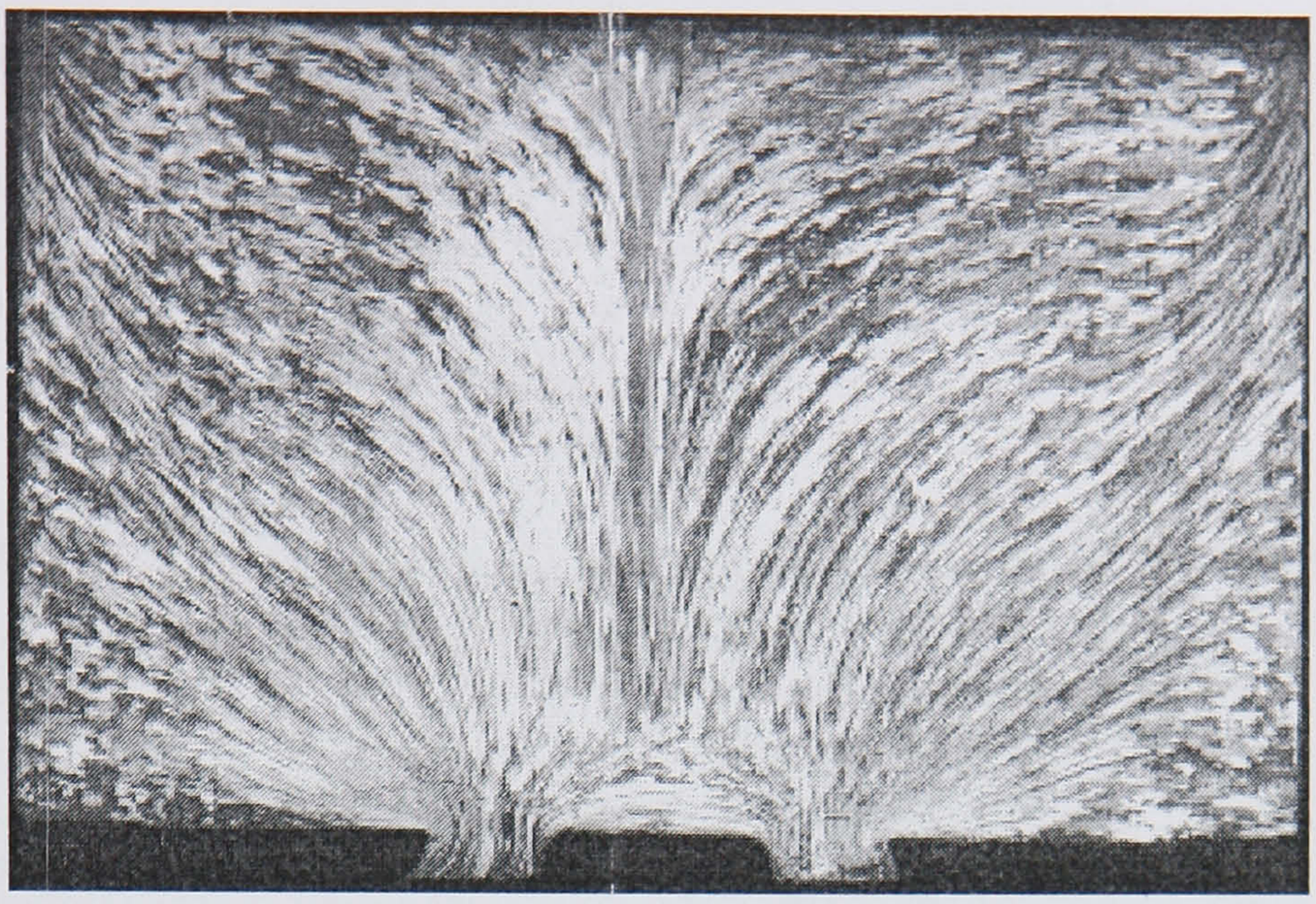

(a) Experimental results of material flow

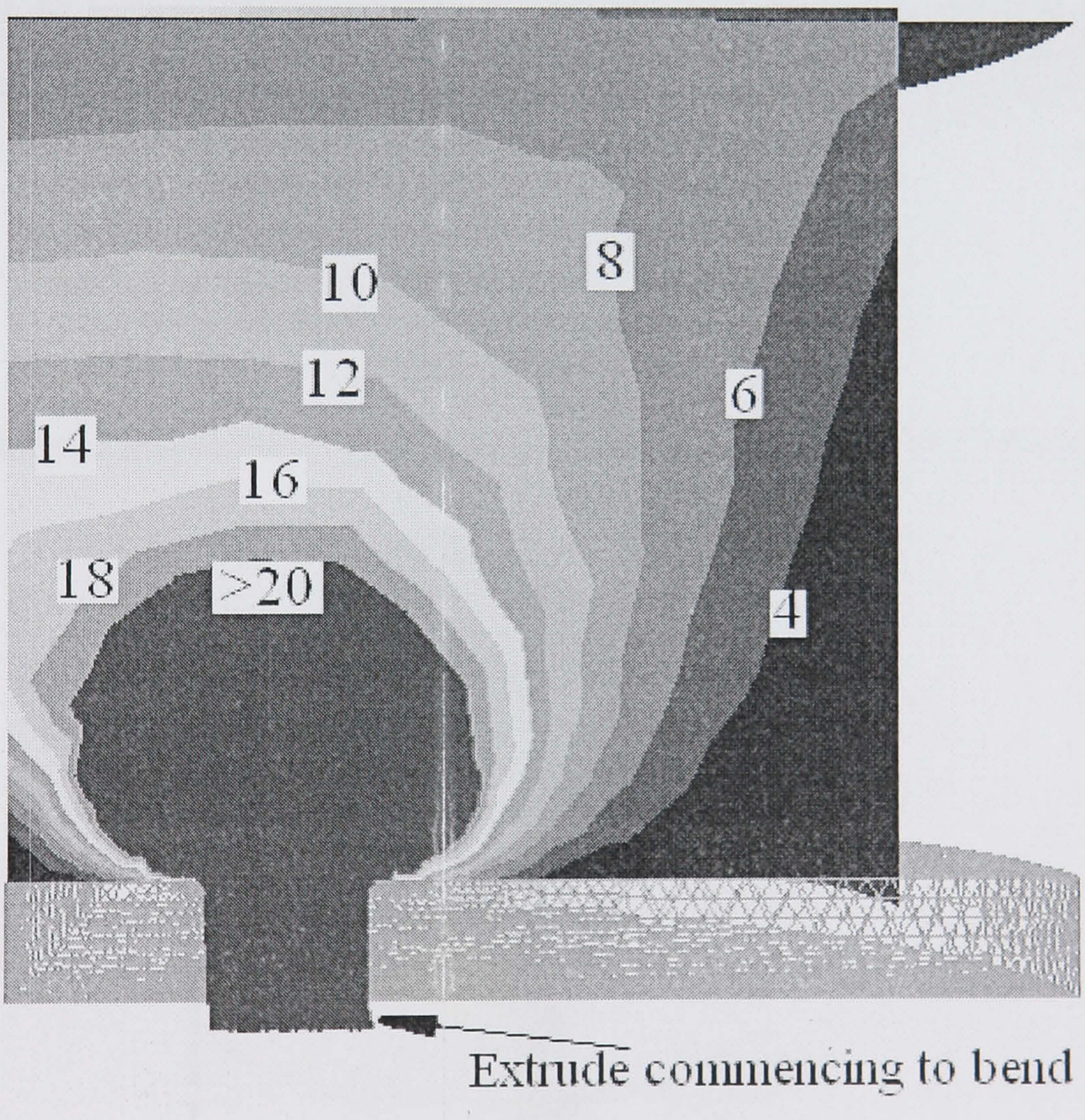

(b) Simulation results of material flow (numbers represent the flow velocity mm/sec)

Figure 6.4 Material flow observed from run 1.

The fourth run, with an offset of -0.5mm in the opposite direction is simulated and the results can be seen in Figures 6.7(a) and 6.7(b). It can be seen from these two figures that

the material flow is far more balanced than the three runs discussed above. At the die exit area, the contours of the velocity lines are almost symmetrical to the die orifice centre. The iso-velocity surfaces with the velocity of 40mm/sec and 230mm/sec are also in the configurations of a quarter of a sphere, which indicates the homogeneous nature of the material flow.

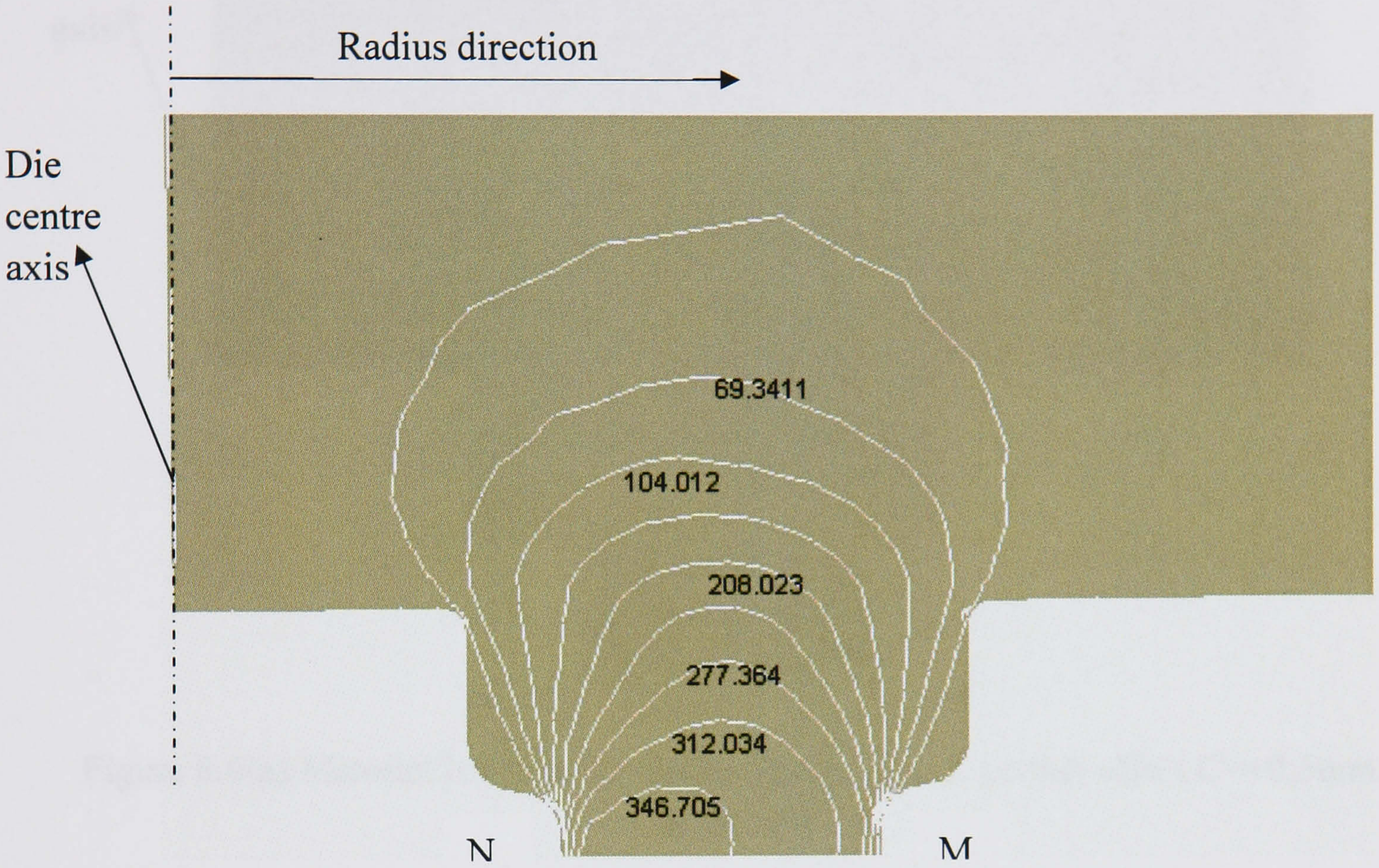

Figure 6.5a Material iso-velocity vector field in run 2, pocket offset *C*=0mm, (mm/sec)

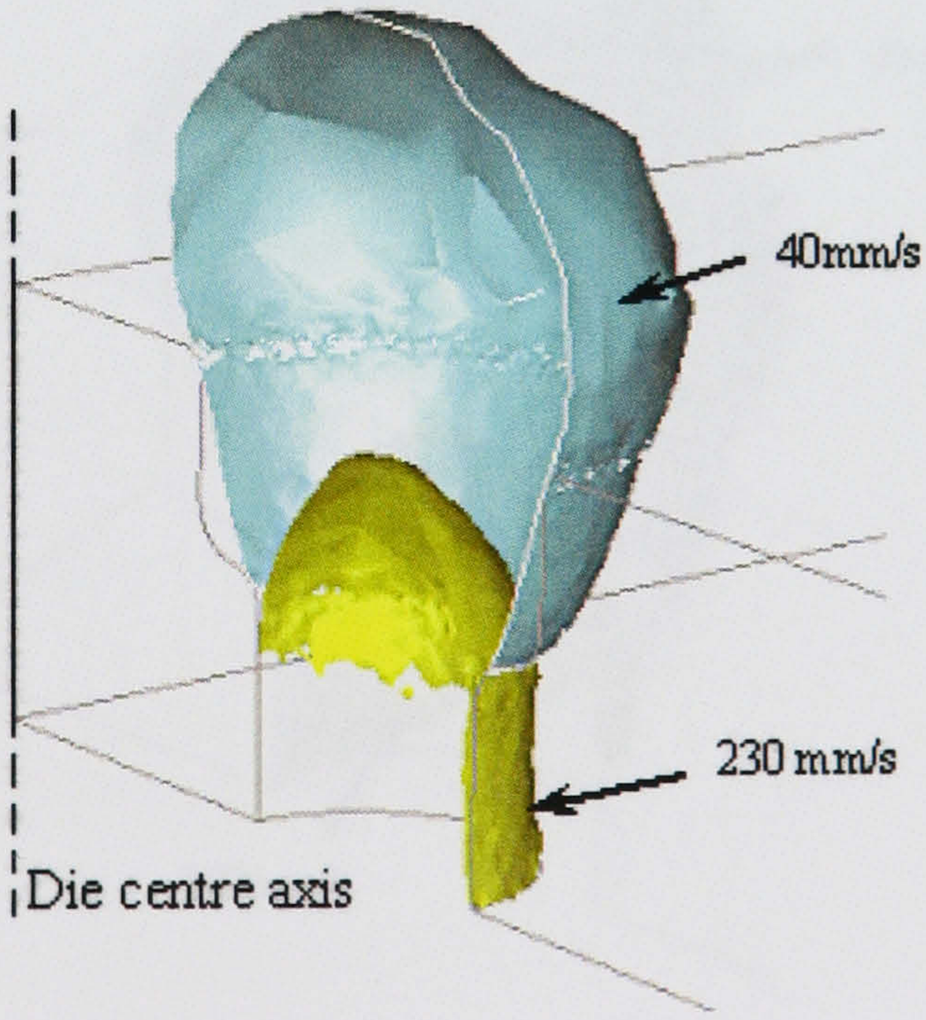

Figure 6.5b Iso-velocity surfaces in run 2 (40mm/sec and 230 mm/sec)

Figure 6.5 FEM simulation output in run 2.

Figure 6.6 and 6.7 also indicate the variation in dead metal zone around the circumference of the pocket, which is partially caused by the offset.

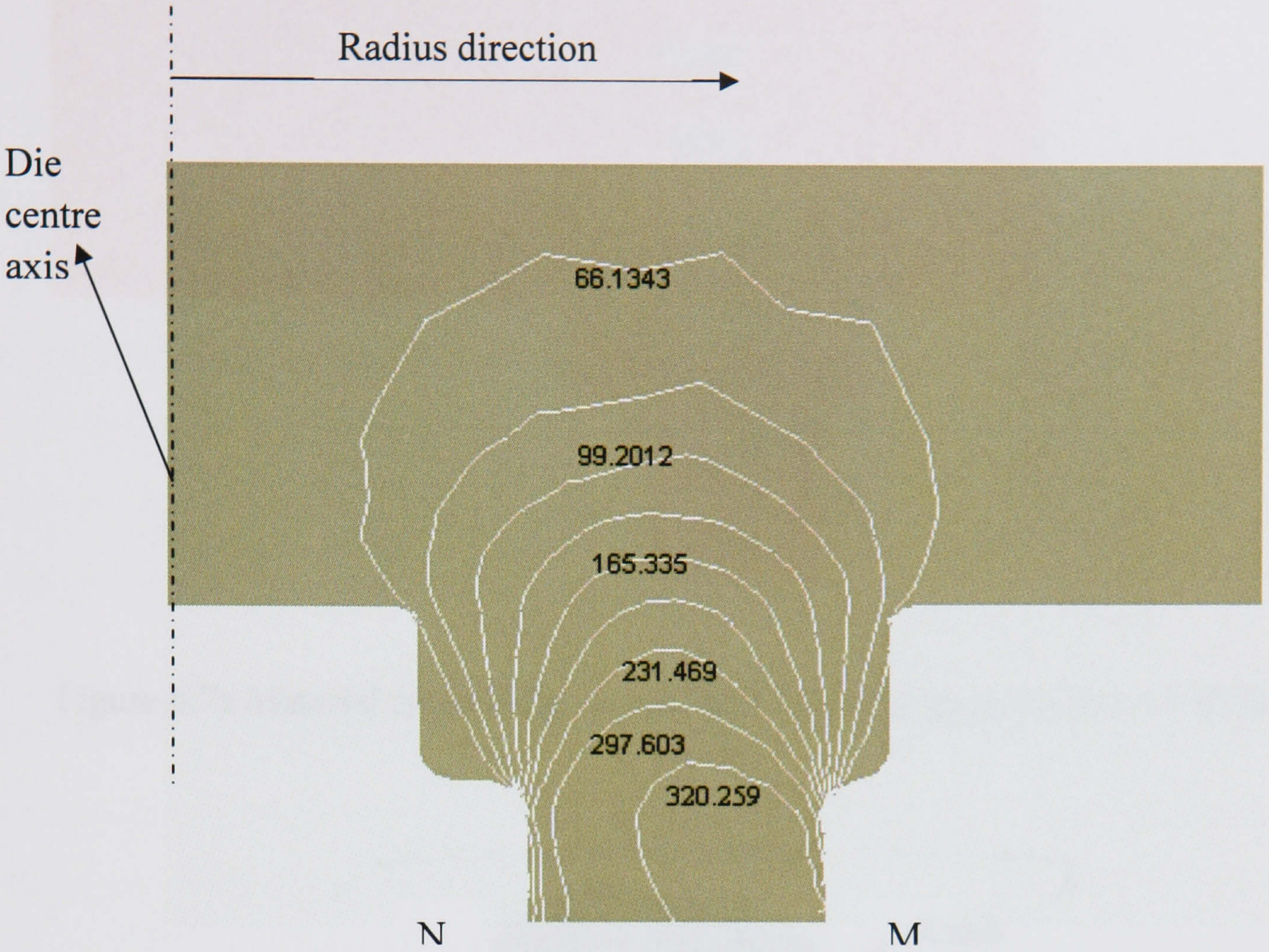

Figure 6.6(a) Material iso-velocity vector field in Run 3, pocket offset *C*=+0.5mm, (mm/sec)

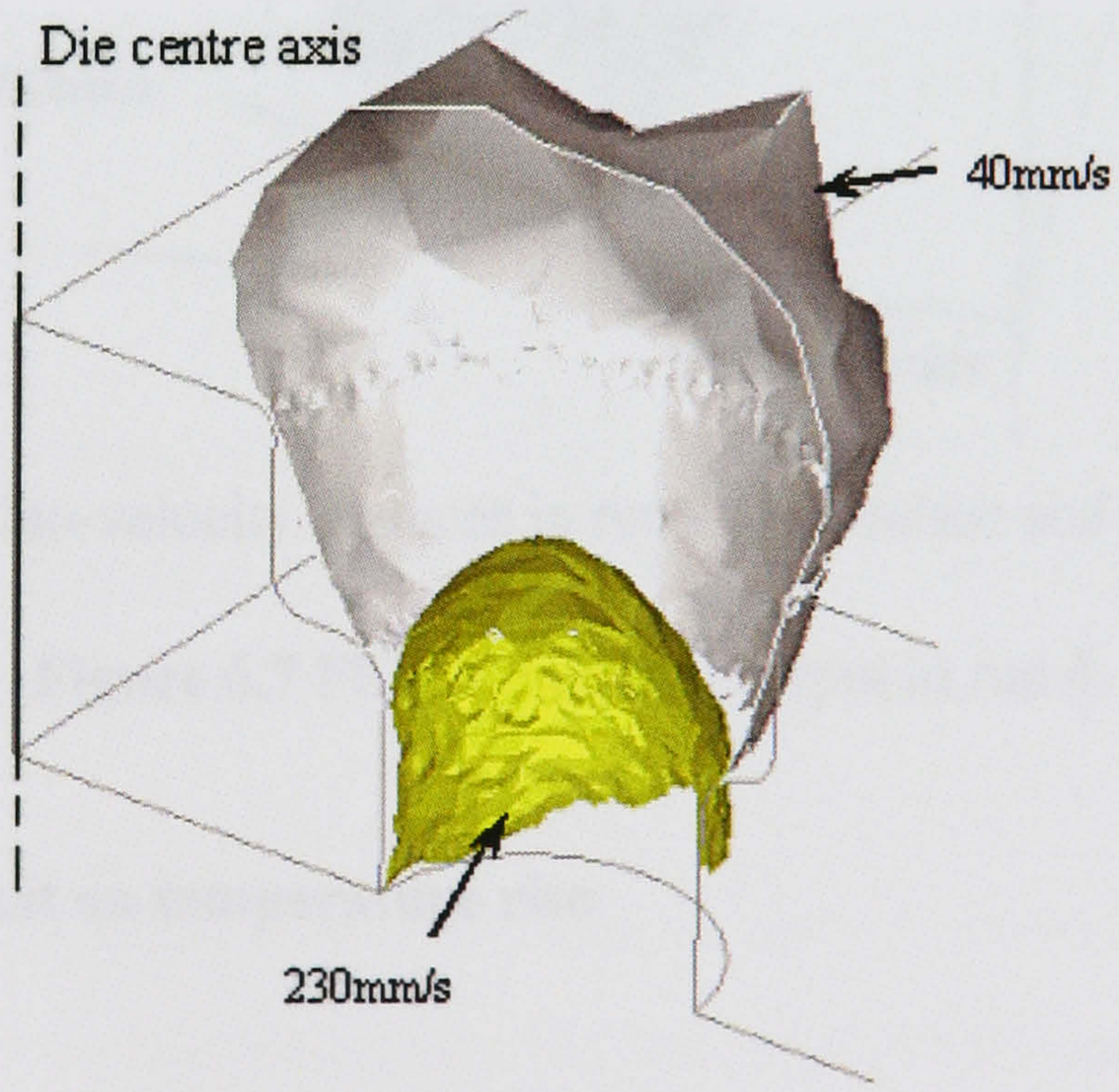

Figure 6.6(b) Iso-velocity surfaces in run 3 (40mm/sec and 230 mm/sec)

Figure 6.6 FEM simulation output in run 3.

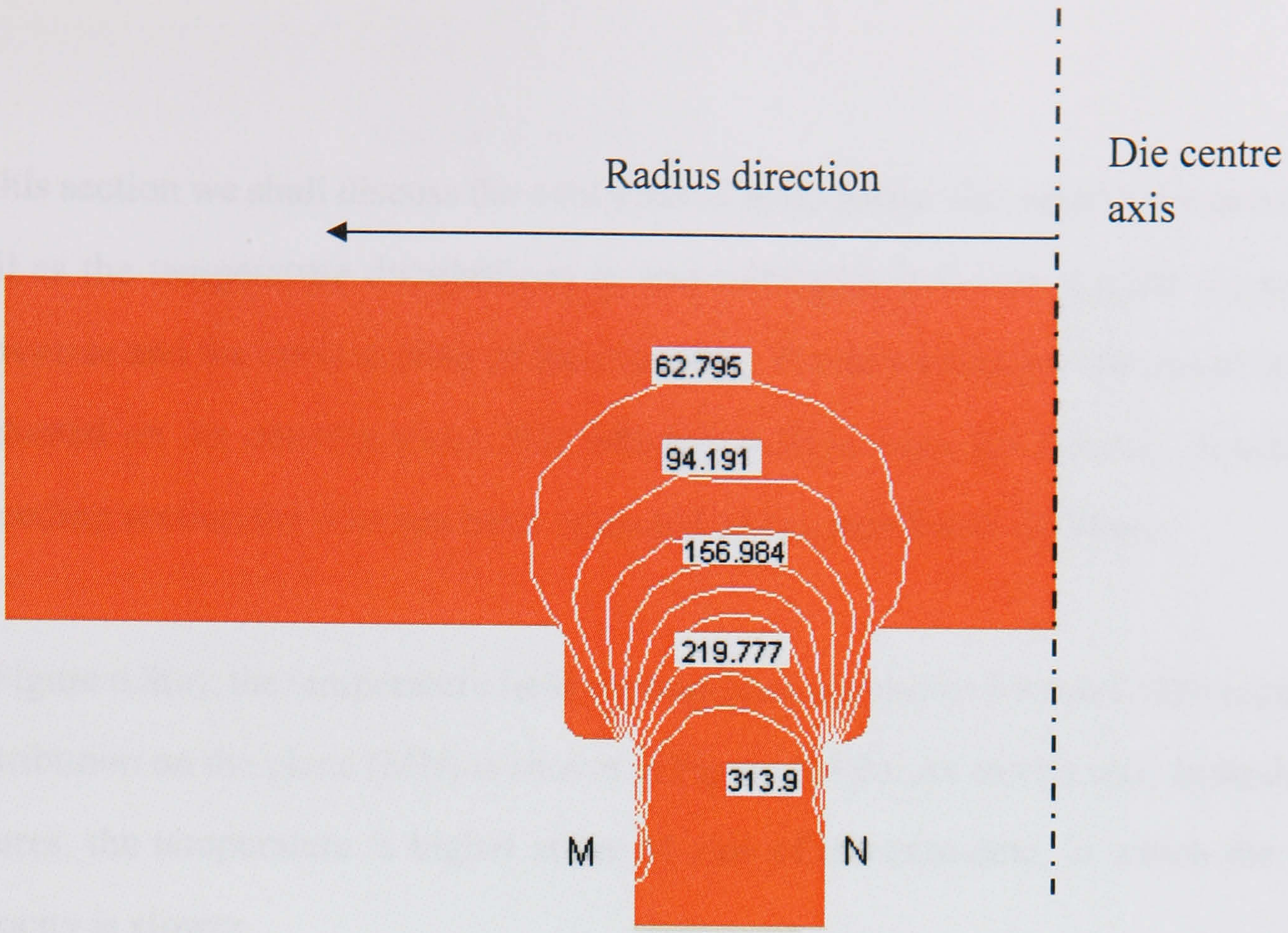

Figure 6.7a Material iso-velocity vector field in Run 4, pocket offset *C*=-0.5mm, (mm/sec)

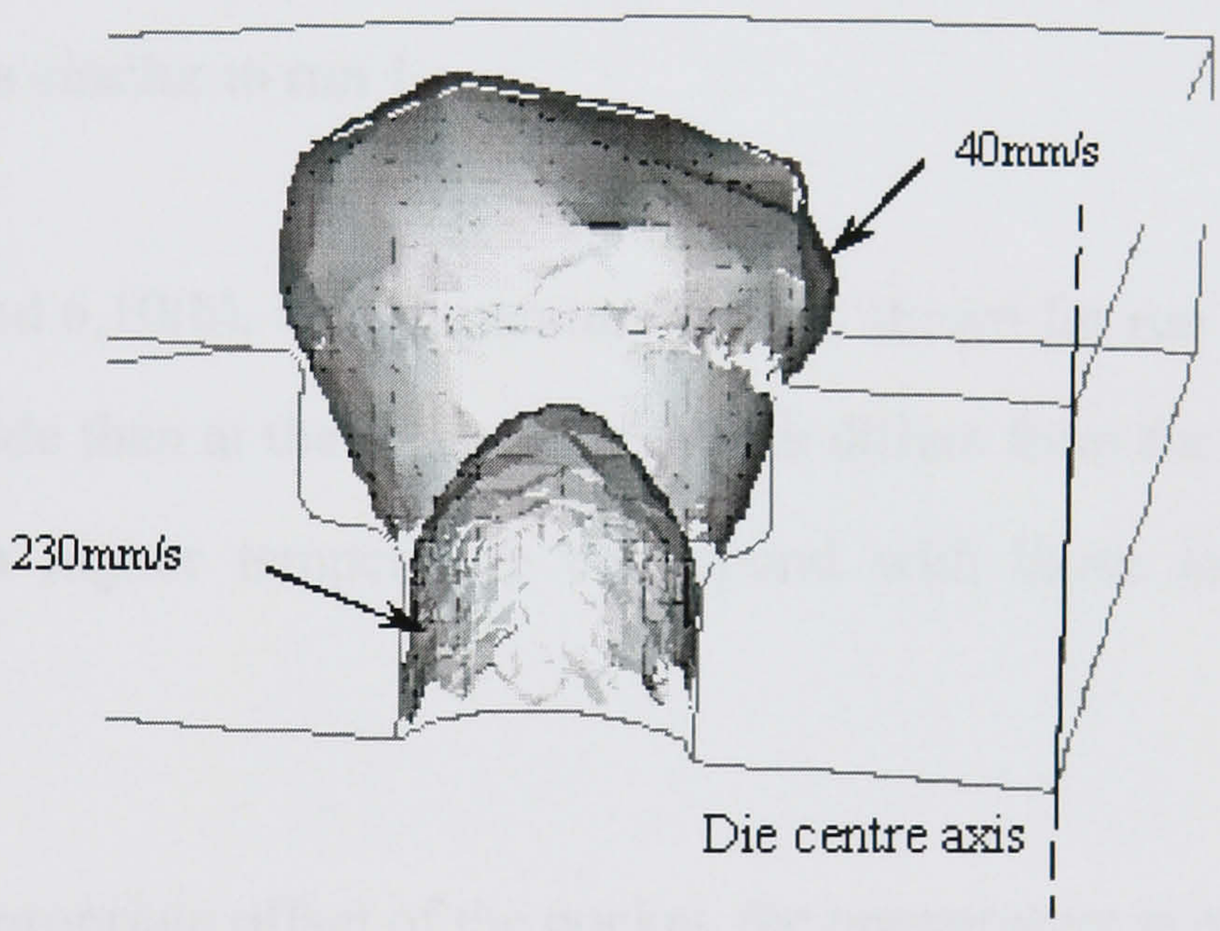

Figure 6.7b Iso-velocity surfaces in run 4 (40mm/sec and 230 mm/sec)

Figure 6.7 FEM simulation output in run 4.

6.1.2 Effect of pocket on temperature rise

It is well known that there is also an intrinsic relationship between the metal flow and the temperature distribution at the deformation area. The more homogeneous flow should lead to a more homogeneous temperature and hence homogenous extrudate properties.

In this section we shall discuss the evolution of temperature throughout the ram stroke as well as the temperature distributions in and surrounding the die and die pocket in the transverse and the cross section of the extrudate. The cross sections discussed have been evaluated on the deletion plane MN which is 0.5mm from the die exit. Similar to the preceding section the data has been extracted after a ram travel of 20mm.

In Figure 6.8(a), the temperature field contour lines are shown for run 1. The temperature distribution on the plane (MN) is shown in Figure 6.8(b). As can be seen from these two figures, the temperature is higher at the M side of the extrudate, in which the flowing velocity is slower.

In Figure 6.9(a), the temperature field contour lines are shown for run 2. The temperature distribution on the plane MN is shown in Figure 6.9(b). The temperature is still higher at the M side, which is similar to run 1.

In Figure 6.10(a) and 6.10(b), the temperature field is shown for run 3. The temperature is higher at the N side than at the M location, which differs from the previous two runs. The locations with higher temperature correspond with those locations where the velocity is lower.

In run 4, with an appropriate offset of the pocket, the temperature is more homogeneous. As can be seen from in Figure 6.11(a) and 6.11(b), both the temperature contour lines and cut plane indicate the temperature is balanced at the M and N side.

The complete histories of the temperature rise at side M and N in run 4 are shown in Figure 6.12, in which the temperatures at the two sides can be seen to equal throughout the extrusion. In contrast, the complete histories of the temperature of M and N in run 1 are shown in Figure 6.13. A temperature difference between M and N side of the extrudate was found throughout the extrusion.

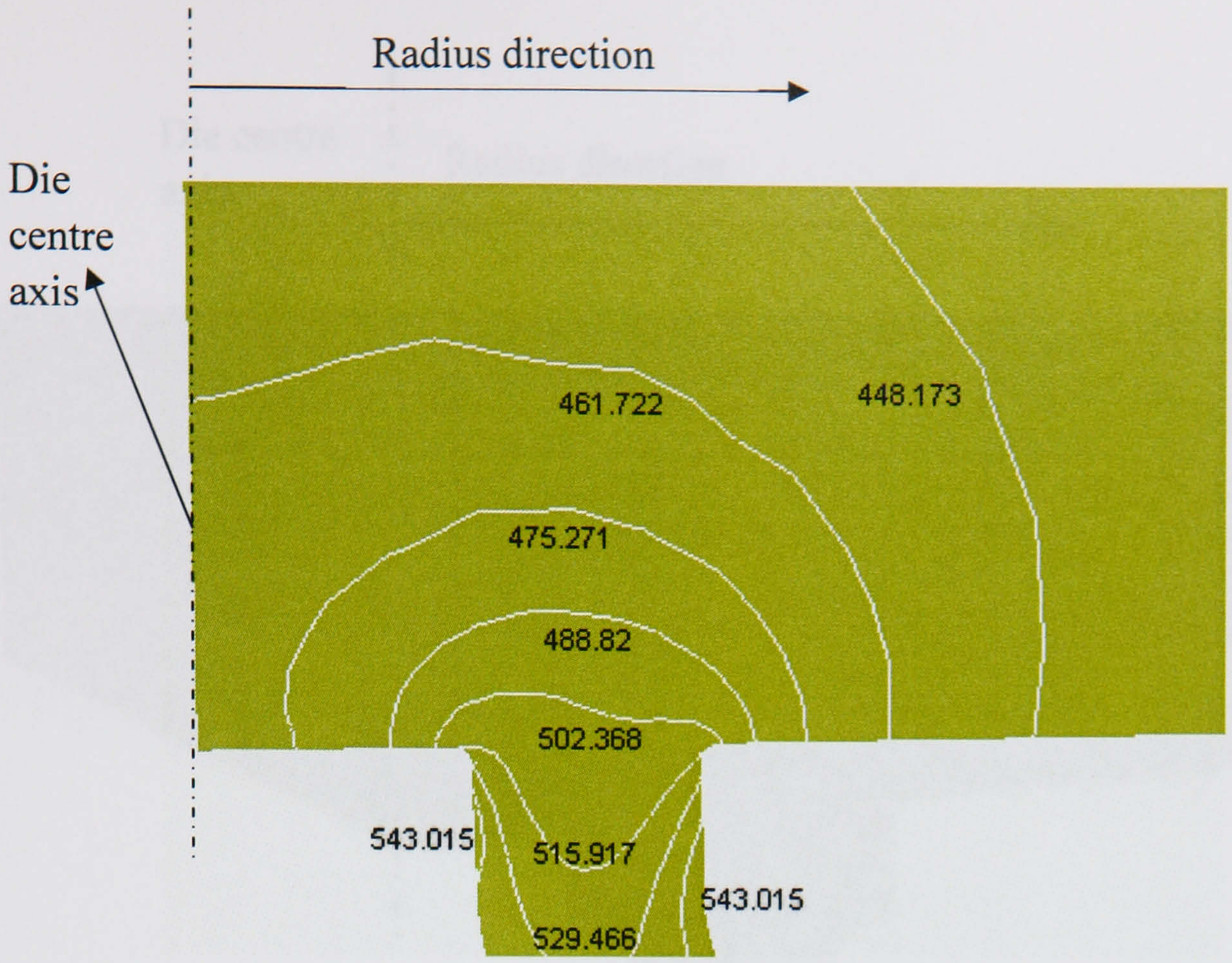

Figure 6.8(a) Temperature contour lines in run 1 (in Celsius)

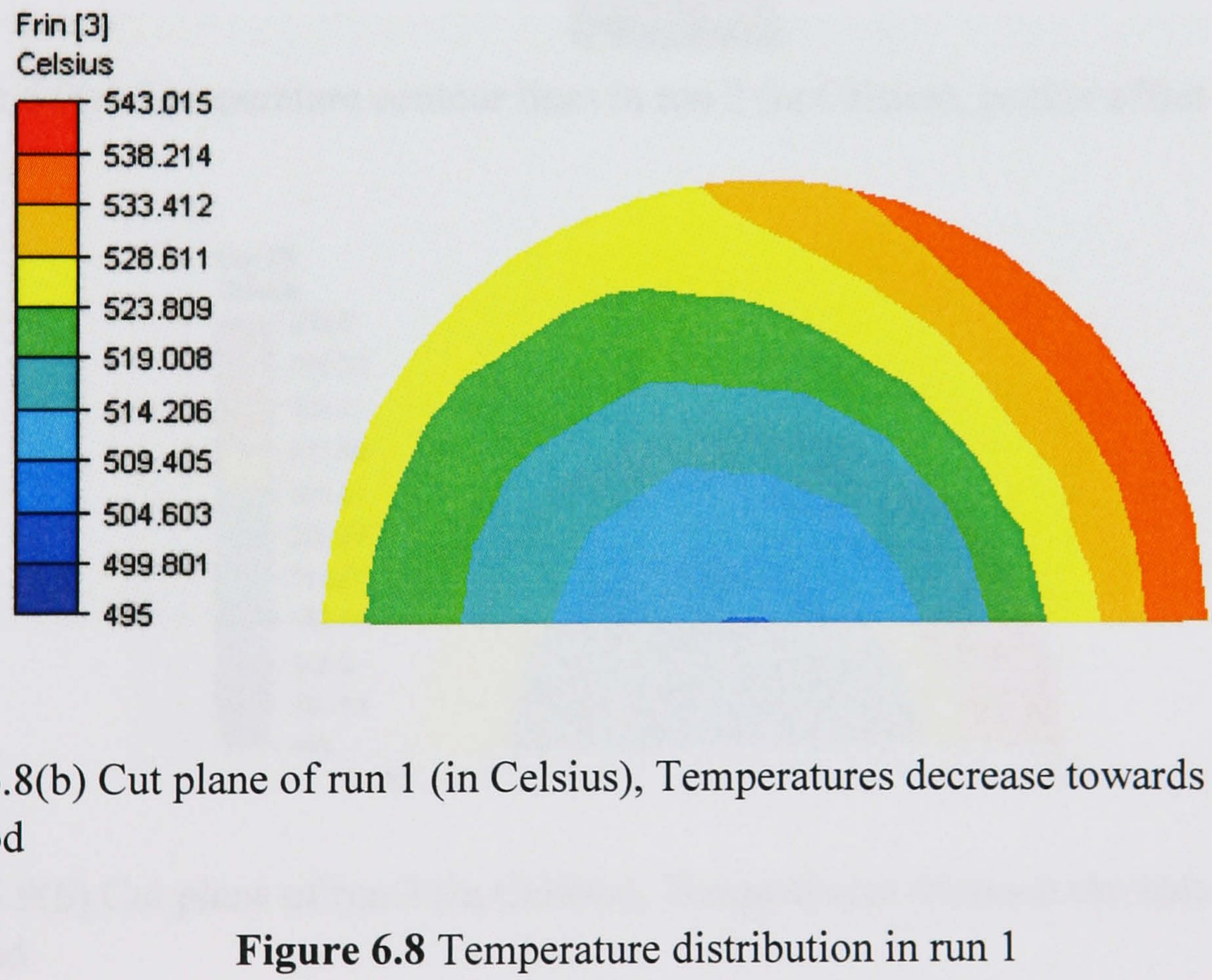

Figure 6.8(b) Cut plane of run 1 (in Celsius), Temperatures decrease towards the centre of the rod

Figure 6.8 Temperature distribution in run 1

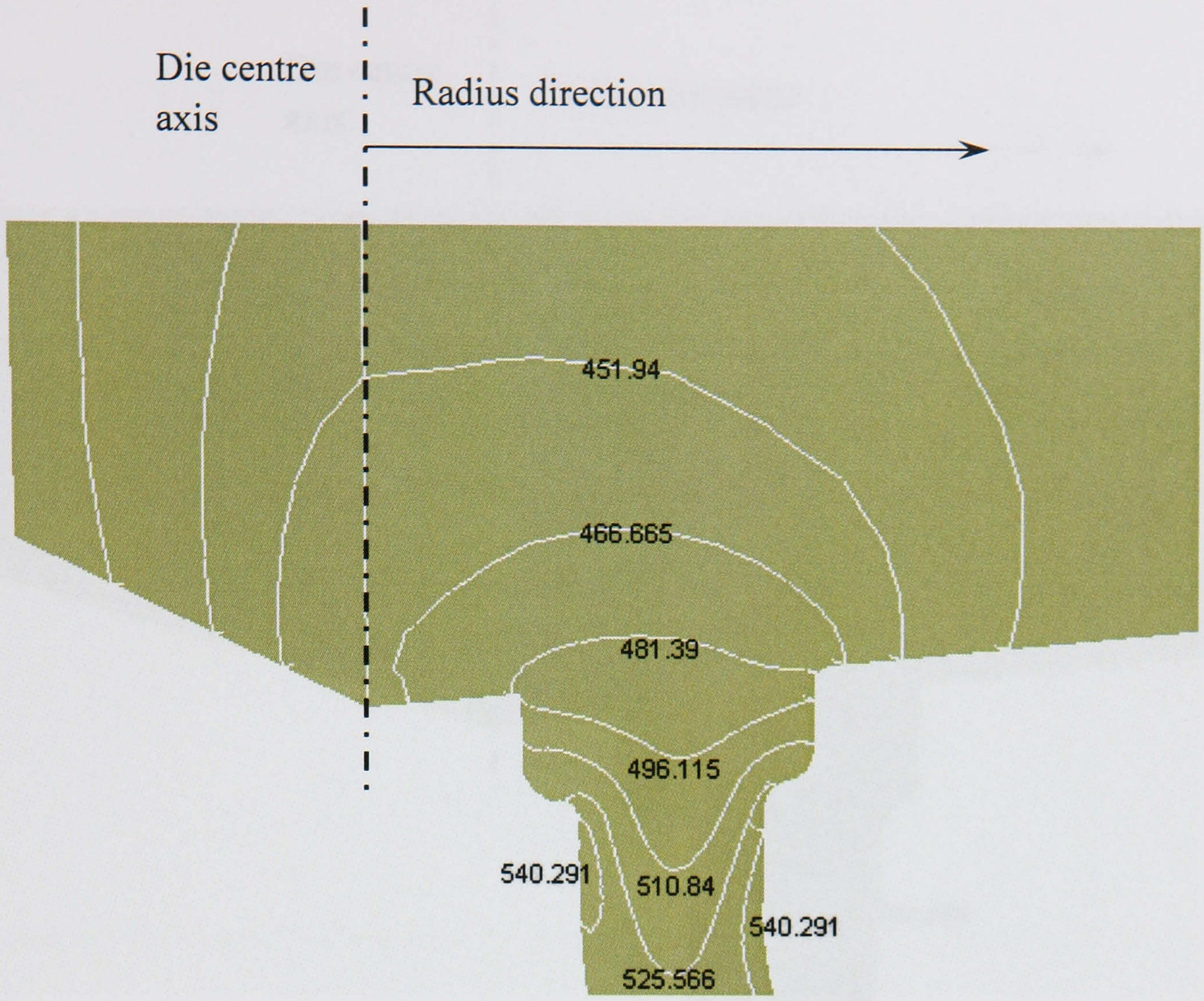

Figure 6.9(a) Temperature contour lines in run 2 (in Celsius), pocket offset *C*=0mm

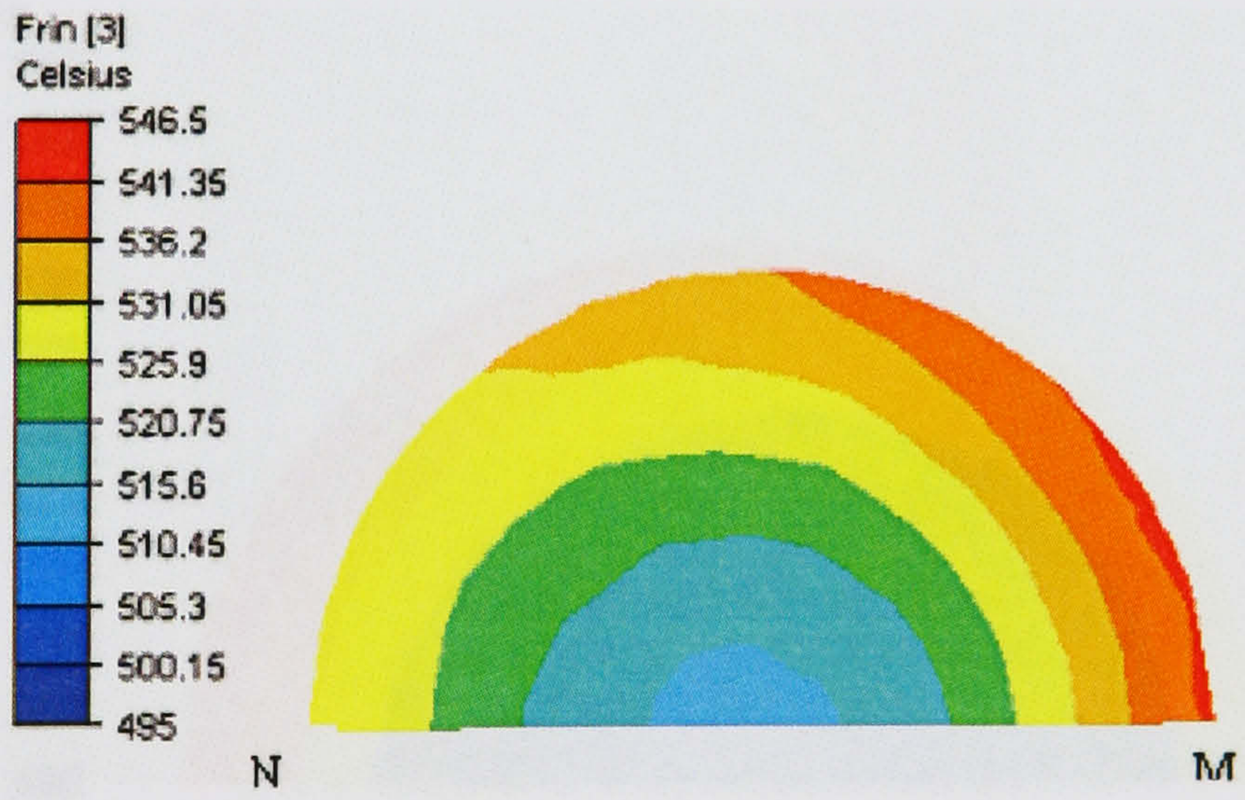

Figure 6.9(b) Cut plane of run 2 (in Celsius), Temperatures decrease towards the centre of the rod

Figure 6.9 Temperature distribution in run 2.

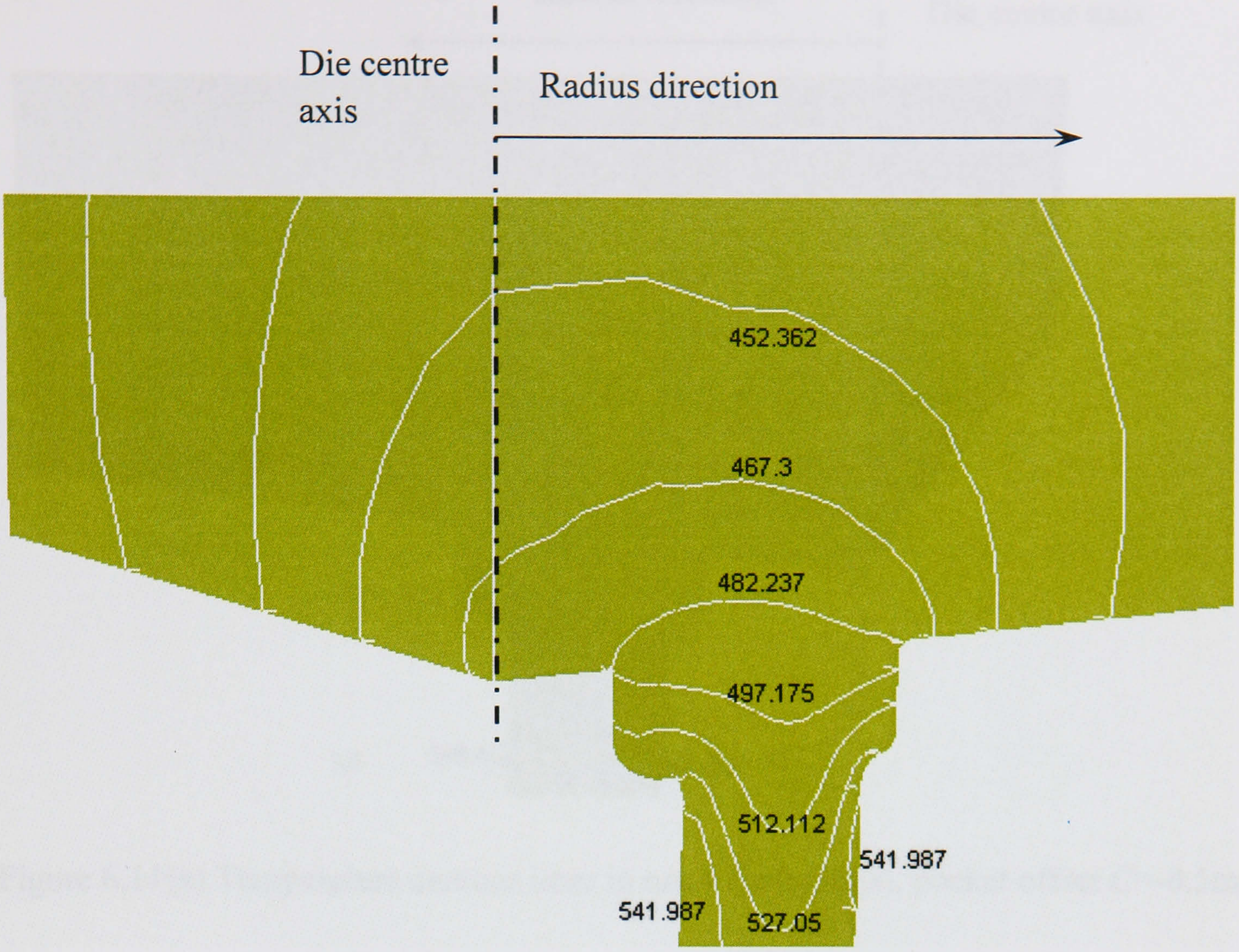

Figure 6.10(a) Temperature contour lines in run 3 (in Celsius), pocket offset C=+0.5mm

Figure 6.10(b) Cut plane of run 3 (in Celsius), Temperatures decrease towards the centre of the rod

Figure 6.10 Temperature distribution in run 3.

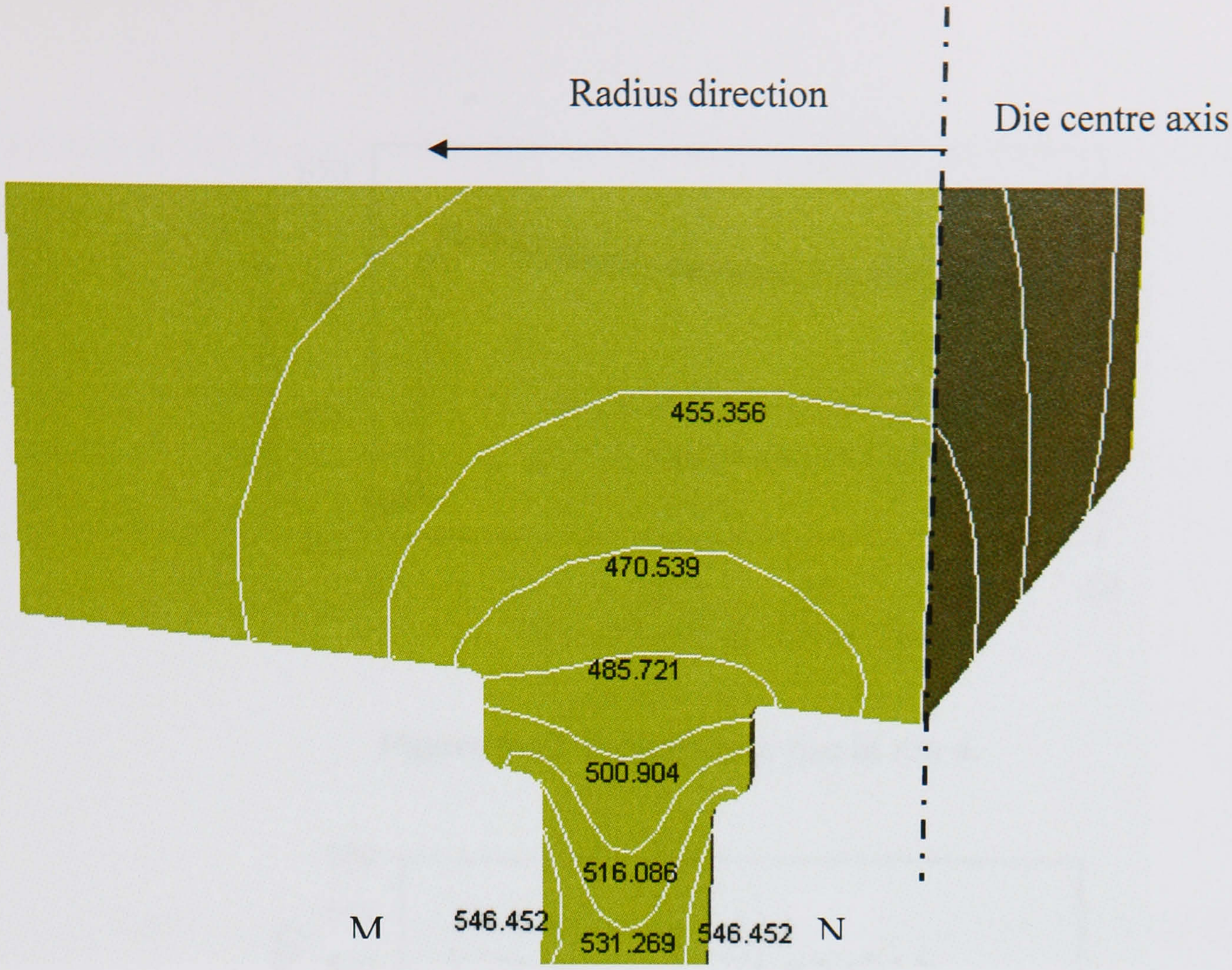

Figure 6.11(a) Temperature contour lines in run 4 (in Celsius), pocket offset *C*=-0.5mm

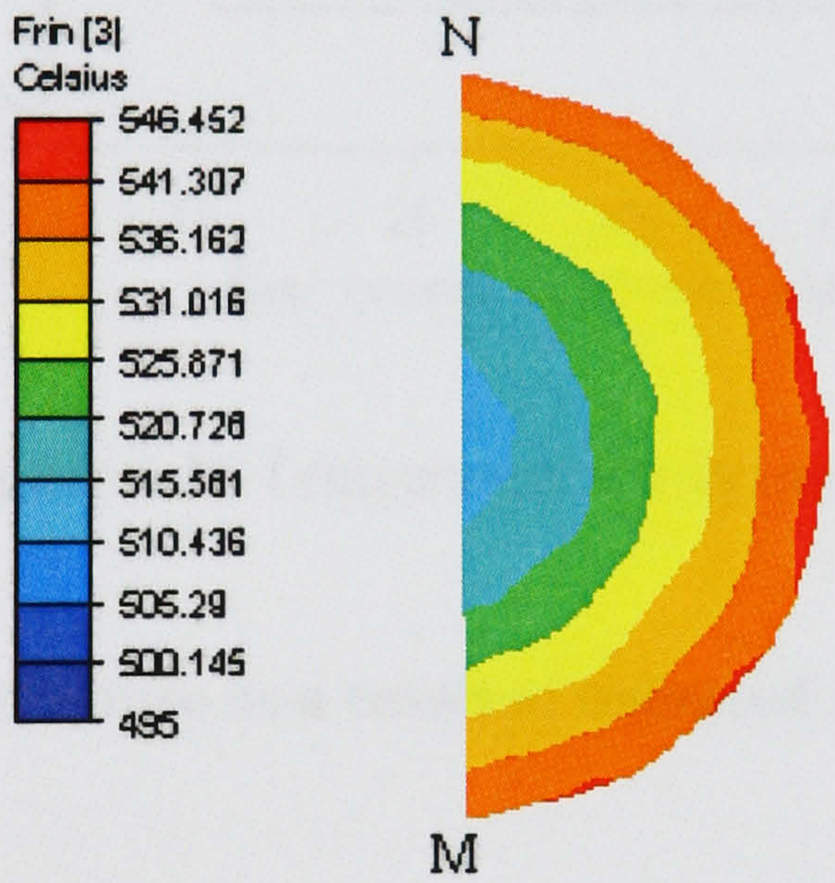

Figure 6.11(b) Cut plane of run 4 (in Celsius), Temperatures decrease towards the centre of the rod

Figure 6.11 Temperature distribution in run 4.

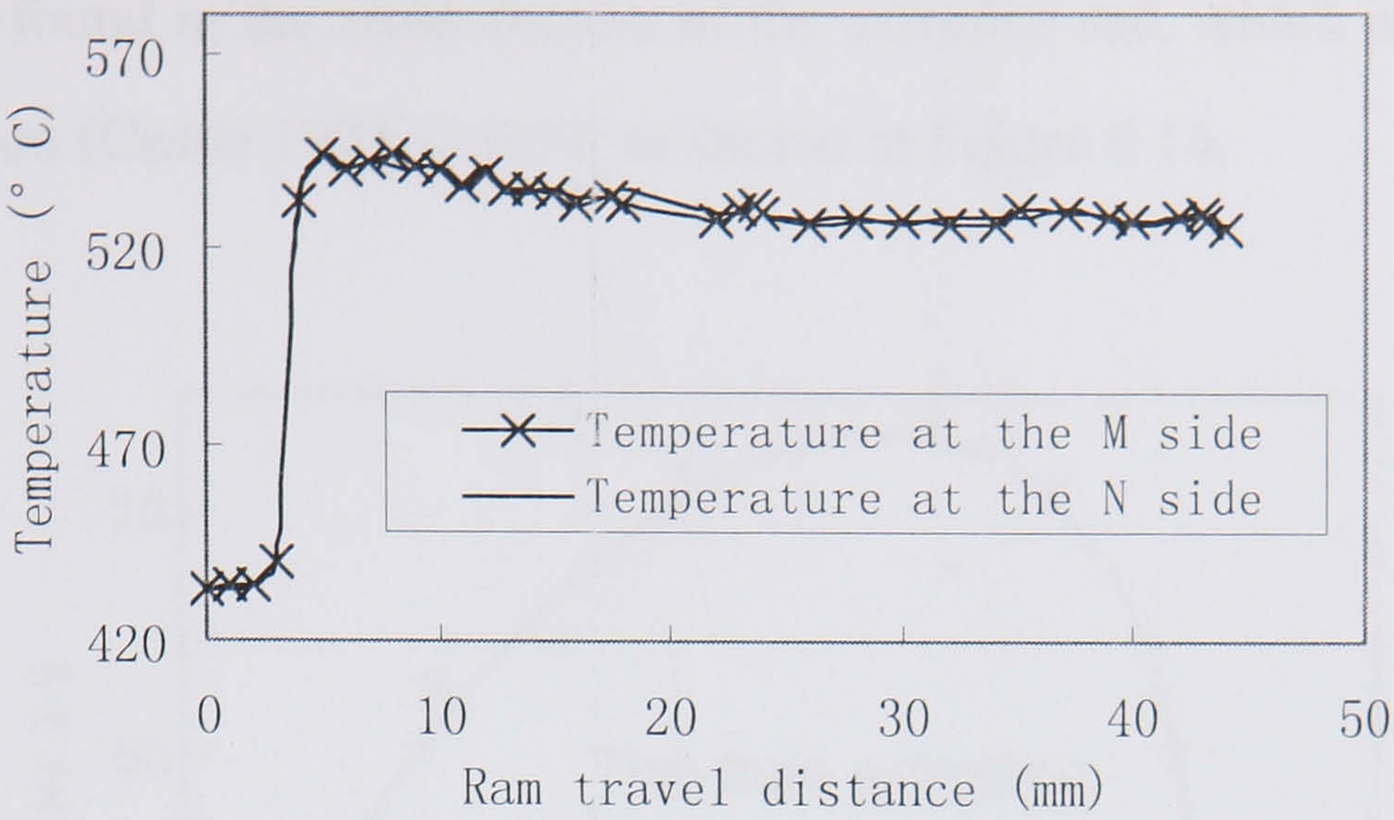

Figure 6.12 Temperature rise in run 4.

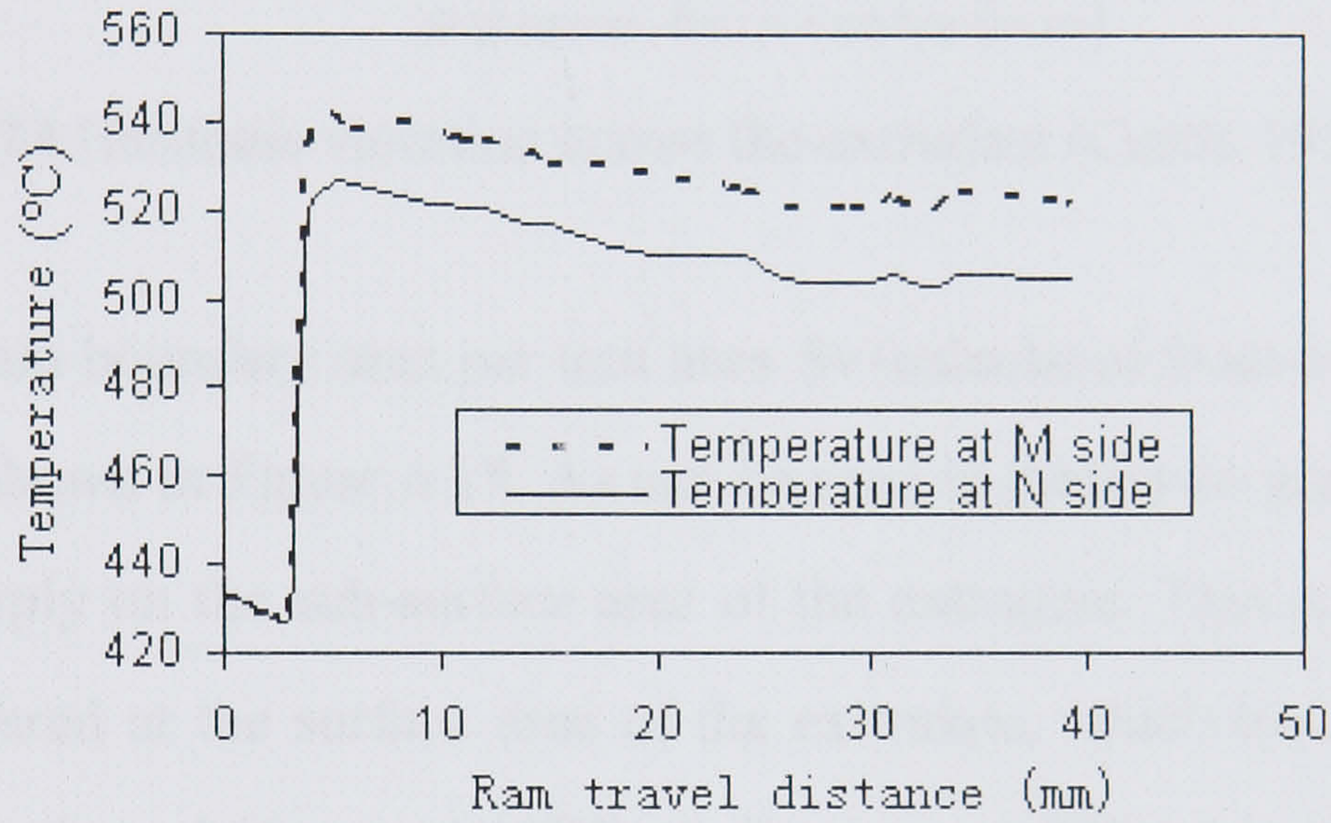

Figure 6.13 Temperature rise in run 1.

6.1.3 Homogeneous substructure as a result of balanced material flow

The discussions above indicate that, in run 4, the material flow is more balanced. The temperature and hence we assume the substructure distribution in the extrudate of run 4 have been proved to be more homogeneous than the other runs. However, the most important properties of the extrudate depend on the structure and substructure. Although over the range of flow stress studied no clear variation in mechanical properties within experimental error, between the multi-hole extrudates (two extrudates from different holes) was found, the properties within and across an extrudate are indeed influenced by the eccentricity. Direct evidence has already been shown in Figure 6.1. A variation of

hardness is also found in the cross-section of the extruded rod, which is produced from two hole extrusion (Castle 1974, p.169), as shown in Figure 6.14.

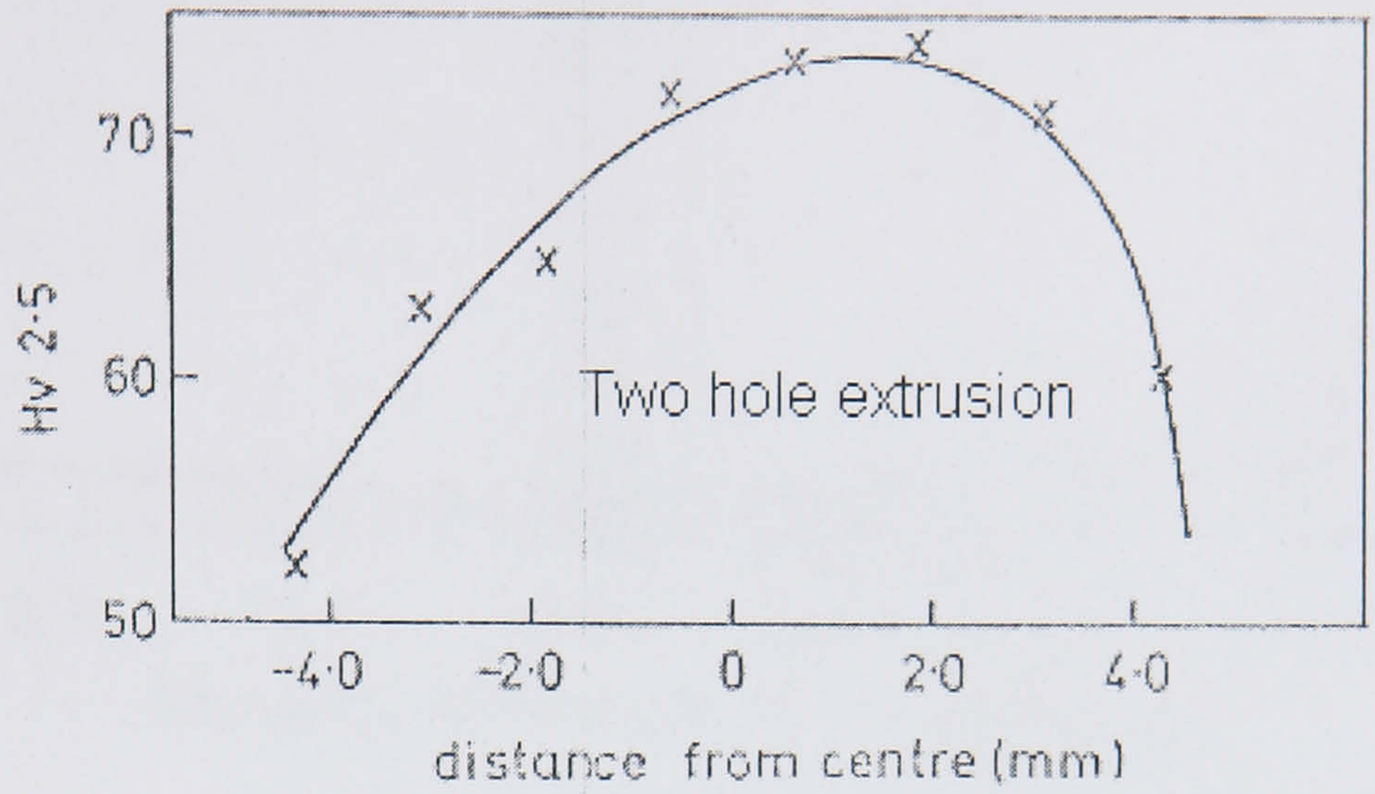

Figure 6.14 Hardness variation across the extrudate (Castle 1974, p.169)

The values of grain boundary area per unit area Sv (calculated from equation 2) across the extrudate is shown in Figure 6.15. As can be seen in these two graphs, the value of Sv increases sharply on the sub-surface area of the extrudate. This is due to the shear deformation suffered at the surface area of the extrudate, which has been reported in many studies (Castle and Sheppard 1976). Aukrust etc. (1997) also give a quantitative study of the sheared surface of aluminium extrudates.

In the analyses performed by Aukrust, a transition from grains that are lamella to the point at which the lamella structure is broken up was found. It was reported to take place about 200 μm below the surface. Results in another experiment carried out by the same author reported that the transition from a bulk region with a rolling type of texture to a surface boundary layer with shear type of texture takes place between 400 μm and 165 μm . The main component of the texture in the surface in both experiments mentioned above is close to (113)[332], which corresponds to the idealised shear texture, the skew cube (001)[110], rotated approximately 25° about the transversal axis.

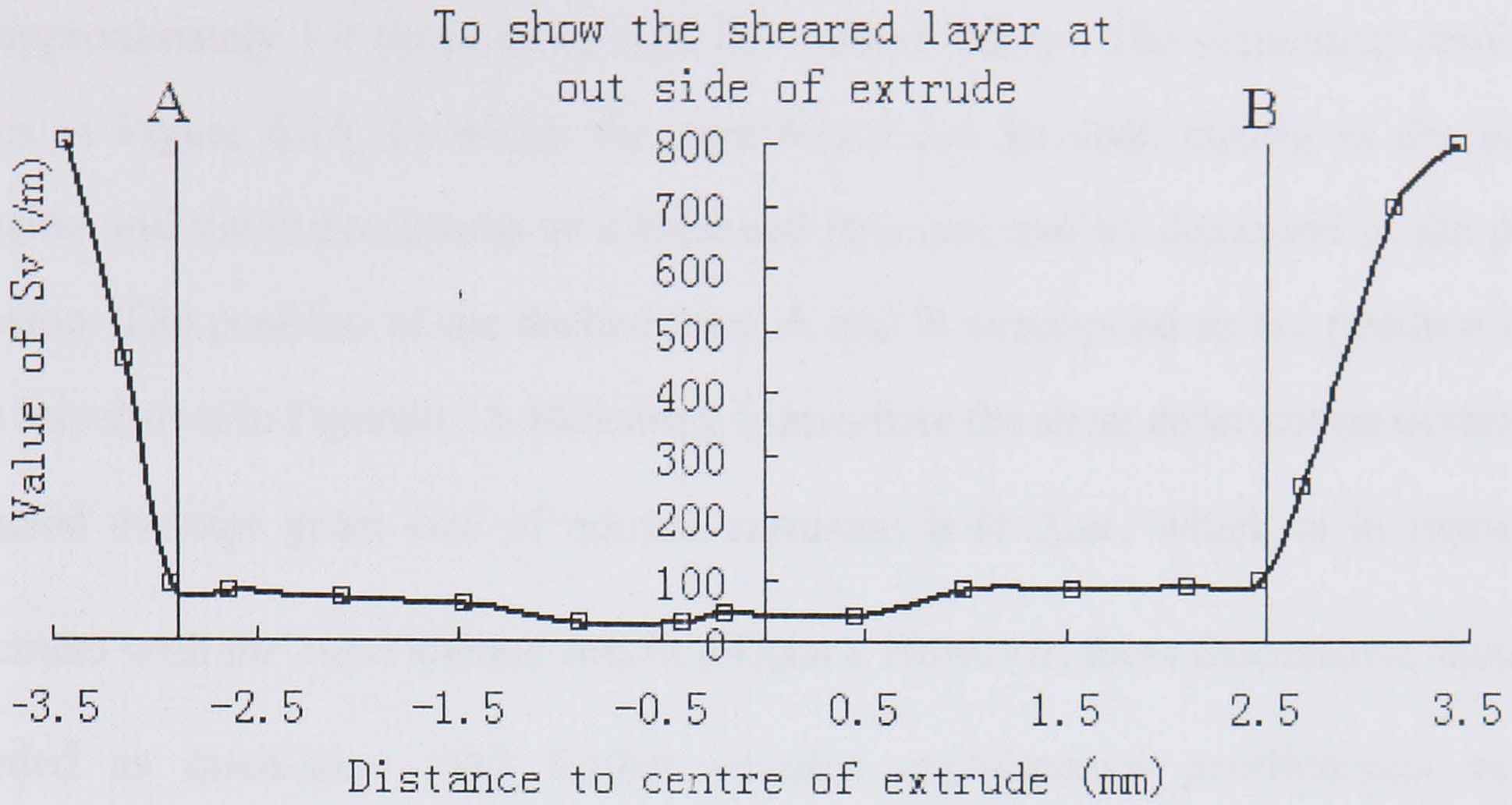

Figure 6.15 The sharp increase of Sv at the subsurface area

In the present study, the transition points discussed above are found to locate below the surface approximately at 500μm at the N side and 900μm at the M side, due to the asymmetric nature of two-hole die extrusion, where the sharp rise of Sv occurs (marked as the cross point between the curve of Sv and straight line A and B individually) as shown in Figure 6.15.

According to the physically based model, the density of nucleation sites is much higher and the recrystallised grain size is therefore expected to be smaller at this subsurface volume under shear deformation than the volume below. However, in experiments, this phenomenon has not been observed, only a relatively small decrease of the grain size was found in this area. Two facts could lead to this phenomenon: one is that the physically based model needs to be improved to predict the recrystallisaton in extremely sheared structures, and the second is that secondary recrystallisation is likely to occur in this special area. However, with the lack of experimental evidence, it is difficult to make any conclusion.

According to the experiments (Vierod 1983), the nuclei number at this surface volume was approximately 1.4 times more than the volume below. The simulation results are shown in Figure 6.16, in which the asymmetry can be seen clearly in the normal extrusion and the improvement to a balanced structure can be discerned in the pocket extrusion. The position of the dashed lines A and B correspond to the position of the same line shown in Figure 6.15, indicating from where the shear deformation occurs. The predicted average grain size of normal extrusion is $41.2\mu m$, which is in reasonable agreement with the experimental results ($43\mu m$). However, these discussions should be regarded as qualitative until further detailed experimental justifications become available.

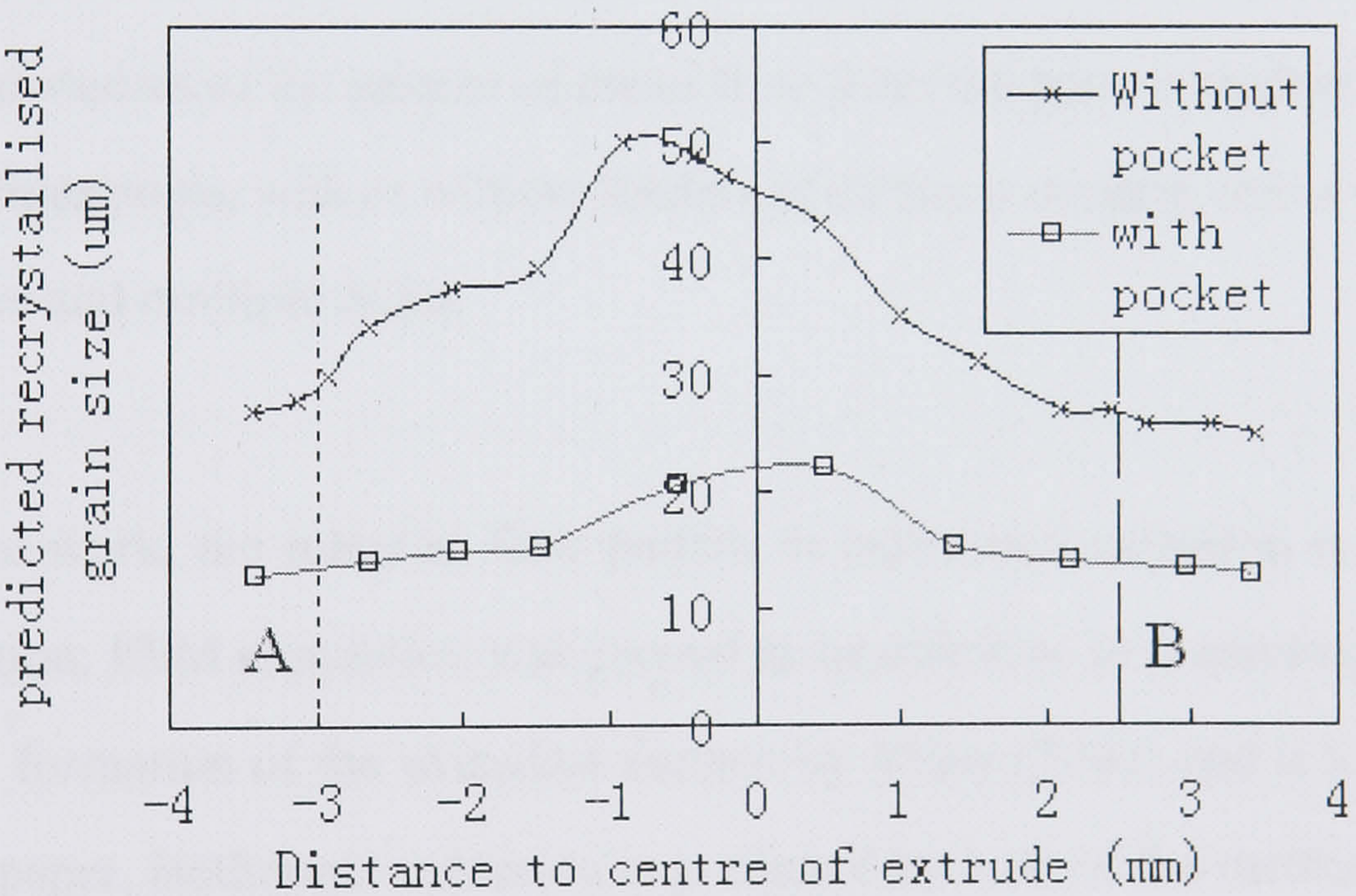

Figure 6.16 Recrystallised grain size

6.2 Isothermal extrusion

Although there are many benefits that could be attained, there are also some uncertainties with regard to isothermal extrusion. It was pointed out by Pinkham (2002) that "If the velocity gradient varies it could cause a part to bend or twist, thereby creating stresses and this is also true for variations in temperature. Hence it is important to understand how the material flows through the die. The material flow pattern has been studied previously by many experiments, but among them there are few concerning material flow in isothermal extrusion. Valberg (1986) discussed the formation of the outer surface layers of the extrudate in direct and indirect conventional extrusion based on the advanced grid pattern technique. Complex effects were found and reported by Akeret (1988) and Valberg et al. (1995). For the modelling of isothermal extrusion, Hardouin studied (1992) die design by starting from classic plasticity theory and taking account of temperature/strain rate-dependent criteria linked to those of Tresca and von Mises. He made detailed studies of the pattern of metal flow from the press container through dies of many configurations, with or without feeders of different designs, into a wide range of section shapes and multiple holes.

In the present work, the material flow pattern in isothermal extrusion is produced by FEM simulation. FEM simulation was proved to be effective in predicting the material flow and the formation of the extrudate surface by Velay (2003) and it is not repeated here. In this paper, isothermal extrusion is predicted by both of the methods mentioned above.

The material flow pattern and the formation of the extrudate surface are shown by the output of the simulation. The influence of the tapered billet and the varying ram speed on the flow pattern during extrusion is discussed in detail. All of the simulations were performed to the very end stage of extrusion. The temperature history and the load-time history are extracted to assist in understanding of the isothermal extrusion process.

The simulation process used in this study is shown in Table 6.2. The billet length is 95mm. The extrusion ratio is 30.

Table 6.2 Process parameter for FEM model

RUN	Extrusion mode	Initial billet temperature (C°)	Container temperature (C°)	Ram speed (mm/s)
1	Conventional	530	580	10
2	Tapered billet	530(front)-495(back)	580	10
3	Vary ram speed (1)	530	580	10 (initial)
4	Vary ram speed (2)	530	580	10 (initial)

Run 1 is a conventional extrusion, Run 2 is an isothermal extrusion established by employing a tapered billet, in which the temperature decreases non-linearly from the front of the billet to the end. The temperature field is set up by the software and the distribution can be seen in Figure 6.17. The maximum temperature is 542°C and the minimum is 520°.

In Run 3, the ram speed is controlled by the FEM program according to the maximum allowed exit temperature, which is set at $565^{\circ}C$. When the exit temperature falls under the pre-set allowed temperature, the ram speed will be increased and when the exit temperature exceeds the upper limit, the program will decrease the ram speed to keep the exit temperature at approximately $565^{\circ}C$.

In Run 4, the ram speed at different stages was determined according to the ram speed history in Run 3. The detail of the experiment will be discussed later.

The hyperbolic sine function was integrated into the FEM to describe the material behaviour. For aluminium alloy AA6063, the constants used in equation 3.12 are:

ΔH =144408KJ/mol, α =0.0152 m^2 / MN , n=5.27, LnA= 24.41 (Sheppard and Jackson 1997). .

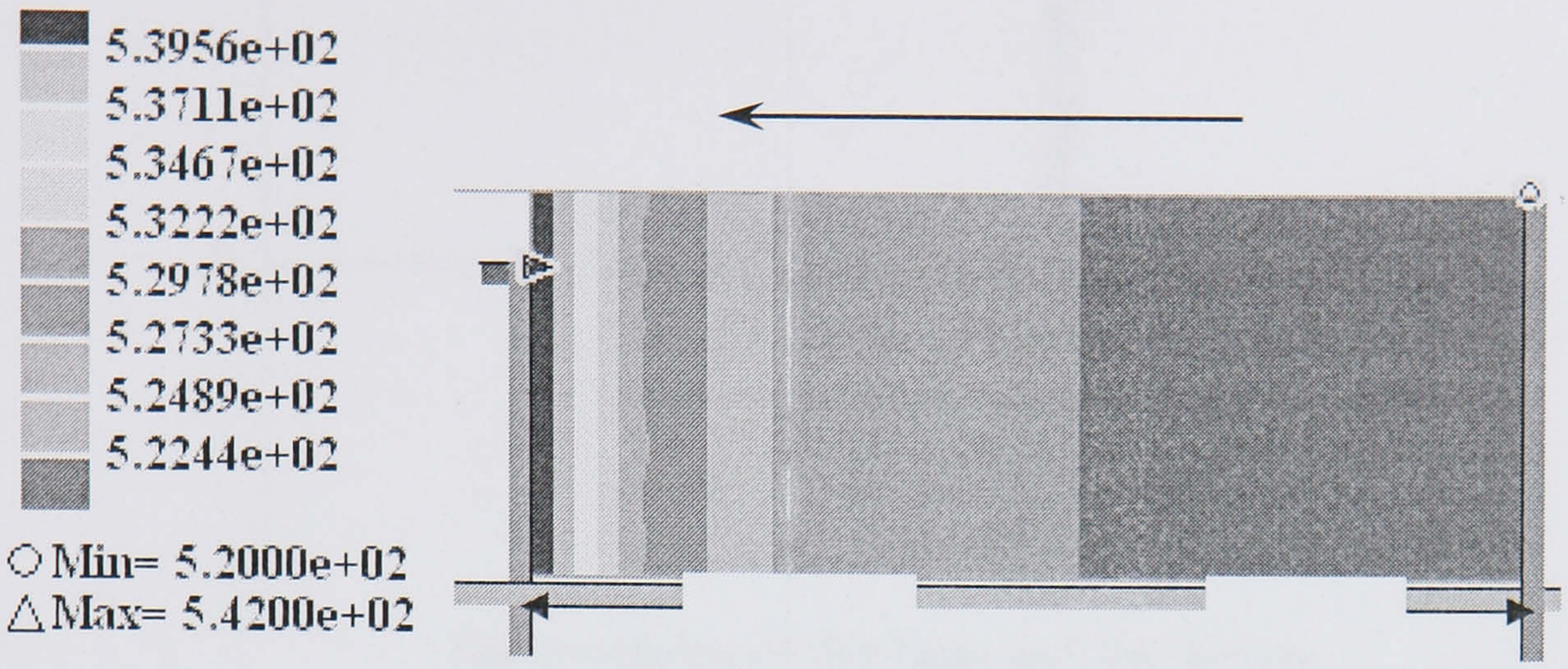

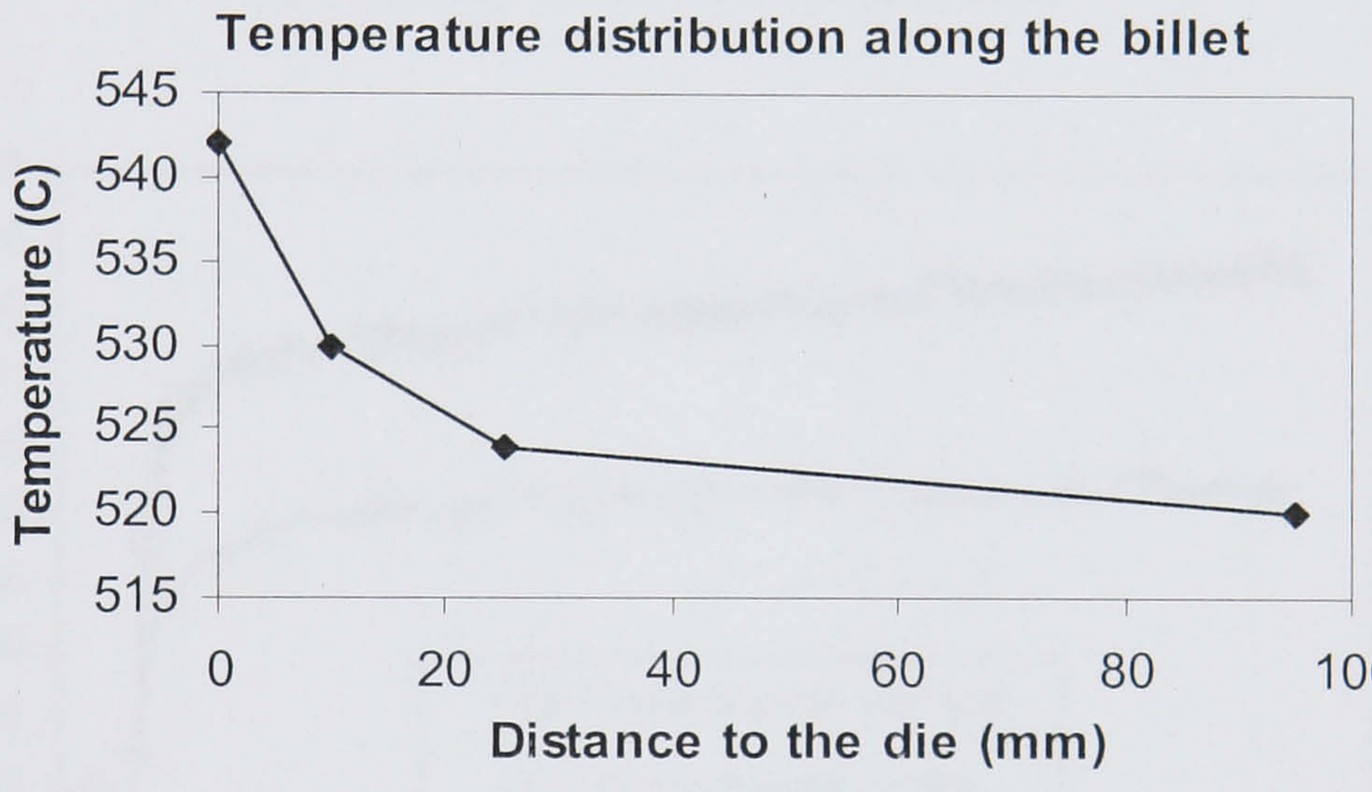

Figure 6.17 Temperature distribution

6.2.1 Effect of isothermal extrusion on temperature rise and load

In this study, both of the two methods mentioned above were adopted to establish isothermal extrusion. The nomenclature used in the regions near the die land is shown in Figure 6.18. The positions of the points that will be used in the following discussion are also shown in this picture.

The temperature evolution at the extrudate centre and surface (extracted from the centre point and the side point, as shown in Figure 6.18) of the first three extrusions shown in Table 6.2 can be seen in Figs 6.19-6.21.

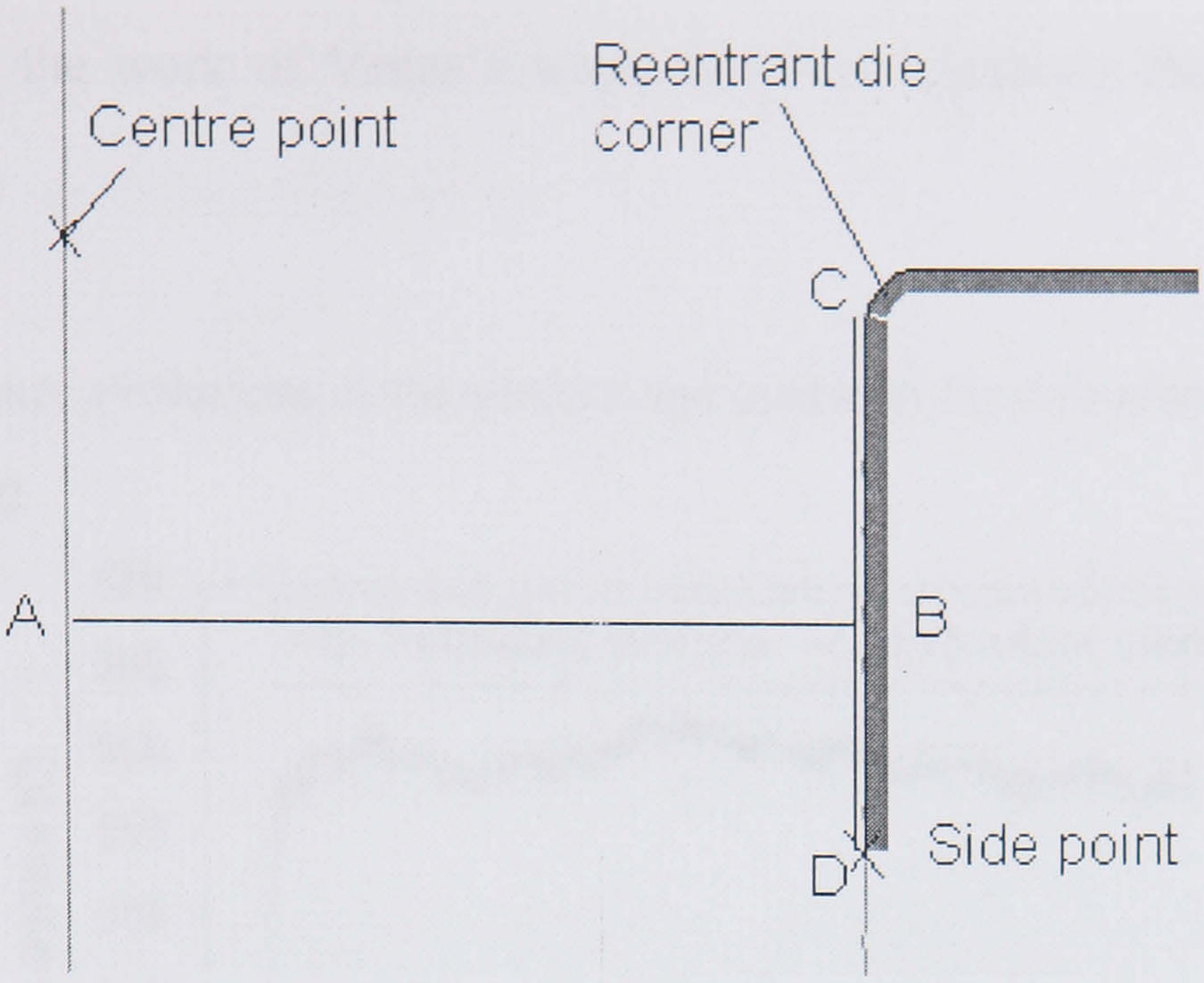

The positions of the lines and the points

Figure 6.18 The deformation area

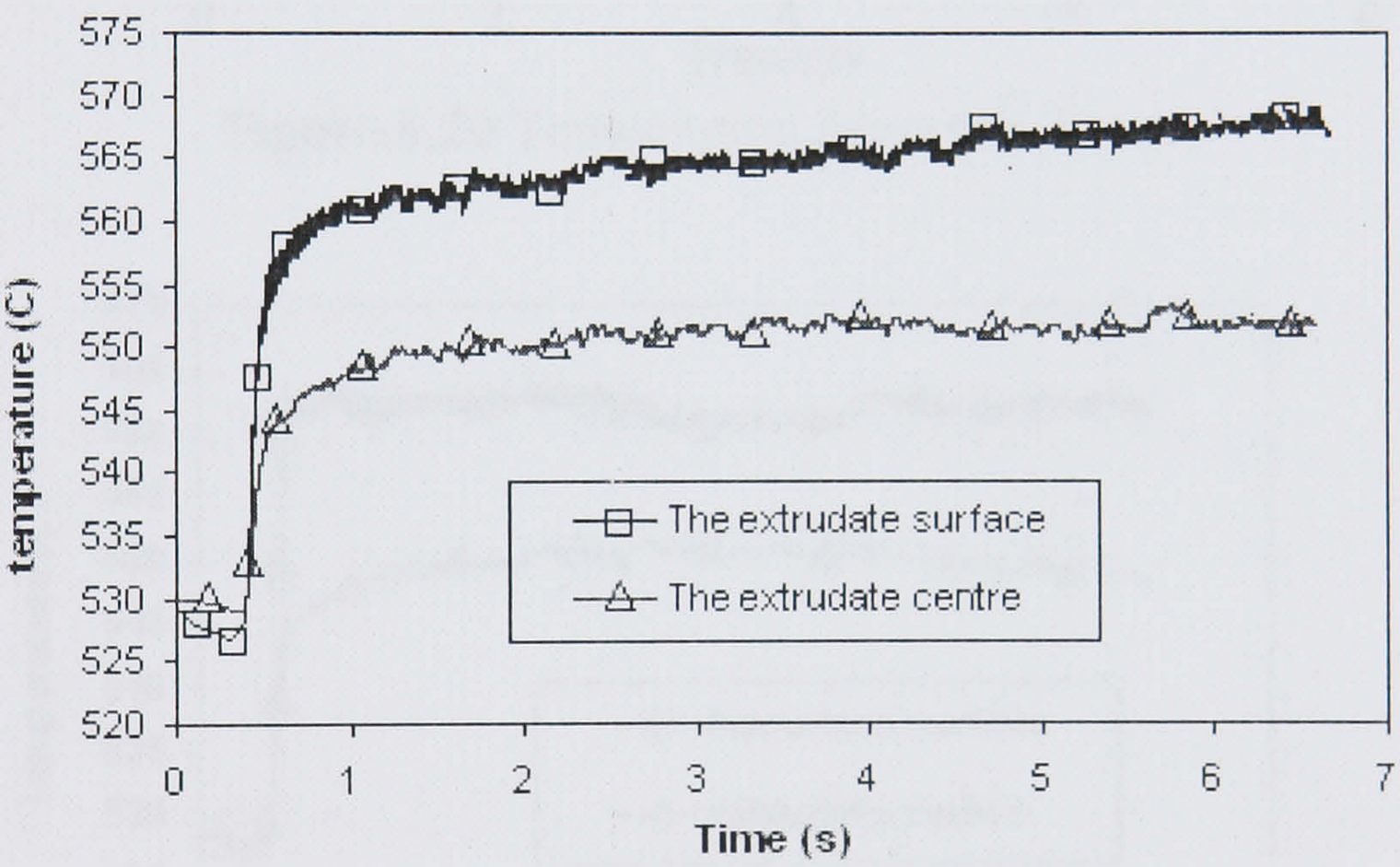

Figure 6.19 Temperature history in Run 1

As can be seen in Figure 6.19, the temperature rises throughout conventional extrusion.

On the surface, the temperature rises from 530 $^{\circ}C$ to 570 $^{\circ}C$ gradually and at the extrudate centre, it rises from 530 $^{\circ}C$ to 550 $^{\circ}C$. The temperature difference between the surface and the centre of the extrudate remains at approximately 15 $^{\circ}C$ throughout the extrusion. This phenomenon had been reported previously by Herberg (1993), where the difference was found to be 60 $^{\circ}C$. Because the billet size used in this study was quite different to that

employed in the work of Venas's work, it is not surprising that the values do not coincide.

The temperature evolutions at the surface and centre of the extrudate in Run 2 are shown in Figure 6.20.

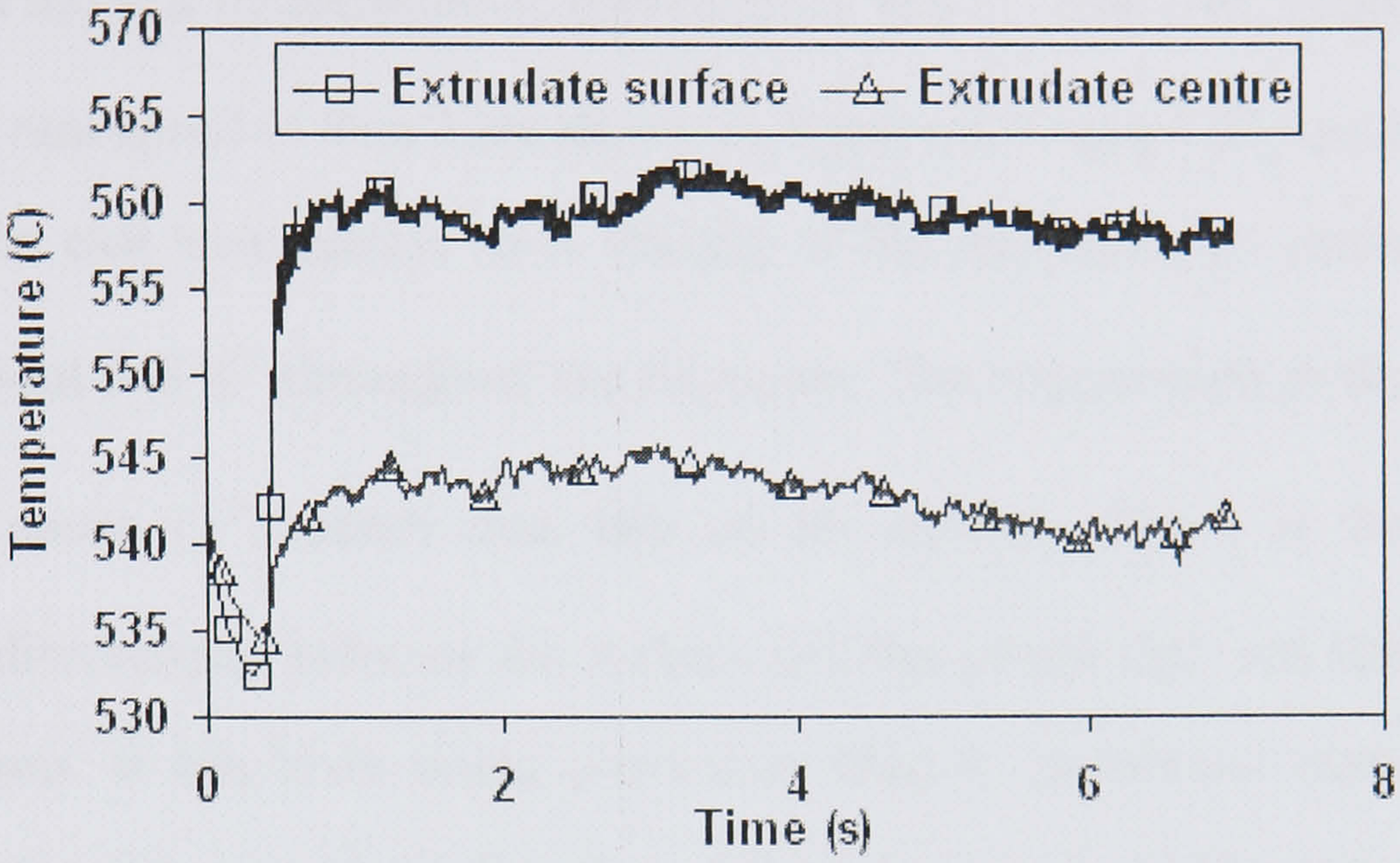

Figure 6.20 Temperature history in Run 2

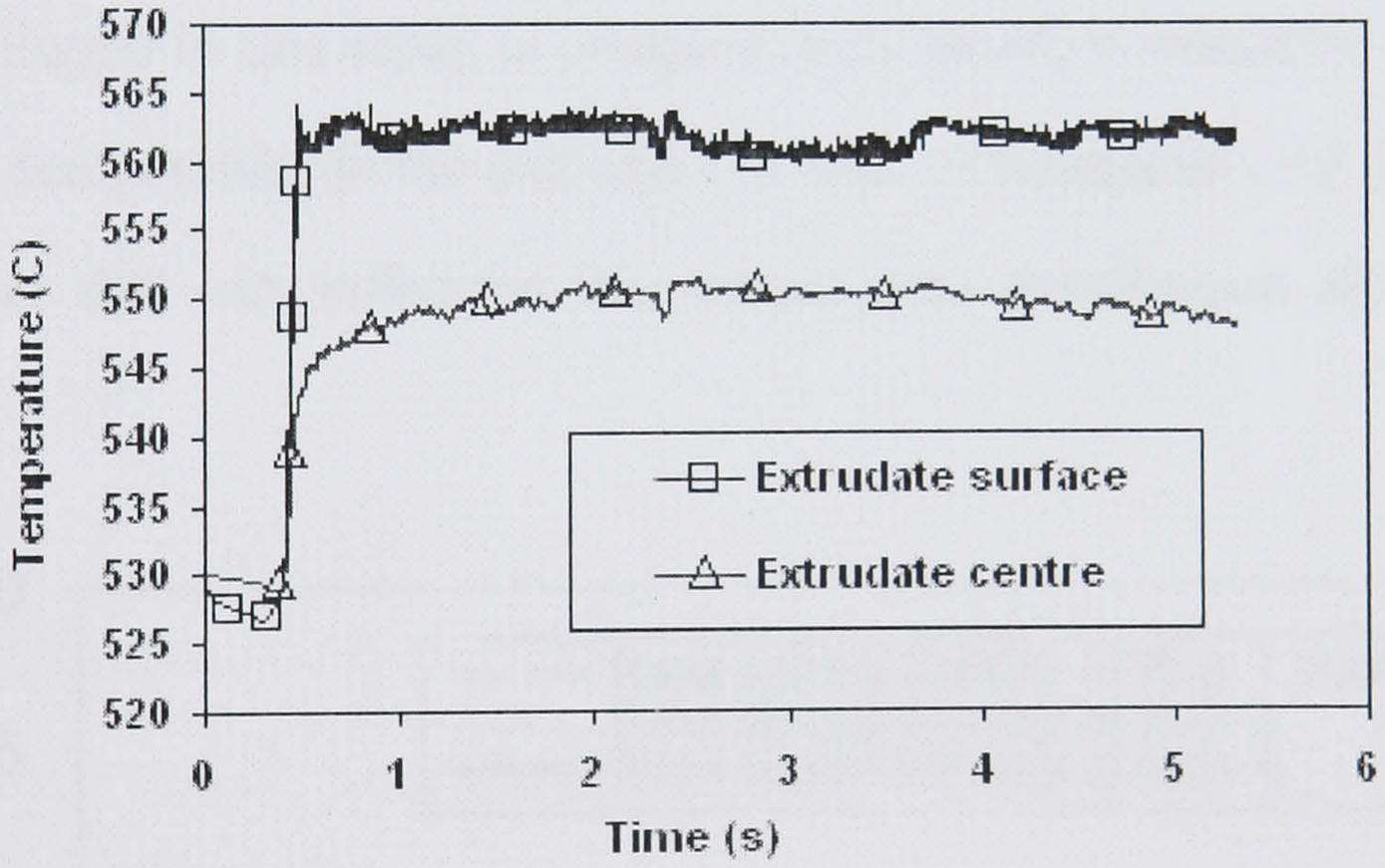

Figure 6.21 Temperature history in Run 3

The temperature rises to $562\,^{\circ}C$ at the surface at the beginning of extrusion, then it remains approximately unchanged until the end of extrusion. As in the conventional extrusion, the temperature on the surface is approximately $15\,^{\circ}C$ higher than that of the centre point throughout the extrusion.

Isothermal extrusion was also simulated utilising the varying speed method in Run 3. In this run, the maximum allowed exit temperature is set at 565 $^{\circ}C$. When the exit temperature is lower than the pre-set temperature, the ram speed will be increased until the exit temperature exceeds the upper limit, and then the program will decrease the ram speed to keep the exit temperature at approximate 564 $^{\circ}C$. The exit temperature and the history of the ram speed of Run 3 are shown in Figures 6.21 and 6.22 respectively. At the side point, the exit temperature rises sharply at the beginning of extrusion and then remains at about 565 $^{\circ}C$ throughout the extrusion. The temperature at the centre of the extrudate is about 15 $^{\circ}C$ lower than that on the surface, which is the same as the temperature discrepancy between the surface and the centre that was found in the first two simulations. It has been stated previously that, in isothermal extrusion, the exit temperature along the transverse direction of the extrudate should be more homogenous, but it is obviously not the case in the present study. Because the dimension of the extrudate employed in this study is comparatively small, it would be of great interest to study the exit temperature in the extrusion of rods of comparatively larger size and find out the factors that can influence the temperature distribution along the transverse direction.

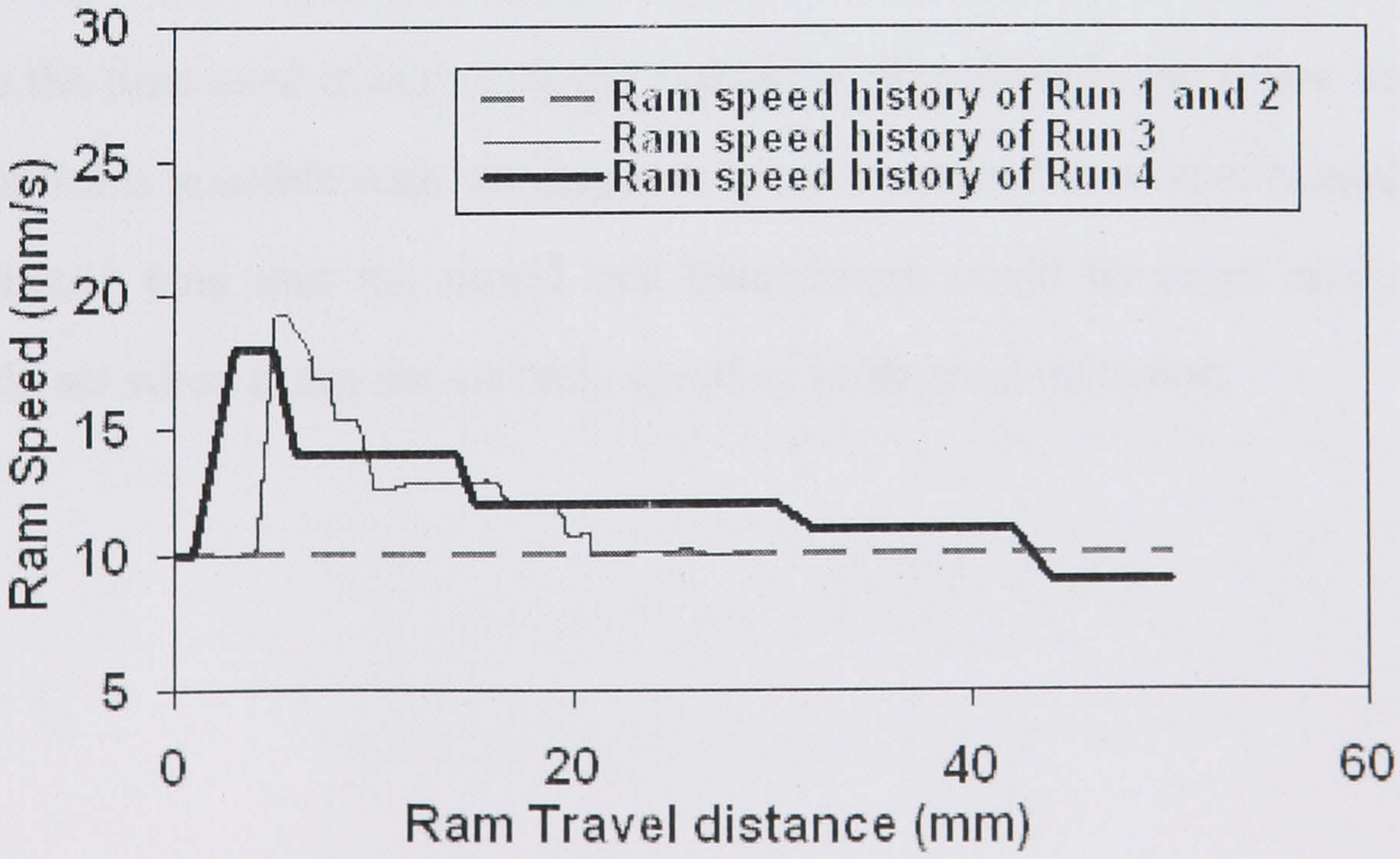

Figure 6.22 Ram speed history

We should note that there is a significant difference between the surface and centre temperature since it is the surface temperature but not the average exit temperature that is critical for surface failure such as cracking.

As for the ram speed history in Run 3, the initial ram speed was 10 mm/s and was increased to 19.4mm/s at the beginning of extrusion. Then the ram speed was decreased to lower speeds gradually to 9.4 mm/s. The extrusion time for the ram travel of 70 mm is about 5.3 seconds, which is much less than in the iso-speed extrusion (7 seconds). This has been discussed frequently and is regarded as one of the benefits of isothermal extrusion.

Depending on the simulation output of Run 3, a different ram speed setting, which is varying in a non-continuous manner, was developed. The initial ram speed applied was 10mm/s over a ram displacement of 3mm (upsetting stage). Then it was increased to 18mm/s and subsequently decreased to 11.5 mm/s and finally to 9.0mm/s. The profile of the ram speed varying with ram travel distance is shown in Figure 6.22. The temperature rise during this simulation was similar to Run 3, which is shown in Figure 6.23. The peak temperature remains at $565^{\circ}C$ and the centre temperature is still $15^{\circ}C$ lower than the surface temperature. The total extrusion time is about 5.1 seconds, which is also much less than the time used in conventional extrusion. Significantly the figure indicates that better control is possible with varying ram speed compared to a taper heated billet. The reader should note that the actual exit temperature could be more easily and more accurately set when using the variable speed of isothermal extrusion.

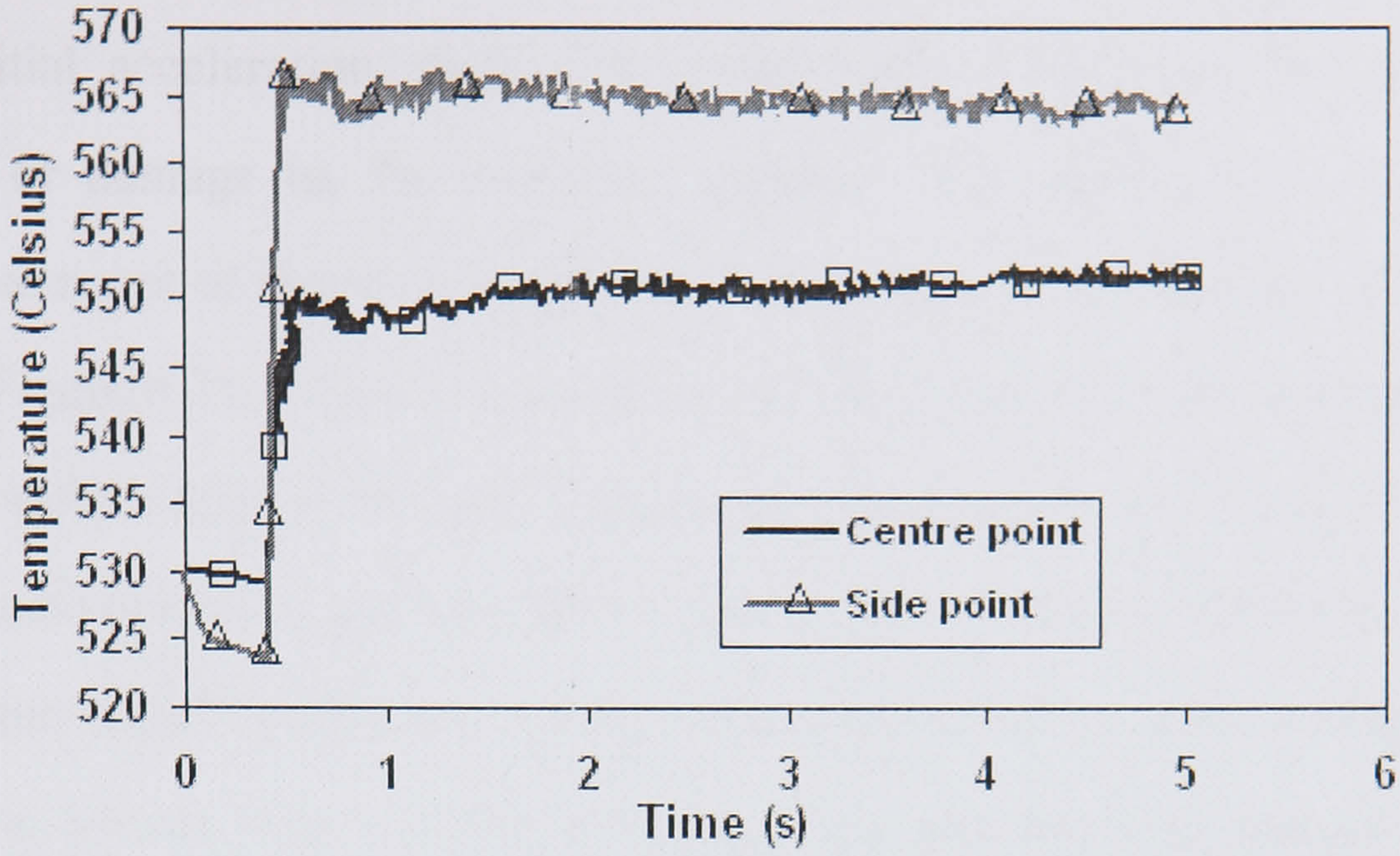

Figure 6.23 Exit temperature evolution in Run 4

The load on the ram, the container and the die of the Run 3 is also shown in Figure 6.24. The Friction force, which is caused by the friction between the container and the billet, decreases gradually during the extrusion with the decreasing of contact area. This simulation result corresponds well with previous studies and experiments (Renne and Sumarokova 1989).

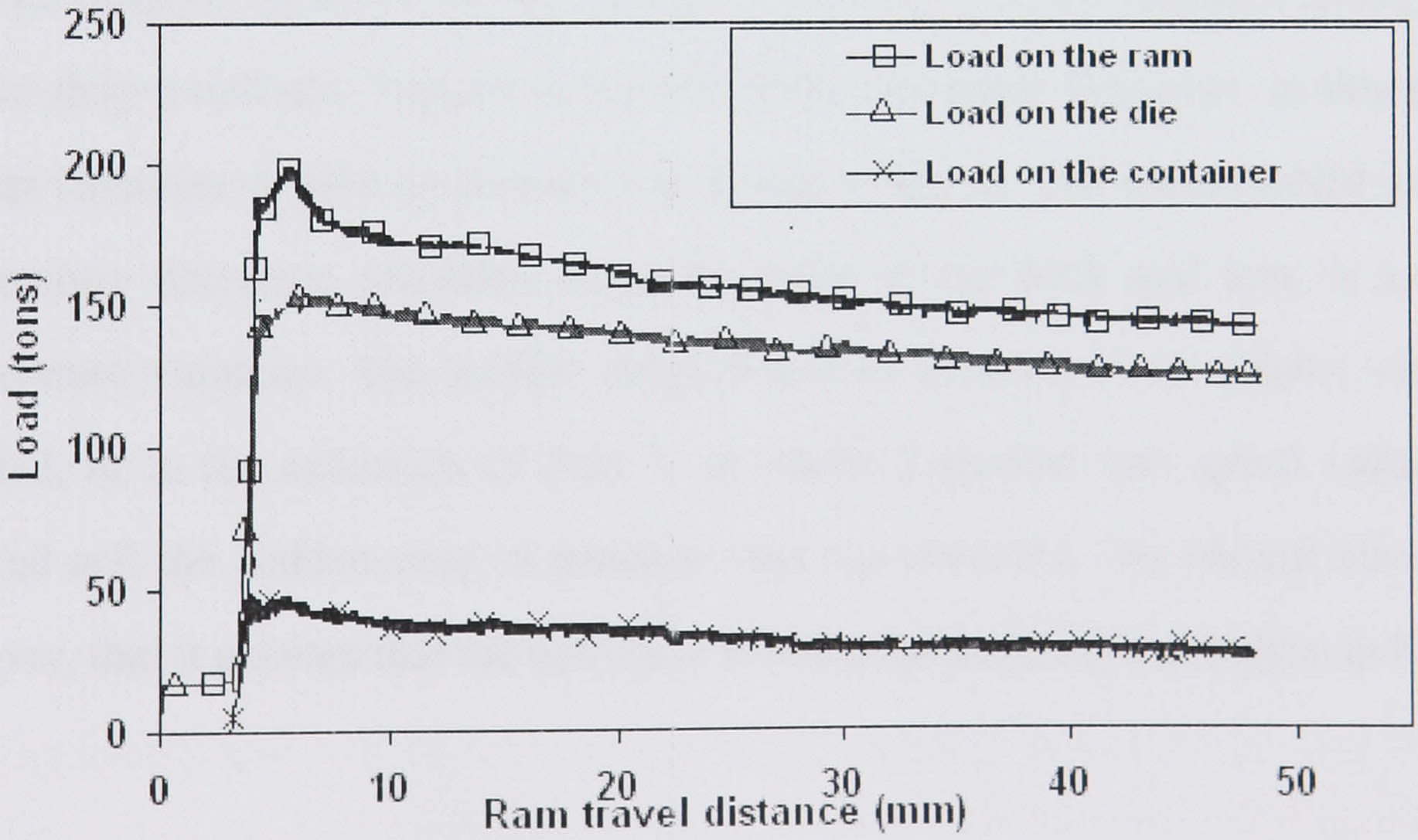

Figure 6.24 Load on the tooling in Run 3

It can be seen from the load-time (ram travel) curves that the peak load on the tooling appears at the beginning of extrusion and decreases during the subsequent extrusion.

Therefore, it is necessary to draw attention to the need to consider the load on the die during the initial acceleration stage. This could lead to the associated problem of distortion of, or damage to, the extrusion product. The speed profile setting must therefore take account of the peak load on the tooling (Bryant and Dixon 1999). As can be seen from Figure 6.25, there are some discontinuous changes in the load-time curves in Run 4. The sudden drop of the load was discussed previously by Chanda et al. (2001) and has also been reported experimentally. It has been observed in FEM simulations that there were some slight fluctuations in the calculated load-time curves, which can be attributed to the remesh in the FEM simulation process and the discontinuous variation of contact conditions at different time steps. The sharp drop found here is much more significant than the fluctuations mentioned above and could only be caused by the speed variation. As reported by Chanda, the drop of pressure is regarded as beneficial since the positive principle stresses (tensile stresses) at critical regions will be reduced, thereby reducing the tendency of friction-related tearing. However, the sudden variation can also create stresses and cause the product to bend or twist, hence influencing product quality. The abrupt change in speed could also cause surface 'stop' marks. However, there seems to be no reported literature on this feature. It was reported by Pinkham (2002) that the sudden drop could also happen in tapered billet extrusion. However, in this study, no sudden variation of load or stresses was found in Run 2. The reason could be that the temperature decreases smoothly from the front to the back and here is no sudden temperature variation. The sudden drops could be avoided when sudden variation is avoided, as in the extrusion of Run 3, in which a gradual ram speed variation was adopted and the sudden drop in pressure was not observed. We should also observe, however, that it appears that the extrusion is closer to isothermal extrusion in Run 4.

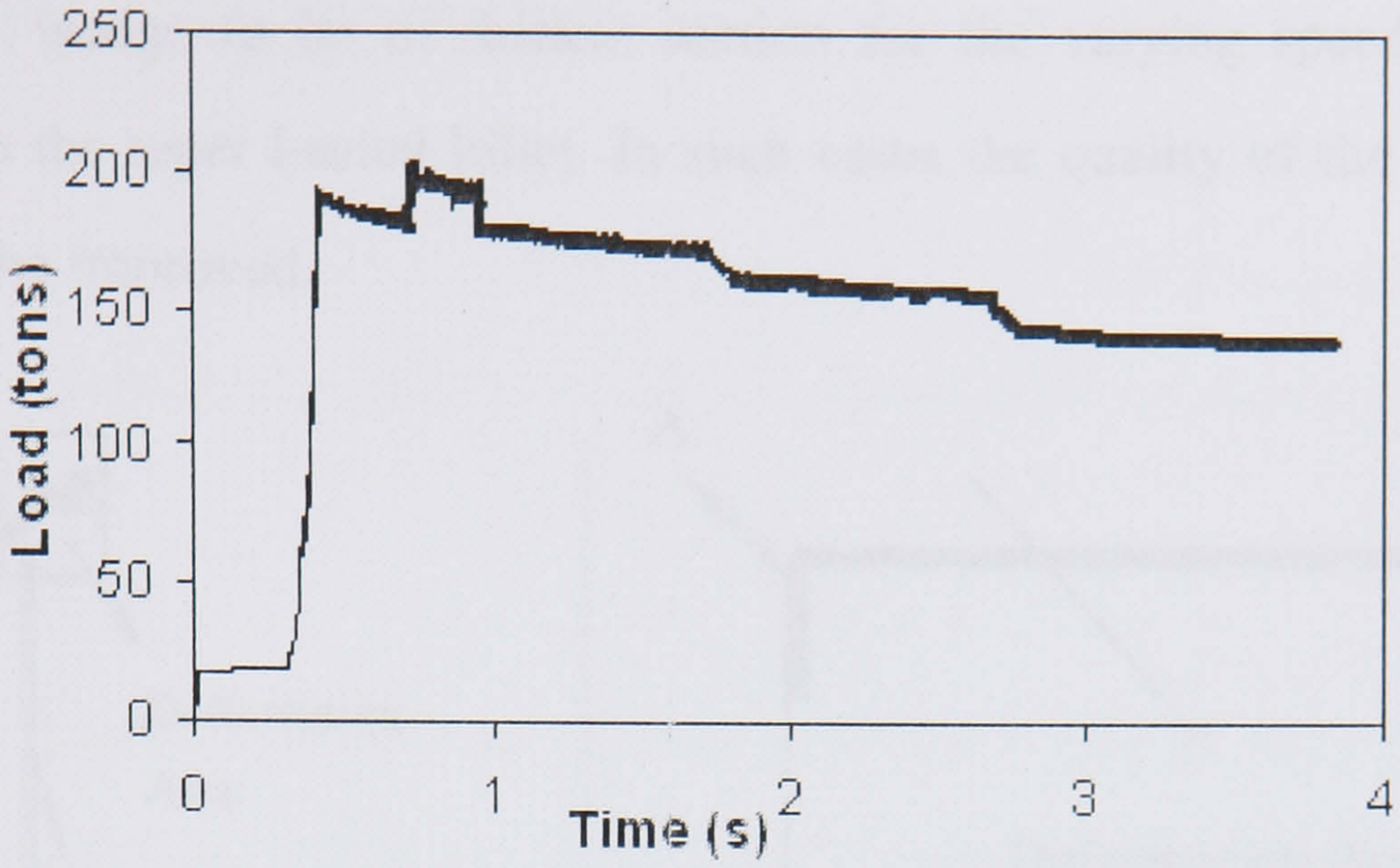

Figure 6.25 Load on the Ram in Run 4

6.2.2 Effect of isothermal extrusion on surface formation and material flow

The methodology and the procedures used in the study on surface formation can be found in the literature (Velay et al. 2003) and are not repeated here. The billet was extruded down to a length of 30mm in all of the simulations as shown in Table 6.2.

One vertical line (AB, with a length of 2000 mm, as shown in Figure 6.26) that is 0.05 mm under the extrudate surface is adopted to study the flow behaviour of the billet skin. The surface location points are shown in Figure 6.26 in detail. It can be determined with good precision the location in the billet from which the outer surface layers of the profile originates. As can be seen from Figure 6.26, a 0.05mm thick outer surface layer of the rod in axisymmetric direct extrusion would form from a relatively small crescent wedge-shaped region located near to the dead metal zone during the extrusion. This has been reported previously in the study of outer surface layer formation in extrusion of AlMgSi allloy (Valberg 1986). In Valberg's study (1986), the experiments were performed by implanting a complete grid pattern inside the billet, as shown in Figure 6.27.

The same analysis was performed for the other extrusions. The results are shown in Figure 6.28. The material flows from the wedge-shaped region gradually during

extrusion to form a surface layer that completely covers the rod. We can clearly discern the crescent wedge to be of thicker section for the varying speed extrusion when compared to the taper heated billet. In such cases the quality of the surface could be expected to be improved.

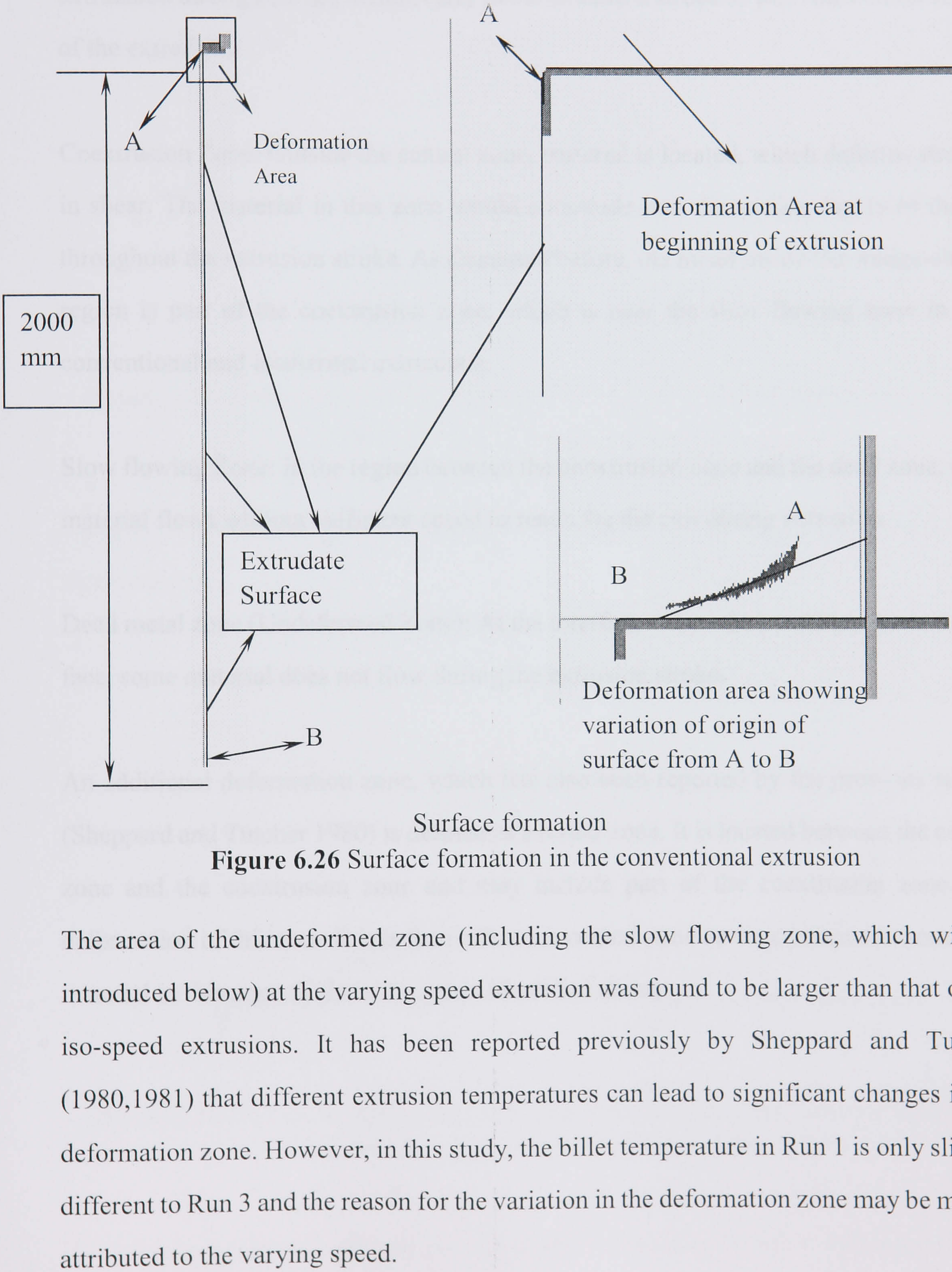

Surface formation

Figure 6.26 Surface formation in the conventional extrusion

The area of the undeformed zone (including the slow flowing zone, which will be introduced below) at the varying speed extrusion was found to be larger than that of the iso-speed extrusions. It has been reported previously by Sheppard and Tutcher (1980,1981) that different extrusion temperatures can lead to significant changes in the deformation zone. However, in this study, the billet temperature in Run 1 is only slightly different to Run 3 and the reason for the variation in the deformation zone may be mainly attributed to the varying speed.

The following zones have been identified previously in direct extrusion by experiments. as shown in Figure 6.29 (Herberg 1993, Renne and Sumarokova 1989):

Central Zone: Metal located in the centre of the deformation zone, which will be extrudated through the die orifice early in the extrusion stroke to form the central section of the extrudate.

Coextrusion Zone: Outside the central zone, material is located, which deforms strongly in shear. The material in this zone would coextrude into the surface layers of the rod throughout the extrusion stroke. As discussed before, the metal inside the wedge-shaped region is part of the coextrusion zone, which is near the slow flowing zone in both conventional and isothermal extrusions.

Slow flowing Zone: In the region between the coextrusion zone and the dead zone, some material flows without sufficient speed to reach the die exit during extrusion.

Dead metal zone (Undeformed Zone): At the interface where the container meets the die face, some material does not flow during the extrusion stroke.

An additional deformation zone, which has also been reported by the previous studies (Sheppard and Tutcher 1980) is defined as a buffer zone. It is located between the central zone and the coextrusion zone and may include part of the coextrusion zone. The deformation of this zone is less than either the central zone or the coextrusion zone. The material in this zone feeds to the zones identified above.

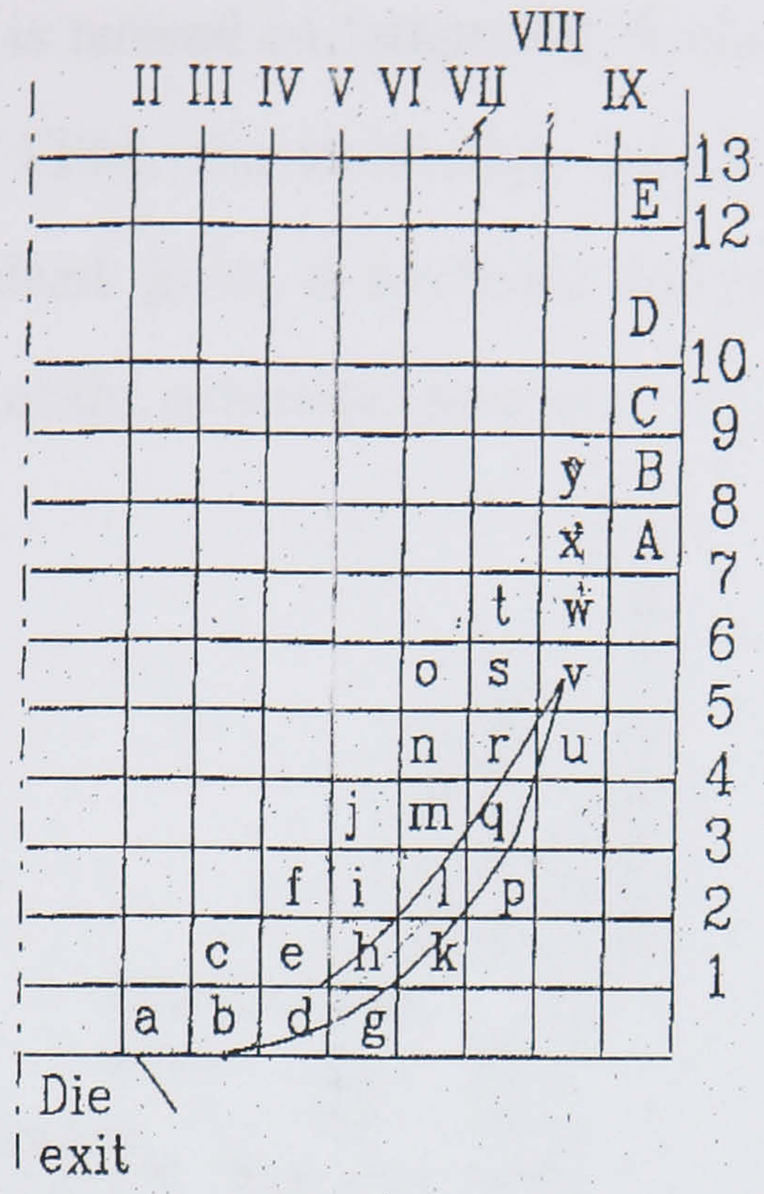

Figure 6.27 Grid elements of the billet in direct extrusion (R=40) forming the outer surface layers of the rod (Valberg 1986)

The five deformation zones are the typical deformation zones established in steady state direct extrusion.

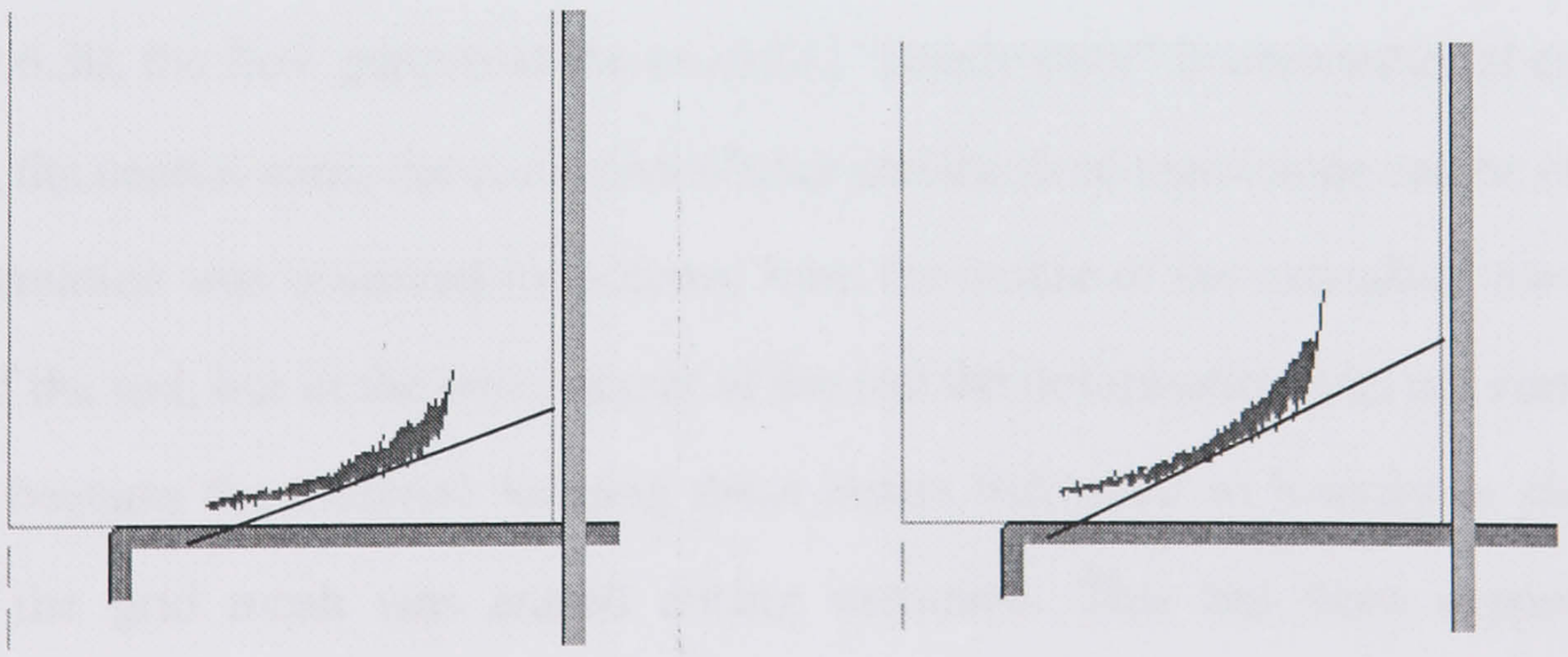

Figure 6.28 Surface formation area in isothermal extrusion (Left: the tapered billet extrusion; Right: varying speed extrusion)

In this study, a reference grid pattern, as shown on the left of Figure 6.30, was employed to study the flow pattern. The technique is based on comparing the deformed grid pattern

with the original undeformed pattern introduced into the billet. It has been used in previous experiments and is termed an 'emptying diagram' (Walbert 1992). Presently, with the development of FEM, the technology can be used in a more precise but economic way and it indeed gives a pertinent description of the metal flow and deformation in simulation of the extrusion process.

Figure 6.29 Regions inside the as-cast billet which flow differently during extrusion (Venas, Herberg and Skauvik 1993)

In Figure 6.30, the flow pattern at the so-called "steady state" in conventional extrusion is shown, the central zone, the coextrusion zone and the dead metal zone can be observed. The deformation was observed to increase from the centre of the extrudate towards the surface of the rod, but in the outer layers of the rod the deformation was not completely recorded because the material forming these layers deformed so heavily in shear that some of the grid mesh was erased during extrusion. This has been supported by experiments in the study of Valberg (1992). The slow flowing zone lies between the coextrusion zone and the dead metal zone and the buffer zone lies between the central zone and the coextrusion zone and they can be regarded as the transition zones. From the shape of the elements the overall deformation can be estimated. The reference grid deformed heavily in the centre area and the coextrusion area. In the buffer area and the

slow flowing area, the deformation of the grid is at a medium level and in the dead metal zone, the reference grid remains unchanged. In the sub-surface layers near to the billet skin the transverse lines are located very close to each other. The material flow at the interface of the billet and the container is influenced strongly by sticking friction. The simulation results correspond well with the experimental result, which is shown in Figure 6.31. The flow patterns of isothermal extrusions are shown in Figure 6.32. Taper heating of the billet appears to result in a different deformation pattern; the speed variation extrusion produces deformation at the horizontal closure, which is more intense. This supports the comment above concerning the effect of the crescent wedge.

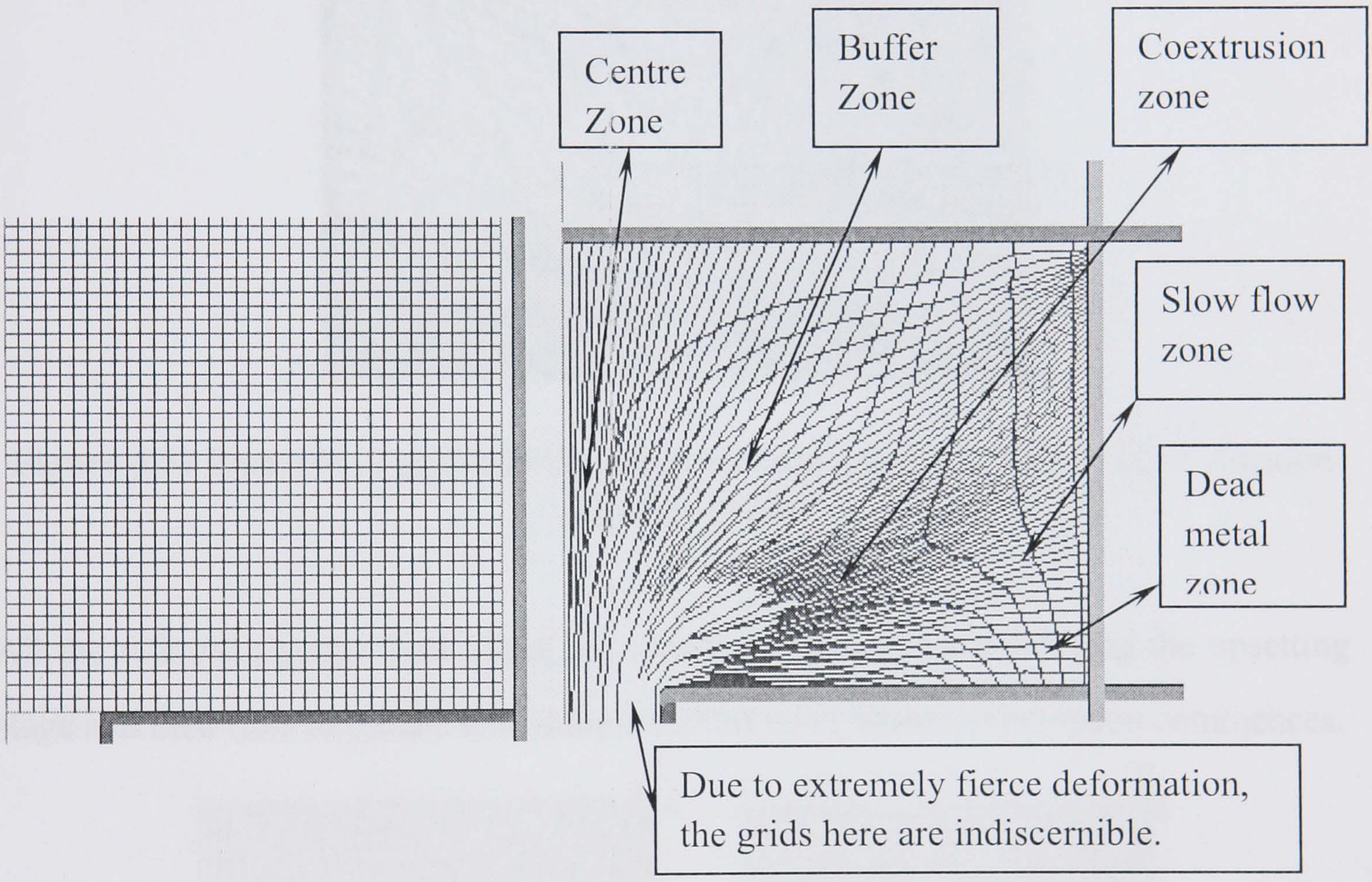

Figure 6.30 Reference grid pattern (Left: before deformation, Right: after deformation)

As can be seen in Figures 6.30-6.32, the five zones can be discerned in all of the extrusion processes. The area of the dead metal zone in the varying speed extrusion is larger than that in the first two runs.

However, it is difficult to observe the detail of the material flow from the macro-scale analysis results. In this study, a group of material points (reference points) located in

different deformation areas is selected and the traces of these points are shown from the output of the program, as shown in Figure 6.33. By tracing back the travel route of these points, the difference between the deformation zones can be discerned clearly. The initial and final coordinates (after a ram travel of 40mm) of these reference points are shown in Table 6.3.

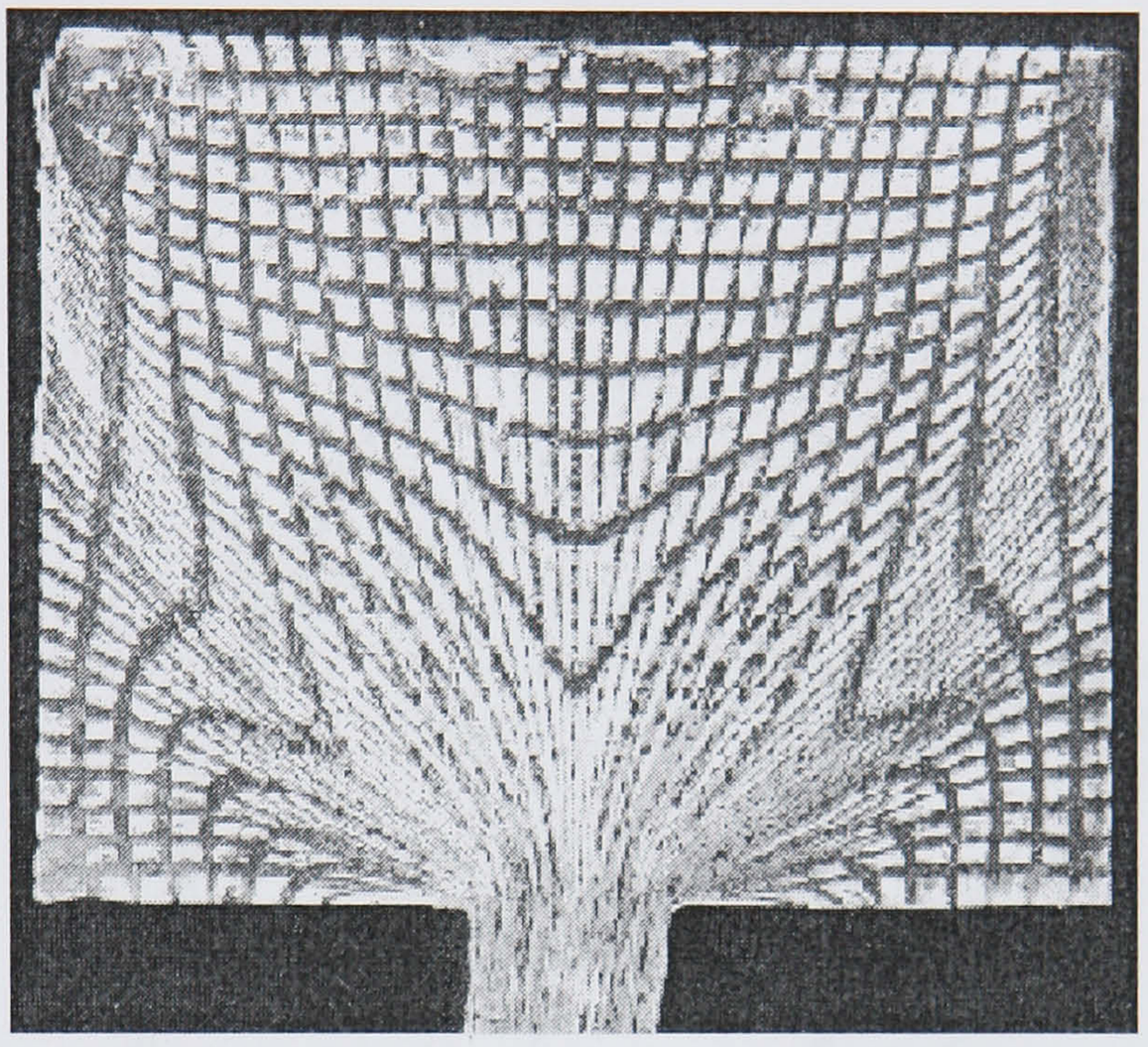

Figure 6.31 Example of gridded billet when extracted from the 'steady state' location (Tutcher 1979)

All the reference points flow along the direction to the container during the upsetting stage and then flow to the die exit along a curved route when the extrusion commences.

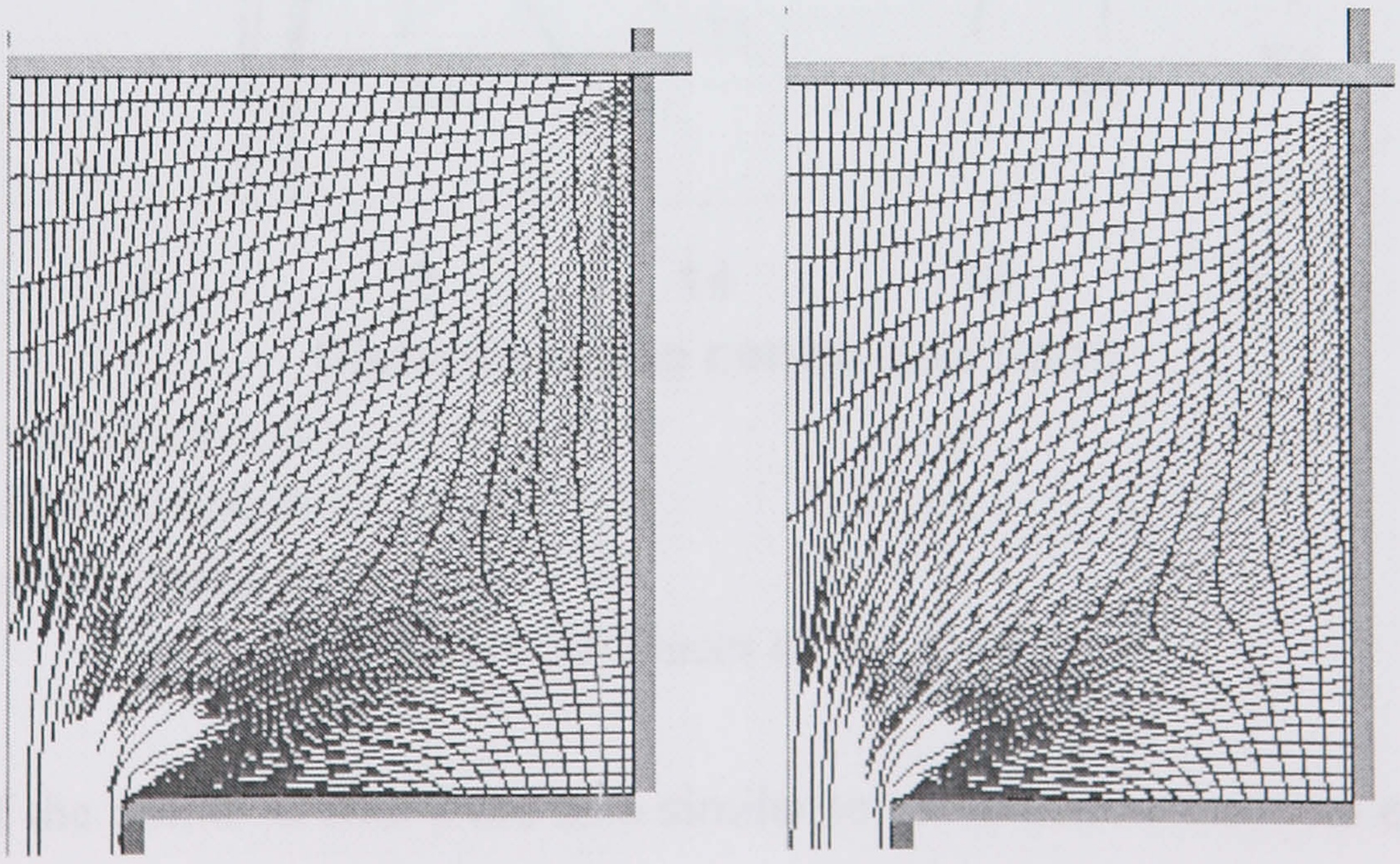

Figure 6.32 The material flow pattern in tapered billet extruson (left) and in varying speed extrusion (right)

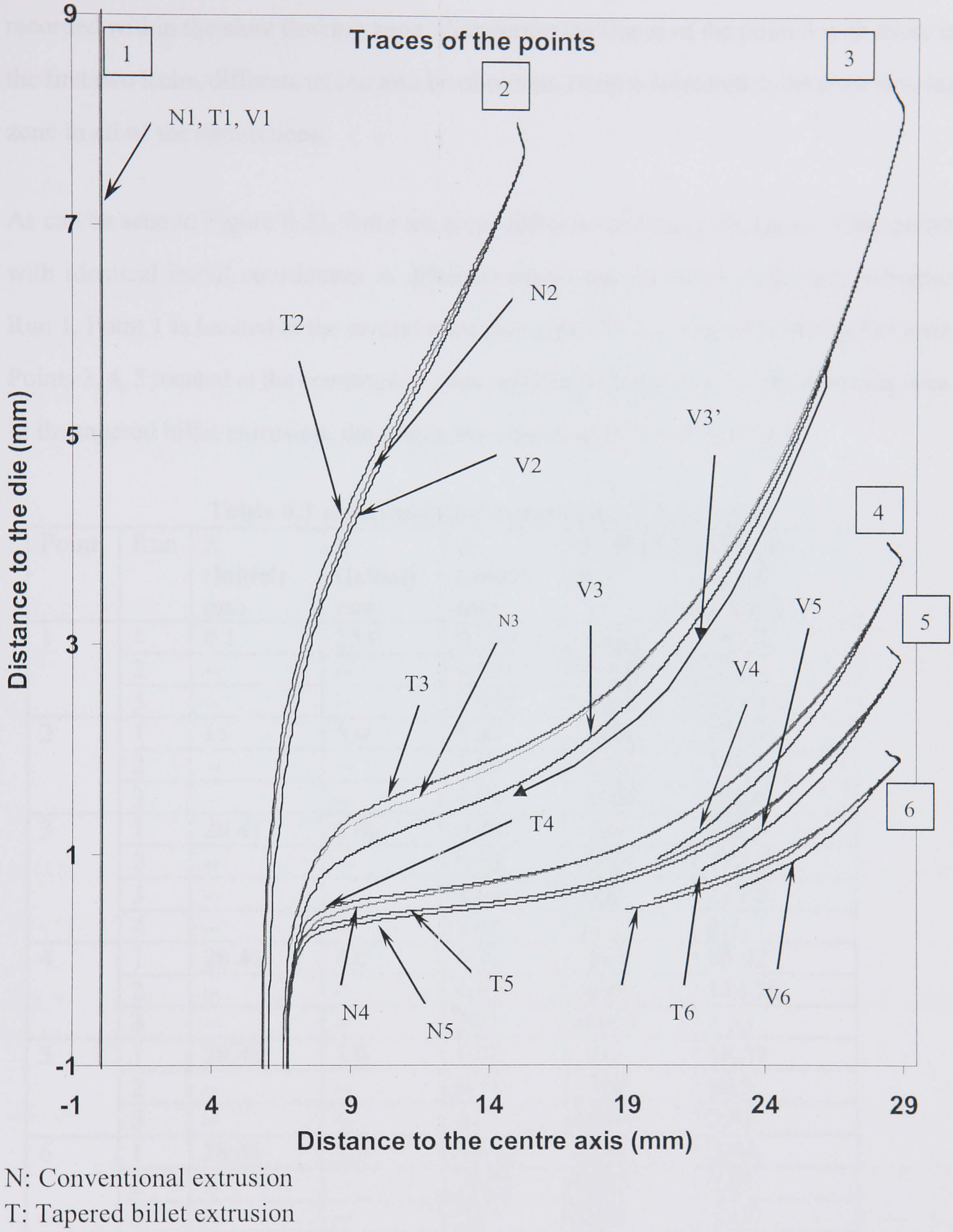

N: Conventional extrusion
T: Tapered billet extrusion
V: Varying speed extrusion

Figure 6.33 Traces of the points

The traces of the points in Run 2 are also similar to those in conventional extrusion. In Run 3, where the ram speed was varying in a continuous manner, the points 4 and 5 travelled along a wedge shaped route for a short distance during the varying speed

extrusion and were not extrudated out of the die. We may observe that they have been recorded within the slow flowing zone. Comparing the traces of the point 3 with those in the first two Runs, differences can also be observed. Point 6 relocated to the slow flowing zone in all of the simulations.

As can be seen in Figure 6.33, there are some differences among the traces of the points with identical initial coordinates in different extrusions. In the conventional extrusion Run 1, Point 1 is located at the central extrusion area, Point 2 located in the buffer zone, Points 3, 4, 5 located at the coextrusion zone and Point 6 located at the slow flowing area. In the tapered billet extrusion, the points are located at identical positions.

Table 6.3 Initial and final coordinates of the points

Point	Run	X (Initial) mm	Y (Initial) mm	X (Final) mm	Y (Final) mm	Average speed (mm/s)
1	1	0.1	25.0	0.039	-1420	362.5
	2	--	--	0.051	-1420	362.5
	3	--	--	0.030	-1030	415.76
2	1	15	8.0	5.87	-1400	354.25
	2	--	--	5.83	-1410	356.75
	3	--	--	6.04	-1060	430.8
3	1	28.41	8.46	6.58	-544	143.5
	2	--	--	6.58	-655	171.25
	3	--	--	6.69	-553	233.2
	4	--	--	17.4	20.1	6.4
4	1	28.41	4.0	6.72	-313	85.42
	2	--	--	6.67	-459	114.75
	3	--	--	20.1	0.963	3.53
5	1	28.41	3.0	6.71	-245	68.39
	2	--	--	6.71	-398	99.5
	3	--	--	21.7	0.851	2.81
6	1	28.41	2.0	18.92	0.62	2.40
	2	--	--	20.21	0.65	2.07
	3	--	--	23.1	0.68	2.19

† The coordinate system is shown in Figure 6.33.

The average flow speed of each point can be determined from the co-ordinates shown in Table 6.3. The material flow velocity decreases from the centre to the edge of the extrudate. Although the material in the coextrusion zone experiences the heaviest

deformation, the material flow speed is not as high as in the central zone. It can also be seen from Table 6.3 that the slow flowing zone can be regarded as a transitional zone. in which the average material flow speed decrease gradually from the coextrusion zone to the dead metal zone, which can be judged from the final coordinate of the reference points.

It was noticed that when the drop of the ram speed occurred in Run 4, the route of the reference point deviated slightly, as can be seen from the trace of V3' in Figure 6.33. It can also be seen from the trace that Point 3 moves into the slow flowing zone. which has not been extrudated out of the die during extrusion.

The variation of the trace indicated that the material flow is unstable in varying speed extrusion, which combined with the variation of the stress, can influence the product quality during extrusion. It is thus confirmed that a sudden alteration of ram speed should be avoided during extrusion.

The loci shown in Figure 6.33 imply that there are indeed differences in the flow of the extrusions simulated. However, the differences are small and unlikely to cause large property variation in the differing modes of extrusion.

6.2.3 The unsteady nature of flow during extrusion and the influence of FEM mesh on the simulation result

Although in the above discussions, the term 'steady state extrusion' was adopted, it should be pointed out here that non-steady characteristics throughout the complete extrusion process are found. It is reflected in the expanding coextrusion zone and shrinking undeformed zone (as well as the slow flowing zone). Figure 6.34 shows the evolution of the undeformed zone (including the slow flowing zone). The simulation results correspond well with former experimental results, as shown in Figure 6.35 (Tutcher 1979).

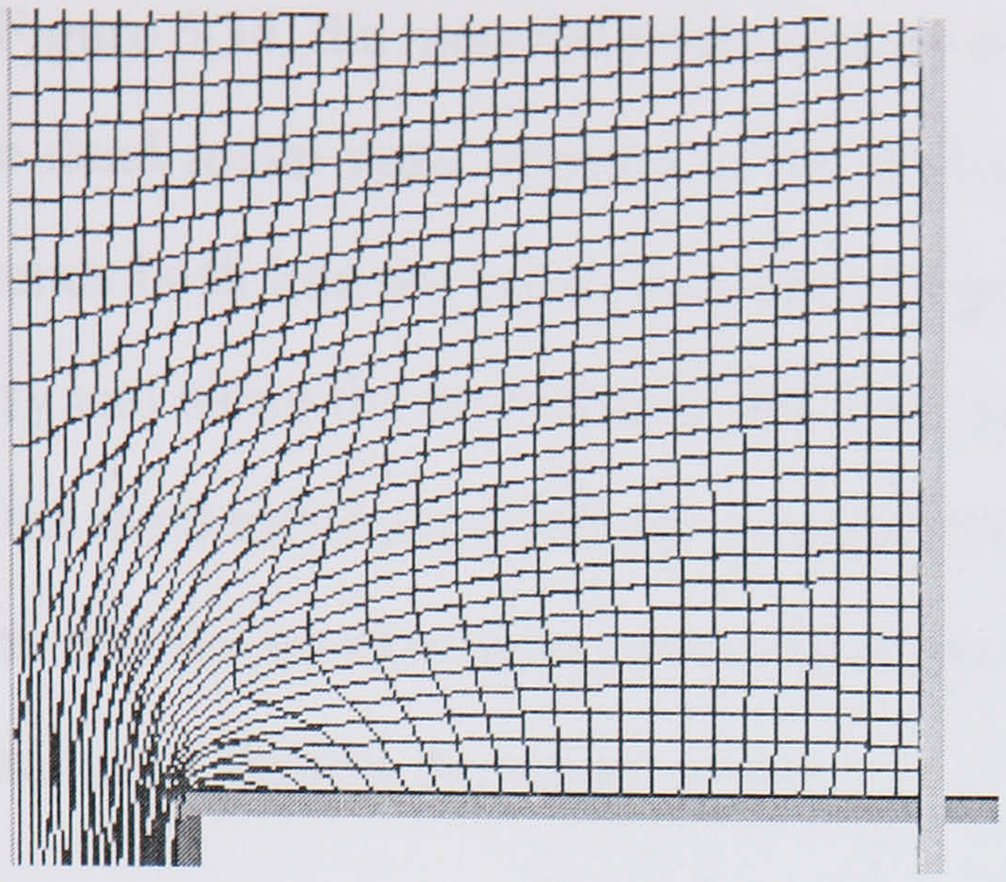

a) Ram travel = 5mm

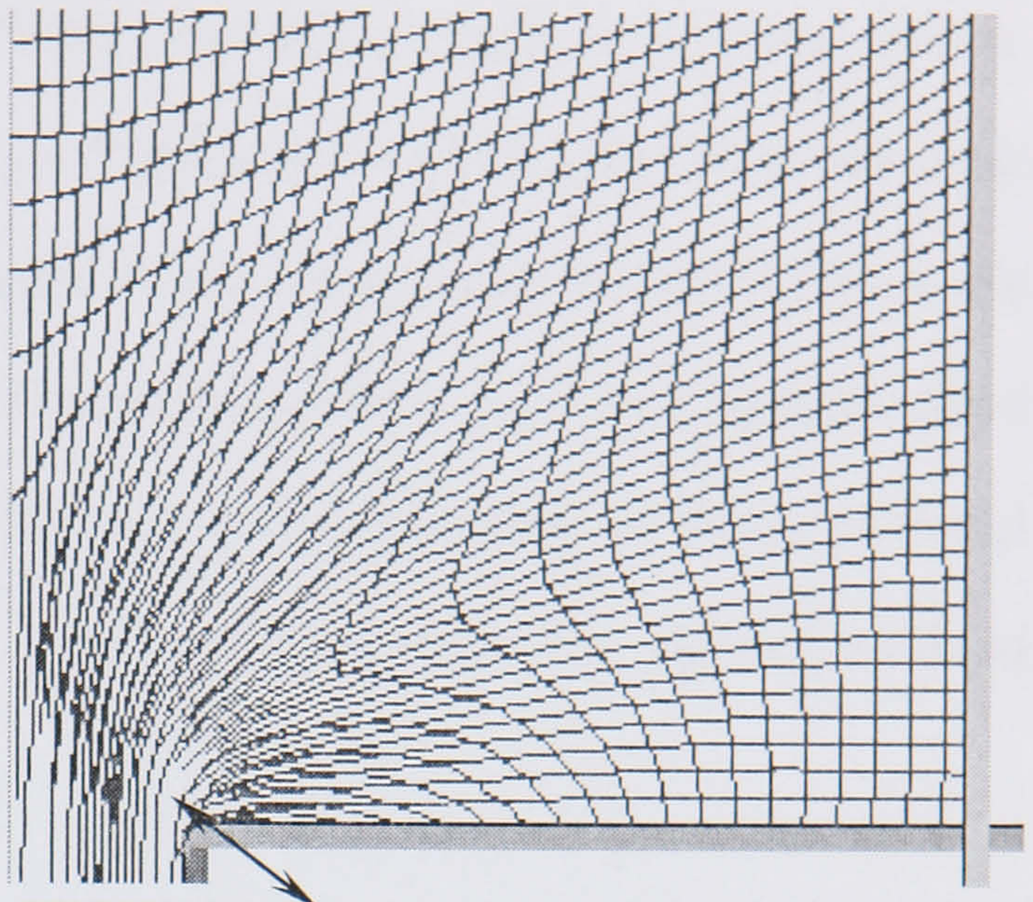

b)Ram travel = 12mm

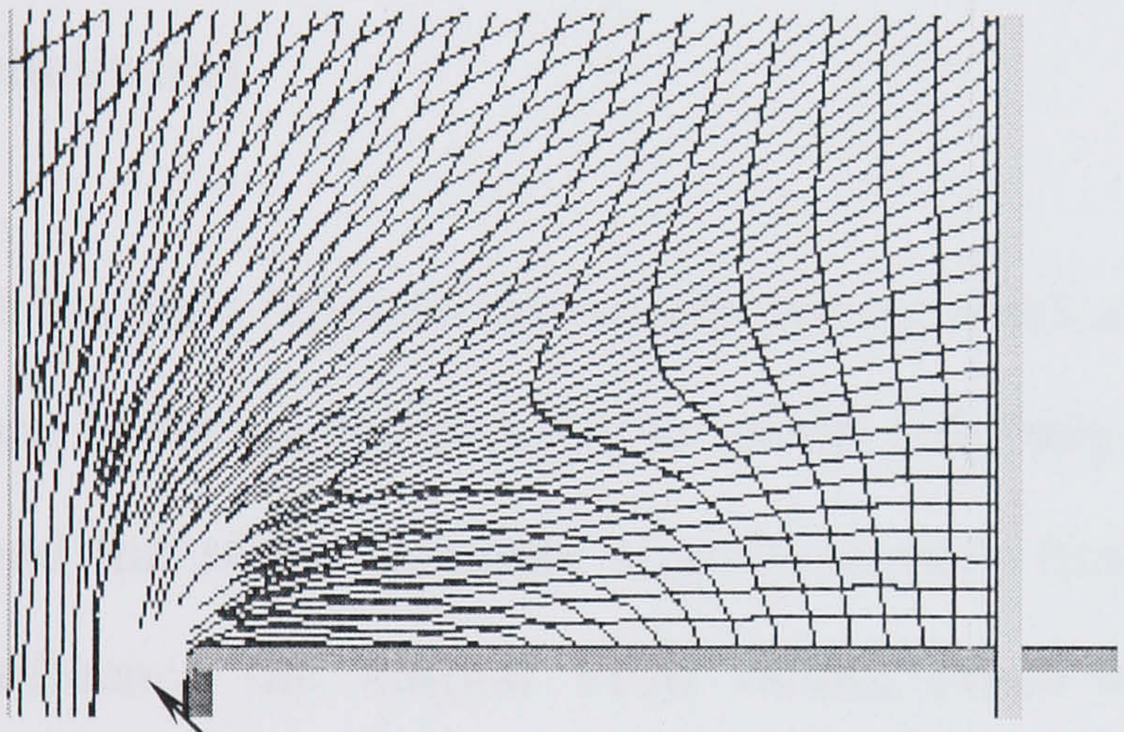

c) Ram travel = 40 mm

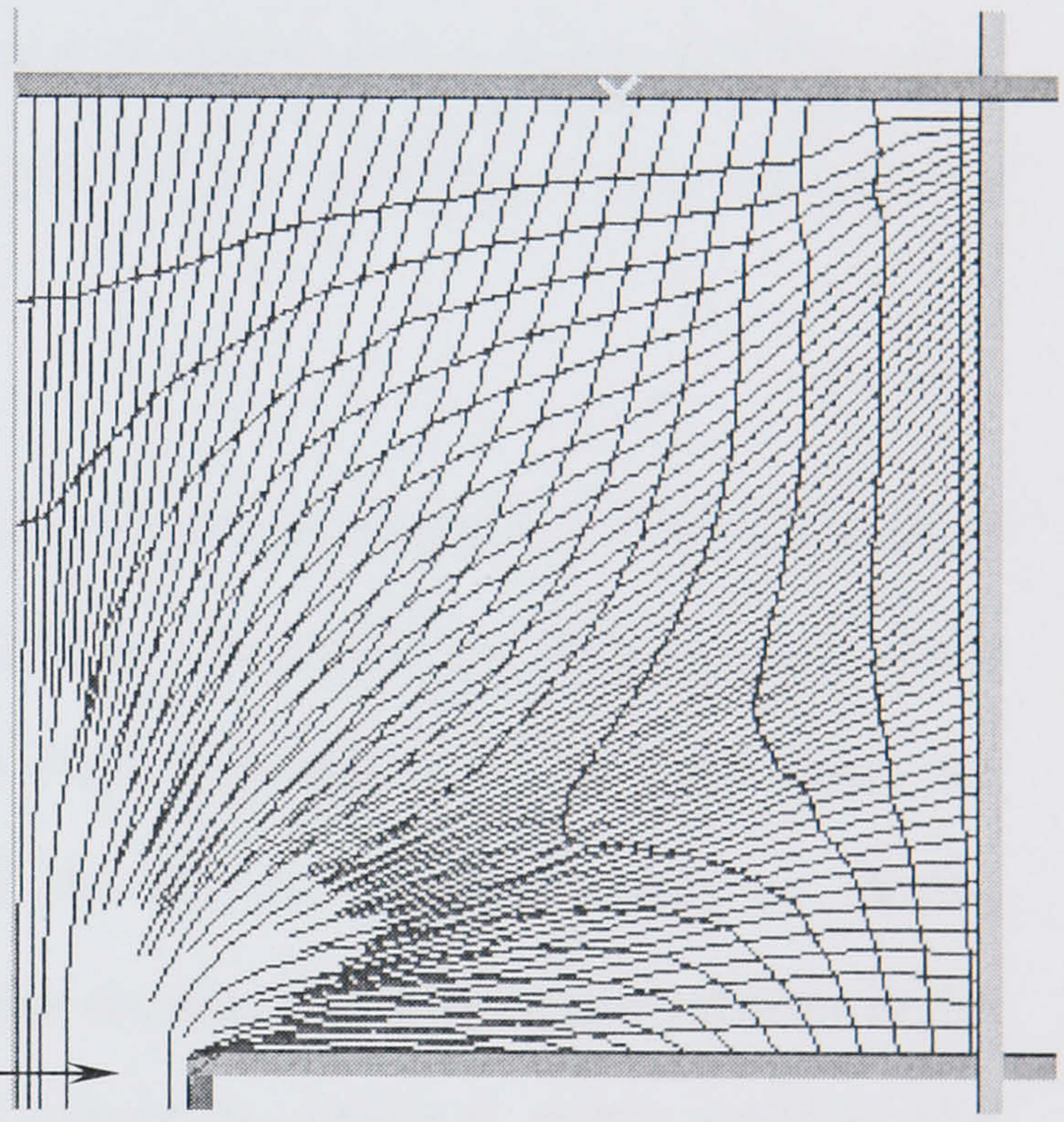

e) Ram travel = 60mm

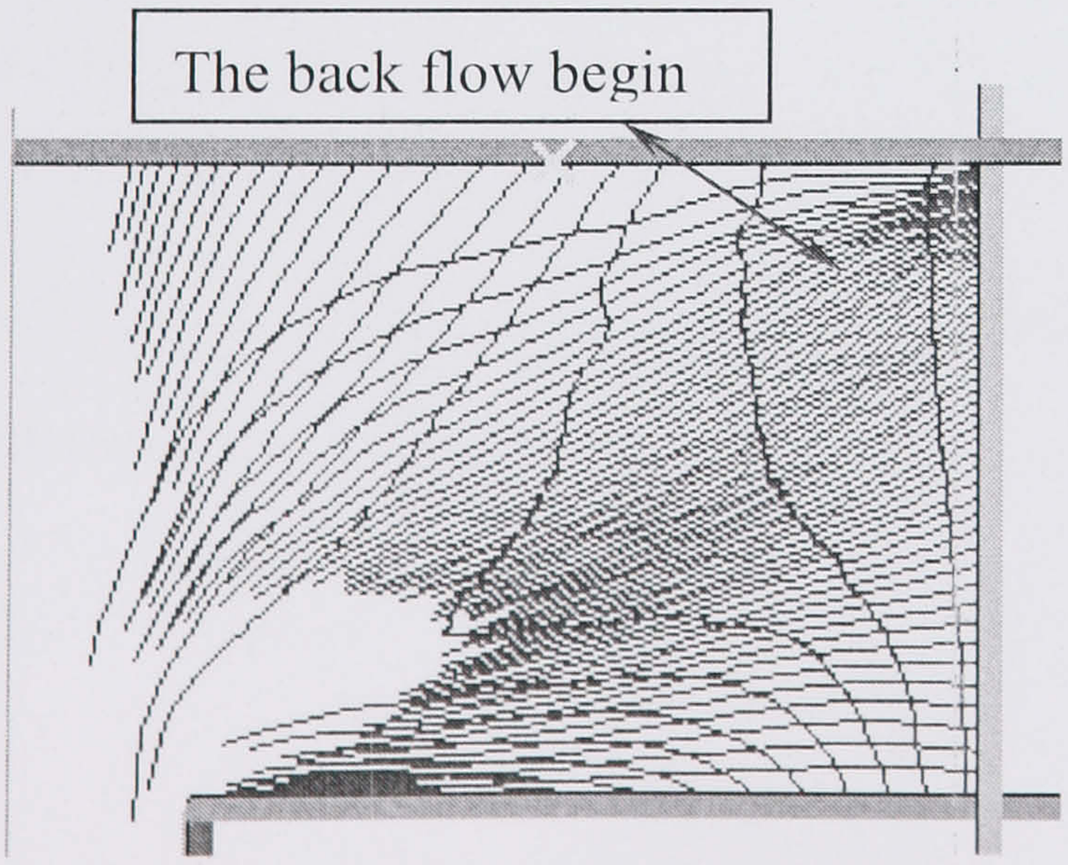

f) Ram travel = 70mm

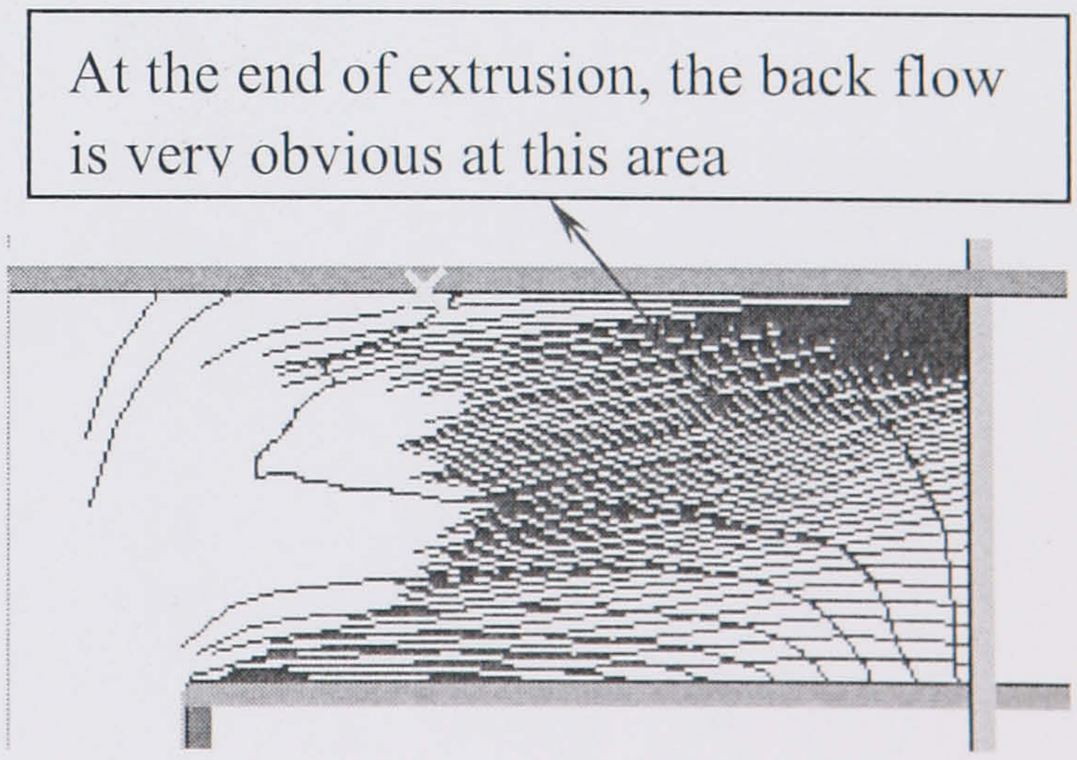

g) Ram travel = 80mm

Figure 6.34 The evolution of the extrusion zones

In Figure 6.34, the material flow patterns at different extrusion stages are clearly shown. The dead metal zone appears at the beginning of extrusion and the deformation zone extends back into the billet. Regions of significant shear can be seen extending from die entry and along the central axis and from die entry to the periphery of the billet bounded by the dead metal zone and the container/billet interface. The interface of the dead metal zone and the co-extrusion zone migrate to the dead metal zone and the volume of dead metal zone shrinks during extrusion.

Considering the unsteady character of extrusion, the comparison between the conventional and isothermal extrusion may be influenced. However, in this study, as mentioned before, all comparisons are performed at the extrusion stage with the same ram travel distance. In this way, the influence of the unsteady extrusion can be eliminated.

It has been reported previously that the mesh and remesh setting used in FEM simulation can influence the simulation results (Herberg 1993). The predicted load, the strain rate and the stress fluctuate slightly at each time step. Although the deviation does not influence the normal FEM output (such as the calculated flow stress or strain) significantly, it would be critical if it can influence the simulated trace of the points in the present study. By comparing the simulation output at different mesh settings, the influence of the mesh was checked carefully as discussed below.

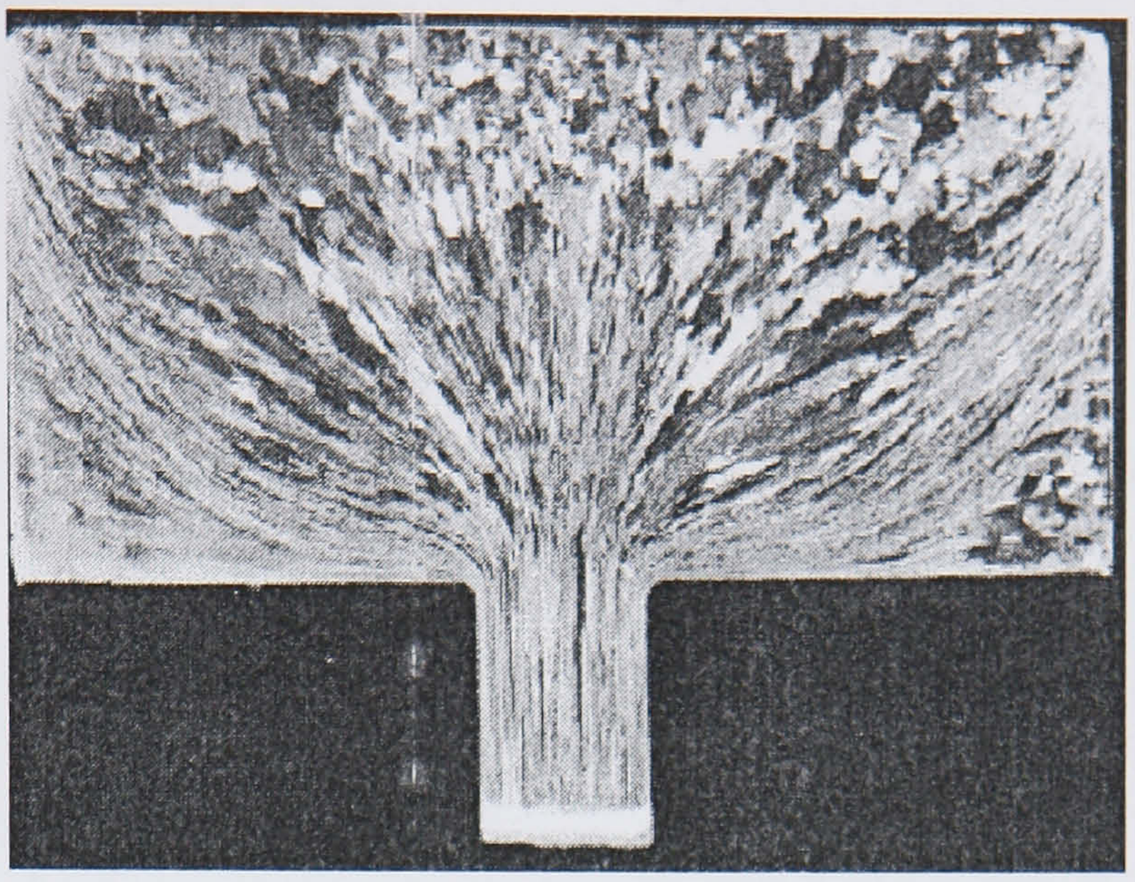

Figure 6.35 Experimental results concerning the microscopic flow at 'steady state' (Tutcher, 1979)

Two simulations concerning one identical extrusion (Run 1, as shown in Table 4) but at different mesh setting (as shown in Figure 6.36) are performed. The calculated traces of the reference points 2 and 3, which were used in the previous section, are compared as shown in Figure 6.37.

As can be seen from Figure 6.37, the traces of the points with identical initial locations are coincident. It is clear that the influence of the mesh size on the simulation of material can be ignored according to this test result. The medium mesh was adopted in this study with the objection of shortening the simulation time. Furthermore, the mesh setting in all of the four simulations is identical to each other and the influence of the mesh can be even smaller. Then it can be said that the simulation is effective in predicting the material flow history.

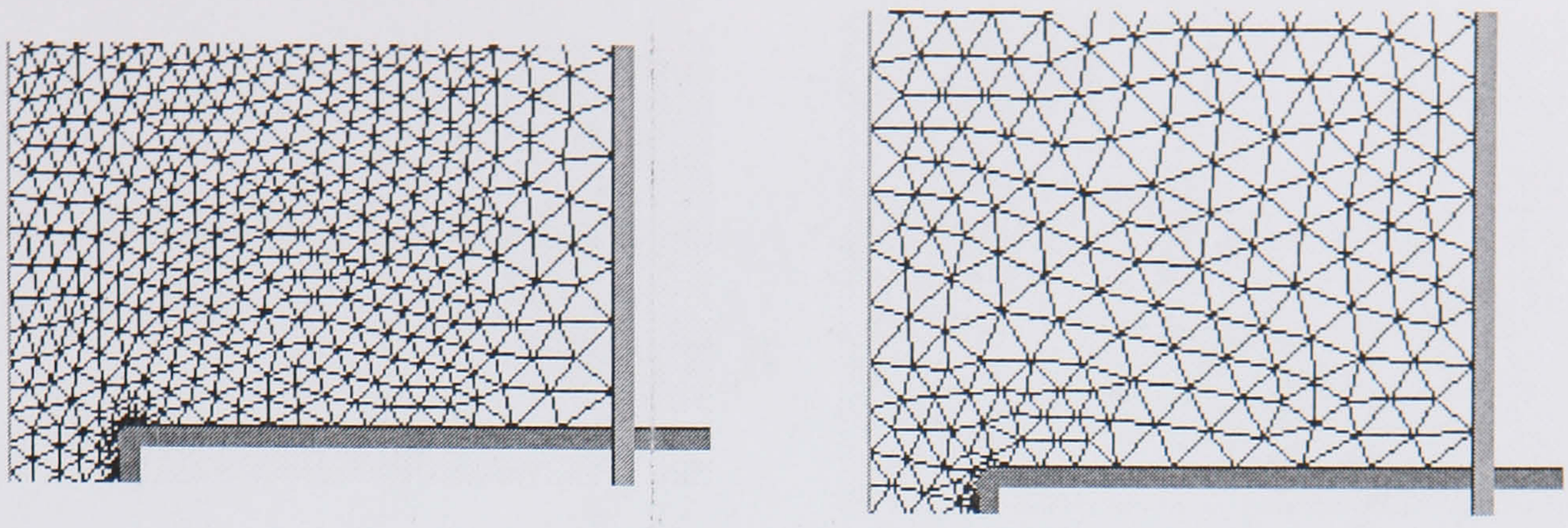

(a) Fine mesh (With the size of 1.2)　　(b) Medium mesh (With the size of 3.0)

Figure 6.36 Different mesh

6.3 Conclusion

(1) Balanced material flow and temperature distribution can be achieved by suitable location of pockets. The material substructure is also shown to be homogeneous around the extrudate perimeter when the optimum pocket position is situated.

(2) Even a small offset of the pocket can cause a significant change of the metal flow during extrusion. Unsuitable design of the pocket die results in a deterioration of velocity, temperature and hence structural homogeneity around the surface.

(3) These results demonstrate that the problems presented in Chapter 4 can be at least partially solved by the method presented here.

(4) The location and extent of the coextrusion zone in varying speed extrusion is higher than that in conventional extrusion, which indicates that varying ram speed can influence the flow pattern significantly.

(5) By comparing the deformed grid-pattern inside the billet with the original underformed pattern, precise information concerning the location of the different deformation zones can be provided in detail by FEM simulation.

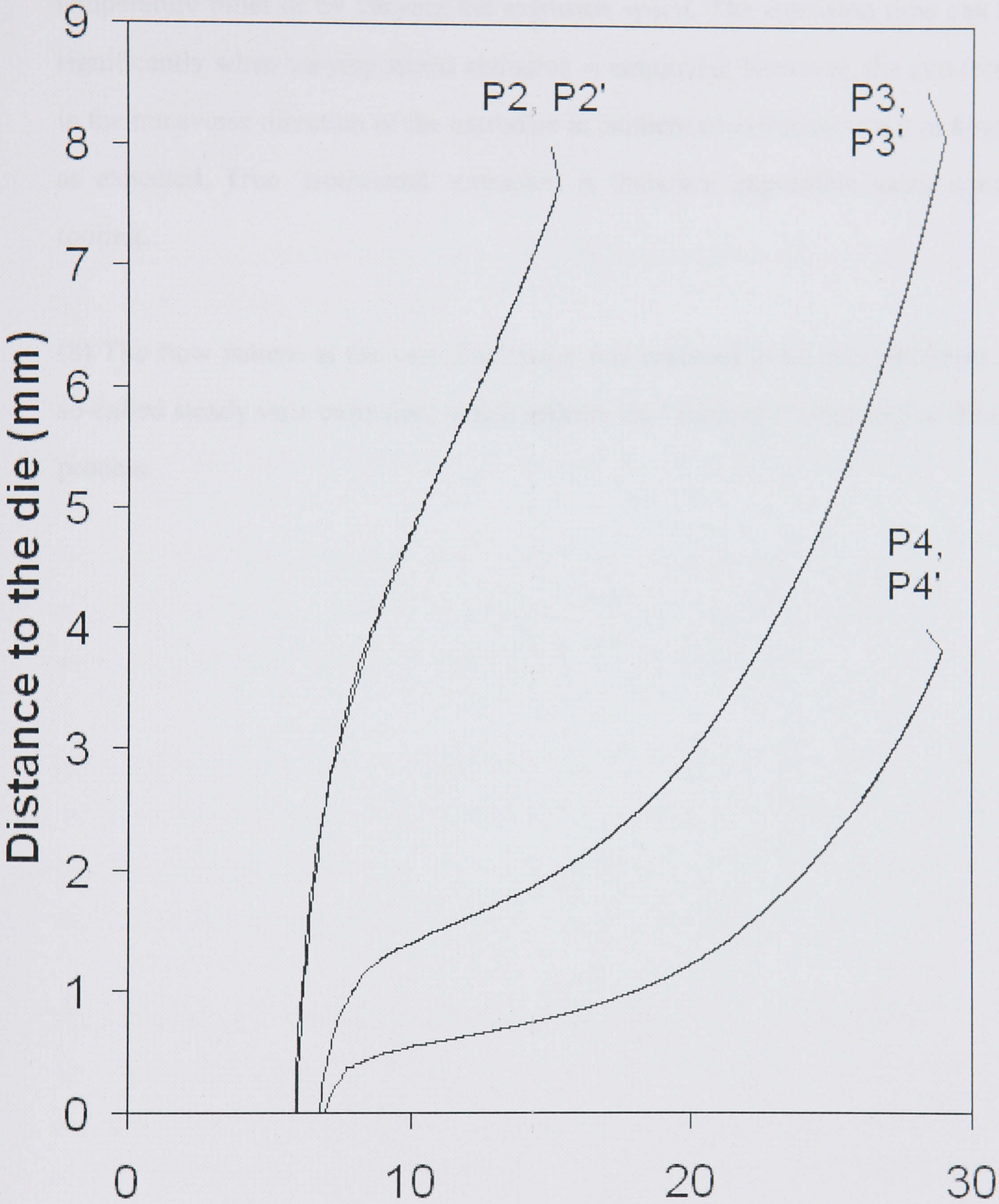

Figure 6.37 The influence of mesh size on the trace simulation

(6) The loads on the tooling drop sharply when the ram speed is decreased suddenly. This could affect the product quality. By the use of gradually changing ram speed or smooth distribution of the temperature in the billet, the sharp drop can be avoided.

(7) Isothermal extrusion could be approximately established by either the tapered temperature billet or by varying the extrusion speed. The extrusion time can be saved significantly when varying speed extrusion is employed. However, the exit temperature in the transverse direction of the extrudate in isothermal extrusion is not as homogenous as expected. True 'isothermal' extrusion is therefore impossible using conventional tooling.

(8) The flow pattern at the very final stage was reported to be quite different from the so-called steady state extrusion, which reflects the "unsteady" character of the extrusion process.

7 Conclusion and suggestion for future work

(1) FEM and other numerical models have been successfully applied to the modelling and simulation of hot extrusion processes and subsequent heat treatment processes. FEM has been proved to be effective in predicting the thermal-mechanical parameters, such as temperature, strain, stress, velocity, etc.

(2) Detailed and visualised studies of the mechanical deformation history (i.e. material flow) by FEM have been realised.

(3) Most of the important information required by industry, such as extrusion load, velocity control and extrusion die optimisation has been predicted by FEM simulation.

(4) FEM has been integrated with other numerical models, such as physically based metallurgical models, cellular automata models and Taylor-Bishop models, which are the basic meso-scale models of computational material science.

(5) Integrated modelling commenced by using FEM and these results were used as subsequently the initial settings for the substructural models. Detailed studies of the metallurgical behaviour after extrusion and during the heat treatment have been performed and agree with published experimental results.

(6) The empirical models, the internal state variables model (physically based model) and cellular automata are effective in simulation of the recrystallisation process occurring in the extrusion and heat treatment of aluminium extrudes. The recrystallisation dynamics, recovered structure and the recrystallised grain size could be approximately predicted.

(7) Typical applications of the integrated model are the analysis and synthesis of the individual influence of forming parameters during extrusion using the Taguchi method and the comprehensive modelling of complex shape extrusions.

(8) The visualisation of both the deformation history and structural evolution after extrusion have been computed using the integrated model reported in this thesis.

(9) The calculated recrystallised grain size, the subgrain size and the volume fraction recrystallised in the study of T shape extrusion are in agreement with the previously reported experimental results. It is also shown that the FEM method can predict deformation in three dimensional complex shape extrusions.

(10) In multi-hole die extrusion, the peak load increases as the number of holes increases for any given reduction ratio. The extrusion pressure can be reduced by choosing the most suitable value of eccentricity.

(11) In multi-hole die extrusion, there is no significant difference among the recrystallised grain sizes in the centre of bars that are extruded from the different die orifices. For the bars extruded from the side hole, the surface recrystallised grain sizes are different at different areas. The recrystallised grain size on the surface, which is nearer to the die centre, is smaller than the grain size on the opposite surface. The substructure is also heterogeneous.

(12) The unbalanced material flow caused by multi-hole die extrusion can be partially solved by adding pocket to the die. Balanced material flow and temperature distribution can be achieved by suitable pocket design. The material substructure is also shown to be homogeneous around the extrude perimeter.

(13) During pocket die extrusion, even a small offset of the pocket can cause a significant change of the metal flow during extrusion. Unsuitable design of the pocket die results in a deterioration of structure homogeneity around the surface.

(14) The influence of the scaled down modelling on the predicted results of numerical simulation is significant. Although the average strain rate, the temperature and the Zener-Hollomon parameter could be similar to the model with the original size in separate runs, it is difficult to reproduce all of the variables in one simulation run.

(15) Scaled modelling could reproduce some information at the macro level: for

example, the material flow pattern. However, quantitative analysis using scaled down numerical modelling should be avoided. Full size modelling is recommended for the simulation of manufacturing processes, but requires detailed comparison with parameters collated from industry with suitable mesh. Industrial scale extrusion can be simulated without loss in computing time.

(16) Using subroutines integrated into commercial software Forge 2 and Forge3, special studies of quality control, such as the commencement of surface cracking have been performed.

(17) A study of isothermal extrusion has been achieved by FEM simulation. The flow pattern at the very final stage was reported to be quite different from the so-called steady state extrusion, which reflects the "unsteady" character of the extrusion process. Control by ram speed was more accurate than by utilising a taper heated billet.

Suggestions for future work:

The range of possible applications of the finite element method extends to all engineering disciplines, but civil, mechanical and aerospace engineers are the most frequent users of the method. The method is also finding acceptance in multidisciplinary problems where there is a coupling between one or more of the disciplines.

However, to give a precise simulation of virtual manufacturing processes, much work is still required. For example, when modelling the hot extrusion process in the present work, the extrusion tooling is assumed to be rigid. The heat transfer between the billet and the tooling exists in the software. However, the deformations of the dies are ignored. Although the influence of the rigid model on the simulation result is generally regarded as minimal, there is an uncertainty concerning the simulation result.

To act as a general numerical modelling tool to study material evolution, FEM has to be integrated with other numerical models, such as physically based metallurgical models, cellular automata models and Taylor-Bishop models, which are the basic meso-scale model of computational material science. Integrated modelling commences

by using FEM and subsequently transfers the simulation results to the initial settings of the substructural models. Recrystallisation dynamics, the recovered structure and the recrystallised grain size can be approximately predicted. Most of these physically based models have not been well researched and in this area work is required to experimentally determine the constant involved.

The advantage of the integrated model comes from grouping the disciplines from different research fields, which are related to each other. However, the individual models may have assumptions and uncertainties. For example, the incomplete and vague understanding of the physical principle of recrystallisation strongly limits the development of the metallurgical models. Either the cellular automata or the physically based models have limits in their applications concerning the deformation conditions and material components. In almost all of the numerical models, assumptions are unavoidable since it is impossible to consider minor factors. Therefore, when developing the integrated model, precautions have to be taken for the application field and the limitations of the model. This also requires further study.

It should also be borne in mind that there is no intrinsic scale limitation of the application of either the FEM or the CA model. Although most of the work in the present study concentrated on continuum macro or meso-scale simulations, both the FEM and the structural model can be applied to micro-scale simulations.

In future studies, the numerical modelling by FEM and metallurgical model could be refined and developed according to the directions below.

(1) Subroutines of Forge2 and Forge3 have been developed to predict the metallurgical behaviour required to be standardised regarding the material and deformation conditions.

(2) Texture models are to be integrated into the FEM program to predict the deformed structure, such as the orientation and misorientations of the grains, which is one of the most critical inputs for the initial state of metallurgical models.

(3) Effects of secondary particles should be studied further and more precise structural modelling by CA as regards the retardation of recrystallisation by small particles or the promotion of recrystallisation by large particles should be examined.

(4) With the development of the computing hardware, more complicated extrusion simulations with the deformable dies can be established.

(5) Experiments using EBI and EBSD are required to give detailed information of the deformed structure and as a means to justify the simulation results.

The contour of an expert system is emerging which is shown in Figure 7.1. However, because of the lack of experimental justification, the constants used in the various continuum models and metallurgical models require standardisation. The integration of the varying content of the system into a single software package is required. Considerably greater computing times would, at the present, be a deterrent.

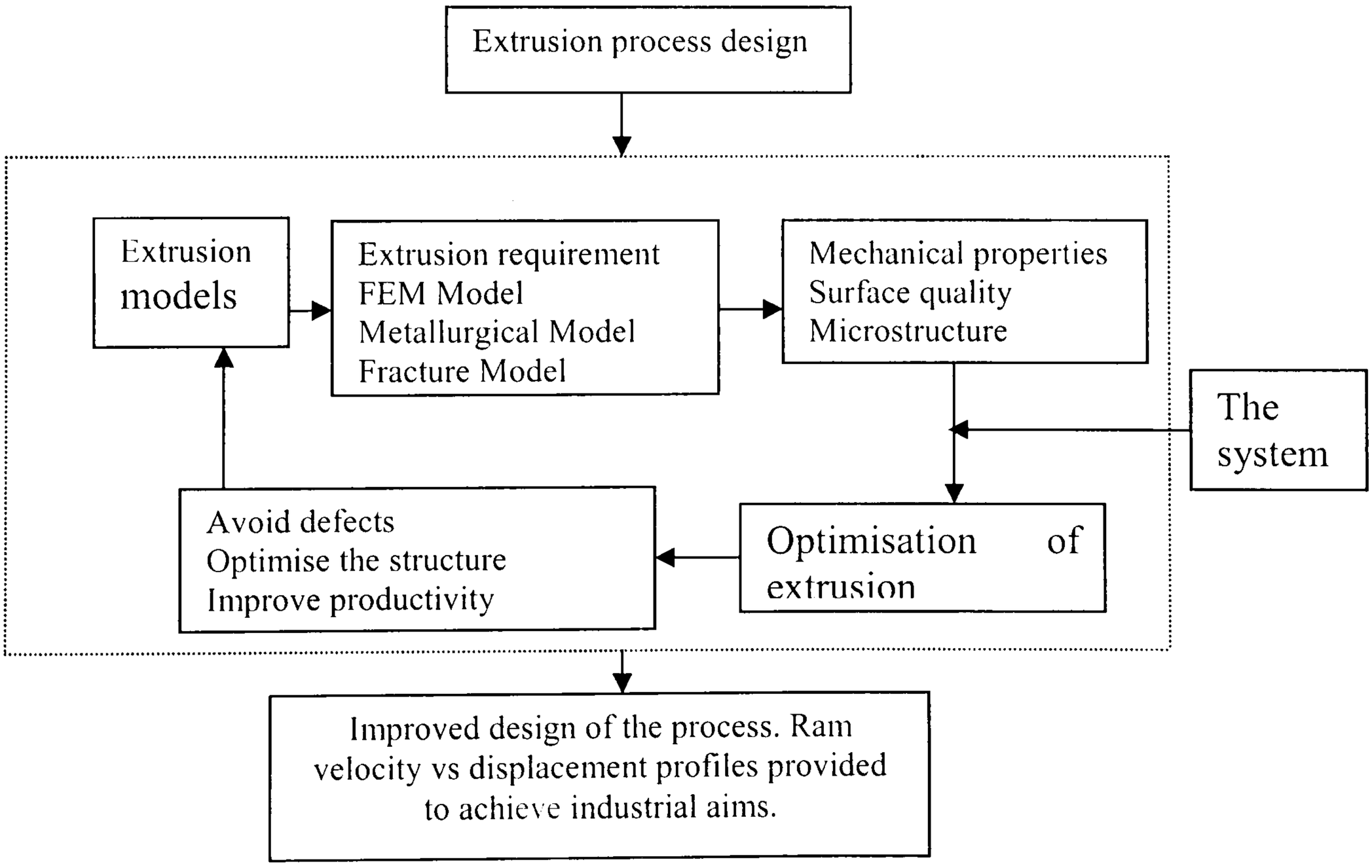

Figure 7.1 The function of the system

Reference

Abtahi, S., Furu, T., Bratland, D. H., Vatne, H. E., Bengtsson, B., Hou, J., 2001. Extrusion of different aluminium alloys, Experimental work and modelling treatments. *Journal of Computational and Applied Mathematics*, 174(1), 79-99.

Akeret, R., 1988. Control of metal flow in extrusion dies. *Light Metal Age*, 46 (7-8), p. 8.

Alonso-Sanz, R., 2005. Phase transitions in an elementary probabilistic cellular automaton with memory. *Physica A: Statistical Mechanics and its Applications*, 347, 383-401.

Anderson, M. P., Srolovitz, D. J., Grest, G. S., Sahni, P. S., 1984. Computer simulation of grain growth- I. kinetics. *Acta Metallurgica*, 32 (5), 783-791.

Arentoft, M., Bjerregaard, H., Andersen, C.B., Wanheim, T. 1998. Influence of the constitutive behaviour of materials on the formability in radial extrusion of tubular components. *Journal of Materials Processing Technology*, 75 (1-3), 122-126.

Arentoft, M., Gronostajski, Z., Niechajowicz, A., Wanheim, T., 2000. Determination of six stiffnesses for a press. *Journal of Materials Processing Technology*, 106, 2-18.

Aretz, H., Luce, R., Wolske, M., Kopp, R., Goerdeler, M., Marx, V., Pomana, G., Gottstein, G., 2000. Integration of physically based models into FEM and application in simulation of metal forming processes. *Modelling and Simulation in Materials Science and Engineering*, 8(6), 881-891.

Arif, A.F.M., Sheikh, A.K., Qamar, S.Z., Al-Fuhaid, K.M., 2001. Variation of pressure with ram speed and die profile in hot extrusion of aluminum-6063. *Materials and Manufacturing Processes*, 16 (5), 701-716.

Ashby, M.F., 1992. Physical modelling of materials problems. *Materials Science and Technology*, 8(2), 102-111

Aukrust, T., Tjotta, S., Vatne, H. E., Van, H.P., 1997. Coupled FEM and texture modelling of plane strain extrusion of an aluminum alloy. *International Journal of Plasticity*, 13 (1-2), 111-125.

Baskes, M. I., 1999. The status role of modeling and simulation in materials science and engineering. *Current Opinion in Solid State and Materials Science*, 4(3), 273-277.

Bathe, K. J., 1996. *Finite Element Procedure.* 2nd ed. London: Englewood Cliffs, N.J.: Prentice-Hall.

Baxter, G.J., Furu, T., Whiteman, J.A., Sellars, C.M. 1996. Influence of transient deformation conditions on strength, microstructure and recrystallisation during thermomechanical processing of an aluminium alloy Al-1% Mg. *Materials Science Forum*, 217-222 (1), *Aluminium Alloys - Their Physical and Mechanical Properties*, 1996. 459-464.

Baxter, G.W., Behringer, R.P. 1991. Cellular automata models for the flow of granular

materials. *Physica D: Nonlinear Phenomena*, 51 (1-3), p. 465.

Becker, R. 1991. Applications of crystal plasticity constitutive models *Model Deform Cryst Solids presented Annu Meet Miner Met Mater Soc*, 249-269.

Benedyk, J.C. 2001. Review and analysis of emerging extrusion processes. Part II: The evolving role of friction in hot extrusion. *Light Metal Age*, 59 (9-10), 6-14.

Berezhnoy, V. L., 1997. Friction-assisted extrusion as an alternative to the indirect and direct extrusion of hard aluminum alloys. *Light Metal Age*, 55 (3-4), 8-13

Bessey, G. 2004. The front-loading compact extrusion press comes of age *Aluminium International Today*, 16 (5), 34-38.

Bianchi, J. H. and Sheppard, T., 1987. Comparison of a viscoplastic finite-element model with slip-line field and upper-bound solutions for nonhardening material subjected to plane strain and axisymmetric extrusion. *International Journal of Mechanical Sciences*, 29 (1), 61-81.

Biner, S. B., 1992. Simulation of forward-backward extrusion with numerical and model material techniques. *Proceedings of a Symposium on Concurrent Engineering Approach to Materials Processing, Nov 1-5 1992, Chicago, IL, USA*. Publ by Minerals, Metals & Materials Soc (TMS), p. 203.

Biswas, A. K. and Repgen, B. 1996. Isothermal and isopressure extrusion results of press optimisation in various extrusion plants. *Proc. 6th international extrusion technology seminar, Aluminium Association, Washington DC.* 1, 37-44.

Bolt, J. H., Van Der Gaag, L, C., Renooij, S., 2005. Introducing situational signs in qualitative probabilistic networks. *International Journal of Approximate Reasoning*, 38 (3), 333-354.

Bowden, F. P. and Tabor, D., 1964. *The friction and lubrication of solids, part II.* Oxford: Oxford University Press.

Bryant, A. J. B., Dixon, W. B., Roger, A. P. 1999. Isothermal extrusion. *Light metal age.* 8-34.

Bunting, C. D. 1983. Closed loop control of extrusion lines increases product quality and reduces cost. *SPE PACTEC '83 - 7th Annual Pacific Technical Conference: Advances in Technology Yield Profitability., Anaheim, Calif, USA.* Soc of Plastics Engineers, 69-75

Castle, A. F., 1974. Continuum and Structural Aspects of Aluminium Allou Extrusion. Theiss (PhD). Imperial College, University of London.

Castle, A. F., Sheppard, T., 1976a. Development of product structure at commencement of extrusion. *Metals Technology*, 3 (9), 433-436.

Castle, A. F. and Sheppard, T., 1976b. Hot Working Theory Applied to Extrusion of Some Aluminium Alloys. *Met Technol.* 3 (10), 454-464.

Castle, A. F. and Sheppard, T., 1976. Hot-working theory applied to extrusion of some aluminium alloys. *Metals Technology*, 3 (10), 454-464.

Castle, A. F., Kelly, F. J., 1980. Application of programmable logic controllers to extrusion plant control. *Aluminium*, 56(11), 703-705.

Chadwick, H. 1982. Cold impact extrusion of closed ended aluminium tubes for high pressure gas cylinders and other components. *WireAsia/TubeAsia, Oxted, Surrey, Engl Tl*. B, p. 17.

Chadwick, R., 1970. Relevance of lubrication in extrusion. *Metals Mater*, 4 (5), 201-207.

Chanda, T., Zhou, J., Duszczyk, J., 2000. FEM analysis of aluminum extrusion through square and round dies. *Materials and Design*, 21 (4), 323-335.

Chanda, T., Zhou, J., Duszczyk, J., 2001. A comparative study on iso-speed extrusion and isothermal extrusion of 6061 Al alloy using 3D FEM simulation. *Journal of Materials Processing Technology*, 114 (2), 145-153.

Chen, B. K., Thomson, P.F., and Choi, S. K., 1992. Computer modelling of microstructure during hot flat rolling of aluminium. *Materials Science and Technology*, 8, 72-77.

Chen, P. C., Kaminski, D. A., Messler Jr., R.W., Shie, J. R. 2000. Application of Inverse Method to Determine Heat Transfer Coefficients for Post-Extrusion Spray Quenching of Aluminum Alloys. *ASM Proceedings: Heat Treating*, 2, 1125-1131.

Chenot, J. L., Tronel, Y., Soyris, N. 1992. Finite element calculation of thermo-coupled large deformation in hot forging. *Conduction, Radiation and Phase Change*, 493-511.

Cheung, Y. K., Lo, S. H., Leung, A. Y. T., 1996. *Finite Element Implementation.* Oxford : Blackwell Science.

Childs, T. H. C., 1974. Metal flow in the hot extrusion of mild steel. *Metals Technology*, 1 (7), 305-309.

Clift, S. E. , Hartley, P., Sturgess, C. E. N., Rowe, G. W., 1990. Fracture prediction in plastic deformation processes. *International Journal of Mechanical Sciences*, 32 (1), 1-17.

Clode, M.P. and Sheppard, T., 1990. Formation of die lines during extrusion of AA 6063. *Materials Science and Technology*, 6 (8), 755-763.

Cockcroft, M. G., Latham, D. G., 1968. Ductility and the workability of metals. *Journal of the Institute of Metals*, 96, 2444-2477.

Cockroft, R. 1969. Glass Lubricated Extrusion of Steel. *Metals & Matls*, 3 (9), 351-355.

Crotaz, C. R., Shercliff, H.R., Mackay, D.J.C., 2002. Advanced Statistical Modelling of Processing of Aluminium Alloys. *Materials Science Forum.* 396-402, 643-648.

Davies, C. H. J., 1995. The effect of neighbourhood on the kinetics of a cellular automaton recrustallisation model. *Scripta metallurgica at materialia*, 33 (7), 1139-1143.

Davies, C. H. J. 1997. Growth of nuclei in a cellular automaton simulation of recrystallisation. *Scripta materialia*, 36 (1), 35-40.

Davies, C. H. J. and Hong, L. 1999. The cellular automaton simulation of static recrystallisation in cold-rolled AA1050. *Scripta materialia*, 40 (10), 1145-1150.

Dawson, P.R., Beaudoin, A.J. and Mathur, K. K., 1994. *In proceedings 15th RISO International Symposium on Materials Science,* eds.: Andersen, S. I., BildeSorensen, J. B., Lorentzen, T., Pedersen, O. B. and Sorensen, N.J., Roskilde: RISO National Laboratory, p. 33.

Dixon, B., 2004. Billet surface flow during extrusion of aluminium alloys. *Aluminium International Today*, 16 (2), 44-46.

DOAR, J. L. 1969. Co-extrusion. Easy way to complex films. *Package Eng*, 14 (9), 86-93.

Doherty, R. D., Samajdar, I., Necker, C. T., Vatne, H. E., Nes, E., Hansen, N., Jensen, D. J., Liu, Y. L., Ralph, B., 1995. Microstructure and crystallographic aspects of recrystallization, *16 Riso International Symposium on Materials Science. Riso National Lab.*, Roskilde, Denmark, 1-23.

Domanti, T., Horrobin, D. J. and Bridgeater, J., 2002. An investigation of fracture criteria for predicting surface fracture in paste extrusion. *International Journal of Mechanical Science*, 44, 1381-1410.

Duan, X., Sheppard, T., 2002a. Three dimensional thermal mechanical coupled simulation during hot rolling of aluminium alloy 3003. *International Journal of Mechanical Sciences*, 44 (10), 2155-2172.

Duan, X., Sheppard, T., 2002b. Simulation of substructural strengthening in hot flat rolling. *Journal of Materials Processing Technology*, 125-126, 179-187.

Duan, X., Sheppard, T. 2002c. Influence of forming parameters on static recrystallization behaviour during hot rolling aluminium alloy 5083. *Modelling and Simulation in Materials Science and Engineering*, 10 (4), 363-380.

Duan, X., Sheppard, T., 2002d. Influence of forming parameters on static recrystallization behaviour during hot rolling aluminium alloy 5083. *Modelling and simulation in materials science and engineering.* 10, 363-400.

Duan, X., Sheppard, T., 2003. Computation of substructural strengthening by the integration of metallurgical models into the finite element code. *Computational Materials Science*, 27 (3), 250-258.

Duan, X., Velay, X., Sheppard, T., 2004. Application of finite element method in the hot extrusion of aluminium alloys. *Materials Science and Engineering*, A 369 (1-2), 66-75.

Dyja, H. and Korczak, P., 1999. Thermal-mechanical and microstructural model for the FEM simulation of hot plate rolling. *Journal of Materials Processing Technology*. (92-93), 463-467.

Evans, R. W., 1993. Modelling of the hot-working of high performance alloys. *Key Engng Mater.* 77-78, 227-240.

Fagan, M. J., 1992. *Finite Element Analysis, theory and practice.* England: Longman Scientific and Technical, Longman Group UK Limited.

Farag, M. M. and Sellars, C. M. 1973. Low stress in hot extrusion of commercial-purity aluminium. *Journal of the Institute of Metals (London)*, 101, 137-145.

Ferguson, D. Complex extrusions. 1996. *Advanced Materials & Processes*, 149 (4), 27-28.

Ferguson, H., 1993. Physical simulation makes inroads in advanced materials testing. *Advanced materials & processes.* 4, 33-36.

Fielding, Roger A.P., Bryant, A.J., Macey, G.E., 2002. Homogenization of aluminum alloy extrusion billet-part I. *Light Metal Age*, 60(3-4), 6-10.

Fleck, N. A., Muller, G. M., Ashby, M. F., Hutchinson, J. W., 1994. Strain gradient plasticity: theory and experiment. *Acta Metallurgica et Materialia*, 42 (2), 475-487.

Flitta, I. and Sheppard, T., 2003. Nature of friction in extrusion process and its effect on material flow. *Materials Science and Technology*, 19 (7), 837-846.

Fowlkes, W. Y., 1995. *Engineering methods for robust product design: using Taguchi methods in technology and product development.* Reading, Mass.: Addison-Wesley Pub. Co.

Furu, T., Shercliff, H. R., Sellars, C. M., Ashby, M. F. 1996. Physically-based modelling of strength, microstructure and recrystallisation during thermomechanical processing of Al-Mg alloys. *Materials Science Forum*, 217-222 (1), *Aluminium Alloys - Their Physical and Mechanical Properties*, 453-458.

Furu, T., Shercliff, H. R., Baxter, G. J., Sellars, C. M., 1999. Influence of transient deformation conditions on recrystallization during thermomechanical processing of an Al-1% Mg alloy. *Acta Materialia*, 47 (8), 2377-2389.

Gallas, J. A. C., Grassberger, P., Herrmann, H. J., Ueberholz, P., 1992. Noisy collective behaviour in deterministic cellular automata. *Physica A: Statistical and Theoretical Physics*, 180 (1-2), p. 19.

Gamache, E., Lafleur, P. G., Peiti, C., Vergnes, B. 1999. Measurement of the coefficient of dynamic friction at extrusion processing conditions. *Polymer Engineering and Science*, 39 (9), 1604-1613.

Geiger, J., Roosz, A., Barkoczy, P., 2001. Simulation of grain coarsening in two dimensions by Cellular-Automaton. *Acta Materialia*, 49(4), 623-629.

Gelin, J. C., Ghouati, O., Shahani, R., 1994. Modelling the plane strain compression

test to obtain constitutive equations of aluminum alloys. *International Journal of Mechanical Sciences*, 36 (9), 773-796.

Gittus, J. and Zarka, J., 1986. *Modelling Small Deformation of Polycrystals*. London: Elsevier Applied Science.

Gopalakrishna, S., Jaluria, Y., 1991. Heat transfer and flow of a non-Newtonian fluid in an extrusion process. *American Society of Mechanical Engineers, Heat Transfer Division, (Publication) HTD*, 174, *Fundamentals of Heat Transfer in Non-Newtonian Fluids*, 13-19.

Gouveia, B. P. P. A., Rodrigues, J. M. C., Martins, P. A. F., Bay, N., 2001. Physical modelling and numerical simulation of the round-to-square forward extrusion. *Journal of Materials Processing Technology*, 112 (2-3), 244-251.

Grassberger, P. 1983. Chaos and diffusion in deterministic cellular automata. *Physica D: Nonlinear Phenomena*, 10D (1-2), 52-58.

Grong, O. and Shercliff, H. R. Microstructure modelling in metals processing. Progress in materials science. 47 (2002) 163-282.

Guha, R. M. and Lengyel, B., 1974. Temperatures in high speed hydrostatic extrusion em dash drawing with friction. *Journal of the Institution of Engineers (India), Part MC: Mechanical Engineering Division*, 54 (3), 117-124.

Guice, W. L. and Witte, L. C., 1987. Heat transfer following an extrusion process. *American Society of Mechanical Engineers, Heat Transfer Division, (Publication) HTD*, 69, 61-68.

Gunasekera, J. S., Gegel, H. L., Doraivelu, S. M., Malas, J. C., Graham, J. C., 1984. Computer aided design of 'MULTI-HOLED', streamlined extrusion dies. *CIRP Annals*, 33 (1), 129-131.

Gupta, A. K., Hughes, K. E., 1979. Hot extrusion of aluminium brass. *Metallurgia*, 46 (10), 644-645.

Hambli, R. and Reszka, M., 2002. Fracture criteria identification using an inverse technique method and blanking experiment. *International Journal of Mechanical Sciences*, 44, 1349-1361.

Hardouin, J. P., 1992. Bearing length calculation by control of metal flow pressure. Aluminium association, *Fifth extrusion technology seminar*, 1992, Vol. II, 291-303.

Harrison, G. F. 1994. Role of material modelling techniques in stress analysis and life assessment of modern aero-engine components. *Proceedings of the Institution of Mechanical Engineers, Part G: Journal of Aerospace Engineering*, 208 (1), 19-31.

Herberg, J. and Skauvik, I. FEM simulations of flow through porthole dies for extrusion of aluminium. *Proceedings of the Safety and Reliability Society Symposium - SARSS, Safety & Reliability Assessment- an Integral Approach*, 1993, p. 671.

Hesselbarth, H. W. And Gobel, I. R. 1991. Simulation of recrystallization by cellular automata. *Acta metall. Mater.* 39 (9). 2135-2143.

Hodges, W. C. 1970. Designing with aluminium extrusions. *Engineering Design Show Conf*, 2- 6 (18B), p. 16.

Huang, Y. 1998. Integrated computer aided extrusion process simulation, die design/manufacturing/management planning system. *Light Metal Age*, 56 (5-6). 76-81.

Humphreys, F. J., 1979. Local lattice rotations at second phase particles in deformed metals. *Acta Metallurgica*, 27, 1801-1814.

Humphreys, F.J. A Network Model for Recovery and Recrystallisation. Scripta Metallurgica et Materialia. 27, 1557-1562, 1992.

Humphreys, F. J. Network model for recovery and *Scripta Metallurgica et Materialia*, v 27, n 11, Dec 1, 1992, p 1557-1562

Hunter, K.L., Snook, I.K., Swingler, D.L., Wagenfeld, H.K. Monte Carlo calculation of the contribution of backscattered electrons to secondary electron emission from aluminium. *Journal of Physics D: Applied Physics*, v 23, n 12, Dec 14, 1990, p 1738-1743

Hurley, P.J. and Humphreys, F.J. The application of EBSD to the study of substructural development in a cold rolled single-phase aluminium alloy. Acta materiallia 51 (2003a) 1087-1102.

Hurley, P.J. and Humphreys, F.J. Modelling the recrystallization if single-phase aluminium. Acta Materialia 51 (2003b) 3779-3793.

Iwata, K., Osakada, K., Fujino, S., 1972. Analysis of hydrostatic extrusion by the finite element method. *Journal of Engineering for Industry, Transactions of the ASME*, 94B (2), 697-703.

Janssens, K. G. F. 2003. Random grid, three-dimensional, space-time coupled cellular automata for the simulation of recrystallisation and grain growth. *Modelling Simul. Mater. Sci. Eng.* 11, 157-171.

Jekl, M., Zupancic, B., Matko, D., Sehic, Z. 1991. The role of analog simulation in the hybrid simulation system. *Melecon*, 884-887.

Johnson, W. and Kudo, H., 1962. *The mechanics of metal extrusion.* Manchester: Manchester University Press.

Jonas, J. J., Sellars, C. M., and Tegart, W. J. McG. 1969. Strength and structure under hot-working conditions. *Metallurgical Review,* 130, 1-23.

Jones, M. J. and Humphreys, F. J., 2003. Interaction of recrystallization and precipitation: The effect of Al_3S_c on the recrystallization behaviour of deformed aluminium. *Acta Materialia.* 51, 2149-2159.

Johnson, W. and Kudo, H. 1962. *The mechanics of metal extrusion.* Manchester: Manchester University Press.

Kagaris, D., Tragoudas, S., Karayiannis, D., 1997. Improved nonenumerative path-delay fault-coverage estimation based on optimal polynomial-time algorithms. *IEEE*

Transactions on Computer-Aided Design of Integrated Circuits and Systems, 16 (3), 309-315.

Kaida, K., Hirano, M., Fujii, T., Yoshida, M. 1997. Aluminium extrusion bend processing technologies. *R&D: Research and Development Kobe Steel Engineering Reports*, 47 (2), 17-20.

Kamal, M. R. and Kalyon, D. 1983. Heat transfer and microstructure in extrusion blowmolding. *Polymer Engineering and Science*, 23 (9), 503-509.

Kirtley, N. 2001. The role of test in the age of simulation. *S V Sound and Vibration*, 35 (4), 14-16.

Ko, D., Kim, B. and Choi, J., 1996. Prediction of surface-fracture initiation in the axisymmetric extrusion and simple upsetting of an aluminum alloy. *Journal of Materials Processing Technology,* 62, 166-174.

Kowalsky, U., Ahrens, H., 1997. FE-analysis of the recipient of an extrusion press applying microstructure-related material model. *Computers and Structures*, 64 (1-4), 655-665.

Krishnamoorthy, C. S., 1994. *Finite Element Analysis-Theory and programming.* Second editioin. New Delhi: Tata McGraw-Hill Publishing Company Limited.

Lange, G., 1971. Heat balance of the extrusion process- 1, (Der Waermehaushalt beim Strangpressen) *Z Metallk*, 62 (8), 571-577.

Langseth, M., Berstad, T., Hopperstad, O.S., Clausen, A.H., 1994. Energy absorption in axially loaded square thin-walled aluminium extrusions. *Proceedings of the 3rd International Conference on Structures under Shock and Impact III*, p. 401.

Li, L., Zhou, J., Duszczyk, J. 2003. A 3D FEM simulation study on the isothermal extrusion of a 7075 aluminium billet with a predetermined non-linear temperature distribution. *Modelling and Simulation in Materials Science and Engineering.* 11. 401-416.

Li, L., Zhou, J., Duszczyk, J. 2004. Prediction of temperature evolution during the extrusion of 7075 aluminium alloy at various ram speeds by means of 3D FEM simulation. *Journal of Materials Processing Technology*, 145 (3), 360-370.

Li, Q., Smith, C. J., Harris, C., Jolly, M. R. 2003. Finite element modelling investigations upon the influence of pocket die designs on metal flow in aluminium extrusion: Part II. Effect of pocket geometry configurations on metal flow. *Journal of Materials Processing Technology*, 135, 197-203.

Li, S., Bourke, M. A. M., Beyerlein, I. J., Alexander, D. J., Clausen, B. 2004. Finite element analysis of the plastic deformation zone and working load in equal channel angular extrusion. *Materials Science and Engineering.* A382 (1-2), 217-236.

Lin, X. B., Xiao, H. S., Zhang, Z. L. 2003. Research on the selection of friction models in the finite element simulation of warm extrusion. *Acta Metallurgica Sinica (English Letters)*, 16 (2), 90-96.

Liu, W. F., Peng, D. S., Jin, X. Y. 2000. FEM simulation of extrusion of 3003 alloy tubes. *Transactions of Nonferrous Metals Society of China (English Edition)*. 10 (5). 656-659.

Liu, Y. Baudin, T. and Penelle, R., 1996. Simulation of normal grain growth by cellular automata. *Scripta materialia*, 34(11), 1679-1683.

Livesley, R. K., 1983. Some aspects of structural computing: 1943-1983. *Instability and Plastic Collapse of Steel Structures, Proceedings of The Michael R. Horne Conference., Manchester* Dobbs Ferry, 16-25.

Lof, J. and Blokhuis, Y., 2002. FEM simulations of the extrusion of complex thin-walled aluminium sections. *Journal of Materials Processing Technology*, 122 (2-3), 344-354.

Lof, J., 2001, Elasto-viscoplastic FEM simulations of the aluminium flow in the bearing area for extrusion of thin-walled sections. *Journal of Materials Processing Technology*, 114(2), 174-183.

Long, H. W. 1986. Some differences between direct and indirect extrusion of aluminium alloys. *Inst of Metals,* 252-257.

Lopez, M. J., Martinez, M., Bracho, S., 1999. Method for designing a deterministic test pattern generator based on cellular automata. *Journal of Electronic Testing: Theory and Applications (JETTA)*, 14 (3), 245-258.

Luton, M. J., Sellars, C. M., 1969. Dynamic recrystallization in nickel an nickel0iron alloys during high temperature deformation. *Acta Metallurgica*, 17 (8), 1033-1043.

Maccarini, G., Giardini, C., Bugini, A., 1990. Extrusion operations. FEM approach and experimental results. *Journal of Materials Processing Technology*, 24, 395-402.

Makowice, D., 1993. Probabilistic approach to the dynamics of deterministic homogeneous and symmetric two-dimensional cellular automata. *Physica A: Statistical and Theoretical Physics*, 199 (2), 1993, p. 299.

Marthinsen, K., Nes, E., Brechet, Y., 2002. On the mechanisms of dynamic recovery. *Scripta Materialia*, 47 (9), 607-611.

Marthinsen, K., Holmedal, B., Abtahi, S., Valle, R., Chen, S., Nes, E. 2003. Coupled FEM and microstructure modeling applied to rolling and extrusion of aluminium alloys. *Materials Science Forum*, 426-432 (5), 3777-3782.

Marx, V., Reher, F. R., Gottstein, G., 1999. Simulation of primary recrystallization using a modified three-dimensional cellular automaton. *Acta Materialia*, 47 (4), 1219-1230.

Mathur, K. K., Dawson, P. R., 1989. On modeling the development of crystallographic texture in bulk forming processes. *International Journal of Plasticity*, 5 (1), 67-94.

McClintock, F. A., Kenney, K. L., Jung, S., Reuter, W. G., Parks, D. M., 1996. Asymmetric, fully plastic crack growth mechanics and tests for structures and piping. *American Society of Mechanical Engineers, Pressure Vessels and Piping Division*

(Publication) PVP, v 343, *Development, Validation, and Application of Inelastic Methods for Structural Analysis and Design*, 153-167.

McHugh, P. E., Asaro, R. J., Shih, C. F., 1993. Computational modeling of metal matrix composite materials - I. Isothermal deformation patterns in ideal microstructures. *Acta Metallurgica et Materialia*, 41 (5), 1461-1476.

Mclaren, J. W., Halicz, L, Lam, J. W. H., 1994. On-line method for the determination of lead and lead isotope ratios in fresh and saline waters by inductively coupled plasma mass spectrometry. *Spectrochimica Acta, Part B: Atomic Spectroscopy*, 49 (7), 637-647.

Mclaren, A. J. and Sellars, C. M., 1992. Modelling distribution of microstructure during hot rolling of stainless steel. *Mater. Sci. Technol.* 8, 1090-1094.

McShane, H., Tutcher, M. G., Sheppard, T. 1978. Analysis of specific pressure necessary to extrude aluminium alloy compacts. *Powder Metallurgy*, 21 (2), 47-51.

Meghdadi, A. H., Akbarzadeh-T, M. R., 2002. Probabilistic fuzzy logic and probabilistic fuzzy systems. *IEEE International Conference on Fuzzy Systems*, 3, 1127-1130.

Meguid, S. A., Shagal, G., Stranart, J. C., 2001. 3D FE analysis of peening of strain-rate sensitive materials using multiple impingement models. *International Journal of Impact Engineering*, 27 (2), 119-134.

Milennin, A. A., Golovko, A. N., Mamuzic, I., 2002. The application of three-dimensional computer simulation when developing dies for extrusion of aluminium shapes. *Metalurgija* 41 (1), 53-55.

Miller, D. P., 1988. Low-level determination of nitrogen dioxide in ambient air using the palmes tube. *Atmospheric Environment*, 22 (5), 945-947.

Mondolfo, L. F.; Barlock, J. G.; Tomeo, A. P., 1976. Control of manganese distribution in 3003 aluminium alloy. *Energies: Journal of the Solar Energy Society of America*, 2, 365-386.

Morse, C.G. Extrusion coating 1970, retrospection, expectation. 2-1. CODEN: TAPPA. *Conference: TAPPI, 25th Plast Pap Conf, Sept 28-30.* 71-83.

Moshksar, M. M. and Ebrahimi, R. 1999. New upper bound analysis for prediction of load and flow pattern in backward extrusion forging. *Iranian Journal of Science and Technology*, 23 (3), 251-266.

Mueller, K. M., Liu, M., Burns, S. A., 2002. Fully stressed design of frame structures and multiple load paths. *Journal of Structural Engineering*, 128 (6), 806-814.

Muller, K. B., 2002. Indirect extrusion with active friction (ISA). *Key Engineering Materials*, 233-236 (I), 323-328.

Murphy, C. A., Perera, T., 2002. The definition of simulation and its role within an aerospace company. *Simulation Practice and Theory*, 9 (6-8), 273-291.

Nakamura, T. and Ishibashi, I., 1995. Forward-backward extrusion type friction testing method. *Technical Paper - Society of Manufacturing Engineers. MF*, n MF95-127. p. 6.

Nes, E., Vame, H. E., Daaland, O., Furu, T., Orsund, R., Marthinsen, K., 1994. Physical modelling of microstructural evolution during thermomechanical processing of aluminium alloys. *SINTEF Materials Technology*, STF24 S94003.

Nes, E. 1998. Modelling of work hardening and stress saturation in FCC metals. *Progress in Materials Science.* 41, 129-193.

Nes, E., Marthinsen, K., 2002. Modeling the evolution in microstructure and properties during plastic deformation of f.c.c.-metals and alloys - An approach towards a unified model. *Materials Science and Engineering,* A322 (1-2), 176-193.

Nes, E., Marthinsen, K., Holmedal, B., 2004. The effect of boundary spacing on substructure strengthening. *Materials Science and Technology*, 20 (11), 1377-1382.

Ohuchi, Kiyoyuki and Takahashi, Hiroo, 1988. Load and material flow in hot extrusion of aluminium and copper powder compacts. *Bulletin of Mechanical Engineering Laboratory (Sakura-mura)*, 50, p. 21.

Oki, Y., Yoshida, Y., Yamashita, T., 1990. Mathematical model used in calculating extrusion pressure of an aluminum alloy with regard to an extrusion die structure. *Keikinzoku/Journal of Japan Institute of Light Metals*, 40 (11), p. 833.

Onawola, O. O., Adeyemi, M. B., 2003. Warm compression and extrusion tests of aluminium. *Journal of Materials Processing Technology*, 136 (1-3), 7-11.

Oyane, M., Yoshinaga, R., Goto, Y., 1978. Testing method for investigation friction and lubrication in metal working process. *Digest of Technical Papers - IEEE MTT-S International Microwave Symposium*, 339-346.

Pahl, G. and Beitz, W., 1977. *Engineering design.* 2nd ed. London: the Design Council, Berling: Springer.

Patterson, S. J., 1981, The direct and indirect extrusion of aluminium alloys. Thesis (Phd). Imperial College, University of London.

Paterson, S. J., Sheppard, T., 1982. Structural changes occurring during thermal treatments during extrusion of Al-Cu-Mg-Mn-Si (AA2014) Alloy. *Metals Technology*, 9, 389-398.

Pearson, C. E., Parkins, R. H., 1961. *The extrusion of Metals*, London: Chapman and Hall Ltd.

Peng, Z. and Sheppard, T. 2003. Prediction of static recrystallisation during extrusion of Aluminium Alloy AA2024. *Proceedings of 15th European Simulation Symposium (ESS2003), Delft, The Netherland.* Society for Modelling and Simulation International, 391-398.

Peng, Z. and Sheppard, T., 2004a. Individual influence of forming parameters on surface recrystallization during aluminium extrusion. *Modelling and simulation in materials science and engineering.* 12, 43-57.

Peng, Z. and Sheppard, T., 2004b. Simulation of multi-hole die extrusion. *Materials science and engineering.* A367, 329-342.

Peng, Z. and Sheppard, T., 2004c. A Study on Surface Cracking in Extrusion of Aluminium Alloy AA2014. *Materials science and technology*. 20, 1179-1191

Peng, Z. and Sheppard, T., 2004d. A Discussion on the Scaling Effect on Numerical Simulation of the Extrusion Process. *Materials science and technology*. 20, 1335-1339.

Peng, Z. and Sheppard, T., 2004e. A study on material flow in isothermal extrusion by FEM simulation. *Modelling and simulation in materials science and engineering.* 12, 745-763.

Peng, Z. and Sheppard, T. 2004f. Prediction of static recrystallisation during shape extrusion. *8th International Aluminium Extrusion Technology Seminar, May 2004 (ET04)*, The united states. Florida: Aluminium association and aluminium extruder councils, 79-92.

Peng, Z. and Sheppard, T. 2004g. Application of FEM to modelling of multi-hole die extrusion. *8th International Aluminium Extrusion Technology Seminar, May 2004 (ET04)*, The united states. Florida: Aluminium association and aluminium extruder councils, 93-106.

Peng, Z. and Sheppard, T. 2004h. Simulation of multi-hole die extrusion by Finite Element Method. *Proceedings of the 7th Esaform Conference on Material Forming ESAFORM 2004, Trondheim, Norway*. Norwegian University of Science and Technology, 605-608

Peng, Z. and Sheppard, T. 2005a. Effect of die pockets on multi-hole die extrusion. *Materials Science and Engineer A*. Received.

Peng, Z. and Sheppard, T. 2005b. Numerical simulation by FEM and Cellular Automata of static recrystallisation after hot extrusionand solution treatment of aluminium alloys. *Modelling and simulation in materials science and engineering.* In review.

Peng, Z. and Sheppard, T. 2005c. A Discussion on the Scaling Effect on Numerical Simulation of the Extrusion Process. *Materials Science and Technology. Received.*

Pemantle, R., 2005. A probabilistic model for the degree of the cancellation polynomial in Gosper's algorithm. *Journal of Algorithms*, 54 (1), 58-71.

Pezzee, C. F. And Dunand, D. C., 1994. Simulation by cellular automata of the (re)crystallization of a matrix containing an inert second phasse. *Materials research society symposium proceedings*, 321, 295-300.

Pinkham, M. 2002. Simulation software benefits extrusion process. *Aluminium Today*, 14(7), 31-32.

Potente, H., Krell, B., 1996. Continuous Process Control for improved quality assurance in extrusion blow molding. *Annual Technical Conference - ANTEC, Conference Proceedings*, 1, 991-995.

Ross, Phillip J., 1988. *Taguchi techniques for quality engineering : loss function, orthogonal experiments, parameter and tolerance design.* London : McGraw-Hill.

Ruppin, D. and Strehmel, W., 1977. Direktes atrangpressen mit konstanter austrit tstemperature em dash einsatz axialer block tempera tuprofile. (Direct extrusion with constant exit temperature – Introduction of axial ingot temperature gradients). *Aluminium*, 53(4), 233-239.

Raabe, D. 1998a. *Computational material science: the simulation of materials, microstructures and properties.* New York, Chichester, Brisbane, Singapore, Toronto: Weinheim.

Raabe, D., 1998b. Discrete mesoscale simulation of recrystallization microstructure and texture using a stochastic cellular automation approach. *Materials Science Forum*, 273-275, 169-174.

Raabe, D., 2002. Cellular automata in materials science with particular reference to recrystallization simulation. *Annual Review of Materials Science*, 32, 53-76.

Rahman, L., Rowe, P., Cheyne, A., Wilson, D. I., 2002. Ram extrusion of potato starch dough through multi-holed dies. *Food and Bioproducts Processing: Transactions of the Institution of of Chemical Engineers, Part C*, 80 (1), 12-19.

Raghunathan, N. and Sheppard, T., 1989. Microstructural development during annealing of hot rolled Al-Mg alloys. *Materials Science and Technology*, 5 (6), 542-547.

Raghunathan, N., Sheppard, T., 1986. Hot worked and annealed microstructures in Al-Mg alloys. *Inst of Metals*, 357-372.

Reinikainen, T., Welo, T., Korhonen, A.S., Kivivuori, S., 1994. Comparison of two commercial FEM codes in cold extrusion simulation. *Journal of Materials Processing Technology*, 42 (2), 137-146.

Renne, I.P., Sumarokova, A.I., 1989. Friction forces on container and die contact surfaces during extrusion. *Soviet Forging and Sheet Metal Stamping Technology (English Translation of Kuznechno-Shtampovochnoe Proizvodstvo)*, 1, 87-92.

Rice, J. R., Trace, D. M., 1969. On the ductile enlargement of voids in triaxial stress field. *Journal of mechanics and physics of solids*, 17, 201-218.

Rollett, A. D. Raabe, D., 2001. A hybrid model for mesoscopic simulation of recrystallization. *Computational Materials Science*, 21 (1), 69-78.

Rong, H., Inoue, K., 1998. Die designs for wide-thin shape extrusion. *R&D: Research and Development Kobe Steel Engineering Reports*, 48 (1), 72-75.

Ryen, O., Holmedal, B., Nes, E., 2002. Characterisation and modelling of work hardening in Al-Mg and Al-Mn alloys. *Materials Science Forum*, 396-402 (2), 1145-1150.

Sara, P.K. 1998. Thermodynamics and Tribology in Aluminium Extrusion. *Wear*, 218-124.

Saha, K., 2000. *Aluminum extrusion technology*. Ohio, USA: ASM international. Materials Park.

Sarma, G. B., Dawson, P. R., 1996. Texture predictions using a polycrystal plasticity model incorporating neighbor interactions. *International Journal of Plasticity*, 12 (8), 1023-1054.

Schey, J. A., 1983. Surface treatment. *Metals Soc (Book 301)*, 235-241.

Schmauder, S., Weichert, D., 1996. Proceedings of the 1994 4th International Workshop on Computational Modelling of the Mechanical Behaviour of Materials. *Computational Materials Science*, 5 (1-3), p. 276.

Sellars, C. M. 1986. Modelling of structural evolution during hot working processes. *Riso Natl Lab*, 167-187.

Sellars, C. M. and Zhu, Q., 1998. Microstructural evolution during hot deformation of aluminium - magnesium alloys. *Proceedings of the TMS Fall Meeting*, 185-197.

Sellars, C.M. and Zhu, Q., 2000. Microstructural modelling of aluminum alloys during thermomechanical processing. *Materials Science and Engineering* A280 (1), 1-7.

Sheikh, A. K., Qamar, S. Z., Arif, A. F. M., 2004. A new definition of shape complexity for metal extrusion. *Journal of Materials Processing Technology*, 155-156 (1-3), *Proceedings of the International Conference on Advances*, 1734-1739.

Sheppard, T. and Chare, P. J. M. 1972. Extrusion of atomized aluminium powders. *Industrie-Anzeiger*, 15 (29), 17-41

Sheppard, T. and Raybould, D., 1973a. Axisymmetric extrusion: the effect of temperature rise and strain rate on the activation enthalpy and material constants of some aluminium alloys and their relation to recrystallisation, substructure, and suvsequent mechanical porperties. *J Inst Met (London)*, 101, 65-72.

Sheppard, T. and Raybould, D., 1973b. On load and temperature rise during the extrusion of superpure Al, Al-Zn and Al-Zn-Mg alloys. *J Inst Met (London)*, 101, 33-44.

Sheppard, T. and Raybould, D. 1973c. New approach to the construction of extrusion-limit diagrams, giving structural information with application to superpure aluminium and Al-Zn-Mg alloys. *J Inst Met (London)*, 101, 73-78.

Sheppard, T., Tutcher, M. G., Flower, H. M. 1979a. Development of recovered dislocation substructures during plastic flow. *Metal Science*, 13 (8), 473-481.

Sheppard, T. and Wright, D. S., 1979b. Determination of flow stress –constitutive equation for aluminium alloys at elevated temperatures. *Met Technol*, 6 (6), 215-223.

Sheppard, T., Tutcher, M. G., 1980a. Development of duplex deformation substructure during extrusion of a commercial Al-5Mg-0.8Mn alloy. *Metal Science*, 14 (12), 1980a, 579-589.

Sheppard, T. and Wood, E. P., 1980a. Effect of section geometry on extrudability of Al-Cu-Mn alloy. *Metals Technology*, 7(2), 58-66.

Sheppard, T. and Wood, E. P., 1980b. Effect of section geometry on extrudability of Al-Cu-Mn ALLOY. *Metals Technology*, 7 (2), 58-66.

Sheppard, T., Tutcher, M. G., 1981. Eeefect of process parameters on structure and properties of Al-5Mg-0.8Mn alloy (AA5456). *Metals Technology*, 8 (8), 319-327.

Sheppard, T., Paterson, S. J., 1982. Direct and indirect extrusion of aluminium alloys. *MET TECHNOL*, 9 (PT 7), 274-281.

Sheppard, T. and Vierod, R. P., 1985. Effects of preheat modification on extrusion characteristics of aluminium alloy 2014. *Materials Science and Technology*, 1 (4), 321-324.

Sheppard, T. and Richards, P., 1987. Structural and substructural observations during thermomechanical processing of two ferritic stainless steels. *Journal of Materials Science*, 22(5), 1642-1650.

Sheppard, T. and Vierod, R. P., 1987. Effect of thermomechanical process on as-extruded and solution soaked structures of Al-Cu-Mn alloys. *Materials Science and Technology*, 3 (4), 285-290.

Sheppard, T., 1993. Extrusion of AA2024 alloy. *Materials science and Technology*. 9, 430-440.

Sheppard, T. and Jackson, A. 1997. Constitutive equations for use in prediction of flow stress during extrusion of aluminium alloys. *Materials Science and Technology*, 13, 203-209.

Sheppard, T., 1999a. Extrusion of aluminium alloys. Dordrecht, The Netherlands: Kluwer Academic Press.

Sheppard, T., 1999b. Temperature changes occurring during extrusion of metals: comparison of bulk, numerical and integral profile predictions with experimental data. *Materials Science and Technology*, 15, 459-463.

Sheppard, T. and Duan, X., 2002. Modelling of static recrystallisation by combining FEM with empirical models. *Journal of Materials Processing Technology*, 130-131, 250-252.

Sheppard, T. and Duan, X. 2003. Modelling of static recrystallisation by the combination of empirical models with the finite element method. *Journal of Materials Science*, 38 (8), 1747-1754.

Shercliff, H. R., 1997. *Modelling of materials and processes*. Department of Emgineering, University of Cambridge, Technical Report CUED/C-MATS/TR243.

Shercliff, H. R. and Lovatt, A. M., 1999. Modelling of microstructure evolution in hot deformation. *Phil. Tran. R. Soc. Lond.* A 357, 1621-1633.

Shercliff, H.R. and Lovatt, A.M., 2001. Selection of manufacturing processes in design

and the role of process modelling. *Progress in Materials Science*, 46 (3-4), 429-459.

Sivaram, K. and Rao, K. P., 1988. Effect of friction and temperature on forming force, material flow and strain distribution in extrusion-forging of Al-5Si alloy. *Journal of the Institution of Engineers (India), Part ME: Mechanical Engineering Division*, 68, 85-88.

Sliwa, R., Zasadzinski, J., 1985. Extrusion on Metals Using Multihole Dies. I. Method and Technique for Investigating Metal Flow During Extrusion Using Multihole Dies. *Archiwum Hutnictwa*, 30 (3), 329-342. Language: Polish

Smolander, K. J., 1985. Monte carlo study of aluminium in liquid and amorphous states. *Physica Scripta*, 31 (5), 427-432.

Sonmez, H. 2002. Research of the effect of lubrication on extrusion load in direct extrusion. *Technical Paper - Society of Manufacturing Engineers. MF*, MF02-301, 1-6.

Spiers, R. M., Winsper, C. E., Sansome, D. H., 1969. Direct extrusion of metal with applied oscillatory energy. *Metal Forming*, 36 (10), 271-277.

Spittel, T. and Spittel M. 1990. Mathematical modelling of process-independent parameters of metal forming. *Scandinavian Journal of Metallurgy*, 19, 85-94.

Sreekumar, P., Jayaraman, V. K., Kulkarni, B. D., 1998. Monte Carlo and cellular automata modeling of CO oxidation on a catalytic surface including the Eley-Rideal step and CO diffusion. *Industrial & Engineering Chemistry Research*, 37 (6), 2188-2192.

Srolovitz, D. J., Grest, G. S. and Anderson, M. P., 1986. Computer Simulation of Recrystallisation – I. Homogeneous Nucleation and Growth. *Acta metall.* 34 (9), 1833-1845.

Subramaniyan, J., 1989. Extrusion of 2024 Aluminium Alloy Sections. Theiss (PhD). Imperial College, University of London.

Surdon, G. and Chenot, J. L., 1987. Finite element calculation of three-dimensional hot forging, *Int. J. for Numerical Methods in Engineering*, 24, 2107-2117.

Taver, E., 2004. Fundamentals of conscious control of product quality. *Standarty i Kachestvo*, 2, 86-94.

Thomsen, E. G., Yang, C. T., Kobayashi, S., 1965. *Plastic deformation in metal processing,* New Zealand: Macmillan Co.

Tibbetts, B. R., Wen, J. T. 1998. Extrusion process control: modeling, identification, and optimization. *IEEE Transactions on Control Systems Technology*, 6 (2), 134-145.

Tjotta, S., Vatne, H. E., Van, H.P., 1997. Coupled FEM and texture modelling of plane strain extrusion of an aluminum alloy. *International Journal of Plasticity*, 13 (1-2), 111-125.

Tokizawa, M., Dohda, K., Murotani, K., 1976. Mechanical of friction at the interface between tool surface and metals in hot extrusion of aluminium alloys em Dash 1.

Effects of dies and extrusion temperature. *Bulletin of the Japan Society of Precision Engineering*, 10 (4), 145-150.

Tuschy, E., 1971. Differences in the flow behavior of different materials during extrusion, (Unterschiede im Fliessverhalten beim Strangpressen verschiedener Werkstoffe). *Z Metallk*, 62 (7), 513-516. Language: German

Tutcher, M. G. 1979. Deformation processing applied to the Al-Mg alloy system. Thesis (PhD). Imperial college, London.

Tutcher, M. G., Sheppard, T. 1980. EXTRUSION LIMITS OF Al-5Mg-0. 8Mn ALLOY (AA 5456). *Metals Technology*, 7 (12), 488-493.

Udagawa, T., Kropp, E., Altan, T. 1992. Investigation of metal flow and temperatures by FEM in the extrusion of Ti-6Al-4V tubes. *Journal of Materials Processing Technology*, 33 (1-2), 155-174.

Ulysse, P., Johnson, R. E., 1998. Study of the effect of the process variables in unsymmetrical single-hole and multi-hole extrusion processes. *Journal of Materials Processing Technology*, 73 (1-3), 213-225.

Urcola, J. J., Sellars, C. M., 1987. Influence of changing strain rate on microstructure during hot deformation. *Acta Metallurgica*, 35 (11), 2649-2657 .

Valberg, H., 1986. Surface formation mechanism in direct extrusion of aluminium alloys. *Inst of Metals*, 240-251

Valberg, H., 1992. Metal flow in the direct axisymmetric extrusion of aluminium. *Journal of Materials Processing Technology*, 31, 39-55.

Valberg, H., Loeken, T., Hval, M., Nylus, B., Thaulow, C., 1995. Extrusion of hollow profiles with a gas pocket behind the bridge. *International Journal of Materials & Product Technology*, 10 (3-6), 222-267.

Vater, M., Heil, H. P., 1969. Effect of section shape on energy requirement for extrusion. *Aluminium*, 45 (3), 141-149.

Vater, M. and Koltzenburg, K., 1970. Study of material flow in the extrusion of copper and copper alloy tubes, *Baender Bleche Rohre*, 11 (11), 587-595.

Velay, X., Duan, X., Sheppard, T., 2003. Prediction of material flow pattern in the hot extrusion of aluminium alloys by the finite element method. *Materials Science Forum*. 426-432 (5), 3807-3812.

Venas, I., Herberg, J.; Skauvik, I., 1993. FEM simulations of flow through porthole dies for extrusion of aluminium. *Proceedings of the European Safety & Reliability Conference, May 10-12 1993, Munich, Ger.* Elsevier Science Publishers B.V. p. 671.

Venkatesan, G., 2003. Process control of product quality. *ISA Transactions*. 42 (4). 631-641.

Vernon-Parry, K. D., Furu, T., Jensen, D. J., Humphreys, F. J., 1996. Deformation microstructure and texture in hot worked aluminium alloys. *Materials Science and Technology*, 12 (11), p. 889.

Vierod, R. P., 1983. Effect of copper additions on deformation processing of aluminium alloys. Theiss (PhD). Imperial College, University of London.

Wang, L., Chessari, C., Karpiel, E., 2001. Inferential control of product quality attributes - Application to food cooking extrusion process. *Journal of Process Control*, 11 (6), 621-636.

Wanheim, T., 1988. In physical simulation of metal working processes, *Fourth Cairo University Conference on Mechanical Design and Production,* Egypt: Cairo University. December 27-29.

Wagener, H. W., Wolf, J., 1994. Coefficient of friction in cold extrusion. *Journal of Materials Processing Technology*, 44 (3-4), 283-291.

Wood, E. P. and Sheppard, T. 1975. Evaluation of shape factors for aluminium alloy extrusions. *Aluminium*, 51(12), 760-764.

Wu, P. Y., Huang, L. M., Liu, T. J., 1995. Simple model for heat transfer inside an extrusion die. *Polymer Engineering and Science*, 35 (21), 1713-1724.

Yokota, H., Hayashi, H., 1974. Indirect extrusion of aluminium alloy. *Sumitomo Light Metal Technical Reports*, 15 (4), 306-310.

Zaidi, M. A. and Sheppard, T., 1982. Development of microstructure throughout roll gap during rolling of aluminium alloys. *Metal Science*, 16 (5), 229-238.

Zaidi, M. A. and Sheppard, T., 1983. Recrystallisation mechanisms in commercial Al-2Mg alloy. *Metal Science*, 17 (5), 219-228.

Zaidi, M. A. and Sheppard, T., 1984. Effect of high-temperature soak and cooling rate on recrystallization behaviour of two Al-Mg alloys (AA 5252 and AA 5454). *Metals Technology*, 11, 313-319.

Zandler, G., Rein, A., Saraniti, M., Vogl, P., Lugli, P., 1994. Can cellular automata methods compete with Monte Carlo semiconductor device simulations? *Proceedings of the 23rd European Solid State Device Research Conference, Sep 13-16 1993, Grenoble, Fr.* Editions Frontieres, p. 21.

Zhang, S., Arentoft, M., Shang, Y., 2000. Physical modeling of metal forming processes. *Suxing Gongcheng Xuebao/Journal of Plasticity Engineering*, 7 (1), 45-49.

Zhou, J., Li, L., Duszczyk, J., 2003. A 3D FEM simulation study on the isothermal extrusion of a 7075 aluminium billet with a predetermined non-linear temperature distribution. *Modelling and Simulation in Materials Science and Engineering*, 11 (3), 401-416.

Zhu, Q., Sellars, C. M., 2000. Microstructural evolution of aluminium-magnesium alloys during thermomechanical processing. *Materials Science Forum*, 331 (1), 409-420.

Zhu, Q., Abbod, M. F., Talamantes-Silva, J., Sellars, C. M., Linkens, D. A., Beynon, J.H., 2003. Hybrid modelling of aluminium-magnesium alloys during thermomechanical processing in terms of physically-based, neuro-fuzzy and finite element models. *Acta Materialia*, 51 (17), 5051-5062.

Zienkiewicz, O. C., Taylor, R. L., Papadopoulos, P., Onate, E., 1990. Plate bending elements with discrete constraints. New triangular elements. *Computers and Structures*, 35 (4), 505-522.

Appendix A: Metallurgical Model

By empirical and physical means, a modest degree of prediction of microstructure can now be achieved. Excellent reviews on modelling of static recrystallisation (SRX) have been given by Gottstein et al. (1999,2000) and by Shercliff and Lovatt (1999). Some of the modelling work has been achieved in the field of hot rolling (Chen 1992, Duan 2002 , and recently in the field of hot extrusion by Duan and Sheppard (2004). Some models introduce many tuning parameters, especially for the physically based models. These parameters depend mainly on the material. To estimate their real values, specific and numerous experiments would be required. Recently, the inverse method combined with FEM has been adopted to define the values of these parameters from those in the literature. The FEM is run iteratively until the appropriate value is found to match the experimental measurement. Duan and Sheppard (2002, 2003) have used the inverse method to give the parameters for alloy 5083 and 2014.

The relationship between the volume fraction recrystallised (Xv) and the holding time (t) is generally represented by the Johnson-Mehl (1939)-Avrami (1939)-Kolmogorov (1937) equation (JMAK), which predicts the relationship between the volume fraction recrystallised (Xv) and the holding time (t) and is generally represented as:

$$Xv = 1 - \exp\{-0.693(\frac{t}{t_{50}})^{k}\} \qquad (A1)$$

where t is annealing time, k is the Avrami exponent with a commonly reported value of 2, t_{50} is the time to 50% recrystallisation. For the calculation of t_{50}, the physical model is commonly regarded as revealing the mechanics driving the transformation. Previous studies (Furu etc. 1999) have shown that the physical models describe the experimental results well for uniform processing conditions. The model was also successfully applied to tests in which the strain rate was increased (when

microstructure transients were not observed). Recently, Sheppard and Duan (2003) have confirmed that the physical model will give better computed results than the empirical model in the simulation of aluminium extrusion. Only the physical model proposed by Furu and Zhu et al (1999, 2000) has been used in this study.

In equation (A1), t_{50} is calculated based on the stored energy (P_D) and the density of recrystallisation nuclei (N_V) (Furu 1999).

$$t_{50} = \frac{C}{M_{GB} P_D} \left(\frac{1}{N_V}\right)^{1/3} \tag{A2}$$

where C is a calibration constant. M_{GB} is the boundary mobility. N_V is the density of nucleation sites and defined as:

$$N_V = (C_d / \delta^2) S_V(\varepsilon) \tag{A3}$$

where C_d is a further calibration constant, δ is the subgrain size, S_V is the grain boundary area per unit volume

$$S_V(\varepsilon) = (2/d_0)[\exp(\varepsilon) + \exp(-\varepsilon) + 1] \tag{A4}$$

d_0 is the grain size after homogenisation. The stored energy P_D is approximated by

$$P_D = \frac{Gb^2}{10}\left[\rho_i (1 - \mathrm{Ln}(10b\rho_i^{1/2})) + \frac{2\theta}{b\delta}\left(1 + \mathrm{Ln}\left(\frac{\theta_c}{\theta}\right)\right)\right] \tag{A5}$$

where G is the shear modulus, b is the burgers vector, ρ_i is the internal dislocation density, θ is the misorientation and θ_c is the critical misorientation for a high angle boundary ($\sim 15^0$), d_0 is the initial grain size.

The evolution of δ, ρ_i and θ has been explicitly expressed in differential form based on the most classical theories of work hardening and dynamic recovery.

$$d\delta = \frac{\delta}{\varepsilon_\delta \delta_{ss}}(\delta_{ss} - \delta)d\varepsilon \qquad (A6)$$

$$d\theta = \frac{1}{\varepsilon_\theta}(\theta_{ss} - \theta)d\varepsilon \qquad (A7)$$

$$d\rho_r = d\rho_r^+ + d\rho_r^- = (C_1 \rho_r^{1/2} - C_2 \frac{\sigma_f}{Z}\rho_r)d\varepsilon \qquad (A8)$$

where δ_{ss} and θ_{ss} are the subgrain size and misorientation at steady state deformation. ε_δ and ε_θ are characteristic strains, ρ_r is random dislocation density, C_1 and C_2 are constants. The internal dislocation density consists of two parts, ρ_r and ρ_g (the geometrical necessary dislocation density).

$$\rho_i = \rho_r + \rho_g \qquad (A9)$$

$$\rho_g = \frac{1}{b}(\frac{1}{R_g} - \frac{\theta}{\delta}) \qquad (A10)$$

where ρ_i is the internal dislocation density, $1/R_g$ is the local lattice curvature.

For site-saturated nucleation, the recrystallised grain size is simply calculated from nucleation density as:

$$d_{rex} = DN_V^{-1/3} \qquad \text{(A11)}$$

where D is a constant.

The constants used in this study are taken from previous studies by Furu (1999): $C/M_{GB} = 3.1\times10^{11}$ and $C_d = 1.48\times10^{-4}$ (when grain size and subgrain size are in units of meters), G =2.05 × 10^{10} MPa (Duan 2002), b=2.86 × 10^{-10} m (Duan 2003), $\rho_0 = 10^{11}\ m^{-2}$ (Furu 1999), $\delta_0 = 1.8\times10^{-6}$ m, $\theta_0 = 0^0$, $\varepsilon_\delta = 9\times10^{10}Z^{-1}$, $\varepsilon_\theta = 8\times10^{-5}Z^{1/4}$ (Zhu 2000), $1/R_g = 5\times10^{-4}m^{-1}$ (Baxter 1999), $C_1 = 90$, $C_2 = 2\times10^7$, D=2.347 (Furu 1999). While some of the constants (activation energy, Burgers vector, etc.) have been determined experimentally (fundamental tuning), it should be pointed out that some other constants are necessarily adjustable parameters that must be determined from a range of values as part of an experimental tuning procedure. For example, the initial dislocation density is reported to be in the range of 10^9 to $10^{11}\ m^{-2}$,(depending upon alloy composition and pre-heat treatment) and C/M_{GB} is given the range of 10^9 to 10^{13} for different alloys (Duan 2003, Furu 1999, Sellars 2000, Duan 2002).

C_d is reported in the range of 10^{-6} (Duan 2002) to 10^{-3} (Duan 2002) for different alloys. For the constants C1 and C2, Sellars has given equations expressed as:

$$C_1 = M/b \qquad \text{(A12)}$$

where M is the Taylor factor, b is the Burgers vector,

$$C_2 = 2D_0 b\beta \tag{A13}$$

where D_0 is the diffusion coefficient, β is the drag force. The relationship between these two parameters is given as:

$$C_2 = (Z/\sigma_f \rho_r^{1/2})_{ss} C_1 \tag{A14}$$

where ss means steady state, σ_f is the friction stress, effectively driving dislocation motion. Although the relation was given in equation A14, it is still difficult to give a precise value for any of the two parameters due to the lack of experimental measurements. The method of "curve fitting" or "inverse iteration" had to be adopted to give the precise values of these constants. Although the exact value should be determined from the experiments, the approximate values are critical as starting points for their exact determination.

The procedure of tuning the constants is of primary importance for the prediction of metallurgical behaviour by these models. Although the sensitivity test of these have being performed previously by Shercliff and Lovatt (1999), further discussion should be continued because the integration of the deformed structure into the metallurgical model is of paramount interest.

Appendix B: Analysis of the gap

To eliminate the gap between the material and the die at the die land area, several methods are employed and results are reported below:

Rod extrusion:

Table B1 Numerical experiments to eliminate the orifice between the material and the die

Test	Experimental result	Different methods tried to eliminate the orifice						
		Master With 6.2	Master With 6.1	Smaller element*	Elastic plastic	RK2	Time step	Visco-plastic friction
GAP		0.4191 (mm)	0.3298 (mm)	0.2310 (mm)	0.3929 (mm)	0.6976 (mm)	0.3470 (mm)	0.3358 (mm)
TIME		2:54	3:25	38:39	2:55	4:24	3:09	2:51
Peak load	669.41 MN/M^2 = 295.6 Tons	260 Tons	280 Tons	256 Tons	264 Tons	276 Tons	268 Tons	264 Tons
Volume loss		Begin 100600 End 99499	100600 99633	100600 99457	100600 99452	100600 99852	100600 99571	100600 99571
Remarks (contact)		Step76	Step77	Step121	Step70	Step45	Step86	Step74

*Smaller element: 0.2mm, normal: 0.5

Extrusion Conditions:

(original experimental settings can be found in the PhD thesis of Vierod 1983, as D4343A in Appendix II)
material: AA2014
Ratio: 30 Storage :400
Die diameter: 27.38 Rod travel distance: 5.5mm, speed:7mm/s
Friction : container: 0.9 , rod : 0.8 , die: 0.4

FEM Mesh setting up:

Cylinder Mesh size: Box1 Size:5.0
52 0 160 0 0 –50
Box2 Size:2.0
12 0 34 0 0 -30
Box3 Size:1.0
10 2 32 0 0 –30
Box4 Size:0.5
9 3.6 31 0 0 –30
Box5 Size:0.2 (only used in smaller element)
8 4.8 15.6 0 0 -15

Appendix C: Communication concerning subroutines

(1) Some parameters used in subroutines:
In subroutine "**loiv_intg**", there is a parameter "**delta_t**", how to use it in subroutine "**loiv_util**".
In subroutine "**loiv_util**", there are "**gs_eta**" and "**gs_eta_point**", but in subroutine "**loiv_intg**", there is only "**gs_eta0**" or "**gs_eta1**" but no **"XXX_point"**. Can we add the "**gs_eta_point0**" or "**gs_eta_point1**" in "**loiv_intg**"?

(2) How can I get the real value of a defined **gs_eta** parameter in "**loiv_intg**".
The output of a parameter from the subroutine "**loiv_intg**" always shown as **"XXX [3D Element]"**. It is different from "**loiv_util**", from which we can get the real values from the output.

For example, I define an OYANE parameter in "**loiv_intg**",

```
!!!!!!!!!!!!!!!!!!!!!!!!!!!!!!!!!!!!!!!!!!!!!!!!!!!!!!!!!!!!!!!!!!!!!!!!!!!!!!!!!!!!!!!!!!!!!!!!!!!!!!
else if (nom.eq.'OYANE') then
C**********************************************************************
*
C    Oyane damage criterium / Critere d endommagement d'Oyane :

C    Oyane=Integrale[(1-aa*press/Sigeq)dEpsb]
C
C    LOIV INTG
C    OYANE
C    PAR AA      = <valeur/value>
C    PAR EQ_STRESS= EXIST
C    PAR STRAIN_RATE= EXIST

C    ETA OYANE    = <valeur/value>
C    ETA Dt = 0
C    FIN LOI
C**********************************************************************
*

        if ((nbpar.ne.3).or.(nbeta.ne.2)) goto 99

        aa   = gs_par0(1)
        sigeq= gs_par0(2)+1.d-10
        ebp  = gs_par0(3)


      gs_eta0(1) = gs_eta0(1)+dmax1(0d0,(1.d0 - aa*press0/sigeq)
                   *ebp*delta_t)
      gs_eta0(2) = delta_t
!!!!!!!!!!!!!!!!!!!!!!!!!!!!!!!!!!!!!!!!!!!!!!!!!!!!!!!!!!!!!!!!!!!!!!!!!!!!!!!!!!!!!!!!!!!!!!!!!!!!
```

The output of the parameter **Oyane** is shown below:

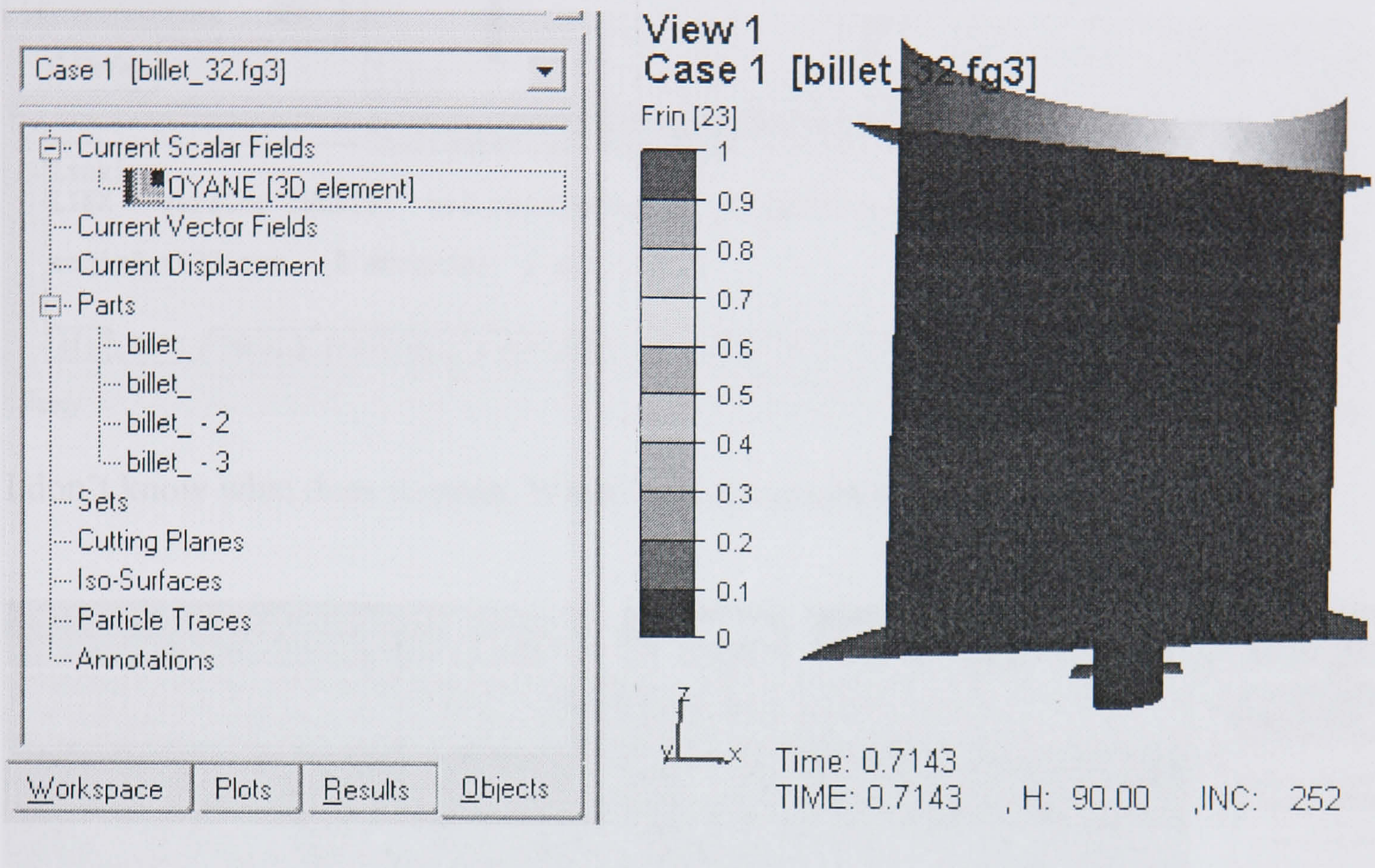

As you can see, there is **Oyane [3D element] (With the value range 0-1).** What is the different between the **Oyane** and **Oyane [3D element]**. If I want to get the real values of the parameter, must I define it in "**loiv_util**"?

(3) I met some problem when I try to build the programs UserProjects_v63 in Fortran:

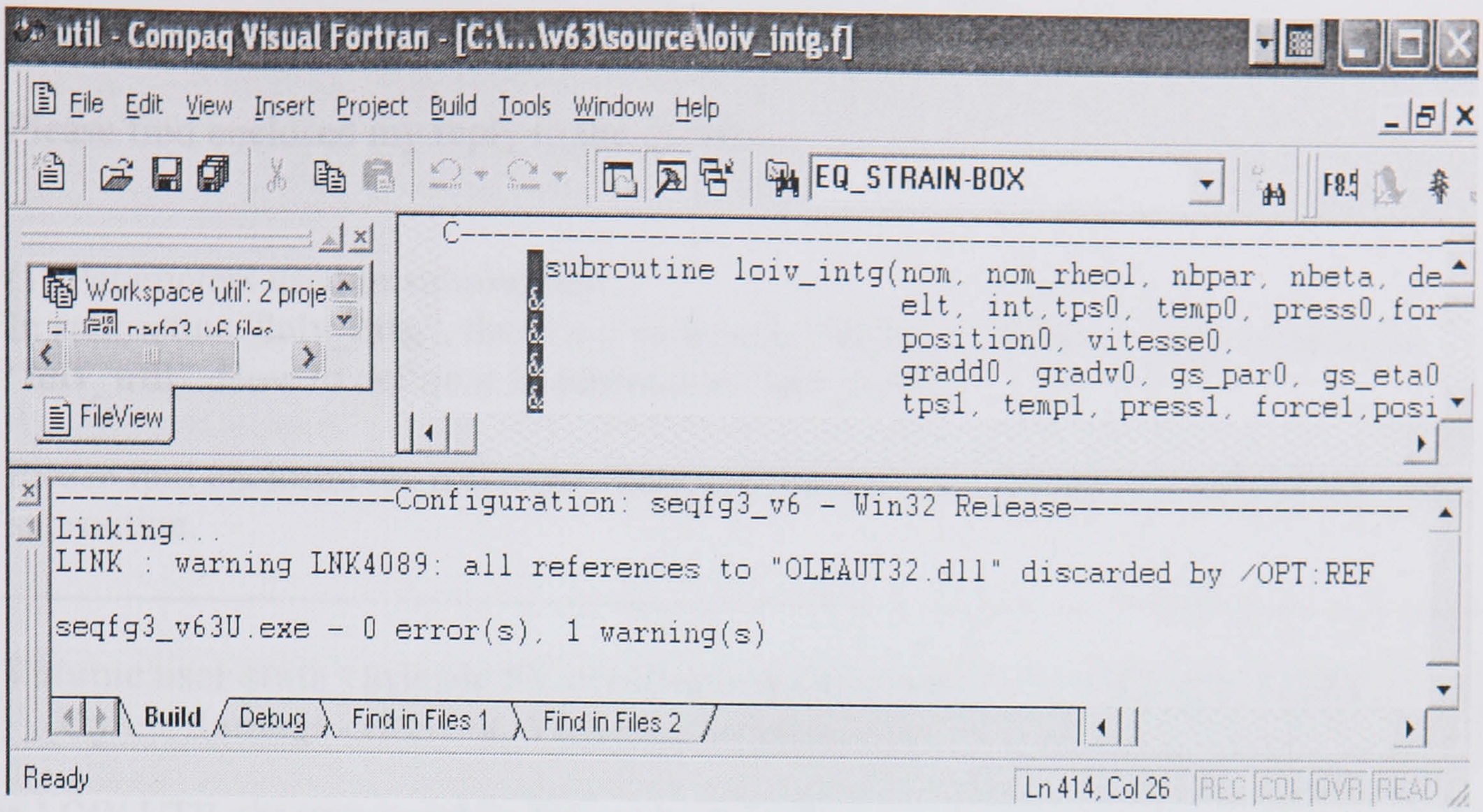

I don't know what does it mean. When I run the projects, a dialog always pops out:

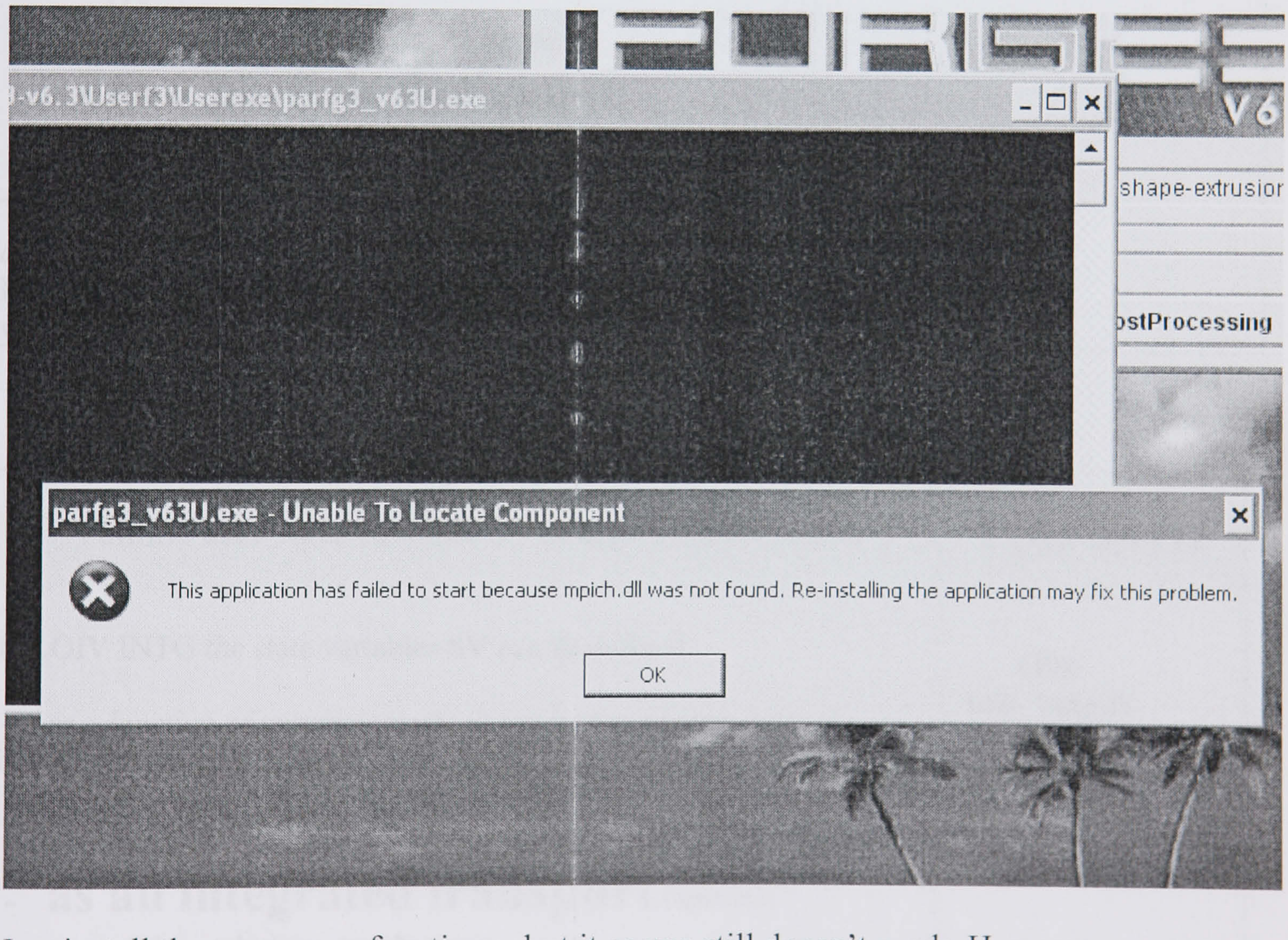

I re-install the program a few times, but it seems still doesn't work. However, UserProjects_v70 works perfectly.

(4) Where can I find the English definitions for all the defined parameters (for example, incr, elt, int, tps0, temp0, press0, force0, position0, vitesse0) used in the subroutines? Do we have some parameters defined for controlling the ram speed (in direct extrusion) in the file of "**loiv_util**".

Dear Sir,

Please find enclosed my reply to the queries.

(1) Parameters used in subroutines:
In subroutine "**loiv_intg**", there is a parameter "**delta_t**", Which I can not find it in "**loiv_util**". How to define it in subroutine "**loiv_util**"?

Please find enclosed the difference between the loiv_intg subroutine and the loiv_util subroutine.

Volume user state variable SV creation/modification (Oyane damage criterion, Vickers hardness, ...)	**LOIV UTIL**
In LOIV UTIL the state variables SV can be defined : - as a function from parameters which can be themselves defined in other laws as SV or DV : $\mathbf{a = f(p_1,p_2,p_3,\ldots p_m)}$ **(type I)** - **as a particle derivative** function of the law parameters: $\mathbf{\Delta a/\Delta t = f(p_1,p_2,p_3,\ldots p_m)}$ **(type II)** The Oyane damage criterion is an example of the latter : ΔOyane/Δt=(1-aa*pressure/Sigeq)*Ebp **In LOIV UTIL it is not possible to create dynamic variables DV.**	**(file loiv_util.f)**

Volume user state variable SV creation/modification	**LOIV INTG**
In LOIV INTG the state variables SV can be defined : as a function of parameters which can be themselves defined in other laws as SV or DV : $\mathbf{a = f(p_1,p_2,p_3,\ldots p_m)}$ **(type I)** - **as an integrated transport** equation summed for each time step Δt as : $\mathbf{a^{(1)} = f(a^{(0)}, \Delta t, p_1^{(0)}, p_2^{(0)},\ldots p_m^{(0)}, p_1^{(1)}, p_2^{(1)},\ldots p_m^{(1)})}$ **(type III)** $\mathbf{a^{(0)}}$ is the state variable SV value at the beginning of the time step, $\mathbf{a^{(1)}}$ its value at the end of the time step and $\mathbf{p_i^{(0)}}$, $\mathbf{p_i^{(1)}}$, are the m parameters values respectively at the beginning and the end of the time step. e type I state variables can be programmed either in LOIV UTIL or in IV INTG.	**(file loiv_intg.f)**

As said previous, in the loiv_intg subroutine you can defined the parameter as an integrated equation. That's why we have the parameter DELTA_T.
In the loiv_intg it is not an integration, that's why we didn't need this parameter.

In subroutine "**loiv_util**", there are "**gs_eta**" and "**gs_eta_point**", but in subroutine "**loiv_intg**", there is only "**gs_eta0**" or "**gs_eta1**" but no **"XXX_point"**. Can we add the "**gs_eta_point0**" or "**gs_eta_point1**" in "**loiv_intg**"?
No it is not possible to add them

(2) How can I get the real value of a defined **gs_eta** parameter in "**loiv_intg**".
The output of a parameter from the subroutine "**loiv_intg**" always shown as **"XXX [3D Element]"**. It is different from "**loiv_util**", from which we can get the real values from the output.
Im am not sure to understand this querie, GLVIEW INOVA (the post processor) write automatically 3D ELEMENT when the variable in calculated in the volume. GLVIEW INOVA write Node if the variable is calculated to the node.

For example, I define an OYANE parameter in "**loiv_intg**",

```
!!!!!!!!!!!!!!!!!!!!!!!!!!!!!!!!!!!!!!!!!!!!!!!!!!!!!!!!!!!!!!!!!!!!!!!!!!!!!!!!!!!!!!!!!!
else if (nom.eq.'OYANE') then
C*************************************************************************
*
C    Oyane damage criterium / Critere d endommagement d'Oyane :

C    Oyane=Integrale[(1-aa*press/Sigeq)dEpsb]
C
C    LOIV INTG
C    OYANE
C    PAR AA        = <valeur/value>
C    PAR EQ_STRESS= EXIST
C    PAR STRAIN_RATE= EXIST

C    ETA OYANE    = <valeur/value>
C    ETA Dt = 0
C    FIN LOI
C*************************************************************************
*


        if ((nbpar.ne.3).or.(nbeta.ne.2)) goto 99

        aa   = gs_par0(1)
        sigeq= gs_par0(2)+1.d-10
        ebp  = gs_par0(3)


      gs_eta0(1) = gs_eta0(1)+dmax1(0d0.(1.d0 - aa*press0/sigeq)
                  *ebp*delta_t)
      gs_eta0(2) = delta_t
!!!!!!!!!!!!!!!!!!!!!!!!!!!!!!!!!!!!!!!!!!!!!!!!!!!!!!!!!!!!!!!!!!!!!!!!!!!!!!!!!!!!!
```

The output of the parameter **Oyane** is shown below:

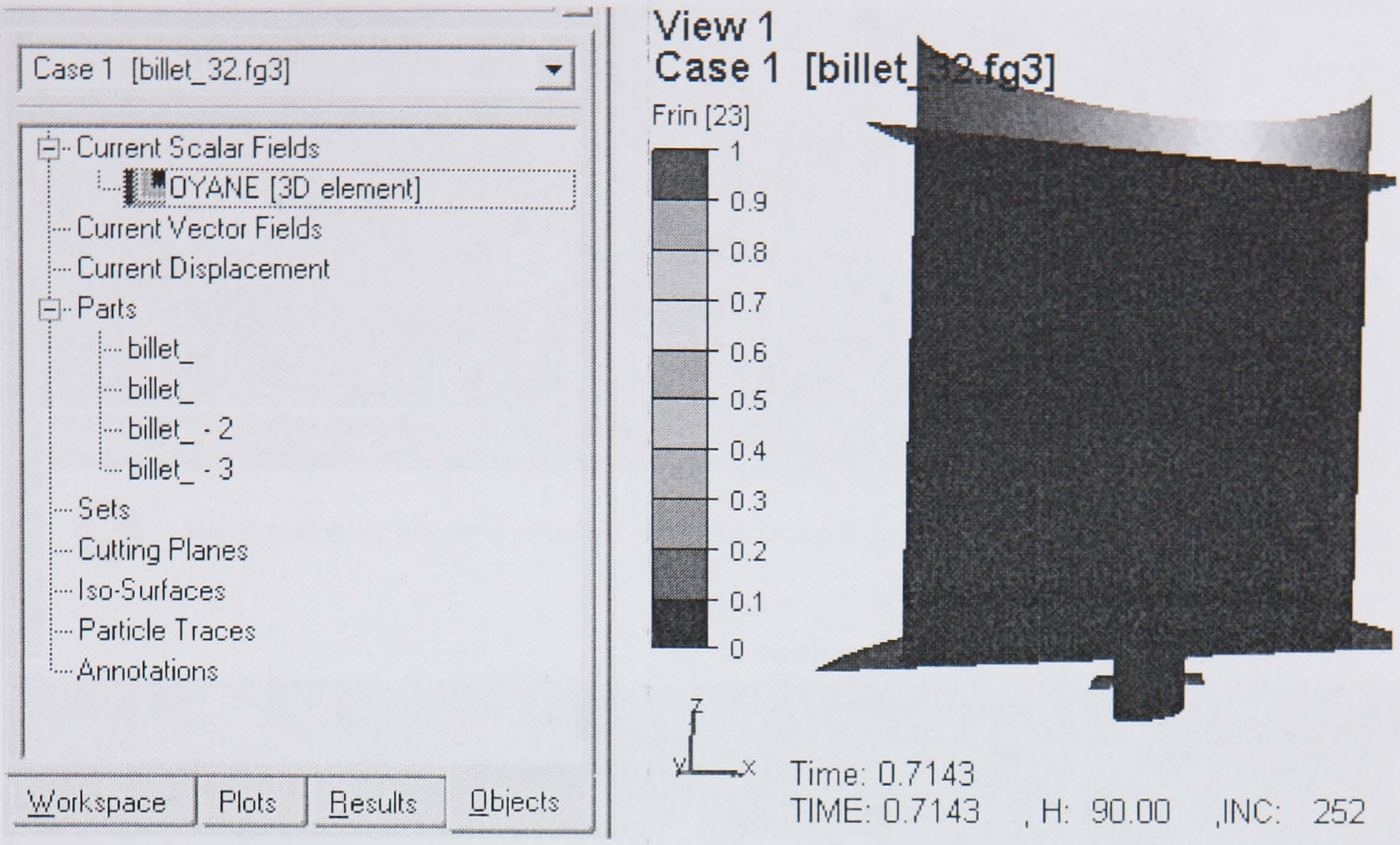

As you can see, there is **Oyane [3D element] (With the range 0-1).** What is the different between the **Oyane** and **Oyane [3D element]**. If I want to get the real values of the parameter, must I define it in "**loiv_util**"?
There is no difference, Inova add automatically this definition

(3) I met some problem when I try to build the programs UserProjects_v63 in Fortran:

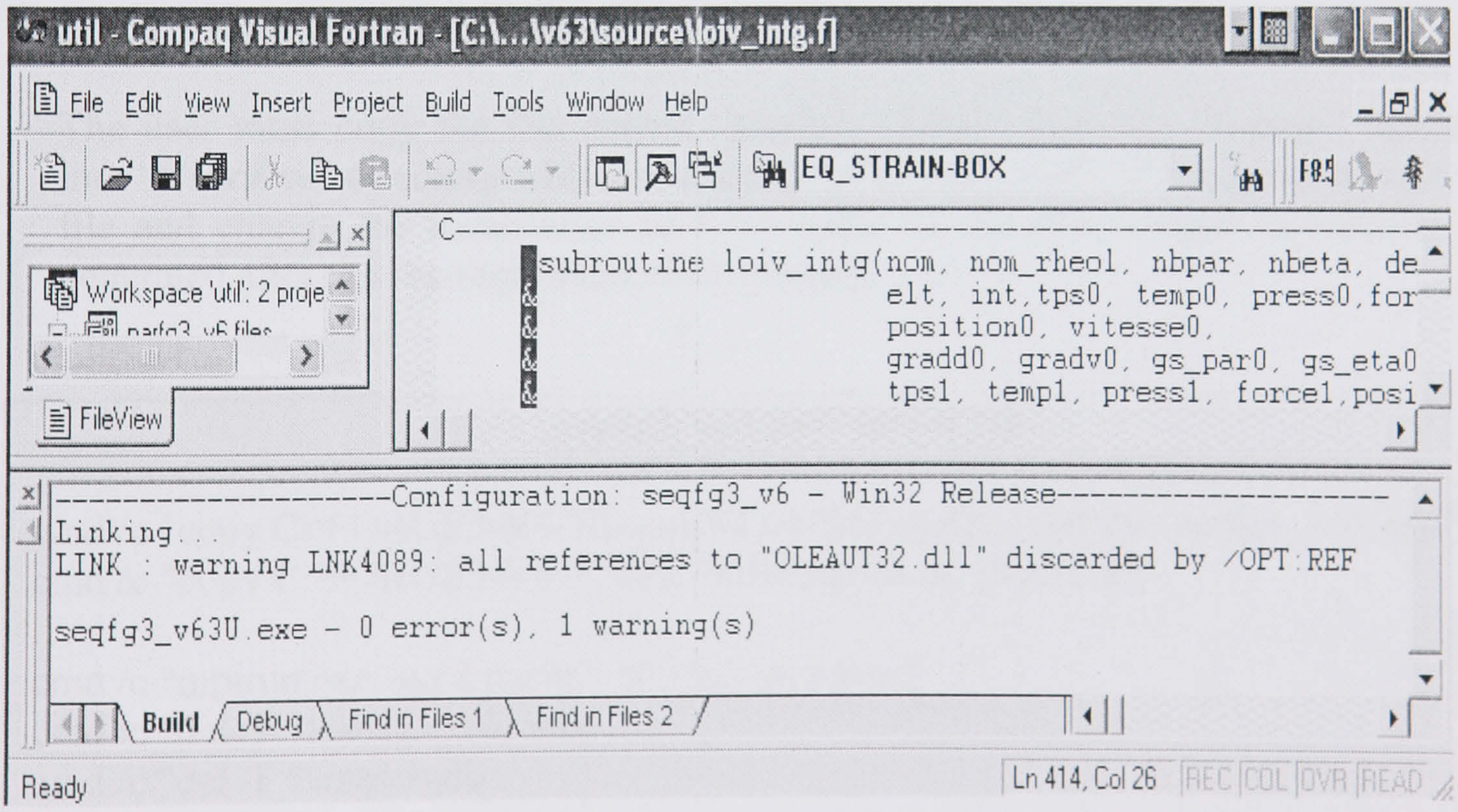

I don't know what does it mean. When I run the projects, a dialog always pops out:

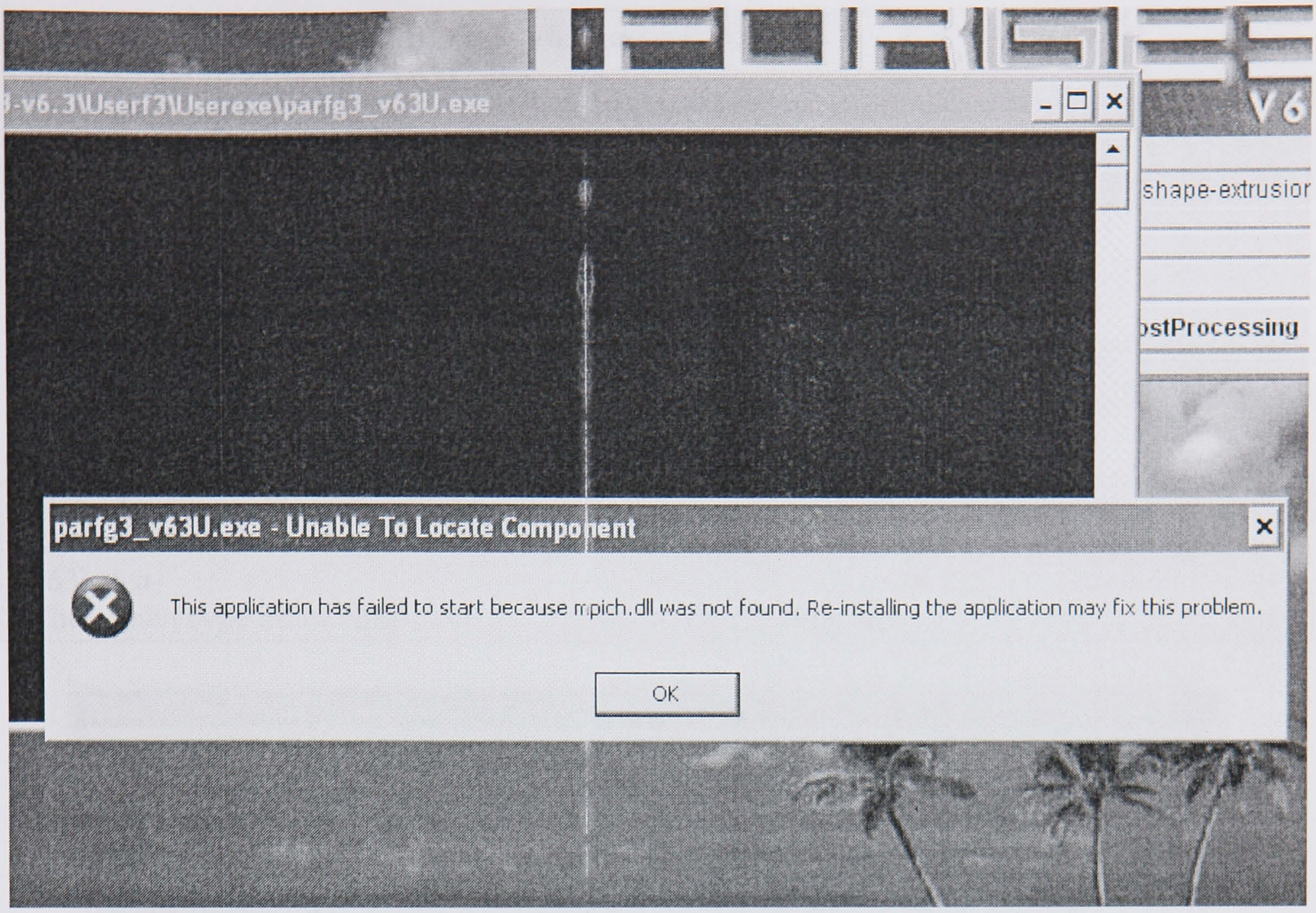

I re-install the program a few times, but it seems doesn't work. However, UserProjects_v70 works perfectly.

Did you follow this procedure to prepare and run your simulation ?

- **FORGE3 multi-processors**

Step 1 : Writing the command file

The user must copy the file named "**parfg3_63.bat**" from the "**tempo**" directory into "**UserExe**" directory with the name "**parfg3_63U.bat**". Then, he must edit this file and change the localisation and the name of the new Forge3 executable file generated after the recompilation of the project.

"parfg3_v63.bat" initial file

```
cmd /c "copy C:\FORGE3-V6.3\UserF3\UserExe\parfg3_v63.exe parfg3_v63.exe"
cmd /c "copy C:\FORGE3-V6.3\MPICH\lib\mpich.dll mpich.dll"
...
cmd /c "mpirun.exe -np 2 parfg3_v63.exe & pause"
cmd /c "del /F %parfg3_v63.exe
cmd /c "del /F %mpich.dll
...
```

"parfg3_v63U.bat" modified file

```
cmd /c "copy C:\FORGE3-V6.3\UserF3\UserExe\parfg3_v63U.exe
parfg3_v63U.exe"
cmd /c "copy C:\FORGE3-V6.3\MPICH\lib\mpich.dll mpich.dll"
...
```

```
cmd /c "mpirun.exe -np 2 parfg3_v63U.exe & pause"
cmd /c "del /F %parfg3_v63U.exe
cmd /c "del /F %mpich.dll
...
```

Step 2 : Writing the "utilexe.3d" file

It is possible (cf. Reference Guide of the Forge3 desktop) to add a user's menu in the Forge3 launcher. The user needs to create a file named "**utilexe.3d**" in the "**Util**"directory from Forge3 package, with this syntax :

First line (title of the user's menu)	: Forge3 Multi-Processors
Second line (localisation of the command file)	: C:\Forge3-v6.3\Usef3\UserExe\parfg3_ v63U.bat
Third line (Type of the file)	: fic_ref

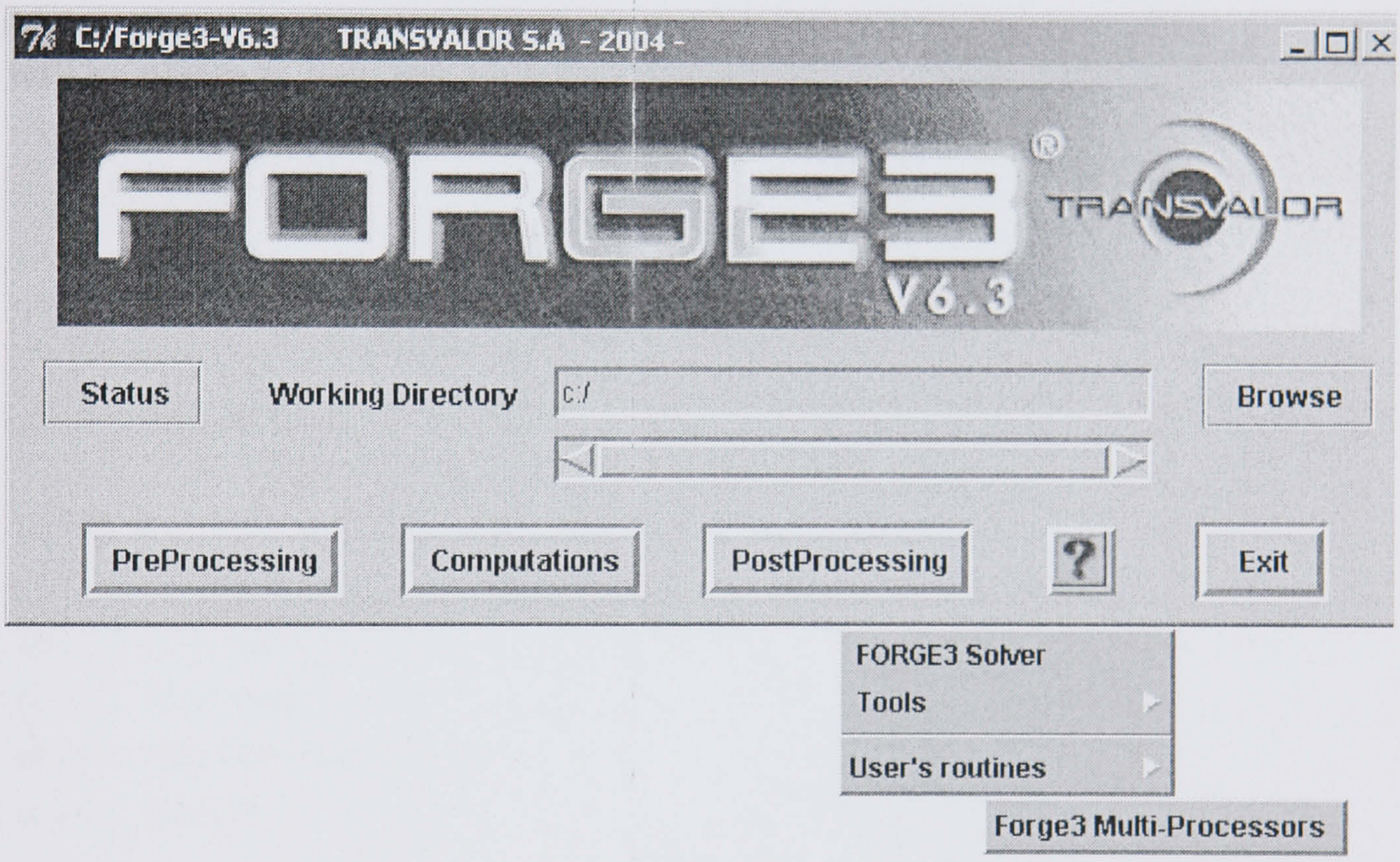

Step 3 : Preparation of the computation

Before running the computation, the user must generate the necessary files to run computation. To do this the user has just to select the menu : "**Computations/Tools/Prepare a computation**", fill in the different fields and then click on the "**OK**" button.

Step 4 : Running the computation

To run the computation, the user must select :

"**Computations/User's routines/Forge3 Multi-Processors**".

The computation will be started automatically.

(4) Do we have a list for all the defined parameters in the subroutines (for example, incr, elt, int, tps0, press0, force0, position0, vitesse0) with both the English and French definitions.
No we didn't not have this list, but there are some information contained in the USER_ROUTINES documentation (English and French).
See C:\Forge3-V6.3\DOC\ENG\User_Routines_V63_Eng.doc
and also before each soubroutine in the diorectory C:\FORGE3\Forge3-V6.3-SGR\USERF3\v63\source\.

Do we have some parameters defined for controlling the ram speed (in direct extrusion) in the file of "**loiv_util**".
Could you please give me more information about what you want to do ?
We will be please to help you to define this, but we need more information.

Appendix D: An example of the input file

```
! File Type:          FORGE3 V7.0 Data File
! Creator:       GLPre Version 2, 3, 0, 20-Release
! Author:        Peng_Zhi
! Creation Date:      2004-06-23 15:06:37
! GLPre active language:English
! System language: English (United States)
! Data File Name:   723.ref
! Data File Location:      C:\pz\Autotrim\Tshape-extrusion-2P.tsv\723
!!!!!!!!!!!!!!!!!!!!!!!!!!!!!!!!!!!!!!!!!!!!!!!!!!!!!!!!!!!!!!!!!!!!!!!!!!!!!!


!=============================== OBJECTS Block
.OBJETS
      ProjectName = Tshape-extrusion-2P
      SimulationName = 723

      Fout = 723.out
      Fres = results\723.res
      Faux = results\723.vtf

      NBSD = 1

      objet 1, NAME=Billet
      objet 1, FMAY=billet.may
      objet 1, NomGen=results\billet_
      objet 1, rheol=1

      outil 1, NAME=Die
      outil 2, NAME=Ram
      outil 3, NAME=Container
.FIN OBJETS
!===============================

!=============================== APPROXIMATION Block
.APPROXIMATION
      Periode_Meca = 1
.FIN APPROXIMATION
!===============================

!=============================== UNITS Block
.UNITES
      MM-MPA-MM.KG.S
```

.FIN UNITES

!==========

!========== RHEOLOGY Block

.RHEOLOGIE

!!!!!!!!!!!!!!!!!!!!

MATERIAU 1 ! (object Billet)

!!!!!!!!!!!!!!!!!!!!

EVP

LOIV SIG0

ZENER-H

PAR DH = 148880.d0

PAR R = 8.31d0

PAR alpha = 0.016d0

PAR n = 4.27d0

PAR A = 325215956.1d0

FIN LOI

!Thermal Coefficients

mvolumique = 2.800000e-06 !Density

cmassique = 1.230000e+09 !Specific Heat

conductmat = 2.500000e+05 !Conductivity

epsilon = 5.000000e-02 !Emissivity

!----------

OUTIL1 !Die

!Friction between deformable object and rigid die

Tresca ! Friction Law

mbarre = 4.000000e-01

!Thermal Exchange between part and rigid die

! Unit = si

alphat = 2.000000e+03 ! Transfert coefficient

Effus = 1.176362E+04 ! tool effusivity

Temp = 300.000000

FIN OUTIL

!----------

!----------

OUTIL2 !Ram

```
!Friction between deformable object and rigid die
Tresca              ! Friction Law
mbarre = 4.000000e-01

!Thermal Exchange between part and rigid die
! Unit = si
alphat          = 2.000000e+03  ! Transfert coefficient
      Effus = 1.176362E+04    ! tool effusivity

      Temp = 300.000000
FIN OUTIL
!------------------------------

!------------------------------
OUTIL3          !Container

      !Friction between deformable object and rigid die
      Tresca              ! Friction Law
      mbarre = 9.5000000e-01

      !Thermal Exchange between part and rigid die
      ! Unit = si
      alphat          = 2.000000e+03  ! Transfert coefficient
      Effus = 1.176362E+04    ! tool effusivity

      Temp = 400.000000
FIN OUTIL
!------------------------------

      !Thermal Exchange between deformable object and air
      AlphaText = 2.000000e+001          ! Global Transfert Coeff.
      TempExt = 50.000000                ! Ambient Temperature

      ! Initial temperature has been set in mesh file: already exists in mesh file

!!!!!!!!!!!!!!!!!!!!
FIN MATERIAU
!!!!!!!!!!!!!!!!!!!!
LOIV MECA
  Sigma1
  Par STRESSTENSOR(6) = EXIST
  Var SIG1 = 0.
FIN LOI
```

```
! *** User Variable Law: Sig1_direction
LOIV MECA
  Sig1_direction
  Par STRESSTENSOR(6) = EXIST
  Var SIG1_VECTOR(3) = 0, 0, 0
FIN LOI

! *** User Variable Law: BOX
LOIV UTIL
  BOX
  Par XMIN = -100
  Par XMAX = 100
  Par YMIN = -100
  Par YMAX = 100
  Par ZMIN = -15
  Par ZMAX = -13
  Par EQ_STRAIN = EXIST
  Eta EQ_STRAIN-BOX = 0.
FIN LOI

LOIV UTIL
     OYANE
    PAR AA              = 3.0
    PAR EQ_STRESS= EXIST
    PAR STRAIN_RATE= EXIST

    ETA OYANE        = 0
FIN LOI

LOIV UTIL
  LATANDCO
    PAR SIG1          = EXIST
    PAR STRAIN_RATE = EXIST

    ETA LATANDCO = 0.0
FIN LOI

LOIV UTIL
  LATANDCN
    PAR SIG1          = EXIST
    PAR STRAIN_RATE = EXIST
    PAR EQ_STRESS       = EXIST
```

```
    ETA LATANDCN = 0
FIN LOI

LOIV UTIL
  Ayada
    PAR STRAIN_RATE = EXIST
    PAR EQ_STRESS       = EXIST

    ETA Ayada = 0.0
FIN LOI

LOIV UTIL
  GW
    PAR STRAIN_RATE = EXIST
    PAR EQ_STRESS       = EXIST

    ETA GW = 0.0
    FIN LOI
.FIN RHEOLOGIE
!=============================================

!=================================== TOLERCONV Block
.TOLERCONV
.FIN TOLERCONV
!=================================

!=================================== INCREMENT Block
.INCREMENT
    Deformation= 1.000000e-002
.FIN INCREMENT
!=================================

!=================================== EXECUTION Block
.EXECUTION
    Inertia
    dtMin = 2.000000e-004
    dtMax = 1.000000e-002
    dhSto = 1.000000e-001
    Fine Sto = 1.000000e+000
    Calcul Outillage
    Folds_Detection
.FIN EXECUTION
!=================================
```

```
!========================================== THERMAL Block
.THERMIQUE
.FIN THERMIQUE
!==========================================

!========================================== MESH BOXES Block
.BOITE

OBJET1
    BOX 1
     Type=10        ! BOX
     Eulerian
     Size= 3
     !Param Info: NbPar, Xmin, Ymin, Zmin, Length, Width, Height
     Parameters:, 6, 0, 0, 0, 81.6585, 41.2335, 65
     Matrix:, 1, 0, 0, -40,
              0, 1, 0, -2.24175,
              0, 0, 1, -50,
              0, 0, 0, 1
END BOX
BOX 2
 Type=10        ! BOX
 Eulerian
 Size= 1
 !Param Info: NbPar, Xmin, Ymin, Zmin, Length, Width, Height
 Parameters:, 6, 0, 0, 0, 40, 25, 55
 Matrix:, 1, 0, 0, -20,
          0, 1, 0, -2.24175,
          0, 0, 1, -50,
          0, 0, 0, 1
END BOX
BOX 3
 Type=10        ! BOX
 Eulerian
 Size= 0.6
 !Param Info: NbPar, Xmin, Ymin, Zmin, Length, Width, Height
 Parameters:, 6, 0, 0, 0, 4, 11.2, 51.2
 Matrix:, 1, 0, 0, -7,
          0, 1, 0, -2.24175,
          0, 0, 1, -50,
          0, 0, 0, 1
END BOX
BOX 4
 Type=10        ! BOX
```

```
Eulerian
Size= 0.6
!Param Info: NbPar, Xmin, Ymin, Zmin, Length, Width, Height
Parameters:, 6, 0, 0, 0, 17, 5.2, 51.2
Matrix:, 1, 0, 0, -7,
        0, 1, 0, 2,
        0, 0, 1, -50,
        0, 0, 0, 1
END BOX
BOX 5
 Type=10        ! BOX
 Eulerian
 Size= 0.6
 !Param Info: NbPar, Xmin, Ymin, Zmin, Length, Width, Height
 Parameters:, 6, 0, 0, 0, 4, 6.2, 51.2
 Matrix:, 1, 0, 0, 6,
        0, 1, 0, -2.24175,
        0, 0, 1, -50,
        0, 0, 0, 1
    END BOX
FIN OBJET

.FIN BOITE
!=================================

!================================= SENSORS Block
.CAPTEURS

.FIN CAPTEURS
!=================================

!================================= BOUNDARY CONDITIONS Block
.CONDLIM

.FIN CONDLIM
!=================================

!================================= DAMAGE CONDITIONS Block
.DAMAGE
      Name = EQ_STRAIN-BOX
      Trigger Value = 0.0001
.FIN DAMAGE
!=================================
```

```
!========================================= REMESHING Block
.MAUTO

OBJET1
        periode = 20
        lbase = 6
FIN OBJET

.FIN MAUTO
!=========================================

!========================================= KINEMATICS Block
.CINEMAT_OUT
     Outil2              ! Ram
       maitre
       Axe = 3
     Fin Outil
.FIN CINEMAT_OUT

.PILOT
NbPass= 1
     Pass1
     Fin Pass
.FIN PILOT
!=========================================

.Histoire
     reprise: incr=14158
.Fin Histoire
```

Published Refereed Papers:

Peng, Z. and Sheppard, T. 2003. Prediction of static recrystallisation during extrusion of Aluminium Alloy AA2024. *Proceedings of 15th European Simulation Symposium (ESS2003), Delft, The Netherland.* Society for Modelling and Simulation International, 391-398.

Peng, Z. and Sheppard, T., 2004a. Individual influence of forming parameters on surface recrystallization during aluminium extrusion. *Modelling and simulation in materials science and engineering.* 12, 43-57.

Peng, Z. and Sheppard, T., 2004b. Simulation of multi-hole die extrusion. *Materials science and engineering.* A367, 329-342.

Peng, Z. and Sheppard, T., 2004c. A Study on Surface Cracking in Extrusion of Aluminium Alloy AA2014. *Materials science and technology.* 20, 1179-1191

Peng, Z. and Sheppard, T., 2004d. A Discussion on the Scaling Effect on Numerical Simulation of the Extrusion Process. *Materials science and technology.* 20, 1335-1339.

Peng, Z. and Sheppard, T., 2004e. A study on material flow in isothermal extrusion by FEM simulation. *Modelling and simulation in materials science and engineering.* 12, 745-763.

Peng, Z. and Sheppard, T. 2004f. Prediction of static recrystallisation during shape extrusion. *8th International Aluminium Extrusion Technology Seminar; May 2004 (ET04)*, The united states. Florida: Aluminium association and aluminium extruder councils, 79-92.

Peng, Z. and Sheppard, T. 2004g. Application of FEM to modelling of multi-hole die extrusion. *8th International Aluminium Extrusion Technology Seminar; May 2004 (ET04)*, The united states. Florida: Aluminium association and aluminium extruder councils, 93-106.

Peng, Z. and Sheppard, T. 2004h. Simulation of multi-hole die extrusion by Finite Element Method. *Proceedings of the 7th Esaform Conference on Material Forming ESAFORM 2004, Trondheim, Norway.* Norwegian University of Science and Technology, 605-608

Peng, Z. and Sheppard, T. 2005a. Effect of die pockets on multi-hole die extrusion. *Materials Science and Engineer A.* Received.

Peng, Z. and Sheppard, T. 2005b. Numerical simulation by FEM and Cellular Automata of static recrystallisation after hot extrusionand solution treatment of aluminium alloys. *Modelling and simulation in materials science and engineering.* In review.

Peng, Z. and Sheppard, T. 2005c. A Discussion on the Scaling Effect on Numerical Simulation of the Extrusion Process. *Materials Science and Technology. Received.*